

Probing the Alzheimer's disease risk gene PTK2B using human-derived induced neurons

Ana Raquel Melo de Farias

▶ **To cite this version:**

Ana Raquel Melo de Farias. Probing the Alzheimer's disease risk gene PTK2B using human-derived induced neurons. Neuroscience. Université de Lille; Universidade federal do Rio Grande do Norte (Natal, Brésil), 2023. English. ⟨NNT : 2023ULILS062⟩. ⟨tel-05327563⟩

HAL Id: tel-05327563

https://theses.hal.science/tel-05327563v1

Submitted on 23 Oct 2025

HAL is a multi-disciplinary open access archive for the deposit and dissemination of scientific research documents, whether they are published or not. The documents may come from teaching and research institutions in France or abroad, or from public or private research centers.

L'archive ouverte pluridisciplinaire **HAL**, est destinée au dépôt et à la diffusion de documents scientifiques de niveau recherche, publiés ou non, émanant des établissements d'enseignement et de recherche français ou étrangers, des laboratoires publics ou privés.



HAL Authorization

UNIVERSITY OF LILLE

Lille Doctoral School in Health Biology (n 446)

PhD in Molecular and Cellular Aspects of Biology

FEDERAL UNIVERSITY OF RIO GRANDE DO NORTE

Postgraduate Program in Neurosciences

PhD in Neuroscience

MELO DE FARIAS Ana Raquel

Probing the Alzheimer's disease risk gene PTK2B using human-derived induced neurons

Directed by Dr. LAMBERT Jean-Charles and Dr. COSTA Marcos

Thesis defense on October 20, 2023

JURY

GIRAULT Jean-Antoine, MD, PhD
DRCE INSERM UMR-S 1270 - Institut du Fer à Moulin, Sorbonne Université, France
Jury President

CROZET Carole, PhD
CR1/INSERM - Institute for Regenerative Medicine and Biotherapy, France
Reviewr

SVAHN LEAO Katarina, PhD
Assistant Professor - Brain Institute/Federal University of Rio Grande do Norte, Brazil
Reporter

HEDIN Cecilia, PhD
Senior Researcher - Fundação Oswaldo Cruz, Brazil
Reviewr

UNIVERSITÉ DE LILLE

Ecole Doctorale Biologie Sante de Lille (n 446)

Doctorat en Aspects Moléculaires et Cellulaires de la Biologie

UNIVERSITÉ FÉDÉRALE DE RIO GRANDE DO NORTE

Programme de Doctorat en Neurosciences

Doctorat en Neurosciences

MELO DE FARIAS Ana Raquel

Mieux comprendre le gene PTK2B, un facteur de risque de la maladie d'Alzheimer, par l'utilisation de neurones dérivés de cellules souches pluripotentes induites humaines

Dirigée par Dr. LAMBERT Jean-Charles et Dr. COSTA Marcos

Soutenue le 20 Octobre de 2023

JURY

GIRAULT Jean-Antoine, MD, PhD
DRCE INSERM UMR-S 1270 - Institut du Fer à Moulin, Sorbonne Université, France
Président du Jury

CROZET Carole, PhD
CR1/INSERM - Institute for Regenerative Medicine and Biotherapy, France
Examinatrice

SVAHN LEAO Katarina, PhD
Assistant Professor - Brain Institute/Federal University of Rio Grande do Norte, Brésil
Rapporteur

HEDIN Cecilia, PhD
Senior Researcher - Fundação Oswaldo Cruz, Brésil
Examinatrice

Abstract

Alzheimer's disease (AD) is the main type of dementia and poses a significant global public health challenge. It is characterized by a progressive decline in cognition, memory, and behavioral functions and affects more than 55 million people worldwide. At the molecular level, AD is defined by the presence of aggregated neurofibrillary tangles (NFTs) within neurons and the accumulation of amyloid-β (Aβ) plaques in the brain. These pathological features are associated with alterations in neuronal activity, synapse loss, gliosis, and neuroinflammation, leading to irreversible neurodegeneration. AD etiology and pathophysiology involves a complex interplay between genetic and environmental factors.

Genome-Wide Association Studies (GWAS) have successfully identified more than 75 genetic loci carrying single nucleotide polymorphisms (SNPs) associated with AD risk. Among these loci, the one harboring the Protein Tyrosine Kinase 2β (*PTK2B*) is highlighted in the present work. This gene encodes a protein tyrosine kinase that is involved in calcium-induced regulation of ion channels and activation of numerous signaling pathways, such as MAP kinase

Non-synonymous genetic variations in the *PTK2B* locus have been associated with an increased risk of AD and are thought to regulate PTK2B expression. However, both the physiological and pathophysiological roles of PTK2B are not fully understood. In the human brain, PTK2B expression is mainly observed in glutamatergic neurons and this expression declines during AD progression. This reduced PTK2B expression in the brain of patients with AD may contribute to neuronal dysfunctions observed in the disease, such as increased electrical excitability and synaptic alterations. Therefore, understanding the role of PTK2B in human neurons may contribute to reveal the mechanisms of neuronal dysfunctions in AD.

Considering that, the aims of this thesis are to uncover the cellular processes and molecular pathways regulated by PTK2B in human neurons. To that, we took advantage of isogenic human induced-pluripotent stem cells (hiPSCs) to generate neurons expressing different levels of PTK2B. Next, we employed functional and molecular assays to probe the consequences of altered PTK2B expression both in a physiological and in an AD-like context.

We show that reduced PTK2B expression leads to increased TAU phosphorylation at various epitopes associated with AD pathology, suggesting a central role of PTK2B in regulating TAU aggregation. Using single-cell transcriptomics, we also show that reduced PTK2B expression leads to specific transcriptional alterations related to neuronal electrical

activity and synaptic transmission mainly in glutamatergic neurons. Calcium imaging experiments indicate that PTK2B downregulation contributes to increased calcium spikes frequency without affecting synchronization, indicating an elevated neuronal electrical activity. Additionally, results from electrophysiological recordings from multi-electrode array (MEA) show increased electrical activity and disrupted bursting patterns in PTK2B mutant neurons.

Overall, this work sheds light on the involvement of PTK2B in AD-related cellular processes, providing insights into the molecular mechanisms and functional alterations associated with PTK2B dysregulation in human iPSC-derived neural cells.

Keywords: Alzheimer's Disease; genetic risk factors; PTK2B; human induced neurons;

Le résumé

La maladie d'Alzheimer

La maladie d'Alzheimer (MA) est l'une des principales causes de démence caractérisée par un déclin progressif de la cognition, de la mémoire et des fonctions comportementales. Elle se définit par la présence de *neurofibrillary tangles (NFTs)* - composés principalement de la protéine *tubulin-associated unit (TAU)* hyperphosphorylé - agrégés dans les neurones et par l'accumulation de plaques amyloïdes-β (Aβ) dans le cerveau. Ces caractéristiques pathologiques sont associées à des altérations de l'activité neuronale, à la perte de synapses, à la gliose et à la neuroinflammation, conduisant à une neurodégénérescence irréversible.

Il existe deux formes principales de la maladie d'Alzheimer : la maladie d'Alzheimer à début précoce (*EOAD*) et la maladie d'Alzheimer à début tardif (*LOAD*). L'*EOAD* est due à des mutations héréditaires, tandis que la *LOAD* est le résultat d'une interaction complexe de facteurs génétiques et environnementaux. La maladie d'Alzheimer à début précoce, qui représente environ 1 à 6 % des cas, se caractérise par l'apparition de la maladie à un âge précoce (vers 40-50 ans) et est due à des mutations héréditaires dominantes dans des gènes tels que la protéine précurseur de l'amyloïde-β (*APP*), la préséniline 1 (*PSEN1*) ou la préséniline 2 (*PSEN2)*. Ces mutations affectent le traitement de l'APP et entraînent une production accrue de peptides Aβ pathogènes, qui s'accumulent sous forme de plaques amyloïdes. Cependant, des niveaux altérés d'Aβ et des plaques sont également présents dans la *LOAD*.

La *LOAD*, également connue sous le nom de MA sporadique, est la forme la plus courante de la MA, représentant 94 à 99 % des cas. Elle se caractérise par une apparition tardive des symptômes cliniques (autour de 65 ans) et a des influences à la fois génétiques et environnementales. L'héritabilité de la *LOAD* est estimée à environ 60-80 % sur la base d'études portant sur des jumeaux monozygotes et dizygotes.

Les modèles animaux, notamment les souris et les rats génétiquement modifiés, ont joué un rôle déterminant dans l'avancement de nos connaissances sur la maladie d'Alzheimer et dans l'expérimentation de thérapies potentielles. Ces modèles impliquent souvent la modification de gènes humains associés à la maladie et peuvent développer certaines caractéristiques pathologiques clés de la MA, telles que les plaques de bêta-amyloïde et les enchevêtrements neurofibrillaires. Cependant, la plupart de ces modèles représentent les rares cas familiaux monogéniques de la maladie d'Alzheimer, qui ne représentent qu'un

faible pourcentage de l'ensemble des cas de maladie d'Alzheimer et ne reflètent peut-être pas entièrement les formes non monogéniques plus courantes de la maladie.

Bien que les modèles animaux aient fourni des informations précieuses sur les mécanismes moléculaires, les changements comportementaux et les thérapies potentielles de la maladie d'Alzheimer, il est essentiel de reconnaître leurs limites. Ils ne rendent pas pleinement compte de la complexité et de l'hétérogénéité de la MA humaine, en particulier en ce qui concerne la complexité génétique de la MA à début tardif (*LOAD*). La plupart des variantes génétiques associées à un risque accru de MA se trouvent dans des régions du génome humain sans homologie dans d'autres espèces, ce qui rend difficile la reproduction complète de ces variantes dans des modèles animaux.

Pour surmonter ces limitations, les cellules souches pluripotentes induites (*iPSC*) sont devenues un outil puissant pour générer des neurones induits (*iNs*) par l'homme qui peuvent modéliser la maladie à l'aide de neurones dérivés directement de patients ayant des antécédents génétiques divers. Ces *iNs* dérivés de patients présentent souvent des caractéristiques spécifiques à la maladie d'Alzheimer, telles que des niveaux accrus de sécrétion de bêta-amyloïde et l'accumulation d'enchevêtrements neurofibrillaires. Ils constituent une ressource précieuse pour l'étude de la pathogenèse de la maladie d'Alzheimer et peuvent être utilisés pour la mise au point de traitements spécifiques aux patients.

Le *GWAS* comme outil efficace pour la détection des facteurs de risque génétiques de la maladie d'Alzheimer

Les études d'association pangénomique (en anglais *Genome-Wide Association Study*, *GWAS*) ont permis d'identifier les facteurs de risque génétiques de la maladie d'Alzheimer, en particulier pour la forme tardive (*LOAD*). Les études à l'échelle du génome analysent la fréquence des polymorphismes d'un seul nucléotide (*SNP*) dans le génome et leur association avec les phénotypes de la maladie d'Alzheimer. Ces études ont permis d'identifier de nombreux *loci* génétiques associés au risque de MA, dont plus de 70 variantes génomiques.

La plupart des variantes génétiques associées à la MA identifiées par les études d'association pangénomique sont situées dans des régions non codantes du génome, ce qui peut affecter l'expression de plusieurs gènes. Il est essentiel de comprendre les effets fonctionnels de ces variantes, leur impact sur l'expression des gènes et les processus biologiques régulés par leurs gènes cibles pour comprendre la pathogenèse de la maladie

d'Alzheimer. Parmi les régions génétiques présentant des signaux forts, les *loci* Bridging Integrator 1 (*BIN1)* et Protein Tyrosine Kinase 2β *(PTK2B)* sont mis en évidence.

Le locus *BIN1* est le deuxième facteur de risque génétique le plus important pour la *LOAD*. Des variations au sein du locus *BIN1* ont été associées à un risque accru de maladie d'Alzheimer. Différentes isoformes du gène *BIN1* sont exprimées dans divers tissus et types de cellules, l'isoforme 1 étant principalement exprimée dans les neurones. Une régulation altérée des isoformes de BIN1 a été observée chez les patients atteints de la maladie d'Alzheimer, et une expression réduite de BIN1 est associée aux stades élevés de Braak de la pathologie de la maladie d'Alzheimer. BIN1 joue un rôle dans l'endocytose, les processus de trafic, la modulation de la réponse immunitaire, l'homéostasie calcique et l'apoptose. Les modifications de l'expression de BIN1 et de la régulation des isoformes peuvent perturber l'activité neuronale et l'homéostasie calcique, ce qui pourrait contribuer à la pathogenèse de la maladie d'Alzheimer.

Le gène *PTK2B*, qui code pour la protéine PTK2B (également dénommé Pyk2), est un autre facteur de risque génétique de la maladie d'Alzheimer identifié par l'étude GWAS. Des variations dans le locus *PTK2B*, y compris des SNP spécifiques, ont été associées à un risque accru de maladie d'Alzheimer. La PTK2B est impliquée dans la réponse inflammatoire, la prolifération et la survie cellulaire. Dans le cerveau humain, l'expression de la PTK2B est enrichie dans les neurones glutamatergiques et diminuée chez les patients atteints de la maladie d'Alzheimer. La régulation à la baisse de la PTK2B dans la MA peut contribuer aux dysfonctionnements neuronaux observés dans la maladie, tels que l'augmentation de l'excitabilité électrique et les altérations synaptiques. Le rôle de la PTK2B dans l'hyper activation neuronale, une caractéristique de la MA, en fait une cible intrigante pour la poursuite des recherches. Cependant, des études sont encore nécessaires pour étudier le rôle de la réduction de la PTK2B dans la maladie d'Alzheimer. Cela est particulièrement vrai pour les modèles neuronaux humains, pour lesquels il existe très peu d'études à ce jour.

Dans l'ensemble, *BIN1* et *PTK2B* représentent des cibles prometteuses pour comprendre la pathogenèse de la maladie d'Alzheimer et développer des interventions thérapeutiques potentielles. Bien qu'une partie de ce doctorat ait également été consacrée à l'étude du rôle de *BIN1* en tant que gène de risque de la maladie d'Alzheimer (ce qui a donné lieu à deux publications - (1) et (2)), l'étude de la modulation de *PTK2B* dans un modèle humain in vitro et sa possible contribution à la pathologie de la maladie d'Alzheimer constituent l'objectif principal de cette thèse et seront discutées en profondeur dans les sections suivantes.

PTK2B en tant que facteur de risque génétique de la maladie d'Alzheimer

Le gène *PTK2B*, situé sur le chromosome 8q21.2, produit de multiples variantes de transcription par épissage alternatif. Il donne naissance à une protéine pleine longueur et à deux isoformes : une isoforme hématopoïétique appelée Pyk2-H, et PRNK, une isoforme courte.

La PTK2B pleine longueur est fortement exprimée dans le système nerveux central, en particulier dans les neurones glutamatergiques de l'hippocampe et du cortex cérébral. Elle est également présente dans d'autres régions du cerveau. Dans les modèles murins, la PTK2B est présente en faible quantité dans les astrocytes, contribuant à la mobilité cellulaire après une lésion cérébrale.

La protéine PTK2B pleine longueur est une tyrosine kinase non réceptrice composée de 1009 acides aminés. Elle se compose d'un domaine FERM N-terminal, d'un domaine kinase central et d'un domaine FAT C-terminal. Ces domaines interagissent pour former une structure auto-inhibée. D'autres régions de la protéine comprennent le linker kinase-graisse (*KFL*), des motifs riches en proline, un élément de liaison à la calmoduline et des séquences impliquées dans le trafic intracellulaire. En résumé, la protéine PTK2B présente divers profils d'expression et possède une structure protéique complexe avec des domaines fonctionnels. Elle joue un rôle dans la signalisation des cellules immunitaires, les fonctions cérébrales et les processus cellulaires.

En tant que une protéine intracellulaire non directement réceptrice, PTK2B subit une régulation importante par le biais d'événements de phosphorylation. La phosphorylation des résidus tyrosine, en particulier Tyr402, joue un rôle crucial dans son activation et son interaction avec d'autres protéines impliquées dans l'adhésion cellulaire, la signalisation en aval et le recrutement des protéines d'échafaudage. D'autres résidus tyrosine, tels que Tyr579, Tyr580 et Tyr881, peuvent également être phosphorylés par les membres de la famille des kinases Src, ce qui renforce encore la signalisation de la PTK2B.

La phosphorylation d'autres résidus, tels que Ser778, influence la localisation de la PTK2B. La phosphorylation de Ser778 régule le motif d'exportation nucléaire, conduisant à l'accumulation nucléaire de PTK2B. La déphosphorylation et d'autres modifications post-traductionnelles, y compris l'ubiquitination, affectent la stabilité, le renouvellement et la localisation intracellulaire de la PTK2B.

Dans le système nerveux central, PTK2B est principalement exprimée dans les neurones glutamatergiques dans le compartiment cytoplasmique, mais cette protéine présente des schémas de localisation subcellulaire dynamiques. Elle peut être enrichie dans la densité

post synaptique (*PSD*) et dans le noyau. Lors de la dépolarisation neuronale, la PTK2B se déplace vers le noyau, favorisant potentiellement la survie cellulaire et régulant l'expression des gènes en interagissant avec des facteurs de transcription et d'autres protéines. Elle est également enrichie au niveau des synapses excitatrices, s'associant au *PSD-95* et aux récepteurs *NMDA*, contribuant ainsi à la signalisation et à la plasticité synaptiques. La PTK2B est également présente dans les épines dendritiques, les cônes de croissance axonale et les corps cellulaires neuronaux.

En résumé, les modifications post-traductionnelles, en particulier la phosphorylation, jouent un rôle crucial dans la régulation de l'activité, de la localisation et de la signalisation en aval de la PTK2B. Sa localisation varie entre le cytoplasme, le noyau et les sites post synaptiques, ce qui suggère des fonctions diverses dans les cellules neuronales.

Dans le contexte de la maladie d'Alzheimer, la PTK2B est impliquée et joue un rôle central dans le dysfonctionnement synaptique lié à la maladie d'Alzheimer. Dans les modèles murins de la maladie d'Alzheimer, la délétion de PTK2B résout la perte synaptique et les déficits de mémoire, tandis que la surexpression de PTK2B réduit la perte synaptique mais augmente la formation de plaques d'Aβ. Dans des modèles de rongeurs, PTK2B protège les neurones de la toxicité synaptique médiée par l'Aβ et participe à l'activation par l'Aβ des cellules microgliales, les macrophages résidents du système nerveux central (SNC). L'activation de la PTK2B entraîne des effets en aval, notamment une excitotoxicité neuronale, par hyperactivation médiée par le neurotransmisseur glutamate, provoquent une entrée massive des niveaux calcium dans la cellule.

Également, PTK2B est associée à la sclérose de l'hippocampe, à la détérioration cognitive et à la progression de la maladie d'Alzheimer. La protéine est impliqué dans l'activation GSK3β médiée par PRKCD et dans l'hyperphosphorylation de TAU. Dans ce cadre, les niveaux endogènes de PTK2B suppriment la phosphorylation de TAU et l'inhibition de PTK2B augmente la phosphorylation de TAU à Ser202/Thr205, un site de phosphorylation important lié à la pathologie de l'Alzheimer. De plus, la protéine PTK2B s'associe physiquement à la TAU et est colocalisée avec la TAU hyperphosphorylée et oligomérique dans les modèles de la maladie. Ainsi, la PTK2B s'avère être un candidat important dans la physiopathologie de l’Alzheimer, bien que sa contribution spécifique aux neurones humains soit peu connue dans ce contexte.

Objectives

Ces données soulignent l'importance de PTK2B dans la modulation des kinases TAU en aval et suggèrent que les voies de signalisation médiées par PTK2B pourraient être des cibles thérapeutiques potentielles pour réduire la pathologie TAU et la toxicité induite par l'Aβ dans la MA. Cependant, des recherches supplémentaires sont nécessaires pour comprendre pleinement ces mécanismes et leurs contributions à la maladie.

C'est pourquoi cette thèse vise à découvrir les processus cellulaires et les voies moléculaires affectés par la PTK2B dans les neurones humains induits (hiNs), à la fois dans la physiologie normale et dans le contexte de la maladie d'Alzheimer.

Les objectifs spécifiques sont les suivants :

I. Générer et caractériser des cultures 2D et 3D exprimant différents niveaux de PTK2B.
II. Examiner l'impact de la délétion de la PTK2B sur les processus clés liés à la maladie d'Alzheimer, tels que les plaques amyloïdes et l'hyper phosphorylation de la TAU.
III. Étudier les voies moléculaires potentielles affectées par la diminution des niveaux de PTK2B dans les neurones et les cellules gliales induits en 2D et en 3D.
IV. Évaluer le rôle de la signalisation PTK2B dans la régulation de l'activité électrique neuronale et son implication potentielle dans les effets médiés par l'Aβ.

Principaux résultats

En abordant ces objectifs, l'étude vise à découvrir les processus cellulaires et les voies moléculaires affectés par la PTK2B dans les neurones humains, à la fois dans la physiologie normale et dans le contexte de la maladie d'Alzheimer.

L'étude révèle qu'une réduction de l'expression de la PTK2B entraîne une augmentation de la phosphorylation de la TAU au niveau de divers épitopes, alors que la production et le métabolisme de la protéine APP ne sont pas affectés, suggérant un rôle spécifique de la PTK2B dans la régulation de la pathologie de l'UAT. En outre, l'analyse des cultures 2D et des organoïdes cérébraux mutants PTK2B met en évidence des altérations transcriptionnelles liées à l'activité électrique neuronale et à la transmission synaptique. Les expériences d'imagerie calcique indiquent que la régulation négative de PTK2B contribue à augmenter la fréquence des pics de calcium sans affecter la synchronisation, ce qui indique une activité électrique neuronale élevée, également observée chez les patients aux premiers stades de la maladie. En outre, les résultats des enregistrements électrophysiologiques

effectués à partir de réseaux multi-électrodes (*MEA*) montrent une activité électrique accrue et des schémas d'éclatement perturbés dans les neurones mutants PTK2B. L'étude explore également le potentiel de sauvetage des effets observés en supprimant l'expression de TAU sur l'activité électrique neuronale, établissant un lien potentiel entre les niveaux de PTK2B, la TAU et l'activité électrique.

Dans l'ensemble, ces travaux mettent en lumière l'implication de la PTK2B dans les processus cellulaires liés à la maladie d'Alzheimer, en donnant un aperçu des mécanismes moléculaires et des altérations fonctionnelles associés à la dysrégulation de la PTK2B dans les cellules neuronales humaines dérivées de l'*iPSC*.

Conclusion

Compte tenu des données examinées, nous pouvons conclure que la PTK2B joue un rôle important dans la maladie d'Alzheimer et qu'elle est impliquée dans divers processus cellulaires et voies moléculaires liés à la maladie. L'expression réduite de PTK2B a été associée à une phosphorylation accrue de TAU, une caractéristique de la pathologie de la MA. Également, nos données corroborent des résultats antérieurs obtenus dans d'autres modèles et soulignent l'importance de PTK2B dans la régulation de l'activité électrique neuronale et de la transmission synaptique. Ces résultats contribuent à notre compréhension des mécanismes sous-jacents à la MA et soulignent le potentiel de la PTK2B en tant que cible thérapeutique pour moduler la pathologie de la TAU et la toxicité induite par l'Aβ dans la MA.

Mots-Clés: Maladie d'Alzheimer ; facteurs de risque génétiques ; PTK2B ; neurones humains ;

Contents

Abstract **4**

Le résumé 6

Contents 13

List of Figures 17

List of Tables 20

Abbreviations list 21

Acknowledgements to Funding Agencies 28

Acknowledgements 29

Laboratories 30

Introduction **31**

Chapter I: Alzheimer's Disease – an overview **32**

1. Diagnosis of Alzheimer's Disease 32
2. Types of Alzheimer's Disease 32
3. Pathological hallmarks of Alzheimer's disease 33
4. From animal to human cell models in Alzheimer's Disease 40
5. Pathophysiological mechanisms of AD 42
6. The recent identification of AD genetic risk factors 44

Chapter II: PTK2B – a Late-Onset Alzheimer's Disease Risk Gene **48**

1. PTK2B expression and structure 48
2. PTK2B signaling pathway 51
3. Functions of PTK2B protein 53
4. PTK2B in Alzheimer's Disease 57

Objectives **59**

1. General aims 59
2. Specific aims 59

Materials and Methods **60**

1. Maintenance of hiPSCs and neural induction 61
2. Differentiation of hiNPCs into mixed cultures of hiNs and hiAs 62
3. Generation of human cerebral organoids 62
4. hiPSCs genetic analyses 63
5. Generation of pure human neuronal cultures from hiNPCs 63
6. Culture of hiNs in Microfluidic Devices 64
7. Immunocytochemistry and immunohistochemistry 65
8. Immunobloting 67
9. Proteome Profiler Array (Phopho panel) 69
10. Viral Transductions 70
11. snRNA-sequencing Library Preparation 71
12. snRNA-seq Dataset Preprocessing 72
13. snRNA-seq datasets integration and annotation 72
14. Differential gene expression and GO enrichment analyses 72
15. Activity-related genes (ARGs) signature enrichment analysis at single cell resolution 73
16. AlphaLISA measurements 73
17. Exposure to $A\beta_{1-42}$ treatment 73
18. Calcium Imaging Experiments 74
19. Analyses of Calcium Transients 74
20. MEA recordings in 2D cultures 75
21. Spike sorting and temporal structure of spontaneous activity 75
22. Statistical Analysis 76

Results 77

1. Characterization of PTK2B hiPSC lines 78
   1.1. ASE 9109 iPSC line 78
   1.2. BION iPSC line 80
2. Generation and characterization of Spontaneous Differentiated 2D cultures under-expressing PTK2B 80

2.1. PTK2B WT, HET and KO hiNPCs readily generate hiNs/hiAs cultures 81
3. Generation and characterization of PTK2B WT, HET and KO cerebral organoids (3D) 85
4. Study of AD biochemical phenotypes in hiPSC-derived neural cells 88
5. Molecular screening of possible targets affected by the under-expression of PTK2B 90
6. Gene expression profiles of *PTK2B* WT, HET and KO neural cells 95
6.1. PTK2B under expression leads to gene expression alterations specifically in glutamatergic neurons 95
6.2. STAT3 may act as a potential key regulator in PTK2B cell lines at both transcriptional and protein levels 97
7. PTK2B signaling in the regulation of neuronal electrical activity 99
7.1. hiNs expressing reduced levels of PTK2B show altered patterns of calcium flux 99
7.2. PTK2B reduced expression correlates with increased single unity electrical properties on MEA system 102
7.3. Altered expression of activity-related genes in PTK2B cerebral organoids 105
7.4. PTK2B-mediated increased neuronal electrical activity depends on TAU 106
8. PTK2B signaling in the regulation of neuronal electrical activity and the Aβ-mediated effects 108
8.1. PTK2B expression decreases along AD Braak stages 108
8.2. PTK2B expression affects neuronal hyperexcitability mediated by $A\beta_{1-42}$ 109
8.3. $A\beta_{1-42}$ affects PTK2B-related molecular pathways at the protein level 112
9. Possible role of PTK2B in neural development 114
10. Cell-autonomous roles of PTK2B in human-induced glutamatergic neurons 118
Discussion 122
1. Role of PTK2B on TAU hyperphosphorylation 123
2. Role of PTK2B in spontaneous neuronal electrical activity 125
3. Molecular pathways altered by reduced PTK2B expression 127
4. A novel activity-dependent transcription pathway in glutamatergic neurons 129
5. Possible role of PTK2B on neuronal and astroglial differentiation 130

6. Is PTK2B the missing link between Aβ, Tauopathy and alterations in neuronal electrical activity observed in AD? 131

Conclusion 134

Appendix 136

Article I 137

1. Differential transcript usage unreveals gene expression alterations in AD human brains 137

1.1. Context and objectives 137

1.2. Personal contributions to the work 137

Article II 153

2. The Alzheimer susceptibility gene BIN1 induces isoform-dependent neurotoxicity through early endosome defects 153

2.1. Context and objectives 153

2.2. Personal contributions to the work 153

Article III 177

3. Alzheimer's disease risk gene BIN1 modulates neural network activity through the regulation of L-type calcium channel expression in human induced neurons 177

3.1. Context and objectives 177

3.2. Personal contributions to the work 177

Article IV 252

4. Amyloid-beta peptides trigger premature functional and gene expression alterations in human-induced neurons 252

4.1 Context and objectives 252

4.2 Personal contributions to the work 253

Bibliography 284

List of Figures

Figure 1. APP processing in physiological conditions and in Alzheimer's Disease.

Figure 2. Abnormal phosphorylated TAU in the pathology of Alzheimer's Disease.

Figure 3. Genetic risk factors for Alzheimer's Disease identified by GWAS.

Figure 4. Scheme on PTK2B full-length protein structure.

Figure 5. Scheme on PTK2B-associated intracellular molecular pathways.

Figure 6. Generation of PTK2B knockout hiPSC lines.

Figure 7. Generation of 2D spontaneously differentiated cultures.

Figure 8. Characterization of ASE 9109–derived hiNPCs and differentiated neural cultures in 2D.

Figure 9: Modulation of PTK2B expression generates similar cultures composition at 5 weeks.

Figure 10: Characterization of BION–derived hiNPCs and differentiated neural cultures in 2D.

Figure 11: Protocol diagram for generation of cerebral organoids from hiPSCs.

Figure 12: Characterization of PTK2B WT, HET, and KO cerebral organoids.

Figure 13: Cerebral organoids exhibit different cellular proportions when modulating PTK2B levels.

Figure 14: PTK2B effects on AD molecular hallmarks on 6 months cerebral organoids.

Figure 15: Reduced PTK2B expression increases total TAU and TAU phosphorylation at different residues in 5-weeks-old human-induced neurons.

Figure 16: PTK2B reduced expression tends to increase TAU phosphorylation in a second cell line (BION-derived cells).

Figure 17: Molecular screening of potential targets of PTk2B modulation.

Figure 18: Analysis of GSK3B and SRC as potential targets of PTk2B modulation.

Figure 19: Investigation of TAU kinases affected by PTk2B expression levels.

Figure 20: mRNA expression of genes encoding for TAU different kinases in cerebral organoids.

Figure 21: I PTK2B under expression leads to gene expression alterations specifically in glutamatergic neurons in 2D cultures.

Figure 22: PTK2B deletion in cerebral organoids leads to gene expression alterations related to synaptic function in glutamatergic neurons.

Figure 23: DEGs in PTK2B HET and KO cerebral organoids are possibly main regulated by STAT3.

Figure 24: PTK2B diminished expression leads to alterations in the phosphorylation of STAT3 at its primary regulatory epitopes at the protein level.

Figure 25: Reduced PTK2B levels correlates with altered neuronal Ca^{2+} transients.

Figure 26: Reduced expression of PTK2B correlates with increased single unity activity.

Figure 27: PTK2B reduced expression and the presence of an AD-related variant impair unity activity properties in a second cell line.

Figure 28: mRNA electrical signature of *PTK2B*-mutated cerebral organoids.

Figure 29: TAU expression correlates with increased neuronal electrical activity in PTK2B HET neurons.

Figure 30: PTK3B expression in the human brain and along AD Braak stages.

Figure 31: The level of PTK2B expression exerts a significant influence on the immediate effects of $A\beta_{1-42}$ exposure on neuronal Ca^{2+} transients.

Figure 32: Acute Aβ1-42 exposition potentially affects PTK2B levels in WT neural cultures.

Figure 33: Acute exposure to Aβ1-42 has the potential to affect the activation of pathways downstream of PTK2B.

Figure 34: Different levels of PTK2B expression influences neural fate after 1 week of differentiation.

Figure 35: Different levels of PTK2B expression influences neural fate after 3 weeks of differentiation.

Figure 36: Different levels of PTK2B expression influences neural fate after 5 weeks of differentiation.

Figure 37: Absence of PTK2B progressively increases the electrical activity of Ngn2-hiNs, reaching the peak at 4 weeks.

Figure 38: Reduced PTK2B expression possibly affects TAU aggregation and neuronal localization in NGN2-hiNs.

Figure 39: PTK2B signaling pathway and the primary molecular insights from its manipulation hiPSC-derives neural cells.

Figure 40: Possible regulation of PTK2B in neurons of healthy individuals and those with Alzheimer's disease.

List of Tables

Table 1: List of PTK2B hiPS cell lines

Table 2: List of primary antibodies used on immunostaining

Table 3: List of secondary antibodies used on immunostaining

Table 4: List of primary antibodies used on immunoblotting

Table 5: List of secondary antibodies used on immunoblotting

Table 6: List of antibodies used on the Proteome Profiler Array

Abbreviations list

Abbreviation	Meaning
2D	Two dimensions
3D	Three dimensions
3R	3-repeat
4R	4-repeat
AD	Alzheimer's disease
AGS	Astrocyte growth supplement
AKT	AKT Serine/Threonine Kinase 1
AM	Acetoxymethyl
APOE	Apolipoprotein E
APP	Amyloid precursor protein
ARGs	Activity-related genes
ASDR	Array-wide spike detection rate
ASO	Antisense oligonucleotides
Astro-I	Immature astrocytes
Astro-II	Mature astrocytes
AT8	Monoclonal antibody anti-phospho-TAU (S202/T205)
Aβ	Amyloid-beta
AβOs	Amyloid-beta oligomers
BCR	B cell receptor
BIC	Bicuculline
BIN1	Bridging integrator 1
BP	BrainPhys
AAV	Adeno-associated virus
CACNA1A	Calcium voltage-gated channel subunit alpha1 A
CACNA1B	Calcium voltage-gated channel subunit alpha1 B
CACNA1C	Calcium voltage-gated channel subunit alpha1 C
CACNA1D	Calcium voltage-gated channel subunit alpha1 D
CACNA1E	Calcium voltage-gated channel subunit alpha1 E
CADM	Stimulated cadmium

Abbreviation	Meaning
CALIMA	CALciumIMagingAnalyzer
CaM	Calmodulin
CaMKII	Ca2+/calmodulin-dependent protein kinase-II
CCND2	cyclin D2
CDK6	cyclin dependent kinase 6
CHO	Chinese hamster ovary
CHO-APPV717L	CHO line expressing London mutated APP695
CHO-APPWT	CHO line overexpressing the human APP695
CHRNA7	Acetylcholine receptor subunit alpha-7
CLAP	Clathrin and AP-2-Binding
CLIC6	Chloride Intracellular Channel 6
CLR	Centered log-ratio
CNQX	Cyanquixaline
CNS	Central Nervous System
COs	Cerebral organoids
CRAN	Comprehensive R Archive Network
CREB	cAMP-response element binding protein
CRISPR	Clustered regularly interspaced short palindromic repeats
CSF	Cerebral spinal liquid
CTF-α	C-terminal fragment α
CTF-β	C-terminal fragment β
DCX	Doublecortin
DEGs	Differentially expressed genes
DLX1	Distal-Less Homeobox 1
DMSO	Dimethyl sulfoxide
DNA	Deoxyribonucleic acid
DPBS	Deionized Phosphate Buffer Saline
dPRGs	Delayed primary response genes
EB	Embryoid Body
EC	Entorhinal cortex
ECM	Extracellular matrix
EEA1	Early endosome antigen 1
EEG	Electroencephalography

Abbreviation	Meaning
EGF	Epidermal growth factor
EMX2	Empty Spiracles Homeobox 2
EOAD	Early-Onset Alzheimer's disease
EPHA	Ephrin-A
ERDF	European Regional Development Fund
ERGs	Early response genes
ERK 1/2	Extracellular signal-regulated kinase 1/2
FAD	Familial Alzheimer's disease
FAK	Focal adhesion kinase
FAT	Focal adhesion targeting
FGSEA	Fast gene set enrichment analysis
fMRI	Functional magnetic resonance imaging
FN1	Fibronectin
Fps	Frames per second
fMRI	Functional magnetic resonance imaging
FYN	Tyrosine-protein kinase Fyn
GABANeu	GABAergic neuron
GAD2	glutamate decarboxylase 2
GFAP	Glial fibrillary acidic protein
GFP	Green fluorescent protein
GLAST	Glutamate/aspartate transporter
GluNeu-I	Glutamatergic neuron
GluNeu-II	Glutamatergic neuron
GO	Gene ontology
GRIN1	Glutamate Ionotropic Receptor NMDA Type Subunit 1
GRM5	Glutamate Metabotropic Receptor 5
GSEA	Gene set enrichment analysis
GWAS	Genome-Wide Association Studies
HES6	HES family bHLH transcription factor 6
HET	Heterozygous
HFS	High frequency stimulation
hiAs	Human induced astrocytes
hiNPCs	Human induced neural progenitor cells

Abbreviation	Meaning
hiNs	Human induced pluripotent stem cells derived neurons
hiPSCs	Human induced pluripotent stem cells
HIST1H2BN	Histone H2B type 1-N
hSYN	Human synapsin
hTAU-C	C-terminal region of human TAU
HTO	Hash Tag Oligonucleotide
Hz	Hertz
ICP	Inverted Control Peptide
iPSCs	Induced pluripotent stem cells
ITGA8	Integrin subunit alpha 8
KFL	Kinase-fat linker
KO	Knockout
L-VGCC	L-type voltage-gated calcium channel
LDP	Long-term depression
LHX1	LIM Homeobox 1
LHX9	LIM Homeobox 9
LKB1	Liver kinase B1
LOAD	Late-onset Alzheimer's disease
LRGs	Late response genes
LRP1	LDL receptor related protein 1
LRRFIP1	LRR Binding FLII Interacting Protein 1
LTP	Long-term potentiation
LVGCC	L-type voltage-gated calcium channels
MAPK	Mitogen-activated protein kinase
MAPT	Microtubule-associated protein tau gene
MBD2	Methyl-CpGbinding domain protein-2
MEA	Multi electrode array
MF	Molecular function
MOI	Multiplicity of infection
MPK1	Mitogen-activated protein kinase 1
MPK3	Mitogen-activated protein kinase 3
MPZ	Myelin protein zero
MTB	Microtubule binding domain

Abbreviation	Meaning
MUA	Multi-unit activity
NES	Nuclear exporting sequence
NFTs	Neurofibrillary tangles
NGN2	Neurogenin2
NHEJ	Nonhomologous end joining
NIF	Nifedipine
NIM	Neural induction medium
NLS	Nuclear localization sequence
NMDA	N-methyl-D-aspartate
NMDAR	N-methyl-D-aspartate receptor
NO	Nitric oxide
NPCs	Neural progenitor cells
NPM	Neural progenitor medium
NRG	Neuregulin
NR2F1	Nuclear Receptor Subfamily 2 Group F Member 1
NTS	Nuclear targeting sequence
OGB-1	Oregon green™ 488 BAPTA-1
PCA	Principal component analysis
PET	Positron emission tomography
PFA	Paraformaldehyde
PHF-1	Monoclonal antibody PHF-1 against TAU
PI3K	Phosphatidylinositol 3-kinase
PKC	Protein kinase C
PLA	Proximity ligation assay
PLO	Poly-L-ornithine
PRNK	Pyk2-related non-kinase
PrP/PRNP	Prion Protein
PS1	Presenilin 1
PS2	Presenilin 2
PSD	Postsynaptic density
PSD-95	Postsynaptic density protein 95
PSEN1	Presenilin 1
PSEN2	Presenilin 2

Abbreviation	Meaning
PTK2B	Protein Tyrosine Kinase-2-beta
Pyk2-H	Pyk2 hematopoietic-specific isoform
RAC1	Rac family small GTPase 1
RhoA	Ras homolog family member A
RID-AGE	Risk Factors and Molecular Determinants of Aging-related Diseases
RNA	Ribonucleic acid
ROIs	Regions of interest
RPKM	Reads per kilobase per million
rPRGs	Rapid primary response genes
rtTA	Reverse tetracycline-controlled transactivator
SAD	Sporadic Alzheimer's disease
sAPPα	Secreted APP ectodomain α
SCENIC	Single-cell rEgulatory network inference and clustering
scRNA-seq	Single-cell RNA-sequencing
SD	Standard deviation
SEMA5	Semaphorin
SFG	Superior frontal gyrus
SFKs	Src family kinase
SH3	Src homology 3 domain
SLC1A3	Solute Carrier Family 1 Member 3
SLC17A6	Solute Carrier Family 17 Member 6
SLC17A7	Solute Carrier Family 17 Member 7
SMADi	SMAD-inhibition
SNAP25	Synaptosome Associated Protein 25
SNPs	Single Nucleotide Polymorphisms
snRNA-seq	Single-nucleus RNA-Sequencing
SPN	Synaptophysin
SRC	Proto-oncogene tyrosine-protein kinase Src
SRGs	Secondary response genes
STAT3	Signal Transducer and Activator of Transcription 3
STDP	Spike-timing-dependent plasticity
STEP	Striatal-enriched phosphatase
STK11	Serine/threonine kinase 11

Abbreviation	Meaning
SUA	Single unit activity
SYN	Synapsin
SYP	Synaptophysin-1
TAU	Tubulin-associated unit
TBS	Theta-burst stimulation
TBST	Tris Buffered Saline Buffer with Tween 20
TCR	T-cell receptor
TF	Transcription factor
TNC	Tenascin C
TWAS	Transcriptome-wide association study
Tyr402	Tyrosine 402
UMI	Unique Molecular Index
UnspNeu	Immature/unspecified neuron
VGCCs	Voltage-gated calcium channels
VGLUT1	Vesicular glutamate transporter 1
vGLUT2	Vesicular glutamate transporter 2
VST	Variance stabilizing transformation
WGS	Whole-Genome Sequencing
WT	Wild-type

Acknowledgements to Funding Agencies

This thesis was fulfilled in France with the support of fundings from the Haut de France Region, Institut Pasteur de Lille, European Union under the European Regional Development Fund (ERDF), the Hauts de France Regional Council (contract no.18006176), the MEL (contract_18006176), the French State (contract no. 2018-3-CTRL_IPL_Phase2), and the Alzheimer's Association Research Grant (AARG-22-972968). In Brazil, the thesis was accomplished with the financial support of the government agencies CNPQ and CAPES.

Acknowledgements

When I came to France to do my Ph.D., I did not know what to expect or who I would be sharing this journey with. But the child version of me was somehow alive, excited about doing science and discovering the world at the same time. Today, I look back with a sense of gratitude that goes beyond the translation of words.

I am grateful to have had Marcos Costa as my advisor in the past nine years, since my undergraduate internship until my doctoral studies. Thank you for letting me learn from your scientific and human examples, from your empathy and from your respect. Your constant curiosity shows me each year that incredible things lie beyond what is obvious and comfortable.

Thank you to my co-supervisor and laboratory director Jean-Charles Lambert. Thank you for the opportunities you gave me in your esteemed laboratory and outside of it, at so many scientific events. Thank you for your empathetic view, beyond the “bonjours” in the corridors.

To my family, thank you for who I am. I know it was brave of you to raise me to fly so far and I will be eternally grateful for that! Daughters with wings were born from parents who could not run. Obrigada!

My dear friends and partners along the way, thank you for allowing me to escape the chaos of a Ph.D. from time to time. You made this road possible and meaningful. I also document here my eternal “saudades” to my friends and colleagues at the Brain Institute in Brazil, especially the former members of Neurocell. You taught me much about the scientist I have become.

To my colleagues at the Pasteur Institute of Lille, I would like to thank you for the moments we shared, for your patience and for your kind efforts to understand the words of a newcomer who barely knew how to say “bonjour” at the beginning. Thank you for so much learning, conversations and beers we shared after hard and good days of work.

To conclude, thank you to the women who came before me, in science and beyond. They have opened invisible doors so that I could graduate today with a double Ph.D. degree.

Laboratories

France

Risk factors and molecular determinants of aging-related disease (RID-AGE)
INSERM U1167 – Institut Pasteur de Lille

Univ. Lille, Inserm, CHU Lille, Institut Pasteur Lille, U1167 - RID-AGE - Facteurs de risque et déterminants moléculaires des maladies liées au vieillissement, F-59000 Lille, France

1 rue du Professeur Calmette, 59000

Campus Institut Pasteur de Lille – Lille, France

Brazil

Laboratory of Cellular Neurobiology (Neurocell)

Brain Institute – Federal University of Rio Grande do Norte

Av. Senador Salgado Filho, 3000
Campus Universitário, Lagoa Nova - Natal / RN, Brazil
59078-970

Introduction

Alzheimer's disease (AD) is the leading cause of dementia worldwide. The disease was firstly described by Alois Alzheimer in the early 1900s as "a peculiar severe disease process of the cerebral cortex" at the 37th Meeting of South-West German Psychiatrists ((3) and (4)). Currently, AD is seen as a complex and heterogeneous neurodegenerative condition, clinically characterized by a progressive decline in cognition, memory, and behavioral functions. At the pathological level, the disease particularly differs from other types of dementia by the presence of both aggregated neurofibrillary tangles (NFTs) inside the neurons and the accumulation of amyloid-β (Aβ) plaques extracellularly in the brain ((5) and (6)). These biochemical hallmarks are associated with alterations in neuronal electrical activity, synapse loss, gliosis and neuroinflammation that, combined, lead to an irreversible neurodegeneration in the brain (7).

1. Diagnosis of Alzheimer's Disease

The prediction of Alzheimer's diagnosis is based on the merge of the patient's clinical history, the detection of biomarkers in the cerebrospinal liquid (CSF), and the analysis of Positron emission tomography (PET) scan imaging. The confirmation, however, is only possible through the post-mortem examination of the brain to attest the presence of NFTs and Aβ plaques, which makes it difficult to render an accurate diagnostic of AD-related dementia. Moreover, it is estimated that 75% of people living with dementia have not received a formal diagnosis, directly affecting the efficiency of treatments. On top of that, with the demographic transition towards aged populations observed in most countries, the prevalence of dementia has been strongly impacted in the past decades. According to the Alzheimer's Disease International Organization (98), over 55 million people were living with dementia in 2020 all over the world and this number is expected to nearly double every 20 years (99). This increasing incidence of AD, together with the lack of effective treatment to date, justifies the urgent need to better understand the pathophysiological mechanisms of this devastating disease.

2. Types of Alzheimer's Disease

Two main forms of AD have been described: the Early-Onset (EOAD), also known as Familial AD (FAD); and the Late-Onset AD (LOAD). EOAD is hereditary and characterized

by disease symptoms appearing at early ages (around 40 to 50 years). In turn, LOAD is a multifactorial condition influenced by genetics and environmental factors, with clinical onset at later ages (> 65 years).

2.1. Early-Onset Alzheimer's Disease

In the minority of the cases - about 1 – 6 % (8), AD is driven by dominant inherited mutations in the genes encoding for the Amyloid-β Precursor Protein (*APP*), Presenilin 1 (*PSEN1*) or Presenilin 2 (*PSEN2*) ((9) and (10)). These mutations lead to an increased processing of APP towards the production of pathogenic Aβ peptides, which are insoluble and accumulate extracellularly into the so-called amyloid plaques. The symptoms of EOAD are like those of late-onset Alzheimer's and include memory loss, confusion, difficulty with problem-solving and decision-making, changes in behavior and personality, and problems with language. Diagnosis involves a comprehensive assessment of medical history, cognitive function, neurological exams, and imaging tests – e.g. magnetic resonance imaging (MRI) – to rule out other conditions.

2.2. Late-Onset Alzheimer's Disease

The LOAD form is named late-onset in view of the later onset of clinical symptoms, above the age of 65 years. Its prevalence increases with age, with the highest rates observed in individuals over 85-years-old. Also called sporadic AD (SAD) due to its heritance, the LOAD constitutes most of the AD cases (94-99 %). While age is the most significant risk factor for LOAD, other factors can also contribute, including genetics, family history, and lifestyle factors. Having a family history of Alzheimer's increases the risk, and certain genetic factors, like carrying the APOE ε4 allele, are associated with a higher risk of developing the disease. Studies with monozygotic and dizygotic twins also indicate that the genetic component could explain between 60% to 80% of the LOAD risk (11). However, a comprehensive understanding of the mechanisms linking this genetic predisposition to LOAD pathogenesis remains largely elusive.

3. Pathological hallmarks of Alzheimer's disease

Despite these differences in age of onset and etiologies, both EOAD and LOAD share common pathological hallmarks, such as the abnormal accumulation of misfolded proteins in the brain, alterations in neuronal circuits and neuroinflammation.

3.1. Amyloid-β plaques

Amyloid-β peptides are metabolites of the APP protein found in the membranes of neurons. In the brain of patients with AD, Aβ peptides tend to aggregate and form insoluble fibrils, which accumulate outside the neurons and form plaques in the brain tissue. These plaques can disrupt normal brain function and contribute to the neurodegenerative processes seen in AD (14). Physiologically, APP plays several important roles as a transmembrane protein at neuronal level. Its biological function includes cell adhesion, neuronal growth and maturation, apoptosis, synaptogenesis, and axonal growth and guidance. The cleavage of APP follows two main excluding pathways, the non-amyloidogenic and the amyloidogenic processing (Fig. 1). The APP fragments produced through these pathways have characteristic structural and solubility properties and play different roles in neuronal functions ((6); (12); (13); (14)).

The non-amyloidogenic and amyloidogenic APP processing differ mainly by the action of α- or β-secretases. In the non-amyloidogenic one, cleavage of APP by α-secretase produces the secreted APP ectodomain α (sAPPα) and the C-terminal fragment α (CTFα). CTFα remains membrane-bound and can be further cut by γ-secretase, producing non-toxic peptides (Fig. 1A) (15).

sAPPα enhances neuronal survival via the activation of protective pathways against pro-apoptotic signals ((16); (17); and (18)) and antagonizes Aβ-mediated effects in neurons such as dendritic spine loss and increased hyperphosphorylated TAU ((19); (20); (21) for review; and (22)). Supporting the trophic role of APPsα in the brain, it was shown that administration of this peptide restores the anatomical, behavioral, and electrophysiological abnormalities observed in a mice model lacking APP (APP-/-) (17). Moreover, stimulation of the non-amyloidogenic APP process improves hippocampal neuronal functions linked to healthy aging (23), suggesting that a reduced activity of this pathway may contribute to AD pathology.

The amyloidogenic APP processing is strongly implicated in the pathogenesis of AD and it is particularly mediated by β-secretase(Fig. 1B). The cleavage of APP by β-secretase (also known as BACE1) produces the soluble APPβ (sAPPβ) released into the extracellular space and the membrane-bound C-terminal fragment β (CTFβ), which can be further cleaved by γ-secretase, resulting in the release of the APP intracellular domain (AICD) and Aβ peptides..

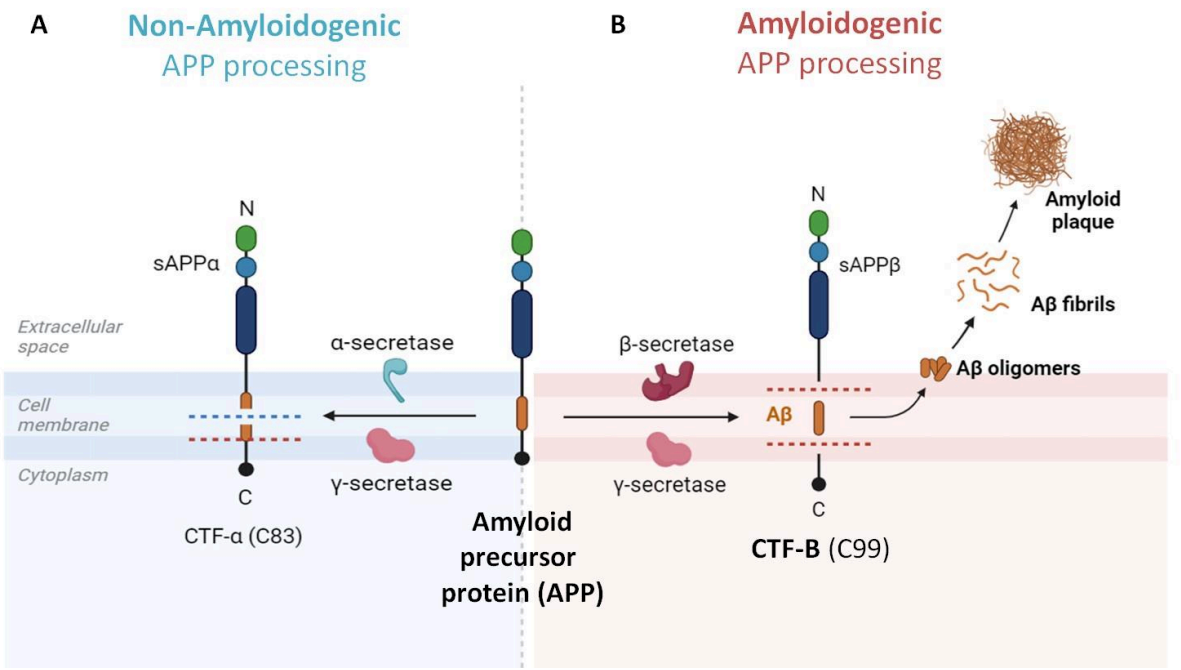

Figure 1. APP processing in physiological conditions and in Alzheimer's Disease. A) Non-Amyloidogenic cleavage of APP leading to the production of sAPPα and CTF-α; process mediated by α- and γ-secretases. **B)** Amyloidogenic cleavage of APP mediated by β- and γ-secretases leading to the production of CTF-β and accumulation of Aβ.

Scheme adapted from BioRender (2022). Cleavage of Amyloid Precursor Protein (APP). https://app.biorender.com/biorender-templates/t-636932609faff9f9ba3d0d39-cleavage-of-amyloid-precursor-protein-app

Among the amyloidogenic Aβ species, $Aβ_{1-40}$ and $Aβ_{1-42}$ are the two mains pathologic species. $Aβ_{1-40}$ is slightly smaller and extensively more abundant (13), although the $Aβ_{1-42}$ is more hydrophobic and more prone to aggregation into amyloid plaques in AD (15), has a greater neurotoxicity ((24) and (25)) and forms fibrils significantly faster than the $Aβ_{1-40}$, suggesting that $Aβ_{1-42}$ plays a key role in the formation of amyloid plaques. Both peptides accumulate as Aβ oligomers (AβOs) and fibrils forming extracellular toxic Aβ plaques in the brain and cerebrospinal fluid (CSF) of patients with AD ((26); (27); (28)), where they induce several neuronal dysfunctions ((29) and (30)).

Among the damages induced by Aβ peptides, one can highlight neuronal hyperexcitability, synaptic dysfunction and degeneration, and neuronal cell death ((25); (31); (32); (33)). Once bound to neurons, AβOs impairs the balance of glutamatergic and GABAergic synapses, disrupt hippocampal synaptic plasticity and inhibits long-term potentiation (LTP) ((34) and (31)). At the axonal level, deposits of Aβ impair fast neuronal trafficking, leading to axonal degeneration (35). All these processes may contribute to the neuronal death observed in the brain of AD patients.

Several lines of evidence indicate that neuronal electrical activity regulates the concentration of Aβ in the brain ((36); (37); (38)). Equally, Aβ deposition leads to neuronal hyperactivity in

the Central Nervous System (CNS) ((39); (40)), both *in vitro* and *in vivo* ((41); (42); (32)). Notably, Aβ-dependent neuronal hyperactivity is only observed in neurons with preexisting baseline activity (32) and can be observed even at picomolar concentration of Aβ oligomers (42). Therefore, there seems to exist a positive feedback loop between Aβ deposition and neuronal hyperactivation at early stages of the AD pathology.

Aβ has been also linked to the disruption of connectivity and integrity of neuronal networks in mice models ((37) and (43)) – corresponding to the dysfunctions observed in the cortex of patients with AD (44). In addition, the presence of Aβ affected the formation of NFTs by accelerating their spatiotemporal progression in an AD mouse model ((45); and (46)). Furthermore, Aβ triggers inflammatory response in the brain, leading to the activation of glial cells. Aβ-activated microglia and astrocytes concentrate around the plaques and contribute to phagocyte the Aβ and reestablish homeostasis ((47); (48); (49)).

Although much progress has been made regarding the contributions of amyloidogenic Aβ species to Alzheimer's pathophysiology, how these processes may be affected by specific genes recently identified as AD risk factors remains unclear.

3.2. Neurofibrillary tangles

Another key pathological feature of Alzheimer's disease is the accumulation of abnormally phosphorylated TAU in the brain. TAU is highly expressed in the CNS, particularly in the cerebral cortex. A major protein in mature neurons, TAU normally has an axonal localization in the adult human brain. Encoded by the Microtubule-associated protein tau gene (*MAPT*), the six TAU isoforms are generated by the inclusion or exclusion of the exons 2, 3 and 10. Among these isoforms, five are present in adult individuals and one is mainly observed in neurons at early stages of brain development ((50); (51); (52)). TAU isoforms are named according to the presence of 4-repeat (4R) and 3-repeat (3R), which are generally expressed in equimolar concentrations within the normal adult brain (53).

The TAU protein has a N-terminal projection domain and a microtubule binding domain (MTB), playing an important role in neuronal functions. As a scaffold protein within the cytoskeleton, TAU facilitates and provides structural support for anterograde and retrograde trafficking mediated by kinesin and dynamin, enabling the axonal transport of nutrients, neurotransmitters and other molecules (50) (Fig. 2A).

However, in AD and other related disorders known as tauopathies (54), abnormal post-translational modifications and accumulation of misfolded TAU occur inside neurons, leading to the formation of NFTs ((51) and (55) for review). The main post-translational modification observed on TAU protein in the form of NFTs is its hyperphosphorylation, which in AD is at

least 3 times higher than in healthy individuals ((56) and (57)). TAU tends to accumulate in the soma and proximal dendrites when hyperphosphorylated at certain amino acid residues (58). In addition to abnormal intraneuronal aggregation, the hyperphosphorylated state may result in a decreased affinity of TAU for microtubules. This leads to incomplete binding between these elements of the cytoskeleton, contributing to its structural destabilization (59) (Fig. 2B). Essential for cellular trafficking, when unstable, microtubules lead to cytoskeleton disorganization, problems in axonal transport and in synapses, impaired neuronal communication, and eventually neuronal death.

In the brain of patients with AD, NFTs are commonly observed in regions of the brain involved in memory processing and cognition. The presence of NFTs follows a regional progression in the brain and corresponds to the stages of the disease ((60) and (61)). Among all the pathologically relevant phosphorylation sites in TAU, the serine (Ser) 202 and threonine (Ther) 205 (commonly identified by AT8 antibody) have been extensively characterized. This specific phosphorylation pattern is classically used as a marker to determine the Braak stage (62) – a semiquantitative classification from I to VI that assesses the severity of the disease based on the localization of NFTs and the gravity of changes observed in different brain areas.

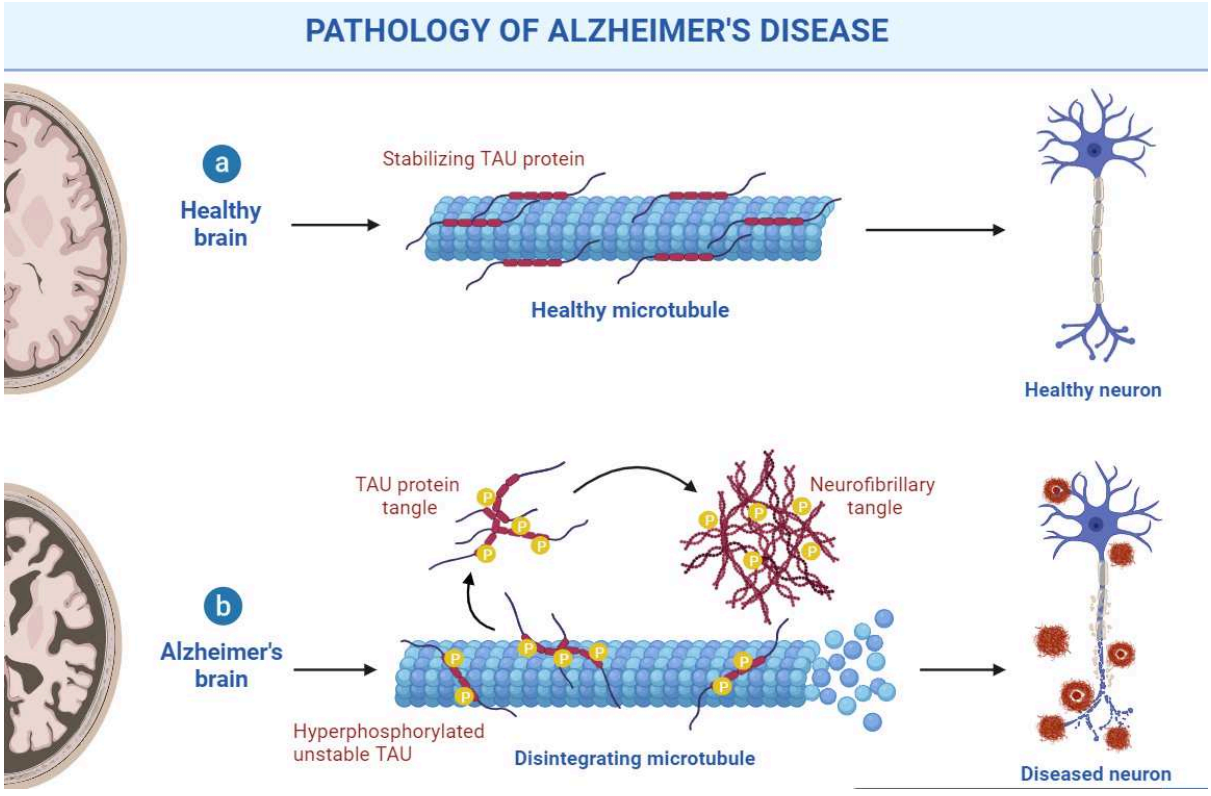

Figure 2. Abnormal phosphorylated TAU in the pathology of Alzheimer's Disease. A) Normal function of TAU protein on stabilizing microtubules in healthy neurons. **B)** Hyperphosphorylated TAU leads to disintegration of microtubules and NFTs formation in neurons of patients with AD.

Scheme adapted from BioRender (2019). Pathology of Alzheimer's Disease. https://app.biorender.com/biorender-templates/t-5d8baeb4f7e1a5007dd46b18-pathology-of-alzheimers-disease

A comprehensive understanding of the molecular pathways contributing to post-translational TAU modifications favoring its aggregation in neurons remains a very active area of research. Approaches targeting TAU expression in neurons, such as the use of antisense oligonucleotides (ASO) to reduce its mRNA expression, have also been recently investigated ((63); and (64)) and may lead to novel therapeutic strategies in the future.

3.3. Alterations in neuronal electrical activity

In different AD models, recordings of neuronal activity at the single unity level, neuronal networks, or even from hippocampus and cortical regions consistently indicate neuronal hyperexcitability during the initial phases of AD ((65); (66); and (69)). Regardless of the technique used – multi-electrode array (MEA), whole-cell patch-clamp, calcium imaging, functional magnetic resonance imaging (fMRI) or electroencephalography (EEG), the observations both in patients and animal models of AD support the notion that neuronal electrical activity is altered at early stages of AD pathology (68).

Previous studies using intracranial foramen ovale electrodes showed that AD patients without a history or EEG evidence of seizures experienced clinically silent hippocampal seizures and non-convulsive epileptiform spikes. These findings suggest that an early development of occult increased hippocampal excitability may contribute to the pathogenesis of AD (69). Moreover, these patients demonstrate an accelerated pace of cognitive deterioration, supporting the hypothesis that the atypical neuronal activity observed could contribute to the progression of the pathology.

The neuronal hyperexcitability observed in AD patients has also been linked to the accumulation of misfolded proteins in the brain. Both increased levels of Aβ plaques and NFTs have been associated with neuronal hyperexcitability in animal and human cell models ((66) and (69)). In a mouse model of AD, the activity patterns of hippocampal CA1 neurons were examined using in vivo two-photon Ca2+ imaging. It was observed that in young mice, there was a selective increase in hyperactive neurons even before the formation of plaques. This suggests that soluble species of Aβ may underlie this impairment (66).

Inversely, neuronal hyperexcitability, induced by various mechanisms, such as seizures or glutamate receptor activation, increases APP endocytosis and Abeta production (37) and promotes TAU phosphorylation (70). In mice models of epilepsy, increased neuronal activity also leads to enhanced TAU phosphorylation (71) and total TAU level (72) in the hippocampus.

Changes in neuronal electrical activity in AD are also associated with dysregulation of ion channels, which highly contribute for maintaining a proper balance of neuronal excitability and inhibition. Previous studies have identified abnormalities in various ion channels, such as voltage-gated sodium channels, voltage-gated potassium channels, and calcium channels ((73); (40); (74); (2)). The modifications include altered intracellular levels in different neural cell types and the imbalanced flux of ions through subcellular compartments (75), which can contribute to hyperexcitability in AD.

Voltage-gated sodium (NaV) channels are crucial for regulating neuronal excitability. Whole cell patch clamp recordings in primary hippocampal neurons showed that exposition to $A\beta_{1-42}$ oligomers increases Na^+ currents in a concentration dependent manner and selectively upregulated the expression of NaV1.6 subtype (74). According to these results, the upregulation of NaV1.6 channels contributes to membrane depolarization and increases spike frequency, resulting in neuronal hyperexcitability.

In early stages of Alzheimer's disease, the Kv3.4 potassium channel subunit – crucial for neuronal spike repolarization – is up-regulated in the cerebral cortex, a trend that persists in advanced stages (73). The alteration of voltage-gated potassium channel subunits, particularly Kv3.4, modifies potassium currents in neurons, leading to changes in synaptic activity. These changes may contribute to the neurodegeneration observed in Alzheimer's disease.

Altogether, these findings support the existence of a vicious cycle of neuronal hyperexcitability and accumulation of misfolded Abeta peptides and TAU proteins in the brain of AD patients.

3.4. Synaptic dysfunction

In Alzheimer's disease, synapse dysfunction is a prominent feature that contributes to cognitive decline ((76) and (77)). A progressive synapse loss is observed in the cortex and hippocampus of AD patients and strongly correlates with the cognitive impairments observed in patients ((78); (79); (80)). Altered expression and dysfunction of key synaptic proteins involved in neurotransmission, including the postsynaptic density protein 95 (PSD-95), Synaptophysin (SYP), and Synapsin (SYN1), contribute to impaired neurotransmitter release and synapse function ((81); (82); (83)).

Both, increased levels of Aβ peptides and hyperphosphorylated TAU play an important role in neuronal synaptic dysfunction. Aβ has been shown to disrupt synaptic structure and function, inhibit neurotransmitter release, and impair synaptic plasticity, thereby contributing to synapse loss ((84); (85); (86)). Distinct mechanisms could be involved in these processes,

including the direct interaction of AβOs with glutamate postsynaptic receptors ((87); (88); and (89)) and the genetic influence of AD genetic risk factors, as will be discussed below on the "Synaptic failure hypothesis" section. Additionally, hyperphosphorylation of TAU observed in AD impairs the protein binding to the microtubules, destabilizing the cytoskeleton and disrupting axonal anterograde and retrograde transport, ultimately leading to synapse loss ((90); (83); (91)).

Alterations in neuronal stimulation can also play a role in synaptic function and plasticity. This activity-mediated modulation can occur through several mechanisms, including the modification of glutamate N-methyl-D-aspartate (NMDA) receptors, intracellular calcium levels, and neurotransmitter release (92). Some rapid and slow homeostatic processes can be raised in response to alterations in electrical activity. The spike-timing-dependent plasticity (STDP) suggests that the precise timing of a synaptic neuronal activity is critical in determining which synaptic plasticity mechanism will be triggered ((93) and (94)). A study using transcranial cortical magnetic stimulation protocols showed that patients diagnosed with AD are not able to establish STDP, evidencing an impaired capacity of electrical-mediated synaptic plasticity (95). In addition to the fast regulation involving STDP, secondary processes can occur and form negative feedback in an attempt to reduce high neuronal stimulation ((96) and (97)).

In sum, AD pathology can be seen as a vicious cycle of altered neuronal electrical activity, synaptic plasticity, APP processing and TAU phosphorylation. It is therefore plausible to speculate that AD risk factors could contribute to AD pathogenesis by affecting one or many of these processes.

4. From animal to human cell models in Alzheimer's Disease

Animal models have played a crucial role in advancing our understanding of AD, develop and test potential therapeutics, and explore the effects of genetic and environmental factors in the AD pathogenesis. Genetically engineered mouse and rat models have been extensively used to study AD and often involve modulation of human genes associated with EOAD ((100) and (101)). Distinct mammalian models develop some of the pathological hallmarks of AD, including the accumulation of amyloid-beta plaques and neurofibrillary tangles (102). However, most of these models carry one or more genetic mutations identified in patients with monogenic FAD (101), which represent 1-6% of AD cases, and may not necessarily help to understand the most frequent cases, which are non-monogenic.

In addition to rodent models, *Drosophila* and *C. elegans* have also been used to study specific aspects of AD pathology and investigate potential therapeutic targets ((103); (104); (105); (1)). Despite the genetic differences from humans, these models offer simplicity, easy genetic manipulation, and shorter life cycles, making them suitable for high-throughput screenings and genetic studies.

While animal models serve as essential tools for investigating the molecular mechanisms, behavioral changes, and potential therapeutic interventions in AD, it is crucial to keep in mind their limitations, as they do not fully replicate the complexity and heterogeneity of human AD. Moreover, animal models cannot fully recapitulate the genetic complexity of late-onset Alzheimer's disease (LOAD), as most genetic variants linked to an increased risk of AD are in regions of the human genome without homology in other species.

4.1. iPSC-based models in Alzheimer's Disease

The use of induced pluripotent stem cells (iPSCs) to generate human-induced neurons (iNs) represents a significant breakthrough in overcoming the limitations of animal models. This approach provides the amazing possibility of modeling the disease employing neurons that can potentially be derived from individuals displaying diverse genetics. Frequently, iNs derived from such patient sources manifest disease-specific characteristics associated with Alzheimer's disease, namely greater Aβ secretion levels and accumulation of NFTs (106). Furthermore, these patient-specific neurons derived from iPSCs hold promise for individualizing therapeutic strategies for patients and potentially improving treatment efficacy for the disease.

In a recent study using hiPSC-derived cerebrocortical neuronal cultures bearing AD-related mutations in presenilin-1 or APP, increased excitatory bursting activity was found, which was explained in part by a decrease in neurite length (67). These findings provide mechanistic insights to investigate the basis of neuronal hyperexcitability and other AD related phenotypes in a human context. In addition to the feasibility of utilizing short-term 2D neural cultures, the iPSC technology offers a remarkable opportunity for the establishment of long-term cultures. The development of iPSC-derived 3D cerebral organoids has established a robust model for investigating early Alzheimer's disease (AD) pathophysiology within a more intricate system (67). This advancement enhances cell-to-cell interactions and promotes higher levels of cellular maturation, contributing to a more comprehensive and physiologically relevant understanding of AD pathology.

5. Pathophysiological mechanisms of AD

As a multifactorial and complex disease, the exact cause of AD is not fully understood. However, a combination of genetic, environmental, and lifestyle factors contributes to its development. Among the environmental risks, aging has the strongest influence for most AD cases (107). In addition, vascular conditions – such as heart disease, stroke, high blood pressure and sedentarism; metabolic disease, educational level and mental stimulation also contributes to the risk of developing AD ((108) and (109)). Although its cause remains elusive, progress has been made in underlying the mechanisms of the disease, and different theories have emerged in the last few years.

5.1. The "Amyloid Cascade Hypothesis"

The remarkable implications of alterations in APP metabolism for the pathophysiology of AD have initially driven the research in this field towards an "Amyloid cascade hypothesis". According to this theory, alterations on APP processing, which lead to the accumulation and aggregation of Aβ in the form of amyloid plaques, would be at the origin of all the modifications observed in the pathophysiology of the disease, including the NFTs formation ((110); (111); (112)). This hypothesis has been largely accepted in the last few decades, specially guided by the strong influence of APP on the familial forms, where it has been suggested to be determinant. However, most of the clinical trials have also been using the results driven by the Amyloid cascade hypothesis to conduct their approaches, aiming to target amyloid plaques via monoclonal antibodies or the secretases involved in the production of β-amyloid. And, despite all the efforts in immunogenic and cell therapy in the last years, no treatment has successfully cured these patients so far.

This raises significant issues concerning current approaches and raises the question of whether there is a causal relationship between Aβ deposits and the onset of other hallmarks. It is noteworthy that accumulation of Aβ is not exclusive to patients with AD, but it is present in aging brains with no signs of dementia ((113); (114); (115)). Given the multifactorial and heterogeneous nature of the disease, it may be oversimplifying to assume that Aβ changes are sufficient to trigger all aspects of the complex AD cascade. Alternative hypotheses and therapeutic targets have therefore been explored in the last few years.

5.2. The "Cellular Phase Hypothesis"

In this regard, the "Cellular phase hypothesis" suggests a pathophysiological cascade with multiple entry points. Together, diverse cell types could differently react to molecular alterations, such as the accumulation of Aβ and hyperphosphorylation of TAU, to regulate the brain homeostasis (116). According to this theory, changes on synapse plasticity,

endosomal trafficking, or inflammatory responses, for example, could initially be a compensatory mechanism resulting from interactions among neurons, astrocytes, microglia, and endothelial cells. Only when these adaptive responses become chronic and the cells can no longer hold it, the alterations would turn into an irreversible state, from where the pathology continually progresses. In this way, distinct mechanisms, or even the same ones, possibly elicit diverse effects during the stages of the disease progression (117). This constitutes the basis of the “cellular phase hypothesis", which is non-exclusive and may occur concomitant with the postulated by other theories, e.g., the “Amyloid cascade”.

5.3. The “Genetically Driven Synaptic Failure Hypothesis”

The “Genetically driven synaptic failure hypothesis” proposes that genetic variations or mutations associated with Alzheimer's disease contribute to the disruption of synaptic function and plasticity, leading to the onset and progression of the disease. This would happen through changes in the cell adhesion core and the connected cellular cascades in neurons (118).

A major scientific support for this theory is the evidence from clinical studies showing neuronal hyperactivity in the cortex and hippocampus of individuals even before the onset of symptoms ((119) and (65)). Vossel et al. investigated neural network activity in individuals with preclinical AD using functional magnetic resonance imaging (fMRI) and electroencephalography (EEG). They found greater cortical spontaneous neural activity and abnormal network synchronization, particularly in regions vulnerable to AD pathology, such as the hippocampus ((120) and (121)). Increased neuronal activity suggests early disruption in the brain networks and highlights the potential role of hyperactivity in the pathogenesis of AD.

Likewise, genetic mutations associated with AD have been linked to disruptions in neurotransmitter systems, including glutamatergic, cholinergic, and GABAergic systems ((122) and (123)). Dysregulation of these neurotransmitter systems could lead to synaptic dysfunction and cognitive impairments observed in AD. Additionally, they could disrupt signaling pathways critical for synaptic function, such as the focal adhesion pathway, Wnt signaling, and calcium signaling. This hypothesis highlights the potential interplay between genetic factors and other pathological mechanisms in AD. Genetic variations may thus interact with these processes, further exacerbating synaptic dysfunction and neuronal damage.

Collectively, these scientific findings support the “genetically driven synaptic hypothesis”, emphasizing the importance of genetic variations and mutations in AD-related genes.

Understanding these genetic influences on synaptic dysfunction and on other molecular aspects of the disease may help in an early diagnosis and to identify novel therapeutic targets for the treatment and prevention of AD. Especially considering the great relevance of several genetic variants recently associated to increased risk of developing AD.

6. The recent identification of AD genetic risk factors

As discussed earlier, the genetic component explains 60 to 80% of the attributable risk to develop the most common form of AD – the LOAD (11). However, it was only in the last 10 years that advances in Whole-Genome Sequencing (WGS) and Genome-Wide Association Studies (GWAS) allowed the identification of several genetic loci potentially implicated on this form of the disease. GWAS analyses have brought to light the association between slight variations in the genome and the occurrence of Alzheimer's phenotype. Single Nucleotide Polymorphisms (SNPs) occur when a single nucleotide in the DNA sequence is different between individuals and, although rare, are notably the most common type of genetic variation. SNPs explain not only most of the variability between individuals but also explain their predisposition to develop a certain trait or disease ((124) and (125)).

GWAS uses genotyped input data from patients and controls to perform associations between the observed frequency of a SNP in a general population and the phenotypes of interest (e.g., AD dementia vs non-dementia). The detection of disease-relevant signals on this type of analysis is a challenge. To powerfully determine them, the population samples tested should be as large as possible. In addition, to minimize other variabilities, the individuals should be descended from identical ethnicities. In 2013, our group led the largest meta-analysis in populations of European ancestry until that time ((116) and (126)). Among AD cases and controls, the genomic data from 74,046 individuals were successfully used to identify 11 new loci possibly associated with increased risk of developing the disease (Fig. 3).

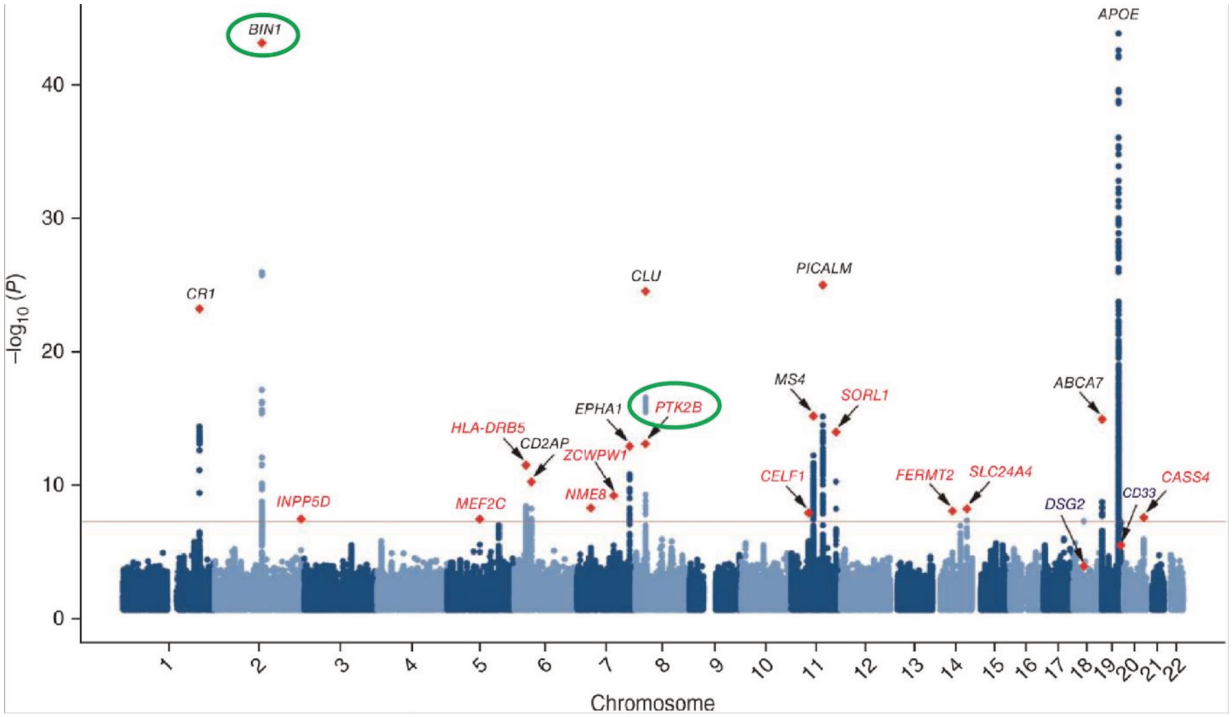

Figure 3. Genetic risk factors for Alzheimer's Disease identified by GWAS. Manhattan plot of GWAS for AD (17,008 cases and 37,154 controls). The red line corresponds to the threshold of significance (P< 5 x 10-8). Genes identified by previous GWAS are shown in black. New genes identified in the Lambert et al. study are represented in red. The red diamonds represent SNPs exhibiting the most statistically significant P values. Green circles highlight the genes investigated in this study.

Figured adapted from Lambert JC, Ibrahim-Verbaas CA, Harold D, Naj AC, Sims R, Bellenguez C, et al. Meta-analysis of 74,046 individuals identifies 11 new susceptibility loci for Alzheimer's disease. Nat Genet. 2013 (Lambert et al., 2013 (53)).

Over the last few years, more than 70 genomic variants have been identified as genetic risk factors for AD using similar methods (127). However, most of these variants are in non-coding regions and might potentially affect the expression of hundreds of genes ((128) and (127)). Identifying functional variants, their effects on gene expression, the biological functions regulated by their target genes, and their potential molecular relevance are, thus, a promising approach towards a comprehensive understanding of AD pathogenesis. Among the genomic regions with the strongest signals, we highlight the Bridging integrator 1 *(BIN1)*, and the Protein Tyrosine Kinase 2β (*PTK2B)* loci, particularly explored in our laboratory (Fig. 3).

6.1. *BIN1* – the second strongest genetic risk factor for LOAD

SNPs within the *BIN1* locus are associated with an increased risk of LOAD ((129); (130); (126)). In our laboratory, we have also been investigating the mechanisms by which changes in BIN1 expression could contribute to AD pathology. This project has resulted in the

publication of three papers on which I am either co-first author or co-author and will be further detailed in the Appendix of this document.

In essence, using scRNA-sequencing data from different human brain regions, we showed that six BIN1 isoforms were differently regulated in AD patients versus control (131). More specifically, the expression of the neuronal-specific isoform 1 is reduced in the brain of AD patients compared to controls. Moreover, we demonstrated that BIN1 expression in glutamatergic neurons is significantly reduced at later stages of the disease compared to earlier stages (2).

BIN1 is situated on chromosome 2d14.3 and undergoes alternative splicing, resulting in the generation of ten isoforms expressed in the central nervous system (CNS) (132). It has been observed that the expression of these isoforms differs according to tissue and cell type (133), where they may have distinct roles. In the brain, isoform 1 and, to a lesser extent, other isoforms containing a Clathrin and AP-2-Binding (CLAP) domain are exclusively expressed in neurons, whereas isoforms and 9 and 10 (lacking the CLAP domain) are mainly observed in glial cells, including microglia ((134) and (133)). The expression of BIN1 isoform 8 is specifically in muscles (132), where it is particularly involved in neuromuscular junctions.

BIN1 protein plays a crucial role in the regulation of endocytosis and trafficking processes, immune response, calcium homeostasis, and apoptosis ((1); (135); and (2)). In rat and mouse models, the overexpression of BIN1 has been associated with greater neuronal activity levels, possibly through the interaction with L-type voltage-gated calcium channels (LVGCC) (136).

Furthermore, we showed that reduced BIN1 expression results in impaired electrical activity in hiPSC-derived neurons (2). Analyses of short-term iPSC-derived 2D cultures from 4-6 weeks showed increased neuronal excitability on multielectrode arrays, enhanced calcium spikes frequency and bursts disorganization in BIN1 KO cells compared to its isogenic WT, also through LVGCC calcium channels – more specifically, CaV1.2. This chronical increased activity could result in a later synapse loss, observed only in long-term 3D cultures (2). These electrical alterations mediated by BIN1 suggest that changes in BIN1 expression impair calcium homeostasis, leading to disrupted neuronal electrical activity, and support the “Genetically driven synaptic failure hypothesis”.

6.2. Detection of *PTK2B* as a LOAD genetic risk factor

Among the new hits identified in one of the largest GWAS association studies in European populations, the third strongest signal was on the locus of the Protein Tyrosine Kinase-2-beta (*PTK2B*) gene (126). Variations in this locus (namely, the rs28834970C SNP) have been identified as a genetic risk factor for the late-onset form of Alzheimer's disease ((126) and (127)). This variant is in an enhancer region adjacent to *PTK2B* gene and has been shown to alter the expression of *PTK2B* and other multiple genes (137). Distinct groups, including ours, have tested different cell lines carrying this variant to determine the full impact of this SNP on AD pathology (see Results section). Later, a combination of transcriptome-wide association study (TWAS), GWAS, and meta-analysis from different groups confirmed *PTK2B* as an important risk gene for AD ((138); (139); and (140)).

The *PTK2B* gene encodes for the Ca^{2+}-activated protein with the same name (PTK2B, also known as Pyk2). Studies of the immune system and cancer cells have implicated PTK2B in processes related to inflammation, proliferation, and cell survival ((141); and (142)). These are the areas in which PTK2B has been primarily studied in humans until its recent discovery as a risk factor for AD.

Highly expressed in forebrain regions and activated in response to various stimuli, PTK2B shares high homology with another focal adhesion protein called FAK (from Focal Adhesion Kinase), but it differs from this one due to its unique property to respond to increased intracellular free calcium (143). Also activated in response to neuronal electrical activity, PTK2B could represent an exceptionally intriguing point for comprehending AD, given that neuronal hyperactivation stands as a primary hallmark of the disease and manifests even from its initial phases. These findings were evident in both clinical studies (144) and *in vitro* models utilizing iPSC-derived systems, as well as animal models ((39); and (67)).

In human brains, PTK2B expression is enriched in the adult forebrain, mainly in glutamatergic neurons (131), and is decreased in the brain of AD patients (145) with a correlation with the disease progression. These observations led us to hypothesize that PTK2B down-regulation could contribute to neuronal dysfunctions observed in the AD human brain, such as increased electrical excitability and synaptic alterations.

Although part of this PhD was also dedicated to investigating the role of BIN1 as an AD risk gene (and resulted in two publications – (1) and (2)), the investigation of PTK2B modulation in a human *in vitro* model, and its possible contribution to the pathology of Alzheimer's disease, is the main objective of this thesis and will be introduced in the following chapter.

1. PTK2B expression and structure

1.1. From the gene to the protein

The AD risk gene PTK2B is localized in the chromosome 8q21.2 and alternative splicing of this gene results in the production of multiple transcript variants. Along with the full-length form of the protein, two isoforms can also be translated – a hematopoietic-specific isoform (called Pyk2-H) and a Pyk2-related non-kinase (PRNK) isoform ((146) and (147)).

The hematopoietic isoform, as the name suggests, is primarily expressed in hematopoietic cells, including B- and T-cells, natural killer cells, and myeloid cells. Important to the immune cell signaling, and in contrast to the PTK2B full-length, the Pyk2-H is primarily activated through immune cell-specific receptors, such as antigen receptors (TCR – from "T cell receptor" and BCR – from "B cell receptor"), and cytokine and chemokine receptors (146). It differs structurally from the non-spliced PTK2B due to the exclusion of an exon containing 42 amino acids in the C-terminal domain, between the kinase and focal adhesion regions.

The PRNK isoform, in turn, is a short variation that lacks both N-terminal and kinase domains and is probably obtained from a second internal initiation site. Like the full-length, the PRNK is also found in the brain, although in lower quantities. Additionally, this short isoform is expressed in many other tissues, including spleen, lung, and kidney (147) and is described to play a role as an endogenous regulator of PTK2B (147). Besides its expression in lymphoid tissue, the non-spliced PTK2B form is highly enhanced within the central nervous system ((148); (149); (150)).

In the human brain, as we previously demonstrated, PTK2B is mainly expressed in human glutamatergic neurons of the middle temporal gyrus (131). Its expression is particularly pronounced in hippocampal pyramidal neurons and, to a lesser extent, in the cerebral cortex ((151); (152); and (153)), regions specially affected in AD pathology. Additionally, PTK2B is also found in other cerebral regions as the amygdala, the thalamus, and the striatum ((150); (154); and (155)). Despite its main expression in glutamatergic neurons, in mouse models, PTK2B was also found in very low quantities in astrocytes ((156); (152); and (153)), where it plays a role in facilitating the cell mobility in response to brain lesion. Additionally, PTK2B was found in less extension in microglial cells, where it plays a role in reacting to stress signals mediated by amyloid beta (157) and ischemia (158). Therefore, PTK2B may play significant roles across various cell types implicated in Alzheimer's disease, with a particular emphasis on glutamatergic neurons. This observation lends support to the 'Genetically

driven synaptic failure hypothesis,' indicating a potential key involvement of PTK2B to the observed electrical activity dysfunction within this specific neuronal population in Alzheimer's pathology.

1.2. Structure of PTK2B protein

The encoded full-length protein PTK2B/Pyk2 is a non-receptor tyrosine kinase composed of 1009 amino acids totaling about 115,8 kDa. It consists of several functional domains, including a N-terminal FERM (Four-point-one, Ezrin, Radixin, Moesin) domain, a central kinase domain, and a C-terminal focal adhesion targeting (FAT) domain ((148); and (159)) (Fig. 4A). These main regions interact with each other, forming a monomeric structure with a close arrangement (143), which is an autoinhibited form of PTK2B (Fig. 4B). Phosphorylation of the Tyr402 is necessary for the reorganization of the protein in a activate state. This residue is in the so-called “activation loop” within the FERM and kinase domains, inaccessible in the close conformation.

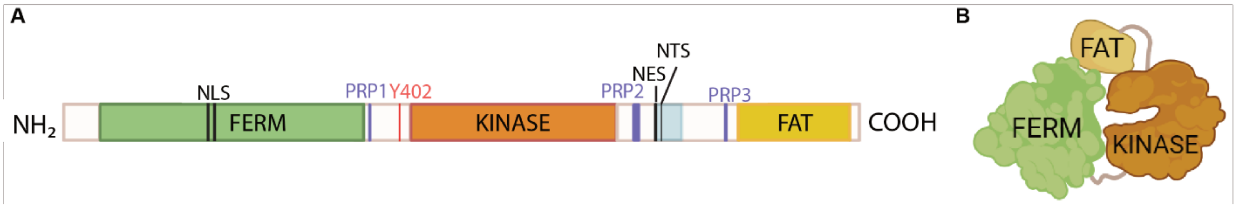

Figure 4. Scheme on PTK2B full-length protein structure. A) Main PTK2B protein domains and its **B)** close and autoinhibited conformation.

Besides the three main PTK2B domains, there are other smaller regions with important roles for protein binding and structure. The kinase-fat linker (KFL) connects the kinase and the FAT domains and is the most contrasting region comparing PTK2B and its homologous FAK. Three proline-rich (PR) motifs are also present – PR1, PR2, and PR3 – and constitute binding sites for other proteins. Two of them are localized within the KFL sequence. In the same region, there is a calmodulin (CaM) binding element, critical for the PTK2B role as calcium sensor (143), a nuclear targeting sequence (NTS), and a nuclear exporting sequence (NES) – important motifs for intracellular trafficking of the protein. The FERM domain enables protein-protein interactions and contains a nuclear localization sequence (NLS). While the kinase domain mediates phosphorylation events, including PTK2B autophosphorylation. The FAT domain assists in focal adhesion, cellular localization and signaling ((160); (161); and (162)).

1.3. Post-translational modifications

PTK2B is extensively regulated by phosphorylation events, which modulate its activity and downstream signaling. Among the different modifications that PTK2B undergoes, phosphorylation at tyrosine residues is one of the most important. The phosphorylation of PTK2B protein affects its activation level, the ability to interact with other proteins, its function in cell adhesion, the recruitment of scaffold proteins, and other important cellular processes.

Tyrosine 402 (Tyr402) is the major autophosphorylation site in PTK2B protein and a key mechanism for its activation ((163); and (164)). Besides leading to the protein activation, phosphorylation at Tyr402 leads to conformational changes, enabling the recruitment and its interaction with Proto-oncogene tyrosine-protein kinase Src (SRC) family members. In response to extracellular stimuli, Src family kinase members (SFKs), including SRC and Tyrosine-protein kinase Fyn (FYN), are also capable of phosphorylating PTK2B (164). This event subsequently leads to the phosphorylation of additional tyrosine residues, namely Tyr579, Tyr580, and Tyr881 ((165); and (166)). As a result, this complex phosphorylation cascade serves to enhance the PTK2B signaling and its interactions with downstream effectors.

The phosphorylation of residues other than tyrosine are also important in PTK2B localization. In this regard, the nuclear export motif is regulated by phosphorylation at Ser778, leading to its inactivation and accumulation of PTK2B in the nucleus (167). Besides its phosphorylation, PTK2B dephosphorylation is also essential in the regulation of its function and cellular localization and it will be explored in the following section.

Additionally, PTK2B undergoes other post-translational modifications ((142); and (168)). Ubiquitination of some residues – as Lys188 and Lys944 – regulates the protein's stability, turnover, and intracellular localization, thereby affecting its activity and degradation ((169); and (170)). Although very close to its homologous FAK, these two proteins do not share all the same post-translational modifications. Acetylation and SUMOylation, e.g., are FAK unique modifications and may be related to the functional differences observed between these proteins (171).

These post-translational modifications on PTK2B serve as important regulatory mechanisms that control its activity, localization, and downstream signaling pathways. They contribute to the dynamic and precise regulation of PTK2B in various cellular processes, including cell adhesion, migration, proliferation, and signaling cascades implicated in normal physiology and disease conditions.

1.4. Temporal and spatial dynamics of PTK2B in neuronal cells

Mainly expressed in glutamatergic neurons in the adult human brain (131), PTK2B is an intracellular protein predominantly found in the cytoplasmatic compartment. Even so, PTK2B may also have distinct subcellular localization patterns according to the neuronal subtype and in response to its activation level, with post-synaptic and nuclear enrichments.

Although enriched in the PSDs and in the nucleus, the protein localization has been described to be dynamic and alternates between cytoplasm and nucleus upon certain conditions ((172); (167); and (173)), such as its activation state or early in the development (174). Treatment with nuclear export inhibitors also have shown its accumulation in the nucleus (175).

Hence, upon neuronal depolarization, PTK2B is translocated to the nucleus in a dephosphorylation dependent of calcineurin and Ca^{2+}/Calmodulin (CaM) in different *in vitro* models ((172); and (176)). The exact function of nuclear PTK2B is under investigation, but it has been suggested that it can promote cell survival and regulate gene expression, by phosphorylating transcription factors and interacting with other proteins such as methyl-CpGbinding domain protein-2 (MBD2) ((177); (178); and (179)).

Also enriched at excitatory synapses, PTK2B localizes within postsynaptic sites. It associates with key postsynaptic density (PSD) proteins, such as PSD-95 and NMDA receptors ((180); (155); (153); and (145)), where it is involved in synaptic signaling and plasticity. When activated upon depolarization and Ca^{+2} influx through NMDA receptor, PTK2B clusters with synapsin and PSD-95 positive regions (180). In addition to its major accumulation regions, PTK2B can also be found in dendritic spines, axonal growth cones, and neuronal cell body (181).

2. PTK2B signaling pathway

In physiological conditions, PTK2B has been identified as a major player in the synapse regulation and plasticity, as well in the regulation of the mitogen-activated protein kinase (MAPK) signaling pathway (159). Together with other kinases – such as the SRC, PTK2B has being involved as well in the postsynaptic regulation of NMDA receptor function (Fig. 5), and in spatial memory and long-term potential (LTP) modulation ((180); (152); and (155)).

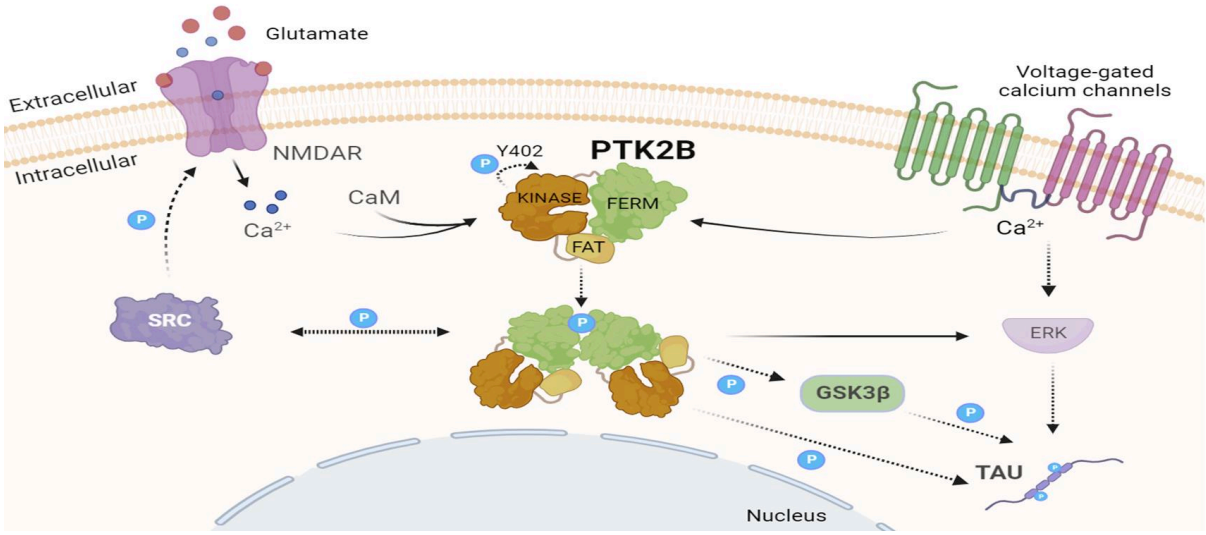

Figure 5. Scheme on PTK2B-associated intracellular molecular pathways in neurons.

2.1. Activation and inhibition of PTK2B

The monomeric form of PTK2B is normally found in its autoinhibited conformation, in which the FERM domain binds to the kinase one, making most binding sites to other proteins inaccessible ((182); (183); and (184)). This closed conformation inhibits the PTK2B kinase function, which requires a ligand-induced clustering, or dimerization, to drive its phosphorylation at Tyr402 ((185); (186); and (187)). This conformational change leading to PTK2B dimerization and activation depends on Ca^{2+} influx through NMDAR, which is in some measure mediated by calmodulin (CaM) binding through KFL and FERM domains ((176); (188); (180); and (143)).

Further studies revealed that Ca^{2+}/CaM may also bind to the postsynaptic density protein 95 (PSD-95), thereby disrupting its basal autoinhibitory interaction and allowing PSD-95 to interact with PTK2B (189). This interaction occurs at the Src homology 3 (SH3) domain of PSD-95 and leads to the clustering and activation of postsynaptic PTK2B ((189); and (180)).

Moreover, other studies of PTK2B cascade in neurons found that PTK2B activation by Ca^{2+}/CaM through NMDAR results in the phosphorylation of extracellular signal-regulated kinase (ERK) (159), leading to increased neuronal survival (190). Hence, K^{+}-induced neuronal depolarization increases the phosphorylation of PTK2B in rat primary neuronal cultures and hippocampal slices (191).

Following its phosphorylation, the Tyr402 and the PR1 motif combine to create a site capable of binding to SRC kinases, namely SRC and FYN (192). This interaction subsequently triggers the activation of these kinases, which further phosphorylates

additional tyrosine residues, enhancing PTK2B activation and other downstream proteins (185).

Besides its autoinhibition through interaction of the FERM and the kinase domains, in neurons, PTK2B can also be physiologically inhibited through its dephosphorylation by the striatal-enriched phosphatase (STEP) ((193); and (194)). Additionally, PTK2B can be inactivated by molecular inhibitors – as PF-719 – which have been investigated for its potential therapeutic applications, especially in inflammatory disease and cancer.

Overall, activated PTK2B serves as a central signaling hub, leading to the activation of various downstream effectors. These include MAPK pathways, phosphatidylinositol 3-kinase (PI3K)/AKT Serine/Threonine Kinase 1 (AKT) pathway, Rho family GTPases, and transcription factors such as CREB (from cAMP response element-binding protein), NMDAR, SRC, STAT3, TAU, and other AD-relevant proteins (195).

3. Functions of PTK2B protein

3.1. A tyrosine kinase

PTK2B facilitates the activation of several signaling cascades, including the phosphatidylinositol 3-kinase (PI3K)/AKT1 pathway, the NOS3 (from Nitric Oxyde Synthase 3) pathway, the MAP kinase signaling cascade (involving MAPK1/ERK2, MAPK3/ERK1, and MAPK8/JNK1), and the Rho family GTPases pathway (including activation of RhoA - from Ras homolog family member A - and RAC1 – Rac family small GTPase 1) (195).

It also phosphorylates NMDA receptors, affecting their biophysical properties and enhancing intracellular calcium influx. Additionally, PTK2B may regulate calcium ion transport through the phosphorylation of calcium channel subunits (196). It enhances SRC kinase activity by phosphorylating SRC (197). Moreover, PTK2B promotes the phosphorylation of ASAP2, RHOU, and PXN, requiring the cooperation of both SRC and PTK2/PYK2.

Its kinase activity has also been associated with TAU phosphorylation at its major tyrosine phosphorylation site – Y18 (198). In this study, HEK293T cells were transfected with TAU alone or in combination with a fused PTK2B-green fluorescent protein (GFP). Results showed that the co-transfection increased 5-fold change the phosphorylation of TAU at Y18 and 2-fold change the total protein levels, compared to cells transfected only with TAU. However, when a mutant form of PTK2B deficient for its kinase activity site (PTK2BY402F-GFP) was used, both the increase in pY18-TAU and total protein were completely abolished.

This suggests that the kinase activity of PTK2B is necessary for TAU phosphorylation and the observed increase in total TAU levels.

Interestingly, the phosphorylation of TAU at Y18 is necessary for TAU excitotoxicity mediated by Ca^{2+} influx through NMDAR in primary neuronal culture (199). On the other hand, as previously discussed in section 3.1, Ca^{2+}/CaM influx activates PTK2B, which may lead to an enhanced phosphorylation of TAU at Tyr18.

Overall, these data indicate that PTK2B acts as a TAU kinase, promoting the phosphorylation of TAU at Y18 and influencing the levels of total TAU protein. These findings provide insights into the molecular mechanisms underlying TAU phosphorylation and suggest a potential role for PTK2B in TAU-related pathologies, including AD.

Moreover, PTK2B has been recently described to play an indirect role in on one of the major Alzheimer's-associated TAU phosphorylation sites (Ser202/T205), possibly through the phosphorylation of GSK3β on Y216 (200). Their study with either HEK cells overexpressing PTK2B concomitant with GSK3β, hiPSC-derived neurons inhibited for PTK2B, or a tauopathy mouse model carrying a deletion or not for the gene have all shown that altered PTK2B expression contributes to a greater phosphorylation of TAU at this residue. Although this data reinforces the importance of this kinase in the pathophysiology of Alzheimer's disease, more studies are required to fully elucidate the process, especially in a human context.

3.2. Focal adhesion

PTK2B is primarily associated with focal adhesion and plays a role in integrin-mediated signaling ((201); (202); and (203)). This cellular process involves a complex network of molecular interactions and signaling events that regulate the attachment and stabilization of cells to the extracellular matrix (ECM) or to other cells.

Cell adhesion mediated by PTK2B primarily occurs through integrin receptors, which connect the extracellular matrix to the cellular cytoskeleton. Upon activation by external stimuli, such as ligand binding or mechanical force, integrins undergo conformational changes, leading to their activation. Active integrins recruit and assemble then focal adhesion proteins at specific focal adhesions sites of the cell membrane, such as PTK2B, FAK, and PAXILIN (205). The binding of PTK2B to the proline-rich regions of these proteins enables its localization to focal adhesions. Then, part of PTK2B activation by autophosphorylation is in response to integrin signaling.

The interaction between PTK2B, integrins, and associated signaling molecules coordinates the complex process of cell adhesion. By integrating extracellular and intracellular signals,

PTK2B plays a crucial role in modulating adhesion dynamics, cytoskeletal organization, and cell migration ((203); (204); and (205)). All these processes are essential for various physiological and pathological processes, including embryonic development, tissue homeostasis, wound healing, and cancer metastasis, highlighting the importance of PTK2B also in this regard.

3.3. Regulation of ion channels

Through its signaling functions and its enrichment in post-synaptic densities, PTK2B can modulate the activity of ion channels via phosphorylation and contribute to the regulation of neuronal excitability ((159); (206); and (151)). Glutamate NMDR is the main ion channel related to PTK2B regulation. As previously discussed, the interaction between PTK2B and PSD-95 promotes PTK2B autophosphorylation and activation, leading to phosphorylation of NMDAR subunits and modulation of NMDAR-mediated currents ((207); (151); (189); (208); and (180)).

Furthermore, PTK2B has been implicated in the regulation of voltage-gated calcium channels (VGCCs), which play critical roles in calcium signaling and neuronal excitability (159). Activation of PTK2B can lead to the phosphorylation and modulation of VGCCs, affecting their activity and calcium influx. This modulation by PTK2B has been observed in rat hippocampal CA1 neurons and has been linked to synaptic plasticity processes (209).

3.4. Synapse plasticity

Synaptic plasticity refers to the ability of synapses to undergo activity-dependent changes in strength and structure. This competence is crucial for physiological processes such as network development, learning and memory, and synapses reorganization (210). Multiple lines of scientific evidence indicate a key role of PTK2B in synapse plasticity ((211) and (151)).

Long-term potentiation (LTP) is a well-studied form of synaptic plasticity associated with the strengthening of synaptic connections. PTK2B has been shown to play a role in LTP induction and maintenance. In hippocampal neurons, PTK2B activation occurs during LTP-inducing stimuli, and its phosphorylation leads to the recruitment and activation of downstream signaling molecules. Genetic knockout or knockdown of PTK2B in a mouse model has been found to impair the induction of LTP in CA1 hippocampal slices when undergoing a high frequency stimulation (HFS), suggesting its involvement in synaptic plasticity processes (152).

In another PTK2B knockout mice model, however, some distinct findings were observed. PTK2B expression was not required for LTP but contributed to long-term depression (LDP).

At the same time, the lack of PTK2B was protective against Aβ-mediated effects on synapse plasticity (153). In this model, a theta-burst stimulation (TBS) protocol induced in CA1 neurons KO for PTK2B had no differences to the LTP observed on the wild-type (WT) ones. The different results obtained in these two experimental models could be likely explained by the different protocols used for the LTP stimulation. Regardless of these discrepancies, both studies support a central role for PTK2B-mediated signaling in synaptic plasticity.

To elucidate whether PTK2B was crucial or either negligible in inducing LTP in hippocampal neurons, another group tested both, HFS and TBS, protocols (212). Constitutive PTK2B KO mice and KO-induced specifically in CA1 neurons all showed LTP dysfunction when stimulated with HFS. However, LTP induced by TBS protocol was unaffected, indicating that PTK2B is specifically involved in HFS-induced LTP, but not in TBS-induced LTP. That brings attention to the fact that different models and stimulation protocols can produce distinct effects in terms of synapse plasticity and the impact of PTK2B on this important cellular process.

3.5. Other functions

Besides its functions in neuronal cells, PTK2B plays a vital role in regulating the humoral immune response and is essential for maintaining normal levels of marginal B-cells in the spleen as well as the proper migration of splenic B-cells. PTK2B is required for normal macrophage polarization and migration towards sites of inflammation. In T-cells, it regulates cytoskeleton rearrangement and cell spreading, contributing to the regulation of T-cell responses. Additionally, PTK2B promotes osteoclastic bone resorption, which necessitates the cooperation of both PTK2B/PYK2 and SRC. It may also inhibit the differentiation and activity of osteoprogenitor cells and affect the murine beige adipocyte differentiation (213). Within microglial cells, PTK2B is activated in response to Aβ and prion protein (PrP) fibrils. This activation is dependent on elevated intracellular calcium levels and requires the assistance of Lyn and PKC (157).

Extensively studied in different types of cancer – where its expression is commonly increased – PTK2B also plays important roles in this regard. Its function on focal adhesion is reported to affect metastasis ((214); (215); and (216)) and its overexpression in cancerous tissues have been correlated to unfavorable diagnosis, possibly through the stimulation of multiple oncogenic signaling pathways ((217); (141), and (142)).

4. PTK2B in Alzheimer's Disease

In addition to the previously discussed functions of PTK2B protein in cellular process also affected in Alzheimer's disease, recent works using mouse models of AD has suggested that PTK2B plays a central role in AD-related synaptic dysfunction mediating Aβ-triggered dysfunction ((153) and (218)).

In the AD mouse model 5XFAD, PTK2B overexpression reduces synapse loss and improves the performance in memory tasks, independently of the accumulation of Aβ plaques in the hippocampus (218). Interestingly, PTK2B overexpression also protects primary rat hippocampal neurons from Aβ-mediated synaptotoxicity (145), suggesting that at least some of the deleterious effects of Aβ exposure in neurons could be counter acted by PTK2B signaling.

Accordingly, PTK2B/ERK signaling pathway has been described as involved in microglial activation by $A\beta_{1-42}$ (219). And soluble Aβ oligomers lead to an increase in intracellular free calcium levels ((220), (221)), leading to PTK2B activation and stimulation of downstream proteins, such as SRC family members that also increase calcium intracellular levels, on a cycle of activation. Moreover, acute Aβo exposition activates Fyn PrPC-dependent signaling, required for later loss of NMDA receptor subunits, promoting excitotoxicity and spine retraction (87). This phenotype correlates with STEP expression, notably, an indirect suppressor of PTK2B activity.

In individuals diagnosed with Alzheimer's disease, meta-analysis of GWAS revealed a strong association of PTK2B loci and hippocampal sclerosis, cognitive deterioration, and the progression of the disease ((222); (223); and (224)).

Besides being correlated to Aβ-mediated effects, PTK2B also has been related to TAU-mediated effects in a mouse model; being involved in PRKCD/PKCδ-mediated GSK3β activation and subsequent TAU hyperphosphorylation. More recently, other evidence indicated that endogenous levels of PTK2B might suppress TAU phosphorylation and tauopathies effects in neurons derived from iPSCs. Conversely, neurons pharmacologically inhibited for PTK2B with PF-719 displayed increased phosphorylation of TAU at Ser202/Thr205 (AT8) (200). Likewise, overexpression of PTK2B in Hek293T cells showed similar enrichment of TAU phosphorylation (200).

As PTK2B is a tyrosine kinase and only phosphorylates TAU at Tyr18 (198), the observed effects of PTK2B on the main TAU AD-related residues, Ser202/Thr205, is likely mediated by other kinases downstream of PTK2B. According to Brody and collaborators (2022), it

possibly passes through the activity of the Liver kinase B1 (LKB1) and the p38 Mitogen-activated protein kinase (p38 MAPK), which might be endogenously inhibited by PTK2B.

At the biochemical level, additional evidence from our and other groups demonstrated a physical association between PTK2B and TAU in Hek293 cells (105) and mouse primary hippocampal neurons (198). Accordingly, in a transgenic TAU mice model (THY-Tau22), the accumulation of PTK2B emerged synchronously with the initial TAU hyperphosphorylation (Ser202/Thr205). In the brain of patients with Alzheimer's disease, the accumulation of PTK2B was specifically noted within neurons exhibiting TAU oligomers, indicating a potential association between PTK2B and the accumulation of TAU at the oligomeric and toxic state (105). Despite the observed accumulation of PTK2B within neurons exhibiting TAU oligomers, it is noteworthy that the overall expression of PTK2B is diminished in Alzheimer's disease-relevant brain regions among patients compared to healthy individuals. Importantly, this reduction in expression correlates with the progression of the disease, as previously mentioned (145).Overall, these data provide evidence of an important role of PTK2B in modulating key aspects associated with AD pathogenesis. However, there is still a need for a comprehensive understanding of the molecular mechanisms that connect PTK2B to TAU hyperphosphorylation and other AD-related phenotypes in human neurons. The PTK2B-mediated signaling pathway could serve as a potential target for future therapeutic interventions aimed at reducing TAU pathology and mitigating Aβ-induced toxicity.

Objectives

Although advances have been made in the last decade after the identification of *PTK2B* as a risk gene for AD, the mechanisms by which PTK2B is implicated in the pathophysiology of the disease are poorly understood, especially in human neurons.

These observations, in conjunction with our analysis indicating that *PTK2B* expression is reduced in patients diagnosed with Alzheimer's disease, led us to hypothesize that PTK2B down-regulation could contribute to neuronal dysfunctions observed in the AD human brain, such as increased electrical excitability and molecular alterations. To address this possibility, we took advantage of human induced pluripotent stem cells (hiPSCs) to generate human neurons expressing different levels of *PTK2B* and evaluated the resulting consequences in both short-term and long-term mixed neural cell cultures within 2D and 3D models (cerebral organoids).

1. General aims

To identify the cellular processes and the molecular pathways regulated by PTK2B in human-induced neurons both in physiological-like state and in an Alzheimer's disease-like context.

2. Specific aims

I. Generate and characterize 2D and 3D cultures expressing different levels of *PTK2B*.
II. Characterize AD-related biochemical phenotypes in human induced neurons expressing reduced levels of PTK2B.
III. Investigate the potential molecular pathways impacted by decreased levels of PTK2B in human-induced neurons and glial cells.
IV. Probe the possible role of PTK2B signaling in the regulation of neuronal electrical activity and the Aβ-mediated neuronal hyperexcitability.

Materials and Methods

1. Maintenance of hiPSCs and neural induction

For this project, we mainly took advantage of a commercially available hiPSC line (ASE-9109, Applied StemCell Inc. CA, USA). The maintenance of the iPSC cultures was done in adherence with manufacturer's protocols which can be found on the webpage of Stemcell Technologies.

Briefly, hiPSCs were maintained in mTeSR1+5X supplemented medium in non-treated cell culture dishes/plates pre-coated with 10 ug/ml of vitronectin fresh-diluted in Cell Adhere Dilution Buffer (StemCell Technologies) during 1h at room temperature. Full medium change was performed daily until the confluence reached about 80-90%, when the cells were passed. Cell number and viability were recorded using a LUNA II™ Automated Cell Counter.

To induce a neural lineage from iPSCs, we used either the monolayer or the embryoid body methods, both consisting of a serum-free system validated by StemCell Technologies and based on the dual SMAD-inhibition (SMADi) method (225). Briefly, on the monolayer system, hiPSCs are cultured at high density and passed for 3 times in STEMdiff™ Neural Induction Medium + SMADi (StemCell Technologies) for approximately 3 weeks. Alternatively, on the embryoid body procedure, the iPSCs are seeded on AggreWell plates (StemCell Technologies) to produce the embryoid bodies. Which are then replated in classic plates followed by a Neural Rosette selection to enrich for human-induced neural progenitor cells (hiNPCs).

After this period, the hiNPCS generated are maintained for up to 9 passages in treated cell culture dishes pre-coated with poly-L-ornithine (PLO) and laminin (10 µg/mL), using supplemented STEMdiff™ Neural Progenitor Medium (NPM; Stemcell Technologies) fully changed daily. PLO solution was made in water (0.001%) while laminin was diluted in PBS 0.01M with Ca2+ and Mg2+.

To circumvent possible clone-specific biases, we used the BION;010-C2 (European Bank of Induced Pluripotent Stem Cells – EBiSC) as a second hiPSC line to confirm the main results previously obtained with ASE-derived cells. This additional line was kindly provided by the laboratory of Dr. Sandrine Thuret (King's College, London - UK) and are named "BION-derived cells" throughout this study.

Table 1: List of PTK2B hiPS cell lines

Cell line	Modification	Clone	Parental line	Source
WT	Isogenic WT	B5	ASE 9109	Applied Stem Cells
HET	14bp deletion in one allele	CL5	ASE 9109	Applied Stem Cells
KO	11bp deletion	CL2	ASE 9109	Applied Stem Cells
C2 (WT)	No modification	Parental cell line	BION;010-C2	EBiSC/Dr. Thurret (King's College)
S5 (SNP)	rs28834970 T→C	-	BION;010-C2	EBiSC/Dr. Thurret (King's College)
PT26 (HET)	KO (heterozygote)	-	BION;010-C2	EBiSC/Dr. Thurret (King's College)

2. Differentiation of hiNPCs into mixed cultures of hiNs and hiAs

To obtain mixed 2D cultures comprising hiNs and hiAs from hiNPCs, we followed the spontaneous differentiation protocol detailed by StemCell Technologies and based on previously published work (226).

Following this spontaneous protocol, 100,000 hiNPCs/well were plated in 24-well cell imaging plates from Eppendorf (Cat # 0030741005) pre-coated with PLO (0.001%) and laminin (10µg/mL). Cells were kept in 0.5 mL of NPC medium per well for 24 hours, and then an equal volume of complete BrainPhys medium (supplemented with BDNF, GDNF, laminin, dibutyryl-cAMP, ascorbic acid, N2, and SM1) was added to each well to begin the process of differentiation. Subsequently, media was partly changed in the plates bi-weekly. The media change consisted of removing half of the existing medium in each well and replacing it with an equal volume of fresh complete BrainPhys medium. Mixed cultures of hiNs and hiAs were characterized at different time points up to 5 weeks from the start of the differentiation process. Cells were either used for electrophysiological analysis, lysed for WB, fixed for immunocytochemistry or isolated for scRNA-sequencing, as described below.

3. Generation of human cerebral organoids

Cerebral organoids (3D Cultures) were generated from *PTK2B* WT, HET and KO hiPSCs employing a 4-stage protocol (227) based on the STEMdiff™ Cerebral Organoid Kit (08570, Stemcell Technologies). The first step consists of the Embryoid Body (EB) Formation Stage, where hiPSCs at 80%-90% confluency were detached from the Vitronectin XF substrate

using Accutase (#AT-104, Innovative Cell Technologies) to form the EB. In a 96-well round-bottom ultra-low attachment plate, 9000 cells were then seeded per well in EB seeding medium (Stemcell Technologies). On day 2 and day 4, EB formation media was added in each well. On day 5, 2 EBs were transferred per well in a 24-well ultra-low attachment plate containing Induction Medium (Stemcell Technologies). Two days later, the EBs were ready for the Expansion Stage. Each EB was embedded in a drop of Matrigel (Corning) and transferred to a 6-well ultra-low attachment plate with Expansion Medium (Stemcell Technologies). After three days, the medium was replaced by Maturation Medium (Stemcell Technologies) and the plate was placed in an orbital shaker (65 rpm speed). During this final Maturation Phase, 75% medium change was done on a biweekly basis. Organoids were allowed to mature for a period of 6.5 months.

4. hiPSCs genetic analyses

A quantitative PCR analysis was performed for detecting the major karyotypic abnormalities previously reported in hiPSC. For that, we used the iPSC Genetic Analysis Kit (07550, Stemcell Technologies). This analysis enabled the genetic screening of the ASE-derived hiPSCs and controls – a genomic DNA control (07562, Stemcell Technologies), human cortical astrocytes (HA; ScienCell #1800), and the ASE-9109 parental cell line (Applied StemCell Inc. CA, USA).

Briefly, the concentration of the genomic DNA samples was measured on NanoDrop. Genomic DNA samples were washed with nuclease-free water and vortex with Master Mix and dye. The samples and the primer-probe mixes were loaded in a 384-well PCR plate, which was runed using a quantitative PCR system. Analyses of results was evaluated as the original protocol and p-values calculated across all loci using one-way ANOVA with Tukey multiple comparisons test.

5. Generation of pure human neuronal cultures from hiNPCs

We have differentiated neurons from virus-transduced hiNPCs using an adapted protocol (228). First, we transduced hiNPCs with the rtTA-Puro lentiviral construct (Vect'UB, ID #pTRIPZ571), followed by transduction with the TetO-NGN2-Puro lentiviral construct (Addgene, #79823) one passage later. The cells were then maintained in NPM medium and expanded before differentiation.

For the production of human induced neurons (hiNs), hiNPCs were plated onto PLO/laminin-coated imaging plates at a density of 100,000 cells per well in NPM. After 24 hours, complete BrainPhys medium (Stemcell Technologies) was added in a 1:1 proportion with 2 µg/mL of doxycycline (Sigma-Aldrich) to induce TetO gene expression. The next day, 1 µg/mL of puromycin (Sigma-Aldrich) was added to initiate cell selection.

After 2-3 days (depending on the effectiveness of antibiotic selection), we performed a full medium change. Next, we added 50,000 human cortical astrocytes to each well with BrainPhys containing doxycycline. Following 24 hours, we added 2 µM of Ara-C (Cytosine β-D-arabinofuranoside; Sigma-Aldrich) to stop the astrocytes from proliferating. Biweekly, we replaced half of the medium in each well with fresh BrainPhys medium containing doxycycline until the 14th day. Afterward, we only performed the biweekly medium change using complete BrainPhys. We allowed differentiation to continue for an additional 2-4 weeks before subjecting the cells to different experimental manipulations. Human cortical astrocytes (HA; ScienCell # 1800) were obtained from ScienCell Research Laboratories, CA, USA and cultured for up to 10 passages in astrocyte medium (ScienCell # 1801) supplemented with astrocyte growth supplement (AGS, ScienCell #1852) and 10 ml of fetal bovine serum (ScienCell # 1800) on poly-l-lysine-coated 75 cm2 flasks.

This co-culture system was analysed using snRNA-seq after 4 weeks of differentiation. Results showed that 70% of cells (n=7120 from 5 independent culture batches) expressed pan-neuronal markers SOX11, SNAP25, DCX, and RBFOX3, with 66% of cells showing co-expression of the glutamatergic neuron marker SLC17A6. Among these cells, less than 1.5% co-expressed the GABAergic neuron markers DLX1, GAD1, and GAD2, and only 5% co-expressed low levels of markers of both neuronal subtypes. The immature astrocytes (Astro-I), mature astrocytes (Astro-II), and undifferentiated NPCs accounted for approximately 15%, 8%, and 4% of the remaining cells, respectively. The initial two cell populations likely reflect distinct astrocyte states integrated into the cultures, while NPCs probably denote cells that failed to reprogram into hiNs following ASCL1 transduction. Thus, the neuronal classes generated by this system consist mostly of glutamatergic neurons (84%), with a small percentage of GABAergic neurons (2.5%) and unspecified neurons expressing low levels of markers from both subtypes (13.5%).

6. Culture of hiNs in Microfluidic Devices

Three-compartment microfluidic devices were utilized for neuron culture. The presynaptic and postsynaptic chambers are connected to the synaptic chamber by long and short micro-channels, respectively. The design and fabrication of the microfluidic device have been previously described (145).

The home-made devices were placed individually in Petri dishes for convenient handling, and UV sterilized for 30 minutes before coating for cell adhesion. The surface coating used poly-L-lysine (Sigma-Aldrich) at a concentration of 20 µg/mL in borate buffer (0.31% boric acid, 0.475% sodium tetraborate, pH 8.5). The coated devices were incubated overnight at 37°C with 5% CO2. After washing with DPBS, the devices were coated with 20 µg/mL

laminin in DPBS and again incubated overnight at 37°C with 5% CO2. The next day, devices were washed once with DPBS prior to cell plating.

Half of the cells were seeded at the entrance of the presynaptic somatic chamber, and the other half at the entrance of the postsynaptic somatic chamber. The devices were microscopically observed under phase contrast to ensure proper cell flow. A total of 30,000 human-induced neural progenitor cells (hiNPCs), resuspended in NPM supplemented with a 10 µM Y-27632 ROCK inhibitor, were seeded per microfluidic device. After a minimum attachment time of 5 minutes, NPM (with 10 µM Y-27632 ROCK inhibitor) was added to the devices. Water was added to the Petri dishes to prevent media evaporation.

The dishes were incubated at 37°C in a humidified 5% CO2 incubator. To induce TetO gene expression in hiPSCs transduced for Neurogenin2, doxycycline (2 µg/mL) was added on the first day of half medium change. The following day, puromycin (1 µg/mL) was added to initiate cell selection. Two days later, 5,000 HAs (ScienCell Research Laboratories, CA, USA) were added per device. After 24 hours, Ara-C (2 µM) was added to stop their proliferation. The medium was changed twice a week with complete BrainPhys medium + 2 µg/mL doxycycline for 14 days. Afterwards, only a partial medium change was carried out using BrainPhys medium.

For each experimental condition (*PTK2B* WT, HET qnd KO), three microfluidic devices were utilized, and two independent cultures were conducted. To evaluate the time-course effect, neuronal cultures were terminated at 4 and 6 weeks.

7. Immunocytochemistry and immunohistochemistry

Neural cultures at the end of the differentiation were pre-fixed in 4% PFA and complete Brain Phys (1:1) for 5 min. The solution was removed, and cells were fixed in 4% PFA for 10 min. Wells were rinsed 3 times with PBS 0.1 M. Blocking was performed in PBS 0.1 M + 5% normal donkey serum + 0.1% Triton X-100. Primary antibodies were diluted in the blocking solution and 300 µL were added to each well following incubation overnight at 4°C under gentle shaking conditions. The following day, wells were washed 3 times with PBS 1X under shaking conditions. Secondary antibodies were diluted in the blocking solution at 1:500 and 300 µL of were added to each well. The plates were covered in aluminum foil and kept gently shaking at room temperature for 2 hours. Subsequently, cells were rinsed 3 times in PBS 0.1 M under shaking conditions, followed by incubation with appropriate volume of Hoechst-33258 solution diluted in PBS 0.1 M. For longer preservation, the solution was removed and 50 µL of aqua Poly/mount (PolySciences Inc) was added to each well and covered with a glass slip.

Cerebral organoids were fixed in 4% PFA (w/v) for 30 min at 4°C followed by three washes with PBS 0.1 M. Cerebral organoids were then placed in sucrose solution (30% w/v) overnight before being embedded in O.C.T (Tissue-Tek). Embedded tissue was sectioned at 20 µm using a Cryostar NX70 Cryostat (Thermo Scientific) and mounted slides were stored at −80°C until immunostaining was performed. For immunostaining, tissue sections were brought to room temperature and then rehydrated with 3 washes with 0.1 M PBS, each for 5 mins. Slides were then washed once with PBS with 0.2% Triton X-100 for 15 mins. Tissue was blocked using 10% of donkey serum in PBS 0.1 M for 1 h at room temperature. After blocking, primary antibodies were added to 0.2 % Triton X-100 and 10% of donkey serum in PBS 0.1 M at appropriate dilutions and incubated overnight at 4°C.The next day, slides were washed with PBS 0.1 M 3 times for 5 min each with gentle shaking. Subsequently, slides were incubated with Alexa Fluor®-conjugated secondary antibodies in 0.2 % Triton X-100 and 10% of donkey serum in PBS 0.1 M for 2 h at room temperature in the dark. After secondary antibody incubation, slides were washed 3 times with PBS for 5 min with gentle shaking. Nuclei were visualized by incubating the tissue for 5 min with Hoechst 33258 stain in PBS 0.1 M. Sections were mounted using aqua Poly/mount (PolySciences Inc). Images were acquired using an LSM 880 Confocal Scanning Microscope in concert with the ZEISS ZEN imaging software housed at the Imaging Platform of the Pasteur Institute, Lille. Alternatively, the X-light V3 Spinning Disk System (Nikon) was equally used to take images from the 2D cultures. The images were processed in Fiji-ImageJ and the figures assembled in Adobe Illustrator 2022.

Table 2: List of primary antibodies used on immunostaining

Target	Specie	Reference	Company
CTIP2	Rat	Ab18465	Abcam
GFAP	Chicken	173006	Synaptic System
GFAP	Rabbit	840001	BioLegend
GFP	Chicken	GFP-1020	Aves
MAP2	Chicken	188006	Synaptic Sytems
NESTIN	Mouse	MAB5326	Millipore
NESTIN	Rabbit	841901	BioLegend
NEUN	Guinea Pig	266,004	Synaptic Systems
PAX6	Rabbit	ab5790	Abcam
PAX6	Rabbit	901301	Biolegend
SOX2	Rat	14-9811-82	Invitrogen
TUBULIN BETA III	Mouse	MAB1637	Millipore
TUBULIN BETA3	Mouse	801202	BioLegend

Table 3: List of secondary antibodies used on immunostaining

Target	Specie	Reference	Company
488	Chicken	703-545-155	Life technology
Alexa 488	Mouse	715-545-151	Jackson ImmunoResearch
Alexa 647	Rabbit	711-605-152	Jackson ImmunoResearch
Alexa 488	Rat	712-545-153	Jackson Immunoreserach
Alexa 488	Guinea Pig	A11073	Life technology
Cy3	Mouse	715-165-151	Jackson
Cy3	Chicken	703-165-155	Jackson
Cy3	Rat	712-165-153	Jackson Immunoreserach
DAPI	-	9564	Life Technology

8. Immunobloting

Samples from the 2D and 3D cultures were collected in RIPA buffer containing protease and phosphatase inhibitors (Complete mini, Roche Applied Science) and sonicated several times at 60%-70% for 10 seconds prior to use for the immunoblotting analyses. Protein quantification was performed using the BCA protein assay (ThermoFisher Scientific). 10 µg of protein from extracts were separated in NuPAGE 4-12% Bis-Tris Gel 1.0 mm (NP0321BOX, Thermo Scientific). As reference, 5-10ul of the leader (Novex Sharp – Invitrogen) was loaded on each extremity of the gel. For the running, MES buffer was used for proteins lower than 45 kDa and MOPS buffer for proteins above that. After that, gels were transferred on nitrocellulose membranes 0.2 µm (#1704158, Bio-Rad). Next, membranes were incubated in milk (5% in Tris-buffered saline with 0.1% Tween-20 (TBST)) or SuperBlock (37536, ThermoFisher Scientific) to block non-specific binding sites for 1 hour at room temperature, followed by several washes with TBST 0.1% as washing buffer.

Immunoblottings were carried out with primary antibodies overnight at 4°C under shaking condition. The membranes were washed four times in the washing buffer, followed by incubation with HRP-conjugated secondary antibodies for 2 hours at room temperature under shaking condition. The membranes were washed four times in washing buffer, and the immune reactivity was revealed using the ECL chemiluminescence system (SuperSignal, ThermoScientific) and imaged using the Amersham Imager 600 (GE Life Sciences). Optical densities of bands were quantified using the Gel Analyzer plugin in Fiji–ImageJ.

Table 4: List of primary antibodies used on immunoblotting

Target	Specie	Reference	Company
APP C-term	Rabbit	A8717	Sigma
ERK1/2	Mouse	4696	Cell signaling
GAPDH	Chicken	AB2302	Millipore
GSK-3β	Mouse	610202	BD bioscience
hTAU pThr231	Mouse	RZ3	P. Davies
hTAU-C	Rabbit	A0024	Dako
LKB1	Rabbit	3047	Cell signaling
p38 MAPK	Rabbit	9212	Cell signaling
P-ERK1/2 pThr202/Tyr204	Rabbit	9101	Cell signalling
P-GSK3B pSer9	Mouse	GTX29769	GeneTex/ Euromedex
P-GSK3B pTyr216	Mouse	612313	BD bioscience
P-hTAU pSer202	Mouse	CP13	P. Davies
P-LKB1 pSer428	Rabbit	3482	Cell signaling
P-p38 pThr180/Tyr182	Rabbit	4511	Cell signaling
P-PTK2B pTyr402	Rabbit	3291	Cell Signaling
P-SRC Family pTyr416	Rabbit	6943	Cell signalling
P-TAU PHF-1 pSer396/Ser404	Mouse	PHF-1	P. Davies
P-TAU pTyr18	Mouse	MM-0194-100	MediMabs
P-TAU AT8 p Ser202/Thr205	Mouse	MN1020	Thermo Scientific
PTK2B	Rabbit	P3902	Merck
SRC	Rabbit	2109	Cell signalling
β-ACTIN	Mouse	A1978	Sigma

Table 5: List of secondary antibodies used on immunoblotting

Target	Reference	Company
HRP-Chicken	A16054	Life technology
HRP-Mouse	115-035-003	Jackson ImmunoResearch
HRP-Rabbit	111-035-003	Jackson ImmunoResearch
HRP-Rabbit	18-8816-33	Rockland

9. Proteome Profiler Array (Phopho panel)

The phosphor panel assay was carried out according to the original protocol from the Human Phospho-Kinase Array Kit (ARY003C, R&D Systems). Briefly, protein extracts from three organoids of each PTK2B WT, HET and KO genotypes were pooled in equal proportions and 10 µg of this pool was used.

On a rocking platform shaker, the Array Buffer was incubated for one hour for blocking. The Array Buffer was Aspirated and 1.0 mL of the prepared samples was added to both the Part A and Part B membrane. Membranes were Incubated overnight at 4 °C under shaker conditions. Membranes were then washed with 1X Wash Buffer for 10min under shaking conditions. Reconstituted Detection Antibody Cocktail A or B were diluted in 1X Array Buffer and 1ml of this solution was added to the respective membranes, which were incubated for 2h at room temperature. Membranes were then washed with 1X Wash Buffer for 10min under shaking conditions and exposed to 1ml of Chemi Reagent Mix during 1 minute. Detection was performed using the ECL chemiluminescence system (SuperSignal, ThermoScientific) and imaged using the Amersham Imager 600 (GE Life Sciences). Optical densities of the bands were quantified using the Gel Analyzer plugin in Fiji-ImageJ.

Table 6: List of antibodies used on the Proteome Profiler Array

Name	Target
AKT 1/2/3	T308
AKT 1/2/3	S473
B-CATENIN	-
CHK-2	T68
C-JUN	S63
CREB	S133
EGFR	Y1086
eNOS	S1177

ERK 1/2	T202/Y204, T185/Y187
FGR	Y412
GSK3-α/β	S21/S9
GSK3β	S9
HSP27	S78/S82
HSP60	-
JNK 1/2/3	T183/Y185, T221/Y223
LCK	Y394
LYN	Y397
MSK 1/2	S376/S360
p38a	T180/Y182
P53	S15
p70 S6 kinase	T389
p70 S6 kinase	T421/S424
PDGF Rbeta	Y751
PLC-γ1	Y783
PRAS40	T246
RSK 1/2	S221/S227
RSK 1/2/3	S380/S386/S377
SRC	Y419
STAT1	Y701
STAT2	Y689
STAT3	Y705
STAT3	S727
STAT5 a/b	Y649/Y699
STAT6	Y641
WNK1	T60
YES	Y426

10. Viral Transductions

Lentiviral constructs were produced by the Vect'UB platform at the TBM Core unit, University of Bordeaux, Bordeaux, France (CNRS UMS 3427, INSERM US 005). The lentiviral constructs used were TTA (Vect'UB; ID # 571) and TetO-Ngn2-Puro (Addgene, # 97329). Lentiviral infections were performed on hiPSCs qt multiple passages, transduced at a multiplicity of infection (MOI) of 2.5. In brief, hiPSCs wsere plated at a density of 400 000 cells per well of a 6-well plate. After plating the cells for 4 hours, we mixed the appropriate volumes of each lentiviral construct in complete mTeSR medium. Next, we added 50 µl of the viral medium mix to each well. We first transduced the TTA construct in the hiPSCs.

After one passage, we transduced the TTA-transduced cells with the NGN2 construct. The cells that had both viral constructs were then expanded further for 1 or 2 passages before being used for differentiation into hiNs. The differentiation process continued for 4-5 weeks before conducting MEA electrophysiology or imaging.

11. snRNA-sequencing Library Preparation

Nuclei isolation and Hash-tagging with oligonucleotides steps were realized on ice with pre-cold buffers and centrifugations at 4°C. *PTK2B* WT, HET, and KO or 6.5-month-old organoids were processed as previously described by our team (1). 2D cultures at 4 or 5 weeks were washed in the imaging plate wells with 500 µL of Deionized Phosphate Buffer Saline 0.1M (DPBS, GIBCO™, Fisher Scientific 11590476). Cells were resuspended in 1 ml of Lysis Buffer (Tris-HCL 10mM, NaCl 10mM, MgCl2 3mM, Tween-20 0,1%, Nonidet P40 Substitute 0,1%, Digitonin 0,01%, BSA 1%, Invitrogen™ RNAseout™ recombinant ribonuclease inhibitor 0,04 U/µL). Multiple mechanical resuspensions in this buffer were performed for a total lysis time of 15 mins., 500 µL of washing buffer was added (Tris-HCL 10mM, NaCl 10 mM, MgCl2 3 mM, Tween-20 0.1%, BSA 1%, Invitrogen™ RNAseout™ recombinant ribonuclease inhibitor 0,04 U/µL) and the lysis suspension was centrifuged 10 mins. at 500 g and 4°C (used for all following centrifugation steps). Nuclei pellets were washed tree times with one filtration step by MACS pre-separation filter 30µm (Miltenyi Biotec). Nuclei pellets were resuspended in 100 µL of staining buffer (DPBS BSA 2%, Tween- 20 0.01%), 10 µL of Fc blocking reagent HumanTruStainFc™ (422302, Biolegend) and incubated 5 min at 4°C. 0.5-1µl of antibody was added to each condition (Total-Seq™-A0453 anti-Vertebrate Nuclear Hashtag 3 MAb414 for the WT and Total-Seq™-A0454 anti-Vertebrate Nuclear Hashtag 4 MAb414 for the KO, 97286 and 97287 respectively, Biolegend) and incubated 15 mins. at 4°C. Nuclei pellets were washed three times in staining buffer with one filtration step by MACS pre-separation filter 30 µm (Miltenyi Biotec) to a final resuspension in 300 µL of staining buffer for Malassez cell counting with Trypan blue counterstaining (Trypan Blue solution, 11538886, Fisherscientific). Isolated nuclei were loaded on a Chromium 10X genomics controller following the manufacturer protocol using the chromium single-cell v3 chemistry and single indexing and the adapted protocol by Biolegend for the HTO library preparation. The resulting libraries were pooled at equimolar proportions with a 9 for 1 ratio for Gene expression library and HTO library respectively. Finally, the pool was sequenced using 100pb paired-end reads on NOVAseq 6000 system following the manufacturer recommendations (Illumina).

12. snRNA-seq Dataset Preprocessing

Unique Molecular Index (UMI) Count Matrices for gene expression and for Hash Tag Oligonucleotide (HTO) libraries were generated using the CellRanger count (Feature Barcode) pipeline. Reads were aligned on the GRCh38-3.0.0 transcriptome reference (10x Genomics). Filtering for low quality cells according to the number of RNA, genes detected, and percentage of mitochondrial RNA was performed. For HTO sample, the HTO matrix was normalized using centered log-ratio (CLR) transformation and cells were assigned back to their sample of origin using HTODemux function of the Seurat R Package (v4) (229). Then, normalizations of the gene expression matrix for cellular sequencing depth, mitochondrial percentage and cell cycle phases using the variance stabilizing transformation (vst) based Seurat:SCTransform function were performed.

13. snRNA-seq datasets integration and annotation

To integrate the datasets from independent experiments, the harmony R package (https://github.com/immunogenomics/harmony) was used. In order to integrate the datasets, the SCTransform normalized matrices was merged and PCA was performed using Seurat::RunPCA default parameter. The 50 principal components (dimensions) of the PCA were corrected for batch effect using harmony::RunHarmony function. Then, the 30 first batch corrected dimensions were used as input for graph-based cell clustering and visualization tools. Seurat::FindNeighbors using default parameters and Seurat::FindClusters function using the Louvain algorithm were used to cluster cells according to their batch corrected transcriptomes similarities. To visualize the cell's similarities in a 2-dimension space, the Seurat::RunUMAP function using default parameters was used. Cell clusters were then annotated based on cell type specific gene expression markers.

14. Differential gene expression and GO enrichment analyses

For snRNA-seq experiments performed from 2 or less culture batches (*i.e.* organoid and nifedipine experiments), gene expression within each main cell type was compared between conditions of interest using Wilcoxon test on the SCTransform normalized gene expression matrix. For snRNA-seq experiments performed from 3 or more culture batches (*BIN1* KO vs WT hiNs comparison), Pseudobulk differential expression analysis was performed using the package DESeq2 (CRAN). For each main cell type, the cell level gene expression matrix was first aggregated at the sample level using Matrix:: aggregate.Matrix function. Genes detected in more than 100 cells or in 10% of the cells were tested for differential expression using DESeq function, including in the model the experiment batch as covariate.

GO enrichment analysis on the differentially expressed genes was performed using the gost function of the gprofiler2 R package (CRAN), using default parameter, or, if specified using fast gene-set enrichment analysis (FGSEA) (230), package (Bioconductor).

15. Activity-related genes (ARGs) signature enrichment analysis at single cell resolution

To study enrichment for activity-related genes (ARGs) signatures across cerebral organoid cells, the CellID R package (https://github.com/RausellLab/CelliD) was used. ARGs obtained from Tyssowski et al. (2018) (231) and Hrvatin et al. (2018) (232), were translated to the corresponding human gene name with the help of the biomaRt package using the respective Ensembl references. Then, the CellID::RunMCA was used to extract cell-specific gene signatures and a hypergeometric test was performed to test enrichment for ARGs in these cell signatures. To test the differential proportion of ARGs enriched cells in BIN1 deleted organoid compared to WT organoid, chi-squared test was performed.

16. AlphaLISA measurements

Cell culture media samples for AlphaLISA measurements were collected at the end of the 3rd and 4th weeks of differentiation of the ASCL1-hiNs. Alpha-LISA kits specific for human Aβ1–X (AL288C, PerkinElmer) and Aβ1–42 (AL276C, PerkinElmer) were used to measure the amount of Aβ1–X and Aβ1–42 respectively in culture media. The human Aβ analyte standard was diluted in the BrainPhys medium. For the assay, 2 µL of cell culture medium or standard solution was added to an Optiplate-384 microplate (PerkinElmer). 2 µL of 10X mixture including acceptor beads and biotinylated antibody was then added to the wells with culture media or standard solution. Following incubation at room temperature for an hour, 16 µL of 1.25X donor beads was added to respective wells and incubated at room temperature for 1 hour. Luminescence was measured using an EnVision-Alpha Reader (PerkinElmer) at 680-nm excitation and 615-nm emission wavelengths.

17. Exposure to $A\beta_{1-42}$ treatment

Spontaneously differentiated 5 week cultures containing hiNs and hiAstros were exposed to low concentrations of $A\beta_{1-42}$ during 24 hours prior to Calcium Imaging recordings. Commercially available $A\beta_{1-42}$ (641-15, Echelon Biosciences Inc./California Peptide) were resuspended in DMSO at the concentration of 100 uM and re-diluted in supplemented BrainPhys medium to reach a final concentration of 100pM. The inverted (42-1) control peptide (ICP) is a peptide with the reverse amino acid sequence of $A\beta_{1-42}$ and was used as control. Additionally, a similar volume of DMSO used as a vehicle was added to blank controls.

After 24h, the medium was changed for fresh supplemented Brain Phys and the cells were treated with Oregon Green to proceed with the calcium imaging recordings.

18. Calcium Imaging Experiments

Real-time calcium imaging recordings were performed in 2D cultures after 5 - 6 weeks of spontaneous differentiation. Prior to imaging, the cells were incubated with Oregon Green™ 488 BAPTA-1 (OGB-1) acetoxymethyl (AM) (ThermoFisher Scientific) for 1 h at 37°C. A 2.5 mM stock solution of the calcium-indicator dye was prepared in Pluronic™ F-127 (20% solution in DMSO) (ThermoFisher Scientific). 1 µL of the dye solution was added to 500 µL of existing BrainPhys medium in each well of a 24-well cell imaging plate. The other half of existing BrainPhys media from the wells of the plate was previously removed and kept aside while the calcium-indicator dye was incubated in fresh BrainPhys medium. After 1 h of incubation, the medium which was kept aside was replaced to each well. The 2D cultures were then ready to be imaged using a Spinning Disk Microscope (Nikon) housed at the Institut Pasteur de Lille, Lille, France using the MetaMorph imaging software.

For imaging the calcium transients, 1000 images were taken using a 20X or 40X long-distance objective, with 10 ms exposure time and 200 ms intervals, during a total of $2.1x10^5$ms. For each well, up to 5 random fields were chosen, and the cellular activity was recorded. Pharmacological assays using competitive antagonists of $GABA_A$ (BIC, from bicuculline) or AMPA/kainate (CNQX) receptors at 100uM confirmed that calcium spikes in hiNs are mediated by chemical synapses.

19. Analyses of Calcium Transients

Time-series data from calcium imaging recordings were at first converted to .avi format after background subtraction by use of ImageJ software. The videos were subsequently opened on CALciumIMagingAnalyzer (CALIMA) software (Eindhoven University of Technology, The Netherlands).

Each video recording of a field of cells was first downscaled to 2X in terms of size with a 10X zoom and was checked for the frame average mode. Moreover, in this first detection stage, pre-set filter parameters were adjusted several times in each field and applied to enable the detection of the maximum number of fluorescent cells. During this step, the automatically detected cells appeared on red and were checked to ensure that only neurons were computed. In cases were needed, manual exclusion was also implemented to eliminate double labeling, ensuring precision in the analysis.

Once at the “Analysis Stage”, detection of the average activity was checked and a median of 3 was applied. All cells within the pre-set filter parameters are detected as regions of interest

(ROIs) in the detection stage. Cell activity from all detected ROIs is then recorded. However, in the subsequent analysis stage, only cells showing a peak detection of Ca^{2+} transients with a standard deviation of at least 2 or more were taken into consideration. At this stage, the parameters for “Spike detection” were individually adjusted for each field, in order to minimize the probability of overlooked peaks and to ensure accurate identification and exclusion of noise from the OGB signal detection. Data in the form of “detected spikes” and “correlation (peak)” are extracted and exported as .csv files. These .csv files were then used to perform the statistical analysis on GraphPad Prism 8.

20. MEA recordings in 2D cultures

PTK2B-mutated cells were cultured on MEA 96- or 24-well plates (CytoView MEA 96/24, Axion Biosystems, USA). Recordings of the extracellular action potentials were performed in 3 independent cultures for each genotype of either ASE- or BION-derived cells. Before recordings, MEA plate were incubated for 5 min in the MaestroPro machine to allow the stabilization of the temperature at 37°C and the CO_2 at 4%. Spontaneous activity was then recorded for 3 min, at 12.5 kHz sampling rate, using AxIS Navigator software (Axion Biosystems). Spikes were detected using a fixed amplitude threshold of 5.5 of the high-pass filtered (>300 Hz) signal for positive- and negative-going signals. The detection included a dead time of 3 ms to account for the refractory period of action potentials. Quantification of the number of detected spikes and spike bursts (defined as at least 5 spikes within 50 ms) in the Multi Unity Activity (MUA) data was performed using Multi- Channel Analyzer 2.16.0 software (Multi-Channel Systems).

Recordings of NGN2-hiNs cultured in microfluidic devices bound to multi-electrode arrays (256MEA100/30iR-ITO, Multi-Channel Systems, Germany) were performed using the MEA2100-256-System (Multi-Channel Systems). Extracellular action potentials were recorded at 2, 3, and 4 weeks of differentiation. Before recordings, MEAs were let stabilize for 5 min on the headstage at 37°C to reduce artifacts due to medium movement. Signals were recorded for 1 min, at 40 kHz sampling rate, using Multi Channel Experimenter 2.16.0 software (Multi-Channel Systems).

21. Spike sorting and temporal structure of spontaneous activity

Channels containing detected waveforms from MUA data were manually processed offline for spike waveform separation and classification using Offline Sorter v3 (Plexon, USA). Briefly, we applied principal component analysis (PCA) to cluster spike waveforms of similar morphologies. Using this approach, we identified from 2 to 10 well-isolated units per channel, and therefore, we considered this single-unit activity (SUA). For each SUA, we

computed the average firing rate, the signal-to-noise ratio, the peak-to-trough amplitude and duration, the average power (square amplitude of the average waveform), the mode of the inter spike interval distribution, and their firing patterns. It has been demonstrated that dissociated neuronal cultures can develop complex discharge structures ((233) and (234)). Here, we considered burst activity if the SUA presents periods of high-frequency discharges interspersed by regular or no discharges at all. Operationally, a burst measured on SUA data must have at least 3 spikes within 100 ms and 200 ms intervals, for the interval between the first and the second, and the second and the third discharge, respectively. After the third spike, the maximal interval to consider a discharge part of the burst was 200 ms. Thus, we computed the SUA that presented bursts, the number of bursts (i.e., the burst frequency), the average burst duration, the number of spikes within each burst, the average burst frequency, and the inter-burst interval. To evaluate the temporal structures of spike trains, we computed the array-wide spike detection rate (ASDR), which is the number of spikes detected per unit of time, summed over all electrodes in the same well. This method is commonly used in the literature to demonstrate synchronous activity (aka, bursts) in MUA data (233).

22. Statistical Analysis

Statistical analysis for the RNA-seq experiments was carried out using RStudio (RStudio Team (2020). RStudio: Integrated Development for R. RStudio, PBC, Boston, MA URL http://www.rstudio.com/).

For all other experiments, statistical analyses and preparation of graphs were performed using GraphPad Prism 8 (San Diego, CA, USA). For all statistical comparisons, we initially assessed the normality of data distribution through the Kolmogorov-Smirnov and/or Shapiro-Wilk tests with an alpha=0.05. Subsequently, we compared group variances using the appropriate parametric or non-parametric tests noted in figure legends. In summary, for comparisons of different genotypes following a normal distribution, Ordinary One-Way ANOVA with Tukey's Multicomparisson's test was performed. For data not meeting normal distribution criteria, a Kruskal-Wallis test was performed with a Dunn's multiple comparison test for comparison between each condition.

Data in plots are represented as mean + standard deviation (SD). An α-error level of $p < 0.05$ was considered significant.

Results

1. Characterization of PTK2B hiPSC lines

We used two different iPSC lines manipulated via Clustered Regularly Interspaced Short Palindromic Repeats (CRISPR)/Cas9 to generate neural cells expressing different levels of PTK2B. ASE 9109-derived cell lines were the main ones used in this work. In a complementary way, in order to confirm in an independent clone some of the main results obtained, BION-derived lines were further employed.

1.1. ASE 9109 iPSC line

ASE 9109 (Applied Stem Cells) were used to generate isogenic *PTK2B* wild-type (WT), heterozygous (HET) and knockout (KO) clones through target gene-editing of the exon7. Cas9/gRNA mediated indel formation at the targeted region caused by nonhomologous end joining (NHEJ) results in frameshift and/or premature stop, thus generating a knockout of the gene of interest (Fig. 6A-B). After the single cell cloning process, cells were subject to genotyping analysis. One homozygous clone CL2 (-11bp), one heterozygous clone CL5 (-14bp/WT), and one isogenic WT clone CL28 were identified for the desired knockout for *PTK2B*.

To check the genetic stability of our cell lines, we performed a quantitative PCR for detection of the most common karyotypic abnormalities in hiPSCs (Stemcell Technologies). Analyses were performed for nine genomic locations (1q, 4p, 8q, 10p, 12p, 17q, 18q, 20q, and Xp) using DNA obtained from *PTK2B* WT, HET, KO and different control cell lines. We observed that our CRISPR/ca9 edited cells have micro duplications in the 20q chromosomes likely inherited from the parental ASE-9109 hiPSc line (Ctrl ASE) (Fig. 6C). This type of microduplication has been described in other cell lines subjected to long term manipulation (235). Moreover, as they are common to all three genotypes studied here, they should not interfere with the results described here after. All other genomic locations analyzed showed no alterations.

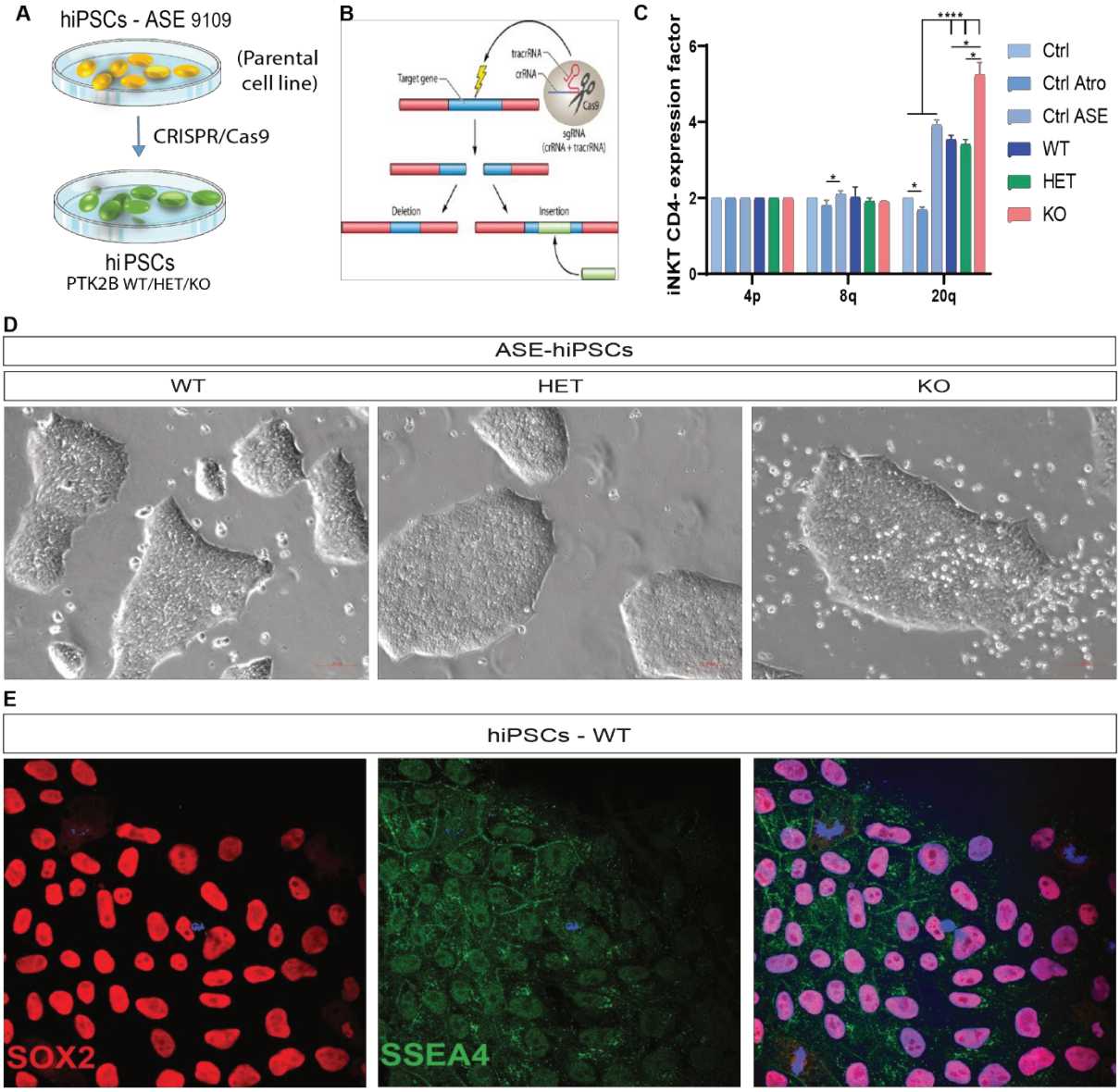

Figure 6. Generation of PTK2B knockout hiPSC lines. A) Scheme of iPSCs from the parental cell line genome edited by CRISPR-Cas9 technology. **B)** Image representing a small guide (sg) RNA designed against a target gene, allowing the hybridization and cleavage by Cas9 enzyme, and thus the editing of PTK2B. **C)** Representation of some of the genome locations (4p, 8q, and 20q) evaluated by qPCR on ASE-derived hiPSCs and controls. **D)** Undifferentiated ASE-derived hiPSCs cultures on phase-contrast - PTK2B WT, HET and KO. Scale bar: 100um. **E)** Representative immunostaining images of PTK2B WT hiPSCs expressing the pluripotent markers SOX2 (red) and SSEA4 (green).

We also characterized the different iPSC lines morphologically and immunophenotypically. In the pluripotent stage, all the cell lines showed similar growth rates and generated hiPSC colonies of similar morphologies, with clear, well-defined edges, prominent nucleoli and a high nucleus/cytoplasm ratio, typical of hiPSCs (Fig. 6D). They also expressed similar levels of the pluripotent markers SOX2 (for SRY-Box Transcription Factor 2) and SSEA4 (for Stage-

specific embryonic antigen 4) (Fig. 6E – representative figure for the WT), indicating that the CRISPR/Cas9 gene-edited ASE-iPSC lines had similar pluripotent properties.

1.2. BION iPSC line

BION;010-C2 (European Bank of induced pluripotent Stem Cells - EBiSC) was used to generate a second pair of *PTK2B* WT (named C2) and *PTK2B* HET (named PT26) iPSC clones, as well an additional iPSC clone carrying the SNP rs28834970:TC (named S5). This variant is deleterious for *PTK2B* and is associated with an increased risk to develop AD (127). These isogenic iPSC clones were kindly provided by Dr. Sandrine Thuret (King's College, London – UK) at the last year of this thesis.

2. Generation and characterization of Spontaneous Differentiated 2D cultures under-expressing PTK2B

To evaluate the effects of *PTK2B* partial and null deletion in human neurons, we first induced the *PTK2B* WT, HET and KO ASE-iPSCs into hiNPCs or neural aggregates, which were subsequently differentiated into neurons and glial cells using 2D or 3D cultures, as previously described by our group (1) (Fig. 7).

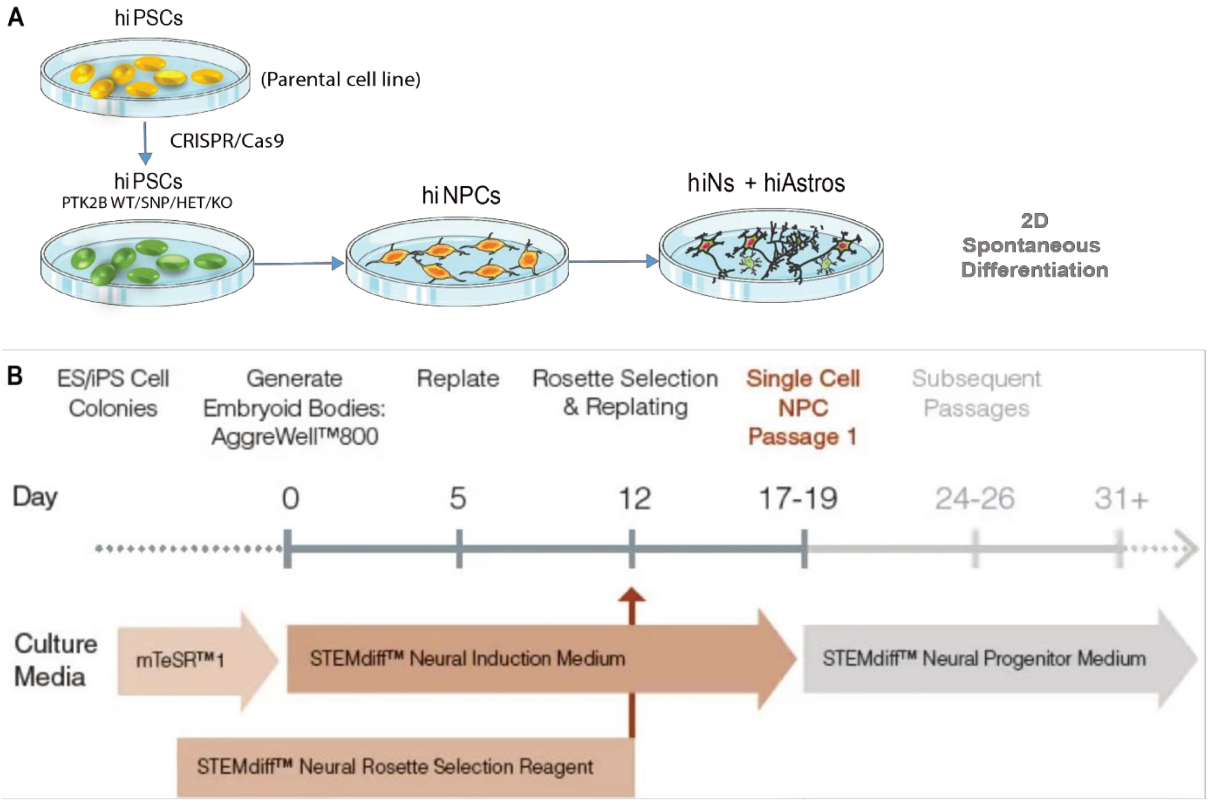

Figure 7. Generation of 2D spontaneously differentiated cultures. Scheme showing **(A)** the hiPSCs from the parental cell lines CRISPR/Cas9-edited to generate either the PTK2B WT, HET, and KO cell lines (ASE-derived) or the C2 (WT), S5 (SNP), and PT26 (HET) cell lines (BION-derived). **B)** The spontaneous differentiation of 2D

cultures from hiPSCs to hiNPCs and hiNs and hiAs. **C)** the 3D generation of cerebral organoids from hiPSCs through neural aggregates stage.

Adapted from STEMdiff™ Neural System technical manual (Stemcell Technologies).

In the 2D model, the process of differentiation into specialized cells is based on changes in the culture medium and is called here "spontaneous differentiation" to distinguish it from the one mediated by transcription factors, such as NGN2. The spontaneous strategy is based on the monolayer method detailed by Stemcell Technologies and was used in this study for the neural induction of hiPSCs to hiNPCs (Fig. 7).

Briefly, this method consists in a serum-free SMAD inhibition-mediated neural induction. It is based on high density seeding of hiPSCs in a supplemented Neural Induction Medium (NIM) (Stemcell Technologies) for approximately three weeks, followed by maintenance in supplemented Neural Progenitor Medium (NPM) until its differentiation into neurons (hiNs) and astrocytes (hiAs). These derived cells were obtained from the seeding of 100,000/well of hiNPCs in NPM for 24 h, followed by an equal volume of BrainPhys medium (supplemented with BDNF, GDNF, laminin, dibutyryl-cAMP, ascorbic acid, N2, and SM1). Subsequently, complete BrainPhys media was changed bi-weekly until 4 or 5 weeks of differentiation.

2.1. PTK2B WT, HET and KO hiNPCs readily generate hiNs/hiAs cultures

The cellular composition of the 2D cultures was evaluated through different methods. Firstly, we performed immunocytochemistry on the ASE-derived cells using antibodies against cell-specific markers for the pluripotent and the specialized cells (Fig. 8). The hiNPCs of all genotypes expressed properly SOX2 and NESTIN, classical markers of neural progenitor cells (Fig. 8B). After 5 weeks, differentiated cultures expressed the neuronal marker MAP2, the astrocyte marker GFAP, and the neural progenitor marker NESTIN, characterizing a successful spontaneous differentiation from hiNPCs (Fig. 8C). At this differentiated stage, PTK2B HET cells expressed 77% less protein than its isogenic WT. The KO cells did not express detectable levels of PTK2B (Fig. 8D-D').

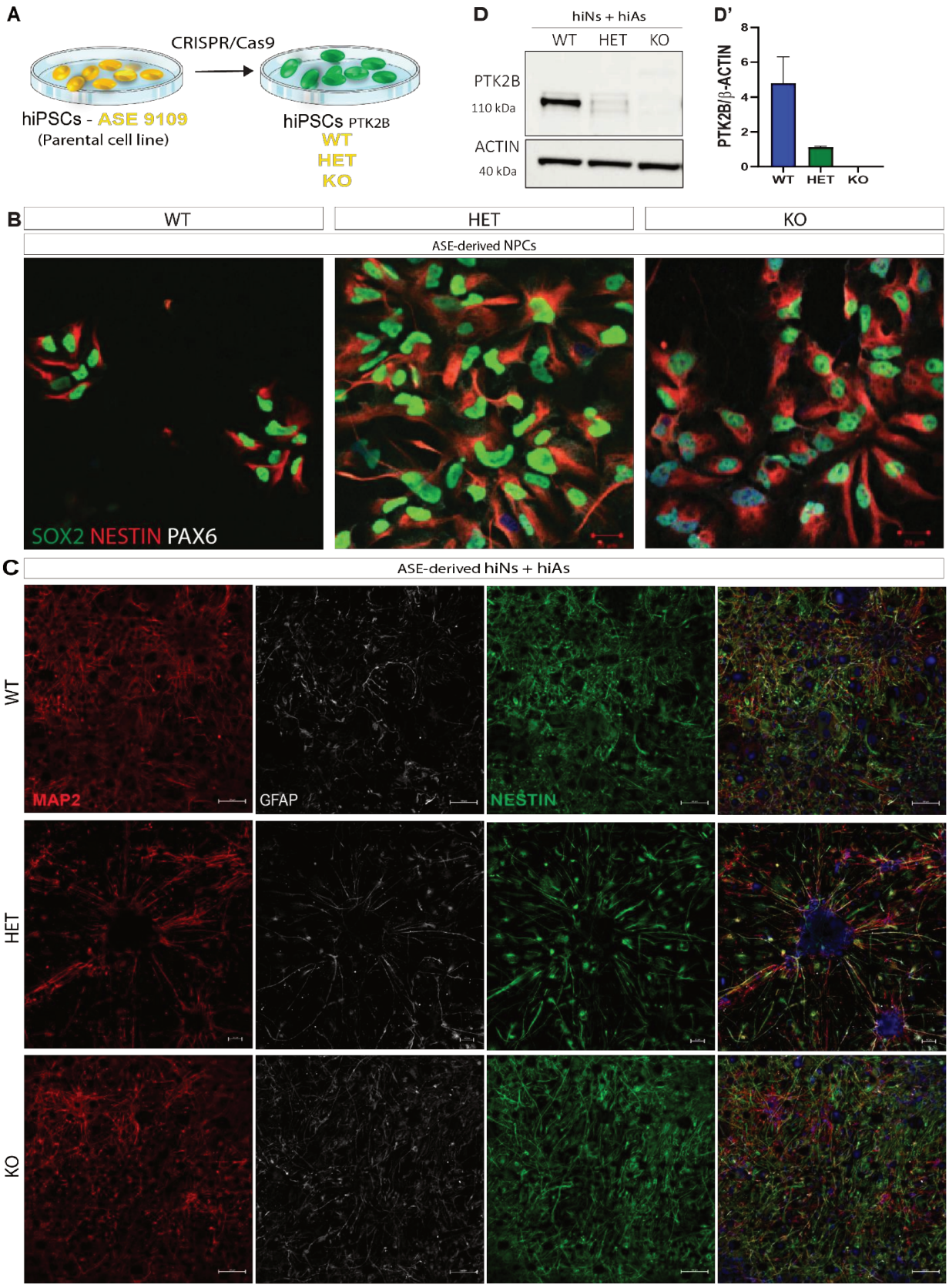

Figure 8. Characterization of ASE 9109–derived hiNPCs and differentiated neural cultures in 2D. A) Scheme representing the obtention of the three cell lines derived from ASE 9109 parental clone (main cell line used in this thesis). **B)** Representative images of PTK2B WT, HET, and KO NPCs stained for the pluripotent markers SOX2 (green), NESTIN (red), and PAX6 (white); and DAPI (blue). **C)** Representative images of mixed neuron/glia 2D cultures derived from hiNPCs after 5 weeks of differentiation and stained for the neuronal marker

MAP2 (red), the astrocyte marker GFAP (white), the neural progenitor marker NESTIN (green), and DAPI (blue). **D-D')** Western blotting showing the PTK2B expression levels normalized by B-ACTIN in WT, HET, and KO 5 weeks differentiated cultures; N = 4 different cell passages.

Next, we performed single-nucleus RNA sequencing (snRNA-seq) experiments to further characterize the cell types/subtypes generated during the spontaneous differentiation of hiNPCs in the 2D cultures (Fig. 9). We found a small proportion of cells expressing genes of hiNPCs, whereas most cells expressed neuronal and astrocyte markers, indicating a successful differentiation of hiNPCs into the major neural lineages.

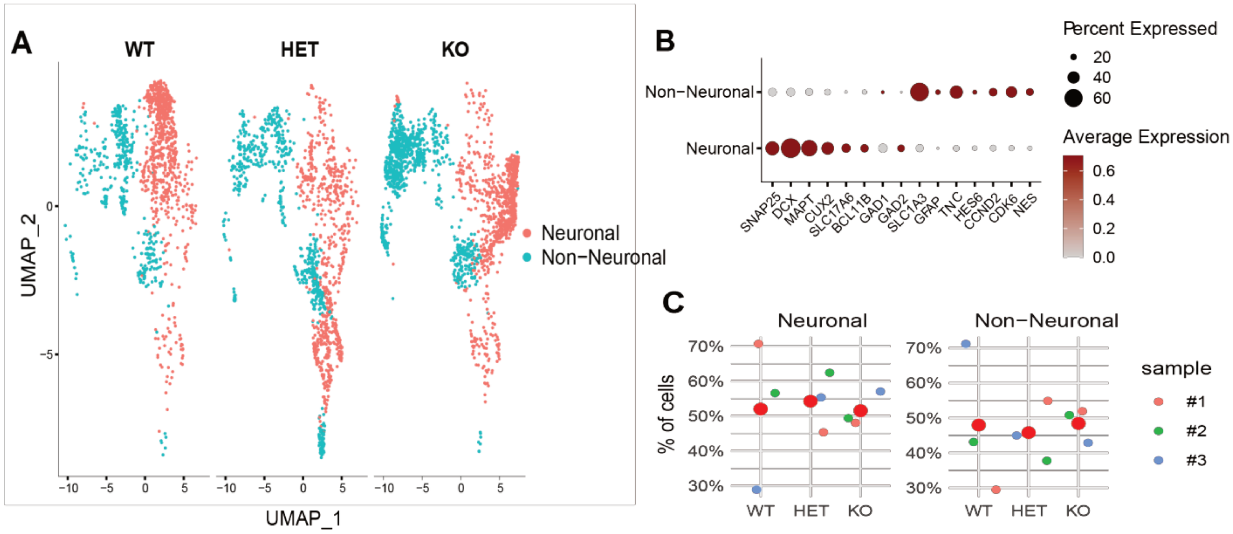

Figure 9: Modulation of *PTK2B* expression generates similar cultures composition at 5 weeks. 5 weeks 2D spontaneously differentiated neural cultures (ASE-derived cells). **A)** UMAP showing the cellular composition of *PTK2B* WT, HET and KO 2D cultures after 5 weeks of differentiation, snRNA-seq. data**. B)** Dot plot showing the list of genes used to classify neuronal and non-neuronal populations. Dots size indicates the percent expressed and the color gradient, the average expression. **C)** Percentage of neuronal and non-neuronal cells per independent experiment on each genotype.

We then proceeded with the characterization of the second hiPSC lines (Fig. 10). The neural differentiation of BION *PTK2B* WT, SNP, and HET hiPSCs in 2D was also characterized by immunocytochemistry. The iPSCs of all genotypes were efficiently induced into NPCs expressing NESTIN, SOX2 and PAX6 (Fig. 10B). The differentiation of NPCs into neurons and astrocytes expressing different levels of PTK2B was validated by western blotting and immunocytochemistry. All three cell lines efficiently differentiated into neurons and astrocytes expressing MAP2 and the glial fibrillary acidic protein (GFAP), respectively (Fig. 10C). PT26 (HET) cells expressed 63% less PTK2B than the C2 (WT) cells, whereas S5 (SNP) cells carrying the genetic variant for *PTK2B* expressed 33% less PTK2B than WT cells (Fig. 10D-D).

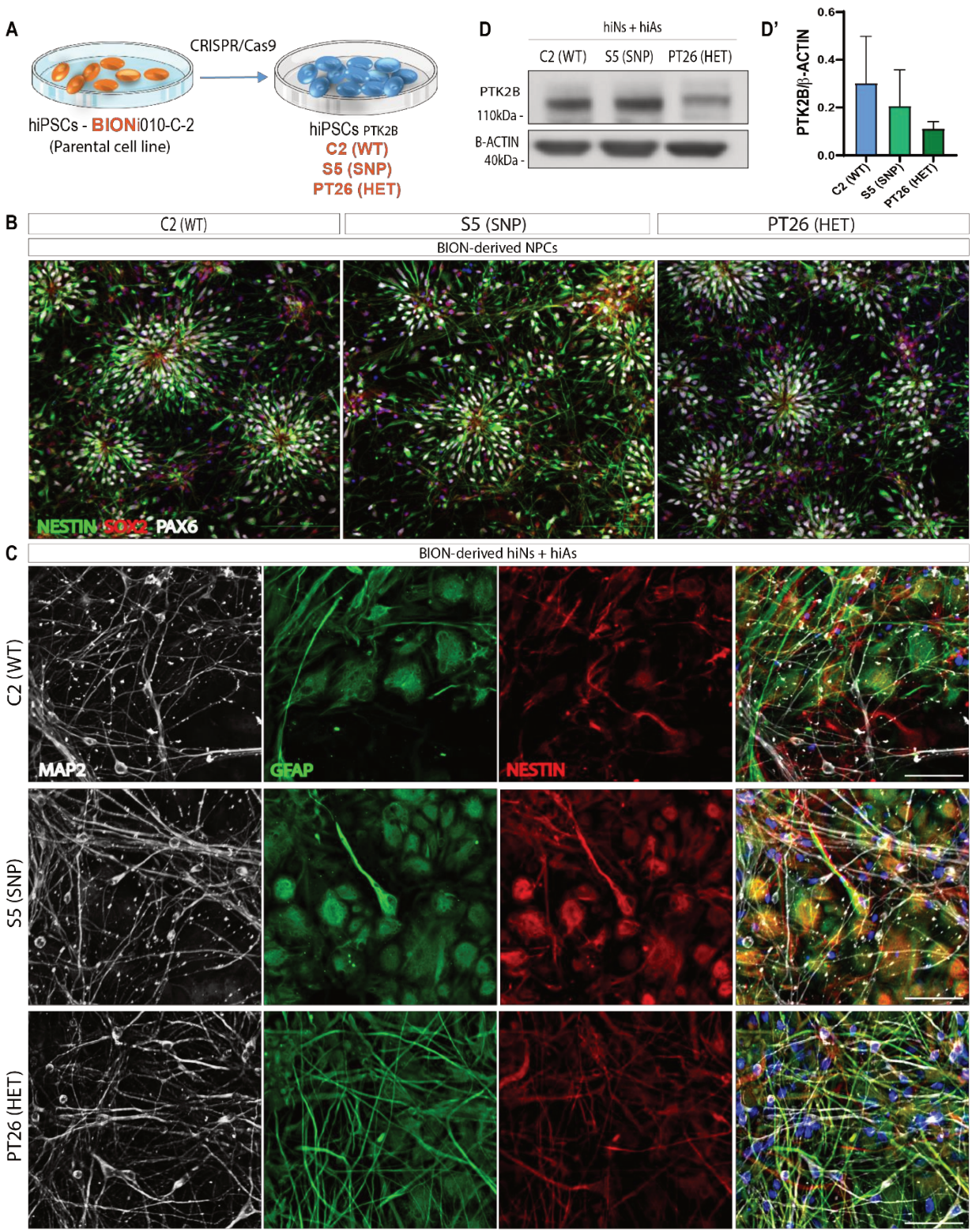

Figure 10: Characterization of BION–derived hiNPCs and differentiated neural cultures in 2D. A) Scheme representing the obtention of the three cell lines derived from BION parental clone. **B)** Representative images of PTK2B C2 (WT), S5 (SNP) and PT26 (HET) NPCs stained for NESTIN (green), SOX2 (red), PAX6 (white) and DAPI (blue) at passage 2. Scale bar 100um. **C)** Representative images of mixed neural 2D cultures derived from hiNPCs after 5 weeks of differentiation and stained for the neuronal marker MAP2 (white), astrocyte marker GFAP (green), NPC marker NESTIN (red), and DAPI (blue). **D-D')** Western blotting showing the PTK2B expression levels normalized by B-ACTIN in C2 (WT), S5 (SNP), and PT26 (HET) 5 weeks differentiated cultures.

3. Generation and characterization of PTK2B WT, HET and KO cerebral organoids (3D)

The monolayer culture protocol described above allowed us to take advantage of the fast differentiation and to easily record neuronal activity by calcium imaging experiments or Multi Electrode Array (MEA) electrophysiology. However, this system is limited in terms of cell maturation and cell-to-cell interactions. To circumvent these limitations, we used a 3D system to generate long-term cultures of human brain organoids from the ASE 9109-derived cell lines (Fig. 11). Besides the variability inherent to the method, the 3D culture provides a more complex and physiological system in terms of cell-to-cell signaling, recapitulating some aspects of the three-dimensional organization of the human brain ((227); (236)) (Fig. 11). It also allows us to work with long-term cultures (up to 6-9 months), harboring more mature neurons and glial cells.

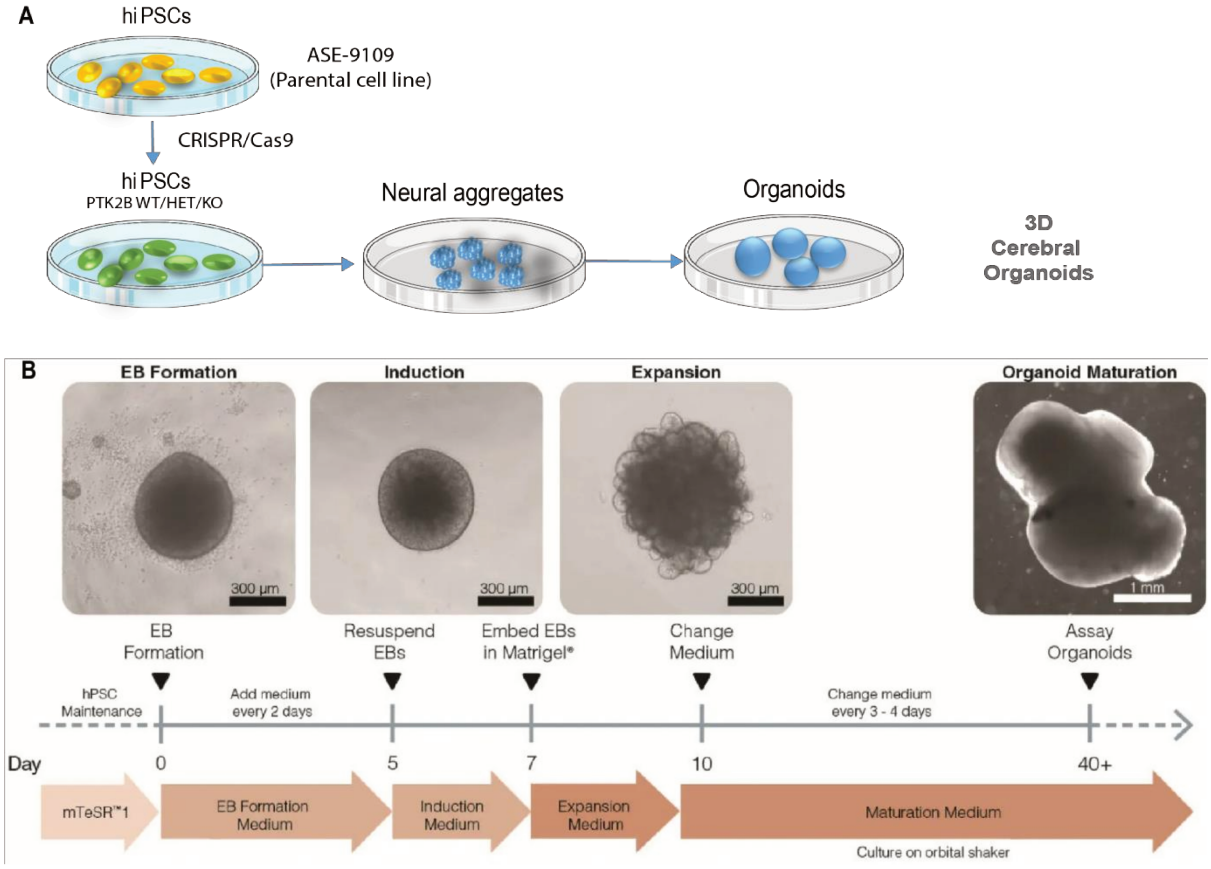

Figure 11: Protocol diagram for generation of cerebral organoids from hiPSCs. A) Scheme showing the hiPSCs from the parental cell line CRISPR/Cas9-edited to generate the PTK2B WT, HET, and KO cell lines (ASE-derived) used to generate 3D cerebral organoids through neural aggregates stage. B) Diagram representing the different culture steps to generate cerebral organoids based on the Stemcell Technologies's protocol.

Adapted from STEMdiff™ Organoid Kit datasheet (Stemcell Technologies).

In order to obtain the 3D cerebral organoids, the STEMdiff™ Cerebral Organoid Kit (Stemcell Technologies) was employed (Fig. 11). In sum, hiPSCs were firstly resuspended in Embryoid Body (EB) seeding medium at the density of 9000 cells per well in a 96-well round-bottom ultra-low attachment plate. After five days, 2 EBs were transferred to a 24-well ultra-low attachment plate with Induction Medium. Following a 2-day induction, the EBs were transferred to a drop of Matrigel for 3D expansion. Once the Matrigel polymerized using an embedding surface, the EBs were transferred to a 6-well ultra-low adherent plate with Expansion Medium. After 3 days, the medium was changed to Maturation Medium and placed in an orbital shaker at 65 RPM. Complete media changes were done bi-weekly until approximately 6 months, when the cerebral organoids were used for immunoblotting and snRNA-sequencing characterization.

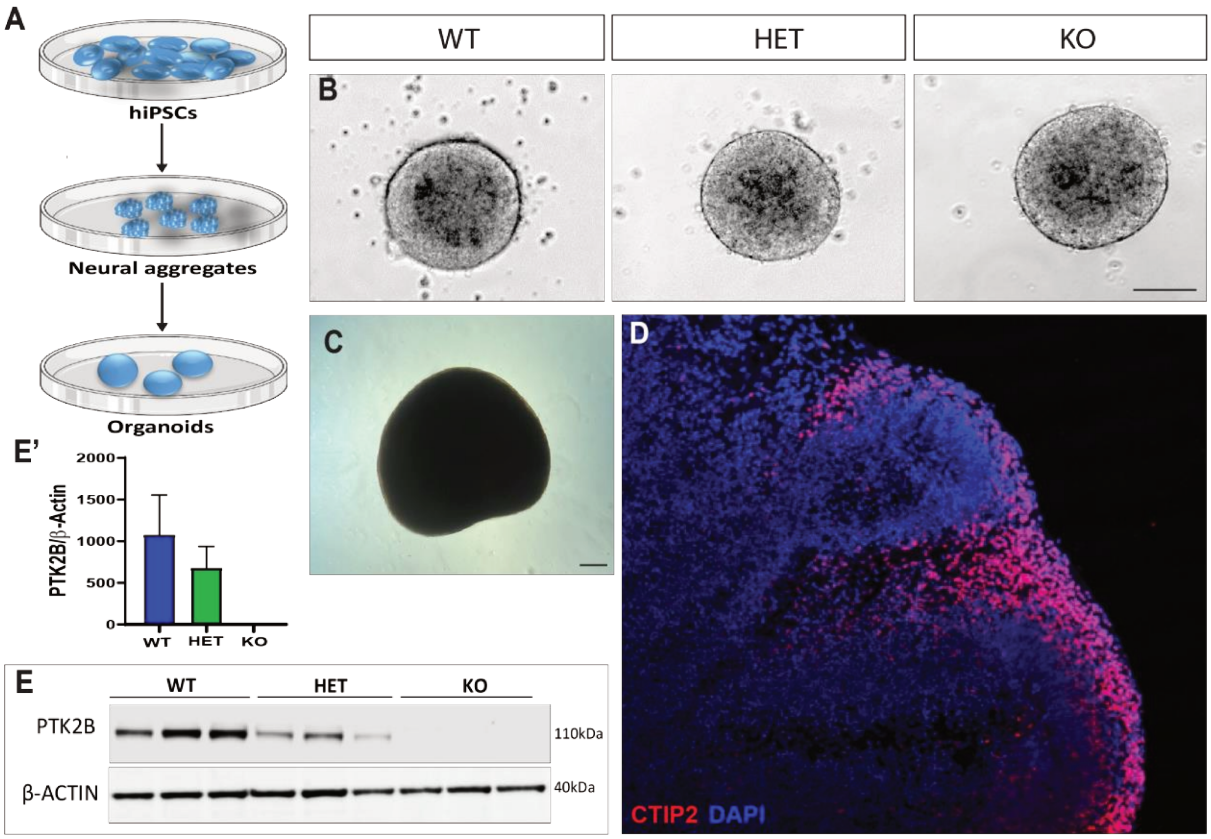

Figure 12: Characterization of *PTK2B* WT, HET, and KO cerebral organoids. ASE-derived 6 months cerebral organoids for *PTK2B* WT, HET and KO. **A)** Scheme showing the hiPSCs differentiation in cerebral organoids. **B)** Representative brightfield images of PTK2B WT, HET and KO 3D cultures at the neural aggregates (embryoid body) stage. Scale bar: 100µm. **C)** Brightfield image of a PTK2B *WT* organoids after 145 days in culture. Calibration bar: 200µm. **D)** Coronal section of a 60 days cerebral organoid showing expression of the neuronal marker CTIP2 (red) and nuclei staining with DAPI (blue). **E-E')** Western blotting of 6 months organoids showing the PTK2B expression levels normalized by B-ACTIN on each genotype, N=3 organoids/genotype.

No gross difference was observed neither in size nor morphology of cerebral organoids from the three genotypes at any step of the protocol (Fig. 12B). At 60 days of differentiation,

cerebral organoids already express the neuronal cell marker CTIP2 (from Coup-TFI interacting protein 2) on immunostaining, as well as a peripheral organization (Fig. 12D). Immunoblot analyses show that at 6 months, PTK2B HET organoids express 41% of the protein when compared to WT. KO organoids properly do not express PTK2B (Fig. 12E-E').

To further characterize this 3D culture model, we performed single nucleus RNA-sequencing (snRNA-seq) in 6.5 months-old PTK2B WT, HET and KO cerebral (Fig. 13). We observed a similar cellular composition of PTK2B WT, HET and KO cerebral organoids (Fig. 13A-C) and confirmed that PTK2B is mainly expressed in glutamatergic neurons, as observed in the human adult brain (131). Following the same direction, genes encoding for several downstream targets of activated PTK2B, such as MAPT, GSK3B and STAT3, are also highly expressed in glutamatergic neurons, but can also be observed in non-neuronal cells (data not shown). This indicates that mainly glutamatergic neurons have the molecular machinery necessary for PTK2B-mediated signaling.

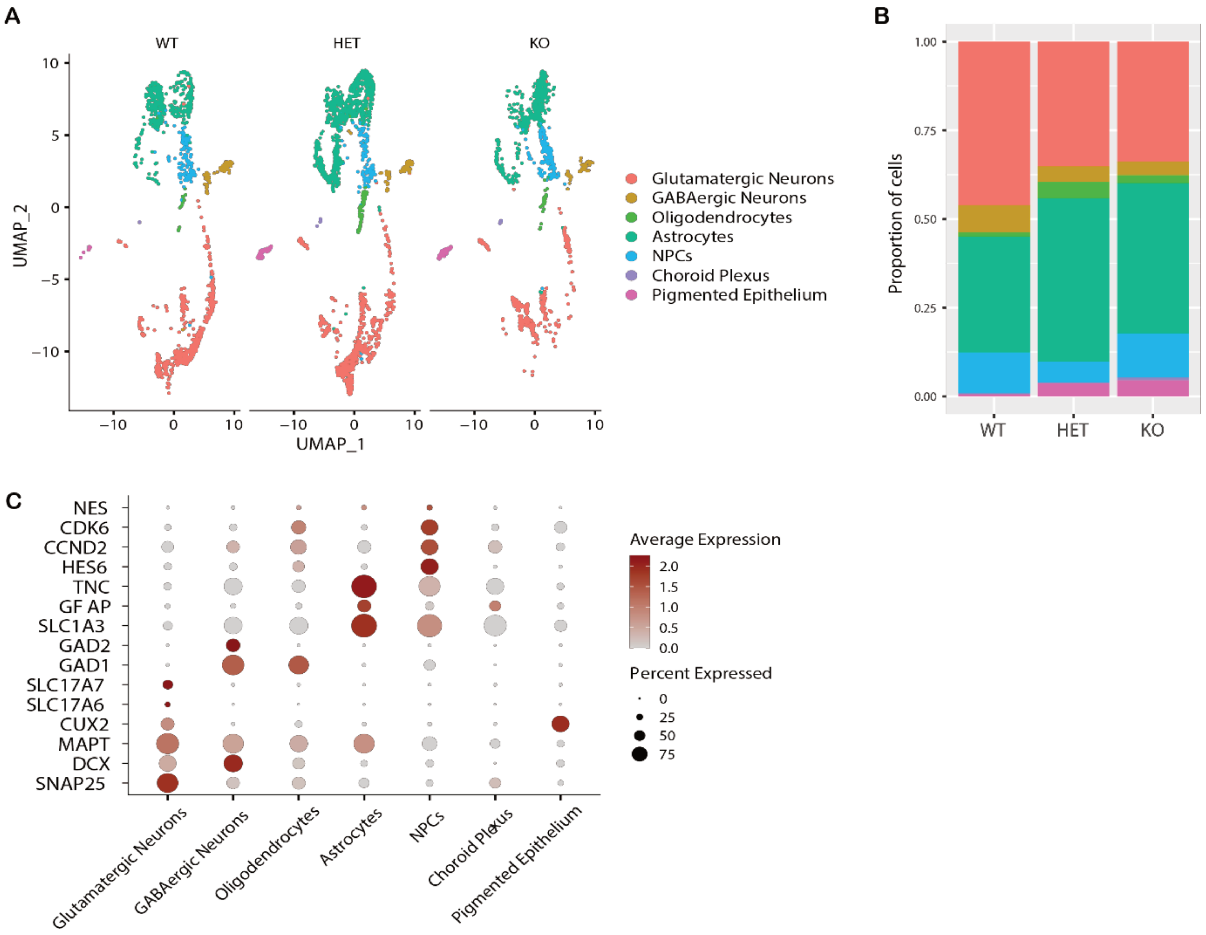

Figure 13: Cerebral organoids exhibit different cellular proportions when modulating PTK2B levels. Data from snRNA-seq of 6 months *PTK2B* WT, HET and KO cerebral organoids (ASE-derived cells). **A)** UMAP showing the cellular composition of the 3D cultures per genotype and the proportion of cells in percentage **(B). C)** Dot plot showing the list of genes used to classify the sub-populations identified. Dots size indicates the percent expressed and the color gradient, the average expression.

4. Study of AD biochemical phenotypes in hiPSC-derived neural cells

Once we characterized the capacity of our hiPSC lines to generate neural cells in 2D and 3D, we employed these models to investigate whether reduced PTK2B expression could affect amyloidogenic APP processing and Tau phosphorylation, two classical hallmarks of AD pathology. To that, we performed immunoblotting assays to measure the levels of full-length APP, beta-CTF, total TAU and TAU phosphorylated at different amino acid residues previously associated with AD pathology. Using 190-days-old cerebral organoids generated from ASE-hiPSCs, we observed similar expression levels of APP and beta-CTF in PTK2B HET or KO compared to WT cerebral organoids (Fig. 14A-A'), suggesting that reduced expression of PTK2B was not sufficient to affect amyloidogenic APP processing. In contrast, levels of phosphorylated TAU (Ser202/Thr205 - P-TAU AT8) were 86% higher in PTK2B HET compared to WT and 72% higher in PTK2B KO compared to WT cerebral organoids when normalized by the total protein (Fig. 14B-B').

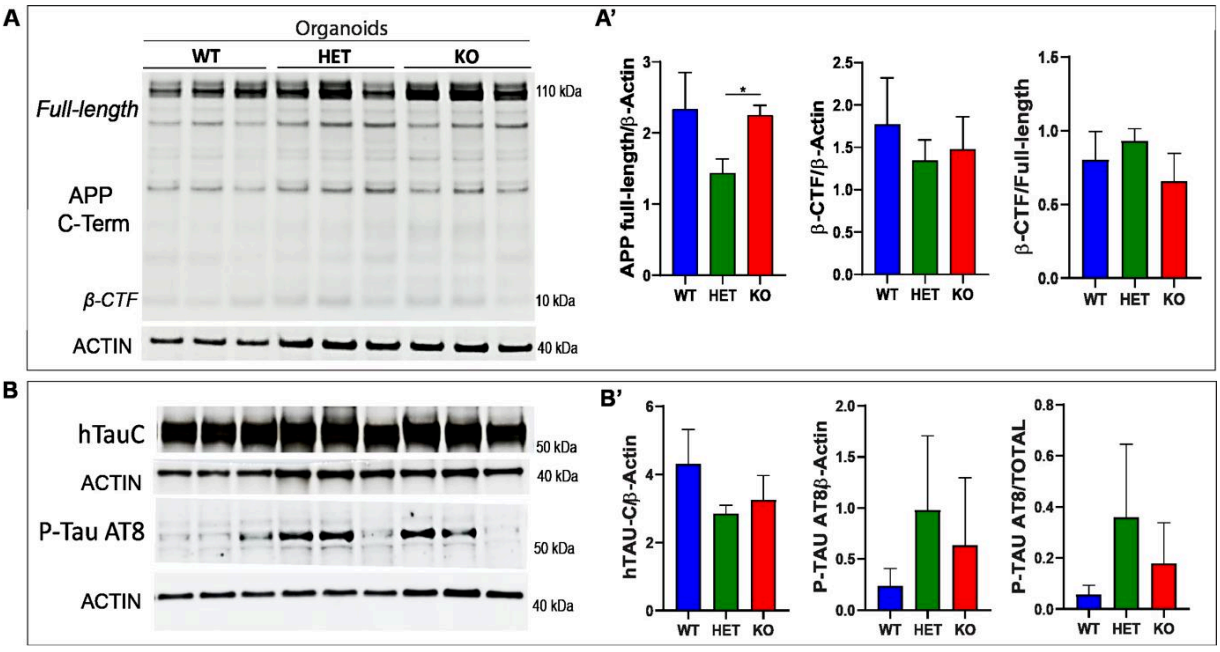

Figure 14: PTK2B effects on AD molecular hallmarks on 6 months cerebral organoids. A-A') Immunoblotting showing the APP metabolism products detected by the APP C-terminal antibody normalized by B-ACTIN on *PTK2B* WT, HET and KO cerebral organoids. **B-B')** immunoblotting showing the total (hTAU-C) and phosphorylated levels of TAU at Ser202/Thr205 (AT8) normalized by B-ACTIN on 6-months-old organoids; Statistical significance analyzed either by ordinary one-way ANOVA - Tukey's multiple comparisons test. N=3 organoids per genotype.

Similar analyses were performed in 2D neural cultures generated from ASE-hiPSC lines (Fig. 15). We observed that *PTK2B* HET cells expressed consistently higher levels of TAU phosphorylated at the Ser202/Thr205 (AT8), Ser396/Ser404 (PHF-1), Thr217, Thr231, Ser202, and Tyr18, compared to both WT and KO (Fig. 15A-B). Although *PTK2B* KO cells expressed slightly higher levels of TAU phosphorylated at the Ser202/Thr205 (AT8), Thr217

and Thr231 compared to WT, this difference was not statistically significant. These results indicate that reduced expression of PTK2B, but not complete depletion of this protein, has a strong impact in TAU phosphorylation.

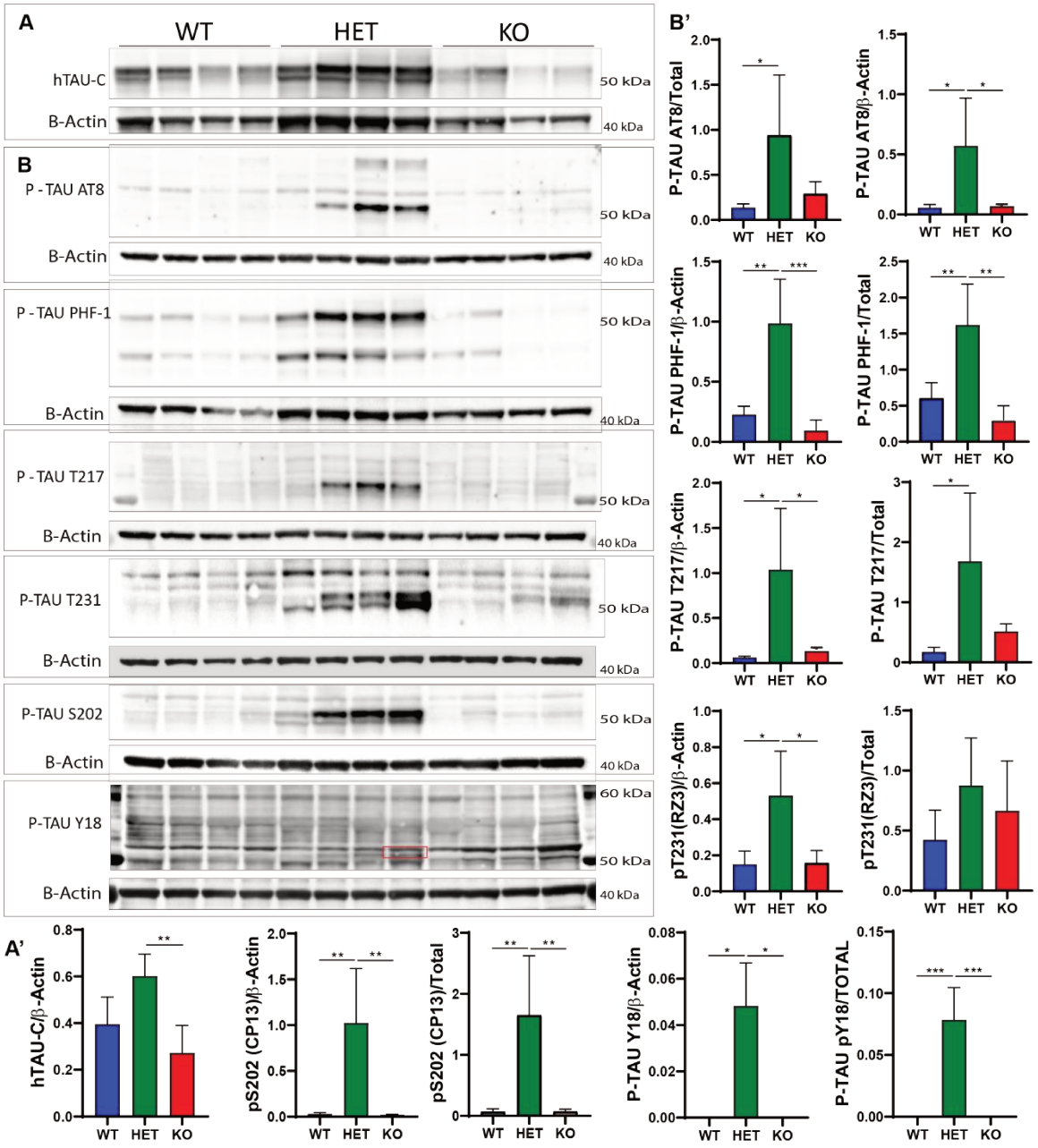

Figure 15: PTK2B under expression increases total TAU and TAU phosphorylation at different residues in 5-weeks-old human-induced neurons. A) immunoblotting showing the levels of total (hTAU-C) and (B) phosphorylated TAU at Ser202/Thr205 (AT8), Ser396/Ser404 (PHF-1), Thr217, Thr231, Ser202 or Tyr18 on PTK2B WT, HET, and KO 5 weeks mixed neural cultures and their respective quantifications (A' and B'). Statistical significance analyzed either by ordinary one-way ANOVA - Tukey's multiple comparisons test. Significant P values range from 0.04 to 0.0001. N=4 independent experiments.

To further confirm this phenotype in an independent *PTK2B* HET cell line, we took advantage of our BION-hiPSC lines. Preliminary results (n=1) reveal that PT26 (HET) neural

cultures after 5 weeks of differentiation express higher levels of phospho-TAU (Ser202/Thr205) compared to WTs (Fig. 16). The effect of *PTK2B* heterozygous mutation on this TAU phosphorylation was milder in the BION-hiPSC line (2-fold increase) than in ASE-hiPSC (8-fold increase), what could likely be explained by the different impacts of the mutations in PTK2B expression in human-induced neurons generated from these two different cell lines (Fig. 8 and 9). In agreement with this interpretation, we observed that S5 cells that expressed intermediate levels of PTK2B compared with C2 (WT) and PT26 (HET) also express higher levels of phosphorylated TAU (Ser202/Thr205) compared to WT, but lower compared to HET (Fig. 16).

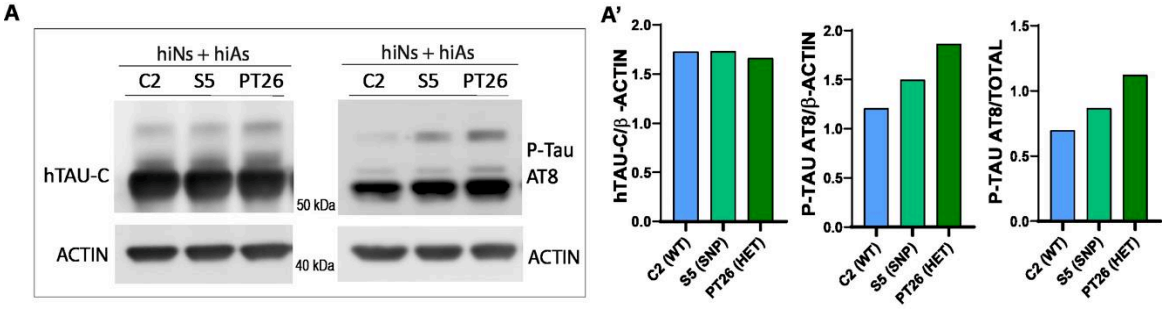

Figure 16: *PTK2B* reduced expression tends to increase TAU phosphorylation in a second cell line (BION-derived cells). 5 weeks PTK2B C2 (WT), S5 (SNP) and PT26 (HET) 2D cultures derived from BION clone. **A-A')** Western blotting for total and phosphorylated (Ser202/Thr205) TAU levels normalized by B-ACTIN. N=1 experiment.

Altogether, these findings in two independent cell lines suggest that reduced PTK2B expression contributed to increase TAU phosphorylation at multiple AD-related epitopes but does not affect amyloidogenic APP processing in human neurons.

5. Molecular screening of possible targets affected by the under-expression of PTK2B

The possible role of PTK2B in the regulation of TAU phosphorylation in hiNs could be mediated by several downstream pathways. To first screen some of these potential signaling pathways, we used a Phospho-kinase panel to measure the levels of 39 phosphorylated proteins in *PTK2B* WT, HET, and KO cerebral organoids after 6 months of culture (Fig. 17).

To select the most interesting candidates, we used a cut-off of 10% to detect increased or decreased levels of phosphorylated proteins in *PTK2B* HET or KO compared to WT cerebral organoids. Proteins were then clustered into three different groups according to the phosphorylation pattern: going in opposite directions between HETs and KOs; increased

expression in both HET and KO relative to the WT; and decreased expression in both HET and KO compared to the WT (Fig. 17B-D).

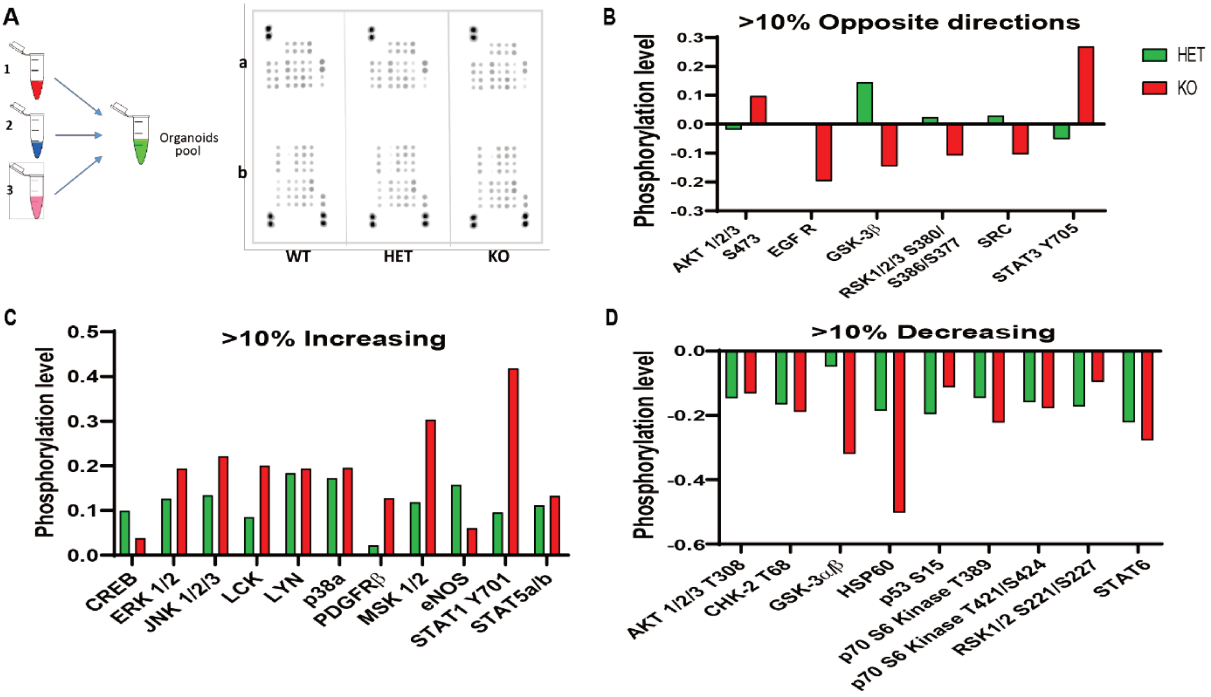

Figure 17: Molecular screening of potential targets of PTk2B modulation. A) Scheme showing a phospho kinase panel used to detect to likely affected proteins on PTK2B WT, HET, KO 6 months cerebral organoids; pool of 3 organoids per genotype. **B)** Phosphorylated proteins detected with > 10% of change in relation to the WT, where the HET and KO go in opposite directions. **C)** Phosphorylated proteins that showed an increase of at least 10% compared to WT. **D)** phosphorylated proteins that showed a decrease of at least 10% compared to WT. List of phosphorylated epitopes is detailed on Materials and Methods section.

GSK3β and SRC

Notably, the direct targeting of GSK3β's Tyr216 by PTK2B offers insight into this phenomenon, as it has been previously described to correlate with the phosphorylation of TAU at Ser202/Thr205 (200). To test this possibility, we measured the levels of total GSK3β and P-GSK3β (Tyr216) in 2D cultures. We observed a slight increase in the levels of P-GSK3β (Tyr216) in *PTK2B* HET compared to WT cells, but this difference was not statistically significant (Fig. 18A-A'), possibly due to the large variability between samples. GSK3β is constitutively activated through autophosphorylation at Tyr216 (237). This mechanism potentially elucidates the greater impact observed on TAU phosphorylation within the *PTK2B* HET cerebral organoids in contrast to the KO.

A member of the Src family kinase and a direct target of PTK2B, the proto-oncogene tyrosine-protein kinase (SRC) protein was identified on the phospho panel as a potential

contributor to the increased TAU phosphorylation seen in the *PTK2B* HET cells relative to the WT. These primary results showed that the phosphorylation of SRC also goes in opposite directions between HET and KO related to the WT (Fig. 17B). To confirm these findings, immunoblotting was performed in 2D cultures after 5 weeks of differentiation. The results showed a trend for both HET and KO cells to have lower levels of phosphorylated SRC at Tyr416 compared to the WT, either normalized by B-ACTIN or by total SRC levels (Fig. 18B-B'). The phosphorylation of SRC at this residue enhances its kinase activity by stabilizing the activation loop (238). Despite the trend observed in SRC phosphorylation, as it is reduced in *PTK2B* HET and KO cells, it is unlikely that this explains the increase in TAU phosphorylation observed in HET cells.

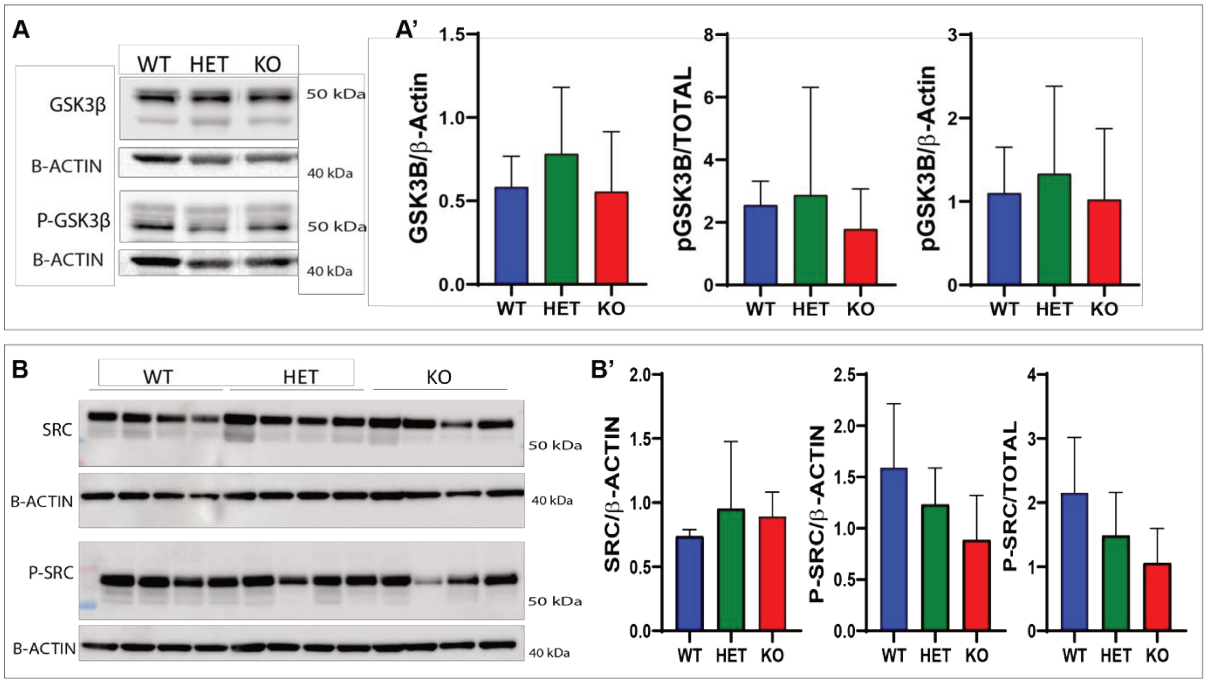

Figure 18: Analysis of GSK3B and SRC as potential targets of PTk2B modulation. 5 weeks *PTK2B* WT, HET and KO 2D cultures derived from ASE clone. **A-A') ** Representative images showing **w**estern blotting for total and phosphorylated (Y216) GSK3B normalized by B-ACTIN. **B-B')** Western blotting for total and phosphorylated (Y416) SRC normalized by B-ACTIN. Statistical significance analyzed by ordinary one-way ANOVA - Tukey's multiple comparisons test. N=4 independent experiments.

p38 MAPK, ERK, and LKB1

We decided then to further investigate which other kinases could possibly explain the relation between PTK2B haploinsufficiency and the increased phosphorylated TAU observed. Based on the analysis of the phospho panel and the literature, P38 MAPK, ERK1/2 and LKB1 are potential candidates. These kinases have already been described as been regulated by PTK2B and important for TAU phosphorylation in different *in vitro* models ((239); and (240)), including a model of pharmacological inhibition of PTK2B (200).

Interestingly, the total level of p38 MAPK was significantly reduced in PTK2B HET cells compared to the WT. However, its activation through phosphorylation on Thr180/Tyr182 appears to be increased. Although confirmation requires a larger N due to variability, this increase seems to be a 3-fold change (Fig. 19A-A').

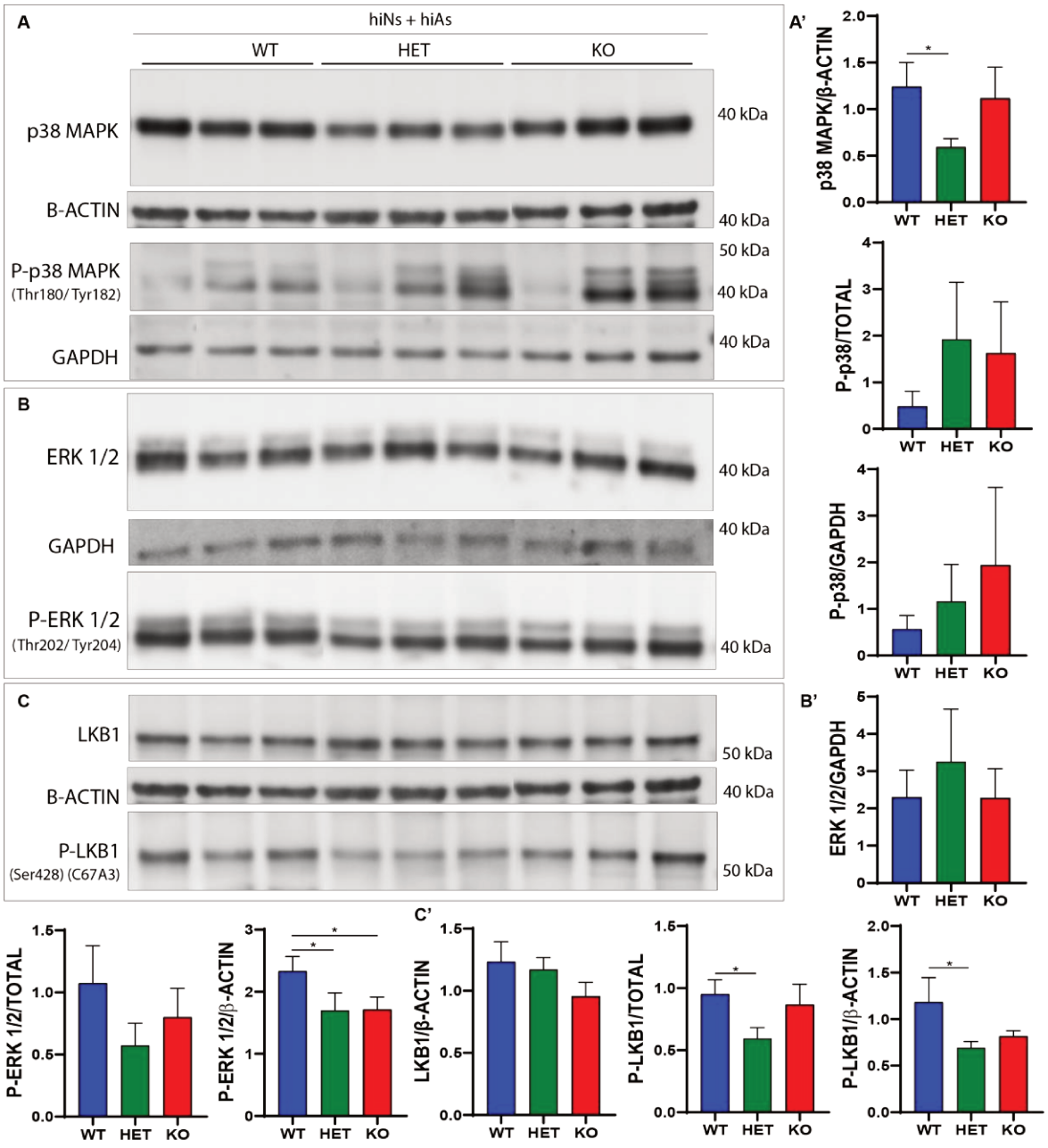

Figure 19: Investigation of TAU kinases affected by PTk2B expression levels. Western blotting of 5-weeks-old spontaneously differentiated PTK2B WT, HET and KO cultures derived from ASE clone. **A-A')** Total and phosphorylated (Thr180/Tyr182) levels of p38 MAPK normalized by B-ACTIN or GAPDH. **B-B')** Total and phosphorylated (Thr202/Tyr204) levels of ERK 1/2 normalized by GAPDH. **C-C')** Total and phosphorylated (Ser428) levels of LKB1 normalized by B-ACTIN. Data are mean ± SD. Statistical significance analyzed by ordinary one-way ANOVA - Tukey's multiple comparisons test. P=0.02-0.04. N = 3 independent experiments.

The phosphorylation of ERK1/2 at the Thr202/Tyr204 and LKB1 at Ser428 are also affected by PTK2B expression levels. Analyses of 5 weeks differentiated cultures revealed that P-ERK1/2 is decreased in both PTK2B HET and KO compared to the isogenic control (Fig. 19B-B'). The phosphorylation of LKB1, in contrast, was exclusively observed in HET cells compared to the WT (Fig. 19C-C'). These analyses suggest that p38 MAPK, ERK1/2 and LKB1 likely have their activity affected by PTK2B expression levels and might contribute to the effects observed on TAU hyperphosphorylation in neural cells.

Taking advantage of our snRNA-sequencing data from cerebral organoids, we checked whether the expression of these TAU kinases was also affected at a later time point - 6 months (Fig. 20). Our observations indicate that the gene encoding ERK2, Mitogen-activated protein kinase 1 (MPK1), is expressed in most cells in all three genotypes. However, it is expressed at lower levels in HET cells. The gene that encodes ERK1, Mitogen-activated protein kinase 3 (MAPK3), is expressed in less than 25% of the cells in all PTK2B genotypes and also at reduced levels in the heterozygous cells. Similar pattern was observed for the gene encoding for LKB1, Serine/threonine kinase 11 (STK11), with reduced expression in the HET when compared to the WT. This data is consistent with the lower activation of these proteins observed by immunoblotting.

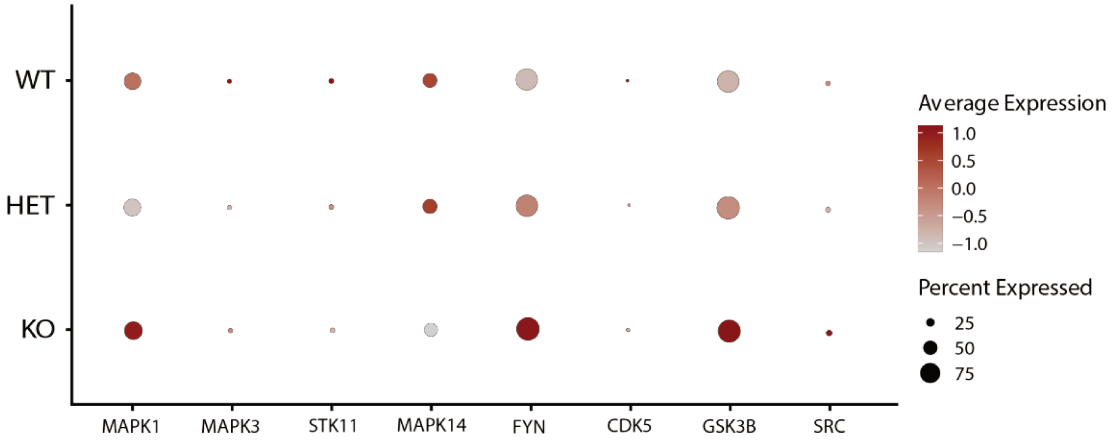

Figure 20: mRNA expression of genes encoding for TAU different kinases in cerebral organoids. snRNA-seq data from *PTK2B* WT, HET and KO cerebral organoids at 6 months. Dot-plot showing the expression of different TAU kinases across *PTK2B* genotypes. Color intensity represents the average expression and dot's size, the percent of cell expressing the gene. N = 4 cerebral organoids per genotype.

In contrast, the expression of the gene encoding for p38 MAPK, Mitogen-activated protein kinase 11 (MPK14), seems to be slightly increased in HET compared to WT. On the other hand, the expression of the genes encoding for GSK3B and FYN is significantly increased in *PTK2B* HET and KO cerebral organoids compared to the WT (Fig. 20). Overall, these data suggest that other relevant TAU kinases are upregulated in neural cells when *PTK2B* expression is reduced and may contribute to the molecular effects observed in these cells.

6. Gene expression profiles of *PTK2B* WT, HET and KO neural cells

6.1. PTK2B under expression leads to gene expression alterations specifically in glutamatergic neurons

In order to better understand the effects mediated by the reduction of *PTK2B* in human neurons, we took advantage of the data obtained through snRNA-seq of 2D cultures and cerebral organoids cultures. Analysis of differential gene expression in individual cell types of *PTK2B* WT, HET and KO cultures revealed significant transcriptional alterations in *PTK2B* KO and HET compared to WT in glutamatergic neurons, but not in any other cell type identified (Fig. 21A (2D) and 22A (3D)), including other neuronal subtypes and astrocytes (data not shown). The differentially expressed genes (DEGs) in *PTK2B* HET and KO vs WT share 23.7% of similarity. In terms of gene ontology (GO) analysis, we found that the DEGs in PTK2B mutant glutamatergic neurons were enriched for biological processes related to neuronal electrical activity and synaptic transmission (Fig. 21C).

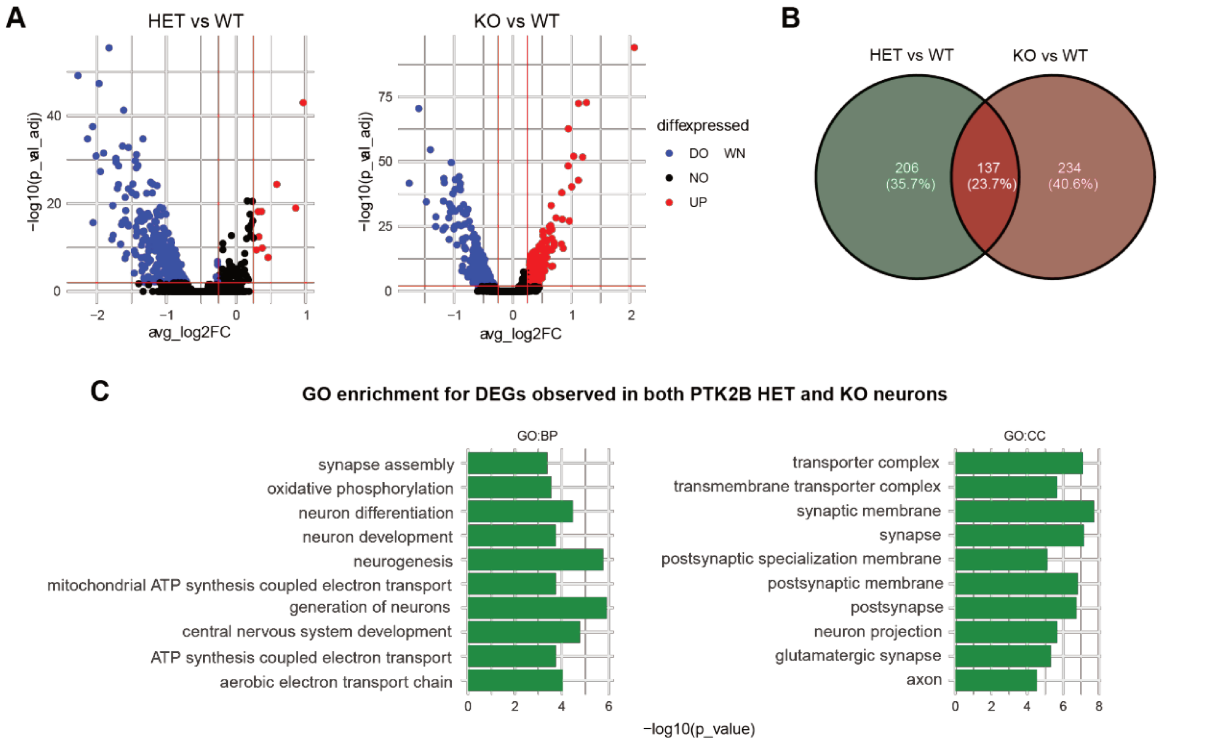

Figure 21: I PTK2B under expression leads to gene expression alterations specifically in glutamatergic neurons in 2D cultures. 5w 2D spontaneously differentiated neural cultures (ASE-derived cells). **A)** Volcano plots showing differentially expressed genes (red dots, FC>1.3 and Padj<0.01; blue dots corresponds to the genes downexpressed; black dots, genes with no difference) in *PTK2B* HET or KO compared to WT neurons. **B)** Venn diagram showing the overlap of differentially expressed genes between *PTK2B* HET vs. WT and KO vs. WT in glutamatergic neurons**. C)** Gene ontology enrichment analysis for DEGs commonly identified in HET and KO neurons. N = 3 independent experiments.

Accordingly, analysis of differential gene expression in individual cell types of *PTK2B* WT, HET and KO cerebral organoids revealed significant transcriptional alterations in *PTK2B* KO and HET compared to WT glutamatergic neurons, but not in any other cell type identified in our cerebral organoids (Fig. 22A-B). The DEGs detected in *PTK2B* HET and KO vs WT share 21.4% of similarity between the *PTK2B* genotypes. Gene ontology analysis found that DEGs in PTK2B mutant glutamatergic neurons were enriched for biological processes related to neuronal electrical activity and synaptic transmission (Fig. 22C).

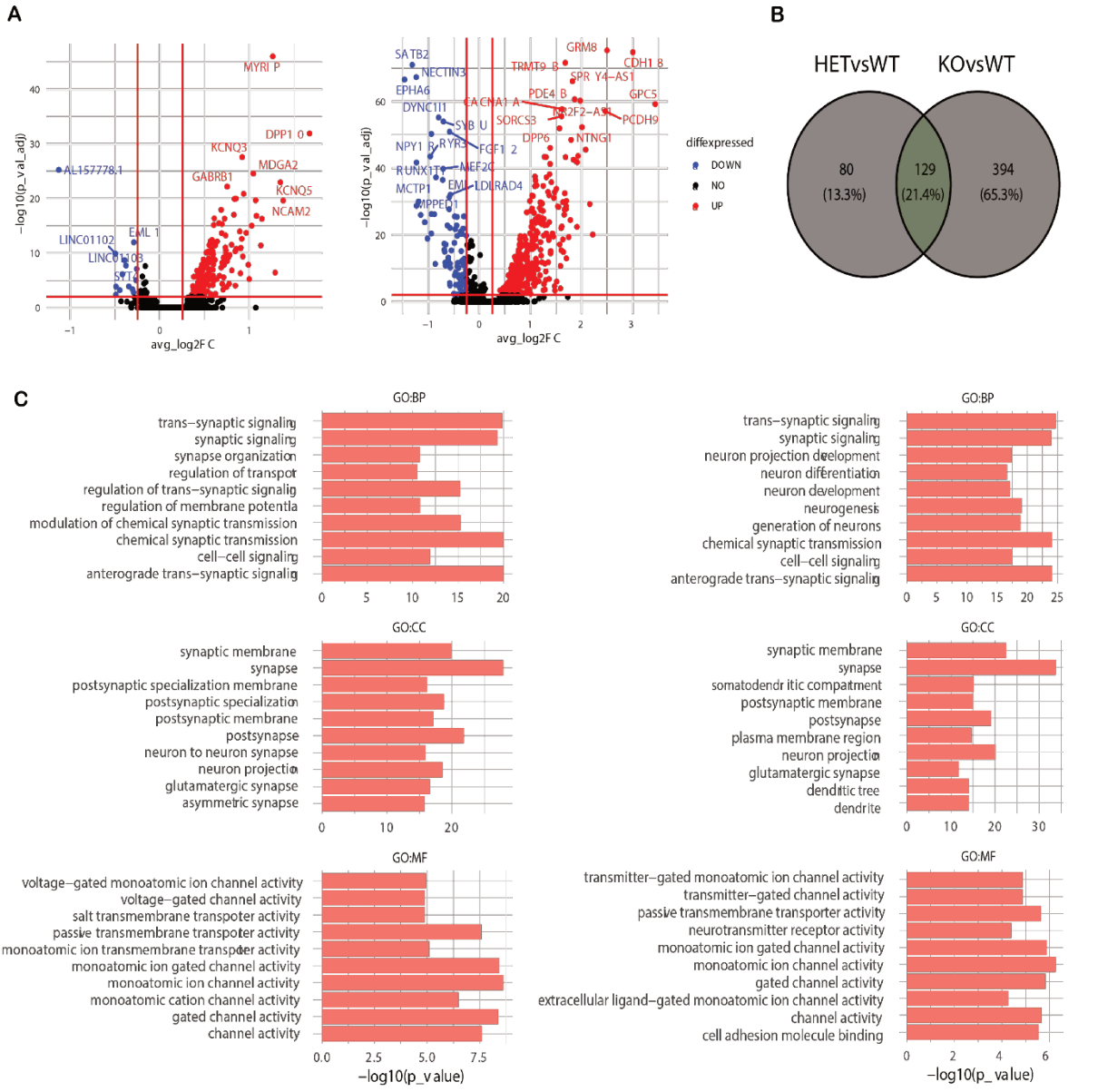

Figure 22: PTK2B deletion in cerebral organoids leads to gene expression alterations related to synaptic function in glutamatergic neurons. A) Volcano plots showing differentially expressed genes (red dots, FC>1.3 and Padj<0.01; blue dots corresponds to the genes downexpressed; black dots, genes with no difference) in *PTK2B* HET or KO compared to WT glutamatergic neurons. **B)** Venn diagram showing the overlap of differentially expressed genes between *PTK2B* HETvsWT and KOvsWT in glutamatergic neurons. **C)** Gene ontology enrichment analysis for DEGs commonly identified in HETvsWT and KOvsWT glutamatergic neurons. N = 4 cerebral organoids/genotype; 6 months old.

6.2. STAT3 may act as a potential key regulator in PTK2B cell lines at both transcriptional and protein levels

Analyses of transcriptome

Using a gene regulatory network strategy (SCENIC, from Single-Cell rEgulatory Network Inference and Clustering), we identified the transcription factors (TF) that could act as the main regulons for the genes differentially expressed (Fig. 23B). As most of the genes were upregulated, we selected among these TFs the ones commonly increasing in HET and KO when compared to the WT – NR2F1 (Nuclear Receptor Subfamily 2 Group F Member 1), HIST1H2BN (Histone H2B type 1-N), EMX2 (Empty Spiracles Homeobox 2), LHX1 (LIM Homeobox 1), STAT3, LHX9 (LIM Homeobox 9), and LRRFIP1 (LRR Binding FLII Interacting Protein 1) (Fig. 20B). HIST1H2BN, EMX2, and LHX9 are barely expressed in glutamatergic neurons, and could not explain the alterations observed on this population. NR2F1, STAT3, and LRRFIP1 are higly expressed on excitatory neurons. However, the snRNA-seq data showed that only STAT3 is particularly more expressed in HET and KO 6 months cerebral organoids compared to the WTs (Fig. 23C). We identified STAT3 as a possible master regulator of genes differentially expressed in glutamatergic neurons and a gradual increase of its regulon activity in *PTK2B* HET and KO.

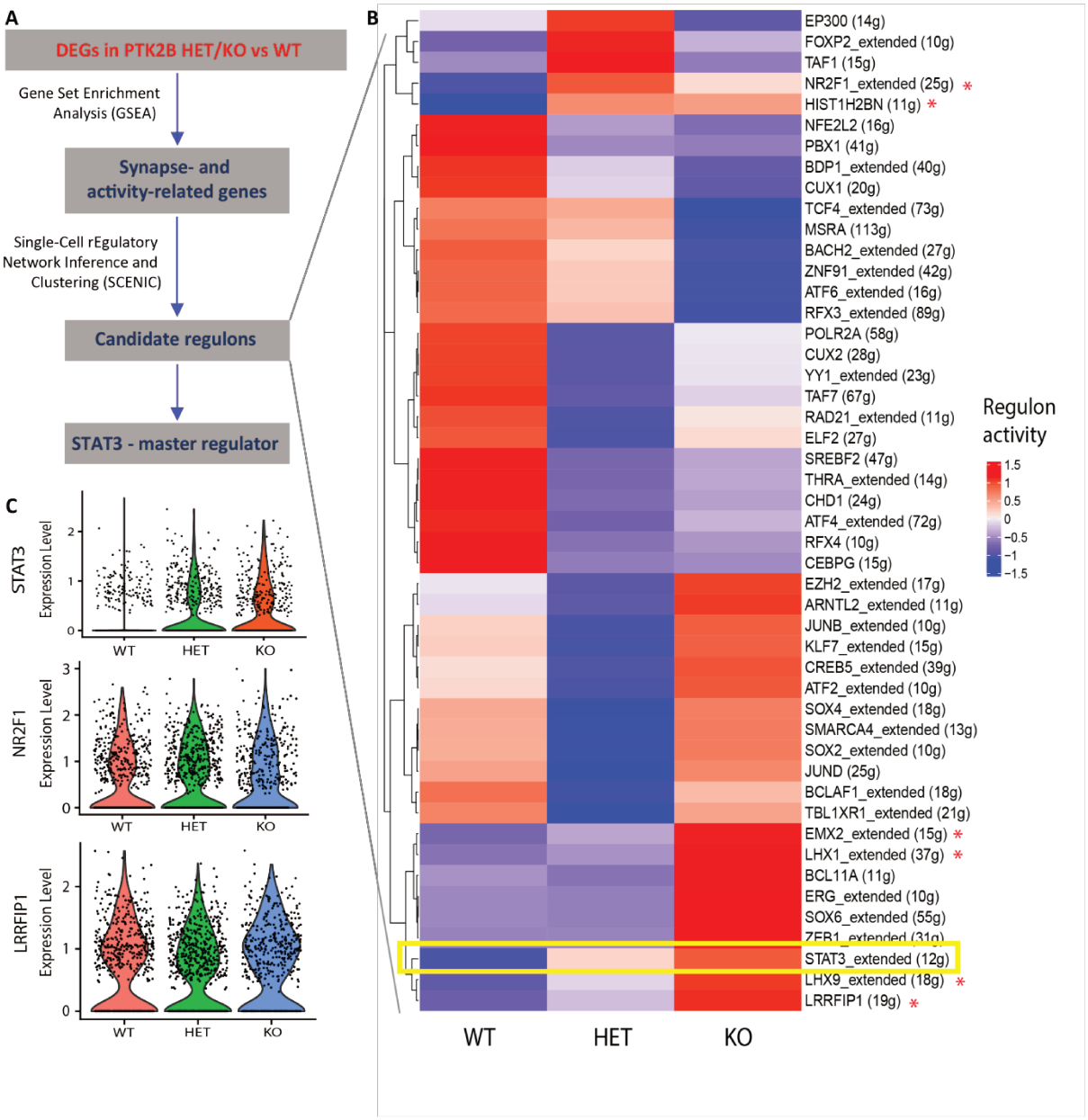

Figure 23: DEGs in PTK2B HET and KO cerebral organoids are possibly main regulated by STAT3. Data from snRNA-seq of PTK2B cerebral organoids at 6 months. **A)** Schematic representation showing the analyses performed on the differentially expressed genes in *PTK2B* HET/KO vs WT leading to identify STAT3 as a potential master regulator. **B)** Heatmap showing the expression of the TFs identified by SCENIC analyses as potential regulons of the DEGs. Yellow rectangle highlights STAT3; red asterisk identify the genes upregulated in *PTK2B* HET and KO vs WT. **C)** Violin plots showing the expression of TFs that popped-out as possible regulators in glutamatergic neurons from *PTK2B* WT, HET and KO cerebral organoids. N = 4 cerebral organoids per genotype.

Protein analysis

STAT3-mediated transcription is regulated by phosphorylation and several kinases, including PTK2B, play a role in this regulation. To evaluate whether STAT3 phosphorylation could be altered in *PTK2B* HET and KO cells, we measured STAT3 total protein levels, as well as its phosphorylation on Tyr705 or Ser727, residues particularly implicated in its transcriptional

regulation. We observed that in 6 months cerebral organoids, the STAT3 total levels show a trend to be dose-dependent enhanced in *PTK2B* HET and KO compared to the WT. The effect, however, is only significant for the STAT3 phosphorylation at the Tyr705, which showed to be reduced in HET and KO cells compared to the WT (Fig. 24A-A'). A similar phosphorylation pattern, but even stronger, was also confirmed at earlier maturation stages on 2D mixed-cultures at 5 weeks (Fig. 24B-B').

Taken together, these results suggest that PTK2B signaling through STAT3 in glutamatergic neurons may be involved in the regulation of neuronal electrical activity/synaptic transmission. However, the interpretation of these results should take into account that STAT3 is highly expressed not only in glutamatergic neurons, but also in other cell types, in particular astrocytes.

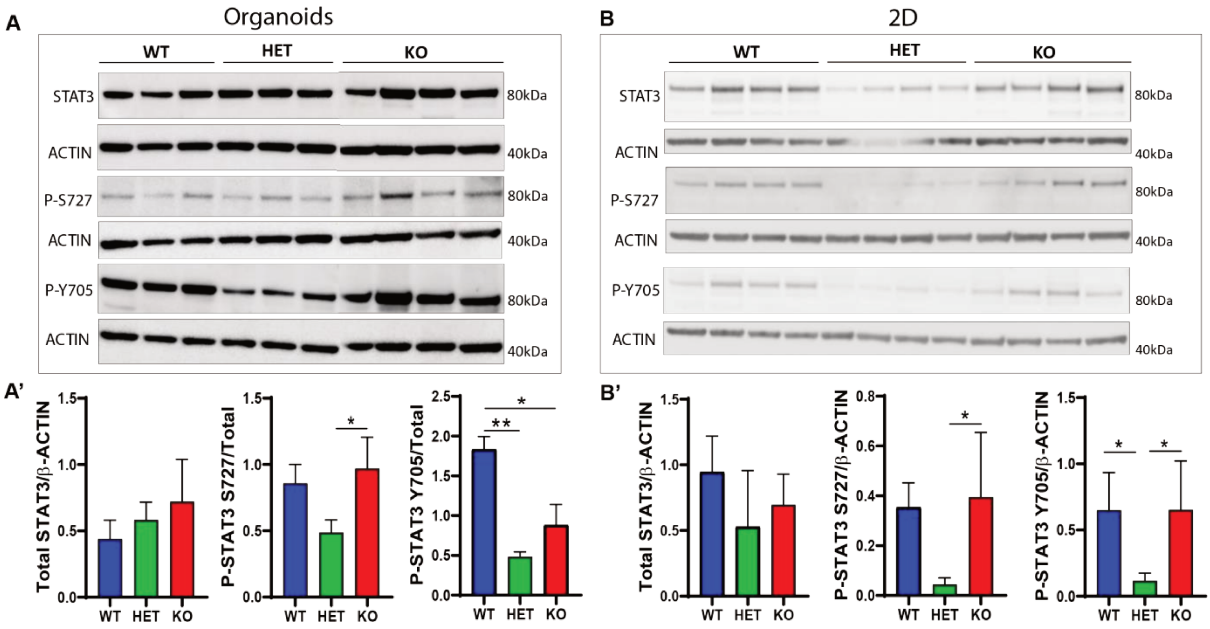

Figure 24: PTK2B diminished expression leads to alterations in the phosphorylation of STAT3 at its primary regulatory epitopes at the protein level. A-A') Immunoblotting showing the levels of total and phosphorylated STAT3 at Ser727 or Tyr705 in WT, HET, and KO 6 months cerebral organoids and in 2D mixed neuronal cultures at 5 weeks **(B-B')**. Statistical significance analyzed by ordinary one-way ANOVA - Tukey's multiple comparisons test. N=3 cerebral organoids and 4 independent 2D cultures per genotype.

7. PTK2B signaling in the regulation of neuronal electrical activity

7.1. hiNs expressing reduced levels of PTK2B show altered patterns of calcium flux

To address the possible role of PTK2B signaling in the regulation of hiNs electrical properties, we first performed calcium imaging experiments as a readout of the electrical activity of spontaneously differentiated 5 weeks mixed neural cultures and analyzed them

using CALIMA software (241). We observed that *PTK2B* HET cells have a higher frequency of calcium transients compared to WT, without significant changes in the percentage of active neurons. The frequency of calcium transients in *PTK2B* KO cells was higher than in HET and WT cells, suggesting a dose-dependent effect of *PTK2B* expression in the regulation of neuronal calcium transients when detected by OGB calcium sensor (Fig. 25A-D).

Next, we measured the synchronicity among neurons using the cross-correlation matrices of calcium transients and calculating the eigenvalues from these matrices. To reduce possible biases introduced by the increased electrical activity in HET and KO cultures in relation to the WT, we normalized the eigenvalues by the frequency of calcium transients peaks and observed that although the PTK2B neurons has more peaks, this does not significantly affect the synchronization observed in HET and KO neurons compared to the control ones (Fig. 25E-E').

Pharmacological assays using competitive antagonists of $GABA_A$ (BIC) or AMPA/kainate (CNQX) receptors at 100uM confirmed that the calcium spikes in hiNs are mediated by chemical synapses (Fig. 25F-G). Interestingly, blockade of $GABA_A$-mediated currents caused an increase in the electrical activity for all genotypes (Fig. 25G), indicating that GABA polarity switch from excitatory to inhibitory has already occurred in our cultures (another sign of neuronal functional development). Although these cultures show a high electrical activity and it has been previously described as related to Aβ-mediated effects (153), the modulation of PTK2B leads to no significant difference in the $Aβ_{1-42}$ and $Aβ_{1-x}$ production secreted on the media on the differentiated 2D cultures at 5 weeks (Fig. 25H).

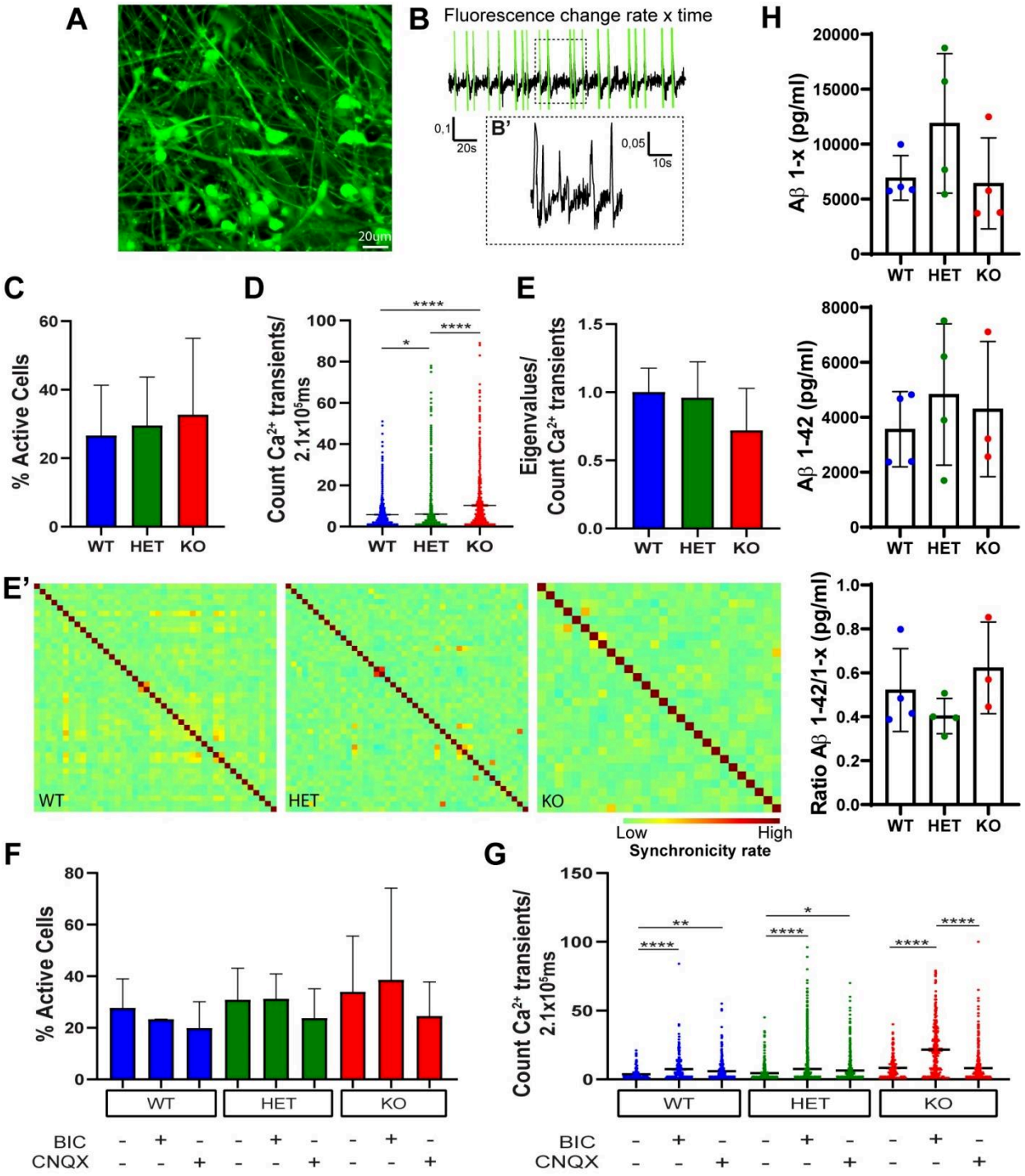

Figure 25: Reduced PTK2B levels correlates with altered neuronal Ca^{2+} transients. Calcium imaging of 2D *PTK2B* neuronal cultures at 5 weeks. **A-B)** Representative images of cultures labeled of Oregon green calcium sensor, scale bar=20um; **(A)** and the spikes detected by the CALIMA softwere based on the fluorescence changes over time in 1000 frames **(B). C)** Percentage of active cells per field and **D)** Counts of Ca^{2+} transients within $2.1x10^5$ms on the different PTK2B genotypes. **E-E')** Correlation among the neurons measured by the ratio between the detected eigenvalues and the counts of of Ca^{2+} transients within $2.1x10^5$ms, **E')** Representative images of the PTK2B genotypes's heatmaps showing the correlation peak detected per field. **F-G)** Pharmacological assays using competitive antagonists of $GABA_A$ (BIC) or AMPA/kainate (CNQX) receptors, **F)** Percentage of active cells per field and **G)** Counts of Ca^{2+} transients/$2.1x10^5$ms under exposition to BIC or CNQX and non-treated controls. **H)** AlphaLISA measurements of the Aβ products 1-42 and 1-x on WT, HET and KO 5 weeks 2D cultures. Statistical significance analyzed either by ordinary one-way ANOVA - Tukey's multiple comparisons test or Kruskal-Wallis multiple comparison test for non-Gaussian distributions. Significant P values range from 0.02 to <0.0001. N=4 independent experiments.

7.2. PTK2B reduced expression correlates with increased single unity electrical properties on MEA system

Our calcium imaging data suggest an increase in neuronal firing rate and/or changes in the firing pattern (number of bursts etc) based on the peaks of Ca^{2+} transients. However, analyses of our previous electrophysiological data using hiNs mutated for another AD risk gene (*BIN1*) suggested that calcium transients detected in calcium imaging are better associated with spike bursts, not with single action potentials (2). Thus, to directly probe the electrical activity of *PTK2B* mutated neurons in a single-cell basis, we performed weekly MEA electrophysiological recordings in spontaneous differentiated cultures using the MaestroPro MEA system (Axion Biosystems, Inc, USA).

While the analyses of 5 weeks cultures are under processing, results from 4 weeks hiNs show that they are already functional at this time point (Fig. 26A). When sorted as single unit activity (SUA), different neurons could be classified and distinguished regarding their firing patterns based on analyses of principal components (Fig. 26B). Representative raster plots showing the activity of WT, HET and KO cultures illustrate a clear different temporal organization between these genotypes (Fig. 26C). Once sorted, we analyzed their mean firing rate and observed a trend to increase electrical activity on the ASE 9109-derived *PTK2B* HET and KO compared to WT neurons, even though there was inter-wells variability in this experiment (Fig. 26C). In addition, to evaluate whether PTK2B also disrupts neuronal synchronization, we analyzed the bursting patterns of these cultures. We observed a clear temporal disorganization of bursts in *PTK2B* HET and KO hiNs compared to WT (Fig. 26C-E). The frequency of bursts is increased in *PTK2B* HET neurons compared to the WT (Fig. 26E). These data show that, although these bursts are more frequent, they are also shorter, indicating that normal levels of PTK2B are critical for proper neuronal synchronization.

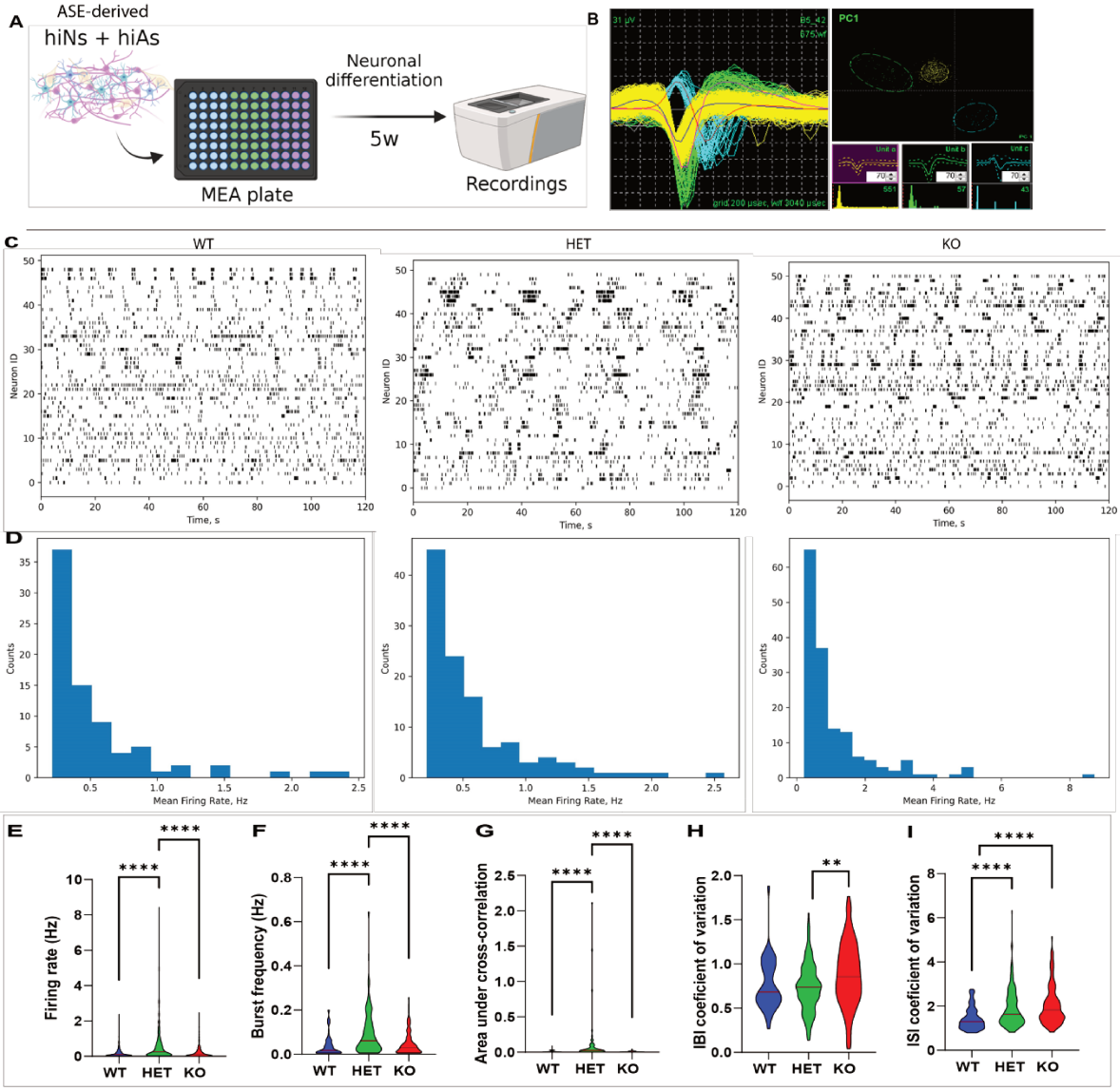

Figure 26: Reduced expression of PTK2B correlates with increased single unity activity. A) Scheme of 4 weeks ASE-derived mixed neural culture on a 96-wells MaestroPro MEA plate. **B)** Representative image of a single unit activity sorting that identified three different neurons firing at the same time on the top of one electrode based on principal component analysis. **C)** Raster plot showing the firing activity of 50 representative single unity neurons per genotype during a recording of 120s. **D)** Histogram of the mean firing rate (Hz) of WT, HET and KO single unity neurons. The quantification of firing rate (Hz) **(E)**, inter-spikes interval **(F)**, burst frequency (Hz) **(G)**, inter-bursting interval **(H)**, and area under cross-correlation **(I)** of single unity neurons. Statistical significance analyzed either by ordinary one-way ANOVA - Tukey's multiple comparisons test or Kruskal-Wallis multiple comparison test for non-Gaussian distributions. Significant P values range from 0.01 to <0.0001. N=3 independent experiments.

To confirm these electrophysiological alterations, we performed similar experiments using the BION-derived cell lines (Fig. 27H-L). It is important to mention that in an attempt to improve cellular survival and neuronal maturation, these cultures were seeded at 40% higher density than the ASE-derived ones, what played a crucial impact on the culture activity basal levels. Although not achieving the exact same results, the use of this second cell line was an important approach and confirms that the modulation of *PTK2B*, either in HET or SNP cells,

leads to changes in neuronal electrical activity. Overall, neurons HET for *PTK2B* or carrying the SNP showed smaller area under cross-correlation than the WT, indicating a reduced synchronization (Fig. 27G).

Taken together, our calcium imaging and preliminary MEA data suggest that PTK2B regulates important biological processes involved in neuronal electrical activity and maturation. Thus, altered expression of this risk gene in the AD brain could play a role in the neuronal hyperexcitability observed in patients at the early stages of the disease.

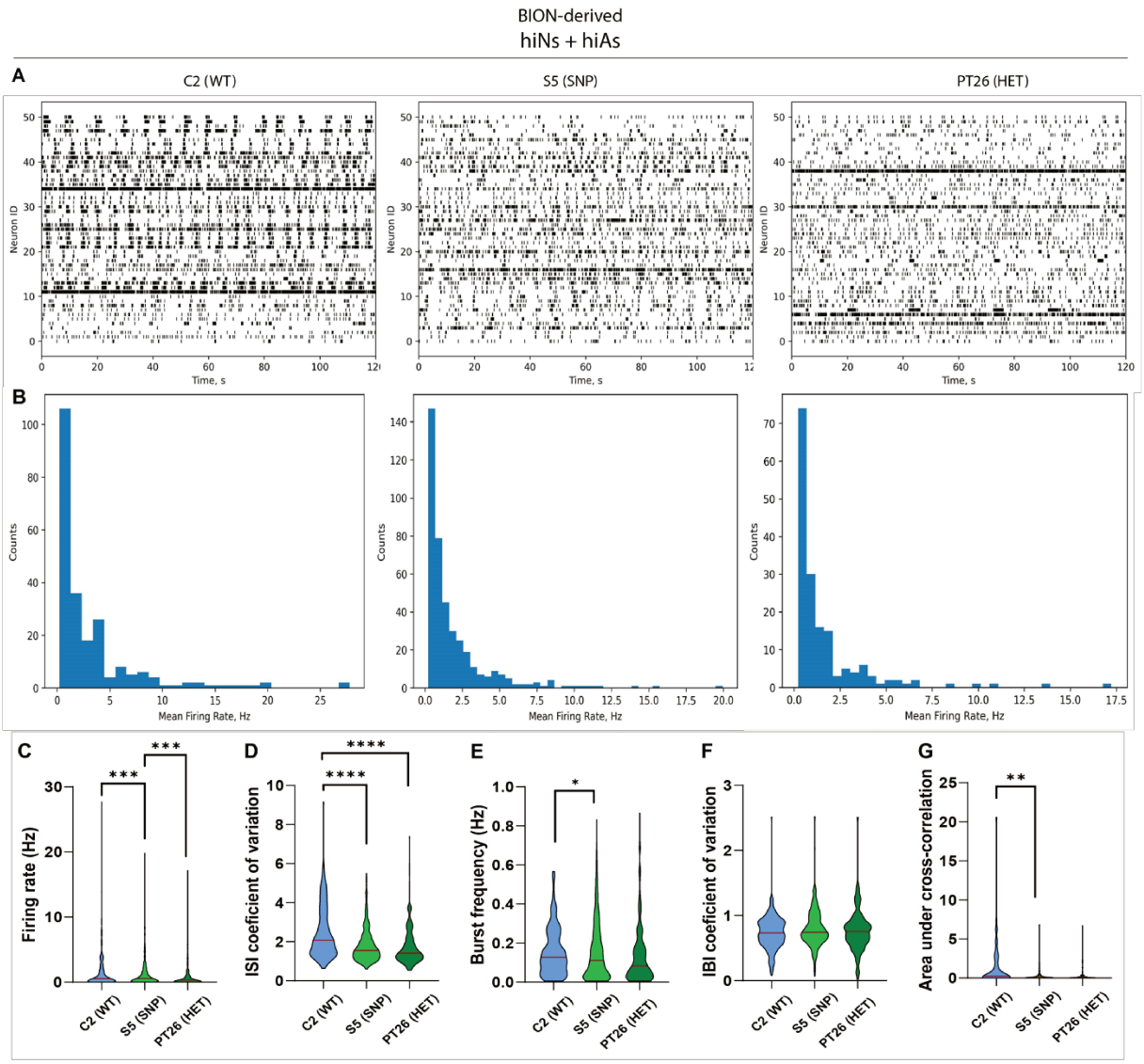

Figure 27: PTK2B reduced expression and the presence of an AD-related variant impair unity activity properties in a second cell line. SUA data from BION-derived hiNs. **A)** Raster plot showing the firing activity of 50 single unity neurons during a recording of 120s. **B)** Histogram of the mean firing rate (Hz) of C2 (WT), S5 (SNP), and PT26 (HET) single unity neurons. The quantification of firing rate (Hz) **(C)**, inter-spikes interval **(D)**, burst frequency (Hz) **(E)**, inter-bursting interval **(F)**, and area under cross-correlation **(G)** of single unity neurons. Statistical significance analyzed either by ordinary one-way ANOVA - Tukey's multiple comparisons test or Kruskal-Wallis multiple comparison test for non-Gaussian distributions. Significant P values range from 0.04 to <0.0001. N=3 independent experiments.

7.3. Altered expression of activity-related genes in PTK2B cerebral organoids

To better characterize the neuronal and glial subtypes in this system, we performed snRNA-seq and could identify 7 main cell types clusters and up to 21 sub clusters (Fig. 13A-B) based on the expression of cell type markers as SLC1A3 (Solute Carrier Family 1 Member 3, encoding for GLAST), GFAP and TNC (Tenascin C) for astrocyte; SNAP25 (Synaptosome Associated Protein 25), DCX (Doublecortin), MAPT for pan-neuronal; SLC17A7 (Solute Carrier Family 17 Member 7, encoding for VGLUT1) and SLC17A6 (Solute Carrier Family 17 Member 6) for glutamatergic neurons; DLX1 (Distal-Less Homeobox 1) and GAD2 (glutamate decarboxylase 2) for GABAergic neurons; HES6 (hes family bHLH transcription factor 6), CCND2 (cyclin D2) and CDK6 (cyclin dependent kinase 6) for NPCs; ITGA8 (integrin subunit alpha 8) for choroid plexus; and CLIC6 (Chloride Intracellular Channel 6) for pigmented epithelium.

We observed a slight change in the proportion of astrocytes and neurons in *PTK2B* HET and KO compared to WT cerebral organoids (Fig. 13B), modifying the ratio of neuronal/non neuronal populations. A similar phenotype has been observed in *BIN1* KO cerebral organoids (2) and it is tempting to speculate that it could result from a possible neuronal loss as a consequence of neuronal hyperexcitability at earlier stages, similar to the toxicity observed in the brain of AD patients.

To directly address this possibility, we first tried to perform calcium imaging in slices of 4-5 months-old cerebral organoids. However, the slices did not recover well from the injury and we could not observe robust patterns of calcium dynamics. To transpose this challenge and taking into account that neuronal electrical activity leads to the expression of activity-related genes (ARGs), which can be used as molecular markers to identify neurons exposed to different patterns of electrical activity ((231); (232)). We decided thus to take advantage of our snRNA-seq data to check the expression of these ARGs on the 6 months organoids (Fig. 28).

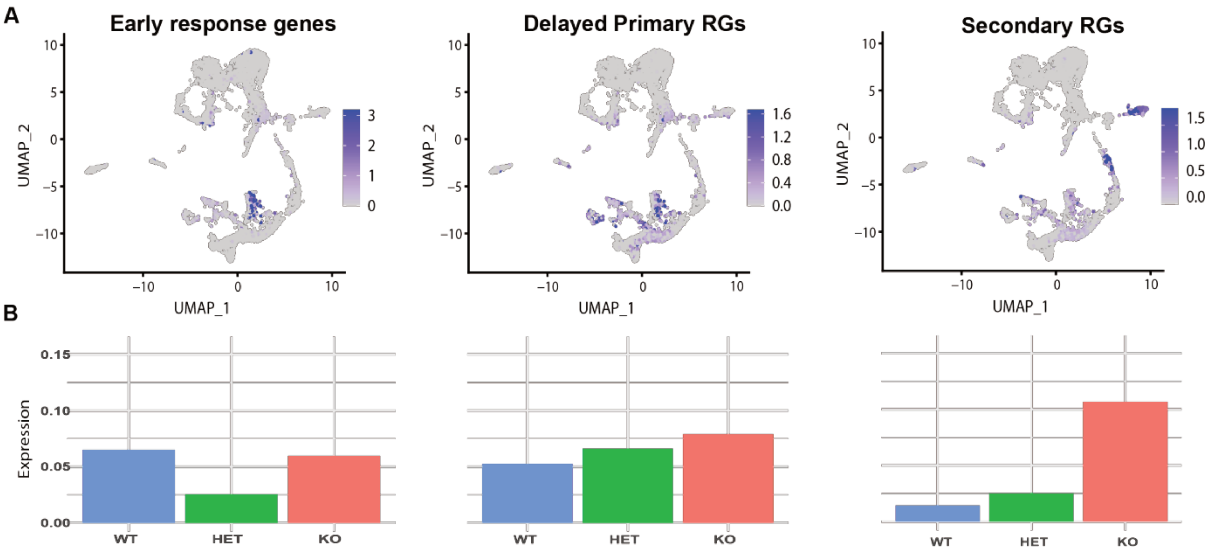

Figure 28: mRNA electrical signature of *PTK2B*-mutated cerebral organoids. Activity-regulated genes (ARGs) expression on PTK2B clusters based on Hrvatin et al., 2018 or Tyssowski et al., 2018 notations. **B)** Expression of the ARGs across the PTK2B genotypes. N=4 independent organoids per genotype.

The transcriptomic analyses could detect the expression of three main groups of activity-related genes: the early response genes or rapid primary response genes (rPRGs) - induced by brief activity patterns; the delayed primary response genes (dPRGs) - induced by sustained activity; and the secondary response genes (SRGs) - which activation often involves a cascade of gene regulatory events. We observed that the proportion of glutamatergic neurons expressing dPRG and SRG signatures were strongly increased in *PTK2B* KO and, to a lesser extent, HET glutamatergic neurons compared to the WT, indicating that these cells were also hyperactive in *PTK2B* HET and KO cerebral organoids (Fig. 28B).

Importantly, this electrical activity pattern was not observed in GABAergic neurons (data not shown) that do not express *PTK2B* in this system. These results support our previous observations in 2D cultures suggesting that under-expression of PTK2B leads to neuronal hyperexcitability.

7.4. PTK2B-mediated increased neuronal electrical activity depends on TAU

As previously discussed, modulation of TAU expression can lead to increased neuronal electrical activity. Given the pronounced impact of *PTK2B* HET on enhancing neuronal firing and its concomitant influence on TAU hyperphosphorylation, we decided to explore whether this electrical phenotype could be attributed to the effects of PTK2B on TAU.

Thus, we evaluated whether by knocking down TAU expression, we could rescue the effects observed on neuronal activity on *PTK2B* WT and HET cultures. To that, we took advantage

of an antisense oligonucleotide (ASO) targeting TAU (kindle provided by Dr. Ravi Jagasia, Roche, Switzerland) to selectively inhibit TAU mRNA expression in 2D cell cultures of the different *PTK2B* genotypes. *PTK2B* WT and HET mixed cultures were treated at three weeks with either saline or ASO TAU at 1uM for two weeks (n=2 experiments). At the end, calcium imaging recording was performed, and proteins collected to check TAU total and phosphorylated levels by WB (Fig. 29).

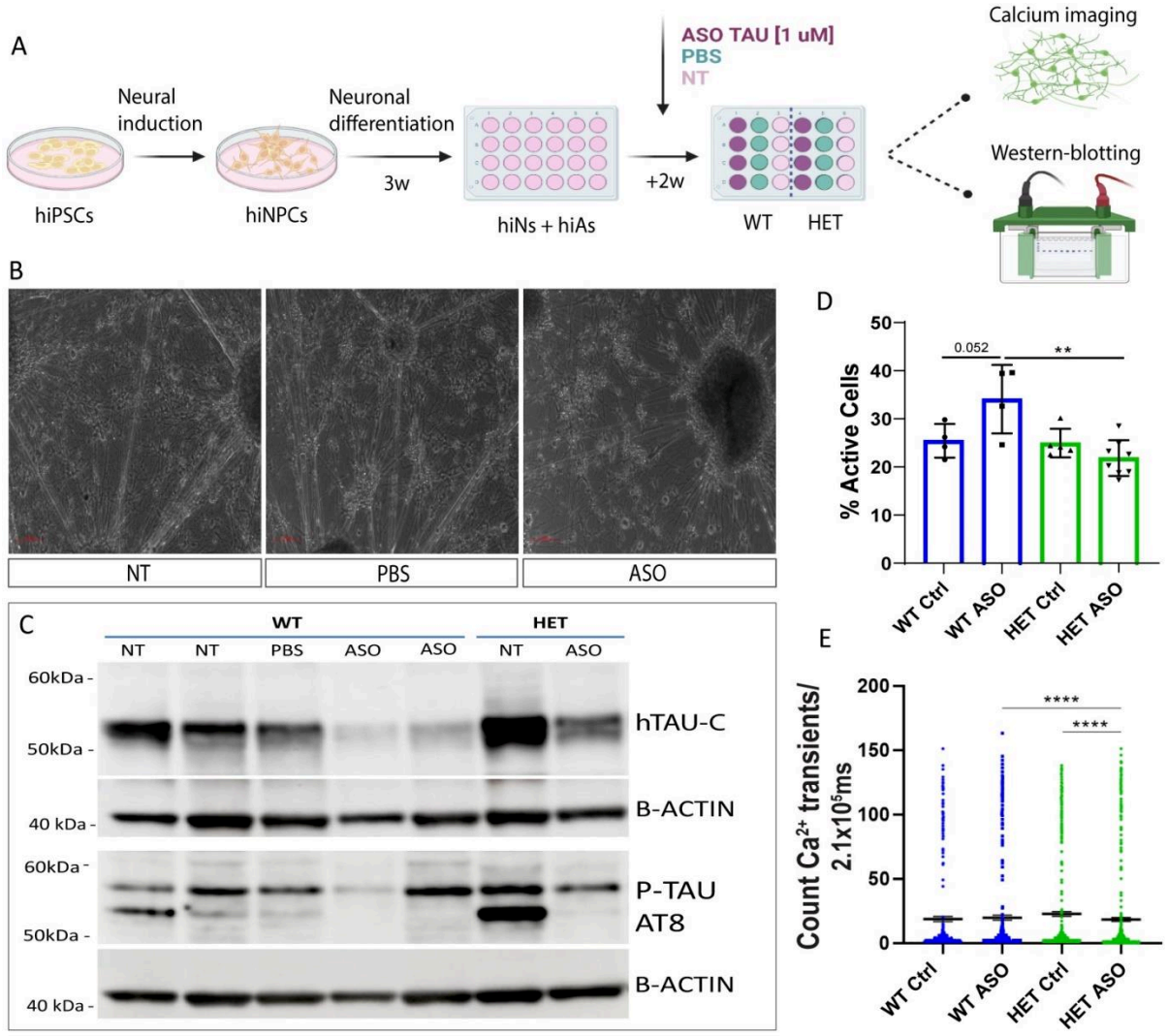

Figure 29: TAU expression correlates with increased neuronal electrical activity in PTK2B HET neurons. A) Scheme of the experimental design showing the spontaneous differentiation of iPSCs to hiNs and hiAs treated with ASO TAU 1uM or PBS 1x during the last 2 weeks of differentiation. **B)** Brightfield images of WT cultures at 5 weeks of differentiation; Scale bar: 100um. **C)** Western blotting showing the total levels of TAU and P-TAU (Ser202/T205) of 5 weeks differentiated cultures for PTK2B WT, HET and KO, either non-treated or treated with ASO TAU or PBS. **D-E)** Calcium imaging data of 5 weeks WT and HET cultures either treated with PBS or ASO TAU 1uM. **D)** % of active cells per field for Ctrls (PBS 0.1M) and ASO TAU. **E)** Counts of Ca^{2+} transients within $2.1x10^5$ms on the different *PTK2B* genotypes and treatments and ASO TAU 1uM or PBS 0.1M as control). Statistical significance analyzed either by ordinary one-way ANOVA - Tukey's multiple comparisons test or Kruskal-Wallis multiple comparison test for non-Gaussian distributions. N=2 independent experiments; 2 wells of each.

Visually, although neurons remain present and active, neuronal morphology appears to be affected by ASO TAU treatment, as expected once TAU is a microtubule binding protein (Fig. 29B, D and E). Immunoblotting analyses revealed that the use of the ASO TAU at 1uM during two weeks effectively reduced TAU expression compared to NT and saline (Fig. 29C). Additionally, preliminary calcium imaging analyses show that the ASO TAU treatment tends to increase the percentage of active cells in the WT ASO compared to vehicle of the same genotype. Interestingly, regarding the genotype, the ASO treatment in HET cells significantly reduces the percentage of active cells compared to ASO treatment in WTs (Fig. 29D).

In terms of counts of Ca^{2+} transients, the ASO TAU treatment demonstrates no significant correlation with alterations in WT cells compared to the vehicle. However, noteworthy observations emerge when PTK2B expression is reduced. The treatment with ASO TAU decreases the counts of Ca^{2+} transients in the HET cells compared to the corresponding vehicle (Fig. 29E). Hence, analyses within the HET genotype showed that the ASO TAU treatment decreases the neuronal electrical activity compared to the HET control.

When comparing *PTK2B* WT and HET neurons, both exposed to ASO TAU treatment, we observed a remarkable reduction in the Ca^{2+} transients in PTK2B HET compared to the corresponding WT (Fig. 29E).

8. PTK2B signaling in the regulation of neuronal electrical activity and the Aβ-mediated effects

8.1. PTK2B expression decreases along AD Braak stages

Analysis of the human brain transcriptome data available in the Atlas of the Developing Human Brain (BrainSpan - Allen Institute for Brain Science) revealed significant changes in PTK2B expression with aging. A progressive increase in PTK2B expression was observed throughout the entire brain during normal human aging (Fig. 26A – it shows the expression only in the hippocampus, although a similar pattern was observed throughout the whole brain). FAK, despite its significant similarity to PTK2B and shared function as tyrosine kinase, has a relatively constant expression throughout life (Figure 30A).

The assessment of public bulk RNA-seq data (242) indicates that PTK2B expression in the human brain is primarily found in excitatory neurons, which are predominantly glutamatergic (Fig. 26B). Remarkably, when analyzing patients at different AD Braak stages, we observed a significant decrease in PTK2B expression in the glutamatergic population of the entorhinal cortex (EC) and superior frontal gyrus (SFG) - regions that are particularly affected by the disease (Fig. 26C). In the EC, the reduction is 65% from Braak 0 to II, 60% from 0 to VI, and

not significant from II to VI. Similarly, in the SFG, there is a 63% reduction from Braak stages 0 to II, a 53% reduction from 0 to VI, and no significant reduction from stages II to VI (Figure 30C).

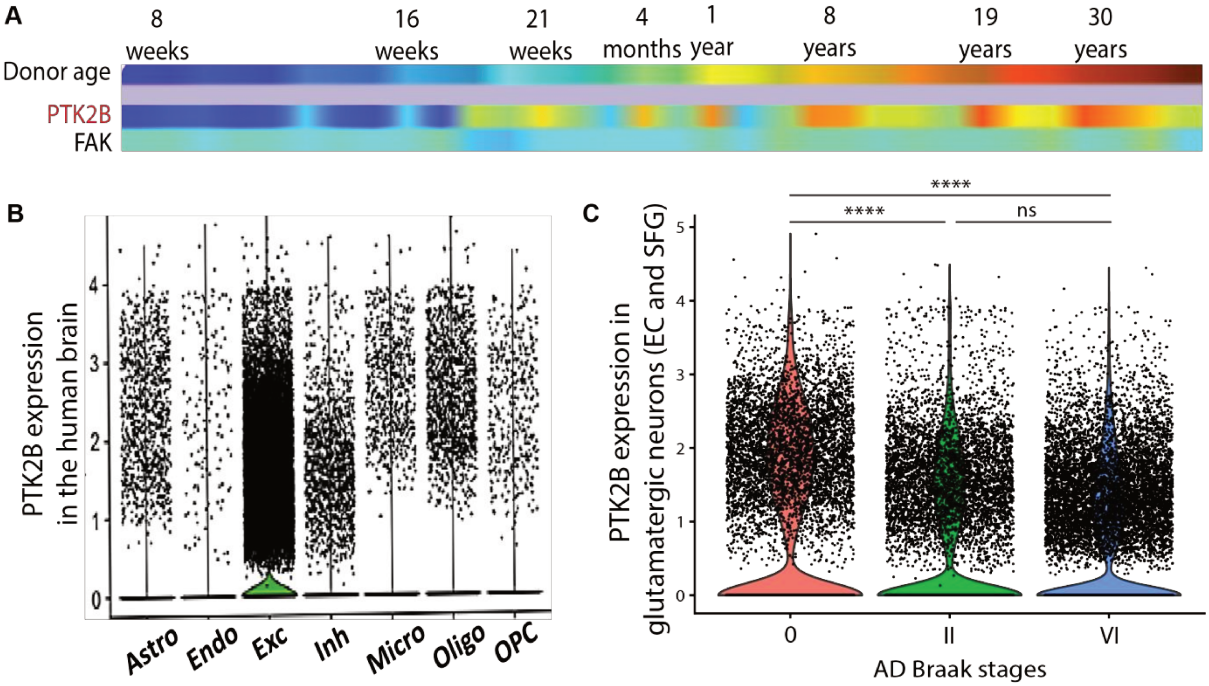

Figure 30: PTK3B expression in the human brain and along AD Braak stages. A) Transcriptome bulk RNA-seq data from 42 human hippocampus specimens, spanning pre- and postnatal-development in both males and females. Color code on the "Donor" row goes from younger ages (blue) to older ages (red). Color code on the gene rows represents the intensity of the expression – from the lowest expression (blue) to highest expression (red). "Weeks" refears to post conceptional weeks. Expression measurement: log2 RPKM (reads per kilobase per million) values **(B-C)** Analyses of public scRNA-seq data (Leng et al., 2021). **B)** Violin plots showing the expression of PTK2B per cell type in the entire human brain. **C)** Violin plots showing the expression of PTK2B throughout AD Braak stages in glutamatergic neurons from the EC and SFG regions of the human brain.

** The original search with the data from the BrainSpan **(A)** can be reproduced on: https://www.brainspan.org/rnaseq/searches?exact_match=false&search_term=PTK2&search_type=gene&page_num=0*

Notably, this finding indicates that instead of a gradual rise in PTK2B expression throughout adulthood, individuals with Alzheimer's progressively experience a decline in PTK2B expression in significant brain regions associated with the disease. This indicates that PTK2B may serve as a potential marker for the progression of Alzheimer's disease and an important player in the pathophysiology of the disease.

8.2. PTK2B expression affects neuronal hyperexcitability mediated by $A\beta_{1-42}$

Several lines of evidence indicate that neuronal electrical activity regulates Aβ concentration in the brain ((36); (37); (38)). Equally, Aβ deposition leads to neuronal hyperactivity in the brain ((39); (40)) and Aβ1-42 oligomers can increase neuronal activity, both *in vitro* and *in*

vivo ((41); (42); (32)). Notably, Aβ-dependent neuronal hyperactivity is only observed in neurons with preexisting baseline activity (32) and can be observed at picomolar concentration of Aβ oligomers (42). Therefore, there seems to exist a positive feedback loop between Aβ deposition and neuronal hyperactivation at early stages of the AD pathology.

Recent work in mice models has suggested that PTK2B plays a central role in AD-related synaptic dysfunction mediating Aβ-triggered dysfunction ((153); (145)). Thus, to probe the possible role of this protein on Aβ-mediated increased electrical activity in human neurons, we acutely exposed hiNs to low concentrations of synthetic $A\beta_{1-42}$ (100pM) and analyzed the effects of this treatment on the calcium dynamics of *PTK2B* WT, HET and KO hiNs after 24 hours (Fig. 23).

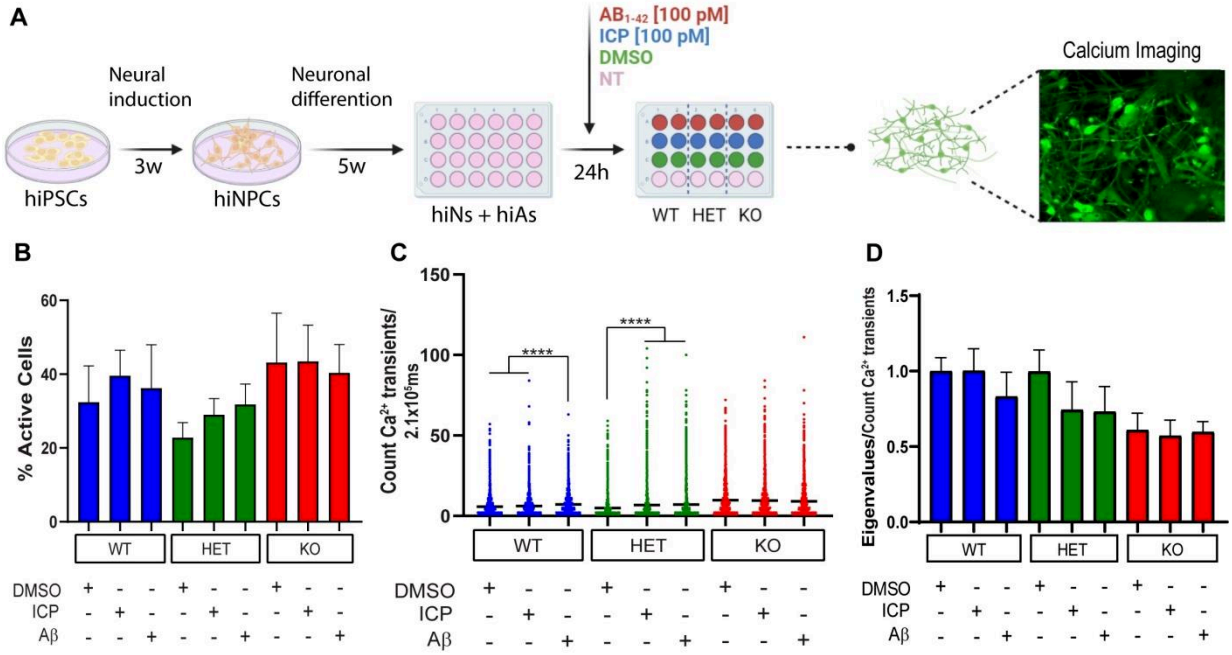

Figure 31: The level of PTK2B expression exerts a significant influence on the immediate effects of $A\beta_{1-42}$ exposure on neuronal Ca^{2+} transients. A) Scheme showing the exposition of PTK2B 5 weeks neuronal cultures to $A\beta_{1-42}$ (100pM) during 24h or to the inverted peptide (ICP), vehicle (DMSO) or non-treated controls. **B)** Percentage of active cells and **C)** Counts of Ca^{2+} transients within $2.1x10^5$ms among the different *PTK2B* genotypes and both $A\beta_{1-42}$-exposed and control conditions. **D)** Correlation among the neurons measured by the ratio between the detected eigenvalues and the counts of Ca^{2+} transients/$2.1x10^5$ms for each genotype and treatment condition. Statistical significance was analyzed using either ordinary one-way ANOVA with Tukey's multiple comparison test or Kruskal-Wallis multiple comparison test for non-Gaussian distributions. Significant P is <0.0001. N=4 independent experiments.

We observed that Aβ but not ICP treatment was sufficient to increase the frequency of calcium transients in *PTK2B* WT neurons compared to controls (Fig. 31C). In *PTK2B* HET hiNs, both Aβ and ICP cultures had higher frequencies of calcium transients compared to controls. In contrast, neither Aβ nor ICP treatments affected the frequency of calcium transients in *PTK2B* KO neurons (Fig. 31C). Despite the high frequency of calcium

transients, treatment with AB1-42 for 24 hours had no effect on the percentage of active cells or their synchronization in any *PTK2B* genotype (Fig. 31A and D). This experiment suggests that neurons with some level of PTK2B expression, either on the WT or HET, have increased calcium transients in response to Aβ1-42. However, neurons with full deletion of PTK2B did not respond differently in the presence of Aβ1-42.

8.3. $A\beta_{1-42}$ affects PTK2B-related molecular pathways at the protein level

Taking that into account, we decided to check whether Aβ exposition for 24 hours was already enough to alter PTK2B expression and phosphorylation. Interestingly, the treatment led to a slight increase in PTK2B total and phosphorylated levels at Tyr402, its main activation site (Fig. 32) in parallel with the increased neuronal electrical activity observed on this condition (Figs. 25, 26, and 28).

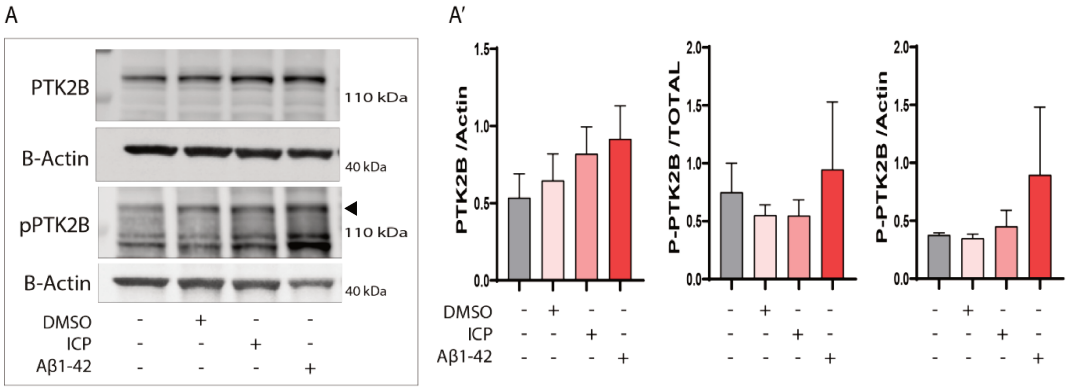

Figure 32: Acute $A\beta_{1-42}$ exposition potentially affects PTK2B levels in WT neural cultures. A) Immunobloting showing the levels of total and phosphorylated PTK2B at Thy402 and its quantifications (A') in WT 5 weeks spontaneous differentiated neural cultures. Statistical significance was analyzed using either ordinary one-way ANOVA with Tukey's multiple comparison test. N=4 independent experiments.

In order to characterize whether the possible increase in PTK2B total expression and phosphorylation mediated by Aβ would lead to alterations in downstream targets of PTK2B, we extended the immunoblotting analyses to other proteins (Fig. 33). Treatment with $A\beta_{1-42}$ for 24h, although sufficient to increase electrical activity, was not sufficient to significantly alter the expression of proteins such as total STAT3 and its phosphorylation sites Tyr705 and tyr727 (Fig. 33A), total and phosphorylated GSK3B at tyr216 and total and phosphorylated SRC at Tyr416 (Fig. 33B).

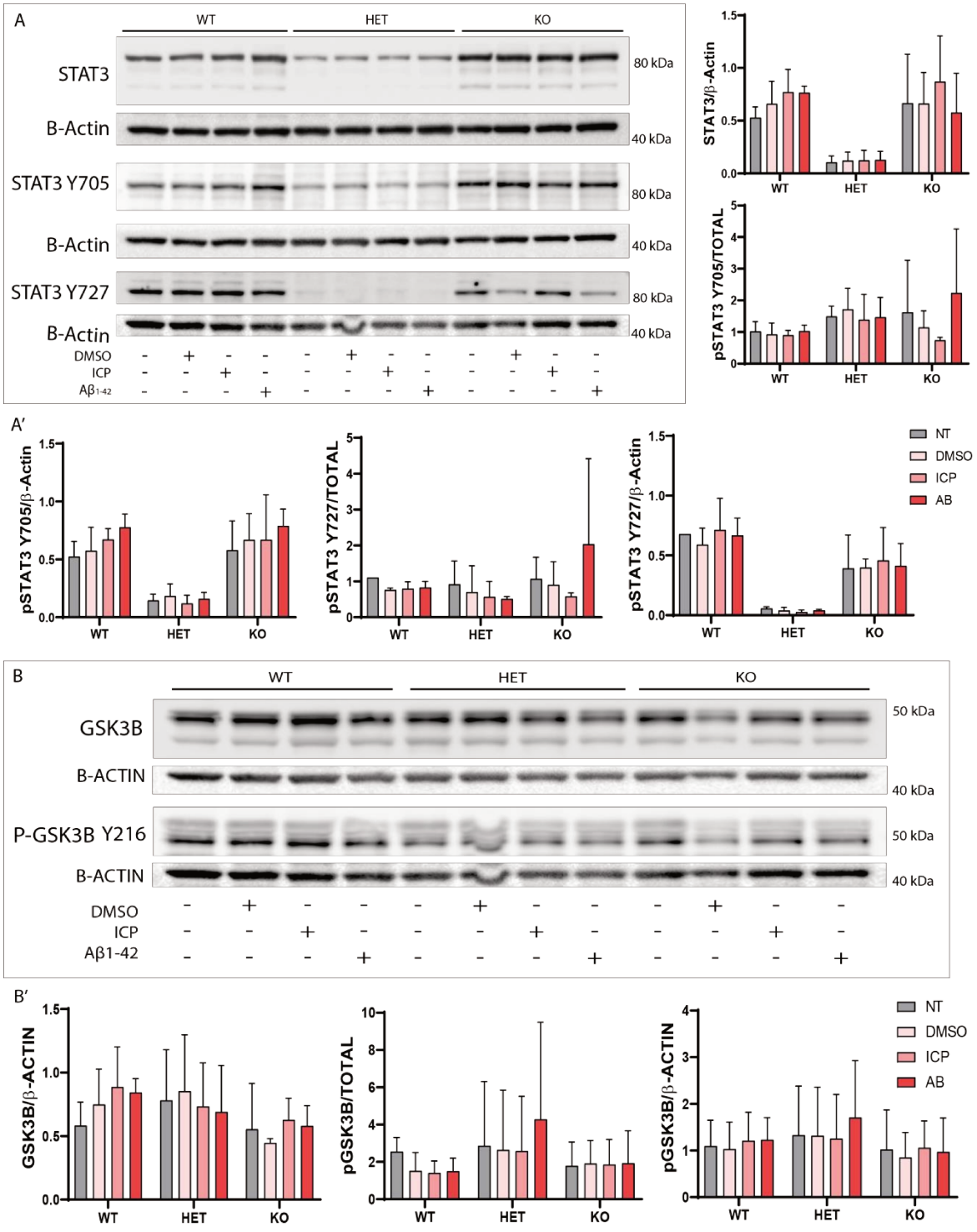

Figure 33: Acute exposure to Aβ1-42 has the potential to affect the activation of pathways downstream of PTK2B. Immunoblotting showing the levels of downstream STAT3 and GSK3B proteins across the different PTK2B genotypes in 5 weeks spontaneous differentiated cultures after 24h of Aβ exposition. **A)** Total and phosphorylated STAT3 at Tyr705 and Tyr727 followed by its quantifications (A')**.** B) Total and phosphorylated GSK3B at Tyr216 followed by its quantifications (B'). Statistical significance was analyzed using either ordinary one-way ANOVA with Tukey's multiple comparison test. N=4 independent experiments.

However, a trend towards Aβ-mediated increase expression can be observed for some of these proteins. This leads us to hypothesize that the cascades leading to AB-mediated

changes at the protein level would require longer exposure. To verify this hypothesis, we plan to further treat these cells with $A\beta_{1-42}$ for longer periods and observe its later effect on electrical activity and PTK2B-modulated molecular pathways.

9. Possible role of PTK2B in neural development

Morphological observations of the 2D cultures during the differentiation process from NPCs to induced neurons and astrocytes revealed that the PTK2B HET and KO cultures could be different from the WT one since early steps of differentiation. To evaluate the potential effect of PTK2B on neural cell differentiation from iPSCs, we fixed 2D cultures at different timepoints, 1, 3 and 5 weeks after seeding, and performed immunocytochemistry staining for different cellular markers. Interestingly, two main aspects could be highlighted, the morphological organization of the cultures and the effect of PTK2B modulation on astrocyte and neuronal differentiation.

Analyses of cultures at 1 week of differentiation showed that at this time point, PTK2B HET and KO cultures have more astrocytes than WTs, revealed by the higher expression of the astrocyte marker GFAP. Additionally, PTK2B HET neurons appear to be more differentiated than WT and KO neurons and are already organized into clusters (a feature observed at all stages of differentiation in this lineage) (Fig. 34).

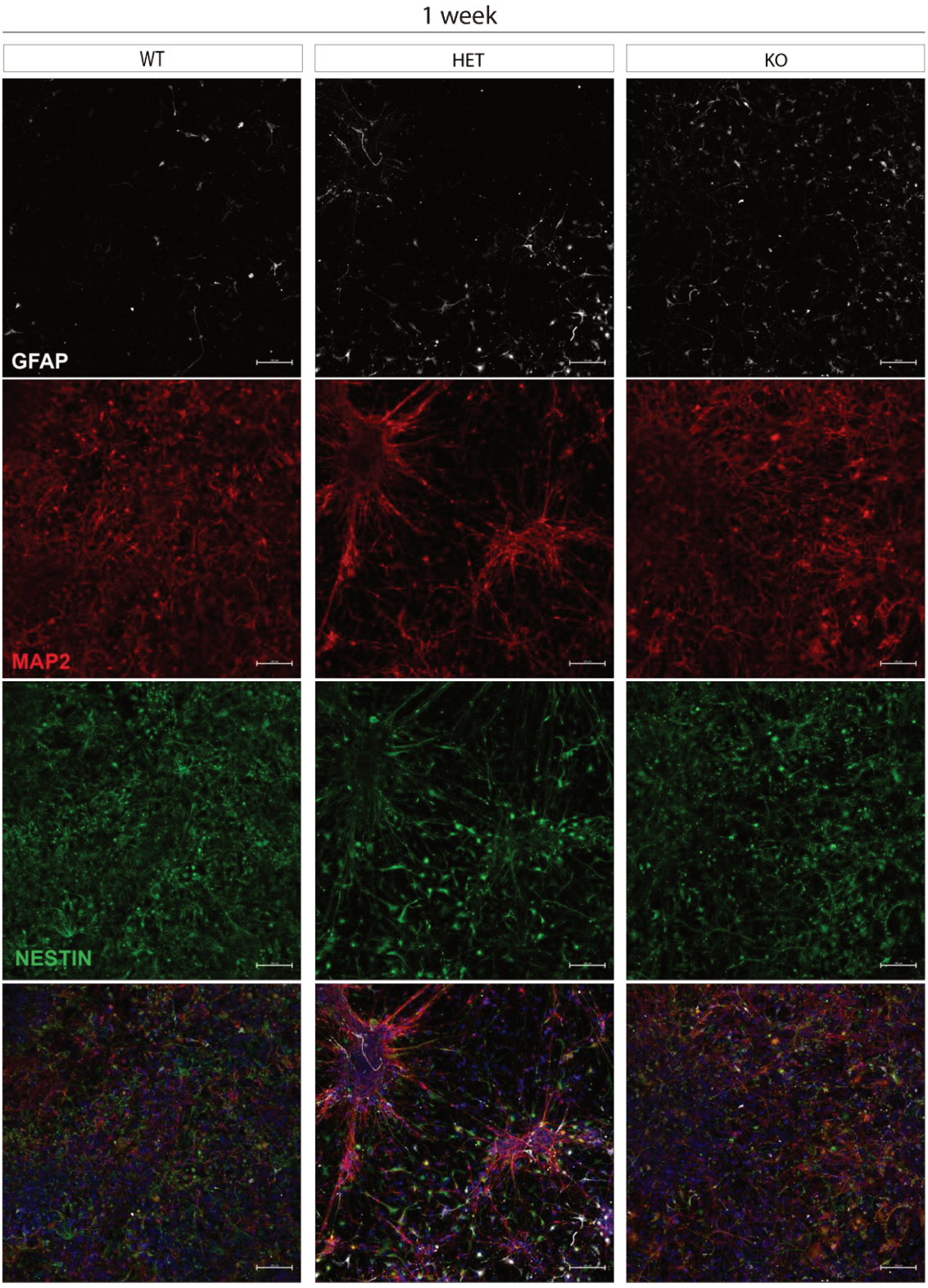

Figure 34: Different levels of PTK2B expression influences neural fate after 1 week of differentiation. Representative images of mixed neural 2D cultures derived from hiNPCs (ASE cell line) after 1 week of differentiation and stained for the astrocyte marker GFAP (white), neuronal marker MAP2 (red), NPC marker NESTIN (green), and DAPI (blue).

At the third week of differentiation, the GFAP expression in WT cultures increased compared to that observed at 1 week, but remained lower than the GFAP expression in HET and KO cultures. At the morphological level, PTK2B HET neurons tend to organize even more in the form of clusters than observed at 1 week, always different from the neuronal organization observed in WT and KO cultures (Fig. 35).

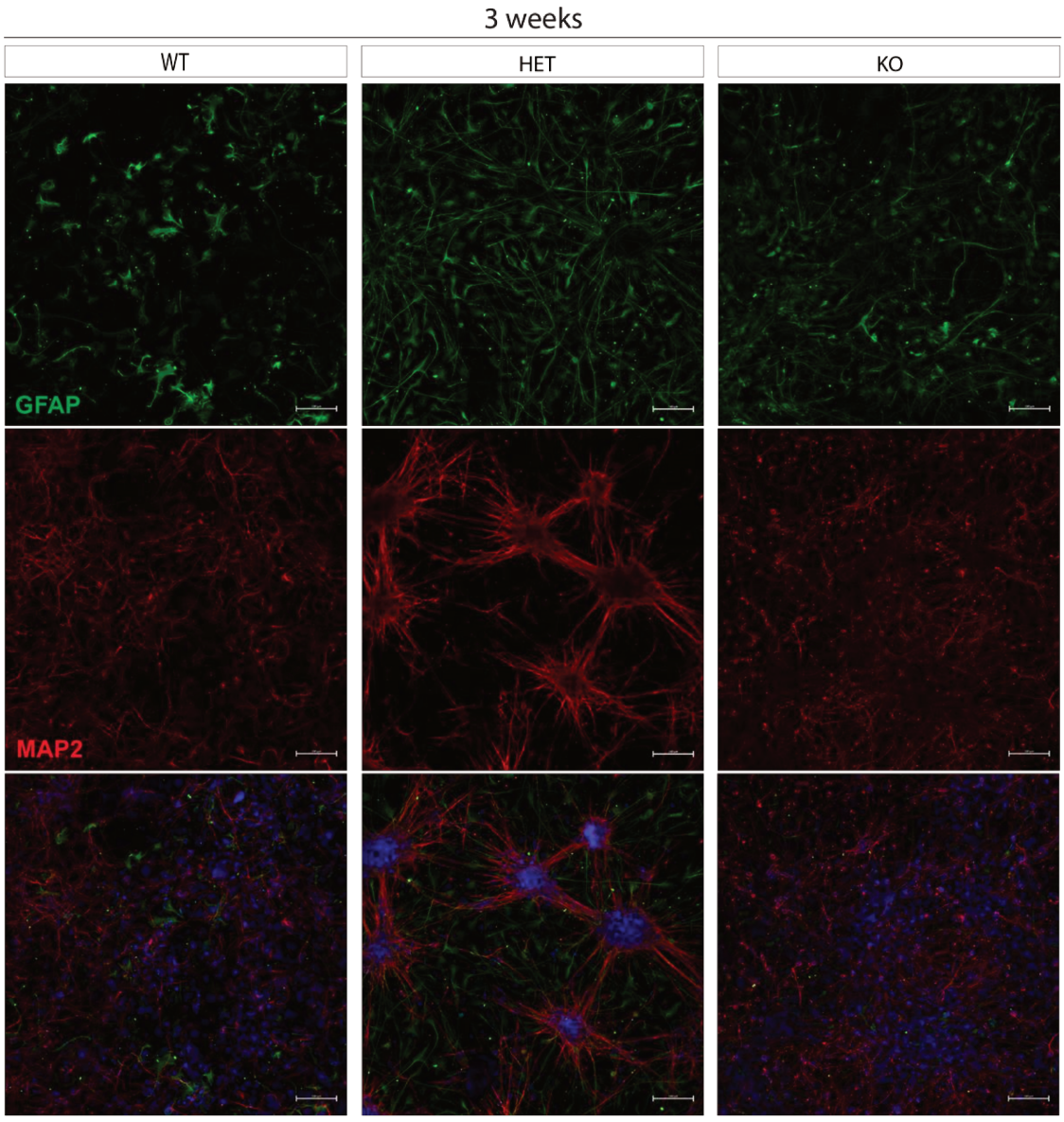

Figure 35: Different levels of PTK2B expression influences neural fate after 3 weeks of differentiation. Representative images of mixed neural 2D cultures derived from hiNPCs (ASE cell line) after 3 weeks of differentiation and stained for the astrocyte marker GFAP (green), neuronal marker MAP2 (red), and DAPI (blue).

At the end of the neural differentiation, at 5 weeks, PTK2B WT, HET and KO cultures are slightly more similar in terms of the proportion of GFAP+ astrocytes. The HET condition consistently shows large neuronal clusters, although, at this time point smaller scale clusters can also be observed in WT and KO conditions (Fig. 36).

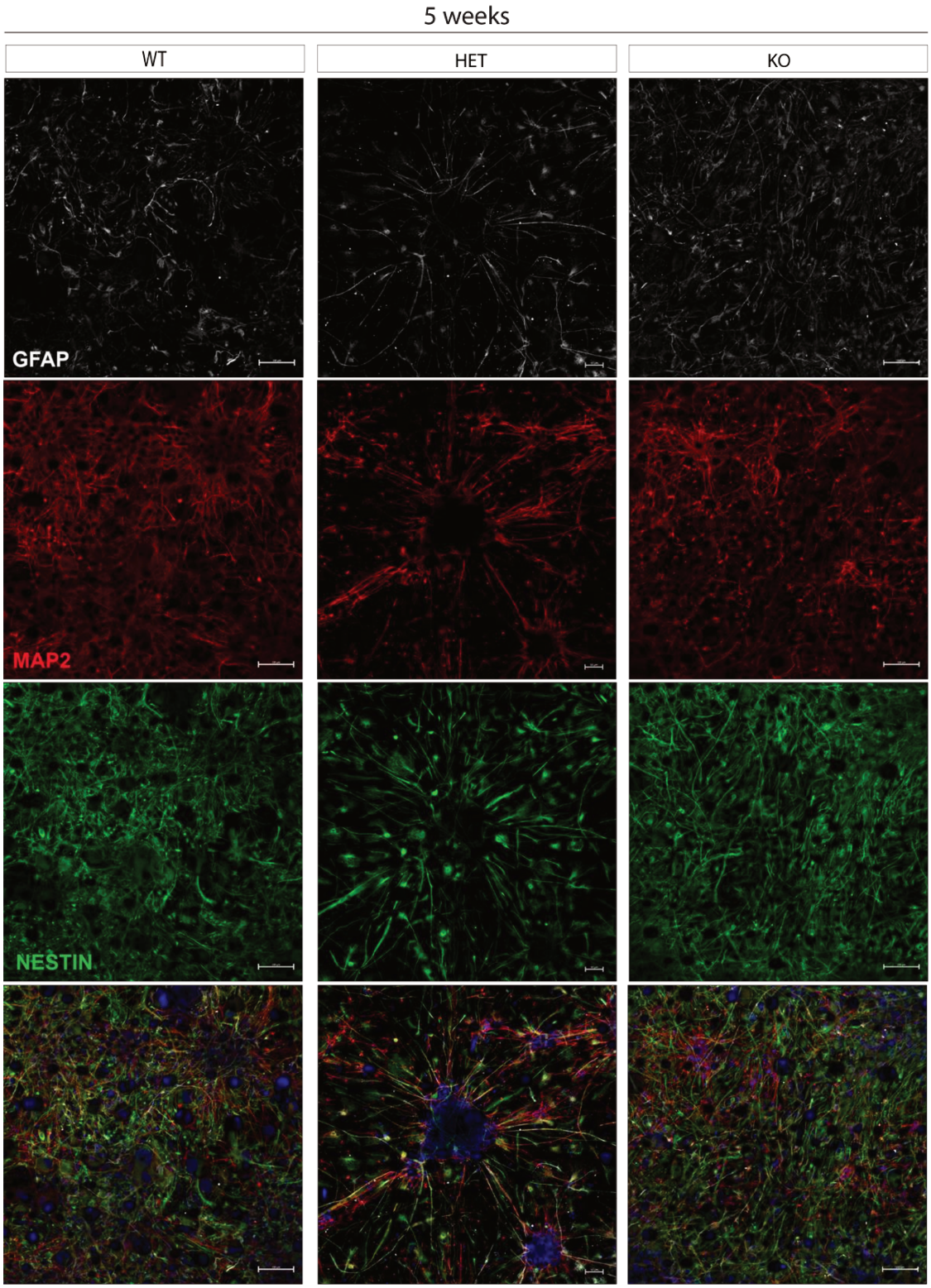

Figure 36: Different levels of PTK2B expression influences neural fate after 5 weeks of differentiation. Representative images of mixed neural 2D cultures derived from hiNPCs (ASE cell line) after 5 weeks of differentiation and stained for the astrocyte marker GFAP (white), neuronal marker MAP2 (red), NPC marker NESTIN (green), and DAPI (blue).

These immunocytochemistry analyses were also repeated on the BION-derived PTK2B cell lines and similar results were observed. Overall, this data suggests that PTK2B under expression levels may affect the neural differentiation of NPCs into neurons and astrocytes in an iPSC-derived 2D model by accelerating it.

Despite these differences, the overall cellular composition of the cultures was similar at 5 weeks (Fig. 9 – snRNAseq), but the different developmental dynamics observed in the different PTK2B genotypes must be taken into account for the interpretation of our data.

10. Cell-autonomous roles of PTK2B in human-induced glutamatergic neurons

As discussed in the previous section, an important drawback of the experiments described above is the possible effect of PTK2B under-expression in neuronal differentiation. To control these undesired effects, we employed a previously described protocol to generate enriched glutamatergic cultures by direct lineage-reprogramming of hiPSCs using doxycycline-inducible expression of Neurogenin2 (*NGN2*) (243). This protocol bypasses the stages of neural induction and differentiation and is believed to generate a homogeneous population of glutamatergic neurons. After NGN2 induction, exogenous human cerebral cortex astrocytes are added to support neuronal maturation and electrical function. Since this direct reprogramming speeds up the neuronal maturation, this methodology also allowed us to anticipate the analysis to 4 weeks of differentiation instead of 5, what is especially useful considering the effect observed on cell adhesion when knocking down/out PTK2B.

On this system, we took advantage of a reverse tetracycline-controlled transactivator (rtTA) and co-transfected it with the NGN2 plasmid with a 2 for 1 ratio, to punctually turn on the NGN2 expression, whose plasmid has a tetracycline-dependent promoter (Fig. 37A). Although this system has its advantages, both plasmids used (rtTA and *NGN2*) carried a sequence that confers puromycin resistance, to select out the non-transfected cells. As a result, iPSCs transfected only with rtTA occasionally survived the reprogramming, generating a culture with some other unexpected cell types. To circumvent this limitation, we developed a novel non-puromycin-resistant rtTA plasmid, which allows a proper antibiotic selection only of cells transfected with both plasmids, generating a pure culture of glutamatergic neurons. These new cell lines have already been expanded and experiments are now ready to be continued.

We have already performed some preliminary electrophysiological experiments in these cultures using a different MEA system (MEA2100-256-Systems, MCS), which requires the use of microfluidics devices to increase the sensibility of the recordings (2). The microfluidic

chambers were designed with three compartments – a pre, a post, and a synaptic compartment – that guide the neuronal process into microchannels over the electrodes. To avoid the quantification of the same action potential navigating along axonal processes, we concentrated our analysis in a single row of electrodes. We observed a trend towards an increase in the frequency of calcium transients in PTK2B HET and KO compared to WT *NGN2*-hiNs (Fig. 37C and D). This increase is more prominent in KO neurons at 4 weeks. After this time point, analysis of the cultures on microscopy and their electrical activity suggest that most cells had already died.

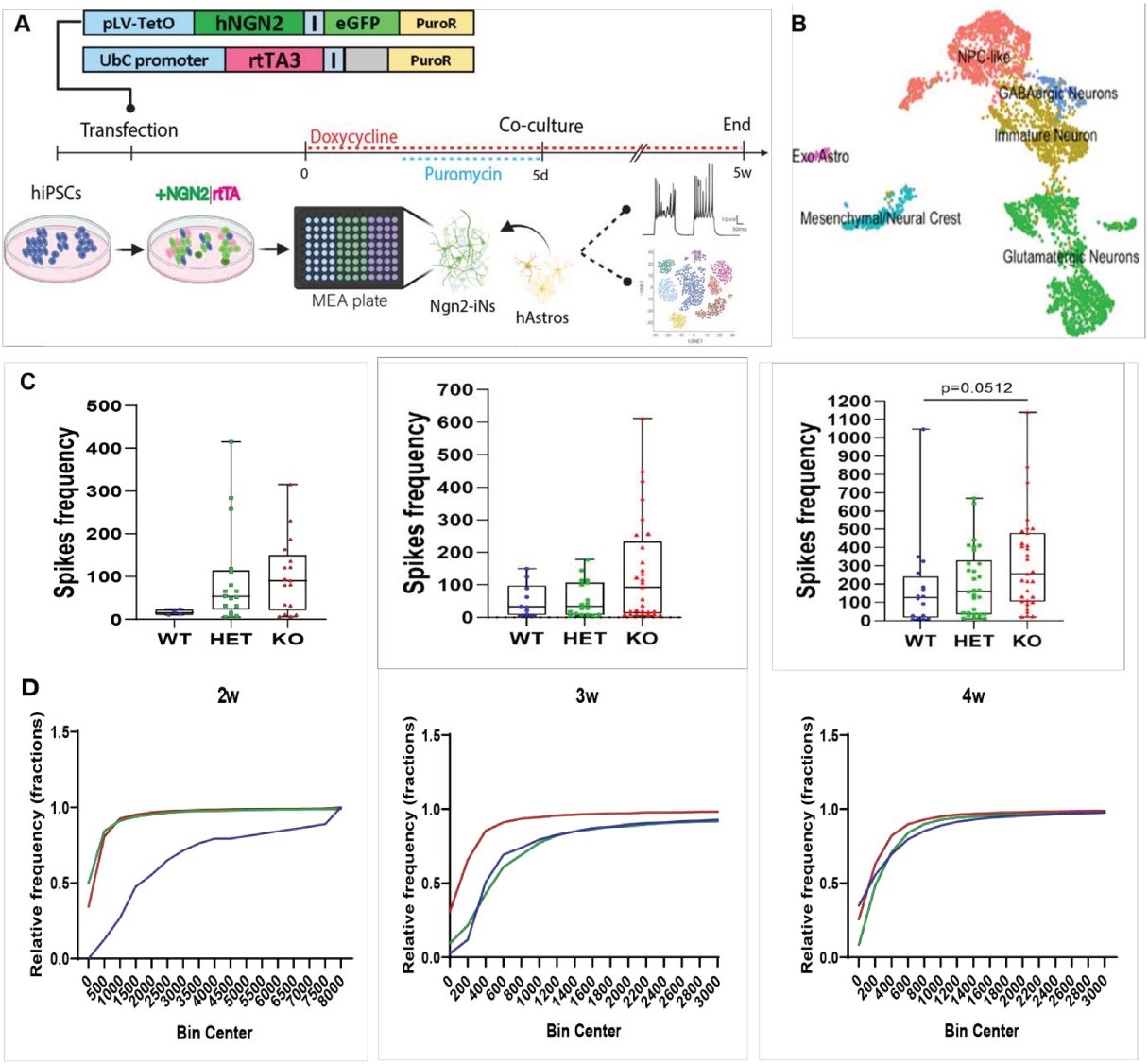

Figure 37: Absence of PTK2B in KO cells progressively increases the neuronal spikes frequency in glutamatergic cultures, reaching the peak at 4 weeks. A) Scheme of the experimental design showing the transfection of hiPSCs with the hNGN2 and the rtTA plasmids and their later differentiation into neurons coc-cultured with exogenous astrocytes. **B)** Dimension plot showing the main cell types identified by scRNA-sequencing of 5-weeks-old NGN2-hiNs cultures. **C)** Spikes frequency and relative spikes frequency per fractions from two to four weeks of differentiation among the *PTK2B* genotypes **(D)**. Non-parametric Kruskal-Wallis test. Data from 1 independent experiment; 3 sets of MEA per genotype;

Although these data come from one preliminary experiment and relates to multi-unit activity, they support our observations using calcium imaging and MEA in spontaneous differentiated cultures. Ongoing experiments will help to confirm these findings and further characterize the functional phenotype of our PTK2B mutated neurons.

In addition to the analyses of electrical activity and transcriptomic profile, we took advantage of the NGN2-induced cultures to verify the second AD hallmark observed in the ASE spontaneously differentiated cultures, the TAU hyperphosphorylation. Interestingly, preliminary immunocytochemical analyses of these cultures at 4 weeks showed an interesting pattern of total and phosphorylated TAU (AT8) labeling (Fig. 38). PTK2B HET and KO neurons showed more frequently an arrangement of TAU in the cell body and proximal dendrites, a pattern typically observed when TAU is hyperphosphorylated.

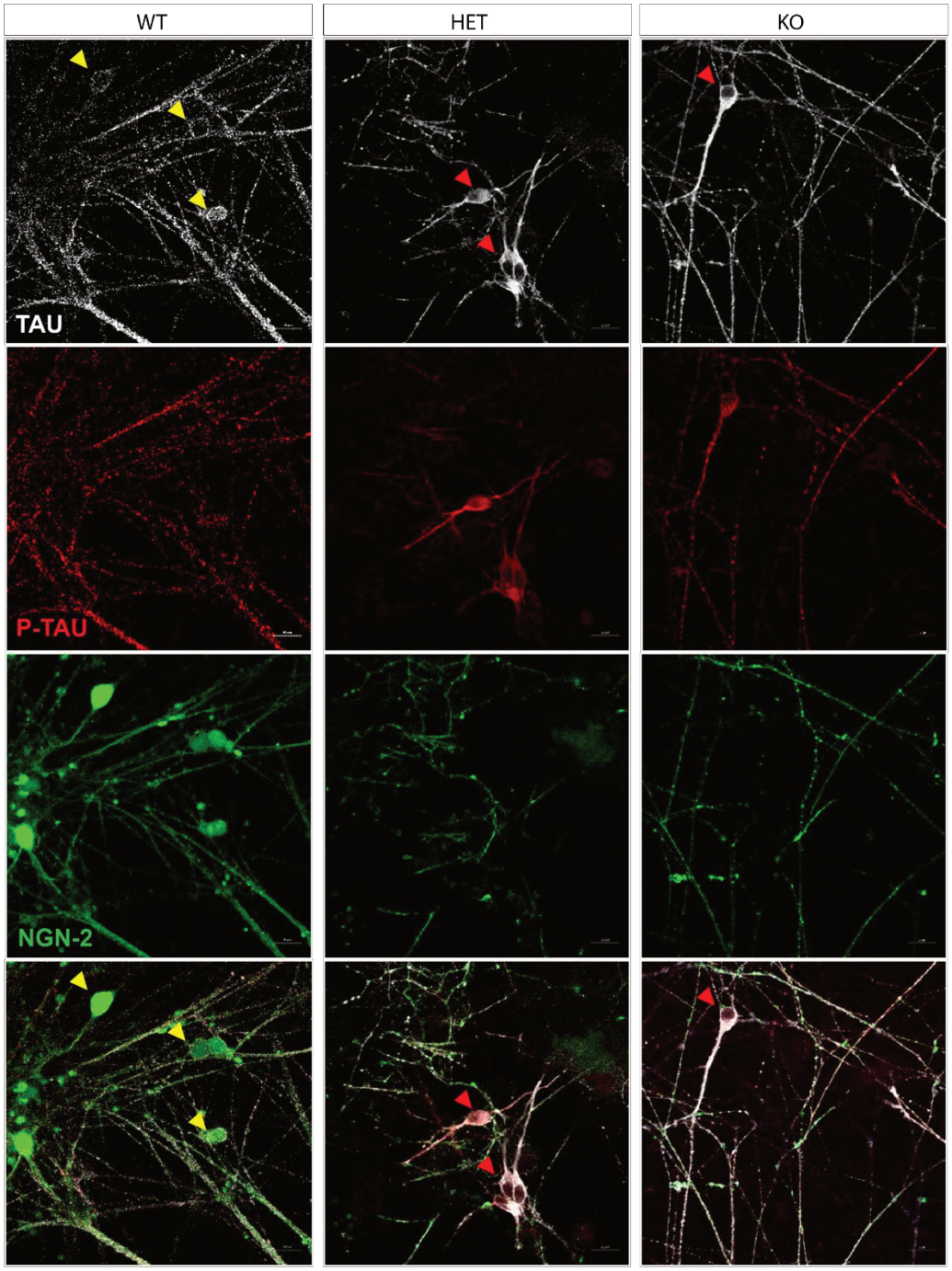

Figure 38: Reduced PTK2B expression possibly affects TAU aggregation and neuronal localization in NGN2-hiNs. Representative images of mixed neuronal 2D cultures (ASE cell line) at 4 weeks of differentiation and stained for total TAU (white), phosphorylated TAU at Ser202/Thr205 (red), and GFP (green) to label NGN2 transduced neurons. Scale bar: 20um.

The results with Ngn2-hiNs reinforce, in a third cell model, the previously discussed evidence that different expression levels of PTK2B are affecting neuronal activity and this is concomitant with changes in TAU phosphorylation.

Discussion

Genetic variants in the *PTK2B* locus are associated with an increased risk to develop AD. However, the impact of these variants for *PTK2B* expression and their pathophysiological consequences remain elusive. In this work, we investigated the impact of altered *PTK2B* expression in human-induced neural cells and started to tackle the effect of one genetic variant identified in AD patients. We show that *PTK2B* plays seminal roles in the regulation of neural cell differentiation, neuronal electrical activity, gene expression and TAU phosphorylation. Using two independents isogenic hiPSC lines genetically modified to express different levels of *PTK2B*, we show that both heterozygous and knockout mutations are associated with altered patterns of neuronal electrical activity and gene expression alterations mainly in glutamatergic neurons. Interestingly, we show that the reduced expression of PTK2B in HET cells, but not the full deletion of the protein in KO cells, leads to a significant increase in TAU phosphorylation at multiple AD-related epitopes. This molecular phenotype is associated with the increased activity of p38 MAPK and GSK3B, and reduced activity of ERK1/2 and LKB1. Preliminary data using a hiPSC line carrying the patient specific PTK2B variant rs28834970 suggests that this variant can also lead to a reduced expression of PTK2B and increased TAU phosphorylation, thus contributing to AD pathogenesis. Moreover, we show preliminary results suggesting that PTK2B-mediated signaling could be activated by increasing amyloid-beta peptides concentrations, potentially linking amyloidopathy to tauopathy phenotypes. Altogether, our results begin to shed light on the possible contribution of PTK2B to the neuronal dysfunctions observed in AD.

1. Role of PTK2B on TAU hyperphosphorylation

Our results in three different in vitro systems - 2D spontaneous differentiation, cerebral organoids and Neurog2-hiNs - show that reduced expression of PTK2B leads to greater levels of phosphorylated TAU at multiple residues. Immunoblotting analysis in cerebral organoids and spontaneously differentiated 2D cultures shows that reduced PTK2B expression significantly increases TAU phosphorylation at Ser202/Thr205 about 5- to 9-fold above controls. The detection of Ser202/Thr205 phosphorylation by the AT8 antibody is widely used to determine the temporal and spatial pattern of TAU phosphorylation in different stages of the disease. However, it is interesting to note that this increase is not restricted to the epitopes detected by AT8. PTK2B HET cells also show a significant increase in the phosphorylation of other five different TAU epitopes - Ser396/Ser404 (PHF-1), Thr217, Thr231, Ser202, and Tyr18. The phosphorylation of TAU at Thr231 and Tyr18 was already reported to be significantly increased at later Braak stages (V/VI) in the brain of patients diagnosed with AD (244), suggesting a relevant contribution of these residues to the

progression of the disease. Notably, phosphorylation of TAU at Tyr18 is directly mediated by PTK2B and required for TAU to modulate NMDA receptor-dependent excitotoxicity in primary neuronal culture (199). Moreover, our results on the NGN2-induced system show that a higher proportion of *PTK2B* HET and KO compared to WT exhibit TAU accumulation in the cell body and proximal dendrites, a pattern compatible with the aggregation of hyperphosphorylated TAU in the brain (58).

Our molecular findings on TAU phosphorylation are in agreement with recent work showing that pharmacological inhibition of PTK2B-mediated signaling by PF-719 increases TAU phosphorylation in iPSC-derived human neurons (200). Moreover, previous studies of our lab have demonstrated that PTK2B is an early marker and an *in vivo* regulator of TAU-related toxicity in Drosophila eyes and wings (105).

Lastly, we and others (242) have shown that the total levels of PTK2B mRNA expression in glutamatergic neurons of patients with AD are reduced at late compared to early stages of tauopathy as indicated by Braak stages (62), which is a classification of the severity of the disease based on the occurrence of NFTs (formed of hyperphosphorylated TAU). In fact, we show a significant decrease in PTK2B expression in mid (II) and late (VI) compared to early (0) Braak stages, but not when comparing late to mid stages. This could suggest that the decrease of PTK2B occurs at early stages of tauopathy, potentially contributing to this pathological event. Therefore, it is plausible to speculate that either neurons expressing lower levels of PTK2B are more prone to TAU hyperphosphorylation or that other pathological processes in the AD brain leads to a reduced PTK2B expression in neurons, contributing to tauopathy.

Future experiments in the lab will try to establish the possible causal relations between the activation of PTK2B-mediated signaling in human-induced neurons and TAU phosphorylation. To that, we will employ genetic strategies to selectively express dominant-negative forms of PTK2B in fully differentiated neurons, thus circumventing the possible effects of PTK2B in cell differentiation (see below) and allowing us to confirm whether the reduction of PTK2B signaling precedes the increase in TAU phosphorylation in hiNs.

According to this possibility, our results using different hiPSC lines - ASE, BION, and a third line (data not shown) - show that different levels of PTK2B expression are associated with proportional effects on TAU phosphorylation. In fact, cell lines expressing less PTK2B protein showed higher levels of total and phosphorylated TAU, and vice-versa. This can be observed, for example, when comparing the expression of PTK2B in hiNs derived from our three isogenic BION hiPSC lines – C2 (WT), S5 (SNP), and PT26 (HET) – where we observe that the insertion of the SNP observed in patients lead to both an intermediary

reduction in PTK2B expression and an increase in TAU phosphorylation compared to WT and HET mutation (Fig. 9 – characterization of BION cell lines).

Also consistent with this interpretation, the reduction of *PTK2B* in HET organoids compared to WT is 41%, while the same ASE cells in 2D cultures have a reduction of 77%. This may explain why the effect of *PTK2B* HET on TAU was less pronounced in 3D cultures than in 2D. This evidence indicates a dose-dependent effect of PTK2B on TAU homeostasis, which we plan to investigate in more detail in the future.

Notably, the study of Leng et al. (242) using single-cell RNA-seq data from the brain of patients diagnosed with AD showed the existence of a cellular subpopulation of excitatory neurons selectively vulnerable to decrease during the progression of the disease (242). Interestingly, analysis of the different expressed genes on this subpopulation revealed that PTK2B expression is reduced in Braak stage VI vs. 0. It is tempting to speculate that the lower PTK2B expression in this neuronal subpopulation contributes to its selective vulnerability in the brain of patients with AD. Along these lines, we could also suggest that physiological levels of PTK2B could be protective against TAU-related pathology, whereas reduced PTK2B expression in vulnerable neurons promotes TAU phosphorylation, as indicated in our hiPSC-derived models.

2. Role of PTK2B in spontaneous neuronal electrical activity

Multielectrode array experiments performed on two different hiPSC cell lines showed that reduced PTK2B expression alters the electrical properties of neurons. Once sorted as single units, PTK2B heterozygous and knockout neurons exhibit increased electrical activity compared to wild type. In addition, these PTK2B mutant cell cultures also exhibited temporal disorganization of bursts, suggesting a potential involvement of PTK2B in neuronal synchronization. These findings are consistent with those of Giralt and collaborators in a mouse model, where they showed that no LTP could be observed in CA1 hippocampal slices of either *Pyk2* heterozygous or knockout mice compared to wild type (152), suggesting a role for PTK2B in memory functions and synaptic plasticity.

Other AD models using hiPSC-derived neurons also succeeded to recapitulate changes in neuronal excitability. Ghatak and collaborators showed that hiPSC-derived neurons carrying mutations in *APP* and/or *PSEN1* display increased sodium current density and increased excitatory synaptic activity (67). Moreover, our work using isogenic *BIN1* WT, HET and KO hiPSC lines showed that reduced BIN1 expression is sufficient to elicit changes in the electrical properties of human induced neurons in a cell-autonomous fashion. In this study,

BIN1 KO hiNs display greater firing frequency compared to the WT, notably through modulation of L-type calcium channel expression (CaV1.2) (2). Our work on *PTK2B* and *BIN1* provides evidence supporting a role of AD risk genes for the regulation of neuronal electrical activity. Interestingly, BIN1 mediates neuronal electrical activity via calcium channels and PTK2B is downstream of calcium modulation in hiNs. Therefore, it is likely that these two genes may converge into a similar pathophysiological mechanism. According to this interpretation, we observed that reduced expression of both *PTK2B* and *BIN1* lead to alterations in calcium transients in hiNs**.** Data from calcium imaging recordings show that the reduced expression of PTK2B in HET cells results in an increase in calcium spike frequency, without significant alterations in the percentage of active neurons. In KO cells, this frequency is further accentuated, indicating a dose-dependent effect of PTK2B on the regulation of neuronal activity.

Taken together, our electrophysiological data suggests that PTK2B regulates crucial biological processes involved in the regulation of neuronal electrical activity and/or synaptic transmission. Therefore, altered expression of this risk gene in the AD brain may contribute to the alterations of neuronal functional properties observed in patients during the early stages of the disease.

Changes in neuronal electrical activity and TAU phosphorylation are associated in many other AD models. For instance, increased neuronal excitability observed in individuals with AD has been associated to greater levels of NFTs (mainly formed by hyperphosphorylated TAU) (69). The presence of TAU in human cerebrospinal fluid induces increased neuronal excitability and alters hippocampal theta oscillations in mouse hippocampal brain slices (245). Conversely, increased neuronal excitability induced by various mechanisms, such as seizures or glutamate receptor activation, has been shown to increase TAU phosphorylation, in part due to activation of TAU kinases ((70) for review). In animal models of epilepsy, increased neuronal activity resulted in increased TAU phosphorylation (71) in the hippocampus.

In this context, it is possible that reduced PTK2B expression first leads to an increased TAU phosphorylation and, as a consequence, this causes the changes in electrical activity, or the contrary. Our preliminary data using ASO TAU on *PTK2B* HET cultures suggest that the neuronal electrical alterations observed in *PTK2B* HET can be, at least partially, explained by TAU-mediated effects. Although more experiments, including MEA electrophysiology, are needed to confirm this possibility, these preliminary findings establish an interesting link between TAU expression, TAU phosphorylation, PTK2B expression and neuronal electrical activity – all of them affected by AD pathology. Additionally, ongoing experiments in the lab

aim at investigating whether electrical stimulation alone is sufficient to modulate PTK2B activation and TAU hyperphosphorylation.

3. Molecular pathways altered by reduced PTK2B expression

Protein level analysis indicates that the increase in TAU phosphorylation observed in PTK2B HET compared to WT cultures is unlikely to be explained by altered SRC phosphorylation, although this kinase is a direct target of PTK2B and has been shown to interact with TAU and phosphorylate it at Tyr18 in response to Aβ peptides (246). In contrast, GSK3β activation through phosphorylation on Tyr216 appears to be enhanced in PTK2B HET cultures compared to the WT. Notably, the earlier mentioned study from Brody and collaborators revealed that inhibiting PTK2B pharmacologically in hiPSC-derived cultures did not result in significant changes to GSK3β, despite an increase in TAU phosphorylation (200). Interestingly, GSK3β played a role in amplifying TAU phosphorylation at Ser202/Thr205 when co-expressed with PTK2B. This observation is intriguing as GSK3β is a direct target of PTK2B, which activates GSK3β by phosphorylating it at Tyr216. On the contrary, PKC suppresses GSK3β function by phosphorylating it at Ser9, and this suppression becomes more pronounced with increased intracellular calcium levels, which also influences PTK2B activation. Therefore, the combined impact of these two calcium-dependent pathways affects GSK3β balance, subsequently influencing its role in TAU phosphorylation.

Besides the slight increase on GSK3β activation, other TAU kinases can be presumed to mediate this process and lead to higher levels of total and phosphorylated TAU in *PTK2B* HET cultures. Our results showed that despite the reduction in total p38 MAPK levels in *PTK2B* HET cells, its activation through phosphorylation at Thr180/Tyr182 is increased 3-fold. Moreover, *PTK2B* HET cells show reduced levels of phosphorylated LKB1 at Ser428 compared to the WT. LKB1 was previously described to regulate TAU through modulation of the activity of p38 MAPK. Similarly, *PTK2B* HET cells show reduced phosphorylation of ERK 1/2 at Thr202/Tyr204 when compared to WT. An effect on ERK was also observed in a mouse model knockout for *PTK2B*, where decreased ERK 2 expression is observed in hippocampal synaptosomes (200).

Although NMDA receptors play a critical role in synaptic plasticity and neuronal viability, their excessive activation can lead to elevated intracellular calcium levels. This increased calcium influx can lead to excitotoxicity and subsequent neurodegeneration (247) a process known as glutamate excitotoxicity. Notably, in the context of Alzheimer's disease, recent research

has shown that this activity triggers the activation of pro-apoptotic pathways involving p38 MAPK, GSK3B, JNK, and nitric oxide (NO). These events may coincide with the suppression of survival pathways, including the inhibition of ERK activity and other molecules such as Ca2+/calmodulin-dependent protein kinase-II (CaMKII) and CREB (248). Significantly, this hypothesis is consistent with our biochemical findings in PTK2B HET cultures, which showed activation of p38 MAPK kinase and GSK3B, along with inhibition of ERK 1/2. This suggests that these pathways may be prioritized when PTK2B is reduced, potentially culminating in subsequent neuronal death (Figure 39). Future experiments should address whether reduced PTK2B expression in hiNs induce activation of pro-apoptotic pathways.

In addition, increased intracellular Ca2+ can activate other protein kinases – including PTK2B – leading to hyperphosphorylation of TAU ((249); and (143)). PTK2B also indirectly regulates NMDA through the phosphorylation of FYN and SRC. This may contribute to the increased calcium transients observed in *PTK2B* HET and KO neurons compared to the WT through calcium imaging, and lead to a vicious cycle of neuronal excitability. These observations can also help to explain the central role of NMDA receptor function and its blocker mechanisms in AD pathology progression (122).

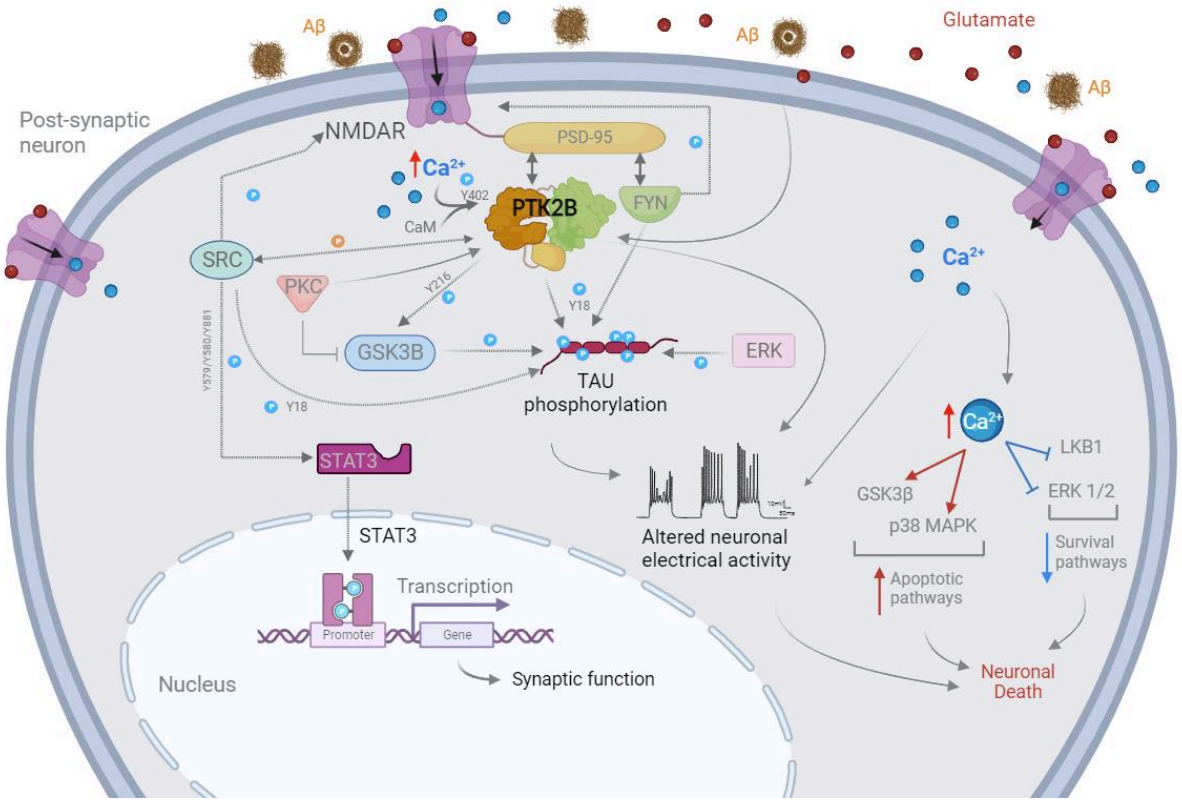

Figure 39: PTK2B signaling pathway and the primary molecular insights from its manipulation hiPSC-derives neural cells.

In Figure 39, I try to summarize our main findings studying hiNs expressing reduced levels of PTK2B and put these data in a broader context of glutamate-mediated neurotransmission. PTK2B-mediated signaling contribute to regulate TAU phosphorylation at specific Alzheimer's disease-related sites, modifications in the activity of TAU kinases, shifts in intracellular calcium transients, adjustments in neuronal electrical activity, and differences in gene expression linked to synaptic function, possibly regulated by STAT3.

Despite both *PTK2B* HET and KO hiNs showing higher electrical activity and disruptions in network synchronization when compared to WT, the molecular profiles observed in hiNs of those different genotypes suggest that reducing PTK2B expression or completely removing it lead to different modifications. PTK2B HET cells exhibit a clear increase in TAU phosphorylation and changes in its intracellular localization, whereas this impact is less noticeable in the KO cells. Conversely, the influence of STAT3 as the main regulator of genetic changes observed in glutamatergic neurons, along with the effect of PTK2B on intracellular calcium transients are more pronounced in KO cells. Due to the strong similarity between PTK2B and FAK, it is possible that compensatory mechanisms could become active when PTK2B is absent, leading to FAK to assume specific functions of PTK2B. Ultimately, this could result in two distinct molecular mechanisms.

4. A novel activity-dependent transcription pathway in glutamatergic neurons

Our analysis of single cell transcriptomic data shows that altering the expression levels of PTK2B leads to genetic changes mainly in glutamatergic neurons. This finding is consistent with our previously published results that PTK2B is mainly expressed in excitatory neurons in the adult human brain (131).

Gene ontology analysis shows that differentially expressed genes in PTK2B KO and HET compared to WT hiNs are mainly associated to biological and molecular processes involved in synaptic transmission and regulation of electrical activity. These findings are consistent with our electrophysiological results showing that modulation of PTK2B alters electrical activity and neuronal synchronization. Furthermore, regulon analysis reveals that STAT3 may be a central transcription factor regulating the expression of these genes downstream of PTK2B.

Although STAT3 expression at the mRNA level is predominantly increased in PTK2B HET and KO cells compared to WT, the results at the protein level are less clear. Analysis of protein extracts from the same cerebral organoids used on the scRNA-seq showed

decreased phosphorylation of STAT3 at its main activation site at Tyr705 in HET and KO cells compared to WT. In the 2D cultures at 5 weeks, the decrease in STAT3 phosphorylation at Tyr705 is even stronger and extends to Ser727 - which has been linked to the duration of STAT3 activity (250). For the interpretation of these results, it is important to keep in mind that although STAT3 is highly expressed in glutamatergic neurons, we also observed a significant expression in other cell types, especially astrocytes. Thus, the culture composition can make a significant impact on the effects observed on the STAT3 total and phosphorylated levels.

To circumvent this limitation, we designed plasmid vectors carrying full-length or dominant-negative STAT3 under the control of the neuronal-specific human SYN promoter. These vectors were transfected in *PTK2B* WT, HET and KO hiPSCs previously transfected with NGN2 to generate pure glutamatergic cultures, later co-cultured with exogenous astrocytes for neuronal maturation. Due to technical reasons, new sets of cultures are currently ongoing and, in the near future, will be able to better elucidate the effect of STAT3-mediated transcription in the different *PTK2B* genetic backgrounds. Additionally, to unbiasedly measure the possible increase in STAT3 phosphorylation in neurons, immunocytochemical assays for total and phosphorylated STAT3 levels on NEUN+ neurons will be performed in frozen sections of cerebral organoids, enabling us to specifically measure the STAT3 total and phosphorylated levels in hiNs and eliminate the impact on astrocytes. By combining these methods, we will be able to confirm whether STAT3 is a significant regulator of *PTK2B* genetic changes in glutamatergic neurons, without bias.

5. Possible role of PTK2B on neuronal and astroglial differentiation

Since PTK2B expression is observed in glutamatergic neurons at early postnatal stages, the severe alterations observed in *PTK2B* HET and KO cultures could be partially attributable to developmental effects during their differentiation from hiNPCs to neurons and astrocytes. Despite PTK2B's role in various fundamental cellular processes, such as cell adhesion and migration, no reports to date have mentioned its involvement in human neural development. However, analyzing 2D cultures at various differentiation stages, we observe that the decreased expression of *PTK2B* in HET cells accelerates the differentiation of neurons and astroglia in hiPSC-derived cultures. If PTK2B truly impacts neural differentiation, its reduced expression at early stages of cell differentiation could differently affect the composition of cultures across the genotypes, potentially influencing the observed phenotypes.

In this regard, if PTK2B expression levels may influence neuronal and/or glial differentiation, this could influence the results in our biochemical assays as well as the electrophysiological patterns of cultures derived from hiPSCs of different genotypes. Therefore, it is necessary to normalize the overall composition of the culture and modulate PTK2B at later stages of development to circumvent this possible technical bias and confirm our previous findings. To this end, we have already started to use an alternative protocol to obtain pure glutamatergic cultures directly from hiPSCs via forced expression of Neurog2 and our preliminary data suggest that at least part of the alterations observed in TAU phosphorylation and electrical activity of *PTK2B* HET and KO hiNs compared to WT are indeed a consequence of reduced PTK2B-mediated signaling, rather than a result of altered cell culture compositions.

Moreover, we have designed plasmid vectors carrying a mutation for PTK2B at its main phosphorylation site (Y705F) or at its main kinase activity site (K457A). These plasmids are located under the promoter of human Synapsin promoter and also contain the sequence for puromycin selection and GCaMP7. Current experiments are ongoing to evaluate whether the expression of those PTK2B dominant-negative constructs only in fully differentiated hiNs will be sufficient to replicate our findings in *PTK2B* HET and KO hiNs, thus ruling out any possible developmental effect.

6. Is PTK2B the missing link between Aβ, Tauopathy and alterations in neuronal electrical activity observed in AD?

We show that exposure to Aβ1-42 for 24 hours increases the frequency of calcium transients in *PTK2B* WT and HET neurons compared to non-treated controls. However, in PTK2B KO neurons, the presence of Aβ has no effect on the frequency of calcium transients, which is already 2-fold higher than in WT hiNs. This experiment suggests that neurons expressing some level of PTK2B, whether on WT or HET, show increased calcium transients in response to Aβ1-42. However, neurons with complete PTK2B deletion may have already reached a plateau of hyperexcitability and, therefore, do not show further responses in the presence of Aβ1-42. Interestingly, treatment with Aβ1-42 during 24 hours results in a small increase in total and phosphorylated levels of PTK2B at its primary activation site, Tyr402 (Figure 32), in WT cells. This increase coincides with the greater neuronal electrical activity observed under this condition. Taken together, these results may suggest that PTK2B activation is involved in the Aβ1-42-mediated effects on neuronal electrical activity in an AD context.

Supporting this hypothesis, previous experiments by other groups have shown that soluble Aβ oligomers increase calcium influx, leading to activation of PTK2B (221). Accordingly, PTK2B has been reported as required for Aβ-mediated synapse dysfunction (200), and its overexpression increases the number of Aβ plaques in the hippocampus (218). Moreover, accumulation of PTK2B coincides with progressive TAU-mediated effects in AD (105).

On the other hand, PTK2B has an important role in LTP-induced hippocampal synapse plasticity ((152), (153)) and its overexpression is also protective to synapsis and behavior ((218); (145)). Recent work of Mastrolia et al., (2021) (212) has shown that the role of PTK2B in synapse plasticity depends on the electrical stimulation protocols used. Null-deletion of PTK2B in mice impairs LTP only when using high-frequency stimulation, but not the theta simulation. PTK2B has thus an apparent dual role concerning the electrical activity and the effects of Aβ and TAU depend on the experiment performed and the disease window.

Taking all that into account, it is possible that PTK2B may act as a sensor of the electrical activity and contribute to firing homeostasis in neurons. According to this idea, increased neuronal activity induced by Aβ, for example, would lead to the activation of PTK2B-pathways important to bring activity back to basal levels. On the other hand, decreased PTK2B expression due to the presence of a genetic variant associated to increased risk of AD would fail to counteract Aβ-mediated neuronal excitability, leading to a persistent increase in neuronal electrical activity and excitotoxicity.

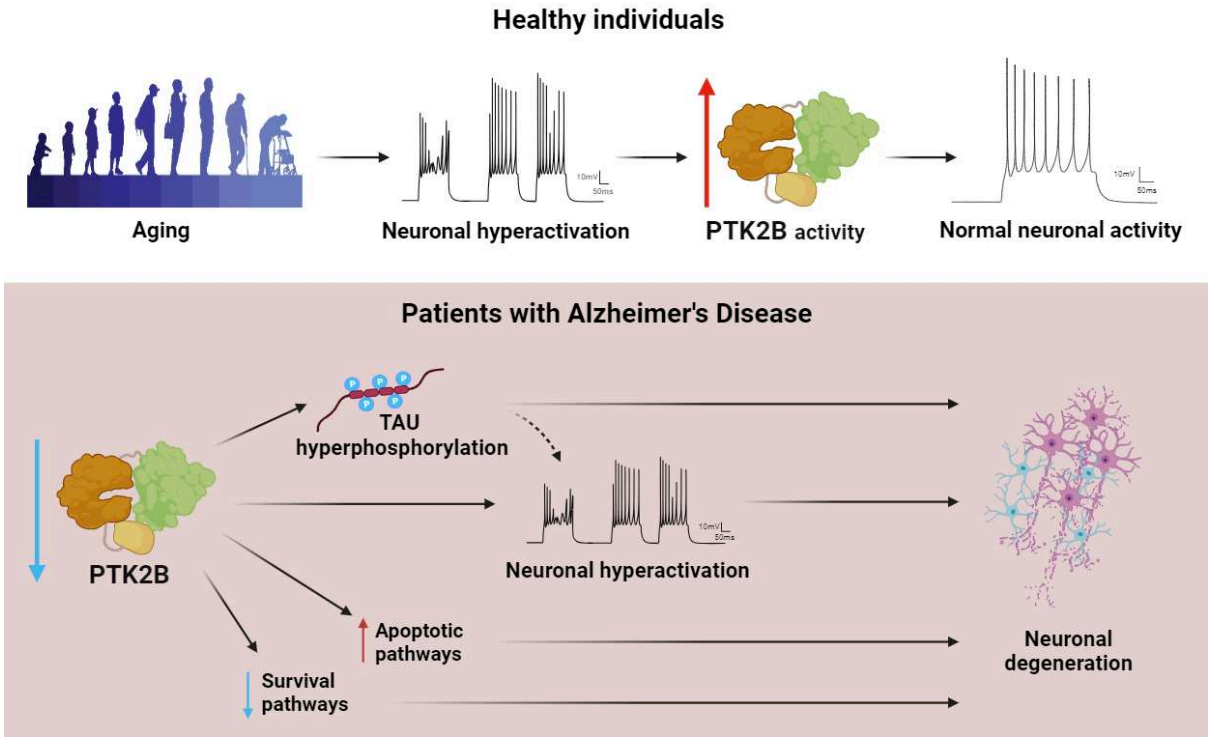

Figure 40: Possible regulation of PTK2B in neurons of healthy individuals and those with Alzheimer's disease.

Thus, an imbalance in PTK2B expression could be critical for several steps observed in the pathophysiology of AD (Fig. 40). These include hyperphosphorylation of TAU, neuronal hyperexcitability, activation of apoptotic pathways and inhibition of survival signaling. All of which contribute to posterior neuronal degeneration observed in the brain of patients with AD.

Conclusion

Genetic variants in the *PTK2B* locus have been associated with a greater risk of Alzheimer's disease, but the effects on PTK2B expression and their pathophysiological consequences are not fully understood. Using different isogenic hiPSC lines, we showed that HET and KO mutations of *PTK2B,* as well as the introduction of patient specific SNPs*,* alter neuronal activity and gene expression, mainly in glutamatergic neurons, with STAT3 as a key regulator of these genetic changes. Interestingly, reduced PTK2B expression in heterozygous cells, but not its complete deletion in knockout cells, led to a substantially higher TAU phosphorylation at several AD-associated sites. This result coincided with increased activity of p38 MAPK and GSK3β, and decreased activity of ERK1/2 and LKB1. Preliminary evidence indicates that the SNP associated to increased risk of developing AD may lead to decreased expression of PTK2B and increased phosphorylation of TAU, thereby contributing to the development of Alzheimer's disease pathology.

Our findings also suggest a correlation between PTK2B and calcium transients' dynamics, which are directly associated with neuronal electrical activity. Notably, exposure to Aβ1-42 amplified calcium transients in neurons with partial or endogenous PTK2B expression but did not induce any effect in neurons with complete PTK2B deletion. This suggests a role for PTK2B in mediating the effects of Aβ1-42 on neuronal electrical activity.

In conclusion, our study reveals the potential role of PTK2B in mediating important aspects of AD-related pathology. Furthermore, it indicates that PTK2B may be a critical intermediary linking Aβ, modifications in neuronal electrical activity and Tauopathy. This information could provide insights for a deeper understanding of AD mechanisms and potential therapeutic strategies.

Appendix

Article I

1. Differential transcript usage unreveals gene expression alterations in AD human brains

Diego Marques-Coelho, Lukas da Cruz Carvalho Iohan, Ana Raquel Melo de Farias, Amandine Flaig and The Brainbank Neuro–CEB Neuropathology Network, Jean-Charles Lambert and Marcos Romualdo Costa

Nature Partner Journals | Aging and Mechanisms of Disease, January 2021, 7:2

1.1. Context and objectives

Alzheimer's disease (AD) is a major cause of dementia in older people, but we still don't fully understand how it works in the brain. In this study, we aimed to better elucidate AD by looking at specific genetic signature in the brain, by using data from three big studies that looked at gene activity in healthy brains and brains affected by AD. For the analyses, we compared gene activity in different parts of the brain in healthy people and those with AD, namely, at the temporal and frontal lobes, which are affected at different stages of AD. Further, we analyzed which types of brain cells were showing changes in gene activity in AD, how these genes are used, and where in the brain they are active.

In summary show that certain genes have different activity levels in the brain of patients diagnosed with AD. Moreover, we show isoform switches in the AD causal gene encoding for APP and the LOAD risk gene BIN1 and observed that expression of BIN1 isoform 1 is reduced in AD brains. Overall, our study presents a novel integrative approach to the analysis of RNAseq data in AD and other neurodegenerative diseases, incorporating both gene/transcript expression and regional/cell type specificities.

1.2. Personal contributions to the work

In this work, I contributed by analyzing the protein expression levels of different BIN1 isoforms in the cerebral frontal cortex and the hippocampus of patiens diagnosed with AD and controls.

npj | Aging and Mechanisms of Disease

www.nature.com/npjamd

ARTICLE OPEN

Check for updates

Differential transcript usage unravels gene expression alterations in Alzheimer's disease human brains

Diego Marques-Coelho[1,2], Lukas da Cruz Carvalho Iohan[1,2], Ana Raquel Melo de Farias[1,3], Amandine Flaig[3] and The Brainbank Neuro–CEB Neuropathology Network*, Jean-Charles Lambert[3] and Marcos Romualdo Costa[1,3]✉

Alzheimer's disease (AD) is the leading cause of dementia in aging individuals. Yet, the pathophysiological processes involved in AD onset and progression are still poorly understood. Among numerous strategies, a comprehensive overview of gene expression alterations in the diseased brain could contribute for a better understanding of the AD pathology. In this work, we probed the differential expression of genes in different brain regions of healthy and AD adult subjects using data from three large transcriptomic studies: Mayo Clinic, Mount Sinai Brain Bank (MSBB), and ROSMAP. Using a combination of differential expression of gene and isoform switch analyses, we provide a detailed landscape of gene expression alterations in the temporal and frontal lobes, harboring brain areas affected at early and late stages of the AD pathology, respectively. Next, we took advantage of an indirect approach to assign the complex gene expression changes revealed in bulk RNAseq to individual cell types/subtypes of the adult brain. This strategy allowed us to identify previously overlooked gene expression changes in the brain of AD patients. Among these alterations, we show isoform switches in the AD causal gene amyloid-beta precursor protein (APP) and the risk gene bridging integrator 1 (BIN1), which could have important functional consequences in neuronal cells. Altogether, our work proposes a novel integrative strategy to analyze RNAseq data in AD and other neurodegenerative diseases based on both gene/transcript expression and regional/cell-type specificities.

npj Aging and Mechanisms of Disease (2021)7:2 ; https://doi.org/10.1038/s41514-020-00052-5

INTRODUCTION

Changes in gene expression characterize a multitude of human diseases and have been successfully used to predict molecular and cellular mechanisms associated with pathological processes[1]. Alzheimer's disease (AD) is the most prevalent type of dementia and causes a progressive cognitive decline, for which there is no effective treatment or cure. Although expression analyses in brain diseases are generally limited by tissue availability, RNA sequencing (RNAseq) data have been generated from *postmortem* brain samples of healthy and AD individuals[2–4]. However, a comprehensive description of the gene expression alterations in the AD brain remains elusive.

Recent work has begun to address this important gap in the study of AD pathology using bulk brain tissue RNA sequencing (RNAseq)[5] or single-cell RNA sequencing (scRNAseq)[6,7]. However, these studies have focused on samples obtained from different brain regions, namely the dorsolateral prefrontal[5,7] and entorhinal cortices[6], which could lead to important discrepancies in the results. In fact, AD pathology shows a progressive impact on different brain regions, characterized at early stages by the presence of TAU protein inclusions in the locus coeruleus, the transentorhinal and entorhinal regions (stages I and II). This is followed by the presence of TAU inclusions in the hippocampal formation and some parts of the neocortex (stages III and IV), followed by large parts of the neocortex (stages V and VI)[8]. This temporal progression of AD pathology could differently impact gene expression in those brain areas. Accordingly, a recent study has shown that changes in protein expression are much more prominent in areas affected at early and intermediate stages, such as the hippocampus, entorhinal cortex, and cingulate cortex in the temporal lobe, compared to other brain regions affected at later stages of AD pathology, such as sensory cortex, motor cortex, and cerebellum[9].

Another important aspect to consider is the descriptive relevance of gene expression analysis based solely on the identification of differentially expressed genes (DEG), which fails to detect dynamics in the expression of multiple related transcripts[10]. Recently, new approaches using transcripts-level analysis, so-called differential transcript usage (DTU), enables identification of alternative splicing and isoform switches with the prediction of functional consequences[11,12]. Therefore, important gene expression modifications in the AD brain could occur at the transcript level and be overlooked in classical DEG analyses.

Here, we took advantage of three available RNAseq datasets, generated using samples from different brain regions, to systematically probe gene expression changes (DEG and DTU) in AD. In Mayo's clinic study, both the temporal cortex and cerebellum were used to obtain bulk RNAseq[2]. In the Religious Orders Study (ROS) and Memory and Aging Project (MAP), henceforth called ROSMAP, the dorsolateral prefrontal cortex was used[3]. Finally, in the Mount Sinai/JJ Peters VA Medical Center Brain Bank (MSBB), four different Brodmann areas of the brain were studied: areas 22 and 36 from the temporal lobe, areas 10 and 44 in the frontal lobe[4]. We also added another level of complexity using an indirect approach to assign DEGs and gDTUs to unique cell types in order to identify AD gene expression signatures for neural cells, microglia, and endothelial cells. Finally, we linked these alterations with AD causal and risk genes, identifying novel isoform switches in BIN1 and APP genes of potential functional consequences for pathology progression.

[1]Brain Institute, Federal University of Rio Grande do Norte, Av. Nascimento de Castro, 2155 Natal, Brazil. [2]Bioinformatics Multidisciplinary Environment (BioME), Federal University of Rio Grande do Norte, Natal, Brazil. [3]Unité INSERM 1167, RID-AGE-Risk Factors and Molecular Determinants of Aging-Related Diseases, Institut Pasteur de Lille, University of Lille, Lille Cedex, France. *A list of authors and their affiliations appears at the end of the paper. ✉email: marcos.costa@pasteur-lille.fr

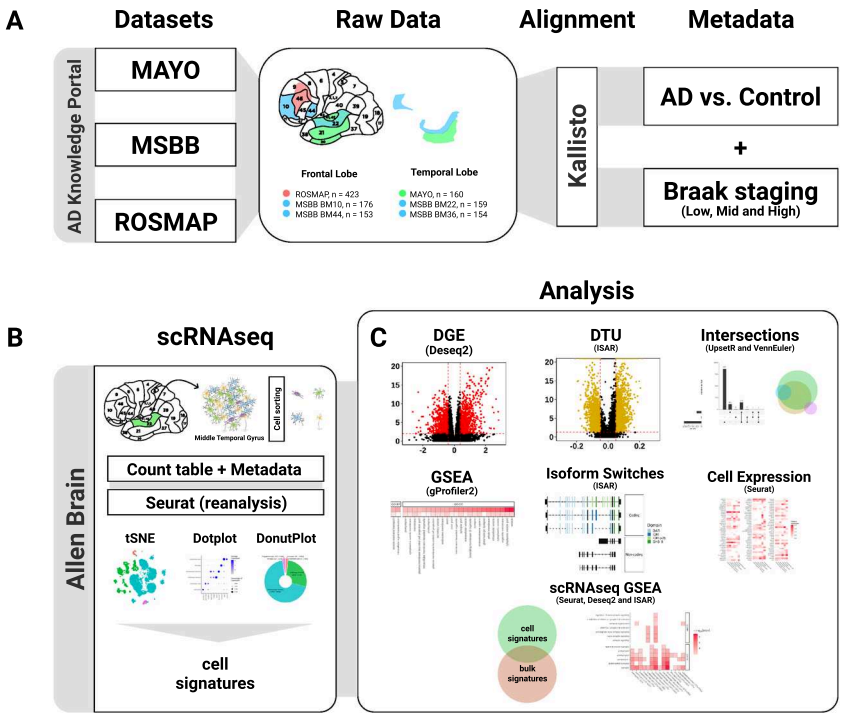

Fig. 1 Schematic summary of the methodology. A Datasets obtained from three consortia (Mayo, MSBB, and ROSMAP) were grouped according to the brain region sampled in the frontal lobe (FL) or temporal lobe (TL). Next, RNAseq data were pseudo-aligned using Kallisto. Clinico-pathological classifications were included as metada. **B** scRNAseq data from the midle temporal gyrus (MTG, Allen Brain Atlas) were analyzed using the R package SEURAT. **C** Gene expression analyses were performed using the R packages DESeq2, IsoformSwitchAnalyzeR (ISAR), and gene set enrichment analysis (GSEA). Assignment of differentially expressed genes or isoform switches to specific cell types/subtypes was performed indirectly using scRNAseq signatures obtained from the MTG (B).

RESULTS

Regional gene expression alterations in the AD brain correlates with pathological progression

Several consortia have generated RNAseq data from brains of individuals with a clinical and/or pathological diagnostic of AD[2–4]. Considering the regional progression of AD pathology[8], we set out to identify and compare differentially expressed genes (DEG) in the temporal lobe (TL), encompassing brain regions affect at early stages of the AD such as the hippocampus and entorhinal cortex, and in the frontal lobe (FL), affect at more advanced stages of the pathology (Fig. 1). Comparisons between control and AD individuals were performed independently for each dataset and only genes with fold change >1.3 and FDR > 0.01 were considered as DEGs. We found 3348 (1244 down- and 2104 upregulated genes) and 2172 (1170 down and 999 upregulated genes in BM22 and BM36; three genes regulated in opposite directions in these two areas) DEGs in the TL of AD individuals compared to their respective controls in the MSBB_TL and Mayo datasets, respectively (Fig. 2A, B and Supplementary Table 1). Of those DEGs, 734 genes (145 down and 520 up) were commonly regulated in both Mayo and MSBB_TL (88.4% of genes altered in the same direction; 15.33% of overlap; $P = 8.56 \times 10^{-59}$, hypergeometric test). In contrast, only 327 (113 down and 214 up) and 209 (97 down and 112 up) DEGs were detected in the MSBB_FL and ROSMAP, respectively. Of those, 31 genes (18 down and 13 up) were found in both datasets (7.34% of overlap; $P = 1.67 \times 10^{-14}$, hypergeometric test) (Fig. 2A, B and Supplementary Table 1). This small number of DEGs in the FL is in agreement with previous data obtained from the DLPFC (106 down- and 158 upregulated genes with FC > 1.3)[13]. Among DEGs detected in the FL, 62.5% were also detected in the TL (Fig. 2B), suggesting that similar molecular changes occur in these brain areas, but at different stages of the disease progression. The differences in the number of DEGs detected in the FL and TL can neither be attributed to lack of statistical power nor potential biases due to tissue processing, since the number of samples in the FL is larger than in the TL groups (Fig. 1) and differences are observed even in samples obtained from the same donors (compare MSBB_TL and MSBB_FL in Fig. 2). Thus, changes in gene expression are much more prominent in brain areas affected at the early stages of AD pathology.

To select genes consistently altered in AD brains, considering the several sources of measurement variations in RNAseq experiments[14], we decided to focus only on DEGs replicated in at least two independent datasets obtained from related brain areas. This resulted in a set of 734 DEGs detected in both Mayo and MSBB TL (temporal lobe intersection—TLI), and 31 DEGs shared between ROSMAP and MSBB FL (frontal lobe intersection—FLI) (Supplementary Table 2). Among TLI DEGs, we observed ABCA1 and 2 (ATP-binding cassette subfamily A member 1 and 2), primarily involved in the maintenance of normal brain homeostasis and associated with AD and other neurological diseases[15]; Complement C1R and C1S, involved in the immune/inflammatory response and previously shown to be upregulated in the brain of a 3 × Tg mouse model of AD when Aβ plaques start to accumulate[16]; RE1 silencing transcription factor (REST), which regulates neural circuit activity during aging[17]; glutamate decarboxylase 1 and 2 (GAD1 and 2), solute carrier family 32 GABA vesicular transporter, member 1 (SLC32A1), calbindin 1 (CALB1), parvalbumin (PVALB), somatostatin (SST), and vasoactive intestinal peptide (VIP), all expressed in GABAergic neurons and involved in cognitive decline in AD and other neurological diseases[18]. Among the few DEGs common to TLI and FLI, we observed a significant downregulation of the neurosecretory protein VGF (VGF nerve growth factor inducible), recently suggested as a key regulator of Alzheimer's disease[19].

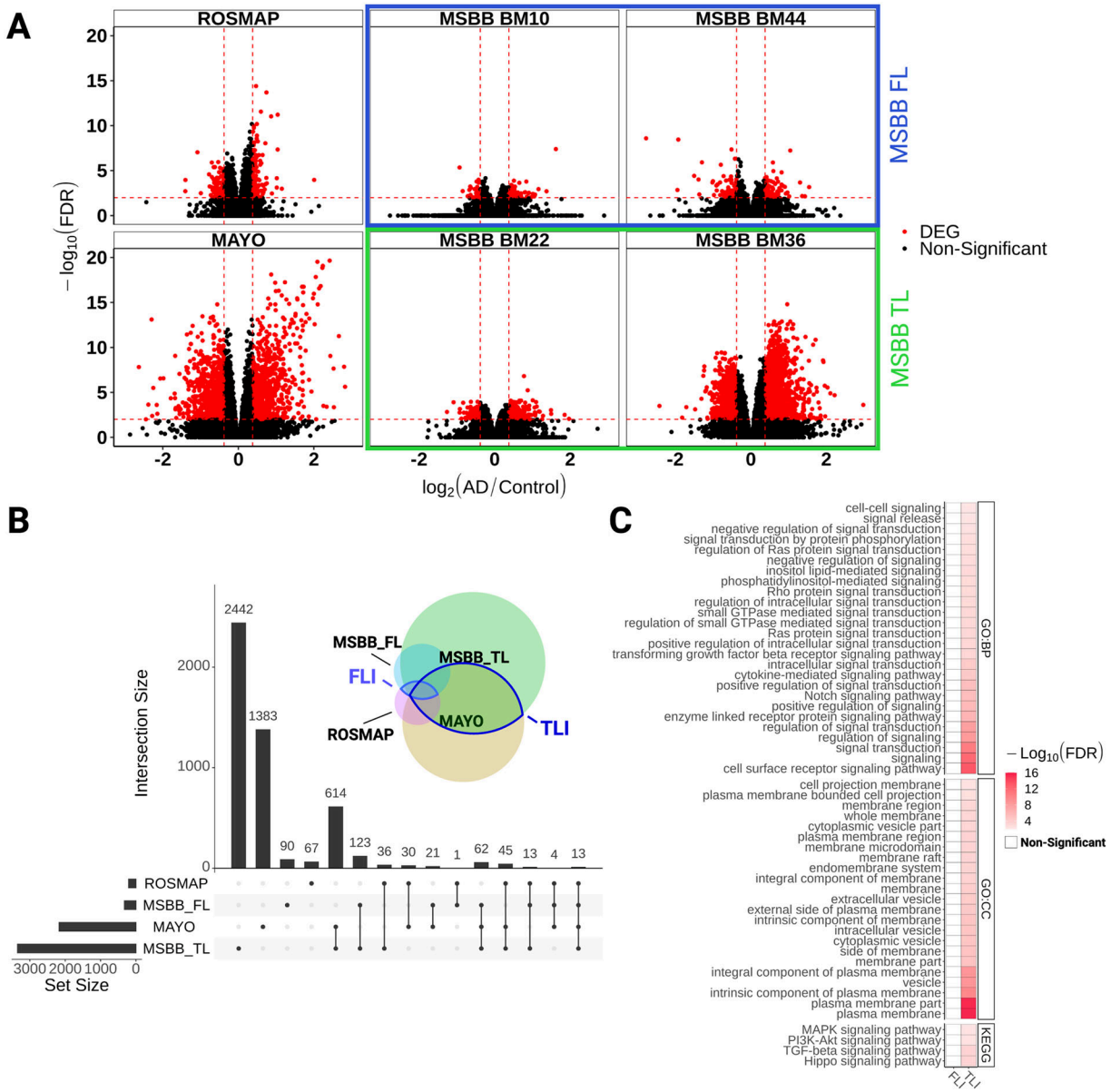

Fig. 2 Gene expression alterations are more prominent in the temporal than the frontal lobe of AD patients. A Volcano plots showing differentially expressed genes (DEG, red dots; FC > 1.3 and FDR < 0.01) in the frontal lobe (ROSMAP and MSBB FL - BM10 and BM44) and temporal lobe (Mayo and MSBB TL - BM22 and BM36). **B** Upset plot showing the total number of DEGs identified in each dataset (horizontal bars) and the number of DEGs exclusive of one dataset (first four vertical bars) or shared by different datasets (other vertical bars). Black dots below vertical bars indicate datasets quantified. Venn diagram illustrates the same results in colors and circle sizes. **C** Gene ontology terms enriched for DEGs identified in the TL or FL intersections (TLI and FLI, respectively).

Next, we used gene set enrichment analyses (GSEA) to assess the functional profile of the DEGs identified in our analysis. Again, we used only genes commonly altered in two datasets (TLI or FLI) to avoid inaccurate results associated with the use of large gene sets in functional analysis[20]. We found that TLI DEGs were significantly enriched for terms (GO:BP, GO:CC and KEGG) associated with generic biological processes, such as cell-signaling pathways and cell-cell signaling, whereas the small number of DEGs in the FLI were not significantly enriched for any term (Fig. 2C and Supplementary Table 3). The limited number of significant gene set enrichment observed in our analysis after inputting DEGs is in disagreement with results reported by Canchi et al.[13]. This discrepancy can likely be explained by the use of stringent criteria to detect TLI DEGs in our study (only genes detected in at least two independent datasets with FC > 1.3 and FDR < 0.01), which significantly reduce the number of genes used in the GSEA.

Differential transcript usage analysis reveals novel genes associated with AD pathology

Gene-level expression analysis lacks the sensitivity to detect possible changes at the transcript-level caused, for example, by alterations in alternative splicing[10,21]. To overcome this limitation, we used differential transcript usage (DTU) analysis to identify additional alterations of gene expression in the AD brains compared to controls. We observed 2509 and 1843 genes with differential transcript usage (gDTU) in the temporal lobe of AD brains studied in the Mayo and MSBB datasets, respectively (Fig. 3A, B and Supplementary Table 1). Similar to what we observed for DEGs, a much smaller number of gDTUs were

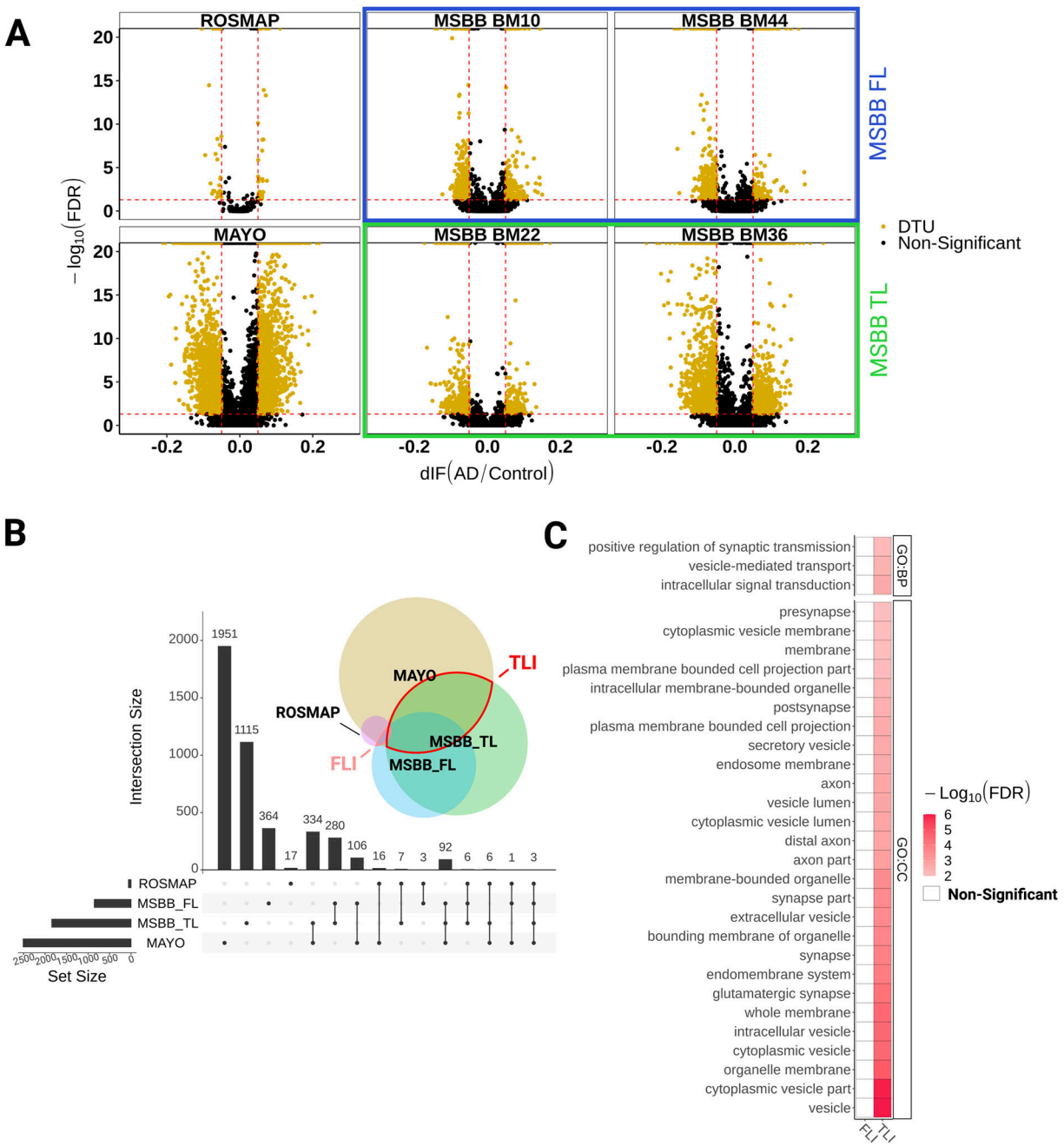

Fig. 3 Differential transcript usage analysis identifies gene expression alterations in AD associated with synapse transmission. A Volcano plots showing genes with differential transcript usage (gDTU, yellow dots; Differential isoform fraction (dIF) >0.05 and FDR < 0.05) in the frontal lobe (ROSMAP and MSBB_FL - BM10 and BM44) and temporal lobe (Mayo and MSBB_TL - BM22 and BM36). **B** Upset plot showing the total number of gDTUs identified in each dataset (horizontal bars) and the number of gDTUs exclusive of one dataset (first four vertical bars) or shared by different datasets (other vertical bars). Black dots below vertical bars indicate datasets quantified. Venn diagram illustrates the same results in colors and circle sizes. **C** Synapse-related terms enriched for gDTUs in the TLI are not observed in the FLI.

detected in the frontal lobe, both in ROSMAP and MSBB studies (59 and 855 genes with transcripts altered, respectively). We found 435 gDTUS in TLI (11.1% of overlap; $P = 6.16 \times 10^{-25}$, hypergeometric test) and 13 gDTUs in FLI (1.47% of overlap; $P = 2.56 \times 10^{-3}$, hypergeometric test) (Supplementary Table 2). In TLI, most gDTUs did not overlap with DEGs (TL—34 gDTUs that are DEGs out of 435 gDTUs, Fig. 4A), whereas in FLI, we found no overlap at all. Consistent with this small overlap, GSEA using only DEGs, only gDTUs or both showed complementary results (Fig. 4B). GSEA using gDTUs (alone or in combination with DEGs) showed significant enrichment for vesicle-mediated transport and other synapse-related terms, which were not observed while inputting only DEGs (Figs. 3C and 4B; Supplementary Table 3). The functional enrichment annotation using both DEGs and gDTUs is in agreement with previous studies using scRNAseq to identify gene expression alterations in unique cell types[6,7] and clearly improves the annotation observed using only DEGs, suggesting that the use of DTU analysis could contribute to unraveling gene expression alterations overlooked in the classical DEG analysis.

Among genes with isoform switches enriched in synaptic-related terms, we observed the AD causal gene APP, previously associated with regulation of synapse transmission and long-term

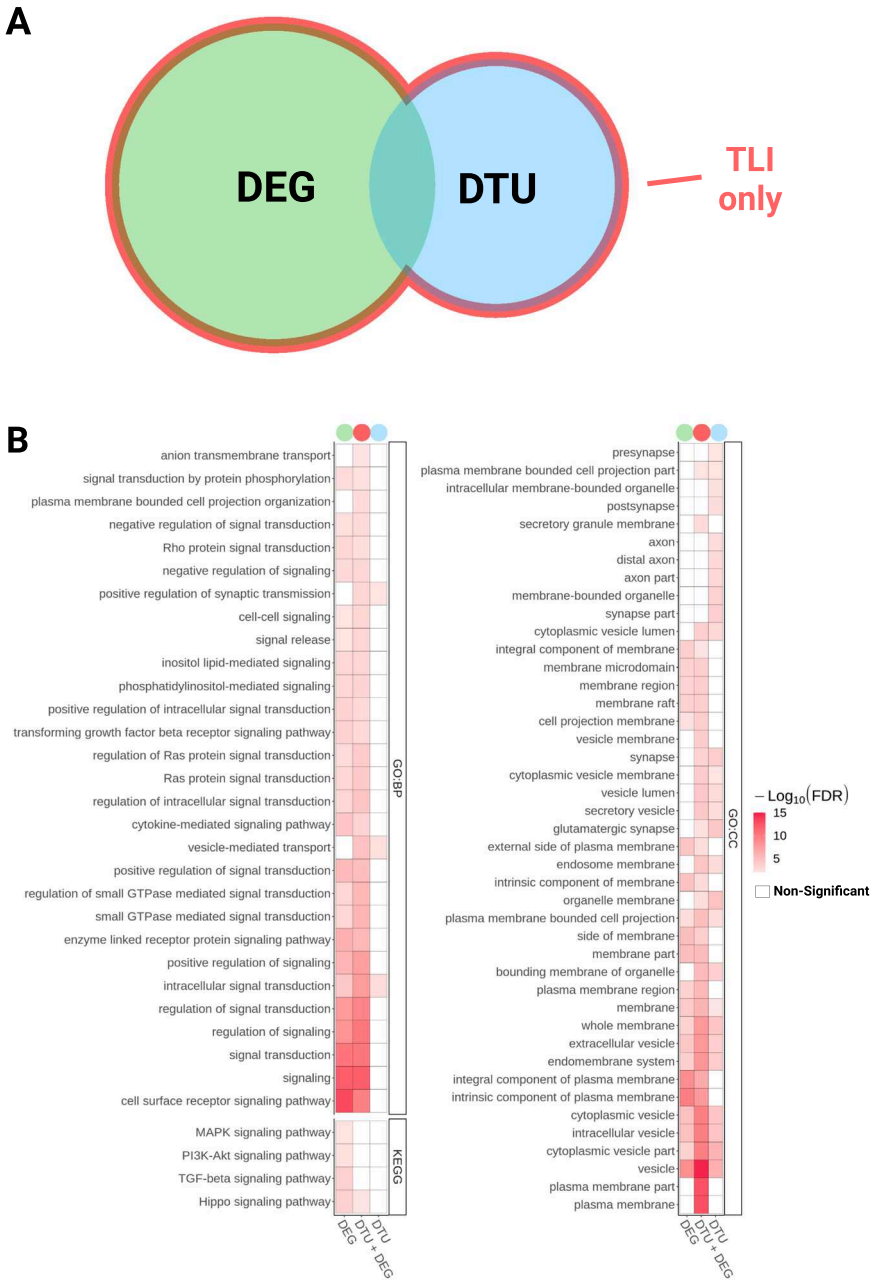

Fig. 4 Differential transcript usage analysis in AD brains reveals gene expression alterations overlooked in DEG analysis. A Venn diagram showing DEGs and gDTUs identified in the TLI. **B** Comparison of GO and KEGG terms enriched for DEG, gDTU, or DEG + gDTU identified in the TLI.

plasticity in AD[22]; neuronal vesicle trafficking associated 1 (NSG1), which has been implicated in the regulation of AMPA receptors (AMPAR) and APP trafficking, thus affecting synaptic transmission, plasticity, and Aβ production[23,24]; RELN (Reelin) that plays important role in synaptic transmission and has been associated with AD[25]; gamma-aminobutyric acid type A receptor subunit alpha 1 (GABRA1), which encodes for a subunit of the main ionotropic GABA receptor in the brain and has previously been shown to be downregulated in the AD brain[26].

Alternative splice events in AD brains and functional consequences

To identify the causes subjacent to gene isoform switches in the AD brain, we quantified the frequency of splicing events associated with the isoform switches detected in AD compared to control brains (Fig. 5 and Supplementary Table 4). We found that alternative transcription start site (ATSS), alternative transcription termination site (ATTS), and exon skipping (ES) were the most frequent splicing events in AD brains (Fig. 5B). Other common splicing events observed were alternative 3′ or 5′ splice sites (A3 and A5, respectively), multiple exons skipping (MES) and intron retention (IR) (Fig. 5B). These observations suggest that changes in alternative splicing could be implicated in AD pathogenesis, corroborating previous analyses in the ROSMAP cohort using intronic usage ratios to identify abnormal splicing events in the AD brain[5].

Alternative splicing events may have diverse functional consequences for protein expression, such as shifting the frequency of transcripts containing introns (noncoding) or mRNA

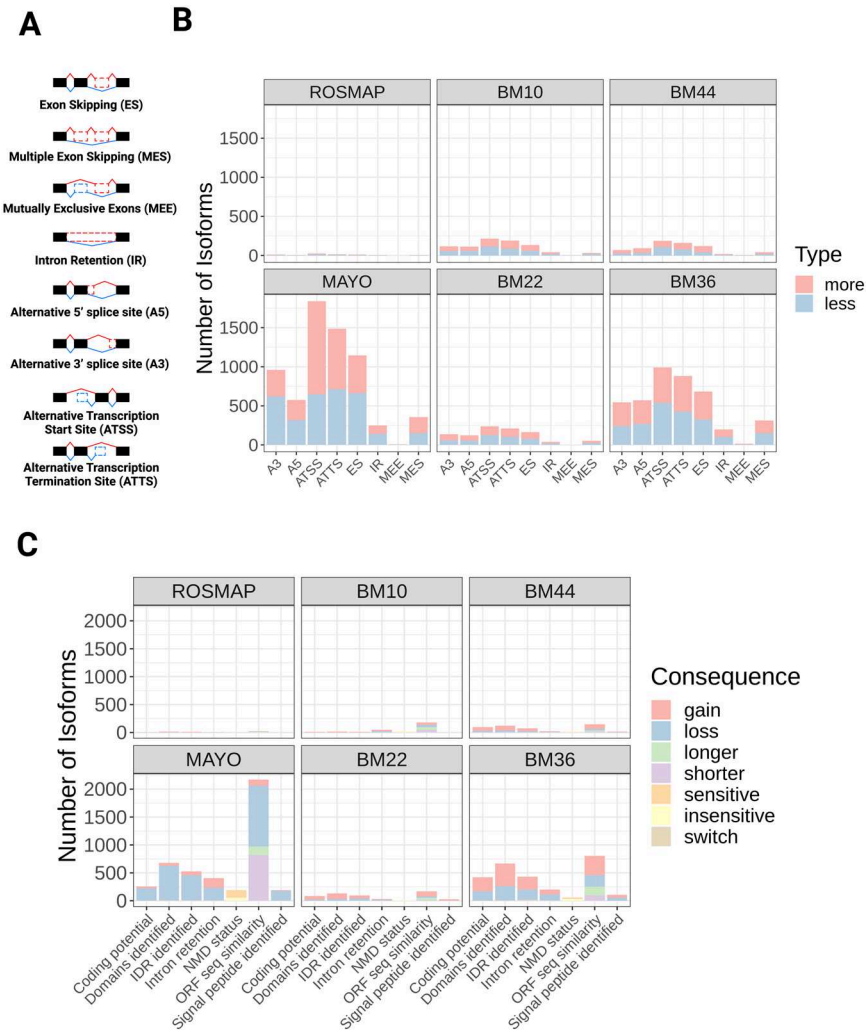

Fig. 5 Alternative splicing mechanisms associated with isoform switches and consequences for protein expression. A Schematic showing different splicing events that can lead to gene isoform switches. **B** Quantification of the number of isoforms showing more or less splicing events in AD compared to controls for each dataset. **C** Quantification of the number of isoforms showing (i) gain or loss of coding potential, domains/signal peptides identified, intrinsically disordered regions (IDR), intron retention, open-reading frame (ORF) sequencing similarity; (ii) switch (simultaneous gain and loss) of domains identified or IDR; (iii) sensitive or insensitive to nonsense-mediated decay (NMD); and (iv) longer or shorter ORF sequencing similarity.

stability (nonsense-mediated decay) or leading to gain/loss of protein domains, intrinsically disordered regions, or signaling peptides[12]. Quantification of these consequences revealed some interesting differences between Mayo and MSBB BM36 (Fig. 5C), the two datasets with the largest numbers of gDTUs. Whereas in the Mayo dataset, a high number of isoforms showed loss of coding potential and protein domains, in the MSBB BM36 isoforms showed an even distribution of loss and gain of coding potential or protein domains (Fig. 5B). These differences could be at least partly explained by the larger number of gDTUs detected in the Mayo compared to MSBB TL (Fig. 3) and are likely related to the different median read depth of these datasets (Mayo—12.58 billion bases; MSBB BM22—3.23 billion bases; MSBB BM36—3.56 billion bases)[27].

Differential expression of genes involved in alternative splicing correlates with isoform switches during disease progression

To evaluate whether the emergence of gDTUs could be correlated with AD pathology hallmarks, we quantified the total of gDTUs observed at different disease stages in the MSBB dataset using the Braak classification (Fig. 6 and Supplementary Table 5). For this purpose, we subdivided samples into three groups: low Braak (0, 1, and 2)— 196 samples (clinical diagnosis: 15 AD and 181 controls); mid-Braak (3 and 4)—133 samples (clinical diagnosis: 58 AD and 75 controls); and high Braak (5 and 6)—308 samples (clinical diagnosis: 305 AD and 3 controls). Next, we evaluated the number of gDTUs when comparing individuals at these different stages (Fig. 6). We observed that most gDTUs were detected only while comparing high with either low or mid-Braak stages (Fig. 6A–D). This pattern was observed both in the FL (BM10 and BM44) and TL (BM22 and BM36), suggesting that gene isoform switches positively correlate with AD pathology progression.

Next, we set out to evaluate alterations in the expression of genes encoding for proteins of the splicing machinery between the same Braak stages. We found that among 441 genes related to "splicing" or "spliceosome" terms (Supplementary Table 6), 79 were DEGs at high compared to low or mid-Braak stages (Fig. 6E). In contrast, we could not detect any DEG in the comparison of mid vs low Braak stages. Among DEGs detected in the comparison between high and low/mid-Braak stages, we observed that several genes specifically associated with the neuronal splicing regulatory network[28], such as RBFOX1 and 2 (RNA binding Fox-1 homolog 1 and 2), ELAVL2 (ELAV like RNA binding protein 2), MBNL3

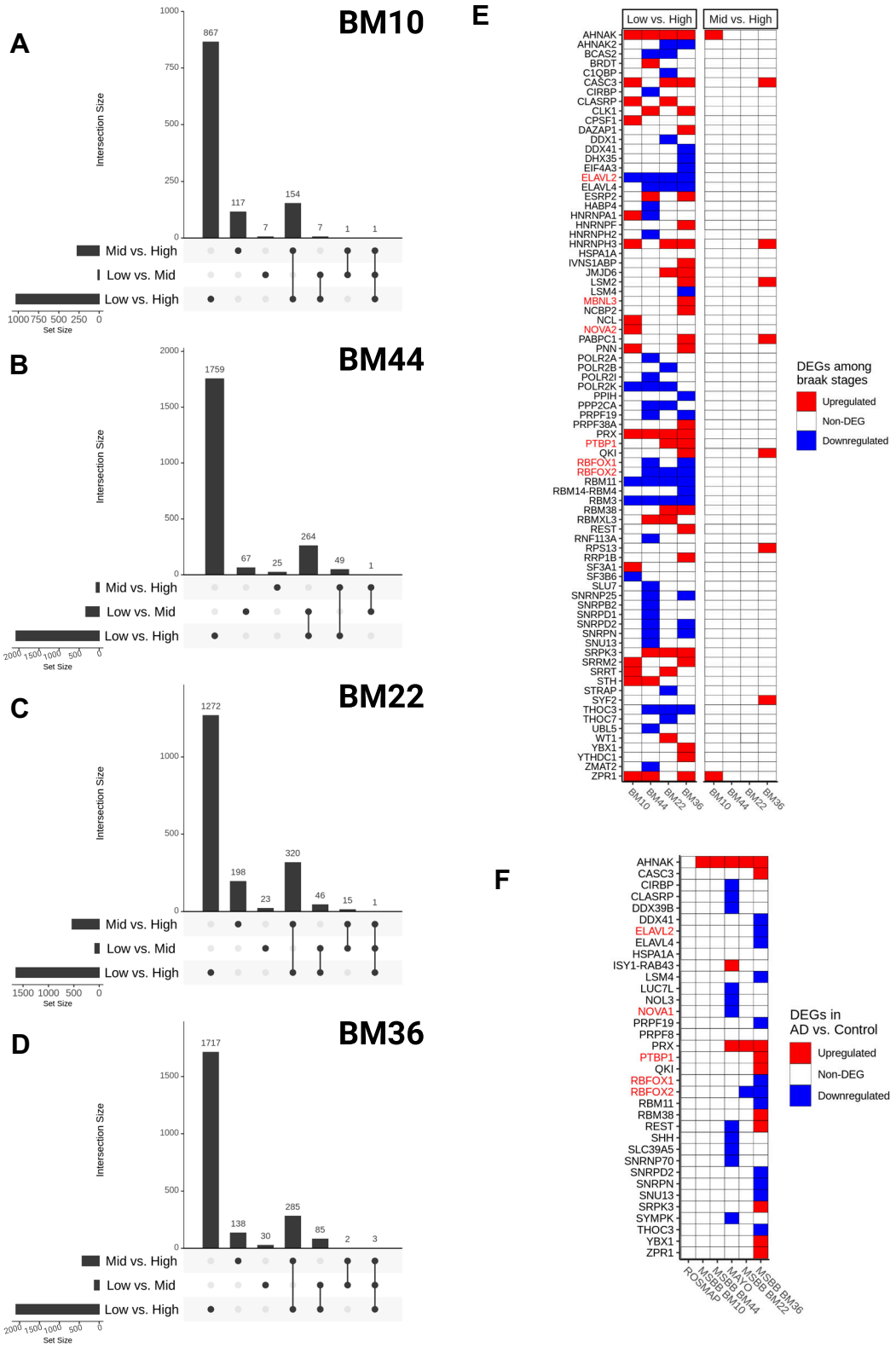

Fig. 6 Coincidence between altered expression of splicing-related genes and gDTUs in advanced pathologic stages of AD. A–D Upset plots showing the total number of gDTU identified in the comparison between different Braak stages (low vs. high, low vs. mid, and mid vs. high) in BM10 (**A**), BM44 (**B**), BM22 (**C**), or BM36 (**D**). Horizontal bars show the total number of gDTUs identified in each comparison (low vs. high, low vs. mid, and mid vs. high), whereas vertical bars indicate the gDTUs exclusive or common to different comparisons. Black dots below vertical bars indicate stages analyzed. **E**, **F** Differential expression of genes associated with splicing/spliceosome after comparison of different Braak stages (**E**) or AD vs controls in different datasets (**F**). Red and blue squares indicate, respectively, up- and downregulated genes. Gene symbols highlighted in red indicate genes belonging to the neuronal splicing machinery.

(muscleblind like splicing regulator 3), PTBP1 (polypyrimidine tract binding protein 1), and NOVA2 (NOVA alternative splicing regulator 2) (Fig. 6E, highlighted in red). A similar correlation between pathological burden and differential expression of the same 441 splice-related genes was observed in the comparison between all AD versus control subjects of the different datasets (Fig. 6F). Changes in the expression of those genes were hardly observed in FL (low number of gDTUs—Fig. 3), but were frequent in TL samples (high number of gDTUs—Fig. 3), albeit to a lesser extent than that observed in the comparison between different Braak stages (likely due to the effects of combining low, mid and high Braak stages in the AD group). Remarkably, the majority of the splicing-related genes with altered expression in the Mayo dataset was not reproduced in the MSBB BM36 dataset, and vice versa (Fig. 6F). This could help to explain the dissimilar consequences of alternative splicing events observed in those datasets (Fig. 5C) and suggest that a myriad of proteins could be involved in altered splicing in the AD brains.

Differential gene expression in separate cell types of the human brain

Considering the cellular diversity in the brain, we took an indirect approach to sort DEGs and gDTUs according to individual cell types. To that, we used scRNAseq data obtained from the adult human brain to identify cell types expressing the genes altered in our DEG/gDTU analysis (Fig. 7 and Supplementary Fig. 1). We found that, out of the 1135 genes with altered expression, i.e., gDTU + DEG, in the TLI (Figs. 2 and 3), 839 were found in at least one cell-type using as cutoff the expression in more than 10% of cells assigned for a specific cell-type (Supplementary Table 7). From these, 239 were identified in unique cell-types/subtypes, 396 in multiple (2–4 cell-types), and 211 in all cell-types analyzed (Fig. 7A, Supplementary Figs. 1 and 2, Supplementary Table 7). Confirming the efficacy of our strategy, GO analyses using cell-type-specific genes revealed that DEGs/gDTUs in the TLI of AD patients were significantly enriched for biological processes associated with inflammation in microglial cells, whereas those associated with cell adhesion were enriched in endothelial cells (Fig. 7B and Supplementary Table 8). Similarly, DEGs/gDTUs identified in neuronal cells were enriched for GO terms such as synaptic signaling, synaptic plasticity, and synapse vesicle cycle (Fig. 7C). Notably, these enrichments were more significant in GABAergic neurons, which could suggest a more pronounced pathological burden on these cells compared to glutamatergic neurons (Fig. 7C). Comparison of the cell-type gene expression signatures identified in our work with previous studies using scRNAseq in AD[6,7] showed a similar degree of overlap (Supplementary Figs. 3 and 4; Supplementary Table 9), further supporting the effectiveness of our strategy to assign gene expression alterations to unique cell types in the AD brain.

DEG/gDTU analyses identify cell-type-specific alterations in AD risk/causal genes

Genomic association studies have revealed about 45 loci containing variants related to an increased or decreased probability of developing AD[29,30]. However, the functional variants and their target genes remain mostly elusive[31]. To contribute to the identification of target genes, we first evaluate the expression of 176 genes located within the 45 loci associated with the AD risk (Supplementary Table 10)[31] and 3 causal AD genes—PSEN1, PSEN2, and APP—in individual cell types of the adult human brain. We found that 116 out of the 179 AD risk/causal genes were expressed by at least one of the major cell types identified in the brain (Fig. 8A and Supplementary Table 11). Subsets of these genes were exclusively expressed either in microglial cells (14 out of 116), neurons (12), astrocytes (2), oligodendrocytes (6), or endothelial cells (6), suggesting cell-type specific roles for these AD risk/causal genes.

Next, we set out to evaluate the differential expression or transcript usage for these genes. Out of the 116 AD risk/causal genes expressed by brain cell types (Fig. 8A), we observed that 54 were also DEGs/gDTUs in at least one of the bulk RNAseq datasets analyzed. Among those genes, two were exclusively identified in the FL (Fig. 8B). We, therefore, decided to focus on the 52 AD risk/causal genes identified in the temporal lobe for further analyses. In this region, we identified 27 and 17 DEGs/gDTUs in the MSBB_TL and Mayo datasets, respectively, including some well-characterized AD risk genes, such as ADAM10 (ADAM metallopeptidase domain 10), BIN1, CLU (Clusterin), and TREM2 (triggering receptor expressed on myeloid cells 2), and the causal AD genes APP, PSEN1 and 2 (presenilin 1 and 2) (Fig. 8A, B). Eight genes were altered in both datasets (Fig. 8B, yellow box; 15,38% of overlap) and were selected for further analysis of isoform switch. Using ISAR to identify the isoforms altered in the AD brains compared to controls, we observed some patterns of isoform switch that could have important functional relevance (Fig. 8C, D). For instance, while BIN1 transcripts ENST00000316724.9 (NP_647593.1—isoform 1) and ENST00000409400.1 (NP_647600.1—isoform 9) were downregulated, transcripts ENST00000393040.7 (NP_647598.1—isoform 6) and ENST00000462958.5, ENST00000046611.5 and ENST00000484253.1 (intron retention) were upregulated (Fig. 8C). This pattern could lead to a decrease of the neuronal-specific BIN1 isoform 1 expression[32], given that retained introns are noncoding sequences. Using western blotting analysis, we confirmed this decrease of BIN1 isoform 1 protein in the frontal cortex and hippocampus of AD brain samples compared to controls (Supplementary Fig. 5).

We also observed isoform switches in the AD causal gene APP with possible functional consequences in neuronal cells. While two APP isoforms were downregulated (ENST00000348990 and ENST00000354192), the isoforms ENST00000346798 and ENST00000357903 were upregulated in Mayo and MSBB datasets (Fig. 8D). Noteworthy, significantly downregulated APP isoforms lack exon 7, which contains the Kunitz protease inhibitor (KPI) domain. KPI is one of the main serine protease inhibitors and increased KPI(+) APP mRNA and protein expression levels have been described in AD brains and are associated with increased amyloid-beta deposition[33–35]. At the exception of ENST00000354192, the other transcripts are mostly expressed in neurons (Marques-Coelho and Costa, unpublished data), indicating that these cells may have a selective increase in the expression of KPI(+)APP and, consequently, enhanced production of Aβ1–42.

DISCUSSION

Comprehensive knowledge of gene expression alterations associated with the onset and progression of human diseases is a key step toward the understanding of their cellular and molecular mechanisms[36]. In this work, we provide a novel framework to identify cell-type-specific gene expression alterations in AD using patient-derived bulk RNAseq. Comparing RNA sequencing data obtained from distinct brain regions of control and AD patients, we show that changes in gene expression are more significant in the temporal than frontal lobe. We also show that a large number of genes present isoform switches without changes in the global expression levels. As a consequence, these genes are overlooked in classical differential expression analysis but can be detected through differential transcript usage analysis. Gene isoform switches are mostly evident at late stages of the pathology and correlate with altered expression of genes encoding for splicing-related proteins. Using an indirect approach to assign genes to unique cell types, we are also able to map DEGs/gDTUs to unique cell populations of the adult brain, and our results are comparable to previously published scRNAseq data[6,7]. Finally, we show that a subset of AD causal/risk factors such as APP or BIN1 is differentially

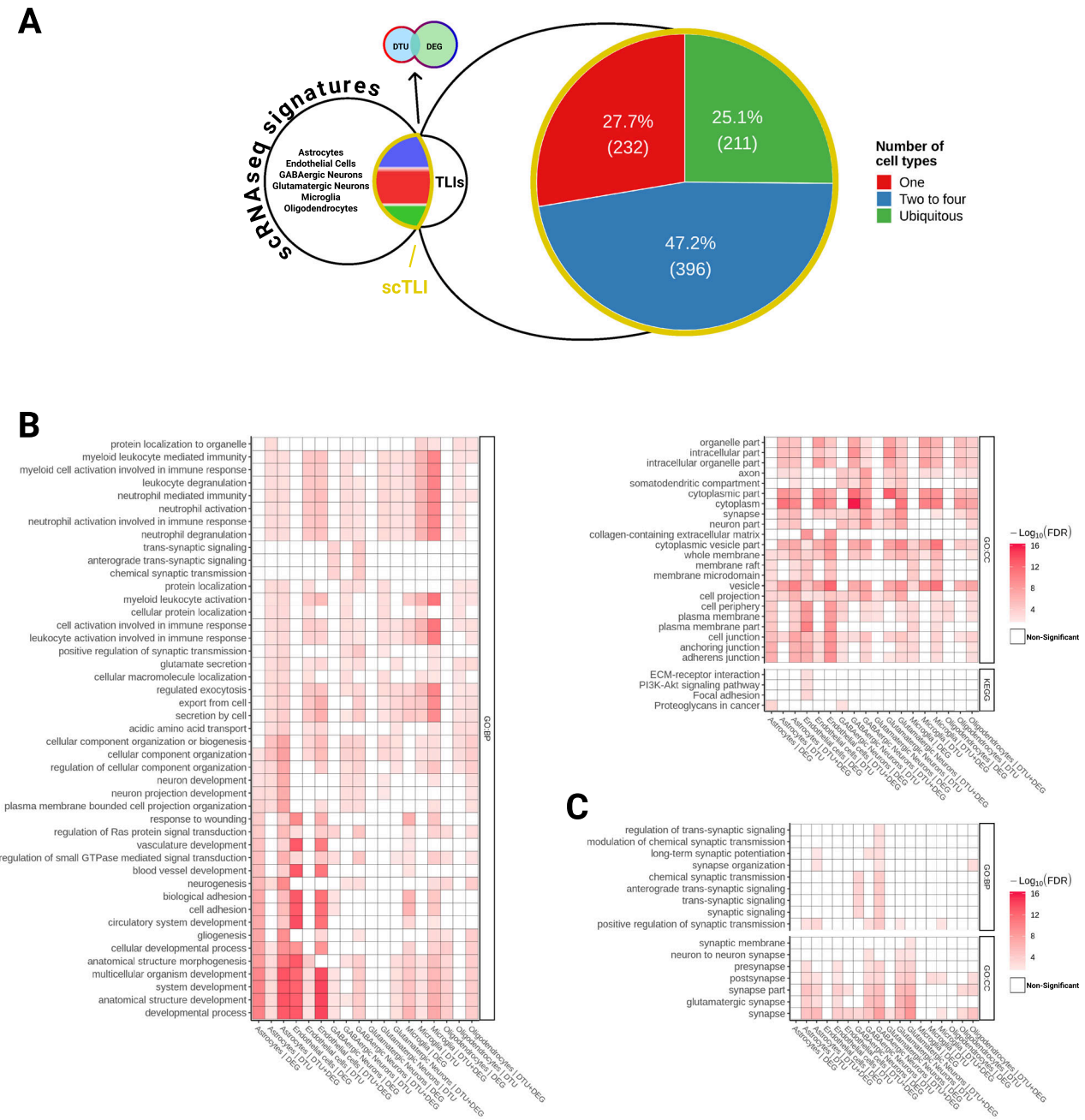

Fig. 7 Cell-type expression pattern for genes altered in AD brains. A Schematic representation showing our strategy to assign DEGs and gDTUs identified in the TLI to specific cell types of the adult human brain (see also Supplementary Fig. 1). Out of 839 single-cell TLI genes (scTLI), 281 were expressed in a unique cell-type, 249 in 2–4 cell-types, and 77 in all cell-types/subtypes analyzed. **B** Gene ontology terms enriched for scTLI DEGs, gDTUs, or both per cell type. **C** Selected GO terms associated with synaptic transmission.

expressed in the AD brain. Altogether, our work provides a comprehensive description of regional and cell-type-specific gene expression changes in the AD brain and suggests that alternative splicing could be an important mechanism for pathological progression.

Despite the availability of RNAseq datasets generated from healthy subjects and AD patients[2–4], a systematic evaluation of the gene expression changes in the AD brain, as well as comparisons of these changes in distinct brain regions, was missing. To the best of our knowledge, only one study aimed at comparing gene expression levels in different AD brain regions[37], but this work was based on microarray data which has limited gene coverage. We show, using bulk tissue RNAseq data, that alterations in gene expression are highly prominent in biological samples obtained from the temporal lobe, which harbors the first brain regions affected in the AD pathogenesis[8]. Conversely, few changes are present in biological samples derived from the frontal lobe, where cells are affected only at advanced stages of AD. These observations are in line with recent data showing that changes in protein expression levels in AD brains are much more prominent in the temporal lobe (hippocampus, entorhinal cortex, and cingulate gyrus) than in the frontal lobe (motor cortex)[9]. They can also help to explain the low number of DEGs identified in scRNAseq data obtained from the frontal lobe[7] compared to a similar study in the entorhinal cortex[6].

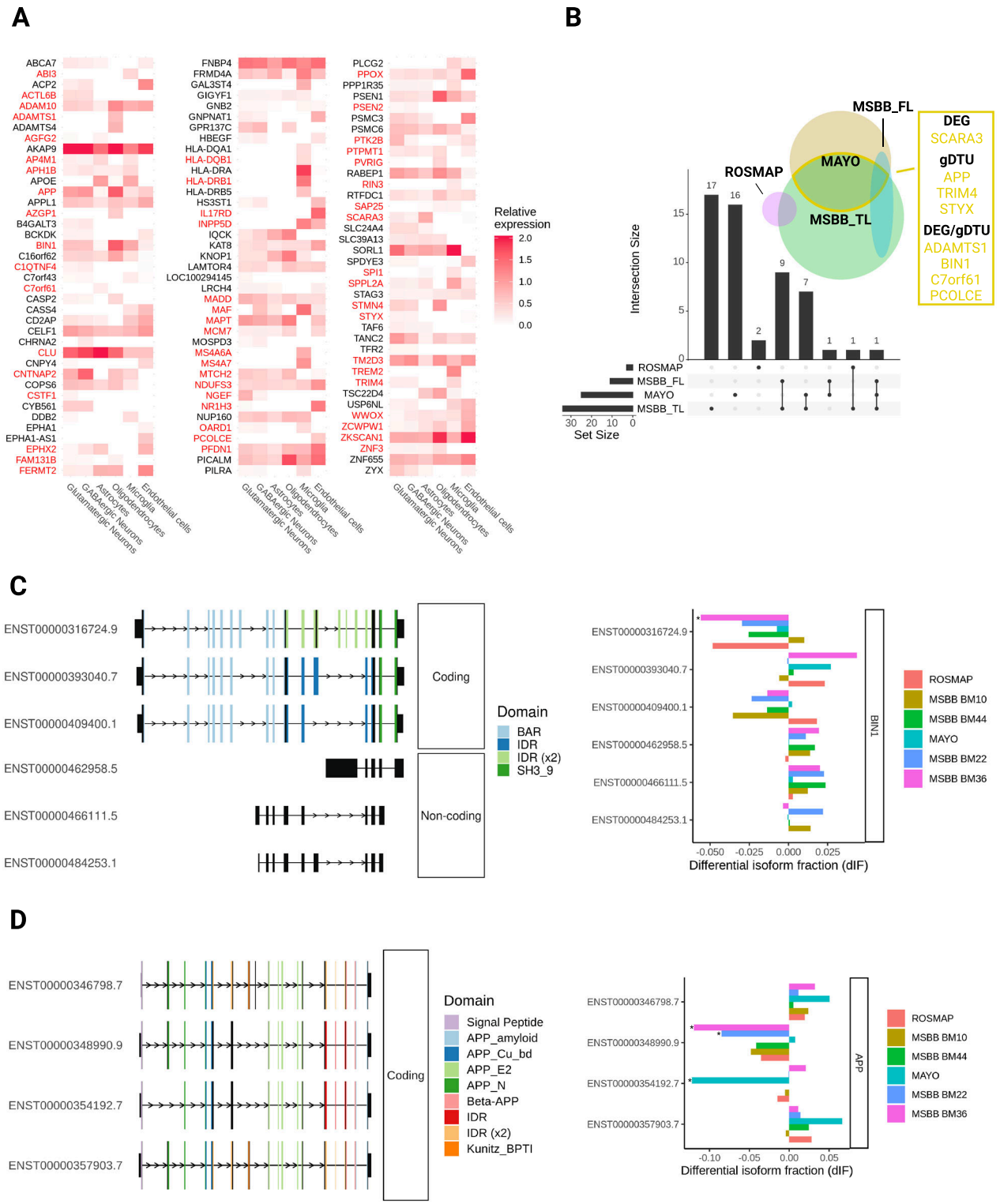

Fig. 8 Expression of AD risk/causal genes is mostly altered in the TL of patients. A Heatmap showing the expression of predicted AD risk/causal genes in different cell types of the adult human brain. DEGs and gDTUs in at least one dataset are highlighted in red. **B** Venn diagram showing the number of AD risk/causal DEGs or gDTUs identified in the different datasets analyzed. The intersection between Mayo and MSBB TL is highlighted in yellow, and genes identified are shown in the yellow box. **C** Representation of the 6 most significant BIN1 isoforms altered (left) and quantification of the differential isoform fraction (dIF) in AD brains compared to controls (right). Main protein domains are indicated with different colors. **D** Similar representation for APP. * dIF >0.05 and FDR > 0.01.

In order to minimize the variability in RNAseq experiments[36], we here focused on DEGs (genes with FC > 1.3 and FDR < 0.01 in AD versus control) detected independently in at least two datasets containing samples of similar brain regions (TLI or FLI). These stringent criteria limited the number of DEGs used in subsequent analyses, but still allowed the uncovering of several genes previously associated with AD pathologies, such as ABCA1, ABCA2, CALB1, C1R, C1S, GAD1/2, PVALB, REST, SLC32A1, SST, VGF, and VIP[15–19] The reduced number of DEGs in FLI and TLI likely explains our failure to detect functional annotations associated with synaptic transmission and immune response in GSEA, as previously reported[13]. However, this study analyzed only the ROSMAP dataset and considered genes with FDR < 0.05 as significant, regardless of the fold change, identifying 1722 DEGs in AD versus control brains. Besides the questionable meaning of DEGs with very small fold changes, the use of such a large set of genes for GSEA can artificially increase the number of significantly enriched functional annotations and is not advised[20].

Nevertheless, our failure to detect key functional annotations associated with AD pathology while inputting TLI DEGs is puzzling and could suggest that DEG analysis fails to detect relevant alterations in gene expression in the AD brain. Indeed, classical DEG analysis using DESeq or edgeR, which rank all gene transcripts, including noncoding sequences[38], are insensitive to the dynamics of gene expression that could, for example, lead to isoform switches with important functional consequences[21]. Therefore, important gene expression alterations could occur at the level of transcripts, without significant changes in the global expression of genes. According to this possibility, we provide convincing evidence that a high number of genes in the AD brain show isoform switches (DTU) but are not detected by DEG analysis, including several genes associated with the regulation of synapse transmission, such as APP, NSG1, RELN, GABRA1[22–26]. Moreover, gDTUs identified in two independent datasets (TLI), alone or in combination with TLI DEGs, were enriched for key biological processes involved in AD pathogenesis, such as synaptic communication, immune response, inflammation, endocytosis, and cell-signaling[39]. Similar gene set enrichment has been described using the analysis of co-expression modules in bulk RNAseq[27,40] or DEG analysis DEGs in unique cell types in scRNAseq[6,7]. This could suggest that the combination of DEG and DTU to analyze bulk RNAseq is comparable to scRNAseq regarding the sensitivity to detect gene expression alteration in AD brains. In agreement with this possibility, we were able to assign DEGs and gDTUs to unique cell types and confirm the similarities among cell-type-specific functional annotations observed in our work compared to previous scRNAseq studies[6,7].

Notably, we show that several DEGs/gDTUs associated with AD pathogenesis, such as NSG1, CALB1, RELN[23–25,41] are exclusively assigned to GABAergic neurons. These genes may be particularly relevant for AD pathogenesis, given the central role of GABAergic neurons for the generation of oscillatory rhythms, network synchrony, and memory in different animal models of AD[42]. Isoform switches in the APP gene could particularly affect GABAergic neurons, which express high levels of that gene, contributing to AD pathogenesis. According to this possibility, conditional knockout of APP/APLP2 only in GABAergic forebrain neurons using DlxCre mice leads to cognitive deficits in hippocampus-dependent spatial learning and memory tasks, associated with altered neuronal morphology and synaptic plasticity[43]. It is tempting to speculate that GABAergic neurons could be particularly vulnerable in AD, contributing to the increased neuronal activity and synapse downscaling observed in AD brains[39,44].

The high number of gDTUs observed in AD brains compared to controls can likely be explained by altered expression of genes encoding for proteins of the splicing machinery, affecting alternative splicing. According to this interpretation, we show that a high number of isoform switches is associated with alternative transcription start site, alternative transcription termination site, exon skipping, alternative 3′ or 5′ splice sites, multiple exon skipping and intron retention. Moreover, we show that several genes encoding for proteins of the splicing machinery have their expression altered in AD brains, especially those showing a high degree of pathology (Braak >5). Also in agreement with the regional differences in gene expression described above, alterations in the splicing machinery are more prominent in the TL than in the FL, which could help to explain the low number of gDTUs in the latter brain region identified in our work and in the previous study using a different strategy to detect isoform switch[5].

Particularly interesting, several genes encoding for proteins involved in the control of alternative splicing in neurons are differently expressed in the TL of AD brains. For instance, RBFOX1 and 2 are downregulated in the MSBB BM36 and could contribute to the altered rate of exon skipping observed in this region[28,45]. Noteworthy, reduced expression of RBFOX1 has been associated with increased inclusion of exon 7 in the APP gene, leading to an enhanced expression of APP isoforms 770 and 751 containing the KPI domain[45]. A similar switch in the APP isoforms has also been associated with somatic gene recombination in AD[46], indicating that increased ratios of APP isoforms containing the KPI domain could be detrimental to neurons. Considering these findings and the well-established associations between KPI(+)APP expression levels, amyloid plaque deposition, and AD pathology progression[33–35], it is tempting to speculate that controlling APP isoform switches by manipulating RBFOX family proteins could be a potential therapeutic strategy to hamper disease progression.

Altered exon skipping could also help to explain the isoform switch observed for BIN1, which is a major risk factor for AD[29,30]. BIN1 comprises a N-BAR domain involved in membrane curvature sensing, an SH3 domain that binds to proline-rich motifs, and a clathrin-binding domain (CLAP) specific of the neuronal isoform 1[32]. We show that the transcript encoding for this latter isoform is significantly reduced in the temporal lobe, suggesting that expression of BIN1 isoform 1 in neurons could be reduced. This observation is in line with decreased BIN1 isoform 1 protein expression in the AD brain compared with controls (our own results)[47]. This would be also in agreement with the observation that overexpression of the BIN1 isoform 1 may be protective in a model of Tauopathy[48].

Although we cannot formally rule out that a stage-dependent increase in the number of DEGs and gDTUs could be due to the loss of neuronal cells in brain regions affected by the pathology, several lines of evidence indicate that this is not the most parsimonious explanation for the data described here. First, we observe that the percentage of up- and downregulated genes in GABAergic and glutamatergic neurons are close to 50%, ruling out the possibility that changes in cell numbers could explain these changes. Secondly, previous scRNAseq studies in AD observed a consistent fraction of cell types isolated across control and AD individuals[6,7], ruling out significant changes in the cellular composition of AD brains. Lastly, a large number of genes with total expression levels unchanged but presenting isoform switches in the AD brains may likely presuppose a steady cellular composition of the tissue.

Altogether, our work proposes a novel strategy to analyze bulk RNAseq data and identify meaningful gene expression alterations in the diseased brain. It also corroborates previous work implicating alternative splicing in AD susceptibility[5] and suggests that isoform switches in the gene BIN1 are involved in the reduced expression of the main neuronal BIN1 isoform 1 in AD brains.

Table 1. Summary of clinical, demographic, and technical variables of samples analyzed from different datasets.

Diagnosis	Sex	*n*	Braak	AOD	CDR	RIN	PMI
Mayo–TL							
AD	F	49	5.55 ± 0.53	83.33 ± 7.23	–	8.58 ± 0.58	6.34 ± 5.8
AD	M	33	5.42 ± 0.55	81.67 ± 8.16	–	8.59 ± 0.5	8.6 ± 5.83
Control	F	37	2.03 ± 0.78	84.81 ± 8.04	–	7.59 ± 1	7 ± 7.69
Control	M	41	2.36 ± 0.87	80.27 ± 9.13	–	7.64 ± 1.05	5.51 ± 6.42
MSBB–BM10							
AD	F	86	5.18 ± 1.21	85.94 ± 6	3.17 ± 1.35	6.05 ± 1.64	6.01 ± 3.97
AD	M	53	5.48 ± 0.99	79.26 ± 7.67	3.23 ± 1.28	6.19 ± 1.42	7.38 ± 4.73
Control	F	52	2.02 ± 1.09	83.04 ± 7.43	0.81 ± 1.1	6.37 ± 1.28	8.69 ± 5.73
Control	M	42	1.62 ± 0.94	78.93 ± 8.56	1.23 ± 1.45	6.73 ± 1.14	11.31 ± 7.47
MSBB–BM22							
AD	F	88	5.25 ± 1.2	85.81 ± 5.95	3.17 ± 1.39	6 ± 1.5	5.34 ± 3.71
AD	M	64	5.41 ± 0.97	79.44 ± 7.67	3.48 ± 1.35	5.53 ± 1.28	7.2 ± 4.8
Control	F	45	2 ± 1.26	82.09 ± 8.1	0.94 ± 1.29	6 ± 1.23	9.18 ± 6.18
Control	M	41	1.72 ± 0.97	79.29 ± 8.66	1.22 ± 1.42	5.72 ± 1.06	11.01 ± 7.29
MSBB–BM36							
AD	F	95	5.35 ± 1.1	86.79 ± 5.2	3.22 ± 1.28	5.59 ± 1.71	5.96 ± 4.14
AD	M	53	5.47 ± 0.91	79.26 ± 7.98	3.42 ± 1.41	5.69 ± 1.61	6.65 ± 4.9
Control	F	44	2.14 ± 1.15	83.45 ± 7.23	0.86 ± 1.28	6.15 ± 1.32	8.3 ± 5.66
Control	M	40	1.65 ± 0.92	78.28 ± 8.79	0.85 ± 1.18	6.2 ± 1.2	12.47 ± 7.92
MSBB–BM44							
AD	F	84	5.2 ± 1.29	85.62 ± 6.02	3.11 ± 1.41	6.9 ± 2.51	5.74 ± 3.82
AD	M	51	5.49 ± 0.98	79.69 ± 7.59	3.2 ± 1.25	6.57 ± 2.41	7.19 ± 4.58
Control	F	45	2.11 ± 1.19	81.82 ± 9.06	0.93 ± 1.26	7.43 ± 2.15	8.19 ± 5.74
Control	M	47	1.82 ± 0.95	78.13 ± 8.16	0.96 ± 1.22	7.35 ± 2.14	11.48 ± 7.3
ROSMAP–DLPFC							
AD	F	147	4.18 ± 0.93	88.55 ± 3.05	–	6.97 ± 0.88	7.25 ± 4.51
AD	M	64	3.92 ± 1.28	87.6 ± 3.18	–	7 ± 1.09	6.58 ± 4.24
Control	F	118	3.04 ± 1.07	85.66 ± 4.83	–	7.31 ± 0.99	7.25 ± 5.18
Control	M	74	2.58 ± 1.4	83.69 ± 5.69	–	7.19 ± 1.08	7.34 ± 4.05

AOD age of death, *CDR* clinical dementia rate, *n* number of samples, *RIN* RNA integrity number, *PMI* postmortem interval (in hours), *AD* Alzheimer disease, *F* female, *M*, male.
Values are mean ± SD. See supplementary Table 13 for individual values.

METHODS

Bulk RNAseq data from human control and disease banks

RNAseq datasets obtained from different brain regions were used (Mayo[2]; MSBB[3]; ROSMAP[4]). Datasets were downloaded from AMP-AD Knowledge Portal (https://www.synapse.org) following all terms and conditions to use the data. The brain area analyzed and the number of individuals per condition was the following: Mayo - Temporal cortex, which neuroanatomically subdivides into the inferior, middle, and superior temporal gyri (STG), and cytoarchitectonically can be subdivided into Brodmann areas (BM, instead of BA) 20/21/22/41/42[49], $N = 160$ subjects (82 AD and 78 controls); MSBB - BM22, which is part of the Wernicke's area in the STG, $N = 159$ subjects (98 AD and 61 controls); MSBB BM36, corresponding to the lateral perirhinal cortex, $N = 154$ subjects (88 AD and 64 controls); MSBB BM10, corresponding to the anterior prefrontal cortex, $N = 176$ subjects (105 AD and 71 controls); MSBB BM44, corresponding to the inferior frontal gyrus, $N = 153$ subjects (90 AD and 63 controls); and ROSMAP - Dorsolateral prefrontal cortex (DLPFC), containing BM46 and part of BM9, $N = 423$ subjects (222 AD and 201 controls). Unless stated otherwise, data obtained from different analyses were grouped in "temporal lobe" (TL) - Mayo, MSBB BM22 and MSBB BM26; or "frontal lobe" (FL) - ROSMAP, MSBB BM10 and MSBB BM44.

Metadata obtained from each study was used to classify patients into Control and Alzheimer's disease groups (Supplementary Table 12). Briefly, for the MSBB dataset, we used patients with Neuropathology Category (NP.1) labeled as "Control" and "definitive Alzheimer". For the Mayo dataset, we used the "Diagnosis" column of the metadata, selecting only "AD" and "Control" patients. For the ROSMAP dataset, we also used the column "Diagnosis" of the metadata, selecting only "Control" (value = 1) and "Alzheimer with no other conditions" (value = 4). In all those datasets, subjects marked as "AD" showed Braak stage values higher than 4. In the MSBB dataset, CDR scores of AD patients were consistently higher than 2. In the Mayo and ROSMAP datasets, all AD patients had also a definitive diagnosis according to NINCDS criteria. Covariates such as "Postmortem interval (PMI)", "RNA integrity number (RIN)", "Age of death", and "Sex" were balanced among the different groups (Table 1; Chi-square test, $p > 0.05$). We used RIN and PMI as covariates in our model to control for possible "batch effects" (linear regression). For detailed information of all individual samples used in this study, please refer to Supplementary Table 13.

For single-cell RNA sequencing (scRNAseq) analyses, we used processed data obtained from the middle temporal gyrus (MTG), available at the Allen Brain Atlas consortium (https://celltypes.brain-map.org/rnaseq).

Realignment of human reads into single pseudoaligner pipeline

Using human GRCh38 cDNA release 94 (ftp://ftp.ensembl.org/pub/release-94) as a reference, we built an index to align all our fastq files. Next, we used pseudoaligner Kallisto[50] (version 0.43.1) with our pre-built index to align fastq files.

Differential gene expression analyses. Differentially expressed genes (DEGs) were identified using differential gene expression at transcript-level using DESeq2 R library[51,52]. To facilitate kallisto output import, transcript-level estimated counts, length, and abundance were extracted using *tximport* function[53]. As described by Michael Love group, transcript-level differential gene expression enhances analysis resolution[52]. Using *DESeqDataSetFromTximport*, a DESeq2 object was created and filtered using rows with sum of all counts bigger than 10. Next, *DESeq* function was used with default values. Using the *results* function, we selected all genes with a false discovery rate (FDR) < 0.01 and fold change (FC) > 1.3. We also used RIN and PMI as covariates (linear regression).

Differential transcript usage (DTU) analysis was performed using the R library IsoformSwitchAnalyzeR[12]. Following pipeline instructions, kallisto abundance tables were imported using *importIsoformExpression* and *importRdata* functions to create a *switchAnalyzeRlist* object. Same cDNA release used in kallisto alignment and correspondent annotation (ftp://ftp.ensembl.org/pub/release-94/gtf/homo_sapiens/Homo_sapiens.GRCh38.94.chr_patch_hapl_scaff.gtf.gz) were applied as input. We filtered data using a gene expression cutoff = 10, isoform expression cutoff = 3, differential isoform fraction (dIF) cutoff = 0.05 and removed single isoform genes. Although DEXSeq is recommended to test differential isoform usage, it does not work efficiently for large datasets (more than 100 samples)[11]. For that reason, we chose *isoformSwitchAnalysisPart1* function using DRIM-Seq[53] to test differential transcript usage. Using part1 fasta files, all external analysis was performed and used as input to *isoformSwitchAnalysisPart2* function. We used CPC2, Pfam, SignalIP and Netsurfp2 as indicated in the pipeline. Next, we performed a confirmation stage using stageR[14] to generate isoforms overall false discovery rate (OFDR). We selected all isoforms with OFDR < 0.01 and dIF >0.05. RIN and PMI metadata were used as covariates (linear regression).

Statistical significance of the intersections among different datasets was calculated using the hypergeometric test (phyper).

Splicing events and event consequences

We used extractSplicingSummary and extractConsequenceSummary functions to quantify gain/loss of predicted splicing events (such as exon skipping and intron retention); and gain/loss (also sensitive/insensitive, shorter/longer and switch) of predicted functional consequences (such as coding potential and domain identified), respectively.

Single-cell RNAseq

Using R library *seurat*[54], we created a seurat object (*CreateSeuratObject*), normalized data (*NormalizeData*), found variable genes (*FindVariableFeatures*), and rescaled data using a linear model (*ScaleData, use.umi = F*). After that, we generated 50 PC's (*RunPCA*) but only used 35 of them based on the PC's visualization distribution (*ElbowPlot*). Since Allen data were already annotated, we only used tSNE (*RunTSNE*) to facilitate visualization. A group classified as "None" by Allen metadata were removed from our analysis. This strategy generated 7 main different cell types: Astrocytes, Endothelial cells, Glutamatergic Neurons, GABAergic Neurons, Microglia, Oligodendrocytes and oligodendrocyte precursor cells (OPCs). To assign genes to specific cell types, we used the AverageExpression function. Using pct.exp bigger than 0.1, we created a list of genes that were expressed by each cell type.

Gene set enrichment analysis (GSEA)

For gene ontology analysis, R library *gprofiler2*[55] was used. Using *gost* function, correction_method = "fdr" and significant=TRUE. To minimize the enrichment of gene ontologies based on a small set of genes, we used three conditions for significance assessment: false discovery rate (FDR) < 0.01; intersection size (intersection between gene set vs. a number of genes in a term) >3; and precision (intersection size divided by gene set) >0.03. We used Gene Ontology (GO or by branch GO:MF, GO:BP, GO:CC), Kyoto Encyclopedia of Genes and Genomes (KEGG), Reactome (REAC), WikiPathways (WP), TRANSFAC (TF), miRTarBase (MIRNA), Human Protein Atlas (HPA), CORUM (CORUM), Human phenotype ontology (HP) as sources. For improved visualization, we plotted results only for GO:BP, GO:CC and KEGG and show only FDR related to terms reaching all criteria of significance.

Selection of splicing-associated genes

To select splicing-related genes, we searched for terms containing the words "splicing" or "spliceosome" in gProfiler bank (https://biit.cs.ut.ee/gprofiler/gost). Taking only GO and WP datasets, 25 terms and 441 genes related to those terms were selected (Supplementary Table 6).

Selection of AD risk/causal genes

The complete list of AD risk/causal genes used in this study is described in Supplementary Table 10. Briefly, AD risk loci were selected from previous work using genome-wide association studies and whole exome sequencing[29,30]. AD risk genes within these loci were determined based on regional association plots, assuming that the functional risk variants are located in the vicinity of the SNP producing the top signal and taking into account the linkage disequilibrium patterns and the recombination peaks within the loci of interest[31]. Early-onset AD causal genes used in this study are APP, PSEN1, and PSEN2.

Western blotting

Frozen brain samples obtained from the frontal cortex (FCx) and hippocampus (hip) of three non-pathology (age: 80.33 ± 3.78 years; Braak: 2.66 ± 1.15; PMI: 37.33 ± 22.50 h) and six AD patients (age: 79.57 ± 6.70 years; Braak: 6; PMI: 26.57 ± 13.40 h) were lysed with RIPA buffer and sonicated at 100% during 10 s before use for the western blotting analyses. The controls for BIN1 isoforms 1 (Iso1) and 9 (Iso9) were obtained using HEK cells transiently transfected with 1 µg/ml DNA solution containing plasmids encoding for BIN1 isoforms mixed with the transfection reagent FuGENE HD (Promega) at the ratio 1:3. Cells were lysed using RIPA buffer 48 h after transfection and frozen for further analyses.

Protein quantification was performed using the BCA protein assay (Thermo Scientific). In total, 10–20 µg of total protein from extracts were separated in SDS–polyacrylamide gels 4–12% (NuPAGE Bis-Tris, Thermo Scientific) and transferred to nitrocellulose membranes (Bio-Rad). Next, membranes were incubated in milk (5% in Tris-buffered saline with 0.1% Tween-20, TTBS) to block non-specific binding sites during 1 h at RT, followed by several washes with TTBS. Immunoblotting was carried out with primary antibodies anti-BIN1 (Abcam, ab182562), anti-β-ACTIN (Sigma-Aldrich, A1978), and anti-GAPDH (Millipore, AB2302) overnight at 4 °C on 20 RPM. The membranes were washed three times in TTBS, followed by incubation with HRP-conjugated secondary antibodies (Jackson, anti-mouse 115-035-003 and anti-rabbit 111-035-003; Thermo Scientific, anti-chicken A16054) overnight at 4 °C on 20 RPM agitation. The membranes were washed three times in TTBS, and the immunoreactivity was revealed using the ECL chemiluminescence system (SuperSignal, Thermo Scientific) and imaged using the Amersham Imager 600 (GE Life Sciences). Optical densities of bands were quantified using "Gel Analyzer" plugin in Fiji[56].

All western blot experiments were performed in compliance with relevant guidelines provided by the Neuro-CEB - Biological Resources Platform and the protocols were approved by the National Institute of Health and Medical Research (INSERM), at the Institut Pasteur de Lille, University of Lille.

Reporting summary

Further information on research design is available in the Nature Research Reporting Summary linked to this article.

DATA AVAILABILITY

MSBB RNAseq[3]: https://doi.org/10.7303/syn3388564; ROSMAP RNAseq[4]: https://doi.org/10.7303/syn3157743; MAYO RNAseq[2]: https://doi.org/10.7303/syn5550404.

CODE AVAILABILITY

Codes used for analyses are available, differentially expressed genes and differential transcript usage in individual datasets can be assessed using https://diegomscoelho.github.io/AD-IsoformSwitch/.

Received: 5 May 2020; Accepted: 12 November 2020;
Published online: 04 January 2021

REFERENCES

1. Masters, C. L. et al. Alzheimer's disease. *Nat. Rev. Dis. Primers* **1**, 15056 (2015).
2. Allen, M. et al. Human whole genome genotype and transcriptome data for Alzheimer's and other neurodegenerative diseases. *Sci. Data* **3**, 160089 (2016).
3. De Jager, P. L. et al. Data descriptor: a multi-omic atlas of the human frontal cortex for aging and Alzheimer's disease research. *Sci. Data* **5**, 180142–180142 (2018).
4. Wang, M. et al. The Mount Sinai cohort of large-scale genomic, transcriptomic and proteomic data in Alzheimer's disease. *Sci. Data* **5**, 1–16 (2018).
5. Raj, T. et al. Integrative transcriptome analyses of the aging brain implicate altered splicing in Alzheimer's disease susceptibility. *Nat. Genet.* **50**, 1584–1592 (2018).
6. Grubman, A. et al. A single-cell atlas of entorhinal cortex from individuals with Alzheimer's disease reveals cell-type-specific gene expression regulation. *Nat. Neurosci.* **22**, 2087–2097 (2019).
7. Mathys, H. et al. Single-cell transcriptomic analysis of Alzheimer's disease. *Nature* **570**, 332–337 (2019).
8. Braak, H. & Braak, E. Neuropathological stageing of Alzheimer-related changes. *Acta Neuropathologica* **82**, 239–259 (1991).
9. Xu, J. et al. Regional protein expression in human Alzheimer's brain correlates with disease severity. *Commun. Biol.* **2**, 1–15 (2019).
10. Yi, L., Pimentel, H., Bray, N. L. & Pachter, L. Gene-level differential analysis at transcript-level resolution. *Genome Biol.* **19**, 53 (2018).
11. Anders, S., Reyes, A. & Huber, W. Detecting differential usage of exons from RNA-seq data. *Genome Res.* **22**, 2008–2017 (2012).
12. Vitting-Seerup, K. & Sandelin, A. IsoformSwitchAnalyzeR: analysis of changes in genome-wide patterns of alternative splicing and its functional consequences. *Bioinformatics* **35**, 4469–4471 (2019).
13. Canchi, S. et al. Integrating gene and protein expression reveals perturbed functional networks in Alzheimer's disease. *Cell Rep.* **28**, 1103–1116.e4 (2019).
14. Van den Berge, K., Soneson, C., Robinson, M. D. & Clement, L. stageR: a general stage-wise method for controlling the gene-level false discovery rate in differential expression and differential transcript usage. *Genome Biol.* **18**, 151 (2017).
15. Abuznait, A. H. & Kaddoumi, A. Role of ABC transporters in the pathogenesis of Alzheimers disease. *ACS Chem. Neurosci.* **3**, 820–831 (2012).
16. Benoit, M. E. et al. C1q-induced LRP1B and GPR6 proteins expressed early in Alzheimer disease mouse models are essential for the C1q-mediated protection against amyloid- β neurotoxicity. *J. Biol. Chem.* **288**, 654–665 (2013).
17. Zullo, J. M. et al. Regulation of lifespan by neural excitation and REST. *Nature* **574**, 359–364 (2019).
18. Prévot, T. & Sibille, E. Altered GABA-mediated information processing and cognitive dysfunctions in depression and other brain disorders. *Mol. Psychiatry* 1–17 (2020) https://www.nature.com/articles/s41380-020-0727-3.
19. Beckmann, N. D. et al. Multiscale causal networks identify VGF as a key regulator of Alzheimer's disease. *Nat. Commun.* **11**, 18 (2020).
20. Subramanian, A. et al. Gene set enrichment analysis: a knowledge-based approach for interpreting genome-wide expression profiles. *Proc. Natl Acad. Sci. USA* **102**, 15545–15550 (2005).
21. Vitting-Seerup, K. & Sandelin, A. The landscape of isoform switches in human cancers. *Mol. Cancer Res.* **15**, 1206–1220 (2017).
22. Kamenetz, F. et al. APP processing and synaptic function. *Neuron* **37**, 925–937 (2003).
23. Alberi, S. et al. The endosomal protein NEEP21 regulates AMPA receptor-mediated synaptic transmission and plasticity in the hippocampus. *Mol. Cell. Neurosci.* **29**, 313–319 (2005).
24. Norstrom, E. M., Zhang, C., Tanzi, R. & Sisodia, S. S. Identification of NEEP21 as a β-amyloid precursor protein-interacting protein in vivo that modulates amyloidogenic processing in vitro. *J. Neurosci.* **30**, 15677–15685 (2010).
25. Yu, N. N., Tan, M. S., Yu, J. T., Xie, A. M. & Tan, L. The role of reelin signaling in Alzheimer's disease. *Mol. Neurobiol.* **53**, 5692–5700 (2016).
26. Limon, A., Reyes-Ruiz, J. M. & Miledi, R. Loss of functional GABA A receptors in the Alzheimer diseased brain. *Proc. Natl Acad. Sci. USA* **109**, 10071–10076 (2012).
27. Wan, Y. W. et al. Meta-analysis of the Alzheimer's disease human brain transcriptome and functional dissection in mouse models. *Cell Rep.* **32**, 107908 (2020).
28. Raj, B. & Blencowe, B. J. Alternative splicing in the mammalian nervous system: recent insights into mechanisms and functional roles. *Neuron* **87**, 14–27 (2015).
29. Lambert, J. C. et al. Meta-analysis of 74,046 individuals identifies 11 new susceptibility loci for Alzheimer's disease. *Nat. Genet.* **45**, 1452–1458 (2013).
30. Kunkle, B. W. et al. Genetic meta-analysis of diagnosed Alzheimer's disease identifies new risk loci and implicates Aβ, tau, immunity and lipid processing. *Nat. Genet.* **51**, 414–430 (2019).
31. Dourlen, P., Kilinc, D., Malmanche, N., Chapuis, J. & Lambert, J. C. The new genetic landscape of Alzheimer's disease: from amyloid cascade to genetically driven synaptic failure hypothesis? *Acta Neuropathologica* **138**, 221–236 (2019).
32. Zhou, Y. et al. Intracellular clusterin interacts with brain isoforms of the bridging integrator 1 and with the microtubule-associated protein Tau in Alzheimer's disease. *PLoS ONE* **9**, e103187 (2014).
33. Kitaguchi, N., Takahashi, Y., Tokushima, Y., Shiojiri, S. & Ito, H. Novel precursor of Alzheimer's disease amyloid protein shows protease inhibitory activity. *Nature* **331**, 530–532 (1988).
34. Johnson, S. A., Rogers, J. & Finch, C. E. APP-695 transcript prevalence is selectively reduced during Alzheimer's disease in cortex and hippocampus but not in cerebellum. *Neurobiol. Aging* **10**, 755–760 (1989).
35. Tanzi, R. E. et al. Protease inhibitor domain encoded by an amyloid protein precursor mRNA associated with Alzheimer's disease. *Nature* **331**, 528–530 (1988).
36. Lee, T. I. & Young, R. A. Transcriptional regulation and its misregulation in disease. *Cell* **152**, 1237–1251 (2013).
37. Haroutunian, V., Katsel, P. & Schmeidler, J. Transcriptional vulnerability of brain regions in Alzheimer's disease and dementia. *Neurobiol. Aging* **30**, 561–573 (2009).
38. Costa-Silva, J., Domingues, D. & Lopes, F. M. RNA-Seq differential expression analysis: an extended review and a software tool. *PLoS ONE* **12**, e0190152 (2017).
39. Canter, R. G., Penney, J. & Tsai, L. H. The road to restoring neural circuits for the treatment of Alzheimer's disease. *Nature* **539**, 187–196 (2016).
40. Milind, N. et al. Transcriptomic stratification of late-onset Alzheimer's cases reveals novel genetic modifiers of disease pathology. *PLoS Genet.* **16**, e1008775 (2020).
41. Odero, G. L. et al. Evidence for the involvement of calbindin D28k in the presenilin 1 model of Alzheimer's disease. *Neuroscience* **169**, 532–543 (2010).
42. Verret, L. et al. Inhibitory interneuron deficit links altered network activity and cognitive dysfunction in alzheimer model. *Cell* **149**, 708–721 (2012).
43. Mehr, A. et al. Lack of APP and APLP2 in GABAergic forebrain neurons impairs synaptic plasticity and cognition. *Cereb. Cortex* **30**, 4044–4063 (2020).
44. Dörrbaum, A. R., Alvarez-Castelao, B., Nassim-Assir, B., Langer, J. D. & Schuman, E. M. Proteome dynamics during homeostatic scaling in cultured neurons. *eLife* **9**, e52939 (2020).
45. Alam, S., Suzuki, H. & Tsukahara, T. Alternative splicing regulation of APP exon 7 by RBFox proteins. *Neurochem. Int.* **78**, 7–17 (2014).
46. Lee, M. H. et al. Somatic APP gene recombination in Alzheimer's disease and normal neurons. *Nature* **563**, 639–645 (2018).
47. Glennon, E. B. C. et al. BIN1 is decreased in sporadic but not familial Alzheimer's disease or in aging. *PLoS ONE* **8**, e78806 (2013).
48. Sartori, M. et al. BIN1 recovers tauopathy-induced long-term memory deficits in mice and interacts with Tau through Thr348 phosphorylation. *Acta Neuropathologica* **138**, 631–652 (2019).
49. Strotzer, M. One century of brain mapping using Brodmann areas. *Clin. Neuroradiol.* **19**, 179–186 (2009).
50. Bray, N. L., Pimentel, H., Melsted, P. & Pachter, L. Near-optimal probabilistic RNA-seq quantification. *Nat. Biotechnol.* **34**, 525–527 (2016).
51. Love, M. I., Huber, W. & Anders, S. Moderated estimation of fold change and dispersion for RNA-seq data with DESeq2. *Genome Biol.* **15**, 550 (2014).
52. Love, M. I., Soneson, C. & Patro, R. Swimming downstream: statistical analysis of differential transcript usage following Salmon quantification. *F1000Research* **7**, 952–952 (2018).
53. Soneson, C., Love, M. I. & Robinson, M. D. Differential analyses for RNA-seq: transcript-level estimates improve gene-level inferences [version 2; referees: 2 approved]. *F1000Research* **4**, 1521 (2016).
54. Butler, A., Hoffman, P., Smibert, P., Papalexi, E. & Satija, R. Integrating single-cell transcriptomic data across different conditions, technologies, and species. *Nat. Biotechnol.* **36**, 411–420 (2018).
55. Kolberg, L., Raudvere, U., Kuzmin, I., Vilo, J. & Peterson, H. gprofiler2—an R package for gene list functional enrichment analysis and namespace conversion toolset g:Profiler. *F1000Research* **9**, 709 (2020).
56. Schindelin, J. et al. Fiji: an open-source platform for biological-image analysis. *Nat. Methods* **9**, 676–682 (2012).

ACKNOWLEDGEMENTS

We thank Charles Duyckaerts (Neuroceb, GIE Neuro-CEB BB-0033-00011) for providing the brain samples. We would also like to thank Dr. Tarciso Velho, Pierre

Dourlen, and Fabien Delahaye for reading and suggestions on the paper. The results published here are in whole or in part based on the data obtained from the AMP-AD Knowledge Portal (https://adknowledgeportal.synapse.org/). Study data were provided by the following sources: The Mayo Clinic Alzheimer's Disease Genetic Studies, led by Dr. Nilufer Taner and Dr. Steven G. Younkin, Mayo Clinic, Jacksonville, FL using samples from the Mayo Clinic Study of Aging, the Mayo Clinic Alzheimer's Disease Research Center, and the Mayo Clinic Brain Bank. Data collection was supported through funding by NIA grants P50 AG016574, R01 AG032990, U01 AG046139, R01 AG018023, U01 AG006576, U01 AG006786, R01 AG025711, R01 AG017216, R01 AG003949, NINDS grant R01 NS080820, CurePSP Foundation, and support from Mayo Foundation. Study data include samples collected through the Sun Health Research Institute Brain and Body Donation Program of Sun City, Arizona. The Brain and Body Donation Program is supported by the National Institute of Neurological Disorders and Stroke (U24 NS072026 National Brain and Tissue Resource for Parkinson's Disease and Related Disorders), the National Institute on Aging (P30 AG19610 Arizona Alzheimer's Disease Core Center), the Arizona Department of Health Services (contract 211002, Arizona Alzheimer's Research Center), the Arizona Biomedical Research Commission (contracts 4001, 0011, 05-901, and 1001 to the Arizona Parkinson's Disease Consortium) and the Michael J. Fox Foundation for Parkinson's Research. Study data were also provided by the Rush Alzheimer's Disease Center, Rush University Medical Center, Chicago. Data collection was supported through funding by NIA grants P30AG10161 (ROS), R01AG15819 (ROSMAP; genomics and RNAseq), R01AG17917 (MAP), the Illinois Department of Public Health (ROSMAP), and the Translational Genomics Research Institute (genomic). For ROSMAP, additional phenotypic data can be requested at www.radc.rush.edu. Part based on the data generated from postmortem brain tissue collected through the Mount Sinai VA Medical Center Brain Bank and were provided by Dr. Eric Schadt from Mount Sinai School of Medicine. This work was co-funded by the European Union under the European Regional Development Fund (ERDF) and by the Hauts de France Regional Council (contrat no.18006176), the MEL (contract_2016_ESR_05), and the French State (contract no. 2018-3-CTRL_IPL_Phase2) to MRC. This work was also funded by the Lille Métropole Communauté Urbaine and the French government's LABEX DISTALZ program (Development of innovative strategies for a transdisciplinary approach to Alzheimer's disease) to J.C.L. D.M.C. and L.I.C.C. are supported by Coordenação de Aperfeiçoamento de Pessoal de Nível Superior (CAPES) scholarships.

AUTHOR CONTRIBUTIONS

M.R.C. conceived of the presented idea and supervised the experiments. D.M-C. performed all bioinformatic analyses and prepared the figures and tables of the paper. L.I.C.C. contributed with bioinformatic analyses. A.F. prepared protein lysates and A.R.M.F. performed western blot analysis in human samples. D.M.-C., J.-C.L., and M.R.C. wrote the paper. All authors revised and approved the final version of the paper.

COMPETING INTERESTS

The authors declare no competing interests.

ADDITIONAL INFORMATION

Supplementary information is available for this paper at https://doi.org/10.1038/s41514-020-00052-5.

Correspondence and requests for materials should be addressed to M.R.C.

Reprints and permission information is available at http://www.nature.com/reprints

Publisher's note Springer Nature remains neutral with regard to jurisdictional claims in published maps and institutional affiliations.

Open Access This article is licensed under a Creative Commons Attribution 4.0 International License, which permits use, sharing, adaptation, distribution and reproduction in any medium or format, as long as you give appropriate credit to the original author(s) and the source, provide a link to the Creative Commons license, and indicate if changes were made. The images or other third party material in this article are included in the article's Creative Commons license, unless indicated otherwise in a credit line to the material. If material is not included in the article's Creative Commons license and your intended use is not permitted by statutory regulation or exceeds the permitted use, you will need to obtain permission directly from the copyright holder. To view a copy of this license, visit http://creativecommons.org/licenses/by/4.0/.

© The Author(s) 2021

THE BRAINBANK NEURO–CEB NEUROPATHOLOGY NETWORK

Franck Letournel[4], Marie-Laure Martin-Négrier[5], Françoise Chapon[6], Maxime Faisant[6], Catherine Godfraind[7], Claude-Alain Maurage[8], Vincent Deramecourt[8], Mathilde Duchesne[9], David Meyronnet[10], Nathalie Streichenberger[10], André Mauès de Paula[11], Valérie Rigau[12], Fanny Vandenbos-Burel[13], Charles Duyckaerts[14], Danielle Seilhean[14], Serge Milin[15], Dan Christian Chiforeanu[16], Annie Laquerrière[17], Florent Marguet[17] and Béatrice Lannes[18]

[4]CHU Hôpital St Jean, Angers, France. [5]CHRU Pellegrin, Bordeaux, France. [6]CHU Côte de Nacre, Caen, France. [7]CHU Gabriel Montpied, Clermont-Ferrand, France. [8]CHRU Hôpital Roger Salengro, Lille, France. [9]CHRU Hôpital Dupuytren, Limoges, France. [10]Groupe Hospitalier Est. Hospices Civils de Lyon, Lyon, France. [11]CHU Hôpital de La Timone, APHM, Marseille, France. [12]CHU de Montpellier, Montpellier, France. [13]CHU Hôpital Pasteur, Nice, France. [14]GH Pitié-Salpêtrière, APHP, Paris, France. [15]CHU La Milétrie, Poitiers, France. [16]CHU Hôpital Pontchaillou, Rennes, France. [17]CHU Hôpital Charles Nicolle, Rouen, France. [18]CHRU Hôpital de Hautepierre, Strasbourg, France.

Article II

2. The Alzheimer susceptibility gene BIN1 induces isoform-dependent neurotoxicity through early endosome defects

Erwan Lambert†, Orthis Saha†, Bruna Soares Landeira, Ana Raquel Melo de Farias, Xavier Hermant, Arnaud Carrier, Alexandre Pelletier, Johanna Gadaut, Lindsay Davoine, Cloe Dupont, Philippe Amouyel, Amelie Bonnefond, Frank Lafont, Farida Abdelfettah, Patrik Verstreken, Julien Chapuis, Nicolas Barois, Fabien Delahaye, Bart Dermaut, Jean-Charles Lambert, Marcos R. Costa† and Pierre Dourlen†

Acta Neuropathologica Communications, 08 January 2022, 10:4

2.1. Context and objectives

The Bridging Integrator 1 (BIN1) gene is known to be a significant contributor to Alzheimer's disease (AD) susceptibility, but understanding how it plays a role in the disease has been challenging.

This study focuses on investigating BIN1 isoforms and their impact on the development of AD, more specifically how the absence of BIN1 or the expression of specific BIN1 isoforms affect early endosomes. To this aim, we explored to in vitro models - Drosophila and human iPSC-derived cultures. We demonstrate that BIN1, particularly BIN1iso1, contributes to the deregulation of early-endosome size, the researchers provided insights into a potential early event in the development of AD pathology.

2.2. Personal contributions to the work

On this work, I personally contributed to the experimental investigations using human iPSC-derived cultures. In summary, I differentiated BIN1 WT and knockout KO human iPSCs into neurons/astrocytes using a 2D culture model. Cerebral organoids from the different BIN1 genotypes were cultured for 6 months and subjected to characterization. Additionally, I extracted protein material and performed the immunoblotting analyses.

Lambert *et al.*
Acta Neuropathologica Communications (2022) 10:4
https://doi.org/10.1186/s40478-021-01285-5

Acta Neuropathologica Communications

RESEARCH Open Access

The Alzheimer susceptibility gene *BIN1* induces isoform-dependent neurotoxicity through early endosome defects

Erwan Lambert[1†], Orthis Saha[1†], Bruna Soares Landeira[1], Ana Raquel Melo de Farias[1,2], Xavier Hermant[1], Arnaud Carrier[3], Alexandre Pelletier[3], Johanna Gadaut[1], Lindsay Davoine[1], Cloé Dupont[1], Philippe Amouyel[1], Amélie Bonnefond[3], Frank Lafont[4], Farida Abdelfettah[1], Patrik Verstreken[5,6], Julien Chapuis[1], Nicolas Barois[4,7], Fabien Delahaye[3], Bart Dermaut[8,9], Jean-Charles Lambert[1], Marcos R. Costa[1,2*†] and Pierre Dourlen[1*†]

Abstract

The *Bridging Integrator 1* (*BIN1*) gene is a major susceptibility gene for Alzheimer's disease (AD). Deciphering its pathophysiological role is challenging due to its numerous isoforms. Here we observed in Drosophila that human *BIN1* isoform1 (BIN1iso1) overexpression, contrary to human *BIN1* isoform8 (BIN1iso8) and human *BIN1* isoform9 (BIN1iso9), induced an accumulation of endosomal vesicles and neurodegeneration. Systematic search for endosome regulators able to prevent BIN1iso1-induced neurodegeneration indicated that a defect at the early endosome level is responsible for the neurodegeneration. In human induced neurons (hiNs) and cerebral organoids, *BIN1* knock-out resulted in the narrowing of early endosomes. This phenotype was rescued by BIN1iso1 but not BIN1iso9 expression. Finally, BIN1iso1 overexpression also led to an increase in the size of early endosomes and neurodegeneration in hiNs. Altogether, our data demonstrate that the AD susceptibility gene *BIN1*, and especially BIN1iso1, contributes to early-endosome size deregulation, which is an early pathophysiological hallmark of AD pathology.

Keywords: BIN1 isoforms, Neurodegeneration, Early endosome, Alzheimer's disease, Drosophila, Human induced neurons

Introduction

Alzheimer's disease is the most common form of dementia, characterized by two main cerebral lesions: the extracellular aggregation of the amyloid beta peptide (Aβ) into senile plaques and the intracellular aggregation of phosphorylated Tau into tangles. In addition, other cytopathological features specific to familial and sporadic AD can be also observed such as abnormally enlarged early endosomes in neurons [8]. At the genetic level, familial AD is due to mutations in *APP*, *PSEN1* and *PSEN2*. Sporadic AD is a multifactorial disease exhibiting a strong genetic component with an estimated attributable risk of 60–80% [20]. Over the last decade, our understanding of this genetic component has strongly progressed with the identification of 76 loci associated with the disease [4]. Among these loci, *BIN1* is the second AD susceptibility gene after *APOE* in terms of association [4, 33, 35].

BIN1 encodes at least 20 exons subject to extensive differential splicing, generating multiple isoforms with different tissue distributions [49]. *BIN1* isoform1 (BIN1iso1) and *BIN1* isoform8 (BIN1iso8) are respectively expressed in the brain and skeletal muscles, the

*Correspondence: marcos.costa@pasteur-lille.fr; pierre.dourlen@pasteur-lille.fr
†Erwan Lambert and Orthis Saha are co-first authors
†Marcos R. Costa and Pierre Dourlen are co-last authors
[1] Univ. Lille, Inserm, CHU Lille, Institut Pasteur Lille, U1167 - RID-AGE - Facteurs de risque et déterminants moléculaires des maladies liées au vieillissement, F-59000 Lille, France
Full list of author information is available at the end of the article

© The Author(s) 2022. **Open Access** This article is licensed under a Creative Commons Attribution 4.0 International License, which permits use, sharing, adaptation, distribution and reproduction in any medium or format, as long as you give appropriate credit to the original author(s) and the source, provide a link to the Creative Commons licence, and indicate if changes were made. The images or other third party material in this article are included in the article's Creative Commons licence, unless indicated otherwise in a credit line to the material. If material is not included in the article's Creative Commons licence and your intended use is not permitted by statutory regulation or exceeds the permitted use, you will need to obtain permission directly from the copyright holder. To view a copy of this licence, visit http://creativecommons.org/licenses/by/4.0/. The Creative Commons Public Domain Dedication waiver (http://creativecommons.org/publicdomain/zero/1.0/) applies to the data made available in this article, unless otherwise stated in a credit line to the data.

two tissues where *BIN1* is mostly expressed, whereas *BIN1* isoform9 (BIN1iso9) is ubiquitously expressed (GTEx portal, http://www.gtexportal.org). In the brain, BIN1iso1 and BIN1iso9 are the most abundant isoforms [11, 61]. All *BIN1* isoforms possess the N terminal BIN1/Amphiphysin/Rvs (BAR) domain, involved in membrane curvature sensing and induction, the C-terminal MYC-Binding Domain (MBD) and the C-terminal SH3 domain, a protein–protein interaction domain that recognizes proline-rich domains like the one in Tau [49, 59]. Muscle-specific isoforms contain a phosphoinositide-interacting (PI) domain, whereas brain-specific *BIN1* isoforms are mainly characterized by inclusion of exons encoding a Clathrin and Adaptor Protein-2 binding (CLAP) domain involved in endocytosis and intracellular trafficking. In the brain, a complex expression pattern is also observed at the cellular level. *BIN1* expression is mainly observed in oligodendrocytes, microglial cells and neurons [1, 41, 52]. However, while neurons express high molecular weight isoforms including BIN1iso1, glial cells express lower molecular weight isoforms such as BIN1iso9 [52, 69].

AD-associated *BIN1* variants are non-coding and likely regulate *BIN1* expression [9]. However, the dysregulation of *BIN1* expression in the brain of AD cases is still highly debated. Some results indicate that overall *BIN1* expression is increased [9], or decreased [21, 41], whereas more complex patterns have been also reported with a decrease in BIN1iso1 and a concomitant increase in BIN1iso9 expression [24]. In addition, according to the pattern of expression, it is not clear if the observed variations of *BIN1* expression are a cause or a consequence of the neurodegenerative process. For example, the decrease in BIN1iso1 and increase in BIN1iso9 expressions may be a consequence of neuronal death and gliosis, respectively, as *BIN1* isoform variations are correlated with neuronal and glial marker variations [52]. Therefore, based on its global and/or isoform expression variation, it is difficult to assess whether BIN1 may be deleterious or protective in AD.

Importantly, impact of such global and/or isoform expression deregulations on the AD pathophysiological process has not yet been elucidated even if several hypotheses have been proposed: (i) modulation of Tau function and neurotoxicity though interaction of the BIN1 SH3 domain with the Tau proline-rich domain in a phosphorylation-dependent manner [39, 54, 59]; (ii) modulation of Tau spreading through its role in endocytosis and intracellular trafficking or extracellular vesicles [6, 11]; (iii) regulation of the APP metabolism despite contradictory results in different models [2, 62]; (iv) regulation of synaptic transmission either in the presynaptic [53] or postsynaptic compartment [56].

Within this complex background, considering the numerous *BIN1* isoforms and the different functions regulated by this gene, it is, thus, pivotal to address isoform-specific functions of BIN1 towards a comprehensive understanding of its role in AD pathophysiology. For this purpose, we investigated the role and potential toxicity of *BIN1* isoforms in neuronal cells by focusing on BIN1iso1, BIN1iso8 and BIN1iso9. We used the highly tractable and readout-rich Drosophila model which allowed the assessment of *BIN1* isoform neurotoxicity in vivo during aging. We further analyzed the role of *BIN1* isoforms in hiNs derived from human induced pluripotent stem cells (hiPSC), a model closer to AD pathology.

Materials and methods

Drosophila genetics and behavioral experiments

Flies were raised at 25 °C under a light/dark cycle of 12 h/12 h (3000 lx) on standard fly medium (Nutri-fly MF, Genesee Scientific, San Diego, CA, USA), unless otherwise stated. UAS-BIN1iso1, UAS-BIN1iso1 ΔEx7, UAS-BIN1iso1 ΔCLAP, UAS-BIN1iso9, UAS-BIN1iso8 and UAS-dAmphA lines were generated in this work (see Additional file 1). Briefly, cDNA were subcloned into pUASTattB vector and injected in attP2 lines (on the III chromosome) and in attP40 lines (on the II chromosome) (BestGene Inc., CA, USA). rh1-Gal4, GMR-Gal4, rh1-GFP, UAS-GFP:ninaC, UAS-evi:GFP, UAS-GFP:LC3 were described previously [13, 17, 36, 40]. The $Amph^{5E3}$ line was a kind gift from GL Boulianne [37]. Other stocks were obtained from the Bloomington Drosophila Stock Center (BDSC, Bloomington, IN, USA): UAS-Luciferase (#35788), UAS-mCD8:GFP (#27400), UAS-GFP (#35786), $Amph^{MI08903\text{-}TG4.0}$ (#77794), $Rab5^{EYFP}$ (#62543), $Rab7^{EYFP}$ (#62545), UAS-GFP-myc-2xFYVE (#42712), UAS-GFP-Rab5 (#43336), UAS-YFP.Rab5.Q88L (#9771), UAS-YFP.Rab5.S43N (#9774), $Rab5^{[2]}$ (#42702), P{TRiP.HMS00147}attP2 Rab5 (#34832), UAS-Rab7.GFP (#42705), UASp-YFP.Rab7.Q67L (#24103), UASp-YFP.Rab7.T22N (#9778), UAS-Rab11-GFP (#8506), UASp-YFP.Rab11.Q70L (#9791), UASp-YFP.Rab11.S25N (#9792), P{TRiP.HMS01056}attP2 Vha68-2 (#64582), P{TRiP.HMS01442}attP2 VhaAC39-1 (#35029), UAS-mCherry:NLS (#38424), attP2 empty line (#8622), UASp-YFP.Rab9 (#9784), $Rab1^{EYFP}$ (#62539), $Rab6^{EYFP}$ (#62544), UAS-GFP.KDEL (#9898), UAS-ManII-EGFP (#65248), UAS-GFP-LAMP (#42714), Appl[d] (#43632), UAS-Appl (#38403), UAS-APP695 (#33796), UAS-YFP:Rab4 (#23269), UAS-YFP:Rab4[S22N] (#9768), UAS-YFP:Rab4[Q67L] (#9770), UAS-Rab4:mRFP (#8505) and UAS-mCD8:mRFP (#27400).

For the climbing test, 5 flies were subjected together to testing in a graduated cylinder. The wall of the cylinder had 5 main graduations, the top one being 13 cm from

the bottom. Flies were tapped down to the bottom of the cylinder and recorded for 10 s to see if they climbed up the wall of the cylinder. This was repeated 5 times in total. A score corresponding to the distance they had climbed was determined by the recorded movies. Flies got a score of between 0 and 5 depending on the main graduation that they were able to reach during the 10 s period. The mean of the 5 trials was calculated and attributed to each fly.

Western blot of Drosophila samples

Drosophila heads (n = 10) and thorax (n = 5) were dissected and crushed in ice-cold LDS lysis buffer (NP0008, NuPAGE, Novex, Life Technologies) supplemented with reducing agent (NP0009, NuPAGE, Novex, Life Technologies). Samples were centrifuged at 8500*g* for 10 min at 4 °C. Supernatants were kept at − 80 °C. Once thawed, they were boiled for 10 min at 85 °C before being loaded and separated in SDS–polyacrylamide gels 4–12% (NuPAGE Bis–Tris, ThermoScientific) in MOPS 1X buffer (NP0001-02, NuPAGE, Novex, Life Technologies). After migration, samples were transferred on to nitrocellulose membranes using the Biorad Trans-blot transfert system kit (Biorad) according to the supplier technical recommendation (7 min, 2.5 A, 25 V). Next, membranes were incubated in milk (5% in Tris-buffered saline with 0.1% Tween-20) to block non-specific binding sites during 1 h at RT, followed by several washes. Immunoblotting was carried out with primary antibodies anti-BIN1 (BIN1 99D, 05-449, Millipore, RRID:AB_309738, 1/2500; BIN1 ab27796, abcam, RRID:AB_725699, 1/1000), anti-α-tubuline (α-tubuline DM1A, T9026, Sigma, RRID:AB_477593, 1/5000), anti-dAmph (#9906, kind gift of Andrew Zelhof, 1/5000)[67] and anti-GFP (anti-GFP, G1544, Sigma, RRID:AB_439690, 1/4000) overnight at 4 °C. After washing, membranes were incubated with HRP-conjugated secondary antibodies (Jackson, anti-mouse 115-035-003, RRID:AB_10015289 and anti-rabbit 111-035-003, RRID:AB_2313567) 2 h at room temperature. Immunoreactivity was revealed using the ECL chemiluminescence system (WBLUC0500, Immobilon Classico Western HRP Substrate, Millipore) and imaged using the Amersham Imager 600 (GE LifeSciences). Optical densities of bands were quantified using Fiji software and results were normalized with respect to tubulin expression [55].

Cornea neutralization

CO2-anesthetized flies were placed in a 35 mm cell culture dish half-filled with 1% agarose and covered with water at 4 °C as described [14]. Flies were observed using an upright confocal microscope (Zeiss LSM710, Wetzlar, Germany) equipped with a 40 × water immersion long-distance objective. Images were acquired using the Zen acquisition software (Zeiss Zen software). Photoreceptor neurons were manually quantified.

Immunofluorescence of Drosophila samples

Fly heads were dissected and fixed in 4% paraformaldehyde phosphate buffer saline (PBS) for 20 min at room temperature. After washing, retinas were finely dissected, permeabilized and depigmented in 0.3% (v/v) Triton X-100 in PBS (0.3% PBT) overnight at 4 °C under gentle agitation. After blocking with 5% normal goat/donkey serum in 0.3% PBT, samples were incubated overnight at 4 °C with the primary antibodies diluted in 0.3% PBT. The following antibodies were used: anti-NA/K ATPase alpha subunit (a5, DSHB, RRID:AB_2166869, 1/100), anti-rhodopsin (4C5, DSHB, RRID:AB_528451, 1/200) and anti-GFP (132004, Synaptic System, RRID:AB_11041999, 1/100). After washing, they were incubated overnight at 4 °C with Alexa 555 Phalloidin anti-F-actin (A34055, ThermoFisher Scientific) and the secondary antibodies diluted in 0.3% PBT: Alexa 488 Donkey anti-guinea pig (706-545-148, RRID:AB_2340472, Jackson ImmunoResearch), Alexa 633 Goat anti-mouse (A-21052, RRID:AB_2535719, ThermoFisher Scientific). After washing, samples were incubated in 90% glycerol PBS for 30 min in the dark before being mounted in the same solution. Retinas were imaged with a LSM710 confocal microscope (Zeiss, Wetzlar, Germany) equipped with a 40X oil objective.

Electron microscopy

Drosophila eyes were dissected and fixed in 1% glutaraldehyde, 4% paraformaldehyde, 0.1 M sodium cacodylate buffer (pH 6.8) 30 min at room temperature and then overnight at 4 °C. After washing, eyes were post-fixed at room temperature in 1% OsO4 and 1.5% potassium ferricyanide for 1 h, then with 1% uranyl acetate for 45 min, both in distilled water at room temperature in the dark. After washing, they were dehydrated with successive ethanol solutions. Eyes were infiltrated with epoxy resin (EMbed 812 from EMS) and were mounted in resin into silicone embedding molds. Polymerization was performed at 60 °C for 2 days. Ultrathin sections of 70–80 nm thickness were observed on formvar-coated grid with a Hitachi H7500 TEM (Milexia, France), and images were acquired with a 1 Mpixel digital camera from AMT (Milexia, France).

Maintenance of cells and generation of hiPSCs and neural derivatives

hiPSCs (ASE 9109, Applied StemCell Inc. CA, USA) modified for BIN1 in exon 3 (Fig. 5) were generated by CRISPR/Cas9. Homozygous null mutants for BIN1 had

a 5 bp deletion on one allele and an 8 bp deletion on the other allele. All hiPSCs, and all subsequent human induced neural progenitor cells (hiNPCs), hiNs, human induced astrocytes (hiAs), and cerebral organoids derived thereof, were maintained in media from Stemcell Technologies, Vancouver, Canada. Maintenance of cell cultures and organoids were done in adherence with manufacturer's protocols which can be found on the webpage of Stemcell Technologies. hiPSCs were maintained in mTeSR1 medium in non-treated cell culture dishes/plates pre-coated with vitronectin. Cell numbers and viability were recorded using a LUNA™ Automated Cell Counter.

In order to obtain hiNPCs, the embryoid body method detailed by Stemcell Technologies was used for the induction of BIN1 WT and KO hiPSCs. Following the generation of hiNPCs, these derived cells were maintained in treated cell culture dishes pre-coated with poly-L-ornithine (PLO) and laminin (5 µg/mL). PLO solution was made in water (0.001%) while laminin was diluted in PBS with Ca^{2+} and Mg^{2+}. BIN1 WT and KO hiNPCs, thus generated, were maintained for up to 10 passages.

2D cultures comprising hiNs and hiAs were produced from hiNPCs. 60,000 hiNPCs/well were plated in 24-well cell imaging plates from Eppendorf (Cat # 0030741005) pre-coated with PLO (0.001%) and laminin (10 µg/mL). Cells were kept in 0.5 mL of NPC medium per well for 24 h. Following this, equal volume of complete BrainPhys medium (supplemented with BDNF, GDNF, laminin, dibutyryl-cAMP, ascorbic acid, N2, and SM1) was added to each well to begin the process of differentiation. Subsequently, media was changed in the plates bi-weekly. The media change consisted of removing half of the existing medium in each well and replacing it with an equal volume of fresh complete BrainPhys medium. Mixed cultures of hiNs and hiAs were obtained at the end of 6 weeks from the start of the differentiation process.

Generation of cerebral organoids

Cerebral Organoids were generated from hiPSCs at 80% confluency. hiPSCs were detached from the Vitronectin XF substrate using Gentle Cell Dissociation Reagent (Stemcell Technologies), centrifuged, pelleted and resuspended in Embryoid Body (EB) seeding medium (Stemcell Technologies) to form EBs. 9000 cells were plated per well in a 96-well round-bottom ultra-low attachment plate. After two days, 1 or 2 EBs were transferred to a well of a 24-well ultra-low attachment plate containing Induction Medium (Stemcell Technologies). The EBs were kept in the induction Medium for 2 days and next they were transferred into Matrigel (Corning) using an embedding surface. When the Matrigel polymerized, the EB were transferred to a 6-well ultra-low adherent plate with Expansion Medium (Stemcell Technologies). After 3 days, the medium was replaced by Maturation Medium (Stemcell Technologies) and the plate was placed in an orbital shaker (65 rpm speed). Complete media changes were done on a bi-weekly basis.

Lentiviral infections

Lentiviral constructs were produced by the Vect'UB platform within the TBM Core unit at University of Bordeaux, Bordeaux, France (CNRS UMS 3427, INSERM US 005). All three lentiviral constructs harbored reporter tags for the expression of tdTomato protein. The lentiviral vectors used were the empty vector—436 (ID # 1770), 436-Bin1Iso1 (ID # 1771), and 436-Bin1Iso9 (ID # 1772). Lentiviral infections were done in 3-week old differentiation cultures obtained from hiNPCs. Viral transductions were performed at a multiplicity of infection (MOI) of 1. In brief, appropriate volumes of each construct were mixed in complete BrainPhys medium and 50 ul of the viral medium mix was then added to each well. Each of the 3 constructs were added in triplicate to respective wells for each of the BIN1 WT and KO cells. Infected cells were maintained for a further 3-week period with bi-weekly changes of half volume of medium in each well.

Immunocytochemistry of 2D cultures

Cells were fixed in PFA (4% w/v) for 10 min. Fixed cells were then washed with PBS 0.1 M. Cells were then blocked with blocking solution (5% normal donkey serum + 0.1% Triton X-100 in PBS 0.1 M) at room temperature for 1 h under shaking conditions. Primary antibodies diluted in the blocking solution were then added and incubation was done overnight at 4°C under shaking conditions. The following day, cells were washed with PBS 0.1 M 3 times for 10 min each before the addition of fluorophore-conjugated secondary antibodies in blocking solution for 2 h at room temperature under shaking conditions ensuring protection from light. 3 washes with PBS were done for 10 min each at room temperature under shaking conditions with protection from light. Hoechst 33258 nucleic acid stain was added to PBS 0.1 M in the second wash. Cells were mounted with fluoromount and imaged directly in the cell imaging plates. All images were acquired using an LSM 880 Confocal Scanning Microscope housed at the Imaging Platform of the Institut Pasteur de Lille using the ZEISS ZEN Imaging Software. Image acquisition was done at 40X for the various cellular markers in Fig. 5. For EEA1 quantifications, we selected 10 random regions positive for MAP2 in 2–3 different wells from 3 independent cell culture batches. Images were taken using a 63X objective and zoom of 2.

Immunohistochemistry of organoid samples

Cerebral organoids were fixed in PFA (4% w/v) for 30 min at 4 °C followed by three washes with PBS 0.1 M. Cerebral organoids were then placed in sucrose solution (30% w/v) overnight before being embedded in O.C.T (Tissue-Tek). Embedded tissue was sectioned at 20 µm using a cryostat and mounted slides were stored at − 80 °C until immunostaining was performed. Mounted tissue was removed from storage and warmed by placing at room temperature for 30 min. Tissue were rehydrated and washed with room temperature PBS 0.1 M 3 times for 5 min. Slides were then washed once with PBS with 0.2% Triton X-100 for 15 min. Tissue was blocked using 10% of donkey serum in PBS 0.1 M for 1 h at room temperature. After blocking, primary antibodies were added to 0.2% Triton X-100 and 10% of donkey serum in PBS 0.1 M at appropriate dilutions and incubated overnight at 4 °C. The next day, slides were washed with PBS 0.1 M 3 times for 5 min each with gentle shaking. Subsequently, slides were incubated with fluorophore-conjugated secondary antibodies in 0.2% Triton X-100 and 10% of donkey serum in PBS 0.1 M for 2 h at room temperature in the dark. After secondary antibody incubation, slides were washed 3 times with PBS for 5 min with gentle shanking. Nuclei were visualized by incubating the tissue for 5 min with Hoechst stain in PBS 0.1 M. Sections were mounted using aqueous mounting medium (Polysciences). Images were acquired using an LSM 880 Confocal Scanning Microscope in concert with the ZEISS ZEN imaging software housed at the Imaging Platform of the Pasteur Institute, Lille. For EEA1 quantifications, we selected 5 random regions in the surface (50-250 µm) of each cerebral organoid, where a high density of MAP2-positive cells could be distinguished. Images were acquired using a 63X objective in 2–3 different sections obtained from at least 3 cerebral organoids of each genotype.

Antibodies used for immunocytochemistry/immunohistochemistry of hiNs and organoid samples

hiPSCs were detected with antibodies for SOX2 (RRID:AB_2651000) and SSEA4 (RRID:AB_2651001) using the Molecular Probes™ Pluripotent Stem Cell 4-Marker Immunocytochemistry Kit (Thermo Fisher Scientific, RRID:AB_2651000). Antibodies used for immunocytochemistry/immunohistochemistry were EEA1 (610457, BD Biosciences, RRID:AB_397830), MAP2 (188006, Synaptic Systems, RRID:AB_2619881), RFP (600-401-379, Rockland Immunochemicals, Inc., RRID:AB_2209751), SOX2 (14-9811-82, Invitrogen, RRID:AB_11219471), NESTIN (MAB5326, Millipore, RRID:AB_2251134), and GFAP (AB5804, Millipore, RRID:AB_2109645). All fluorophore-tagged secondary antibodies were sourced from Jacskon ImmunoResearch Europe Ltd.

Immunoblotting of 2D cultures and cerebral organoid

Samples from the 2D cultures or brain organoids were collected in RIPA buffer containing protease inhibitors (Complete mini, Roche Applied Science, Penzberg, Germany) and sonicated two times at 60–70% during 10 s before use for the western blotting analyses.

Protein quantification was performed using the BCA protein assay (Thermo Scientific). In total, 10 µg of protein from extracts were separated in SDS–polyacrylamide gels 4–12% (NuPAGE Bis–Tris, Thermo Scientific) and transferred to nitrocellulose membranes (Bio-Rad). Next, membranes were incubated in milk (5% in Tris-buffered saline with 0.1% Tween-20 – TTBS, or SuperBlock – Thermo Scientific) to block non-specific binding sites during 1 h at RT, followed by several washes with TTBS. Immunoblottings were carried out with primary antibodies anti-BIN1 (ab182562, Abcam, RRID:AB_725699), anti-APP (C-terminal) (A8717, Sigma-Aldrich, RRID:AB_258409) and anti-β-ACTIN (A1978, Sigma-Aldrich, RRID:AB_476692) overnight at 4 °C on 20 RPM agitation. The membranes were washed three times in TTBS, followed by incubation with HRP-conjugated secondary antibodies anti-mouse (115-035-003, RRID:AB_10015289) and anti-rabbit (111-035-003, RRID:AB_2313567, Jackson ImmunoChemicals, Inc.) overnight at 4 °C on 20 rpm. The membranes were washed three times in TTBS, and the immunoreactivity was revealed using the ECL chemiluminescence system (SuperSignal, Thermo Scientific) and imaged using the Amersham Imager 600 (GE Life Sciences). Optical densities of bands were quantified using the Gel Analyzer plugin in Fiji – ImageJ [55].

Image analysis using Imaris

The "surface" function on Imaris was used for detection of EEA1 puncta. Background subtraction was performed using "local contrast" and automatic threshold, warranting the same processing criteria for all images. Next, a manual filter cut-off was applied to detect all puncta volumes above 0.1 μm^3. MAP2 and tdTomato surfaces were also detected based on background subtraction using "local contrast" and automatic threshold. Automatic thresholds using the filter "absolute intensity" were then applied to find MAP2 and tdTomato surfaces. For the detection of EEA1 puncta on MAP2 and EEA1 puncta on $MAP2^+$/$tdTomato^+$ cells, filters for the standard deviation of intensity were applied in the MAP2 and tdTomato channels respectively. Volume information for the EEA1 puncta were collated from each acquired image as CSV files. The volumes were sorted using Microsoft Excel. We

used a cut-off maximum volume of 10µm^3 for each field. The sorted volume data were then analyzed statistically using the GraphPad Prism software.

snRNA-seq library preparation

Nuclei isolation and Hash-tagging with oligonucleotides steps were realized on ice with pre-cold buffers and centrifugations at 4 °C. BIN1 WT and KO organoids of 6 months (n=4 per genotype) were cut in 2 parts, washed twice with 1 ml of Deionized Phosphate Buffer Saline 1X (DPBS, GIBCO™, Fisher Scientific 11590476) and centrifuged 5 min at 300*g*. Organoids pellets were resuspended in 500 µl lysis buffer (Tris–HCL 10 mM, NaCl 10 mM, $MgCl_2$ 3 mM, Tween-20 0.1%, Nonidet P40 Substitute 0.1%, Digitonin 0.01%, BSA 1%, Invitrogen™ RNAseout™ recombinant ribonuclease inhibitor 0.04 U/µL). Multiple mechanical resuspensions and wrecking steps in this buffer were perform for a total lysis time of 10 min, 500 µl of washing buffer was added (Tris–HCL 10 mM, NaCl 10 mM, $MgCl_2$ 3 mM, Tween-20 0.1%, BSA 1%, Invitrogen™ RNAseout™ recombinant ribonuclease inhibitor 0.04 U/µL) and the lysis suspension was centrifuged 8 min at 500*g* (used for all following centrifugation steps). Nuclei pellets were washed three times with one filtration step by MACS pre-separation filter 20 µm (Miltenyi Biotec). Nuclei pellets were resuspended in 100 µL of staining buffer (DPBS BSA 2%, Tween-20 0.01%), 10 µL of Fc blocking reagent HumanTruStainFc™ (422302, Biolegend) and incubated 5 min at 4 °C. 1 µl of antibody was added (Total-Seq™-A0451 anti-Vertebrate Nuclear Hashtag 1 MAb414 for the WT and Total-Seq™-A0453 anti-Vertebrate Nuclear Hashtag 3 MAb414 10 µg for the KO, 97284 and 97286 respectively, Biolegend) and incubated 15 min at 4 °C. Nuclei pellets were washed three times in staining buffer with one filtration step by MACS pre-separation filter 20 µm (Miltenyi Biotec) to a final resuspension in 300 µl of staining buffer for Malassez cell counting with Trypan blue counterstaining (Trypan Blue solution, 11538886, Fisherscientific). Isolated nuclei were loaded on a Chromium 10 × Genomics controller following the manufacturer protocol using the chromium single-cell v3 chemistry and single indexing and the adapted protocol by Biolegend for the HTO library preparation. The resulting libraries were pooled at equimolar proportions with a 9 for 1 ratio for Gene expression library and HTO library respectively. Finally, the pool was sequenced using 100 bp paired-end reads on the Illumina NovaSeq 6000 system following the manufacturer recommendations.

snRNA-seq analysis and differential expression analysis

UMI Count Matrices for gene expression and for HTO libraries were generated using the CellRanger software (10 × Genomics). After filtering for low quality cells according to the number of RNA, genes detected, and percentage of mitochondrial RNA, and normalizing the HTO matrix using centered log-ratio (CLR) transformation, 2,990 cells were assigned back to their sample of origin using HTODemux function of the SeuratV3 R Package (Satijalab), resulting to 1,794 and 1,196 cells for BIN1 KO and WT, respectively. Then, Seurat Workflow with SCTransform normalization was used to cluster the cells according to their transcriptome similarities. Each cluster was annotated using cell type specific markers. Finally, differential expression analysis between BIN1 KO and WT cells within each identified cell type was performed using DESeq2 package [38].

Statistical analyses

Statistical information are available in the method section and in the figure legends. Two-tailed statistical tests were used. Hypothesis testing was carried out with Kruskal Wallis test followed by Mann–Whitney comparison and ANOVA with post-hoc Tukey. Statistical analyses were performed using R 3.6.0 (R Core Team (2019). R: A language and environment for statistical computing. R Foundation for Statistical Computing, Vienna, Austria. URL https://www.R-project.org/), RStudio 1.2.1335 and GraphPad Prism. For boxplots, the bold segment, lower and upper hinges represent the median, first quartile and third quartile respectively. The upper whisker extends from the hinge to the largest value no further than 1.5 * IQR from the hinge (where IQR is the inter-quartile range, or distance between the first and third quartiles). The lower whisker extends from the hinge to the smallest value at most 1.5 * IQR of the hinge.

Results

Functional conservation of human BIN1 isoforms in Drosophila

BIN1 belongs to the amphiphysin family and in mammals, two genes compose this family: *amphiphysin I* (*AMPH*) and *amphiphysin II* (*AMPH2*) also named *BIN1*. Drosophila has only one ortholog called *Amphiphysin* (*Amph*) that is referred to as *dAmph* henceforth in this article. dAmph has 3 isoforms but only the BAR and SH3 domains are conserved in dAmph. Within this background, we generated 3 transgenic Drosophila lines expressing the human BIN1iso1, BIN1iso8 and BIN1iso9 isoforms. As a control, we also generated transgenic Drosophila lines expressing the longest dAmph isoform, dAmphA (Fig. 1a). We obtained transgenic lines expressing identical basal level of BIN1 isoforms with two additional BIN1iso1 and BIN1iso9 lines expressing high BIN1 levels that we used for dose-dependent effects (Additional file 1 and Additional file 2: Fig. S1).

We assessed the functional conservation of human BIN1 isoforms in Drosophila. Like human subjects harboring *BIN1* coding mutations and suffering myopathy [44], *dAmph* null flies have locomotor defects, due to T-tubule morphogenesis defects in muscle cells [37, 67]. We tested if the expression of muscle human BIN1iso8 could restore the locomotor performance of *dAmph* deficient adult transgenic flies assessed in the so-called climbing test. In addition to the null dAmph^{5E3} allele, we took advantage of a dAmph$^{MI08903\text{-}TG4.0}$ allele that allows Gal4 expression under the control of *dAmph* endogenous promoter while stopping *dAmph* transcription (Additional file 1 and Additional file 3: Fig. S2). We checked by western blot that *dAmph* expression was abolished in dAmph$^{MI08903\text{-}TG4.0/5E3}$ compound heterozygous flies compared to dAmph$^{MI08903\text{-}TG4.0/+}$ heterozygous flies and that BIN1iso8 could be expressed in this genetic background (Fig. 1b). Then, we observed that dAmph$^{MI08903\text{-}TG4.0/5E3}$ compound heterozygous flies had locomotor defects like dAmph$^{5E3/5E3}$ null flies compared to control flies or dAmph$^{MI08903\text{-}TG4.0/+}$ heterozygous flies (Fig. 1c). Expression of human BIN1iso8 restored the locomotor abilities of dAmph$^{MI08903\text{-}TG4.0/5E3}$ compound heterozygous flies to levels similar to the ones observed in control flies or dAmph$^{MI08903\text{-}TG4.0/+}$ heterozygous flies (Fig. 1c). Thus, human BIN1iso8 is able to rescue the locomotor functions of *dAmph* null flies, thereby indicating a functional conservation of human BIN1iso8 in Drosophila.

Next, we addressed the possible functional conservation of BIN1 isoforms in neuronal cells. Overexpression of dAmphA results in development defects of the light-sensitive photoreceptor neurons in Drosophila retina [67]. These neurons possess a specialized compartment, called rhabdomere, which consists of an apical microvillar stack of actin-rich intricately folded membranes containing the light-sensing rhodopsin proteins. We tested if human BIN1 isoforms expression with the early eye-specific GMR driver could phenocopy the dAmphA-induced rhabdomere phenotype. The Drosophila eye is composed of 600–800 units called ommatidia. Each ommatidium contains 6 outer photoreceptor neurons and 2 superimposed inner photoreceptor neurons. We expressed GFP in the outer photoreceptor neurons (Rh1 driver) and used the cornea neutralization technique to assess rhabdomere morphology [13]. While we observed six rhabdomeres per ommatidium, of similar size and organized in a trapezoidal shape in the control condition, some rhabdomeres were missing and others were smaller or deformed in the dAmphA overexpressing condition (Fig. 1d). Thus, we confirmed that expression of dAmphA alters rhabdomere morphogenesis. Individual expression of BIN1iso1, BIN1iso8 or BIN1iso9 recapitulated a similar phenotype respectively (Fig. 1d). In addition, high levels of BIN1iso1 and BIN1iso9 exacerbated the phenotype indicating a dose-dependent effect. We also confirmed these results on whole-mount pupal retina dissection (Fig. 1e). dAmphA-, BIN1iso1-, BIN1iso8- and BIN1iso9-overexpressing retina exhibited strong deformed accumulations of F-actin at the level of the rhabdomere. In conclusion, overexpression of all human BIN1 isoforms phenocopied dAmphA overexpression during the development of photoreceptor neurons suggesting functional conservation also at the neuronal level.

Human BIN1iso1 is neurotoxic in Drosophila photoreceptor neurons

The neurotoxic effects of human BIN1 isoforms in the developing Drosophila prompted us to investigate whether a similar effect could also be observed after expression of BIN1 isoforms in adult Drosophila. To do so, we employed the outer photoreceptor-specific driver Rh1, active in photoreceptor neurons after rhabdomere morphogenesis at the end of pupal development. We quantified the number of outer photoreceptor neurons following cornea neutralization and rhabdomere

(See figure on next page.)

Fig. 1 Functional conservation of human BIN1 isoforms in Drosophila. **a** Scheme of cerebral human BIN1 isoform1 (BIN1iso1), muscular human BIN1 isoform8 (BIN1iso8), ubiquituous human BIN1 isoform9 (BIN1iso9) and Drosophila BIN1, called Amphiphysin, isoformA (dAmphA) for which transgenic lines were generated. **b** Western blot analysis of Amph and BIN1 expression in dAmph$^{MI08903\text{-}TG4.0/+}$, dAmph$^{MI08903\text{-}TG4.0/5E3}$ and dAmph$^{MI08903\text{-}TG4.0/+}$; UAS-BIN1iso8 fly thorax. dAmphA, dAmphB and dAmphC were expressed in the heterozygous dAmph$^{MI08903/+}$ flies, whereas they were not detected in dAmph$^{MI08903/5E3}$ flies (*background staining). BIN1iso8 was expressed in dAmph$^{MI08903\text{-}TG4.0/+}$; UAS-BIN1iso8 flies. **c** Analysis of the climbing locomotor activity of 2 day-old flies with the indicated genotype. dAmph$^{MI08903\text{-}TG4.0/5E3}$ flies exhibited a similar low climbing score as the null dAmph$^{5E3/5E3}$flies. Expression of BIN1iso8 rescued the locomotor defects of dAmph$^{MI08903\text{-}TG4.0/5E3}$ flies (from left to right n = 10, 5, 49, 67, 26, ANOVA F-value = 66.15, Df = 4, p = 2.37×10^{-38} with post-hoc Tukey, n.s. not significant). **d** Visualization of outer photoreceptor neuron rhabdomeres by cornea neutralization in 2-day-old flies expressing mCherry (as a control), BIN1iso1, BIN1iso8, BIN1iso9 and dAmphA under a GMR driver (attP2 is a control with an empty attP2 landing site and no UAS construct). While each ommatidium contained 6 outer photorceptors organized in a trapezoid shape (yellow circles) in the two control conditions, BIN1 isoforms and dAmphA expression resulted in a strong alteration in the number, shape and trapezoid organization of the rhabdomeres with a stronger effect for BIN1iso1 and BIN1iso9 high-expressing lines. **e** Immunofluorescence of whole-mount pupal retina expressing Luciferase (as a control), BIN1iso1, BIN1iso8, BIN1iso9 or dAmphA. They were labelled for the plasma membrane neuronal Na/K ATPase and F-actin. Contrary to the control, BIN1iso1, BIN1iso8, BIN1iso9 and dAmphA induced a strong accumulation of F-actin at the level of the rhabdomere

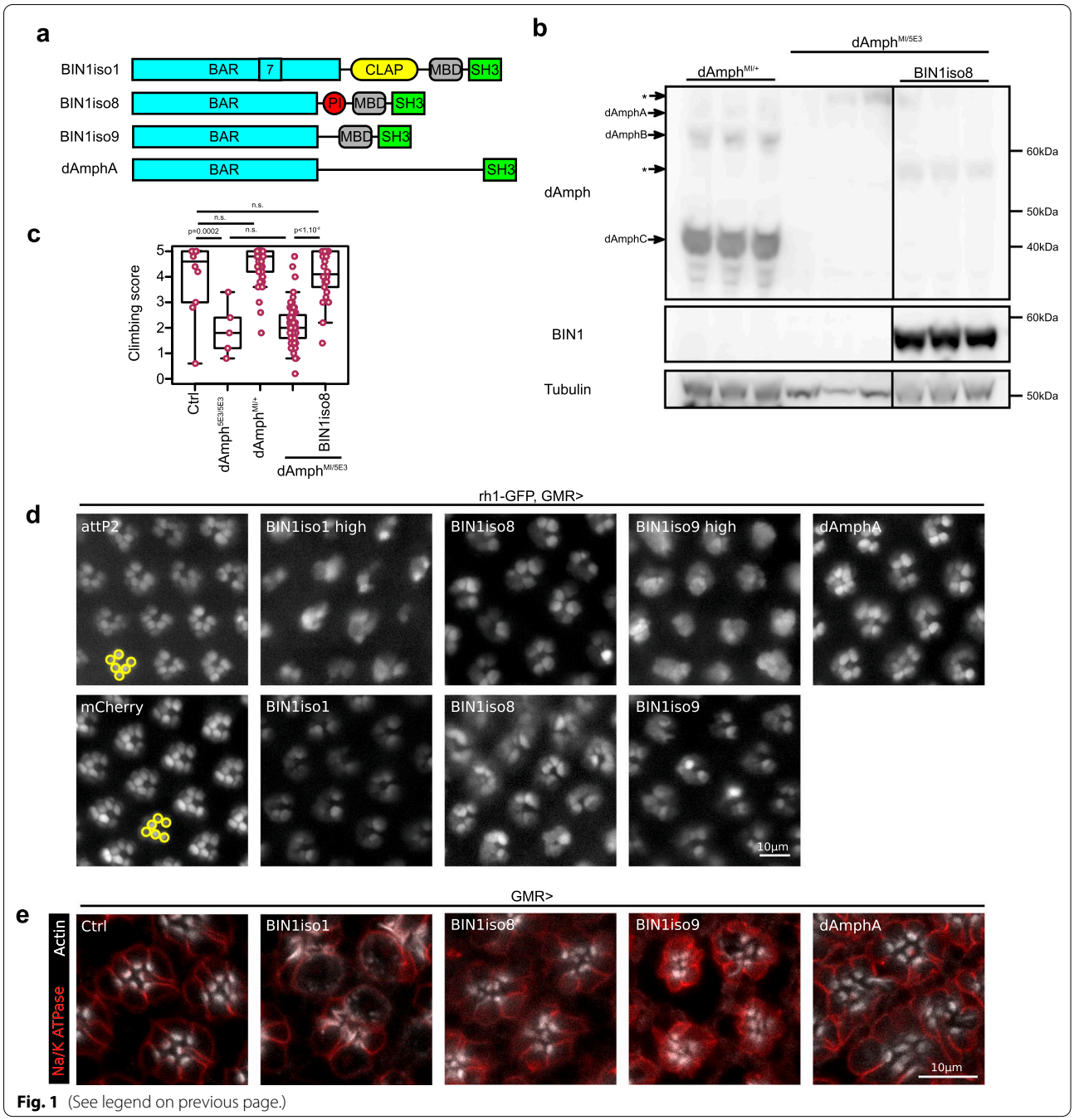

Fig. 1 (See legend on previous page.)

visualization. We observed that young flies (1 day-old) had a normal number of outer photoreceptor neurons (6 per ommatidium) with normal morphology (Fig. 2a, b). These observations indicated that the use of rh1 driver bypasses the developmental retinal defects observed using the GMR driver. We then observed that 4-week-old flies expressing BIN1iso1, but not the ones expressing BIN1iso8, BIN1iso9 and dAmphA, lost around half of their outer photoreceptor neurons (Fig. 2a, b). This phenotype was not dose-dependent as flies expressing basal or high BIN1iso1 levels had a similar outer photoreceptor neuron loss. Of note, flies expressing high levels of BIN1iso9 had nearly no loss of outer photoreceptor neurons (Fig. 2a–d). In conclusion, expression of BIN1iso1 induced a progressive neurodegeneration in adult Drosophila photoreceptor neurons and this effect was isoform-specific and not dose-dependent.

Since photoreceptor neurons are specialized neurons highly dependent on the phototransduction cascade [64], we wondered if a defect in this phototransduction cascade may be the cause of the neurodegeneration. For this purpose, we assessed whether the degeneration was light-dependent. BIN1iso1-expressing flies were allowed to age in the normal 12 h/12 h light/dark cycle or under constant dark condition for 4 weeks. Light absence did not prevent outer photoreceptor neurodegeneration even if occurring to a lesser extent (Fig. 2e). This indicated that the phototransduction cascade was not the main cause of the neurodegeneration and that increased global neuronal activity favors BIN1iso1-induced neurodegeneration.

We asked why BIN1iso1 was more toxic for photoreceptor neurons than the other BIN1 isoforms. We wondered whether it could originate from the subcellular localization of BIN1 isoforms. We labelled retinas of 1-day old flies expressing either BIN1iso1, BIN1iso8 or BIN1iso9 for BIN1 (Fig. 2f). All BIN1 isoforms were similarly enriched at the base of photoreceptor neuron rhabdomeres. We next wondered what in the sequence of BIN1iso1 makes it neurotoxic. BIN1iso1 differs from BIN1iso9 by two sequences: (i) the Exon7 in the BAR domain and (ii) the neuronal specific CLAP domain. We tested the neurotoxicity of truncated BIN1iso1 forms for these two sequences (Fig. 2g) after generating the corresponding transgenic flies (Additional file 4: Fig. S3) and observed that loss of the CLAP domain abrogated outer photoreceptor neurodegeneration contrary to the loss of Exon7, which only partially rescued photoreceptor neurons (Fig. 2h). Hence, the BIN1iso1-induced degeneration depends on its CLAP domain and to a lesser extent on the Exon7 in the BAR domain. Since the CLAP domain is known to interact with AP-1 adaptin, AP-2 adaptin and the Clathrin Heavy Chain, which are involved in endocytosis and intracellular trafficking [26, 50, 65], this suggested that the cause of the degeneration could be a defect in endocytosis/intracellular trafficking.

BIN1iso1 induces vesicle accumulation in photoreceptor neurons

To further understand the cause of the BIN1iso1-induced degeneration, we analyzed the degenerating photoreceptor neurons by electron microscopy. While neurons in 15-day-old flies either expressing luciferase, BIN1iso9 or dAmphA did not show any abnormalities, the degenerating neurons in BIN1iso1 flies exhibited a strong accumulation of vesicles (Fig. 3a and Additional file 5: Fig. S4a). These vesicles were of various sizes, some of them nearly as big as a complete ommatidium. The cytoplasm of some photoreceptor neurons was filled with vesicles, compacting it against the plasma membrane, which seemed intact. The vesicles were surrounded by a single membrane and not a double membrane as observed in autophagosome (Fig. 3a) and did not have any specific content. Rhabdomeres of BIN1iso1 photoreceptor neurons were disintegrated, whereas the chromatin seemed normal although the nucleus was frequently squeezed in between vesicles (Fig. 3a and Additional file 5: Fig. S4b). Eventually, photoreceptor neurons died (Additional file 5: Fig. S4d). Hence, ultrastructural analysis of degenerating photoreceptor neurons indicated that the neurodegeneration induced by BIN1iso1 is characterized by a strong accumulation of single membrane vesicles of unknown origin.

We next evaluated the nature of these vesicles by immunofluorescence using specific organelle GFP- or YFP-tagged markers for endoplasmic reticulum, Golgi, plasma membrane, early endosome, late endosome/multivesicular body, recycling endosome, lysosome and autophagosome [16] (Fig. 3b and Additional file 6: Fig. S5). In 15-day-old flies, many BIN1iso1-induced vesicles were positive for EYFP:Rab5 and GFP:2xFYVE, markers of early endosome and for EYFP:Rab7 and evi:GFP, markers of late endosome/multivesicular body (Fig. 3c, d). These different markers labelled small- to middle- sized vesicles with the exception of evi:GFP which tended to label bigger vesicles. Some big vesicles were

(See figure on next page.)

Fig. 2 Human BIN1iso1 is neurotoxic in Drosophila photoreceptor neurons. **a** Visualization of retina photoreceptor neurons expressing BIN1 isoforms (rh1 promoter) by cornea neutralization in living flies. **b** Quantification (Kruskal Wallis $p = 0.013$ followed by Mann–Whitney comparison, ***$p < 0.001$, ****$p < 0.0001$). At the bottom of the graph, upper numbers indicate the number of quantified eyes per condition and lower numbers indicate the mean number of ommatidia quantified per eye. Contrary to BIN1iso8 and BIN1iso9, BIN1iso1 expression induced a progressive age-dependent neurodegeneration, which was not dose-dependent. **c**, **d** Western blot analysis of BIN1 isoforms expression in the retina and quantification ($n = 3$, ANOVA F-value = 12.98, Df = 5, $p = 0.00017$, with post-hoc Tukey, *$p < 0.05$, **$p < 0.01$, ***$p < 0.001$). **e** Quantification of BIN1iso1-induced photoreceptor neuron degeneration over 4 weeks under a 12 h/12 h light/dark cycle (Ctrl L and BIN1iso1 L) or under constant darkness (Ctrl D and BIN1iso1 D) (Kruskal Wallis $p = 0.0005344$ for Day8-11, $p = 3.264 \times 10^{-05}$ for Day15-16, $p = 1.36 \times 10^{-07}$ for Day28-29, followed by Mann Whitney comparison, *$p < 0.05$, **$p < 0.01$, ***$p < 0.001$, ****$p < 0.0001$). Loss of light did not prevent neurodegeneration although the intensity of degeneration was reduced. **f** Localization of BIN1 isoforms in one-day-old fly photoreceptor neurons. Luciferase was used as a control. Na/K ATPase staining labelled the plasma membrane and actin staining mostly labelled rhabdomere of photoreceptor neurons. Upper panels are longitudinal views of retina, whereas lower panels exhibit sectional views of ommatidium. **g**, **h** Scheme of the truncated BIN1iso1 tested protein and quantification of their toxicity in 15 day-old flies (Kruskal Wallis $p = 5.686 \times 10^{-11}$ followed by Mann Whitney comparison, ***$p < 0.001$, *****$p < 0.00001$). Loss of the CLAP domain totally abrogated BIN1iso1 toxicity

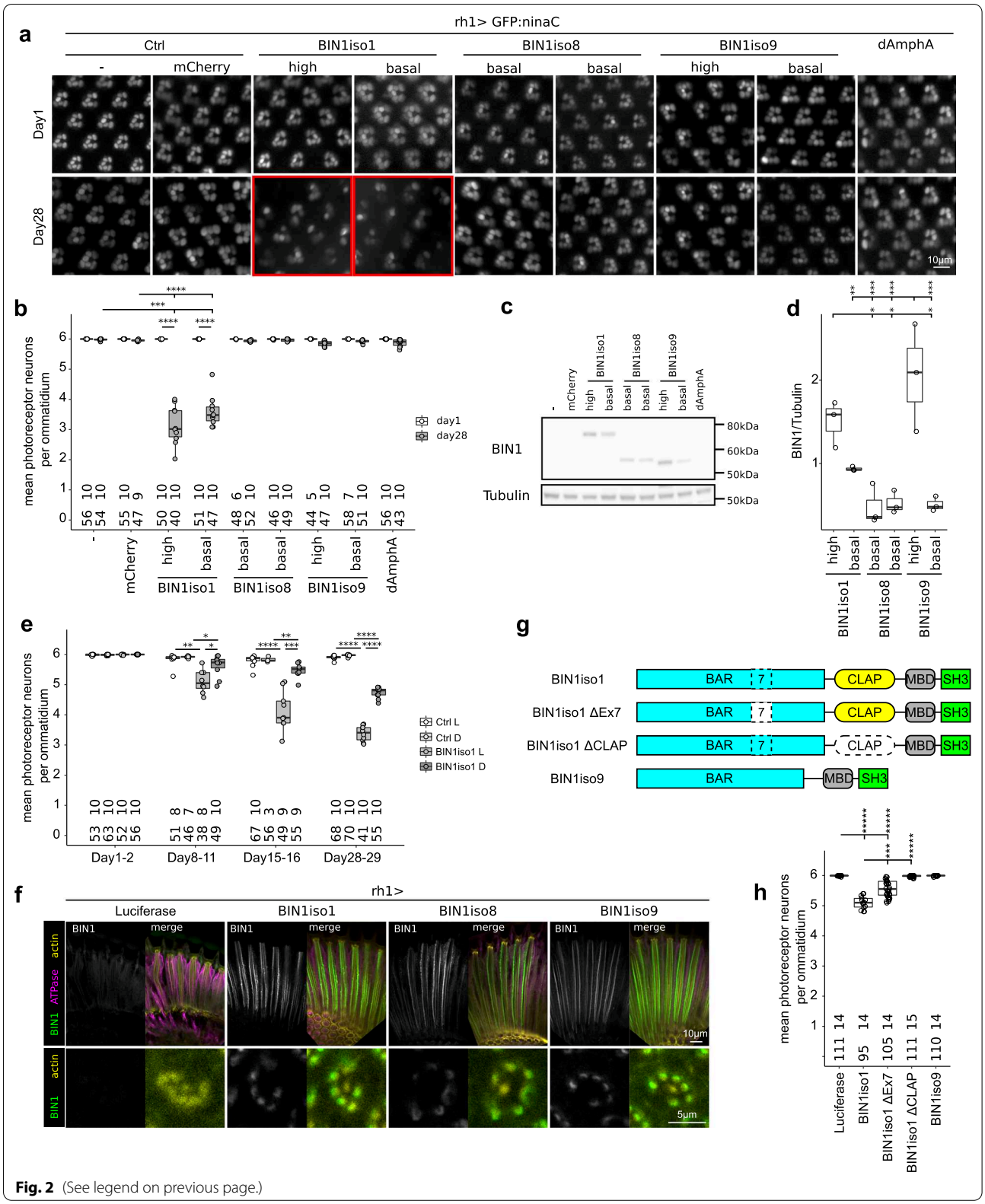

Fig. 2 (See legend on previous page.)

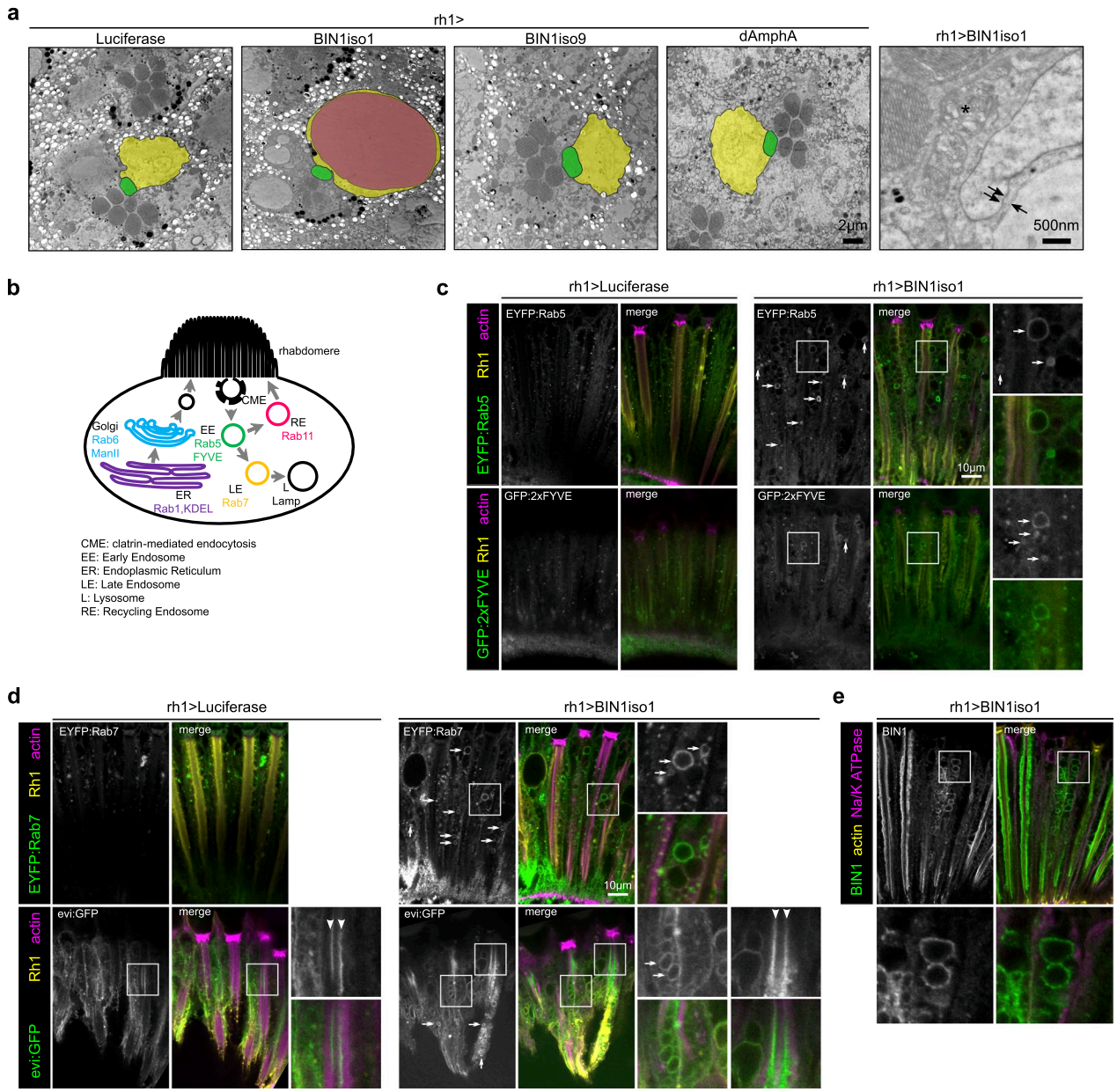

Fig. 3 BIN1iso1-induced degeneration is characterized by a strong accumulation of vesicles showing endosomal markers. **a** Electron microscopy images of retina expressing Luciferase (Ctrl), AmphA, BIN1iso1 and BIN1iso9 from 15-day-old flies. 1 to 2 ommatidia transversal sections are seen on the 4 left images. One photoreceptor neuron is outlined per image, its cytoplasm and nucleus being highlighted in yellow and its rhabdomere in green. Each ommatidium contains 6 outer photoreceptor neurons whose rhabdomeres are organized in a trapezoidal shape, with a 7th rhabdomere in the middle corresponding to one of the two inner photoreceptor neurons. In the BIN1iso1 condition, only 4 rhabdomeres can be seen. In addition, the cytoplasm of the photoreceptor is filled with vesicles, some of them (highlighted in magenta) are very big. These vesicles are surrounded by a single membrane (arrow on the right panel) as compared to the nuclear envelope (double arrow). Their rhabdomere is usually disintegrating (*). **b** Scheme of the organelles tested in photoreceptor neurons with the markers used. **c**, **d** Images of photoreceptor neurons expressing BIN1iso1 and EYFP-tagged endogenous Rab5 and GFP:2xFYVE, as early endosome markers (**c**), or EYFP-tagged endogenous Rab7 and evi:GFP, as late endosome/multivesicular body markers (**d**). Rh1 and actin staining, respectively yellow and magenta in the merge image, are used to label retina structure of 15-day-old flies. The photoreceptor neurons expressed Luciferase as a control or BIN1iso1. In the BIN1iso1 conditions, many vesicles were positive for the tested organelle markers (arrows, green staining in merge images). The extracellular inter-rhabdomeric staining for the evi:GFP marker (arrowhead) corresponds to exosomes. **e** Images of photoreceptor neurons expressing BIN1iso1 stained for BIN1, the photoreceptor neuron plasma membrane Na/K ATPase and actin in 7-day-old flies. BIN1iso1 is localized at the base of the rhabdomeres and around some abnormal vesicles as seen in the inset

also exceptionally labelled by the lysosomal Lamp2:GFP marker and corresponded to rare multilamellar bodies observed by electron microscopy (Additional file 5: Fig. S4c and Additional file 6: Fig. S5g). Of note, we also noticed that the extracellular space between rhabdomeres of the 8 photoreceptor neurons in the middle of ommatidia, called the interrhabdomeric space, was positive for evi:GFP in both the control and BIN1iso1 conditions (arrowhead Fig. 3d). Since evi:GFP labels exosomes either within the multivesicular bodies or in the extracellular environment [3, 36], evi:GFP interrhabdomeric staining likely corresponded to released exosome which did not appear to be compromised by BIN1iso1 expression. In addition, we observed staining for BIN1 around some vesicles suggesting a potential direct action of BIN1iso1 on the membrane dynamics of these vesicles (Fig. 3e). In conclusion, these results suggested that BIN1iso1-induced vesicles accumulation originated from a blockade at the level of early endosome and/or late endosome.

BIN1iso1 induces neurodegeneration through blockade of the early endosome trafficking in drosophila photoreceptor neurons

To test if the intracellular trafficking defects were responsible for the neurodegeneration phenotype, we tested if regulators of endosome trafficking could rescue BIN1iso1-induced neurodegeneration. We tested regulator of early endosome (Rab5), recycling endosome (Rab11), late endosome (Rab7 and Rab9) and lysosome (subunits of the V-ATPase) (mostly a collection of UAS transgenes expressing wild-type, constitutively active and dominant negative Rab proteins [68]). We observed an inhibition of BIN1iso1-induced neurotoxicity through a rescue of photoreceptor neurons for regulators of the early endosome Rab5 and recycling endosome Rab11 (Fig. 4a, c, d). Modulation of the late endosome regulators Rab7 and Rab9, and of lysosome V-ATPase did not modify BIN1iso1-induced neuronal loss (Fig. 4e, f). Of note, we checked by western blot that the rescue effect of Rab5 and Rab11 was not due to a decrease in BIN1iso1 expression, consecutive to a dilution of the Gal4 between the multiple UAS constructs (Fig. 4b). We further tested the constitutively active (CA) and dominant negative (DN) forms of Rab5 and Rab11, respectively named $Rab5^{CA}$, $Rab5^{DN}$, $Rab11^{CA}$ and $Rab11^{DN}$. Surprisingly $Rab5^{DN}$ rescued BIN1iso1-expressing photoreceptor neurons, whereas $Rab5^{CA}$ had no effect (Fig. 4c). This indicated that, although counterintuitive, overexpression of wild-type Rab5 resulted in a loss of function of Rab5 and that loss of function of Rab5 is protective against BIN1iso1-induced neurodegeneration. We confirmed this result when one copy of Rab5 ($Rab5^{2/+}$) was removed or by knocking down Rab5 ($Rab5^{HMS00145}$) (Fig. 4c). Contrary to Rab5, $Rab11^{DN}$ increased BIN1iso1-induced neuronal loss (although not significant) (Fig. 4d). A gain of function of Rab11 seemed, therefore, protective against BIN1iso1-induced neurodegeneration. We also tested the fast recycling endosome regulator Rab4 (Additional file 7: Fig. S6). Although one construct expressing mRFP-tagged Rab4 rescued BIN1-induced neurodegeneration, another YFP-tagged Rab4 construct did not, and neither did the YFP-tagged $Rab4^{DN}$ or $Rab4^{CA}$ construct. Altogether, because the neurodegeneration was rescued by modulation of regulators of early and recycling endosomes, these results indicated that BIN1iso1-induced photoreceptor neuron degeneration is due to a defect in the early endosome trafficking.

We further wondered if BIN1iso1 neurotoxicity may be mediated by APP or one of its metabolites. Indeed, APP-β Carboxy Terminal Fragment (APP-βCTF), the product of APP cleavage by β-secretase and precursor of Aβ peptide through γ-secretase cleavage, induces endosome enlargement in neurons [28]. Drosophila has a single homolog of APP, called APP Like (Appl), which is also processed by several secretases and generates secreted fragments, a neurotoxic Aβ-like peptide and an C-terminal intracellular domain (AICD) [7]. Interestingly, Appl regulates endolysosomal function in Drosophila neurons [30]. In addition, some results support a regulation of APP processing by BIN1 [62]. We tested if loss of function, overexpression of *Appl* or overexpression of human APP could modulate BIN1iso1-induced photoreceptor neuron degeneration. Loss of one copy of *Appl* had no

(See figure on next page.)

Fig. 4 BIN1iso1-induced neurodegeneration is rescued by regulators of the intracellular trafficking. **a** Representative images of 15-day-old retina expressing BIN1iso1 or luciferase (as a control) and constructs modulating Rab5, Rab7 and Rab11 activities. **b** Western blot analysis of BIN1, GFP derivatives in the corresponding conditions showing that BIN1 is not decreased in the conditions in which photoreceptor neurons are rescued. *Non-specific band. **c**–**g** Quantification of the BIN1iso1-induced neurodegeneration upon respective modulation of the early endosome regulator Rab5 activity, the recycling endosome regulator Rab11 activity, the late endosome regulator Rab7 and Rab9 activities, the lysosomal ATPase activity and Appl/APP. At the bottom of the graph, upper numbers indicate the number of quantified eyes per condition and lower numbers indicate the mean number of ommatidia quantified per eye. Statistical analysis was performed using a Kruskal Wallis test ($p = 0.003643$ for Rab5, $p = 6.169 \times 10^{-06}$ for $Rab5^{DN}$ and $Rab5^{CA}$, $p = 0.0001721$ for Rab5 mutant and knockdown, $p = 0.003643$ for Rab11, $p = 0.03487$ for $Rab11^{DN}$ and $Rab11^{CA}$, $p = 0.1408$ for Rab7, $p = 0.24$ for $Rab7^{DN}$ and $Rab7^{CA}$, $p = 0.8959$ for Rab9, $p = 0.1394$ for lysosomal ATPase subunit knockdown, $p = 0.006947$ for Appl/APP) followed by Mann Whitney comparison (*$p < 0.05$, **$p < 0.01$, ***$p < 0.001$)

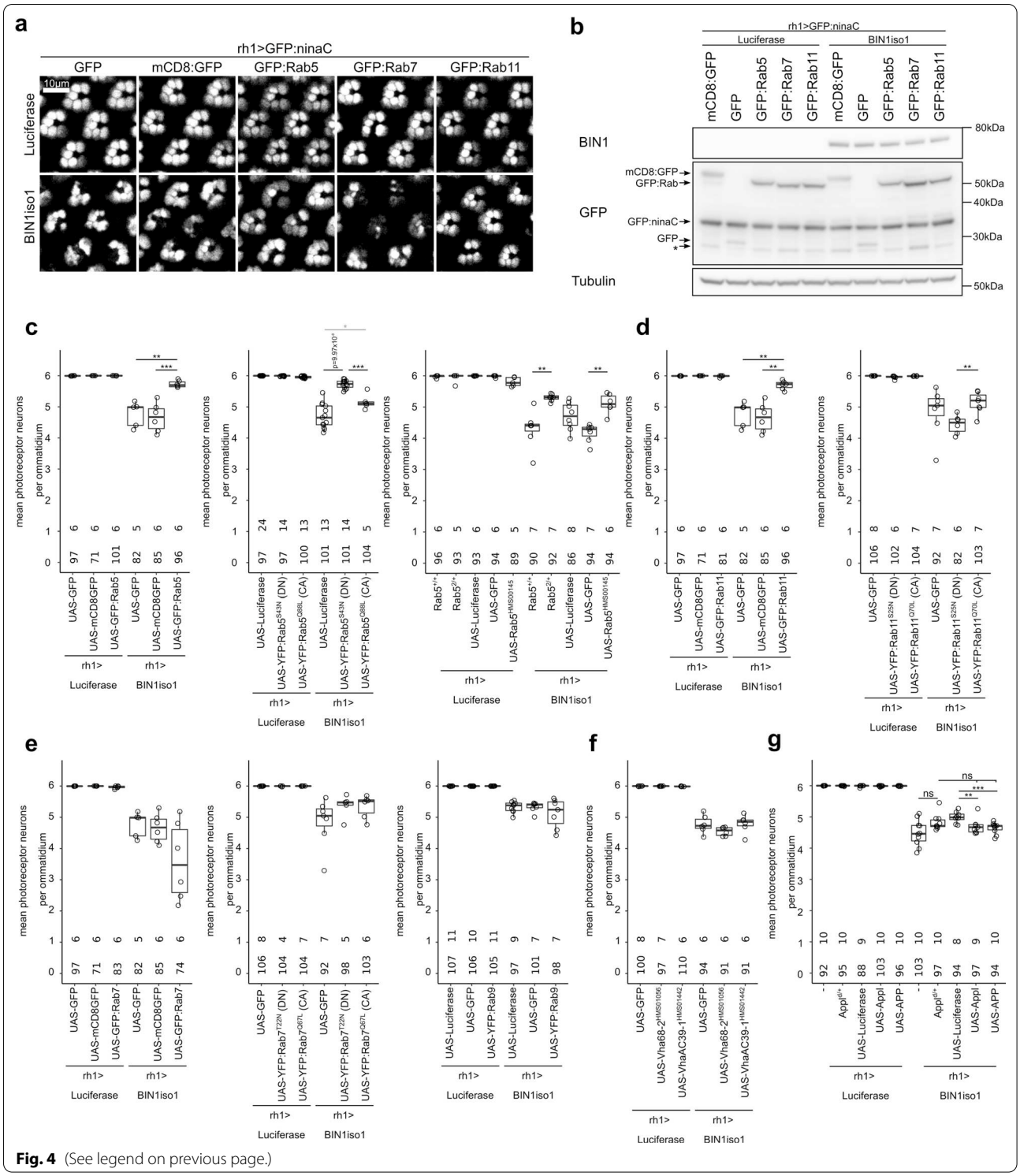

Fig. 4 (See legend on previous page.)

effect suggesting that *Appl* is not required for BIN1iso1 toxicity (Fig. 4g). Overexpression of *Appl* and human *APP* significantly enhanced PR loss but only slightly in terms of fold change and not significantly compared to the loss of one copy of *Appl* (Fig. 4g). Overall, these experiments suggest that APP (and potentially its metabolites) do not contribute to the BIN1iso1 neurotoxicity observed in our Drosophila model.

Generation and characterization of *BIN1* WT and KO human induced neurons

Next, we wondered whether the role of BIN1iso1 in endosome trafficking was conserved in Human. To address this possibility, we generated human isogenic *BIN1* wild type (WT) and knockout (KO) pluripotent stem cell (hiPSC) lines by CRISPR/Cas9 technology. Both hiPSC lines showed similar expression of pluripotency cell markers (SOX2 and SSEA4, Fig. 5c) and growth rates (Fig. 5d). *BIN1* WT hiPSC expressed low molecular weight BIN1 isoforms, including likely BIN1iso9 (Fig. 5i). We then employed these cells to generate hiPSC-derived neurons both in bi-dimensional (2D) cell cultures and in cerebral organoids.

Following neural induction, both *BIN1* WT and KO human induced neural progenitor cells (hiNPCs) expressed similar levels of NESTIN and SOX2 (Fig. 5e). Although *BIN1* KO hiNPCs showed a significant reduction in growth rate when compared to WT (Fig. 5f), both hiNPCs lines were expanded up to 10 passages and readily generated similar proportions of human induced neurons(hiNs) and astrocytes (hiAs) when subjected to conditions of differentiation (Fig. 5g, h). WT hiNPCs mainly expressed low molecular weight BIN1 isoforms, whereas in differentiated cultures both low and high molecular weight isoforms, probably corresponding to BIN1iso9 and BIN1iso1 respectively, were expressed (Fig. 5j). The expression pattern observed for BIN1 isoforms likely reflects the mixed composition of the differentiated cell cultures at 6 weeks, comprising both neurons and astrocytes, which mainly express BIN1iso1 and BIN1iso9, respectively [69].

Likewise, *BIN1* WT and KO hiPSCs were able to generate cerebral organoids with no obvious differences in size and composition (Fig. 6a, b). Expression of BIN1 protein in 190-day-old *BIN1* WT cerebral organoids was confirmed by western blot and showed a similar pattern as the one described in 2D cell cultures (Fig. 6c). Next, using single-nucleus RNA-sequencing (snRNA-seq), we observed that cerebral organoids of both genotypes contain all major neural cell types, with no significant difference in the proportions of cell types (Fig. 6d, e, f and Additional file 8: Fig. S7). We then performed differential gene expression analysis for all different cell types identified in *BIN1* WT and KO cerebral organoids using DESeq2 [38]. We observed 41 differentially expressed genes (DEGs; $0.7 < FC > 1.3$ and $FDR < 0.01$) in glutamatergic neurons and 43 DEGs in astrocytes (Fig. 6g, h and Additional file 9: Table S1). All the other cell types showed none or only 1–2 DEGs (Additional file 9: Table S1), indicating that *BIN1* WT and KO neural cells have similar gene expression profiles. Importantly, even for the 41 DEGs observed in glutamatergic neurons, no significant enrichment for gene ontologies associated with endocytic pathway was observed (Additional file 10: Table S2). These findings indicate that *BIN1* WT and KO hiPSC-derived neurons mainly differ by the expression of BIN1. As a consequence, potential defects in the endosome pathway in these cell models are likely not due to major transcriptional modifications but due to a direct action of BIN1 protein and its interaction with other proteins.

APP metabolism and endosome trafficking are tightly interconnected processes [23, 34] and previous work has suggested a role for BIN1 in their regulation [42, 62].

(See figure on next page.)

Fig. 5 Characterization of hiPSCs and their cell derivatives. **a** Schematic showing the production of *BIN1* WT and KO hiPSCs from parental cell line using CRISPR/Cas9 technology. These hiPSCs, in turn, were used to generate intermediate hiNPCs, and subsequently, mixed cultures of hiNs and hiAs. **b** Representation of exon 3 region of BIN1 was targeted for the production of *BIN1* WT and KO hiPSCs by CRISPR/Cas9 technology. The guide RNA sequence is shown (grey). **c**-**c**" Representative images showing pluripotency markers SOX2 (red), SSEA4 (green) and stained with Hoechst 33258 (**c**") in *BIN1* WT and KO hiPSCs. **d** Plot showing the normalized growth rate of *BIN1* WT and KO hiPSCs (N = 4 independent cell passages; p = 0.77, Unpaired t-test). **e**-**e"** Representative images showing hiNPCs labelled for NESTIN (red), SOX2 (green) and stained with Hoechst 33258 (e", Scale Bar = 20 µm). **f** Plot showing the normalized growth rate of *BIN1* WT and KO hiNPCs (N = 9 independent cell passages: ****p < 0.0001, Unpaired t-test). **g**-**g"** Representative images showing a 6-week-old mixed hiNs/hiAs culture labelled for the neuronal marker MAP2 (red), the astrocytic marker GFAP (green) and stained with Hoescht 33258 (g", Scale Bar = 10 µm) **h** Plot showing the percentage of cells in different cell populations – hiNPCs, hiNs, and hiAs (ANOVA $_{F(5,12)}$, p = 0.45). **i** Immunoblot for BIN1 and actin in BIN1 WT and KO hiPSCs samples. Band indicated on the blot for the WT cells (solid red arrowhead) indicates BIN1-light (BIN1:L) isoforms of BIN1. **j** Immunoblot showing the expression of BIN1:L isoforms (solid red arrowhead) in WT hiNPCs and both BIN1:L (hollow red arrowhead) and BIN1-heavy (BIN1:H; solid green arowhead) isoforms in 6-week-old mixed cultures of hiNs and hiAs

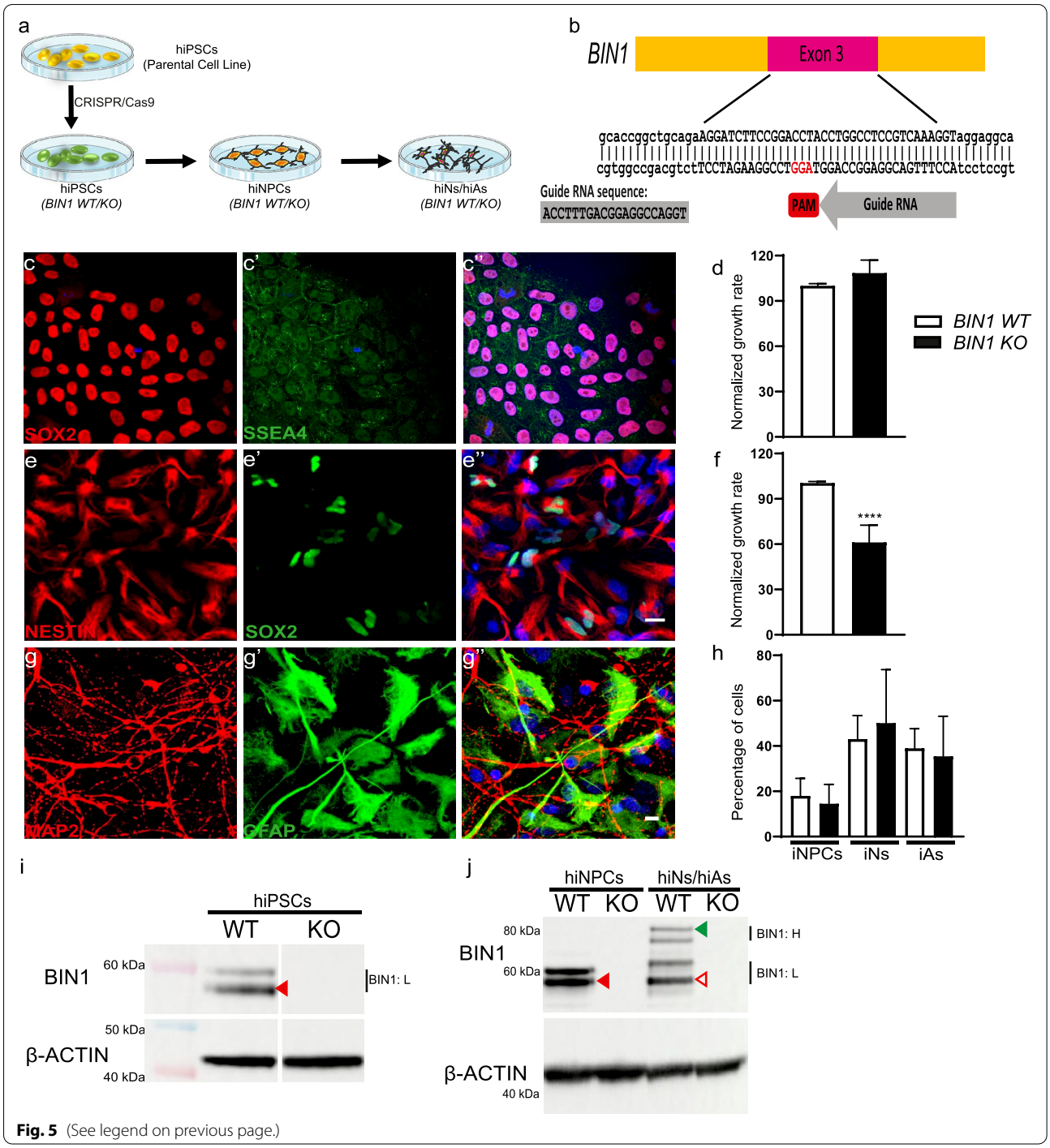

Fig. 5 (See legend on previous page.)

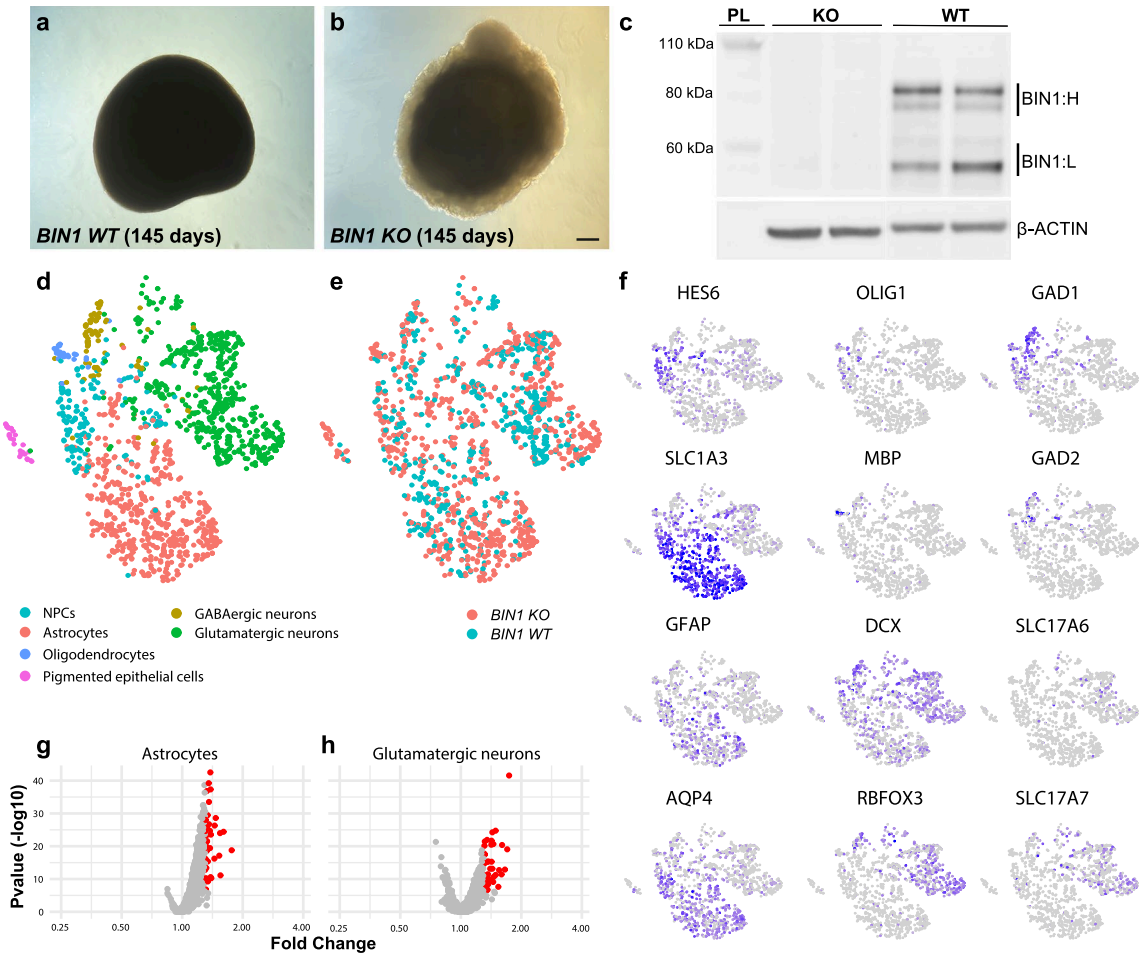

Fig. 6 *BIN1* WT and KO cerebral organoids show similar composition and gene expression. **a**, **b** Brightfield images of a *BIN1* WT (a) and KO (b) cerebral organoids after 145 days (d) in culture. Calibration bar: 200 µm. **c** Western blot for BIN1 and ACTIN in 190 days-old *BIN1* WT and KO cerebral organoids used for snRNA-seq. Bands corresponding to light (BIN1:L) and heavy BIN1 (BIN1:H) isoforms are indicated. MW – molecular weight. **d**, **e** tSNE plots of all 2990 cells from the snRNA-seq color-coded by cell type annotation (d) and genotype (e). **f** tSNE plots showing the expression of neural progenitor cell (HES6 and SLC1A3), astrocytes (SLC1A3, GFAP and AQP4), oligodendrocytes (OLIG1, MBP), pan neuronal (DCX, RBFOX3), GABAergic neurons (GAD1 and GAD2) and glutamatergic neurons (SLC17A6 and SLC17A7) markers. **g**, **h** Volcano plots showing genes differentially expressed in *BIN1* KO astrocytes (g) and glutamatergic neurons (h) compared to WT cells. Red dots indicate genes with fold change (FC) > 1.3 and false discovery rates (FDR) < 0.01

To probe whether BIN1 deletion could affect amyloidogenic APP processing in hiNs, we measured the levels of the APP β- CTF in cerebral organoids and 2D cell cultures (Additional file 11: Fig. S8). We found a significant reduction in the levels of APP β-CTF normalized either by ACTIN or full-length APP in BIN1 KO compared to WT cerebral organoids (Additional file 11: Fig. S8a, b). A similar trend was observed in 2D cell cultures, but without reaching statistical significance (Additional file 11: Fig. S8c, d).

BIN1 null mutation is associated with smaller early-endosome vesicles in hiPSC-derived neurons

In order to probe the impact of *BIN1* null mutation in hiNs, we quantified the number and size of the early endosome antigen 1 (EEA1)-expressing endosomes in microtubule-associated protein 2 (MAP2)-expressing cells in both 2D cultures and cerebral organoids (Fig. 7). EEA1 is an early endosomal Rab5 effector protein that has been implicated in the docking of incoming

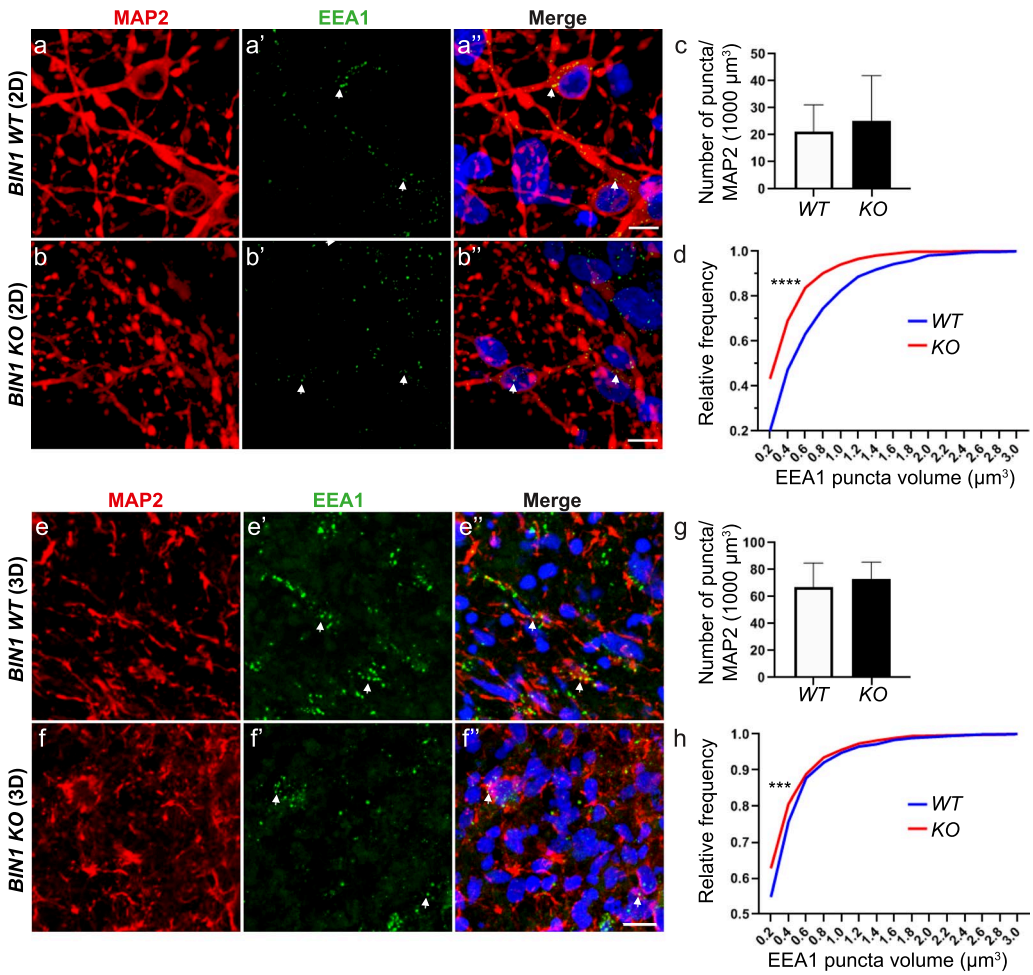

Fig. 7 Increased proportion of small-volume endosomes in *BIN1* null mutant hiNs. **a**– **b"** Representative images of *BIN1* WT and KO hiNs in 6-week-old 2D cultures immunolabeled with antibodies against MAP2 (red, a and b) and EEA1 (green, a' and b') and stained with Hoechst 33258 (blue, a" and b") (Scale Bar = 10 µm). **c** Plot showing the quantification of the number of EEA1$^+$ puncta per 1000 µm^3 of MAP2$^+$ surface (N = 3 independent cell cultures; *BIN1* WT hiNs: 21.15 ± 9.94 EEA1$^+$ puncta per 1000µm^3 of MAP2$^+$ surface; *BIN1* KO hiNs: 25.31 ± 16.58 EEA1$^+$ puncta per 1000µm^3 of MAP2$^+$ surface; p = 0.84, Unpaired t-test). **d** Plot showing the cumulative distribution of EEA1$^+$ puncta volumes in *BIN1* WT (blue line) and KO (red line) hiNs (N = 3 independent cell cultures; Kolmogorov–Smirnov test, ****p < 0.0001). **e**–**f"** Coronal sections of 190-days-old *BIN1* WT and KO cerebral organoids immunolabeled with antibodies against MAP2 (red, e and f) and EEA1 (green, e' and f') and stained with Hoechst 33258 (blue, e" and f"). **g** Quantification of the number of EEA1$^+$ puncta per 1000 µm^3 of MAP2$^+$ surface (N = 3 organoids per genotype; cerebral organoids: *BIN1* WT hiNs: 66.72 ± 18.13 EEA1$^+$ puncta per 1000µm^3 of MAP2$^+$ surface; *BIN1* KO hiNs: 73.18 ± 12.47 EEA1$^+$ puncta per 1000µm^3 of MAP2$^+$ surface; Unpaired t-test, p = 0.96). **h** Cumulative distribution of EEA1$^+$ puncta volumes in *BIN1* WT (blue line) and KO (red line) hiNs (N = 3 organoids per genotype; Kolmogorov–Smirnov test, ***p < 0.001)

endocytic vesicles before fusion with early endosomes [43]. We observed a significant change in the cumulative distribution of EEA1$^+$ endosome volumes in hiNs both in 2D cultures and cerebral organoids, mostly due to a predominance of small volume endosomes in *BIN1* KO compared to WT hiNs (Fig. 7d, h). Conversely, no significant change in the number of endosomes was observed in hiNs of both genotypes (Fig. 7c, g). These data suggested that BIN1 is involved in the regulation of early endosome size in human neurons.

BIN1iso1 specifically modulates sizes of the early-endosome vesicles

We then wondered whether the function of BIN1 in endocytosis could also be isoform-specific in human neurons, as observed in Drosophila. To test this possibility, we set out to perform lentiviral-mediated transfection with fluorophore-expressing BIN1iso1, BIN1iso9 or control plasmids in hiNs at 3 weeks of differentiation. After 3 additional weeks, we quantified the number and size of EEA1-expressing endosomes in transfected hiNs

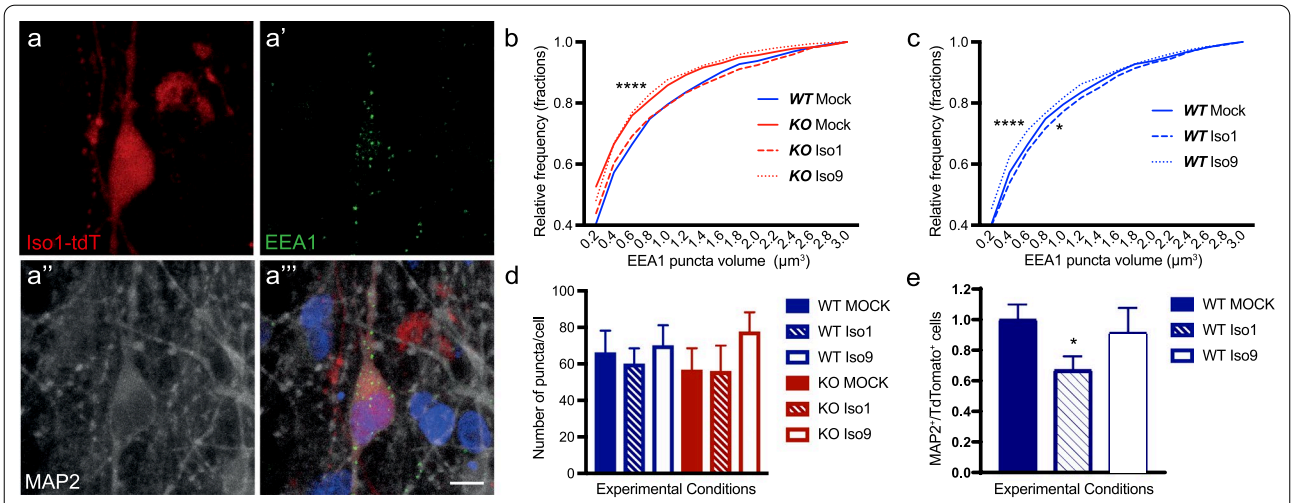

Fig. 8 Rescue of endosomal phenotype in *BIN1* null mutant neurons by transduction of BIN1 Isoform 1. **a**–**a'''** Representative images of *BIN1* WT and KO hiNs in 6-weeks-old 2D culture immunolabeled with antibodies against tdTomato (tdT, red, a), EEA1 (green, a'), MAP2 (grey, a''), and stained with Hoechst 33258 (blue, a''') (Scale Bar = 10 µm). **b** Plot showing the cumulative distribution of EEA1^{+} puncta volumes in transduced *BIN1* KO hiNs with tdT lentiviral constructs; *BIN1iso1* (dashed red line), *BIN1iso9* (dashed red line), and Mock-tdT (solid red line). *BIN1* WT hiNs tranduced with Mock-tdT (solid blue line) is indicated to show the rescue effect of the BIN1iso1 construct (orange line) in *BIN1*-null mutant neurons. Kolmogorov–Smirnov test followed by Bonferroni correction: *BIN1* WT + Mock vs *BIN1* KO + Mock: ****Padj < 0.0001; *BIN1* WT + Mock vs *BIN1* KO + iso9: Padj < 0.0001; *BIN1* KO + Mock vs *BIN1* KO + Iso1: ****Padj < 0.0001; *BIN1* WT + Mock vs *BIN1* KO + Iso1: Padj = 0.174; *BIN1* KO + Mock vs *BIN1* KO + Iso9: Padj = 0.207 (N = 3 independent cell cultures). **c** Plot showing the cumulative distribution of EEA1^{+} puncta volumes in transduced *BIN1* WT hiNs with tdTomato (tdT)-expressing lentiviral constructs; *BIN1iso1* (dashed blue line), *BIN1iso9* (dotted blue line), and Mock-tdT (solid blue line). Kolmogorov–Smirnov test followed by Bonferroni correction: *BIN1* WT + Mock vs *BIN1* WT + Iso1: *Padj = 0.04; *BIN1* WT + Mock vs *BIN1* WT + Iso9: ****Padj < 0.0001 (N = 3 independent cell cultures). **d** Graph showing the quantification of numbers of EEA1 puncta per cell in cells transduced with tdT-tagged lentiviral constructs (N = 3 independent cell cultures. EEA1^{+} puncta/neuron: *BIN1* WT + Mock: 65.86 ± 12.78; *BIN1* WT + Iso1: 59.75 ± 8.895; *BIN1* WT + Iso9: 69.82 ± 11.42; *BIN1* KO + Mock: 56.47 ± 12.27; *BIN1* KO + Iso1: 55.65 ± 14.52; *BIN1* KO + Iso9: 77.31 ± 11.04; p = 0.81, ANOVA $_{F(5,90)}$). **e** Quantification of MAP2^{+}/tdTomato^{+} neurons in BIN1iso1- and BIN1iso9-transduced cells relative to Mock-tdT-transduced cells (N = 3 independent cell cultures; Number of tdT^{+} cells: Mock = 468; BIN1iso1 = 193; BIN1iso9 = 103; ANOVA followed by Dunnett's multiple comparisons test, **p = 0.0289)

identified by tdTomato expression (Fig. 8). We observed that expression of BIN1iso1, but not BIN1iso9, in *BIN1* KO hiNs fully rescued the volume of EEA1^{+} endosomes to values similar of those observed in WT hiNs (Fig. 8b). We also over-expressed BIN1iso1 and BIN1iso9 in WT hiNs. Consistent with our previous observation in flies, we observed that BIN1iso1 overexpression in neurons led to an increase of large volumes EEA1^{+} endosomes, whereas the opposite effect was observed in neurons overexpressing BIN1iso9 (Fig. 8c). Neither in *BIN1* WT nor in KO hiNs did we observe significant changes in the number of puncta per cell after BIN1iso1 or BINiso9 overexpression (Fig. 8d). Lastly, we evaluated whether BIN1iso1 overexpression could have a neurotoxic effect in hiNs. To that end, we quantified the proportion of MAP2^{+} neurons in 6 weeks cultures after transduction with BIN1iso1-, BIN1iso9- or control-tdTomato^{+} cells. We found that BIN1iso1 overexpression led to a 30% reduction in the proportion of neurons compared to controls (Fig. 8e). Interestingly, this effect of BIN1iso1 was not observed in *BIN1* KO cells, suggesting that only supra-physiological expression levels of this isoform could be toxic for neurons.

Altogether, these observations indicate that BIN1iso1 expression is sufficient to regulate endosome volumes, even in the absence of other BIN1 isoforms in *BIN1* KO hiNs, and that increased expression of BIN1iso1 deregulates endosome size and can lead to degeneration of human neurons, as observed in Drosophila photoreceptors.

Discussion

In this work, we assessed the function and potential neurotoxicity of human BIN1 isoforms in Drosophila and human neurons. We show a functional conservation of human BIN1 in Drosophila as BIN1iso1, BIN1iso8 and BIN1iso9 phenocopied dAmphA-induced photoreceptor neuron developmental defects and BIN1iso8 was able to rescue the locomotor defects associated with the loss of *dAmph* in Drosophila. Expression of BIN1iso1 resulted in a progressive neurodegeneration of photoreceptor neurons that was isoform-specific and dose-independent.

The degeneration did not depend on the activation of the phototransduction cascade and was associated with a strong accumulation of vesicles harboring early and late endosomal markers. These results suggested that a BIN1 isoform-specific alteration of the endosome-lysosome pathway could contribute to neuronal degeneration. Accordingly, the degeneration was prevented by a loss of function of the early endosome regulator Rab5 and a gain of function of the recycling endosomal protein Rab11. Lastly, we observed a conservation of BIN1iso1 function in hiNs in 2D cultures and in organoids. Loss of BIN1 resulted in reduced size of early endosomes, whereas expression of BIN1iso1, but not BIN1iso9, was able to rescue the reduced size of early endosomes in the *BIN1* KO hiNs. As in Drosophila, overexpression of BIN1iso1 resulted in enlarged early endosomes and had neurotoxic effects in WT hiNs.

Our results indicate context- and isoform-specific functions of BIN1: (i) Expression of BIN1iso1, BIN1iso8 and BIN1iso9 altered photoreceptor neuron rhabdomere morphogenesis during development in an isoform-independent and dose-dependent manner, whereas in the adult photoreceptor neurons BIN1iso1 expression induced neurodegeneration in an isoform-dependent and dose-independent manner; (ii) in human neurons, we observed a shift in BIN1 isoform expression from low molecular weight isoforms in hiPSCs and NPCs (likely mainly BIN1iso9) to high molecular weight isoforms in hiNs (likely mainly BIN1iso1); (iii) BIN1iso1 expression rescued the size of BIN1-deficient early endosomes contrary to BIN1iso9. Collectively, these results argue for an important role of BIN1iso1 in mature neuronal cells and support the fact that BIN1iso1 is a neuron-specific isoform with specific functions in this cell-type [52, 69]. Furthermore, (i) *BIN1* KO hiNs showed early endosomes of reduced size; (ii) in *BIN1* KO hiNs, BIN1iso1 expression rescued early endosome sizes but did not lead to enlargement of these vesicles; and (iii) in WT hiNs, BIN1iso1 overexpression induced early endosome enlargement. These results suggest that homeostatic BIN1iso1 expression levels need to be tightly regulated to allow proper endocytic trafficking in neurons. Of note, BIN1iso9 overexpression in WT hiNs induced a reduction of early endosome size. Since BIN1 forms dimers through its BAR domain [51], we postulate that BIN1iso9 may dimerize with BIN1iso1 and inhibit BIN1iso1 function in a dominant negative manner. Interestingly, this may also indicate another level of complexity to regulate BIN1 functions at the protein level.

Our results support a direct role of BIN1iso1 in neurons at the early endosome crossroad as indicated (i) by the labeling of large vesicles with early endosome markers in Drosophila, (ii) by the Rab5 rescue experiment in Drosophila and (iii) by the early endosome size modulation in hiNs. Of note, the phenotype with very large vesicles in Drosophila likely results from Drosophila being a heterologous system for human BIN1iso1, and as a consequence, exhibiting stronger phenotypes. Additionally, in Drosophila, some of the vesicles also exhibited markers for late endosome/MVB and exceptionally, lysosome. However, regulation of late endosome/MVB or lysosomal function did not modulate photoreceptor degeneration and secretion of exosomes did not appear to be blocked, suggesting that BIN1iso1 defect do not occur at this level. BIN1 has been proposed to regulate endocytosis by interaction with clathrin, Adaptor Proteins (AP) and dynamins [12, 22, 26, 50, 65]. Since some of these proteins are also involved in vesicle budding of the intracellular organelles [26], we propose that BIN1iso1 may also inhibit vesicle budding of early endosomes, thus, leading to an increase in their size. Overexpressing Rab11 would overcome this inhibition through the activation of endosome recycling, decompress enlarged endosomes and explain the rescuing effect of a gain of Rab11 that we observed. In support of this direct action of BIN1iso1 on endosomes, (i) we observed BIN1iso1 on the large endosomal vesicles in Drosophila, (ii) BIN1 knockout in cerebral organoids reduced endosome size without impacting expression of genes involved in the endosome trafficking pathway, and (iii) in Drosophila, BIN1iso1 toxicity was dependent on the CLAP domain, which is known to directly bind intracellular trafficking proteins like clathrin and APs [50]. This regulation of early endosomes correlates with a broader role of BIN1 in the regulation of intracellular trafficking ranging from endocytosis [6, 65] to recycling endosomes [62] as well as related processes in neuronal pre- or post-synaptic compartments [53, 56].

Interestingly, a growing body of evidence supports a dysregulation of the endosomal-lysosomal system as a plausible underlying mechanism in AD pathogenesis [45, 58]. Several AD susceptibility genes identified by GWAS (*BIN1, PICALM, EPHA1, CD2AP, SORL1* and *RIN3*) encode proteins that function predominantly in endocytic trafficking [15]. Endosome enlargement has been described to be the first cytopathological marker of AD, before the emergence of plaques and tangles [8]. Several human AD cell models, namely hiNs originating from sporadic and familial AD patients [27], hiNs carrying fAD APP and PSEN1 mutations [34] and hiNs knocked-out for the AD risk gene SORL1 [25, 32], recapitulate these endosomal defects similarly to what we observed in the BIN1iso1 overexpressing hiNs. In AD and Down syndrome, these defects are associated with an overactivation of Rab5 [47] and overactivation of Rab5 in mice mimics AD-like endosomal dysfunction [48]. We have

also shown that BIN1iso1 effects in Drosophila are Rab5-dependent. Early endosomes are a major site of APP processing by β-secretase to yield APP β-CTF. Therefore, alterations in endocytic pathways can affect APP metabolism and this likely explain the decrease in APP β-CTF we observed in the BIN1 knocked-out hiNs. Reciprocally, APP β-CTF mediates endosomal defects in fAD mutant hiNs [34]. To do so, APP β-CTF activates Rab5 via APPL1 [31]. However, in our study, loss of *Appl*, the Drosophila ortholog of APP, did not rescue BIN1iso1-induced neurodegeneration, suggesting that APP β-CTF does not mediate BIN1iso1 toxicity. The involvement of APP β-CTF have also been questioned in SORL1 knocked-out hiNs with contradictory results in two studies showing APP β-CTF-dependent or -independent endosomal defects [25, 32]. Another putative intermediate is Ras and Rab Interactor 3 (RIN3), a guanine nucleotide exchange factor (GEF) for the Rab5 small GTPase family, which is located in a GWAS-defined AD susceptibility locus [35]. Upregulation of RIN3 induces endosomal dysfunction through Rab5 [57] and RIN3 interacts with BIN1 [29, 57]. Further experiments would be, thus, of interest to test RIN3 as an intermediate for BIN1iso1 neurotoxicity. Finally, we show that BIN1iso1 endosomal defects and toxicity can be attenuated by a gain of function of Rab11, which dovetails with data showing a colocalization of BIN1 with Rab11 [56] and indicating that Rab11 activity is altered in AD in relationship with endosomal trafficking [5, 63, 66]. Overall, our results strongly support a role of BIN1 in the endosomal dysregulation observed in AD.

Since we observed endosome enlargement and neurodegeneration upon BIN1iso1 overexpression, our results also suggest that an increase in BIN1iso1 may be deleterious to neurons and contribute to early phases of AD pathology through early endosome alterations. It implies an increase in BIN1iso1 levels in neurons, which remains elusive. To date, most experiments showing altered BIN1 expression in the AD brain have focused in samples obtained at late stages of the pathology [1, 9, 21, 24, 41, 52, 60] and none have directly measured the levels of BIN1 isoforms at early stages of the pathology at the single-cell resolution. Therefore, at this point, it is not possible to establish a clear link between levels of BIN1 expression in neurons and AD pathogenesis. Due to the numerous biological roles of BIN1 in AD pathophysiology, it is parsimonious to envisage that both up- and down-regulation of BIN1 isoforms expression in the human brain could affect disease progression through different cell-type specific mechanisms, including the endosomal abnormalities described here.

Future studies should also address the possibility that *BIN1* polymorphisms associated with an increased AD risk could affect the expression of BIN1iso1 in neurons. Interestingly, the variant rs59335482, an insertion allele associated with a higher AD risk, is able to increase transcriptional activity in a luciferase assay in vitro using HEK cells and SH-SY5Y neuroblastoma cells, and is also associated with an increase in *BIN1* mRNA expression in the brain [9]. However, individual BIN1 isoforms were not analyzed in this study. Other variants, rs6733839 and rs13025717, in linkage disequilibrium with the above-mentioned variant, have been shown to be located in a region enriched in microglia-specific enhancers [10, 46]. Deletion of a large 363 bp promoter region containing these variants in hiPSCs resulted in a decrease of *BIN1* expression specifically in human induced microglia, but not in Neurog2-induced hiNs. Unfortunately, neither the transcriptional effect of the exact variants nor the expression of BIN1 in spontaneously differentiated hiNs have been tested yet. In addition, the possibility that the impact of functional variants may depend on specific AD pathophysiological process, e.g. Aβ exposure, has not been assessed. There is, thus, a high uncertainty about functional variants in the BIN1 locus. Even if our current study was not intended to directly assess functional consequences of AD risk-related BIN1 polymorphisms but to focus on BIN1 isoforms function in neurons, which are still insufficiently described and understood, it may provide a context for BIN1-associated risk, namely the dysregulation of early endosome size and function. Up to now and not exclusive from each other, BIN1 polymorphisms have been associated with Tau but not amyloid loads in post-mortem AD brain tissue [9] and they are consistently associated with faster Aβ-associated Tau-PET accumulation and cognitive decline in AD patient [18, 19].

Conclusions

In conclusion, an increase of BIN1iso1 in neurons could contribute to AD pathogenesis by increasing the size of early endosomes observed early in the pathogenic process and by inducing neurodegeneration. Other AD genetic determinants have also been shown to regulate early endosome size, supporting early endosome defects as a major event in the pathogenesis of AD.

Abbreviations

Aβ: Amyloid β peptide; AD: Alzheimer's disease; APP β-CTF: APP β-carboxy terminal fragment; BAR: BIN1/Amphiphysin/RVS; BIN1iso1: Human BIN1 isoform1; BIN1iso8: Human BIN1 isoform8; BIN1iso9: Human BIN1 isoform9; CA: Constitutively active; CLAP: Clathrin and adaptor protein-2 binding; DEG: Differentially expressed genes; DN: Dominant negative; hiA: Human induced astrocyte; hiN: Human induced neuron; hiNPC: Human induced neural progenitor cells; hiPSC: Human induced pluripotent stem cells; KO: Knockout; snRNA-seq: Single-nucleus RNA-sequencing; WT: Wild type.

Supplementary Information

The online version contains supplementary material available at https://doi.org/10.1186/s40478-021-01285-5.

Additional file 1. Supplementary information and supplementary methods.

Additional file 2. Figure S1. Creation of transgenic lines expressing human BIN1 isoforms.

Additional file 3. Figure S2. Scheme of AmphMI08903-TG4.0 allele.

Additional file 4. Figure S3. Generation and test of transgenic Drosophila expressing truncated human BIN1-1 forms for the Exon7 (BIN1-1 ΔEx7) and the CLAP domain (BIN1-1 ΔCLAP).

Additional file 5. Figure S4. Electron microscopy images of BIN1-1-induced photoreceptor degeneration in Drosophila eyes.

Additional file 6. Figure S5. Screening of organelle markers in BIN1-1-induced degenerating photoreceptor neurons.

Additional file 7. Figure S6. Effect of Rab4 modulation on BIN1iso1 neurotoxicity in Drosophila photoreceptor neurons.

Additional file 8. Figure S7. Graphic representation of proportions of cell types (in percentages) in *BIN1* KO and WT cerebral organoids.

Additional file 9. Table S1. Differential gene expression analysis for all different cell types identified in *BIN1* WT and KO cerebral organoids.

Additional file 10. Table S2. Gene ontology enrichment analysis for the 41 DEGs observed in glutamatergic neurons.

Additional file 11. Figure S8. Decreased APP/β-CTF levels in BIN1 KO cerebral organoids.

Acknowledgements
The authors thank the BICeL platform of the Institut Biologie de Lille and the Vect'UB viral platform (INSERM US 005 – CNRS 3427 – TBMCore, Université de Bordeaux, France). The authors also thank the UMR 8199 LIGAN-PM Genomics platform (Lille, France). We thank A. Zelhof, G.L. Boulianne and J Laporte for antibody, fly stock and cDNA. The a5 and 4C5 antibodies developed by Fambrough, D.M. (The Johns Hopkins University) and de Couet, H.G./Tanimura, T. (University of Hawaii) were obtained from the Developmental Studies Hybridoma Bank, created by the NICHD of the NIH and maintained at The University of Iowa, Department of Biology, Iowa City, IA 52242.

Authors' contributions
Conceptualization, PD, MRC, JCL, BD; Methodology, PD, MRC, XH; Investigation, PD, EL, MRC, OS, NB, XH, FA, BSL, ARMF, J G, AC, AP, FD; Resources, XH, LD, CD, JC, AB; Writing—Original Draft, PD, MRC, JCL, EL, OS; Writing—Reviews & Editing, PD, MRC, JCL, EL, OS; Supervision, PD, JCL, MRC, FD, BD, PA, FL, PV; Funding Acquisition, JCL, MRC, PD, BD. All authors read and approved the final manuscript.

Funding
Drosophila cDNA was obtained from the Drosophila Genomics Resource Center, supported by NIH Grant 2P40OD010949. Drosophila stocks obtained from the Bloomington Drosophila Stock Center (NIH P40OD018537) were used in this study. The Genotype-Tissue Expression (GTEx) Project was supported by the Common Fund of the Office of the Director of the National Institutes of Health, and by NCI, NHGRI, NHLBI, NIDA, NIMH, and NINDS. The data used for the analyses described in this manuscript were obtained from dbGaP accession number phs000424.v8.p2 on 04/02/2021. This work was supported by France Alzheimer (#328 ADhesion, #1999 BIN1DROSO), Fondation Vaincre Alzheimer (LECMA Grant The BIN1-Tau neurotoxic link in Drosophila) and la Fondation pour la recherche médicale (ALZ201912009628, ALZ201906008477). This work was co-funded by the European Union under the European Regional Development Fund (ERDF) and by the Hauts de France Regional Council (Contrat No.18006176), the MEL (contract_2016_ESR_05), and the French State (contract no. 2018-3-CTRL_IPL_Phase2). This work was also funded by the Lille Métropole Communauté Urbaine and the French government's LABEX DISTALZ program (Development of innovative strategies for a transdisciplinary approach to Alzheimer's disease). The UMR 8199 LIGAN-PM Genomics platform (Lille, France) belongs to the 'Federation de Recherche' 3508 Labex EGID (European Genomics Institute for Diabetes; ANR-10-LABX-46) and was supported by the ANR Equipex 2010 session (ANR-10-EQPX-07-01; 'LIGAN-PM'). The LIGAN-PM Genomics platform (Lille, France) is also supported by the FEDER and the Region Nord-Pas-de-Calais-Picardie.

Availability of data and materials
The datasets analyzed during the current study are available from corresponding authors on reasonable request.

Declarations

Competing interests
The authors declare no competing interests.

Author details
[1]Univ. Lille, Inserm, CHU Lille, Institut Pasteur Lille, U1167 - RID-AGE - Facteurs de risque et déterminants moléculaires des maladies liées au vieillissement, F-59000 Lille, France. [2]Brain Institute, Federal University of Rio Grande do Norte, Natal, Brazil. [3]Univ. Lille, Inserm, CNRS, CHU Lille, Institut Pasteur de Lille, U1283-UMR 8199 EGID, F-59000 Lille, France. [4]Univ. Lille, CNRS, Inserm, CHU Lille, Institut Pasteur de Lille, U1019-UMR 9017-CIIL-Center for Infection and Immunity of Lille, F-59000 Lille, France. [5]VIB Center for Brain and Disease Research, KU Leuven, Leuven, Belgium. [6]Department of Neurosciences, Leuven Brain Institute, KU Leuven, Leuven, Belgium. [7]Univ. Lille, CNRS, Inserm, CHU Lille, Institut Pasteur de Lille, US41-UMS2014-PLBS, F-59000 Lille, France. [8]Department of Biomolecular Medicine, Faculty of Medicine and Health sciences, Ghent University, 9000 Ghent, Belgium. [9]Centre for Medical Genetics, Ghent University Hospital, 9000 Ghent, Belgium.

Received: 20 October 2021 Accepted: 23 October 2021
Published online: 08 January 2022

References

1. Adams SL, Tilton K, Kozubek JA, Seshadri S, Delalle I (2016) Subcellular changes in bridging integrator 1 protein expression in the cerebral cortex during the progression of Alzheimer disease pathology. J Neuropathol Exp Neurol 75:779–790. https://doi.org/10.1093/jnen/nlw056
2. Andrew RJ, De Rossi P, Nguyen P, Kowalski HR, Recupero AJ, Guerbette T et al (2019) Reduction of the expression of the late-onset Alzheimer's disease (AD) risk-factor *BIN1* does not affect amyloid pathology in an AD mouse model. J Biol Chem 294:4477–4487. https://doi.org/10.1074/jbc.RA118.006379
3. Bartscherer K, Pelte N, Ingelfinger D, Boutros M (2006) Secretion of Wnt ligands requires Evi, a conserved transmembrane protein. Cell 125:523–533. https://doi.org/10.1016/j.cell.2006.04.009
4. Bellenguez C, Küçükali F, Jansen I, Andrade V, Morenau-Grau S, Amin N, et al (2020) Large meta-analysis of genome-wide association studies expands knowledge of the genetic etiology of Alzheimer's disease and highlights potential translational opportunities. medRxiv 17:10
5. Buggia-Prévot V, Fernandez CG, Riordan S, Vetrivel KS, Roseman J, Waters J et al (2014) Axonal BACE1 dynamics and targeting in hippocampal neurons: A role for Rab11 GTPase. Mol Neurodegener. https://doi.org/10.1186/1750-1326-9-1
6. Calafate S, Flavin W, Verstreken P, Moechars D (2016) Loss of Bin1 promotes the propagation of Tau pathology. Cell Rep 17:931–940. https://doi.org/10.1016/j.celrep.2016.09.063
7. Cassar M, Kretzschmar D (2016) Analysis of amyloid precursor protein function in drosophila melanogaster. Front Mol Neurosci 9:61. https://doi.org/10.3389/fnmol.2016.00061
8. Cataldo AM, Peterhoff CM, Troncoso JC, Gomez-Isla T, Hyman BT, Nixon RA (2000) Endocytic pathway abnormalities precede amyloid beta deposition in sporadic Alzheimer's disease and Down syndrome: differential effects of APOE genotype and presenilin mutations. Am J Pathol 157:277–286
9. Chapuis J, Hansmannel F, Gistelinck M, Mounier A, Van Cauwenberghe C, Kolen KV et al (2013) Increased expression of BIN1 mediates Alzheimer

genetic risk by modulating tau pathology. Mol Psychiatry 18:1225–1234. https://doi.org/10.1038/mp.2013.1
10. Corces MR, Shcherbina A, Kundu S, Gloudemans MJ, Frésard L, Granja JM et al (2020) Single-cell epigenomic analyses implicate candidate causal variants at inherited risk loci for Alzheimer's and Parkinson's diseases. Nat Genet 52:1158–1168. https://doi.org/10.1038/s41588-020-00721-x
11. Crotti A, Sait HR, McAvoy KM, Estrada K, Ergun A, Szak S et al (2019) BIN1 favors the spreading of Tau via extracellular vesicles. Sci Rep 9:9477. https://doi.org/10.1038/s41598-019-45676-0
12. Dong J, Misselwitz R, Welfle H, Westermann P (2000) Expression and purification of dynamin II domains and initial studies on structure and function. Protein Expr Purif 20:314–323. https://doi.org/10.1006/prep.2000.1305
13. Dourlen P, Bertin B, Chatelain G, Robin M, Napoletano F, Roux MJ et al (2012) Drosophila fatty acid transport protein regulates rhodopsin-1 metabolism and is required for photoreceptor neuron survival. PLoS Genet 8:e1002833. https://doi.org/10.1371/journal.pgen.1002833
14. Dourlen P, Levet C, Mejat A, Gambis A, Mollereau B (2013) The Tomato/GFP-FLP/FRT method for live imaging of mosaic adult Drosophila photoreceptor cells. J Vis Exp 79:e50610. https://doi.org/10.3791/50610 PMID: 24084155
15. Dourlen P, Kilinc D, Malmanche N, Chapuis J, Lambert J-C (2019) The new genetic landscape of Alzheimer's disease: from amyloid cascade to genetically driven synaptic failure hypothesis? Acta Neuropathol 138:221–236. https://doi.org/10.1007/s00401-019-02004-0
16. Dunst S, Kazimiers T, von Zadow F, Jambor H, Sagner A, Brankatschk B et al (2015) Endogenously tagged Rab proteins: a resource to study membrane trafficking in Drosophila. Dev Cell 33:351–365. https://doi.org/10.1016/j.devcel.2015.03.022
17. Fouillet A, Levet C, Virgone A, Robin M, Dourlen P, Rieusset J et al (2012) ER stress inhibits neuronal death by promoting autophagy. Autophagy 8:915–926. https://doi.org/10.4161/auto.19716
18. Franzmeier N, Ossenkoppele R, Brendel M, Rubinski A, Smith R, Kumar A et al (2021) The BIN1 rs744373 Alzheimer's disease risk SNP is associated with faster Aβ-associated tau accumulation and cognitive decline. Alzheimer's Dement. https://doi.org/10.1002/alz.12371
19. Franzmeier N, Rubinski A, Neitzel J, Ewers M, Weiner MW, Aisen P et al (2019) The BIN1 rs744373 SNP is associated with increased tau-PET levels and impaired memory. Nat Commun. https://doi.org/10.1038/s41467-019-09564-5
20. Gatz M, Reynolds CA, Fratiglioni L, Johansson B, Mortimer JA, Berg S et al (2006) Role of genes and environments for explaining Alzheimer disease. Arch Gen Psychiatry 63:168–174. https://doi.org/10.1001/archpsyc.63.2.168
21. Glennon EBC, Whitehouse IJ, Miners JS, Kehoe PG, Love S, Kellett KAB et al (2013) BIN1 is decreased in sporadic but not familial Alzheimer's disease or in aging. PLoS ONE 8:e78806. https://doi.org/10.1371/journal.pone.0078806
22. Grabs D, Slepnev VI, Songyang Z, David C, Lynch M, Cantley LC et al (1997) The SH3 domain of amphiphysin binds the proline-rich domain of dynamin at a single site that defines a new SH3 binding consensus sequence. J Biol Chem 272:13419–13425. https://doi.org/10.1074/jbc.272.20.13419
23. Haass C, Kaether C, Thinakaran G, Sisodia S (2012) Trafficking and proteolytic processing of APP. Cold Spring Harb Perspect Med 2:a006270. https://doi.org/10.1101/cshperspect.a006270
24. Holler CJ, Davis PR, Beckett TL, Platt TL, Webb RL, Head E et al (2014) Bridging integrator 1 (BIN1) protein expression increases in the alzheimer's disease brain and correlates with neurofibrillary tangle pathology. J Alzheimer's Dis 42:1221–1227. https://doi.org/10.3233/JAD-132450
25. Hung C, Tuck E, Stubbs V, van der Lee SJ, Aalfs C, van Spaendonk R et al (2021) SORL1 deficiency in human excitatory neurons causes APP-dependent defects in the endolysosome-autophagy network. Cell Rep. https://doi.org/10.1016/j.celrep.2021.109259
26. Huser S, Suri G, Crottet P, Spiess M (2013) Interaction of amphiphysins with AP-1 clathrin adaptors at the membrane. Biochem J 450:73–83. https://doi.org/10.1042/BJ20121373
27. Israel MA, Yuan SH, Bardy C, Reyna SM, Mu Y, Herrera C et al (2012) Probing sporadic and familial Alzheimer's disease using induced pluripotent stem cells. Nature 482:216–220. https://doi.org/10.1038/nature10821
28. Jiang Y, Rigoglioso A, Peterhoff CM, Pawlik M, Sato Y, Bleiwas C et al (2016) Partial BACE1 reduction in a Down syndrome mouse model blocks Alzheimer-related endosomal anomalies and cholinergic neurodegeneration: role of APP-CTF. Neurobiol Aging 39:90–98. https://doi.org/10.1016/j.neurobiolaging.2015.11.013
29. Kajiho H, Saito K, Tsujita K, Kontani K, Araki Y, Kurosu H et al (2003) RIN3: A novel Rab5 GEF interacting with amphiphysin II involved in the early endocytic pathway. J Cell Sci 116:4159–4168
30. Kessissoglou IA, Langui D, Hasan A, Maral M, Dutta SB, Hiesinger PR et al (2020) The Drosophila amyloid precursor protein homologue mediates neuronal survival and neuroglial interactions. PLOS Biol 18:e3000703. https://doi.org/10.1371/journal.pbio.3000703
31. Kim S, Sato Y, Mohan PS, Peterhoff C, Pensalfini A, Rigoglioso A et al (2016) Evidence that the rab5 effector APPL1 mediates APP-βCTF-induced dysfunction of endosomes in Down syndrome and Alzheimer's disease. Mol Psychiatry 21:707–716. https://doi.org/10.1038/mp.2015.97
32. Knupp A, Mishra S, Martinez R, Braggin JE, Szabo M, Kinoshita C et al (2020) Depletion of the AD risk gene SORL1 selectively impairs neuronal endosomal traffic independent of amyloidogenic APP processing. Cell Rep. https://doi.org/10.1016/j.celrep.2020.107719
33. Kunkle BW, Grenier-Boley B, Sims R, Bis JC, Damotte V, Naj AC et al (2019) Genetic meta-analysis of diagnosed Alzheimer's disease identifies new risk loci and implicates Aβ, tau, immunity and lipid processing. Nat Genet 51:414–430. https://doi.org/10.1038/s41588-019-0358-2
34. Kwart D, Gregg A, Scheckel C, Murphy E, Paquet D, Duffield M et al (2019) A large panel of isogenic APP and PSEN1 mutant human iPSC neurons reveals shared endosomal abnormalities mediated by APP β-CTFs, not Aβ. Neuron. https://doi.org/10.1016/j.neuron.2019.07.010
35. Lambert J-C, Ibrahim-Verbaas CA, Harold D, Naj AC, Sims R, Bellenguez C et al (2013) Meta-analysis of 74,046 individuals identifies 11 new susceptibility loci for Alzheimer's disease. Nat Genet 45:1452–1458. https://doi.org/10.1038/ng.2802
36. Lauwers E, Wang Y-C, Gallardo R, Van der Kant R, Michiels E, Swerts J et al (2018) Hsp90 mediates membrane deformation and exosome release. Mol Cell 71:689-702.e9. https://doi.org/10.1016/j.molcel.2018.07.016
37. Leventis PA, Chow BM, Stewart BA, Iyengar B, Campos AR, Boulianne GL (2001) Drosophila Amphiphysin is a post-synaptic protein required for normal locomotion but not endocytosis. Traffic 2:839–850
38. Love MI, Huber W, Anders S (2014) Moderated estimation of fold change and dispersion for RNA-seq data with DESeq2. Genome Biol. https://doi.org/10.1186/s13059-014-0550-8
39. Malki I, Cantrelle FX, Sottejeau Y, Lippens G, Lambert JC, Landrieu I (2017) Regulation of the interaction between the neuronal BIN1 isoform 1 and Tau proteins—role of the SH3 domain. FEBS J 284:3218–3229. https://doi.org/10.1111/febs.14185
40. Malmanche N, Dourlen P, Gistelinck M, Demiautte F, Link N, Dupont C et al (2017) Developmental expression of 4-repeat-Tau Induces neuronal aneuploidy in Drosophila Tauopathy models. Sci Rep 7:40764. https://doi.org/10.1038/srep40764
41. Marques-Coelho D, Iohan L da CC, Melo de Farias AR, Flaig A, Letournel F, Martin-Négrier ML, et al (2021) Differential transcript usage unravels gene expression alterations in Alzheimer's disease human brains. NPJ Aging Mech Dis 7. https://doi.org/10.1038/s41514-020-00052-5
42. Miyagawa T, Ebinuma I, Morohashi Y, Hori Y, Young Chang M, Hattori H et al (2016) BIN1 regulates BACE1 intracellular trafficking and amyloid-β production. Hum Mol Genet 25:2948–2958. https://doi.org/10.1093/hmg/ddw146
43. Mu FT, Callaghan JM, Steele-Mortimer O, Stenmark H, Parton RG, Campbell PL et al (1995) EEA1, an early endosome-associated protein. EEA1 is a conserved α- helical peripheral membrane protein flanked by cysteine "fingers" and contains a calmodulin-binding IQ motif. J Biol Chem 270:13503–13511. https://doi.org/10.1074/jbc.270.22.13503
44. Nicot A-S, Toussaint A, Tosch V, Kretz C, Wallgren-Pettersson C, Iwarsson E et al (2007) Mutations in amphiphysin 2 (BIN1) disrupt interaction with dynamin 2 and cause autosomal recessive centronuclear myopathy. Nat Genet 39:1134–1139. https://doi.org/10.1038/ng2086
45. Nixon RA (2017) Amyloid precursor protein and endosomal–lysosomal dysfunction in Alzheimer's disease: inseparable partners in a multifactorial disease. FASEB J 31:2729–2743. https://doi.org/10.1096/fj.201700359
46. Nott A, Holtman IR, Coufal NG, Schlachetzki JCM, Yu M, Hu R et al (2019) Brain cell type–specific enhancer–promoter interactome maps and

disease-risk association. Science (80-) 366:1134–1139. https://doi.org/10.1126/science.aay0793
47. Pensalfini A, Jiang Y, Kim S, Nixon RA (2021) Assessing activation in health and disease. In: Methods in molecular biology (Clifton, N.J.), pp 273–294
48. Pensalfini A, Kim S, Subbanna S, Bleiwas C, Goulbourne CN, Stavrides PH et al (2020) Endosomal dysfunction induced by directly overactivating Rab5 recapitulates prodromal and neurodegenerative features of Alzheimer's disease. Cell Rep 33:108420. https://doi.org/10.1016/j.celrep.2020.108420
49. Prokic I, Cowling BS, Laporte J (2014) Amphiphysin 2 (BIN1) in physiology and diseases. J Mol Med 92:453–463. https://doi.org/10.1007/s00109-014-1138-1
50. Ramjaun AR, McPherson PS (1998) Multiple amphiphysin II splice variants display differential clathrin binding: identification of two distinct clathrin-binding sites. J Neurochem 70:2369–2376
51. Ramjaun AR, Philie J, De Heuvel E, McPherson PS (1999) The N terminus of amphiphysin II mediates dimerization and plasma membrane targeting. J Biol Chem 274:19785–19791. https://doi.org/10.1074/jbc.274.28.19785
52. De Rossi P, Buggia-Prévot V, Clayton BLL, Vasquez JB, van Sanford C, Andrew RJ et al (2016) Predominant expression of Alzheimer's disease-associated BIN1 in mature oligodendrocytes and localization to white matter tracts. Mol Neurodegener 11:59. https://doi.org/10.1186/s13024-016-0124-1
53. De Rossi P, Nomura T, Andrew RJ, Masse NY, Sampathkumar V, Musial TF et al (2020) Neuronal BIN1 regulates presynaptic neurotransmitter release and memory consolidation. Cell Rep 30:3520-3535.e7. https://doi.org/10.1016/j.celrep.2020.02.026
54. Sartori M, Mendes T, Desai S, Lasorsa A, Herledan A, Malmanche N et al (2019) BIN1 recovers tauopathy-induced long-term memory deficits in mice and interacts with Tau through Thr348 phosphorylation. Acta Neuropathol 138:631–652. https://doi.org/10.1007/s00401-019-02017-9
55. Schindelin J, Arganda-Carreras I, Frise E, Kaynig V, Longair M, Pietzsch T et al (2012) Fiji: an open-source platform for biological-image analysis. Nat Methods 9:676–682
56. Schürmann B, Bermingham DP, Kopeikina KJ, Myczek K, Yoon S, Horan KE et al (2020) A novel role for the late-onset Alzheimer's disease (LOAD)-associated protein Bin1 in regulating postsynaptic trafficking and glutamatergic signaling. Mol Psychiatry 25:2000–2016. https://doi.org/10.1038/s41380-019-0407-3
57. Shen R, Zhao X, He L, Ding Y, Xu W, Lin S et al (2020) Upregulation of RIN3 induces endosomal dysfunction in Alzheimer's disease. Transl Neurodegener. https://doi.org/10.1186/s40035-020-00206-1
58. Small SA, Simoes-Spassov S, Mayeux R, Petsko GA (2017) Endosomal traffic jams represent a pathogenic hub and therapeutic target in Alzheimer's disease. Trends Neurosci 40:592–602
59. Sottejeau Y, Bretteville A, Cantrelle F-X, Malmanche N, Demiaute F, Mendes T et al (2015) Tau phosphorylation regulates the interaction between BIN1's SH3 domain and Tau's proline-rich domain. Acta Neuropathol Commun 3:58. https://doi.org/10.1186/s40478-015-0237-8
60. Taga M, Petyuk VA, White C, Marsh G, Ma Y, Klein H-U et al (2020) BIN1 protein isoforms are differentially expressed in astrocytes, neurons, and microglia: neuronal and astrocyte BIN1 are implicated in tau pathology. Mol Neurodegener 15:44. https://doi.org/10.1186/s13024-020-00387-3
61. Taga M, Petyuk VA, White C, Marsh G, Ma Y, Klein HU et al (2020) BIN1 protein isoforms are differentially expressed in astrocytes, neurons, and microglia: neuronal and astrocyte BIN1 are implicated in tau pathology. Mol Neurodegener. https://doi.org/10.1186/s13024-020-00387-3
62. Ubelmann F, Burrinha T, Salavessa L, Gomes R, Ferreira C, Moreno N et al (2017) Bin1 and CD2AP polarise the endocytic generation of beta-amyloid. EMBO Rep 18:102–122. https://doi.org/10.15252/embr.201642738
63. Udayar V, Buggia-Prévot V, Guerreiro RL, Siegel G, Rambabu N, Soohoo AL et al (2013) A Paired RNAi and RabGAP overexpression screen identifies Rab11 as a regulator of β-amyloid production. Cell Rep 5:1536–1551. https://doi.org/10.1016/j.celrep.2013.12.005
64. Wang T, Montell C (2007) Phototransduction and retinal degeneration in Drosophila. Pflugers Arch 454:821–847. https://doi.org/10.1007/s00424-007-0251-1
65. Wigge P, Köhler K, Vallis Y, Doyle CA, Owen D, Hunt SP et al (1997) Amphiphysin heterodimers: potential role in clathrin-mediated endocytosis. Mol Biol Cell 8:2003–2015
66. Woodruff G, Reyna SM, Dunlap M, Van Der Kant R, Callender JA, Young JE et al (2016) Defective transcytosis of APP and lipoproteins in human iPSC-derived neurons with familial Alzheimer's disease mutations. Cell Rep 17:759–773. https://doi.org/10.1016/j.celrep.2016.09.034
67. Zelhof AC, Bao H, Hardy RW, Razzaq A, Zhang B, Doe CQ (2001) Drosophila Amphiphysin is implicated in protein localization and membrane morphogenesis but not in synaptic vesicle endocytosis. Development 128:5005–5015
68. Zhang J, Schulze KL, Robin Hiesinger P, Suyama K, Wang S, Fish M et al (2007) Thirty-one flavors of Drosophila Rab proteins. Genetics 176:1307–1322. https://doi.org/10.1534/genetics.106.066761
69. Zhou Y, Hayashi I, Wong J, Tugusheva K, Renger JJ, Zerbinatti C (2014) Intracellular clusterin interacts with brain isoforms of the bridging integrator 1 and with the microtubule-associated protein Tau in Alzheimer's disease. PLoS ONE 9:e103187. https://doi.org/10.1371/journal.pone.0103187

Publisher's Note

Springer Nature remains neutral with regard to jurisdictional claims in published maps and institutional affiliations.

Ready to submit your research? Choose BMC and benefit from:

- fast, convenient online submission
- thorough peer review by experienced researchers in your field
- rapid publication on acceptance
- support for research data, including large and complex data types
- gold Open Access which fosters wider collaboration and increased citations
- maximum visibility for your research: over 100M website views per year

At BMC, research is always in progress.

Learn more biomedcentral.com/submissions

BMC

Article III

3. Alzheimer's disease risk gene BIN1 modulates neural network activity through the regulation of L-type calcium channel expression in human induced neurons

Orthis Saha#, Ana Raquel Melo de Farias#, Alexandre Pelletier#, Dolores Siedlecki-Wullich, Johanna Gadaut, Bruna Soares Landeira, Arnaud Carrier, Anaïs-Camille Vreulx, Karine Guyot, Amelie Bonnefond, Philippe Amouyel, Cláudio Marcos Queiroz, DevrimKilinc, Fabien Delahaye, Jean-Charles Lambert and Marcos R.Costa

 # Equal contributions

Molecular Neurodegeneration, 2023 (under review)

3.1. Context and objectives

In summary, the objective of this study is to reveal the functions of the BIN1 gene in human iPSC-derived neural cells and its potential contribution to Alzheimer's disease pathology. For this, we employ diverse techniques, including single-cell RNA sequencing, biochemical assays, immunocytochemistry, and multi-electrode array (MEA) electrophysiology. We demonstrate that BIN1 affects calcium regulation, electrical activity, and gene expression in brain cells, implying that approved drugs targeting calcium regulation could be a potent therapeutic for Alzheimer's disease.

3.2. Personal contributions to the work

In this study, I participated in various aspects of the experimental investigation, including the differentiation of BIN1 WT and KO human iPSCs into neurons/astrocytes using a 2D model and the generation of cerebral organoids from the different BIN1 genotypes, followed by their subsequent characterization. As well, I extracted protein material from the 2D and 3D cultures and performed the immunoblotting analyses. Furthermore, I performed and analyzed several of the calcium imaging recordings to access the impact of BIN1 on calcium transients.

Molecular Neurodegeneration

The Alzheimer's disease risk gene BIN1 modulates neural network activity via the regulation of L-type calcium channel expression in human-induced neurons

--Manuscript Draft--

Manuscript Number:	
Full Title:	The Alzheimer's disease risk gene BIN1 modulates neural network activity via the regulation of L-type calcium channel expression in human-induced neurons
Article Type:	Research article
Funding Information:	

European Union under the European Regional Development Fund (ERDF) (18006176)	Dr. Marcos Romualdo Costa
Conseil Régional Hauts-de-France (18006176)	Dr. Marcos Romualdo Costa
Métropole de Lille (18006176)	Dr. Marcos Romualdo Costa
French state (2018-3-CTRL_IPL_Phase2)	Dr. Marcos Romualdo Costa
Fondation pour la Recherche Médicale (ALZ201912009628, ALZ201906008477)	PhD Jean-Charles Lambert
French RENATECH network (P-18-02737)	PhD Jean-Charles Lambert
PTR-MIAD (377)	Dr. Marcos Romualdo Costa
Fondation pour la Recherche sur Alzheimer (PYKAD-2022)	Dr. Marcos Romualdo Costa

Abstract:

Background: Bridging Integrator 1 (BIN1) is the second most important Alzheimer's disease (AD) risk gene, but its physiological roles in neurons and its contribution to brain pathology remain largely elusive. In this work, we show that BIN1 plays a critical role in the regulation of calcium homeostasis, electrical activity, and gene expression of glutamatergic neurons.

Methods: We generated 3D cerebral organoids and 2D enriched neuronal cell cultures from isogenic BIN1 wild-type (WT), heterozygous (HET) and homozygous knockout (KO) human-induced pluripotent stem cells (hiPSCs). Using single-cell RNA-sequencing, biochemical assays, immunocytochemistry and multi-electrode array(MEA) electrophysiology, we characterized the molecular and functional consequences of reduced BIN1 expression in different neural cell types.

Results: We show that BIN1 is mainly expressed by oligodendrocytes and glutamatergic neurons of cerebral organoids, like in the human brain. Both BIN1 HET and KO cerebral organoids show specific transcriptional alterations, mainly associated with ion transport and synapses in glutamatergic neurons. We then demonstrate that BIN1 cell-autonomously regulates gene expression in glutamatergic neurons by using a novel protocol to generate pure culture of human-derived induced neurons (hiNs). Using this system, we also show that BIN1 plays a key role in the regulation of neuronal calcium transients and electrical activity via its interaction with the L-type voltage-gated calcium channel Cav1.2. BIN1 KO hiNs show reduced activity-dependent internalization and higher Cav1.2 expression compared to WT hiNs. Pharmacological treatment with clinically relevant doses of nifedipine, a calcium channel blocker, partly rescues neuronal electrical and gene expression alterations in BIN1 KO glutamatergic neurons. Further, we show that transcriptional alterations in BIN1 KO hiNs affecting biological processes related to calcium homeostasis are also present in glutamatergic neurons of the human brain at late stages of AD pathology.

Conclusions: Together, our findings suggest that BIN1-dependent alterations in neuronal properties could contribute to AD pathophysiology and that treatment with low doses of clinically approved calcium blockers should be considered as an option to dampen disease onset and progression.

Corresponding Author:

Marcos Romualdo Costa, M.D./Ph.D.
Inserm
Lille, Non United States Or Canada FRANCE

Powered by Editorial Manager® and ProduXion Manager® from Aries Systems Corporation

Corresponding Author Secondary Information:	
Corresponding Author E-Mail:	marcos.costa@pasteur-lille.fr
Corresponding Author's Institution:	Inserm
Corresponding Author's Secondary Institution:	
First Author:	Orthis Saha
First Author Secondary Information:	
Order of Authors:	Orthis Saha
	Ana Raquel Melo de Farias
	Alexandre Pelletier
	Dolores Siedlecki-Wullich
	Bruna Soares Landeira
	Johanna Gadaut
	Arnaud Carrier
	Anaïs-Camille Vreulx
	Karine Guyot
	Amelie Bonnefond
	Philippe Amouyel
	Devrim Kilinc
	Cláudio Marcos Queiroz
	Fabien Delahaye
	Jean-Charles Lambert
	Marcos Romualdo Costa, M.D./Ph.D.
Order of Authors Secondary Information:	
Opposed Reviewers:	
Additional Information:	
Question	**Response**
Is this study a clinical trial?<hr>A clinical trial is defined by the World Health Organisation as 'any research study that prospectively assigns human participants or groups of humans to one or more health-related interventions to evaluate the effects on health outcomes'.	No

Manuscript

Click here to access/download;Manuscript;Saha et al_MolNeurodeg_submission.pdf

Click here to view linked References

The Alzheimer's disease risk gene *BIN1* modulates neural network activity via the regulation of L-type calcium channel expression in human-induced neurons

Orthis Saha[1,#], Ana Raquel Melo de Farias[1,2,#], Alexandre Pelletier[3,#,&], Dolores Siedlecki-Wullich[1], Johanna Gadaut[1], Bruna Soares Landeira[1], Arnaud Carrier[3], Anaïs-Camille Vreulx[1], Karine Guyot[1], Amelie Bonnefond[3], Philippe Amouyel[1], Cláudio Marcos Queiroz[2], Devrim Kilinc[1], Fabien Delahaye[3], Jean-Charles Lambert[1] and Marcos R. Costa[1,2,*]

1. Univ. Lille, Inserm, CHU Lille, Institut Pasteur de Lille, U1167-RID-AGE facteurs de risque et déterminants moléculaires des maladies liées au vieillissement, DISTALZ, Lille, France
2. Brain Institute, Federal University of Rio Grande do Norte, Natal, Brazil
3. Univ. Lille, Inserm, CNRS, CHU Lille, Institut Pasteur de Lille, U1283-UMR 8199 EGID, Lille, France

[#]Equal contribution

[&]Current address: The Department of Pharmacology, Physiology & Biophysics. Boston University, Chobanian & Avedisian School of Medicine, MA 02118

* Correspondence should be addressed to:

Marcos Costa, MD, PhD

INSERM UMR1167

Institut Pasteur de Lille

1 rue du Pr. Calmette

59019 Lille CEDEX, France

Tel: 00 33 (0)3 20 87 77 10

marcos.costa@pasteur-lille.fr

Keywords : Human induced neurons ; cerebral organoids ; BIN1 ; neuronal electrical activity ; gene expression ; Alzheimer's disease ; calcium homeostasis

Abstract

Background: Bridging Integrator 1 (*BIN1*) is the second most important Alzheimer's disease (AD) risk gene, but its physiological roles in neurons and its contribution to brain pathology remain largely elusive. In this work, we show that BIN1 plays a critical role in the regulation of calcium homeostasis, electrical activity, and gene expression of glutamatergic neurons.

Methods: We generated 3D cerebral organoids and 2D enriched neuronal cell cultures from isogenic *BIN1* wild-type (WT), heterozygous (HET) and homozygous knockout (KO) human-induced pluripotent stem cells (hiPSCs). Using single-cell RNA-sequencing, biochemical assays, immunocytochemistry and multi-electrode array(MEA) electrophysiology, we characterized the molecular and functional consequences of reduced BIN1 expression in different neural cell types.

Results: We show that *BIN1* is mainly expressed by oligodendrocytes and glutamatergic neurons of cerebral organoids, like in the human brain. Both *BIN1* HET and KO cerebral organoids show specific transcriptional alterations, mainly associated with ion transport and synapses in glutamatergic neurons. We then demonstrate that *BIN1* cell-autonomously regulates gene expression in glutamatergic neurons by using a novel protocol to generate pure culture of human-derived induced neurons (hiNs). Using this system, we also show that BIN1 plays a key role in the regulation of neuronal calcium transients and electrical activity via its interaction with the L-type voltage-gated calcium channel $Cav_{1.2}$. *BIN1* KO hiNs show reduced activity-dependent internalization and higher $Cav_{1.2}$ expression compared to WT hiNs. Pharmacological treatment with clinically relevant doses of nifedipine, a calcium channel blocker, partly rescues neuronal electrical and gene expression alterations in *BIN1* KO glutamatergic neurons. Further, we show that transcriptional alterations in *BIN1* KO hiNs affecting biological processes related to calcium homeostasis are also present in glutamatergic neurons of the human brain at late stages of AD pathology.

Conclusions: Together, our findings suggest that BIN1-dependent alterations in neuronal properties could contribute to AD pathophysiology and that treatment with low doses of clinically approved calcium blockers should be considered as an option to dampen disease onset and progression.

Introduction

The Bridging Integrator 1 (*BIN1*) is the second most associated genetic determinant with the risk of late-onset Alzheimer's disease (LOAD), after the Apolipoprotein E (*APOE*) gene [1–4]. In the adult human brain, *BIN1* is mainly expressed by oligodendrocytes, microglial cells and glutamatergic neurons [5–7] and its expression is reduced in AD patients compared to healthy individuals [7,8]. The consequences of this reduced BIN1 expression to neuronal and glial cells, as well as the mechanisms by which it contributes to AD pathogenesis remain poorly understood.

BIN1 has disputably been associated with amyloidopathy and tauopathy, two pathological hallmarks of AD [9]. Reduced BIN1 expression results in a higher amyloid precursor protein (APP) processing towards the production of amyloid-beta (Aβ) peptides in Neuroblastoma Neuro2a cells [10,11]. However, we previously showed that *BIN1* knockout (KO) does not increase the concentrations of Aβ peptides in hiPSC-derived neurons (human-induced neurons or hiNs) despite impairing endocytic trafficking [12]. Likewise, reduced Bin1 expression in the mouse brain does not affect the production of endogenous Aβ peptides [13]. Concerning Tau pathology, decreased expression of the BIN1 ortholog Amph suppress Tau-mediated neurotoxicity in Drosophila Melanogaster [14]. In contrast, reduced BIN1 expression results in higher Tau aggregation and propagation in primary rat hippocampal neurons [15]. In humans, higher concentrations of phosphorylated Tau are observed in the cerebrospinal fluid of patients with AD and are significantly correlated with genetic variants within the *BIN1* locus [16].

More recently, BIN1 has also been associated with the regulation of synaptic transmission and neuronal electrical activity in animal models. Conditional deletion of *Bin1* in neurons of the adult mice hippocampus leads to altered frequency of mini excitatory post-synaptic currents (mEPSC), likely due to an impaired presynaptic release probability and slower depletion of neurotransmitters [6]. Knockdown of *BIN1* in embryonic rat primary cortical neurons also affects the glutamate AMPA receptor trafficking in the post-synaptic compartment, leading to alterations in the amplitude of mEPSC [17]. Lastly, overexpression of a BIN1-mKate2 fusion protein increases the frequency of spontaneous excitatory postsynaptic currents (sEPSCs) in embryonic rat hippocampal cultures, seemingly by affecting

the localization of L-type voltage gated calcium channels (LVGCC) in the membrane through a Tau-dependent interaction [18].

Despite these advances, no consensus has been reached on the roles of BIN1 in AD pathogenesis and even its physiological functions in human brain cells remain mostly unknown. In this work, we tackled this important question by generating and characterizing human neural cells derived from isogenic *BIN1* wild type (WT), heterozygous (HET) and homozygous knockout (KO) hiPSC lines. We first characterized the transcriptional profile of human neural cells grown in three-dimensional cerebral organoids for more than 6 months and show that reduced BIN1 expression affects mainly glutamatergic neurons. Next, we generated pure *BIN1* WT and KO hiNs cultures and show that BIN1 cell-autonomously regulates electrical activity and gene expression of glutamatergic neurons via the interaction with the regulation of the LVGCC $Cav_{1.2}$. Pharmacological blockage of this channel with nifedipine partly rescues electrical and gene expression alterations in *BIN1* KO hiNs. Our findings suggest that BIN1 is a key regulator of calcium homeostasis in glutamatergic neurons and that repurposing the use of clinically approved calcium channel blockers could be a promising strategy to treat AD.

Results

BIN1 HET and KO cerebral organoids show transcriptional alterations associated with neuronal functional properties

Cerebral organoids (COs) faithfully recapitulate fundamental aspects of the three-dimensional organization of the human brain, including the molecular specification of different neural cell types/subtypes and the generation of complex electrical activity patterns [19,20]. To investigate the potential role of BIN1 in human neural cells, we generated and characterized COs using isogenic *BIN1* wild type (WT), heterozygous (HET) and KO hiPSCs (Fig. 1A). After 6.5 months of culture, COs were composed of all the major neural cell types identified by the expression of MAP2, GFAP and NESTIN and we did not observe any gross difference in size or morphology of COs among the three genotypes (Sup. Fig. 1A). Western blot analyses confirmed the reduction and absence of BIN1 protein in BIN1 HET and KO COs, respectively (Sup. Fig. 1B). We have then employed single-nucleus RNA sequencing (snRNA-seq) to further characterize individual cell types/subtypes and investigate possible gene expression alterations associated with reduced BIN1 expression. COs (n=4 from each genotype) were divided into two halves that were independently processed for western blotting or snRNA-seq. We observed similar expression of general neuronal and glial proteins in these COs (Sup. Fig. 1C), suggesting a low degree of heterogeneity in these samples. Nevertheless, to further reduce potential batch effects, we pooled COs into a single multiplexed library using Cell Hashing (Stoeckius et al., 2018). After sequencing, quality control and demultiplexing, we recovered 4398 singlets that could be grouped into 7 major cell clusters based on the expression of cell type markers *SLC1A3 (GLAST), GFAP* and *TNC* (astrocyte); *SNAP25, DCX, MAPT* (pan-neuronal); *SLC17A7* and *SLC17A6* (glutamatergic neurons); *DLX1, GAD1* and *GAD2* (GABAergic neurons); *HES6, CCND2* and *CDK6* (NPCs); *ITGA8* (choroid plexus); and *CLIC6* (pigmented epithelium) (Fig. 1B-C). *BIN1* expression in COs was mainly detected in glutamatergic neurons and oligodendrocytes (Fig. 1C), similar to the profile described for the human brain [7] - except for brain microglial cells that express *BIN1* but are not present in COs. We also observed a reduction and enlargement, respectively, in the proportions of glutamatergic neurons and astrocytes in *BIN1* KO compared to WT (Fig. 1D; ****p<0.0001; Chi-square test).

To identify possible differentially expressed genes (DEGs) in *BIN1* KO or HET compared to WT cells, we performed Wilcoxon test for each major cell type/subtype identified in COs. Consistent with the predominant expression of *BIN1* in glutamatergic neurons (Fig. 1D), we identified a high number of DEGs in this cell type both in *BIN1* HET (76 genes) and KO (124 genes) compared to WT genotype (Fig. 1E; Sup. Fig. 1D). In astrocytes, we also detected 75 DEGs in *BIN1* KO, but only 6 DEGs in *BIN1* HET compared to WT (Fig. 1E; Sup. Fig. 1D). For all other cell types, we observed a maximum of 1-4 DEGs in the comparison between KO vs WT or HET vs WT (Sup. Table 1). These observations suggest that both BIN1 null (KO) and partial deletion (HET) affect similar biological process in glutamatergic neurons in a dose-dependent manner. Accordingly, similar GO terms were enriched for DEGs identified in *BIN1* KO or HET glutamatergic neurons, including several terms associated with synaptic transmission (Fig. 1F). For *BIN1* KO glutamatergic neurons, we also identified GO terms associated with ion channel complex and calcium ion binding (Sup. Fig. 1E; Sup. Table 2), further suggesting that BIN1 depletion leads to specific transcriptional changes associated with functional properties of this neuronal subtype.

Altered expression of activity-related genes in *BIN1* KO and HET COs

Neuronal firing patterns (such as tonic and burst firing) play a key role on the transcriptional regulation of a particular set of genes designated activity-related genes (ARGs) [21]. While neurons stimulated with brief patterns of electrical activity transcribe rapid primary response genes (rPRGs) or early response genes (ERGs), those stimulated with sustained patterns of electrical activity express delayed primary response genes (dPRGs), secondary response genes (SRGs) or late response genes (LRGs) (Fig. 2A)[22,23]. Using Cell-ID [24], we quantified the enrichment for ARGs signatures (Sup. Table 3) in COs at single-cell resolution as an indirect read-out of neuronal electrical activity patterns in this model. We first confirmed that ARG signatures were predominantly enriched in neurons (Fig. 2B). Then, we quantified the proportion of glutamatergic or GABAergic neurons significantly enriched for such specific response gene signatures ($p_{adj}<0.05$; hypergeometric test). We observed a significantly higher proportion of glutamatergic neurons enriched for dPRGs and LRGs both in *BIN1* HET and KO, as well as SRGs in *BIN1* KO compared to WT glutamatergic neurons, whereas the proportion of glutamatergic neurons enriched for rPRGs and ERGs was reduced in *BIN1* HET and KO (Fig. 2C). In sharp contrast, the only difference observed in GABAergic neurons

was a reduction in the proportion of cells enriched for SRGs (Sup. Fig. 2). These results suggest that reduced BIN1 expression in glutamatergic neurons triggers neuronal firing patterns towards sustained activity leading to a higher expression of late-response ARGs.

Lower numbers of synaptic *puncta* in BIN1 HET and KO COs compared to WT

Transcriptional alterations in *BIN1* HET and KO glutamatergic neurons are also suggestive of synaptic dysfunction, which is an early hallmark of AD pathology [25]. We thus sought to determine whether BIN1 depletion could affect synaptic connectivity in COs. Using immunohistochemistry to detect the expression of the pre-synaptic protein Synaptohysin-1 (SYP) and post-synaptic protein HOMER1, we were able to quantify the frequency of putative synaptic contacts (% SYP assigned) in COs (see methods). We observed a significant reduction in the % of SYP assigned both in *BIN1* HET and KO compared to WT, mainly due to a reduction in the number of post-synaptic spots expressing HOMER1 (Fig. 3A-D).

Next, we investigated whether APP processing and Tau phosphorylation, which have been previously associated with BIN1 and are known to modulate neuronal electrical activity [10,15,26], could also be altered in *BIN1* HET and KO COs. To this end, we measured the intracellular levels of full-length APP and APP β-CTF (as a readout of amyloidogenic APP processing), total and phosphorylated TAU proteins by western blotting. Besides a trend for reduced TAU expression (Fig. 3F) likely explained by the reduced proportion of neurons, we did not detect any significant differences in the intracellular levels of APP, APP β-CTF, TAU or phospho-TAU (Ser202, Thr205) in *BIN1* HET and KO compared to WT COs (Fig. 3E-L). Altogether, these results suggest that BIN1 depletion could alter neuronal functional properties without significantly affecting APP or Tau metabolism in COs.

Cell-autonomous role of BIN1 in the regulation of neuronal gene expression

Our results in COs suggest that reduced BIN1 expression affects mainly glutamatergic neurons. However, at least in BIN1 KO COs, we cannot completely rule out an effect of BIN1 deletion in astrocytes that could indirectly impact glutamatergic neurons. Therefore, to unambiguously probe the cell-autonomous effect of *BIN1* deletion on the electrical activity and gene expression of human glutamatergic neurons, we generated *BIN1* WT or KO pure neuronal cultures by direct lineage-reprogramming of human NPCs (hNPCs) using doxycycline-inducible expression of ASCL1 (Fig. 4A; see online methods). After validation of

the efficient lineage-reprogramming of hNPCs into highly pure neurons (hereafter ASCL1-hiNs) (Fig. 4B), we added exogenous human cerebral cortex astrocytes to trophically support functional neuronal maturation and synaptic connectivity [27]. Using snRNA-seq after 4 weeks of differentiation we identified 5583 cells (n=5 independent culture batches) clustered into two main glutamatergic neuron (GluNeu-I and II), one GABAergic neuron (GABANeu), one immature/unspecified neuron (UnspNeu), two astrocyte (Astro-I and II) and 1 proliferative NPC groups (Fig. 4C-D). Sample-level differential gene expression analysis using DESeq2 [28], revealed 99 DEGs (|log2FC| >0.25 and FDR <0.05) in *BIN1* KO GluNeu-II compared to WT, but only 2 in GluNeu-I and 1 in immature neurons (Fig. 4E; Sup. Table 4). As observed in COs (Fig. 1H-I), GO term enrichment analysis revealed a significant enrichment for terms associated with synaptic transmission, ion channel activity and calcium signaling pathways (Fig. 4F; Sup. Table 5). The percentage of GluNeu-II enriched for late-response ARGs was slightly greater in *BIN1* KO compared to WT, but without statistical differences (Fig. 4G-H). Exogenously added human astrocytes co-cultured with *BIN1* WT and KO hiNs also showed a low number of DEGs (11 in Astro-I; Sup. Table 4), likely reflecting an astrocyte reaction to primary changes in hiNs in response to *BIN1* deletion.

BIN1 KO leads to alteration in the electrical activity pattern of ASCL1-hiNs

The transcriptional changes observed in our 2D and 3D models could suggest that reduced BIN1 expression is associated with altered electrical properties of glutamatergic neurons. To directly address this possibility, we used multi-electrode arrays (MEA) to record and quantify multi-unit activity (MUA) in ASCL1-hiNs. As previously described in spontaneously differentiated hiPSC-derived neuronal cultures [29], ASCL1-hiNs cells exhibited a diverse range of spontaneous activity patterns, including regular discharges, population bursts and period activity (Fig. 5A). In this respect, we found a conspicuous change in the temporal organization of MUA after *BIN1* deletion (Fig. 5A), mainly characterized by a greater number of spike bursts at 4 weeks (Fig. 5D). These alterations may result from changes at the single cell or the population level (different number of neurons contributing to each electrode, for example). To disentangle these possibilities, we used waveform-based spike sorting to examine the functional consequences of *BIN1* deletion at the single neuronal level (Fig. 6A). We identified a similar number of single units per recording electrode between genotypes (WT: 4.92±2.34; KO: 5.27±2.45), indicating that *BIN1* deletion does not affect the

density of active neurons within culture. However, we observed reduced single-unit activity (SUA) frequency (Fig. 6B) and higher SUA amplitude (Fig. 6C) in *BIN1* KO compared to WT ASCL1-hiNs. Interestingly, we could not detect significant changes in the number of bursts per neuron (WT: 11.01±6.71; KO: 10.36±8.59), although both the burst duration and the number of spikes within a burst were significantly lower in *BIN1* KO compared to WT ASCL1-hiNs (Fig. 6D-E). We also observed a prominent temporal disorganization of *BIN1* KO hiNs activity by computing the array-wide spike detection rate (ASDR, Fig. 6G), which reveals the strength of the synchronized population activity, and the autocorrelograms of SUAs (Fig. 6H-I), which allows the apprehension of synchronized periodicity. These analyses revealed that most spikes of *BIN1* WT neurons were organized in bursts occurring at periodic intervals of about 8-10 s, whereas the spikes of *BIN1* KO neurons were randomly distributed, leading to a higher percentage of spikes occurring outside of bursts compared to WT neurons (Fig. 6J).

Altered electrical activity of *BIN1* KO ASCL1-hiNs is associated with normal synapse numbers and altered TAU phosphorylation

These changes in neural network activity observed in *BIN1* KO hiNs could be explained, among other things, by a reduced synaptic connectivity, as observed in our long-term COs cultures (Fig. 3). To test this possibility, we first quantified the number of synaptic contacts in *BIN1* WT and KO ASCL1-hiNs cultures. In contrast with COs, we did not detect any significant differences in the number of putative synaptic contacts (% SYP assigned) in *BIN1* KO compared to WT ASCL1-hiNs, neither after 4 nor 6 weeks of differentiation (Fig. 7A-D). Next, we quantified the number and activity of glutamatergic synapses by using real-time imaging of ASCL1-hiNs expressing the glutamate sensor iGLUSnFr [30]. In accordance with our observations based on immunocytochemistry, we did not detect differences neither in the number of glutamatergic synapses (active spots) nor in the frequency of events (change in fluorescence levels in active spots) in *BIN1* KO compared to WT ASCL1-hiNs (Sup. Fig. 3; Sup. Movies 1 and 2), indicating that changes in neuronal activity observed in our cultures are not related to changes in synaptic transmission.

Taking advantage of this culture system comprising enriched neuronal populations, we also sought to confirm whether BIN1 deletion could be associated with changes in APP processing or Tau phosphorylation. To this end, we measured the extracellular levels of amyloid-beta (Aβ) peptides, as well as the intracellular levels of full-length APP and APP β-

CTF, total and phosphorylated TAU proteins in ASCL1-hiNs cultures. Like COs, we did not detect any significant differences neither in the extracellular levels of Aβ1-x or Aβ1-42, nor in the intracellular levels of APP or APP β-CTF in *BIN1* KO compared to WT ASCL1-hiNs (Sup. Fig. 4). However, in contrast with our observations in COs, we observed significantly higher levels of phospho-TAU (Ser202, Thr205) relative to β-ACTIN and total TAU in in *BIN1* KO compared to WT ASCL1-hiNs (Fig. 7E-F). Together, these observations may suggest that *BIN1* deletion primarily impairs neuronal intrinsic properties regulating electrical activity and Tau phosphorylation prior to detectable changes in synaptic communication (observed only in long-term cultures) and independently of alterations in APP processing.

BIN1 regulates neuronal Ca^{2+} dynamics through LVGCCs

In neurons, electrical activity is always accompanied by an influx of Ca2+ ions, which play a fundamental role in the regulation of neuronal firing and activity-dependent gene transcription [31]. We therefore postulated that reduced BIN1 expression in human glutamatergic neurons could affect Ca2+ dynamics, as previously suggested for cardiomyocytes [32]. To directly test this possibility, we first studied Ca^{2+} dynamics in *BIN1* WT and KO ASCL1-hiNs using real-time calcium imaging experiments. We observed spontaneous synchronous calcium transients among adjacent cells both in *BIN1* WT and KO ASCL1-hiNs cultures (Sup. Movies 3 and 4). By quantifying calcium spike transients (> 2 standard deviations above the noise level) we showed a significantly higher frequency of Ca^{2+} transients in *BIN1* KO compared to WT ASCL1-hiNs (Fig. 8A,B and D). Moreover, the dynamics of individual Ca^{2+} transients in *BIN1* KO were qualitatively different from WT ASCL1-hiNs (Fig. 8C). These differences could be quantitatively measured by a longer time to reach the maximum intracellular Ca^{2+} levels and to recover baseline levels (Fig. 8E-F).

In human heart failure, BIN1 expression is reduced, leading to an impairment in Cav1.2 trafficking, calcium transients, and contractility (Hong et al., 2012). Thus, we sought to determine if BIN1 could also interact and regulate LVGCC expression in human neurons. To that, we performed proximity ligation assay (PLA) to probe a possible interaction between BIN1 and $Cav1_{.2}$ or $Cav_{1.3}$, the two LVGCCs expressed in ASCL1-hiNs (Sup. Fig. 5). We observed a widespread BIN1-$Cav_{1.2}$ PLA signal (Fig. 8G) and, to a lesser extent, a BIN1-$Cav_{1.3}$ PLA signals in neurons (Sup. Fig. 5). Next, we quantified neuronal LVGCC protein by western blotting and observed higher total $Cav_{1.2}$ expression in *BIN1* KO compared to WT ASCL1-hiNs (Fig. 8H-I).

Protein expression of neither $Cav_{1.3}$, nor the members of the Cav_2 family ($Cav_{2.1}$, $Cav_{2.2}$ and $Cav_{2.3}$) were altered in the same cultures (Sup. Fig. 5), suggesting a specific regulation of $Cav_{1.2}$ expression by BIN1.

Notably, LVGCCs are key regulators of neuronal firing [29] and activity-dependent internalization of these channels is a key mechanism in firing homeostasis [33]. We thus set out to investigate whether *BIN1* deletion could impair this mechanism in human neurons. We stimulated ASCL1-hiNs with KCl 65nM for 30 min to induce neuronal depolarization and collected total and endosomal proteins for analysis. We confirmed a higher global level of $Cav_{1.2}$ in *BIN1* KO compared to WT ASCL1-hiNs that was independent of KCl treatment (Fig. 8J). However, $Cav_{1.2}$ expression in the endosomal fraction was 50% higher after KCl treatment in *BIN1* WT, whereas this rise was only of 10% in *BIN1* KO ASCL1-hiNs (Fig. 8K). This effect was specific for $Cav_{1.2}$ since both early endosome antigen 1 (EEA1) and $Cav_{1.3}$ expression rose in both *BIN1* WT and KO ASCL1-hiNs at similar levels after KCl treatment (Fig. 8K). Altogether, these results indicate that BIN1 regulates activity-dependent internalization and expression of $Cav_{1.2}$ in human neurons.

Treatment with the calcium channel blocker nifedipine partly rescues electrical and gene expression alterations in *BIN1* KO ASCL1-hiNs

To investigate whether the network dysfunctions observed in *BIN1* KO ASCL1-hiNs may be related to the higher expression of $Cav_{1.2}$, we treated these cells with a physiologically relevant concentration (50nM) of the $Cav_{1.2}$ blocker nifedipine [34]) for 2 weeks and recorded neuronal activity using MEA electrophysiology. We observed a partial recovery of the oscillatory pattern of neuronal electrical activity observed in WT cells (Fig. 9A). Interestingly, the percentage of spikes outside bursts was not affected by nifedipine treatment in *BIN1* WT but was significantly lower in *BIN1* KO ASCL1-hiNs (Fig. 9B), indicating a partial recovery of burst organization. To note, no difference in firing rates was observed whatever the models and conditions (Fig. 9C). After 2 weeks of nifedipine treatment (4 weeks of differentiation), we also performed snRNA-seq experiments and recovered a total of 1537 cells (n= 2 independent culture batches), which were mapped into the 7 clusters described before (Fig. 4; Sup. Figure 6). Using Wilcoxon test, we found that nifedipine treatment down-regulated several genes in *BIN1* KO ASCL1-hiNs, especially in the GluNeu-II population (Sup. Table 6). Comparison of GO term enrichments between nifedipine-treated and untreated *BIN1* KO vs

WT GluNeu-II population revealed a consistent reduction of the enrichment for several terms associated with ion channel activity and synapse transmission in nifedipine-treated BIN1 KO cells (Figure 9D; Sup. Table 7). Altogether, these data support the view that BIN1 contributes to the regulation of electrical activity and gene expression through the regulation of $Cav_{1.2}$ expression/localization in human neurons.

Molecular alterations in *BIN1* KO organoids and ASCL-hiNshiNs are also present in glutamatergic neurons of the human brain at late stages of AD pathology

We finally sought to evaluate whether molecular alterations in our neural models may recapitulate some of those observed in the brain of AD cases. For this purpose, we used a publicly available snRNA-seq dataset generated from the entorhinal cortex (EC) and superior frontal gyrus (SFG) of AD patients at different Braak stages [35]. We first observed a progressive and significant decrease in BIN1 mRNA levels in glutamatergic neurons (Fig. 10A), suggesting that reduced BIN1 expression in this cell type may be a common feature occurring in the AD pathology progression. We then compared DEGs identified in BIN1 KO glutamatergic neurons (either from COs or ASCL1-hiNs) with those identified in the same cell subtype of AD brains (Sup. Table 8). Remarkably, DEGs identified in *BIN1* KO glutamatergic neurons (either from COs or ASCL1-hiNs) showed a statistically significant overlap with DEGs detected in this cell population in AD brains at different Braak stages (Fig. 10B). In astrocytes, however, a similar significant overlap could only be observed between COs and AD brains (Fig. 10B). GO analysis based on DEG overlap between *BIN1* KO ASCL1-hiNs and AD brain glutamatergic neurons indicated significant enrichment for pathways associated with glutamate receptor activity and gated channel activity (Fig. 10C; Sup. Table 7). Similarly, DEG overlap between *BIN1* KO COs and AD brain glutamatergic neurons was significantly enriched for genes associated with glutamate receptor activity, gated channel activity and calcium ion binding (Fig. 10D; Sup. Table 7). No significant enrichment was observed for DEG overlap between *BIN1* KO COs and AD brain astrocytes (data not shown).

Discussion

In this work, we show that the AD genetic risk factor *BIN1*, plays a critical role in the regulation of neuronal firing homeostasis and gene expression in glutamatergic neurons. Complete deletion of *BIN1* gene in these neurons is sufficient to alter the expression of the LVGCC $Cav_{1.2}$, leading to altered calcium homeostasis and neural network dysfunctions in human neurons *in vitro*. These functional changes are correlated with changes in the expression of genes involved in synaptic transmission and ion transport across the membrane, as well as elevated Tau phosphorylation. In long-term neuronal cultures using COs, we show that reduced BIN1 expression is associated with fewer synapses and specific gene expression alterations in glutamatergic neurons associated with activity-dependent transcription. Notably, reduced BIN1 expression in human-induced glutamatergic neurons is sufficient to elicit gene expression alterations that are also present in AD and converge to biological processes related with calcium homeostasis. Together, our findings support the view that altered BIN1 expression in glutamatergic neurons may contribute to AD pathophysiology by dysregulating neuronal firing homeostasis via LVGCCs.

Neuronal network dysfunctions are observed in AD patients at early stages of the disease and precede or coincide with cognitive decline [36–38]. Under physiological conditions, neuronal networks can maintain optimal output through regulation of synaptic plasticity and firing rate [39]. Our results suggest that normal levels of BIN1 expression in glutamatergic neurons are fundamental to regulating neuronal firing rate homeostasis. Accordingly, *BIN1* deletion in hiNs is sufficient to dysregulate network oscillations even without impacting the number of functional synaptic contacts, suggesting that the desynchronization observed in *BIN1* KO hiNs circuits are a consequence of disordered homeostatic controls of neuronal activity. At later time-points (COs), glutamatergic neurons show both gene expression alterations indicative of altered electrical activity and reduced synaptic densities, which could indicate a synaptic down-scaling in response to earlier augmented electrical activity (Dörrbaum et al., 2020).

One key mechanism controlling neuronal spiking activity is the regulation of Ca^{2+} homeostasis [29,31,40]. Boosted neuronal electrical activity induces the turnover of LVGCCs from the plasma membrane through endocytosis [33] and regulates the transcription of genes

encoding for calcium-binding proteins and calcium-mediated signaling [41], mechanisms aiming to restore local Ca^{2+} signaling cascades and protect cells against aberrant Ca^{2+} influx. We show that BIN1 interacts with $Cav_{1.2}$ in hiNs, similar to previous findings in cardiac T tubules [32] and provide evidence supporting a novel role for BIN1 in the regulation of activity-dependent internalization of $Cav_{1.2}$ in human neurons, thus linking the known role of BIN1 in endocytosis [12] to firing homeostasis in human neurons via the LVGCC. These results confirm in human neurons the interaction between endogenous neuronal BIN1 and $Cav_{1.2}$ as previously suggested in mouse hippocampal neurons, overexpressing a Bin1-mKate fused protein [18].

Loss of Ca^{2+} homeostasis is an important feature of many neurological diseases and has been extensively described in AD [42,43]. Interestingly, DEGs identified in *BIN1* KO glutamatergic neurons in our different cell culture models are enriched for calcium-related biological processes. This is also observed for DEGs detected in glutamatergic neurons of the AD brain at late stages of pathology when the expression levels of BIN1 in those cells is also decreased. Thus, it is plausible to speculate that reduced expression of *BIN1* in glutamatergic neurons may contribute to the breakdown of Ca^{2+} homeostasis in the AD brain, potentially contributing to neuronal circuit dysfunctions. Consistent with this hypothesis, we have previously shown a significant reduction in the expression of the transcript encoding for the neuron-specific BIN1 isoform 1 in bulk RNA-sequencing data from a large number of AD patients [7] and we show in this work that *BIN1* expression is reduced in glutamatergic neurons of AD brains at late Braak stages. Moreover, it has been recently shown that Bin1 conditional knockout in neurons and glial cells of the mouse forebrain is sufficient to elicit gene expression changes associated with calcium-dependent mechanisms (Ponnusamy et al., 2022), further supporting the interpretation that BIN1 plays an important role in cellular processes involved in Ca^{2+} homeostasis in the brain.

Lastly, we show that treatment with the clinically approved calcium channel blocker nifedipine for only 2 weeks is sufficient to partly recover electrical and gene expression alterations in *BIN1* KO hiNs. These findings further support our interpretation that changes in gene expression and electrical activity observed in *BIN1* HET and KO hiNs are a direct consequence of reduced BIN1 expression in glutamatergic neurons and not a possible artifact of CRISPR/Cas9 gene-editing in our hiPSC lines. Moreover, together with our observations of reduced BIN1 expression and transcriptional alterations affecting biological processes related

to calcium homeostasis in human-induced glutamatergic neurons of the human brain at late stages of AD pathology, our data strongly support a link between BIN1 and calcium homeostasis.

Thus, it is plausible to speculate that *BIN1* depletion in glutamatergic neurons primarily undermines Ca^{2+} homeostasis, leading to changes in neuronal electrical activity. In a later stage, gene expression and circuit-level alterations such as synapse loss would occur, likely because of altered neuronal electrical activity. A corollary to this model would be that early treatments aiming to restore Ca^{2+} homeostasis and neuronal electrical activity may have a beneficial impact in AD onset and progression. Supporting this notion, both a Mendelian randomization and a retrospective population-based cohort study found evidence suggesting that treatment with Ca^{2+} channel blockers in human patients are associated with a reduced risk of AD [44,45]. In the future, it would be interesting to study the impact of these drugs for AD onset/progress as a function of genetic variants in the *BIN1* locus.

An important limitation of our work is the absence of microglial cells in our models, hampering the study of BIN1 roles in this cell type of high relevance to AD pathology [46]. However, our findings provide fundamental information about the molecular and cellular processes impacted by reduced BIN1 expression in human neurons, which will require further confirmation in the brain of patients carrying AD-related *BIN1* genetic variants. Moreover, we studied the impact of heterozygous and knockout mutations, which do not necessarily represent the consequences of AD-related *BIN1* genetic variants in gene expression. Nevertheless, it is tempting to speculate that slight changes in *BIN1* expression provoked by those variants could progressively deteriorate neuronal functions in the human brain, contributing to AD pathogenesis in the elderly brain.

Declarations

Ethics approval and consent to participate

The datasets used and/or analysed during the current study are available from the corresponding author on reasonable request.

Consent for publication

Not applicable.

Availability of data and materials

Not applicable.

Competing interests

The authors declare no competing interests.

Funding

This work was co-funded by the European Union under the European Regional Development Fund (ERDF) and by the Hauts de France Regional Council (contract no.18006176), the MEL (contract_18006176), and the French State (contract no. 2018-3-CTRL_IPL_Phase2). This work was partly supported by the French RENATECH network (P-18-02737), Fondation pour la recherche médicale (ALZ201912009628, ALZ201906008477), PTR-MIAD, Fondation Recherche Alzheimer and by the Sanofi i-Awards Europe 2019. This work was also funded by the Lille Métropole Communauté Urbaine and the French government's LABEX DISTALZ program (Development of innovative strategies for a transdisciplinary approach to Alzheimer's disease). The UMR 8199 LIGAN-PM Genomics platform (Lille, France) belongs to the 'Federation de Recherche' 3508 Labex EGID (European Genomics Institute for Diabetes; ANR-10-LABX-46) and was supported by the ANR Equipex 2010 session (ANR-10-EQPX-07-01; 'LIGAN-PM'). The LIGAN-PM Genomics platform (Lille, France) is also supported by the FEDER and the Region Nord-Pas-de-Calais-Picardie and is a member of the "France Génomique" consortium (ANR-10-INBS-009).

Authors' contributions

Conceptualization, M.R.C.; Methodology, M.R.C., F.D., D.K., C.M.Q.; Investigation, M.R.C., O.S., B.S.L., A.R.M.F., J.G., A.C., A.P., D.S.W., F.D., K.G., D.K., A.C.V., C.M.Q.; Writing - Original Draft, M.R.C.; Writing - Reviews & Editing, M.R.C., F.D., J.C.L., C.M.Q., D.K.; Figures preparation: M.R.C., F.D., A.P., B.S.L., A.R.M.F., D.K. Supervision, M.R.C., F.D., J.C.L., D.K.; Funding Acquisition, M.R.C., J.C.L., F.D, D.K., P.A., A.B. All authors have read and approved the manuscript.

Acknowledgements

The authors thank the BICeL platform of the Institut Biologie de Lille and the Vect'UB viral platform (INSERM US 005 – CNRS 3427 – TBMCore, Université de Bordeaux, France). The authors thank Karine Blary at the IEMN Lille for the microfabrication work. The Maestro Pro multiwell microelectrode array was acquired with the "Prix Claude Pompidou pour la Recherche sur l'Alzheimer (2021)" to MRC.

References

1. Lambert JC, Ibrahim-Verbaas CA, Harold D, Naj AC, Sims R, Bellenguez C, et al. Meta-analysis of 74,046 individuals identifies 11 new susceptibility loci for Alzheimer's disease. Nat Genet. Nature Publishing Group; 2013;45:1452–8.

2. Kunkle BW, Grenier-Boley B, Sims R, Bis JC, Damotte V, Naj AC, et al. Genetic meta-analysis of diagnosed Alzheimer's disease identifies new risk loci and implicates Aβ, tau, immunity and lipid processing. Nat Genet. Nature Publishing Group; 2019;51:414–30.

3. Schwartzentruber J, Cooper S, Liu JZ, Barrio-Hernandez I, Bello E, Kumasaka N, et al. Genome-wide meta-analysis, fine-mapping and integrative prioritization implicate new Alzheimer's disease risk genes. Nat Genet [Internet]. Springer US; 2021;53:392–402. Available from: http://dx.doi.org/10.1038/s41588-020-00776-w

4. Bellenguez C, Küçükali F, Jansen IE, Kleineidam L, Moreno-Grau S, Amin N, et al. New insights into the genetic etiology of Alzheimer's disease and related dementias. Nat Genet. 2022;54.

5. De Rossi P, Buggia-Prévot V, Clayton BLL, Vasquez JB, Van Sanford C, Andrew RJ, et al. Predominant expression of Alzheimer's disease-associated BIN1 in mature oligodendrocytes and localization to white matter tracts. Mol Neurodegener. BioMed Central Ltd.; 2016;11.

6. De Rossi P, Nomura T, Andrew RJ, Masse NY, Sampathkumar V, Musial TF, et al. Neuronal BIN1 Regulates Presynaptic Neurotransmitter Release and Memory Consolidation. Cell Rep [Internet]. ElsevierCompany.; 2020;30:3520-3535.e7. Available from: https://doi.org/10.1016/j.celrep.2020.02.026

7. Marques-Coelho D, Iohan L da CC, Melo de Farias AR, Flaig A, Letournel F, Martin-Négrier ML, et al. Differential transcript usage unravels gene expression alterations in Alzheimer's disease human brains. npj Aging Mech Dis. Nature Research; 2021;7.

8. Glennon EBC, Whitehouse IJ, Miners JS, Kehoe PG, Love S, Kellett KAB, et al. BIN1 Is Decreased in Sporadic but Not Familial Alzheimer's Disease or in Aging. PLoS One. 2013;8:1–11.

9. Serrano-Pozo A, Frosch MP, Masliah E, Hyman BT. Neuropathological alterations in Alzheimer disease. Cold Spring Harb Perspect Med. 2011;1:1–24.

10. Ubelmann F, Burrinha T, Salavessa L, Gomes R, Ferreira C, Moreno N, et al. Bin1 and CD 2 AP polarise the endocytic generation of beta-amyloid . EMBO Rep. 2017;18:102–22.

11. Miyagawa T, Ebinuma I, Morohashi Y, Hori Y, Chang MY, Hattori H, et al. BIN1 regulates

BACE1 intracellular trafficking and amyloid-β production. Hum Mol Genet. Oxford University Press; 2016;25:2948–58.

12. Lambert E, Saha O, Soares Landeira B, Melo de Farias AR, Hermant X, Carrier A, et al. The Alzheimer susceptibility gene BIN1 induces isoform-dependent neurotoxicity through early endosome defects. Acta Neuropathol Commun [Internet]. 2022;10:4. Available from: https://doi.org/10.1186/s40478-021-01285-5

13. Andrew RJ, De Rossi P, Nguyen P, Kowalski HR, Recupero AJ, Guerbette T, et al. Reduction of the expression of the late-onset Alzheimer's disease (AD) risk-factor BIN1 does not affect amyloid pathology in an AD mouse model. J Biol Chem [Internet]. NA; 2019;294:4477–87. Available from: http://dx.doi.org/10.1074/jbc.RA118.006379

14. Chapuis J, Hansmannel F, Gistelinck M, Mounier A, Van Cauwenberghe C, Kolen K V., et al. Increased expression of BIN1 mediates Alzheimer genetic risk by modulating tau pathology. Mol Psychiatry. 2013;18:1225–34.

15. Calafate S, Flavin W, Verstreken P, Moechars D. Loss of Bin1 Promotes the Propagation of Tau Pathology. Cell Rep. Elsevier B.V.; 2016;17:931–40.

16. Jansen IE, van der Lee SJ, Gomez-Fonseca D, de Rojas I, Dalmasso MC, Grenier-Boley B, et al. Genome-wide meta-analysis for Alzheimer's disease cerebrospinal fluid biomarkers. Acta Neuropathol [Internet]. Springer Berlin Heidelberg; 2022;144:821–42. Available from: https://doi.org/10.1007/s00401-022-02454-z

17. Schürmann B, Bermingham DP, Kopeikina KJ, Myczek K, Yoon S, Horan KE, et al. A novel role for the late-onset Alzheimer's disease (LOAD)-associated protein Bin1 in regulating postsynaptic trafficking and glutamatergic signaling. Mol Psychiatry. Nature Publishing Group; 2019;

18. Voskobiynyk Y, Roth JR, Cochran JN, Rush T, Carullo NVN, Mesina JS, et al. Alzheimer's disease risk gene BIN1 induces Tau-dependent network hyperexcitability. Elife. 2020;9:1–25.

19. Lancaster MA, Renner M, Martin CA, Wenzel D, Bicknell LS, Hurles ME, et al. Cerebral organoids model human brain development and microcephaly. Nature [Internet]. Nature Publishing Group; 2013;501:373–9. Available from: http://dx.doi.org/10.1038/nature12517

20. Trujillo CA, Gao R, Negraes PD, Gu J, Buchanan J, Preissl S, et al. Complex Oscillatory Waves Emerging from Cortical Organoids Model Early Human Brain Network Development. Cell Stem Cell [Internet]. Elsevier Inc.; 2019;25:558-569.e7. Available from: https://doi.org/10.1016/j.stem.2019.08.002

21. Flavell SW, Greenberg ME. Signaling Mechanisms Linking Neuronal Activity to Gene Expression and Plasticity of the Nervous System. Annu Rev Neurosci [Internet]. Annual Reviews; 2008;31:563–90. Available from: https://doi.org/10.1146/annurev.neuro.31.060407.125631

22. Tyssowski KM, DeStefino NR, Cho JH, Dunn CJ, Poston RG, Carty CE, et al. Different Neuronal Activity Patterns Induce Different Gene Expression Programs. Neuron [Internet]. Elsevier Inc.; 2018;98:530-546.e11. Available from: https://doi.org/10.1016/j.neuron.2018.04.001

23. Hrvatin S, Hochbaum DR, Nagy MA, Cicconet M, Robertson K, Cheadle L, et al. Single-cell analysis of experience-dependent transcriptomic states in the mouse visual cortex. Nat Neurosci [Internet]. 2018;21:120–9. Available from: https://doi.org/10.1038/s41593-017-0029-5

24. Cortal A, Martignetti L, Six E, Rausell A. Gene signature extraction and cell identity recognition at the single-cell level with Cell-ID. Nat Biotechnol. Nature Research; 2021;

25. Styr B, Slutsky I. Imbalance between firing homeostasis and synaptic plasticity drives early-phase Alzheimer's disease. Nat. Neurosci. Nature Publishing Group; 2018. p. 463–73.

26. Harris SS, Wolf F, De Strooper B, Busche MA. Tipping the Scales: Peptide-Dependent Dysregulation of Neural Circuit Dynamics in Alzheimer's Disease. Neuron [Internet]. Elsevier Inc.; 2020;1–19. Available from: https://doi.org/10.1016/j.neuron.2020.06.005

27. Christopherson KS, Ullian EM, Stokes CCA, Mullowney CE, Hell JW, Agah A, et al. Thrombospondins are astrocyte-secreted proteins that promote CNS synaptogenesis. Cell. 2005;120:421–33.

28. Love MI, Huber W, Anders S. Moderated estimation of fold change and dispersion for RNA-seq data with DESeq2. Genome Biol. 2014;15:1–21.

29. Plumbly W, Brandon N, Deeb TZ, Hall J, Harwood AJ. L-type voltage-gated calcium channel regulation of in vitro human cortical neuronal networks. Sci Rep. Nature Publishing Group; 2019;9.

30. Marvin JS, Scholl B, Wilson DE, Podgorski K, Kazemipour A, Müller JA, et al. Stability, affinity, and chromatic variants of the glutamate sensor iGluSnFR. Nat Methods. Nature Publishing Group; 2018;15:936–9.

31. Simms BA, Zamponi GW. Neuronal voltage-gated calcium channels: Structure, function, and dysfunction. Neuron. Cell Press; 2014. p. 24–45.

32. Hong TT, Smyth JW, Gao D, Chu KY, Vogan JM, Fong TS, et al. BIN1 localizes the L-type calcium channel to cardiac T-tubules. PLoS Biol. 2010;8.

33. Green EM, Barrett CF, Bultynck G, Shamah SM, Dolmetsch RE. The Tumor Suppressor eIF3e Mediates Calcium-Dependent Internalization of the L-Type Calcium Channel CaV1.2. Neuron [Internet]. 2007;55:615–32. Available from: https://linkinghub.elsevier.com/retrieve/pii/S0896627307005697

34. Hirasawa M, Pittman QJ. Nifedipine facilitates neurotransmitter release independently of calcium channels. Proc Natl Acad Sci U S A. 2003;100:6139–44.

35. Leng K, Li E, Eser R, Piergies A, Sit R, Tan M, et al. Molecular characterization of selectively vulnerable neurons in Alzheimer's disease. Nat Neurosci [Internet]. Springer US; 2021;24:276–87. Available from: http://dx.doi.org/10.1038/s41593-020-00764-7

36. Vossel KA, Beagle AJ, Rabinovici GD, Shu H, Lee SE, Naasan G, et al. Seizures and Epileptiform Activity in the Early Stages of Alzheimer Disease. JAMA Neurol [Internet]. 2013;70:1158–66. Available from: https://doi.org/10.1001/jamaneurol.2013.136

37. Vossel KA, Tartaglia MC, Nygaard HB, Zeman AZ, Miller BL. Review Epileptic activity in Alzheimer's disease: causes and clinical relevance [Internet]. 2017. Available from: www.thelancet.com/neurology

38. Lam AD, Deck G, Goldman A, Eskandar EN, Noebels J, Cole AJ. Silent hippocampal seizures and spikes identified by foramen ovale electrodes in Alzheimer's disease. Nat Med [Internet]. 2017;23:678–80. Available from: https://doi.org/10.1038/nm.4330

39. Turrigiano GG, Nelson SB. Homeostatic plasticity in the developing nervous system. Nat Rev Neurosci. 2004;5:97–107.

40. Frere S, Slutsky I. Alzheimer's Disease: From Firing Instability to Homeostasis Network Collapse. Neuron. Cell Press; 2018. p. 32–58.

41. Dörrbaum AR, Alvarez-Castelao B, Nassim-Assir B, Langer JD, Schuman EM. Proteome dynamics during homeostatic scaling in cultured neurons. Elife. eLife Sciences Publications Ltd; 2020;9.

42. Bezprozvanny I, Mattson MP. Neuronal calcium mishandling and the pathogenesis of Alzheimer's disease. Trends Neurosci [Internet]. Elsevier; 2008;31:454–63. Available from: https://doi.org/10.1016/j.tins.2008.06.005

43. Carvalho LI, Lambert J-C, Costa MR. Analysis of modular gene co-expression networks reveals molecular pathways underlying Alzheimer's disease and progressive supranuclear

palsy. medRxiv [Internet]. 2021;2021.09.21.21263793. Available from: http://medrxiv.org/content/early/2021/10/05/2021.09.21.21263793.1.abstract

44. Ou YN, Yang YX, Shen XN, Ma YH, Chen SD, Dong Q, et al. Genetically determined blood pressure, antihypertensive medications, and risk of Alzheimer's disease: a Mendelian randomization study. Alzheimer's Res Ther. Alzheimer's Research & Therapy; 2021;13:1–9.

45. Wu CL, Wen SH. A 10-year follow-up study of the association between calcium channel blocker use and the risk of dementia in elderly hypertensive patients. Med (United States). 2016;95.

46. Nott A, Holtman IR, Coufal NG, Schlachetzki JCM, Yu M, Hu R, et al. Brain cell type–specific enhancer–promoter interactome maps and disease-risk association. Science (80-). American Association for the Advancement of Science; 2019;366:1134–9.

47. Wagenaar DA, Pine J, Potter SM. An extremely rich repertoire of bursting patterns during the development of cortical cultures. BMC Neurosci. 2006;7:1–18.

48. Hao Y, Hao S, Andersen-Nissen E, Mauck WM, Zheng S, Butler A, et al. Integrated analysis of multimodal single-cell data. Cell [Internet]. Elsevier Inc.; 2021;184:3573-3587.e29. Available from: https://doi.org/10.1016/j.cell.2021.04.048

49. Korotkevich G, Sukhov V, Sergushichev A. Fast gene set enrichment analysis. bioRxiv. BioAr. 2019;

Figure legends

Figure 1: Similar transcriptional changes in glutamatergic neurons from 6.5-month-old *BIN1* HET and KO COs. (A) Scheme of the experimental design. (B) UMAP representation of the different cell subtypes in COs identified using snRNA-seq. (C) Dot plot representing the expression for *BIN1* and key markers used to annotate cell subtypes. (D) Proportion of cell subpopulations in the three genotypes (****p<0.0001; Chi-squared test). (E) Volcano plots representing DEGs comparing HET vs WT or KO vs WT in astrocytes and glutamatergic neurons. DEGs with adjusted p-value <0.05 and |log2FC| >0.25 are shown in red. (H) Functional enrichment analysis of DEGs commonly identified in HET and KO glutamatergic neurons. GO: gene ontology; BP: biological processes; CC: cellular components; MF: molecular function.

Figure 2: Altered expression of activity-related genes in BIN1 HET and KO glutamatergic neurons. (A) Scheme indicating the different sets of ARGs regulated by brief and sustained patterns of electrical activity [22,23]. rPRGs: rapid primary response genes; dPRGs: delayed primary response genes; SRGs: secondary response genes; ERGs: early response genes; LRGs: late response genes; Exc – glutamatergic neurons; Inh – GABAergic neurons. (B) Feature plots showing the enrichment score of single cells for ARG signatures. Enrichment scores correspond to the $-\log10(p_{adj})$ of the Cell-ID-based enrichment test. (C) Proportions of glutamatergic neurons (right) enriched for the different ARG signatures according to genotype (*p<0.05; **p<0.01; ***p<0.001; Chi-squared test).

Figure 3: Reduced synaptic numbers in BIN1 HET and KO cerebral organoids. (A) Immunohistochemistry for HOMER1 (red), SYP (green) in 6.5-month-old *BIN1* WT, HET and KO COs. Insert (A') illustrates the identification of putative synaptic contacts. (B-D) Quantifications of the SYP and HOMER1 spot density, and the percentage of SYP assigned by HOMER1 spots in *BIN1* WT, HET and KO COs ($^{\#}$p<0.1; *p<0.05; **p<0.01; Dunn's multiple comparison test; n=3 COs per genotype). (E) Western blot for total TAU protein C-terminal (TAU-C), phosphorylated (p)-TAU at Ser202, Thr205 (AT8) and β-ACTIN in 6.5-month-old COs. (F-H) Quantification of TAU-C/β-ACTIN, p-TAU/β-ACTIN and p-TAU/TAU-C levels normalized to WT ($^{\#}$p<0.1; Mann-Whitney test; n=3 COs per genotype). (I) Western blot for APP and β-

ACTIN in 6.5-month-old COs. (J-L) Quantification of APP/β-ACTIN, β-CTF/β-ACTIN and β-CTF /APP levels normalized to WT (n=3 COs per genotype).

Figure 4: Neuronal-specific BIN1 KO cell-autonomously elicit transcriptional changes. (A) Scheme of the Ascl1-induced hiNs experiments. (B) Images showing BIN1 WT and KO hiNs 7 days after the beginning of doxycycline treatment immunolabeled for neuronal markers MAP2 and TUBB3 and astrocyte marker GFAP and stained with DAPI. (C) UMAP representation of the different cell subtypes identified in ASCL1-hiNs cultures using snRNA-seq. (D) Dot plot representing expression of key markers used to annotate cell subtypes. (E) Volcano plot representing DEGs comparing BIN1 KO vs WT glutamatergic neurons (GluNeu-II). Differential expression analysis was performed using DEseq2 on the sample level gene expression matrix, including the experiment batch as covariates. DEGs with adjusted p-value <0.05 and |log2FC| >0.25 are shown in red. Gene labels are shown for calcium- and synapse-related genes. (F) Functional enrichment analysis of DEGs identified in glutamatergic neurons. Bar plots representing the top 15 the enriched GO terms in each category at adjusted p-value <0.01. (G) UMAP representing GluNeu-II enrichment for delayed Primary Response Genes (dPRGs) and Secondary Responses Genes (SRGs) (Tyssowski et al., 2018). Red point indicate enrichment with adjusted p-value<0.05, hypergeometric test using CellID. (H) Barplot of the percentage of enriched GluNeu-II cells by genotype for each gene sets.

Figure 5: *BIN1* KO ASCL-hiNs have a higher spike burst frequency compared to WT. (A) Raster plots showing MUA recorded for 1 minute in *BIN1* WT and KO ASCL1-hiNs after 4 weeks of differentiation. Each line represents one electrode localized side-by-side in our microfluidic/MEA array (as in panel A). (B-C) Quantification of the number of detected spikes at different time points (*p=0.0141; ***p=0.0006; Two-way ANOVA followed by Tukey's multiple-comparison test; n= 5 for each genotype). (D) Quantification of the number of spike bursts at different time points (**p=0.004; $^{\#}$p=0.0888; Mann-Whitney test).

Figure 6: Disorganization of neuronal activity in *BIN1* KO ASCL1-hiNs. (A) Raster plots showing the decomposition of multi-unity activity (MUA, black lines) into single-unit activity (SUA, colored lines) using spike waveform clustering. (B-E) Quantification of single-neuron firing rate (B; **p=0.0034), spike amplitude (C; *p=0.0106), burst duration (D; ****p<0.0001)

and number of spikes per burst (E; ****p<0.0001) at 4 weeks. Mann-Whitney test; n= 5 independent experiments; WT: 376 neurons; KO: 416 neurons). (F) Raster plots showing SUA recorded from 5 different electrodes of *BIN1* WT (left) or KO (right) ASCL-hiNs cultures after 4 weeks of differentiation. (G) Array-wide spike detection rate (ASDR) plots based on SUA recorded in *BIN1* WT and KO ASCL1-hiNs cultures. Each line represents one independent culture batch. (H-I) Normalized autocorrelogram heatmap (H, each line refers to one SUA) and averaged correlation (I) for all SUAs recorded in 5 independent *BIN1* WT and KO ASCL1-hiNs cultures. (J) Percentage of spikes outside of bursts (*p=0.0417, Mann-Whitney test).

Figure 7: Similar synaptic density and higher TAU phosphorylation in *BIN1* KO compared to WT ASCL1-hiNs. (A-B) Immunocytochemistry using the astrocyte marker GFAP, neuronal marker MAP2, pre-synaptic marker SYP and post-synaptic marker HOMER1 in *BIN1* WT ASCL1-hiNs after 4 weeks of differentiation in a three-chamber microfluidic device. Scale bar = 200 µm. Rectangular box in A is magnified in B, allowing the identification of putative synaptic contacts. (C-D) Fraction of SYP spots assigned by HOMER1 spots in MAP2 processes at 4 (C) and 6 weeks (D) ASCL1-hiNs cultures (n= 8 independent devices for each genotype). (E) Western blot for total TAU protein C-terminal (TAU-C), phosphorylated (p)-TAU at Ser202, Thr205 (AT8) and β-ACTIN in 4-week-old ASCL1-hiNs cultures. (F) Quantification of TAU-C/β-ACTIN and p-TAU/TAU-C levels in BIN1 KO ASCL1-hiNs normalized to WT (*p=0.0262; Mann-Whitney test).

Figure 8: Altered frequency of calcium transients in *BIN1* KO ASCL1-hiNs. (A) Snapshot of a 4-week-old ASCL1-hiNs culture labeled with Oregon green BAPTA. (B) Representative plot of fluorescence change over time in 1000 frames. (C) Representative traces showing the fluorescence changes in *BIN1* WT and KO ASCL1-hiNs. Red dashed lines indicate the time to reach the fluorescence maximal intensity (raising time - t1) and to return to baseline (recovery time - t2). (D) Quantification of calcium transients in *BIN1* WT and KO ASCL1-hiNs (****p<0.0001; Mann-Whitney test; n= 3 independent cultures for each genotype; number of active cells per condition: 754 (WT), 1006 (KO)). (E-F) Quantification of rising time (t1) and recovery time (t2) for calcium transients (**p=0.0022; ****p<0.0001; Mann-Whitney test). (G) Images showing PLA spots using anti-BIN1 and anti-$Cav_{1.2}$ antibodies in 4-week-old *BIN1* WT and KO hiNs. Cells were also immunolabeled for the neuronal marker MAP2 (green), the

astrocyte marker GFAP (white), and stained with DAPI (blue). (H) Western blot for Cav1.2 (without and with blocking peptide) and β-ACTIN in 4-week-old ASCL1-hiNs cultures. (I) Quantification of Cav1.2/β-ACTIN levels in *BIN1* WT and KO ASCL1-hiNs cultures (*p=0.0286; Unpaired t-test). (J) Western blot for $Cav_{1.2}$ and β-ACTIN in the total protein extracts from 4-week-old ASCL1-hiNs treated with KCl (+) or vehicle (-). Plot shows the quantification of $Cav_{1.2}$ normalized by β-ACTIN. (K) Western blot for $Cav_{1.2}$, $Cav_{1.3}$ and EEA1 in the endosomal protein extracts from 4-week-old ASCL1-hiNs treated with KCl (+) or vehicle (-). Plot shows the optical density of these proteins (****p<0.0001; Chi-square test).

Figure 9: Nifedipine treatment partly rescues electrical and gene expression alteration in BIN1 KO hiNs. (A) Auto-correlograms of 4-week-old *BIN1* WT and KO hiNs treated or not with 50 nM Nifedipine for 2 weeks. (B) Percentage of spikes outside of bursts (WT vs WT+NIF: **p_{adj}=0.0034; WT vs KO: *p_{adj}=0.0124; Dunn's multiple comparison test). (C) Average firing rates. (D) Comparison of the enrichment for GO terms in genes upregulated in KO vs WT and KO + nifedipine (NIF) vs WT GluNeu-II using fast gene set enrichment analysis (FGSEA). The FGSEA results are shown for the top15 GO terms with reduce enrichment in KO NIF.

Figure 10: Similar molecular alterations in *BIN1* KO hiNs and glutamatergic neurons of the AD brain. (A) Box plot representing *BIN1* mRNA in expression through different Braak stages in entorhinal cortex (EC) and superior frontal gyrus (SFG) (***p_{adj}<0.001; Wilcoxon test). (B) Dot plot representing the overlap between DEGs identified in glutamatergic neurons of the AD brain and *BIN1* KO ASCL1-hiN cultures (left) or *BIN1* KO COs (right). (C-D) Network representation of enriched GO terms in overlapping DEGs between AD brains and glutamatergic neurons in culture. Enriched GO terms were identified using over-representation test.

Supplementary data

Sup. Figure 1: Cellular and molecular characterization of 6.5-month-old cerebral organoids. (A) Immunohistochemistry for GFAP (red), MAP2 (green) and DAPI (blue) in 6.5-month-old *BIN1* WT, HET and KO COs. (B) Western blots showing the isoforms of BIN1 detected in WT, WT, the reduced expression in HET, and the absence of BIN1 protein in KO COs. (C) Western blots showing the expression of neuronal (TAU and vGLUT2) and astrocytic (GFAP) proteins in 14 individual COs at 190 days, including some of the BIN1 WT, HET and KO samples used for snRNA-seq. Note the low variability in protein expression. (D) Volcano plots representing DEGs comparing HET vs WT or KO vs WT in astrocytes and glutamatergic neurons. DEGs with adjusted p-value <0.05 and |log2FC| >0.25 are shown in red. Gene labels are shown for top 10 genes in terms of log2FoldChange and p-value. (E) (H) Functional enrichment analysis showing the top 15 significantly enriched GOs for DEGs identified in the *BIN1* KO vs WT or HET vs WT glutamatergic neurons. GO: gene ontology; BP: biological processes; CC: cellular components; MF: molecular function.

Sup. Figure 2: Reduced BIN1 expression does not enhance activity-dependent transcription in GABAergic neurons. A-B) Proportions of GABAergic neurons enriched for the different ARG signatures according to genotype (*p<0.05; **p<0.01; ***p<0.001; Chi-squared test).

Sup. Figure 3: Normal glutamatergic transmission in *BIN1* KO ASCL1-hiNs. Box plots show the number of active spots per neuron and number of events detected by time-lapse video-microscopy in 4- or 6-week-old ASCL1-hiNs cultures transduced with the glutamate sensor iGLUSnFr (4 weeks: n= 378 BIN1 WT and 266 BIN1 KO ASCL1-hiNs; 6 weeks: n= 685 BIN1 WT and 629 BIN1 KO ASCL1-hiNs).

Sup. Figure 4: Normal APP processing in *BIN1* KO ASCL1-hiNs. (A) Western blots showing the expression of APP full-length, β-CTF and β-ACTIN at 4 weeks. (B) Quantification of the ratios APP/β-ACTIN, β-CTF /β-ACTIN and β-CTF/APP (n = 5 for each genotype). (C) Quantification of soluble A$\beta_{1\text{-}x}$, A$\beta_{1\text{-}42}$ and the ratio A$\beta_{1\text{-}42}$/ A$\beta_{1\text{-}x}$ in ASCL1-hiNs cultures at 3 and 4 weeks.

Sup. Figure 5: Expression of voltage-gated calcium channels in ASCL1-hiNs. (A) Violin plots showing the mRNA levels of Cav1 and Cav2 members of the voltage-gated calcium channel families L-type, P/Q-type, N-type and R-type detected in ASCL1 hiNs. (B) Images showing PLA spots using anti-BIN1 and anti-Cav1.3 antibodies in 4-week-old *BIN1* WT hiNs. Cells were also immunolabeled for the neuronal marker MAP2 (green), the astrocyte marker GFAP (white), and stained with DAPI (blue). (C) Western blots showing the expression of Cav1.3, Cav2.1, Cav2.2, Cav2.3 and β-ACTIN in 4-week-old ASCL1h hiNs. (D) Quantification of protein expression.

Sup. Figure 6: snRNAseq of nifedipine treated ASCL1-hiNs cultures. (A) UMAP of the n=2 nifedipine experiments integrated with the other hiNs snRNA-seq experiments. (B) correlation between the differential gene expression in untreated *BIN1* KO + vehicle vs WT (x axis, DEGs are plotted in red) and in *BIN1* KO + nifedipine (nif) vs WT. Calcium- and synapse-related genes upregulated in *BIN1* KO + vehicle vs WT are labeled if the genes are not upregulated in KO + nif vs WT. (C) Plot showing the total number of DEGs identified in *BIN1* KO ASCL1-hiNs treated or not with nifedipine.

Sup. Movies 1 and 2: Time-series of 1000 frames taken from *BIN1* WT and KO ASCL1-hiNs transduced with iGLUSnFr after 2 weeks of differentiation and imaged 2 weeks later. Videos are played at 100 fps.

Sup. Movies 3 and 4: Time-series of 1000 frames taken from *BIN1* WT and KO ASCL1-hiNs after 4 weeks of differentiation and labeled with Oregon Green BAPTA and imaged. Videos are played at 100 frames per second (fps).

Sup. Table 1: DEGs identified in different cell types/subtypes of COs.

Sup. Table 2: GO terms enriched for DEGs identified in different cell types/subtypes of COs.

Sup. Table 3: List of ARGs used for hypergeometric test in Cell-ID.

Sup. Table 4: DEGs identified in different cell types/subtypes of ASCL1-hiNs cultures.

Sup. Table 5: GO terms enriched for DEGs identified in different cell types/subtypes of ASCL1-hiNs cultures.

Sup. Table 6: DEGs identified in different cell types/subtypes of ASCL1-hiNs cultures treated with nifedipine.

Sup. Table 7: GO terms enriched for DEGs identified in different cell types/subtypes of ASCL1-hiNs cultures treated with nifedipine.

Sup. Table 8: DEGs identified in different cell types/subtypes of the AD brain.

Sup. Table 9: GO terms enriched for DEGs commonly identified in *BIN1* HET or KO cells and the AD brain.

Materials and methods

Maintenance of isogenic hiPSC lines and neural induction

Isogenic hiPSCs (ASE 9109, Applied StemCell Inc. CA, USA) modified for BIN1 in exon 3 were generated by CRISPR/Cas9. Homozygous null mutants for BIN1 had a 5 bp deletion on one allele and an 8 bp deletion on the other allele. Heterozygous for BIN1 had a 1bp insertion on one allele. All hiPSCs, and all subsequent human induced neural progenitor cells (hiNPCs), hiNs, human induced astrocytes (hiAs), and cerebral organoids derived thereof, were maintained in media from Stemcell Technologies, Vancouver, Canada. Maintenance of cell cultures and organoids were done in adherence with manufacturer's protocols which can be found on the webpage of Stemcell Technologies. hiPSCs were maintained in mTeSR1 medium in non-treated cell culture dishes/plates pre-coated with vitronectin. Cell numbers and viability were recorded using a LUNA™ Automated Cell Counter.

To generate *BIN1* WT and KO hiNPCs, we used the dual SMAD-inhibition (SMADi) method (Chambers et al., 2009). Briefly, hiPSCs are cultured and passaged for 3 times in STEMdiff™ Neural Induction Medium + SMADi (Stemcell Technologies) for up to 3 weeks. After this period, hiNPCS are maintained for up to 10 passages in treated cell culture dishes pre-coated with poly-L-ornithine (PLO) and laminin (5 µg/mL), using STEMdiff™ Neural Progenitor Medium (NPM; Stemcell Technologies). PLO solution was made in water (0.001%) while laminin was diluted in PBS with Ca2+ and Mg2+.

Generation of Cerebral Organoids

Cerebral organoids (3D Cultures) were generated from *BIN1* WT, HET and KO hiPSCs using a 4-stage protocol (Lancaster et al., 2013). The first step was the Embryoid Body (EB) Formation Stage, where hiPCSc at 80%-90% confluency were detached from the Vitronectin XF substrate using Accutase (#AT-104, Innovative Cell Technologies). To form the EB, 9000 cells were plated per well in a 96-well round-bottom ultra-low attachment plate containing EB seeding medium (Stem Cell Technologies). At day 2 and day 4, EB formation media is added in the wells. After five days, the EBs were transferred to a 24-well ultra-low attachment plate containing Induction Medium (Stem Cell Technologies), where each well receives 1-2 EBs. Two days later, the EBs were ready for the Expansion Stage. The EBs were embedded in Matrigel (Corning) and transferred to a 24-well ultra-low adherent plate with Expansion

Medium (Stem Cell Technologies). After three days, the medium was replaced by Maturation Medium (Stem Cell Technologies) and the plate was placed in an orbital shaker (100 rpm speed). During this final Maturation Phase, 75% medium change was done on a biweekly basis. Organoids were allowed to mature for a period of 6.5 months.

Generation of pure human neuronal cultures from hiNPCs

We differentiated neurons from virus-transduced hiNPCs according to an adapted protocol (Zhang et al., 2013; Yang et al., 2017). Briefly, hiNPCs are first virally-transduced with the TTA lentiviral construct and a passage later, the TetO-Ascl1-Puro lentiviral construct was transduced. These cells are maintained in NPM medium and expanded prior to differentiation. For differentiation of human induced neurons (hiNs), hiNPCs are plated onto PLO/laminin-coated imaging plates at density 100,000 cells/well in NPM. After 24 h, complete BrainPhys medium (StemCell Technologies) is added 1:1 together with 2 µg/mL doxycycline (Sigma-Aldrich) to induce TetO gene expression. The following day, 1 µg/mL puromycin (Sigma-Aldrich) was added to start cell selection. After 2-3 days (depending on the efficiency of antibiotic selection), 50,000 human cortical astrocytes were added in each well with BrainPhys containing doxycycline. After 24 h, 2 µM of Ara-C (Cytosine β-D-arabinofuranoside; Sigma-Aldrich) was added to arrest the proliferation of astrocytes. Half of the medium in each well was changed biweekly with fresh BrainPhys medium containing doxycycline until the 14th day. After that, the biweekly medium change was performed only with BrainPhys. Differentiation was allowed to continue for another 2-4 weeks prior to subjecting the cells to various experimental manipulations. Human cortical astrocytes (HA; ScienCell # 1800) were sourced from ScienCell Research Laboratories, CA, USA and grown up to 10 passages on poly-l-lysine coated 75 cm^2 flasks using astrocyte medium (ScienCell # 1801) supplemented with astrocyte growth supplement (AGS, ScienCell #1852) and 10 ml of fetal bovine serum (ScienCell # 1800).

This co-culture system was characterized using snRNA-seq after 4 weeks of differentiation showing that 70% of cells (n=7120 from 5 independent culture batches) expressed the pan-neuronal markers SOX11, SNAP25, DCX and RBFOX3, with 66% of cells co-expressing the glutamatergic neuron marker SLC17A6, less than 1.5% of cells co-expressing the GABAergic neuron markers DLX1, GAD1 and GAD2, and 5% of cells co-expressing low levels of markers of both neuronal subtypes. The remaining cells, immature astrocytes (Astro-

I), mature astrocytes (Astro-II) and undifferentiated NPCs, represented about 15%, 8%, 4% of the cells, respectively. The first two cell populations likely represent two different states of astrocytes added to the cultures, whereas NPCs are likely cells that failed to reprogram into hiNs despite ASCL1 transduction. Thus, neuronal classes generated in this system comprise a large fraction of glutamatergic neurons (84%), a small proportion of GABAergic neurons (2.5%) and unspecified neurons co-expressing low levels of markers of both neuronal subtypes (13.5%).

Culture of hiNs in Microfluidic Devices

Three-compartment microfluidic neuron culture devices were used in which the presynaptic and postsynaptic chambers are connected to the synaptic chamber by respectively long and short micro-channels. Details of the microfluidic device design and fabrication have been previously described (Kilinc et al, 2020).

The homemade devices were placed individually in Petri dishes for easy handling and UV sterilized for 30 min before coating for cell adhesion. The primary surface coating consisted of poly-L-lysine (Sigma-Aldrich) at 20 µg/mL in borate buffer (0.31% boric acid, 0.475% sodium tetraborate, pH 8.5). All coated devices were incubated overnight at 37°C, 5% CO2. After a wash with DPBS, devices were then coated with 20 µg/mL laminin in DPBS and incubated overnight at 37°C in 5% CO2. The following day, devices were carefully washed once with DPBS before cell plating.

In total, 30,000 hiNPCs resuspended in NPM containing 10 µM of Y-27632 ROCK inhibitor were seeded per device, half at the entrance of the presynaptic somatic chamber and half at the entrance of the postsynaptic somatic chamber. Microfluidic devices were microscopically checked at the phase contrast to ensure the cells were correctly flowing into chambers. After a minimum of 5 minutes to allow the cells to attach, devices were filled with NPM (containing 10 µM of Y-27632 ROCK Inhibitor). Water was added to the Petri dishes to prevent media evaporation, and these were then incubated at 37°C in a humidified 5% CO2 incubator. For induced neuron culture from hiNPCs transduced for Ascl1, doxycycline (2 µg/mL) was added on the first day of half medium change to induce TetO gene expression. The following day, puromycin (1 µg/mL) was added to start cell selection. Two days after the puromycin selection, a total of 5,000 HAs (ScienCell Research Laboratories, CA, USA) were added per device. After 24 hours, Ara-C (2 µM) was added to stop their proliferation. Half of

the medium was changed twice a week with complete BrainPhys medium + 2 µg/mL doxycycline for 14 days. After that, half medium change was performed only with BrainPhys medium.

Five microfluidic devices were employed for each experimental condition (*BIN1* KO vs WT both for spontaneous neuronal differentiation and Ascl1 induction) and two independent cultures were performed. To assess the time-course effect, neuron cultures were stopped at 4 and 6 weeks.

Viral Transductions

Lentiviral constructs were produced by the Vect'UB platform within the TBM Core unit at University of Bordeaux, Bordeaux, France (CNRS UMS 3427, INSERM US 005). The lentiviral constructs used were TTA (Vect'UB; ID # 571) and TetO-Ascl1-Puro (Addgene, # 97329). Lentiviral infections were done in NPCs at P3 or P4. The viral constructs were transduced at a multiplicity of infection (MOI) of 2.5. In brief, NPCs were plated at a confluency of 1x106 cells per well of a 6-well plate. After 4 hours of plating the cells, appropriate volumes of each lentiviral construct were mixed in complete Neural Progenitor medium and 50 µl of the viral medium mix was then added to each well. We transduced the TTA construct at first in the hiNPCs. Following one passage, the TTA-transduced cells were transduced with the construct for ASCL1. Cells having both viral constructs were then further expanded for 1 or 2 passages before being used for differentiation into hiNs.

The iGluSnFR construct was an adeno-associated viral vector (BS11-COG-AAV8) sourced from Vigene Biosciences, MD, USA. The viral construct was transduced at a MOI of 5,000 at around 10 days of differentiation for the ASCL1-hiNs. Differentiation was allowed to continue for a duration of 4-6 weeks prior to MEA electrophysiology or imaging.

Immunocytochemistry and Immunohistochemistry

Bidimensional (2D) cultures: All cells were fixed in 4% (w/v) paraformaldehyde (Electron Microscopy Sciences, Catalog # 15712) for 10 minutes in the imaging plates. Following, fixation, cells were washed thrice with PBS 0.1 M. Blocking solution (5% normal donkey serum + 0.1% Triton X-100 in PBS 0.1 M) was added to fixed cells at room temperature for 1 hour under shaking conditions. After the blocking step, primary antibodies were added to cells in the blocking solution and incubated overnight at 4°C. The following day, cells were washed

with PBS 0.1 M thrice for 10 mins. Each. Alexa Fluor®--conjugated secondary antibodies in blocking solution were then incubated with the cells for 2 hours at room temperature under shaking conditions ensuring protection from light. Subsequently, 3 washes with 0.1 M PBS were done for 10 min each at room temperature under shaking conditions with protection from light. Hoechst 33258 solution was added during the second PBS wash. Cells were mounted with Aqua-Poly/Mount (Polysciences, Inc.) and imaged directly in the cell imaging plates. All images were acquired using an LSM 880 Confocal Scanning Microscope housed at the Imaging Platform of the Pasteur Institute, Lille. Duolink® Proximity Ligation Assays (PLA) was used to detect endogenous Protein-Protein Interactions. The following pairs of antibodies were used: anti-BIN1 (rabbit, 182562, abcam) and anti-Cav1.2 (mouse, 84814, abcam); or anti-BIN1 and anti-Cav1.3 (mouse, 85491, mouse). Other antibodies used for immunocytochemistry were: MAP2 (188006 and 188004, Synaptic Systems), Beta III Tubulin (MAB1637, Sigma-Aldrich), GFAP (AB5804, Millipore; and 173006, Synaptic Systems). All Alexa Fluor®-tagged secondary antibodies were sourced from Jacskon ImmunoResearch Europe Ltd.

Microfluidic Devices: Cultured induced neurons were fixed in 4% paraformaldehyde in PBS for 15 min at room temperature, washed three times with PBS, and permeabilized with 0.3% Triton X-100 in PBS for 5 min at room temperature. Cells were blocked in PBS containing 5% normal donkey serum for 1 h at room temperature before overnight incubation at 4°C with the following primary antibodies: MAP2 (188006, Synaptic Systems); HOMER1 (160004, Synaptic Systems), Synaptophysin (101011, Synaptic Systems), and GFAP (AB5804, Millipore). Cells were washed twice with PBS and incubated with the following secondary antibodies for 2h at room temperature: DyLight™ 405 Donkey Anti-Chicken (703-475-155, Jackson ImmunoResearch), Alexa Fluor 594 Donkey Anti-Guinea Pig (706-585-148, Jackson ImmunoResearch), Alexa Fluor 488 Donkey Anti-Mouse (715-545-151, Jackson ImmunoResearch) and Alexa Fluor 647 Donkey Anti-Rabbit (711-605-152, Jackson ImmunoResearch). Cells were rinsed three times with PBS and microfluidic devices were mounted with 90% glycerol.

Samples were imaged with a LSM 880 confocal microscope with a 63X 1.4 NA objective. Images were acquired at zoom 2 in z-stacks of 0.5 µm interval. Typically, 6 images were acquired per device from the synapse chamber near the postsynaptic chamber such the image

contains multiple dendrites. Images were deconvoluted using the Huygens software (Scientific Volume Imaging, Netherlands).

Cerebral Organoids: Cerebral organoids were fixed in 4% PFA (w/v) for 30 min at 4°C followed by three washes with PBS 0.1 M. Cerebral organoids were then placed in sucrose solution (30% w/v) overnight before being embedded in O.C.T (Tissue-Tek). Embedded tissue was sectioned at 20 µm using a Cryostar NX70 Cryostat (Thermo Scientific) and mounted slides were stored at −80°C until immunostaining was performed. For immunostaining, tissue sections were brought to room temperature and then rehydrated with 3 washes with 0.1 M PBS, each for 5 mins. Slides were then washed once with PBS with 0.2% Triton X-100 for 15 mins. Tissue was blocked using 10% of donkey serum in PBS 0.1 M for 1 h at room temperature. After blocking, primary antibodies were added to 0.2 % Triton X-100 and 10% of donkey serum in PBS 0.1 M at appropriate dilutions and incubated overnight at 4°C. The next day, slides were washed with PBS 0.1 M 3 times for 5 min each with gentle shaking. Subsequently, slides were incubated with Alexa Fluor®-conjugated secondary antibodies in 0.2 % Triton X-100 and 10% of donkey serum in PBS 0.1 M for 2 h at room temperature in the dark. After secondary antibody incubation, slides were washed 3 times with PBS for 5 min with gentle shanking. Nuclei were visualized by incubating the tissue for 5 min with Hoechst 33258 stain in PBS 0.1 M. Sections were mounted using aqueous mounting medium (Polysciences). Images were acquired using an LSM 880 Confocal Scanning Microscope in concert with the ZEISS ZEN imaging software housed at the Imaging Platform of the Pasteur Institute, Lille. Image acquisition was done at 40X for the various cellular markers in Fig. 1. The antibodies used were MAP2 (188006, Synaptic Systems) and GFAP (AB5804, Sigma-Aldrich).

Quantification of Synaptic Connectivity

Synaptic connectivity was quantified as previously described (Kilinc et al, 2020). Briefly, images were analyzed with Imaris software (Bitplane, Zürich, Switzerland) by reconstructing Synaptophysin I and HOMER1 puncta in 3D. The volume and position information of all puncta were processed using a custom Matlab (MathWorks, Natick, MA) program. This program assigns each postsynaptic spot to the nearest presynaptic spot (within a distance threshold of 1 µm) and calculates the number of such assignments for all presynaptic puncta.

Immunoblotting

Samples from the 2D cultures or brain organoids were collected in RIPA buffer containing protease and phosphatase inhibitors (Complete mini, Roche Applied Science) and sonicated several times at 60%-70% for 10 seconds prior to use for the immunoblotting analyses. Protein quantification was performed using the BCA protein assay (ThermoFisher Scientific). 10 µg of protein from extracts were separated in NuPAGE 4-12% Bis-Tris Gel 1.0mm (NP0321BOX, Thermo Scientific) or 3-8% Tri-Acetate gel (EA03755BOX, Thermo Scientific) and transferred on to nitrocellulose membranes 0.2µm (#1704158, Bio-Rad). Next, membranes were incubated in milk (5% in Tris-buffered saline with 0.1% Tween-20 (TBST)) or SuperBlock (37536, ThermoFisher Scientific) to block non-specific binding sites for 1 hour at room temperature, followed by several washes with TBST 0.1% or TNT 1x as washing buffers. Immunoblottings were carried out with primary antibodies overnight at 4°C under shaking condition. The membranes were washed three times in the washing buffer, followed by incubation with HRP-conjugated secondary antibodies for 2 hours at room temperature under shaking condition. The membranes were washed three times in washing buffer, and the immune reactivity was revealed using the ECL chemiluminescence system (SuperSignal, ThermoScientific) and imaged using the Amersham Imager 600 (GE Life Sciences). Optical densities of bands were quantified using the Gel Analyzer plugin in Fiji–ImageJ. The primary antibodies used for the immunoblots were as follows: BIN1 (ab182562,Abcam), APP C-terminal (A8717, Sigma-Aldrich), Tau (A002401-2, Agilent) Phospho-Tau(Clone: AT8) (MN1020,ThermoFisher Scientific), CaV1.3 (CACNA1D) (ACC-005, Alomone), CaV2.1 (CACNA1A) (ACC-001, Alomone), CaV2.2 (CACNA1B) (ACC-002, Alomone), CaV2.3 (CACNA1E) (ACC-006, Alomone), CaV1.2 (CACNA1C) (AGP-001 and ACC-003, Alomone), blocking peptide for Anti-CaV1.2 (CACNA1C) (BLP-CC003, Alomone) and β-ACTIN (A1978, Sigma-Aldrich). Secondary antibodies used for the immunoblots were Mouse-HRP (115-035-003, Jackson ImmunoResearch), Rabbit-HRP (111-035-003, Jackson ImmunoResearch), and Guinea pig-HRP (106-035-003, Jackson ImmunoResearch).

Activity-dependent endosytosis assay

ASCL1-hiNs (n=9 cultures from each genotype) were subjected to 30 min of depolarization with 65 mM KCl or a mock treatment. Cells were then collected and pulled for

endosomal fraction purification using the Minute™ Endosome Isolation and Cell Fractionation Kit (Invent Biotechnologies). Western blot was performed as described above.

AlphaLISA measurements

Cell culture media samples for AlphaLISA measurements were collected at the endof the 3rd and 4th weeks of differentiation of the ASCL1-hiNs. Alpha-LISA kits specific for human Aβ1–X (AL288C, PerkinElmer) and Aβ1–42 (AL276C, PerkinElmer) were used to measure the amount of Aβ1–X and Aβ1–42 respectively in culture media. The human Aβ analyte standard was diluted in the BrainPhys medium. For the assay, 2 µL of cell culture medium or standard solution was added to an Optiplate-384 microplate (PerkinElmer). 2 µL of 10X mixture including acceptor beads and biotinylated antibody was then added to the wells with culture media or standard solution. Following incubation at room temperature for an hour, 16 µL of 1.25X donor beads was added to respective wells and incubated at room temperature for 1 hour. Luminescence was measured using an EnVision-Alpha Reader (PerkinElmer) at 680-nm excitation and 615-nm emission wavelengths.

Calcium and iGluSnFR Imaging

Calcium imaging was performed in 2D cultures after 4 weeks (Ascl1-induced). Prior to imaging, the cells were incubated with Oregon Green™ 488 BAPTA-1 (OGB-1) acetoxymethyl (AM) (ThermoFisher Scientific) for 1 h. A 2.5 mM stock solution of the calcium-indicator dye was prepared in Pluronic™ F-127 (20% solution in DMSO) (ThermoFisher Scientific). 1 µL of the dye solution was added to 400 µL of fresh BrainPhys medium in each well of a 24-well cell imaging plate. Existing BrainPhys media from the wells of the plate was removed and kept aside while the calcium-indicator dye was incubated in fresh BrainPhys medium. After 1 h of incubation, the medium which was kept aside was replaced to each well. The 2D cultures were then ready to be imaged using a Spinning Disk Microscope (Nikon) housed at the Institut Pasteur de Lille, Lille, France using the MetaMorph imaging software.

For imaging the calcium activity, 1000 images were taken using a 20× long-distance objective, with 10 ms exposure time and 200 ms intervals. For each well, 5 random fields were chosen, and the cellular activity was recorded.

Cells transduced with iGluSnFR were directly imaged after 4 or 6 weeks of differentiation and 500 images were taken with the same imaging parameters. Up to 8 fields per well were filmed, each field containing at least one fluorescent transduced cell along with its processes.

Analyses of Calcium Transients

All live recordings of neuronal calcium transients were first converted into .avi format after background subtraction using the FIJI software. Following the conversion, the videos were subsequently opened using the free software for data analyses of calcium imaging, CALciumIMagingAnalyzer (CALIMA) made available online by Fer Radstake (Eindhoven University of Technology, The Netherlands). Each video recording of a field of cells was first downscaled to 2X in terms of size with a 10X zoom and was checked for the frame average mode. Moreover, in this first detection stage, pre-set filter parameters were adjusted and applied to enable the detection of the maximum number of fluorescent cells in each field. In the analysis tab, detection of the average activity was checked and for pre-processing, a median of 3 was applied. All cells within the pre-set filter parameters are detected as regions of interest (ROIs) in the detection stage. Cell activity from all detected ROIs is then recorded. However, in the subsequent analysis stage, only cells showing spiking frequencies with a standard deviation of at least 2 or more were taken into consideration. Data in the form of detection spikes and the correlation (peak) are extracted and exported as .csv files.

Electrophysiological recordings in 2D cultures and cerebral organoids

ASCL1-hiNs were cultured in microfluidic devices bound to multi-electrode arrays (256MEA100/30iR-ITO, Multi-Channel Systems, Germany). Extracellular action potentials were recorded in 5 different cultures for both genotypes at 2, 3, 4 and 6 weeks of differentiation using the MEA2100-256-System (Multi-Channel Systems). Before recordings, MEAs were let stabilize for 5 min on the headstage to reduce artifacts due to medium movement. Signals were recorded for 1 min, at 40 kHz sampling rate, using Multi Channel Experimenter 2.16.0 software (Multi-Channel Systems). Electrical activity in cerebral organoids was recorded using 256-6wellMEA200/30iR-ITO (Multi-Channel Systems, Germany). Briefly, 5-6-month-old cerebral organoids were mounted onto MEAs and kept for 2 h in complete Brainphys medium. Then, MEAs were placed on the headstage and let stabilize for 5 min before recordings. Signals were recorded for 5 min, at 10 kHz sampling rate

using Multi-Channel Experimenter 2.16.0. For rescue experiments using a calcium channel blocker, ASCL1-hiNs were cultured on MEA 96-well plates (CytoView MEA 96, Axion Biosystems, USA). Extracellular action potentials were recorded in 3 independent cultures for either genotype in the presence of 50nM nifedipine (Tocris Bioscience) or vehicle using the MaestroPro (Axion Biosystems, Inc, USA). Before recordings, MEAs were let stabilize for 5 min on the MaestroPro at 37°C and 5% CO_2. Signals were recorded for 3 min, at 12.5 kHz sampling rate, using AxIS Navigator software (Axion Biosystems).

Spikes were detected using a fixed amplitude threshold of 5.5 and 4.5 standard deviations (for the 2D and 3D cultures, respectively) of the high-pass filtered (>300 Hz) signal for positive- and negative-going signals. The detection included a dead time of 3 ms to account for the refractory period of action potentials. Quantification of the number of detected spikes (MUAs) and spike bursts (defined as at least 5 spikes within 50 ms) was performed using Multi-Channel Analyzer 2.16.0 software (Multi-Channel Systems).

Spike sorting and temporal structure of spontaneous activity

Channels containing detected waveforms were manually processed offline for spike waveform separation and classification using Offline Sorter v3 (Plexon, USA). Briefly, we applied principal component analysis (PCA) to cluster spike waveforms of similar morphologies. Using this approach, we identified from 2 to 10 well-isolated units per channel, and therefore, we considered this single-unit activity (SUA). For each SUA, we computed the average firing rate, the signal-to-noise ratio, the peak-to-trough amplitude and duration, the average power (square amplitude of the average waveform), the mode of the interspike interval distribution, and their firing patterns. It has been demonstrated that dissociated neuronal cultures can develop complex discharge structures [47]. Here, we considered burst activity if the SUA presents periods of high-frequency discharges interspersed by regular or no discharges at all. Operationally, a burst must have at least 3 spikes within 100 ms and 200 ms intervals, for the interval between the first and the second, and the second and the third discharge, respectively. After the third spike, the maximal interval to consider a discharge part of the burst was 200 ms. Thus, we computed the SUA that presented bursts, the number of bursts (i.e., the burst frequency), the average burst duration, the number of spikes within each burst, the average burst frequency, and the inter-burst interval. To evaluate the temporal structures of spike trains, we computed the array-wide spike detection rate (ASDR),

which is the number of spikes detected per unit of time, summed over all electrodes in the array. This method is commonly used in the literature to demonstrate synchronous activity (aka, bursts) in MUA data (Wagenaar, 2006).

snRNA-seq Library Preparation

Nuclei isolation and Hash-tagging with oligonucleotides steps were realized on ice with pre-cold buffers and centrifugations at 4°C. 6.5-month-old BIN1 WT, HET, and KO organoids were processed as previously (Lambert et al., 2022). 4-week-old cultured ASCL1-induced BIN1 WT and KO 2D cultures were washed in the imaging plate wells with 500 µL of Deionized Phosphate Buffer Saline 1X (DPBS, GIBCO™, Fisher Scientific 11590476). Cells were resuspended with wide bore tips in 500 µL Lysis Buffer (Tris-HCL 10mM, NaCl 10mM, MgCl2 3mM, Tween-20 0,1%, Nonidet P40 Substitute 0,1%, Digitonin 0,01%, BSA 1%, Invitrogen™ RNAseout™ recombinant ribonuclease inhibitor 0,04 U/µL). Multiple mechanical resuspensions in this buffer were performed for a total lysis time of 15 mins., 500 µL of washing buffer was added (Tris-HCL 10mM, NaCl 10 mM, MgCl2 3 mM, Tween-20 0.1%, BSA 1%, Invitrogen™ RNAseout™ recombinant ribonuclease inhibitor 0,04 U/µL) and the lysis suspension was centrifuged 8 mins. at 500 g (used for all following centrifugation steps). Nuclei pellets were washed tree times with one filtration step by MACS pre-separation filter 20µm (Miltenyi Biotec). Nuclei pellets were resuspended in 100 µL of staining buffer (DPBS BSA 2%, Tween-20 0.01%), 10 µL of Fc blocking reagent HumanTruStainFc™ (422302, Biolegend) and incubated 5 min at 4°C. 1µl of antibody was added (Total-Seq™-A0453 anti-Vertebrate Nuclear Hashtag 3 MAb414 for the WT and Total-Seq™-A0454 anti-Vertebrate Nuclear Hashtag 4 MAb414 for the KO, 97286 and 97287 respectively, Biolegend) and incubated 15 mins. at 4°C. Nuclei pellets were washed three times in staining buffer with one filtration step by MACS pre-separation filter 20 µm (Miltenyi Biotec) to a final resuspension in 300 µL of staining buffer for Malassez cell counting with Trypan blue counterstaining (Trypan Blue solution, 11538886, Fisherscientific). Isolated nuclei were loaded on a Chromium 10X genomics controller following the manufacturer protocol using the chromium single-cell v3 chemistry and single indexing and the adapted protocol by Biolegend for the HTO library preparation. The resulting libraries were pooled at equimolar proportions with a 9 for 1 ratio for Gene expression library and HTO library respectively. Finally, the pool was sequenced

using 100pb paired-end reads on NOVAseq 6000 system following the manufacturer recommendations (Illumina).

snRNA-seq Dataset Preprocessing

Unique Molecular Index (UMI) Count Matrices for gene expression and for Hash Tag Oligonucleotide (HTO) libraries were generated using the CellRanger count (Feature Barcode) pipeline. Reads were aligned on the GRCh38-3.0.0 transcriptome reference (10x Genomics). Filtering for low quality cells according to the number of RNA, genes detected, and percentage of mitochondrial RNA was performed. For HTO sample, the HTO matrix was normalized using centered log-ratio (CLR) transformation and cells were assigned back to their sample of origin using HTODemux function of the Seurat R Package (v4) [48]. Then, normalizations of the gene expression matrix for cellular sequencing depth, mitochondrial percentage and cell cycle phases using the variance stabilizing transformation (vst) based Seurat:SCTransform function were performed.

snRNA-seq datasets integration and annotation

To integrate the datasets from independent experiments, the harmony R package (https://github.com/immunogenomics/harmony) was used. In order to integrate the datasets, the SCTransform normalized matrices was merged and PCA was performed using Seurat::RunPCA default parameter. The 50 principal components (dimensions) of the PCA were corrected for batch effect using harmony::RunHarmony function. Then, the 30 first batch corrected dimensions were used as input for graph-based cell clustering and visualization tool. Seurat::FindNeighbors using default parameters and Seurat::FindClusters function using the Louvain algorithm were used to cluster cells according to their batch corrected transcriptomes similarities. To visualize the cells similarities in a 2-dimension space, the Seurat::RunUMAP function using default parameter was used. Cell clusters were then annotated based on cell type specific gene expression markers.

Differential gene expression and GO enrichment analyses

For snRNA-seq experiment reproduce 2 times or less (*i.e.* organoid and nifedipine experiments), gene expression within each main cell type was compared between conditions of interest using Wilcoxon test on the SCTransform normalized gene expression matrix. For

snRNA-seq experiment reproduce more than 2 times (*BIN1* KO vs WT hiNs comparison), Pseudobulk differential expression analysis was performed using the package DESeq2 (CRAN). For each main cell type, the cell level gene expression matrix was first aggregate at the sample level using Matrix:: aggregate.Matrix function. Genes detected in more than 100 cells or in 10% of the cells was test for differential expression using DESeq function, including in the model the experiment batch as covariate.

GO enrichment analysis on the differentially expressed genes was performed using the gost function of the gprofiler2 R package (CRAN), using default parameter, or, if specified using fast gene-set enrichement analysis (FGSEA, [49]) package (Bioconductor).

Activity-related genes (ARGs) signature enrichment analysis at single cell resolution

To study enrichment for activity-related genes (ARGs) signature across cerebral organoid cells, the CellID R package (https://github.com/RausellLab/CelliD) was used. ARGs obtained from Tyssowski et al. (2018) and Hravtin et al. (2018) (supplementary Table 7), were translated to the corresponding human gene name with the help of the biomaRt package using the respective Ensembl references. Then, the CellID::RunMCA was used to extract cell-specific gene signature and hypergeometric test was performed to test enrichment for ARGs in these cell signatures. To test the differential proportion of ARGs enriched cells in BIN1 deleted organoid compared to WT organoid, chi-squared test was performed.

Comparative analysis with specific DEGs in AD brains

To compare the transcriptomic change observed in BIN1 deleted cerebral organoid with those observed in AD brain we used the dataset available for download at Synapse.org under the Synapse ID syn21788402 [35]. The raw gene expression matrix was normalized using Seurat::SCTransform and differential expression analysis was performed within each neuronal cell type using Wilcoxon test as used for our organoid dataset. AD related DEGs, thus, obtained were compared with our BIN1 related organoid DEGs in every cell type. To this end, the enrichment for AD-related DEGs in BIN1-related DEGs was tested using hypergeometric test. The background for this test was defined as all genes detected in both datasets. The p-value of this test was used as metrics to compare the significance of the gene overlap between neuronal cell types.

Statistical analyses

Statistical analyses were performed using GraphPad Prism version 8.0.0 (GraphPad Software, San Diego, California USA, www.graphpad.com) and R 4.2.0 (R Core Team, 2022, https://cran.r-project.org/bin/windows/base/old/4.2.0/). Bar plots show mean ± SD and individual values. Box plots show 1-99 percentile. Statistical tests and p values are indicated in figure legends.

Figure 1

Click here to access/download;Figure;Figure 1_MolNeuro.pdf

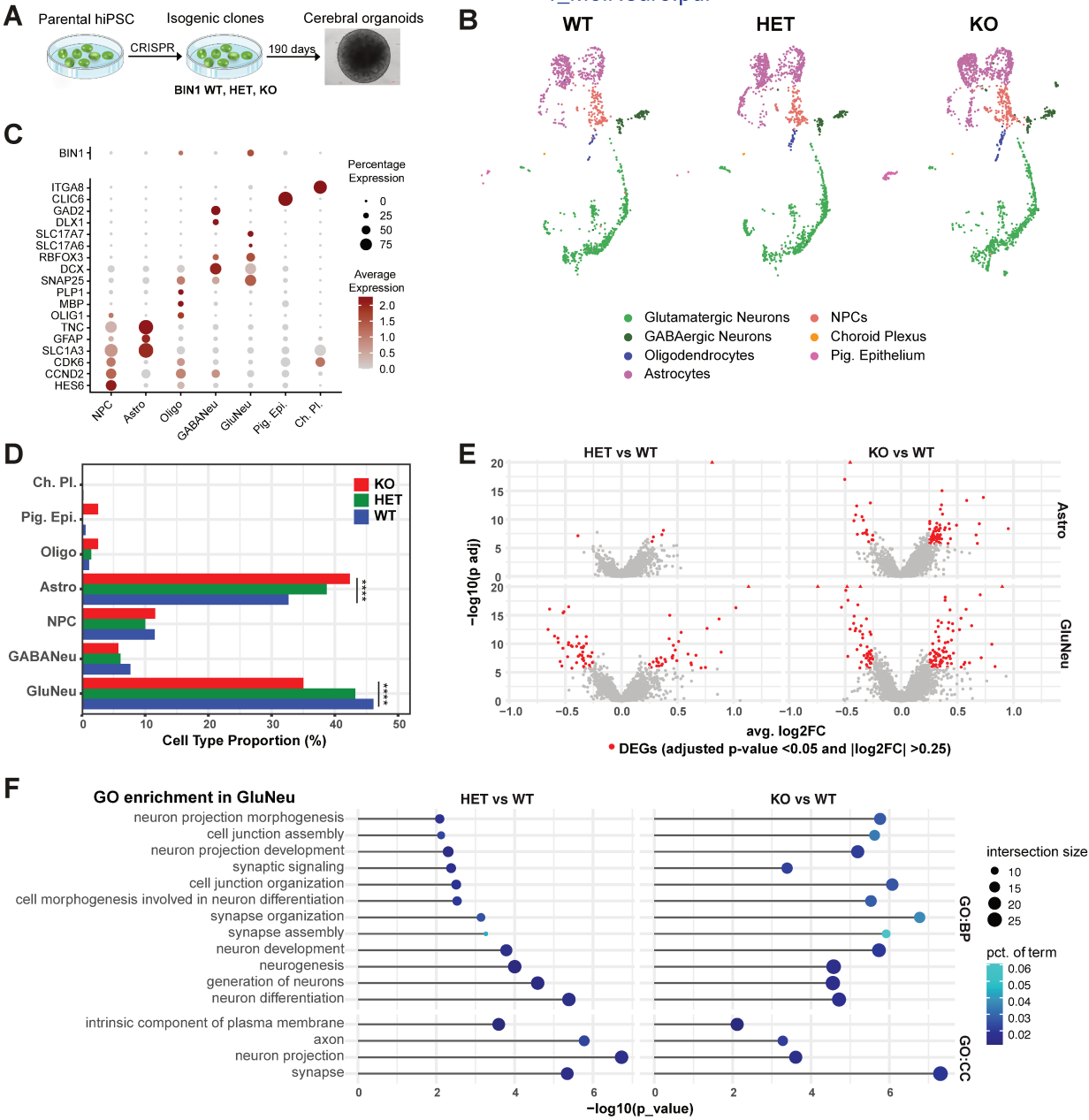

Figure 2

Click here to access/download;Figure;Figure 2_MolNeuro.pdf

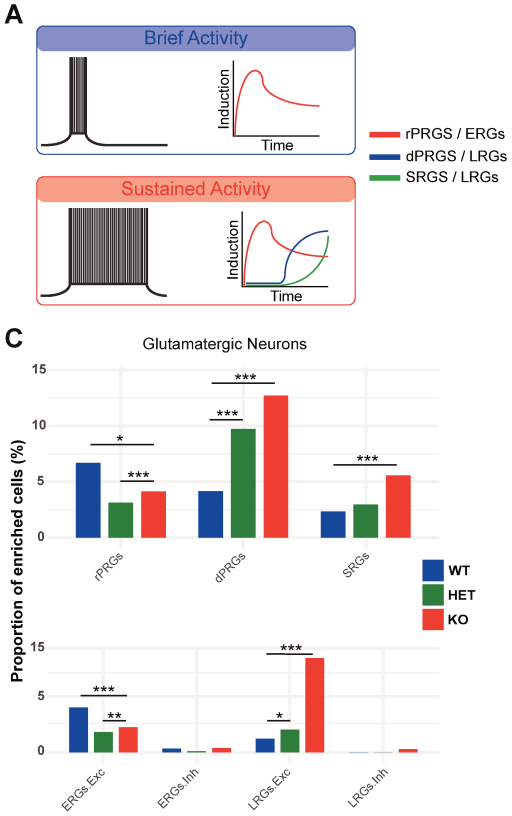

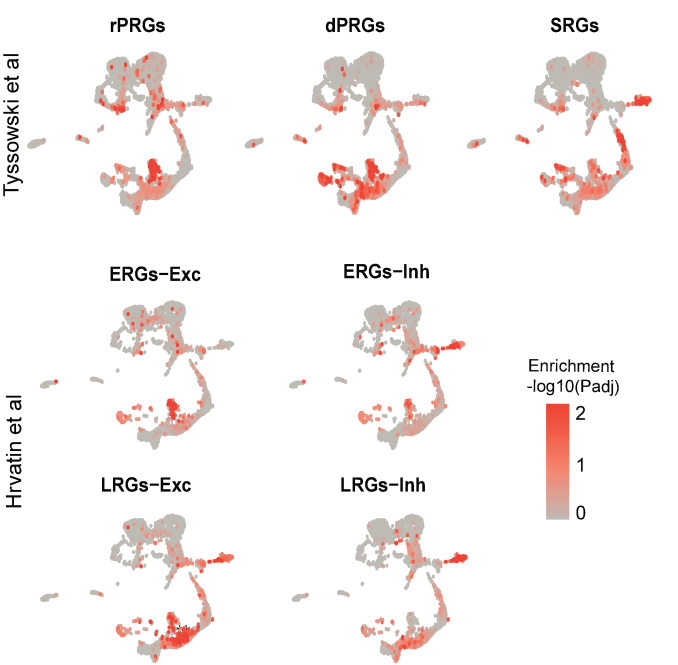

Figure 3

Click here to access/download;Figure;Figure 3_MolNeuro_compressed.pdf

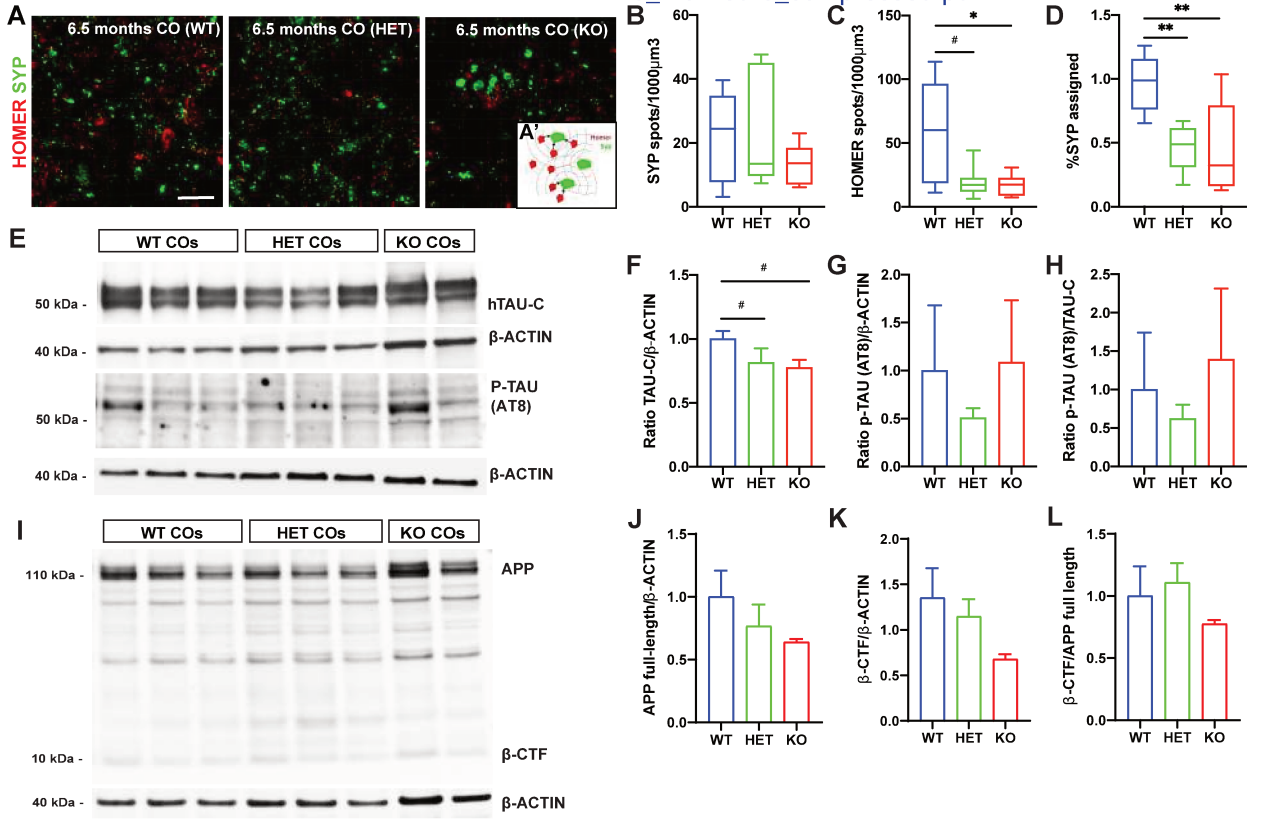

Figure 4

Click here to access/download;Figure;Figure 4_MolNeuro_compressed.pdf

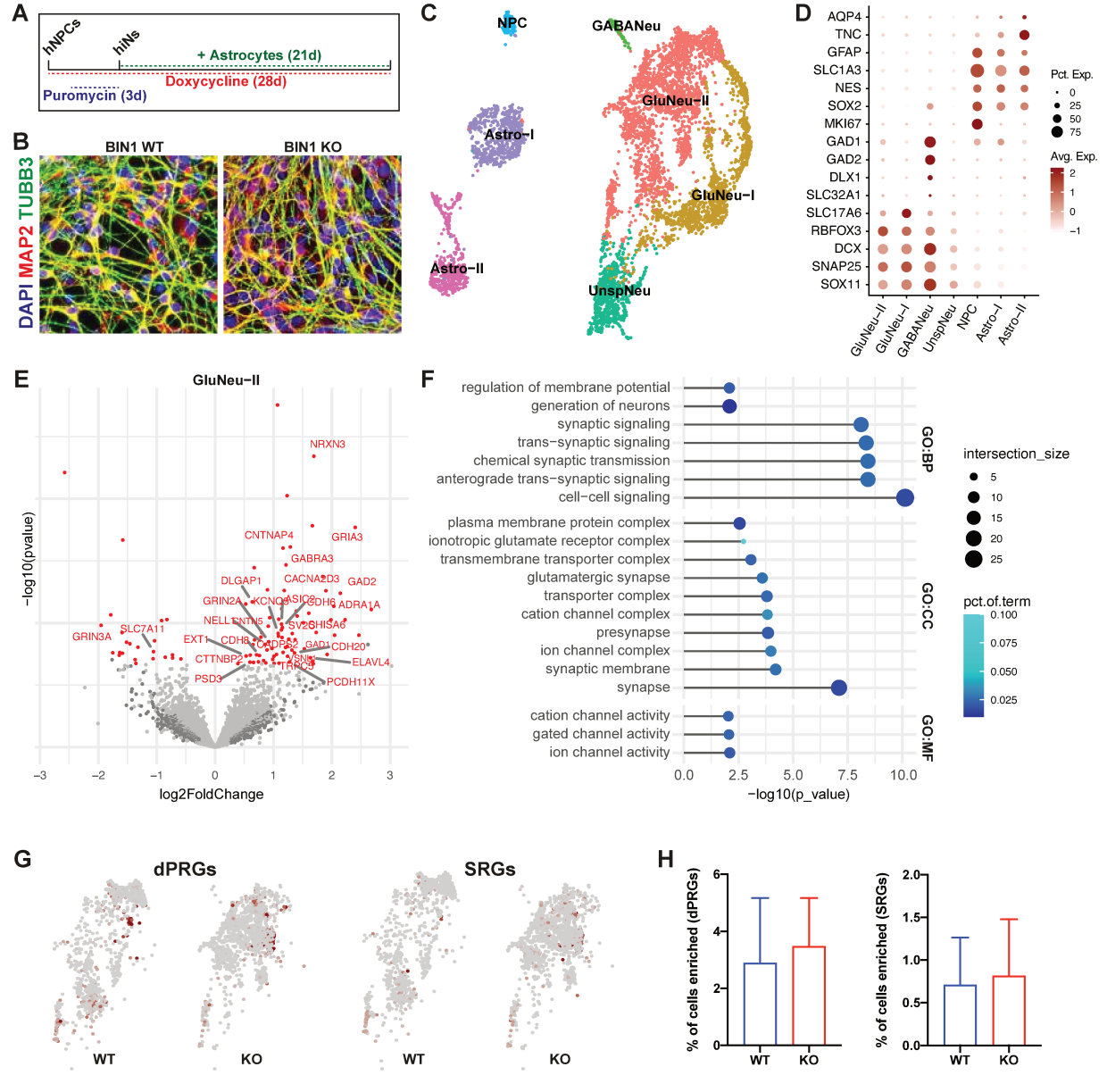

Figure 5

Click here to access/download;Figure;Figure 5_MolNeuro_compressed.pdf

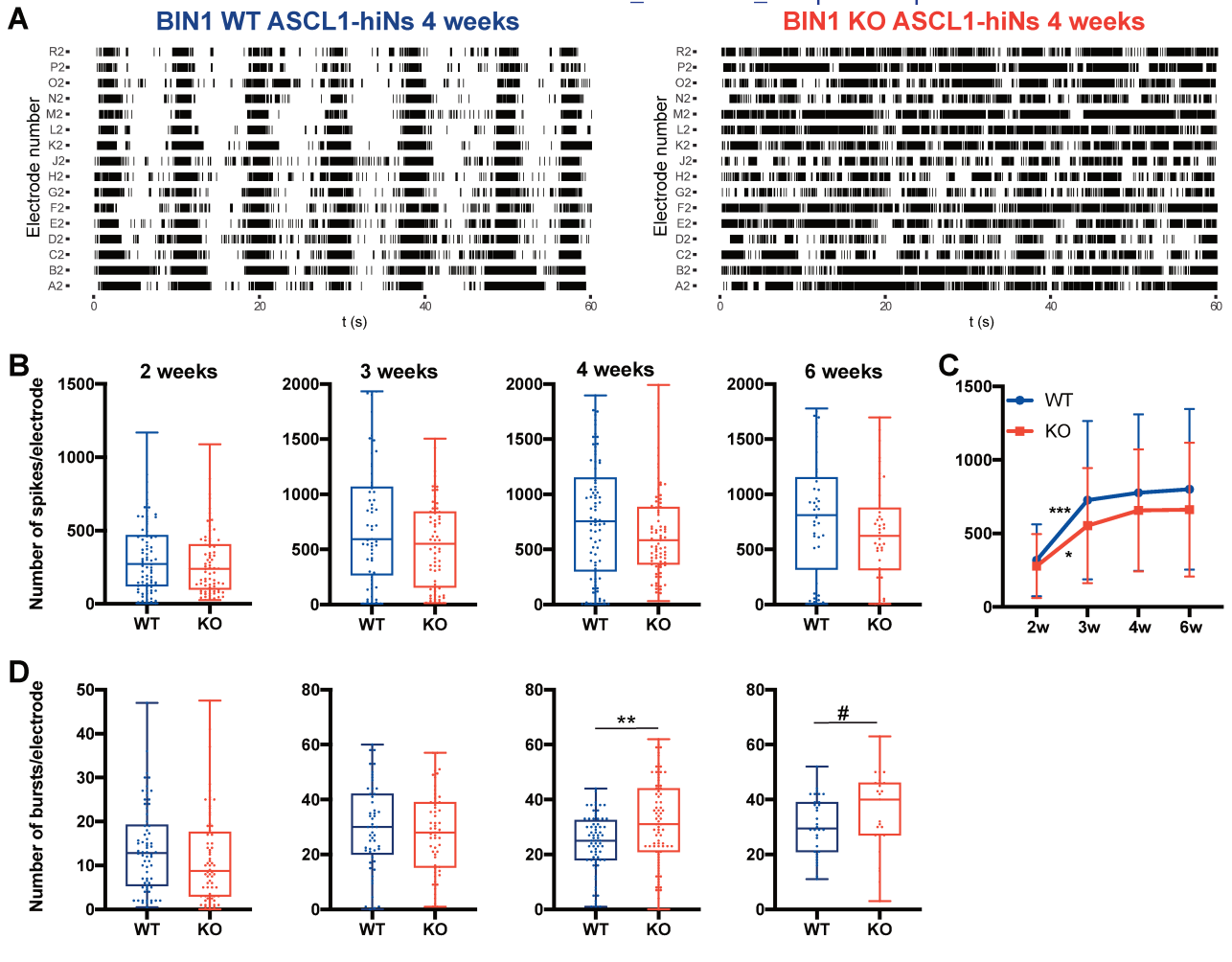

Figure 6

Click here to access/download;Figure;Figure 6_MolNeuro.pdf

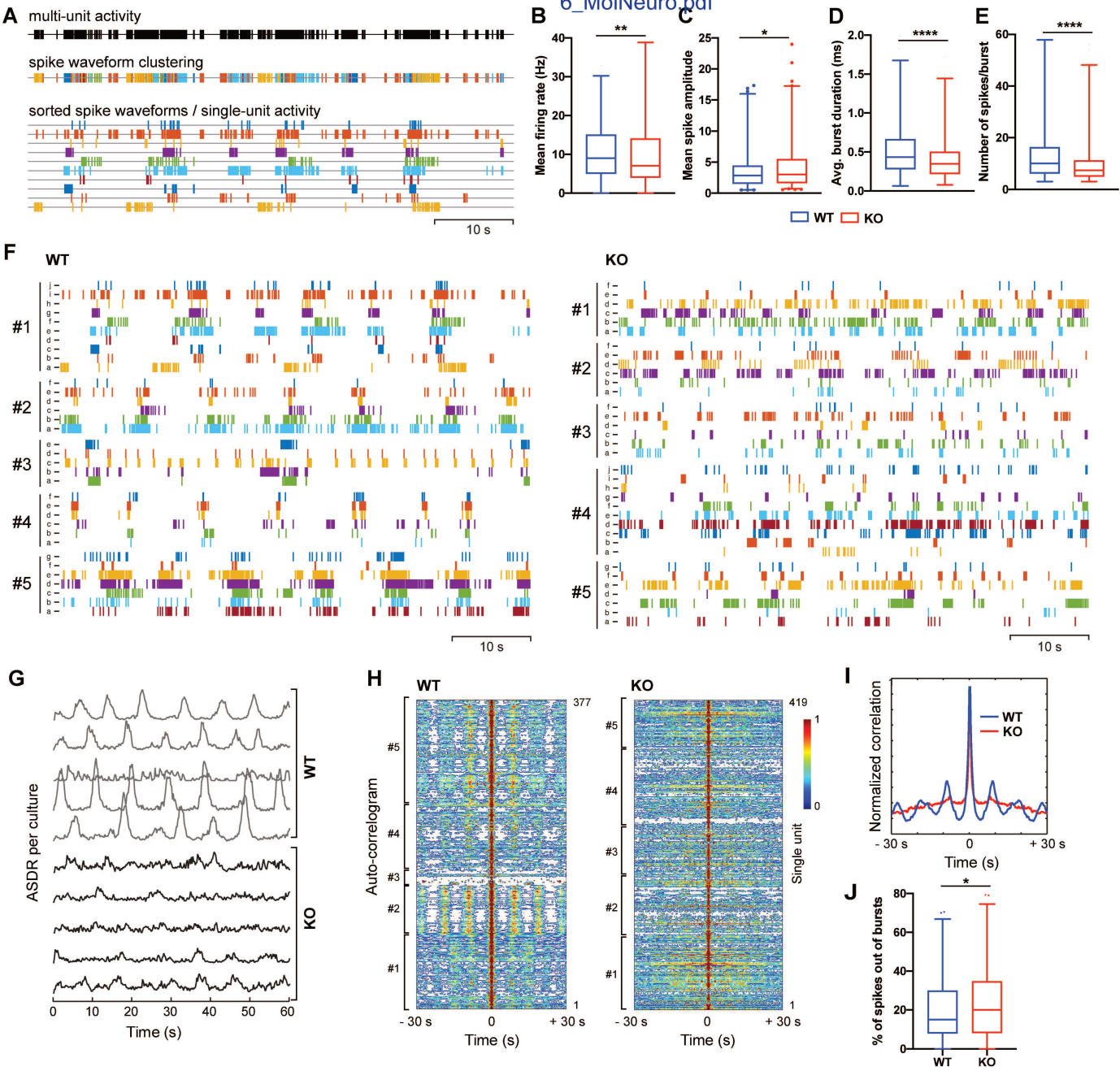

Figure 7

Click here to access/download;Figure;Figure 7_MolNeuro_compressed.pdf

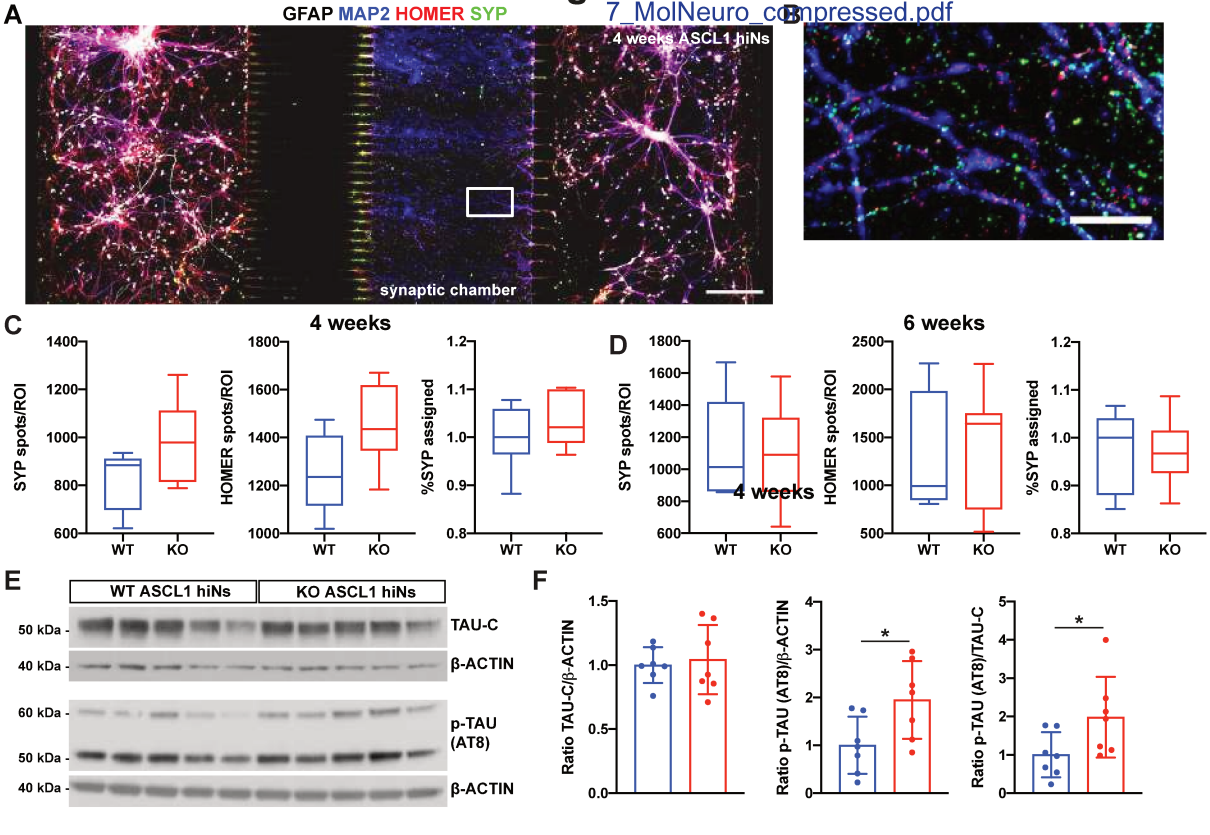

Figure 8

Click here to access/download;Figure;Figure 8_MolNeuro_compressed.pdf

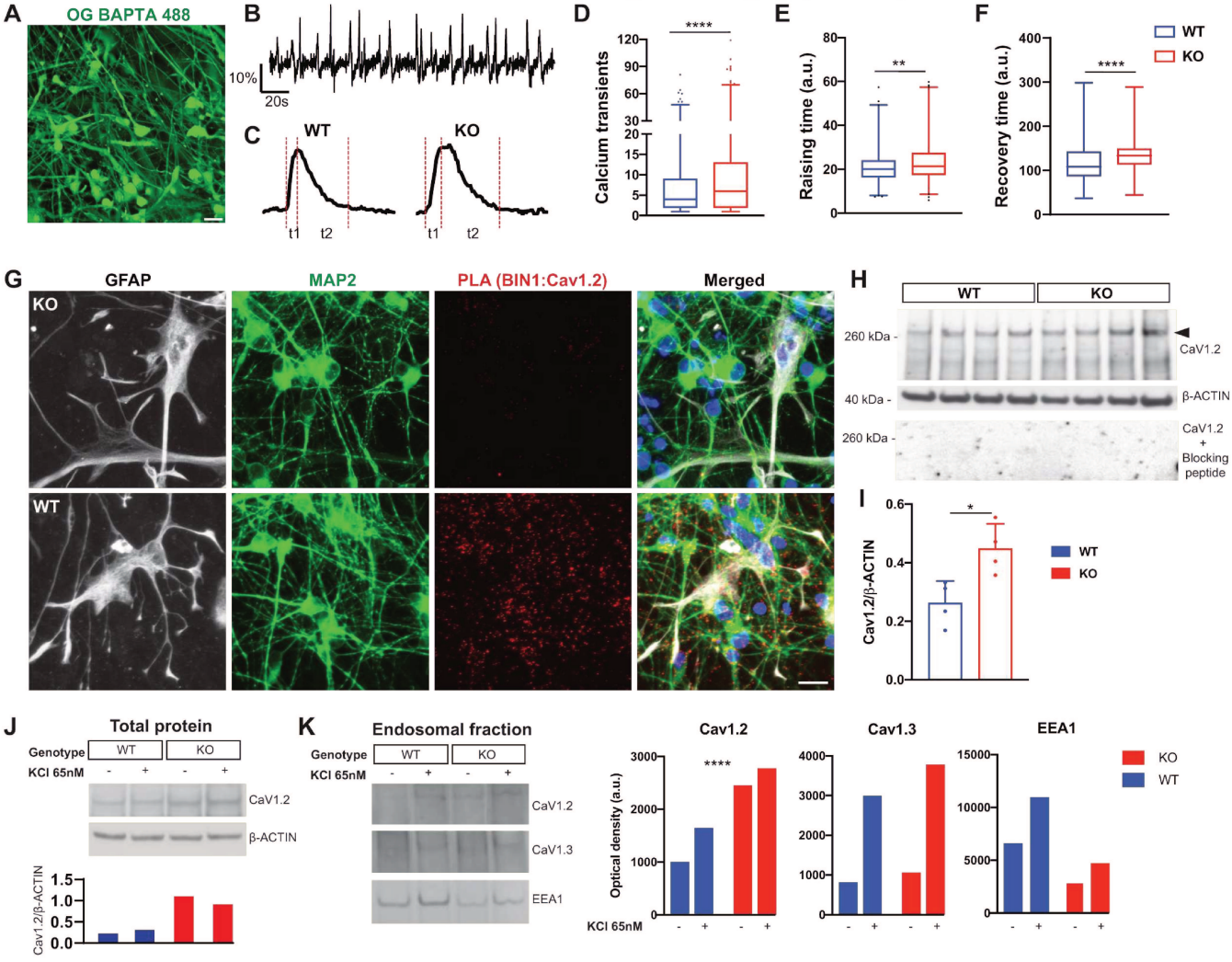

Figure 9

Click here to access/download;Figure;Figure 9_MolNeuro_compressed.pdf

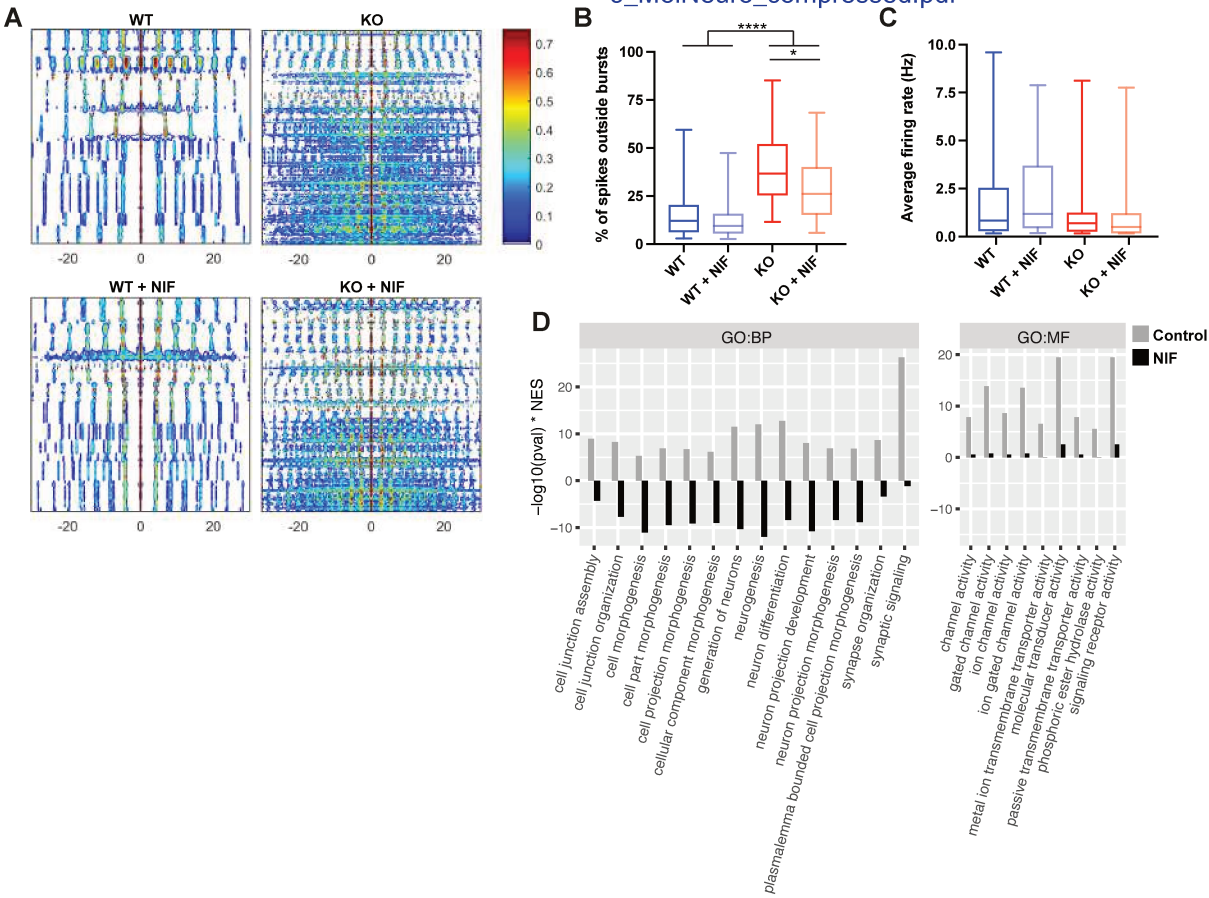

Figure 10

Click here to access/download;Figure;Figure 10_MolNeuro.pdf

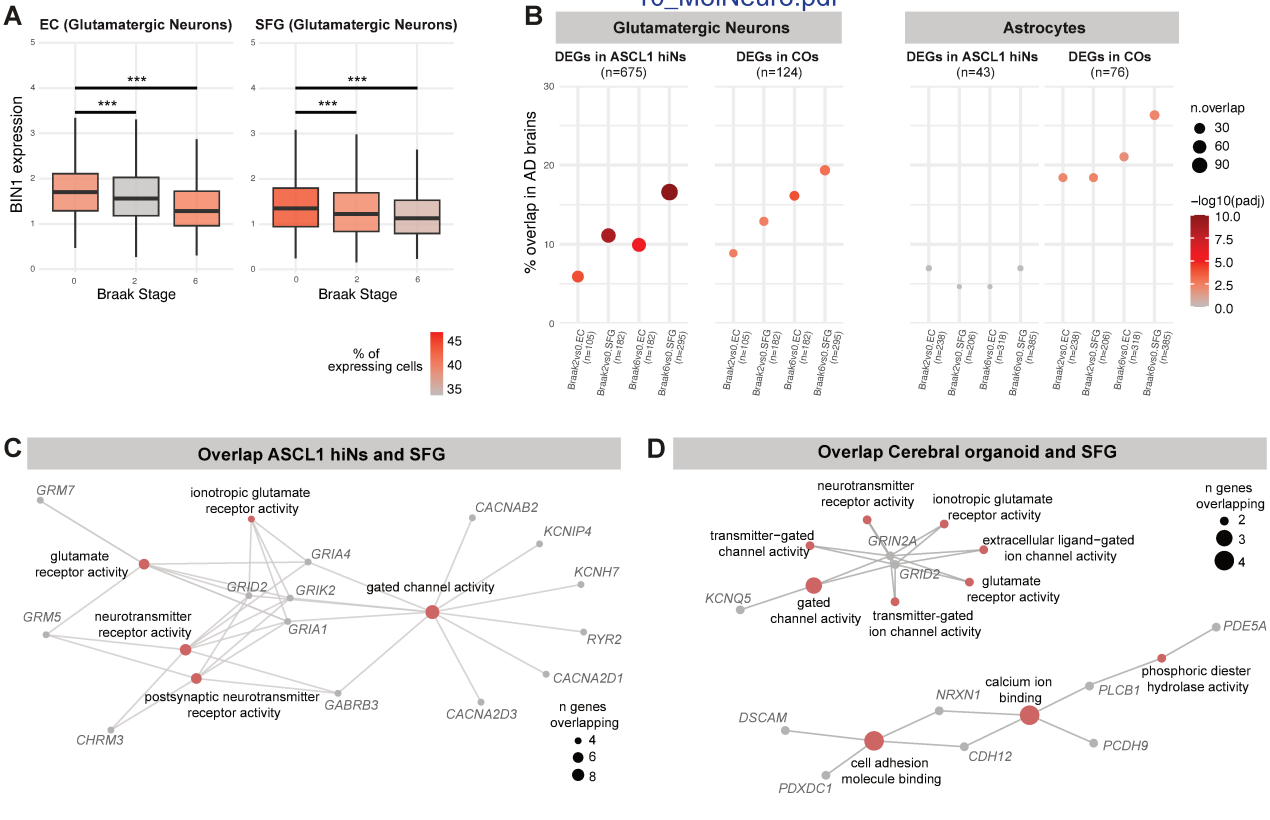

Figure S1

Click here to access/download;Figure;Figure S1_MolNeuro_compressed.pdf

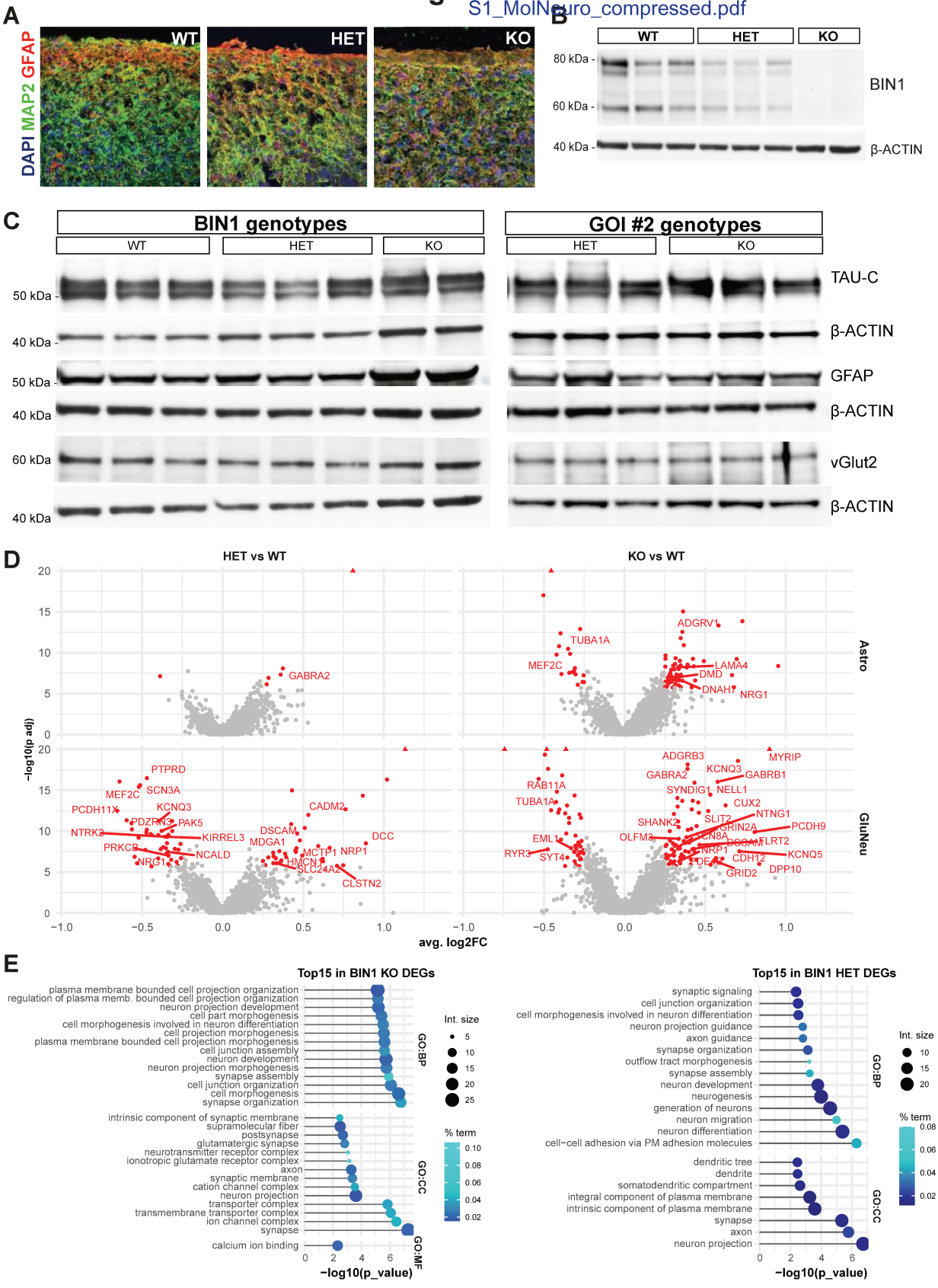

Figure S2

Click here to access/download;Figure;Figure S2_MolNeuro.pdf

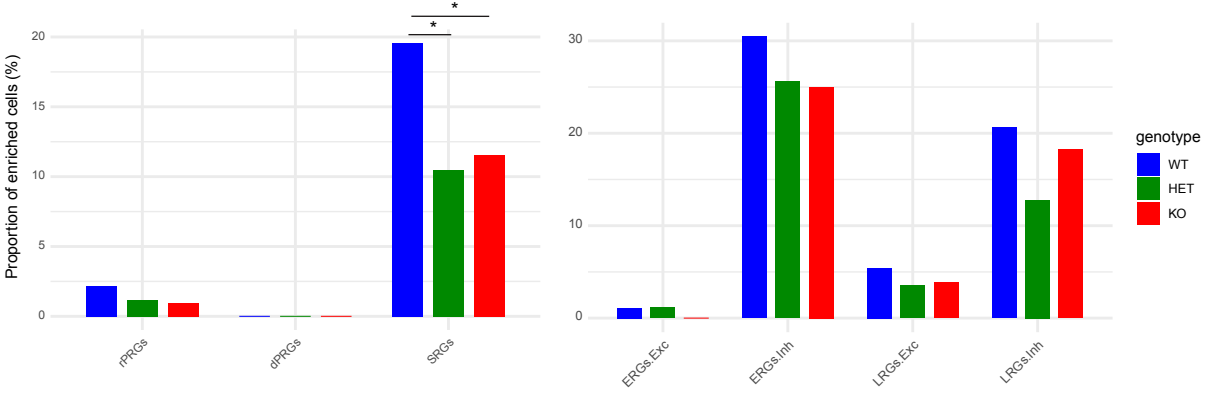

Figure S3

Click here to access/download;Figure;Figure S3_MolNeuro.pdf

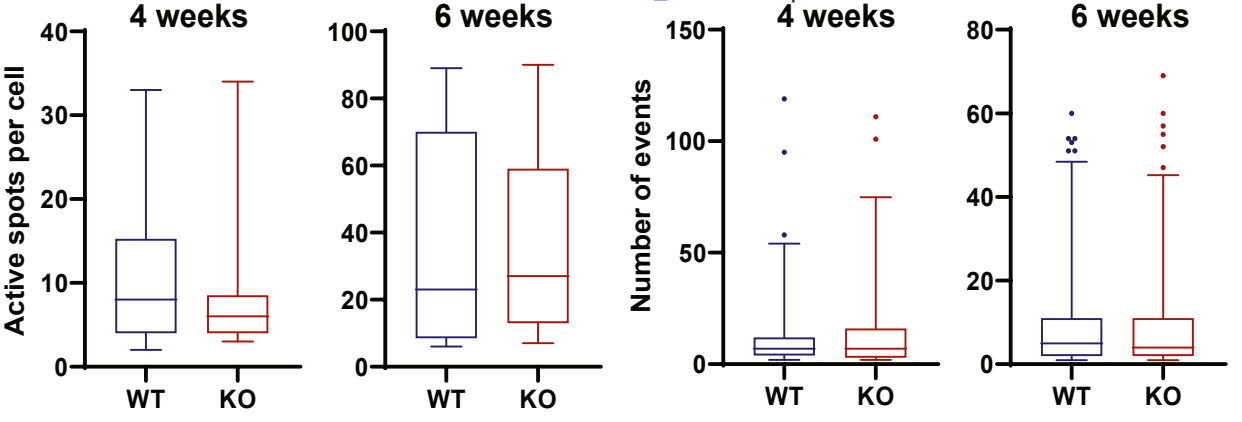

Figure S4

Click here to access/download;Figure;Figure S4_MolNeuro.pdf

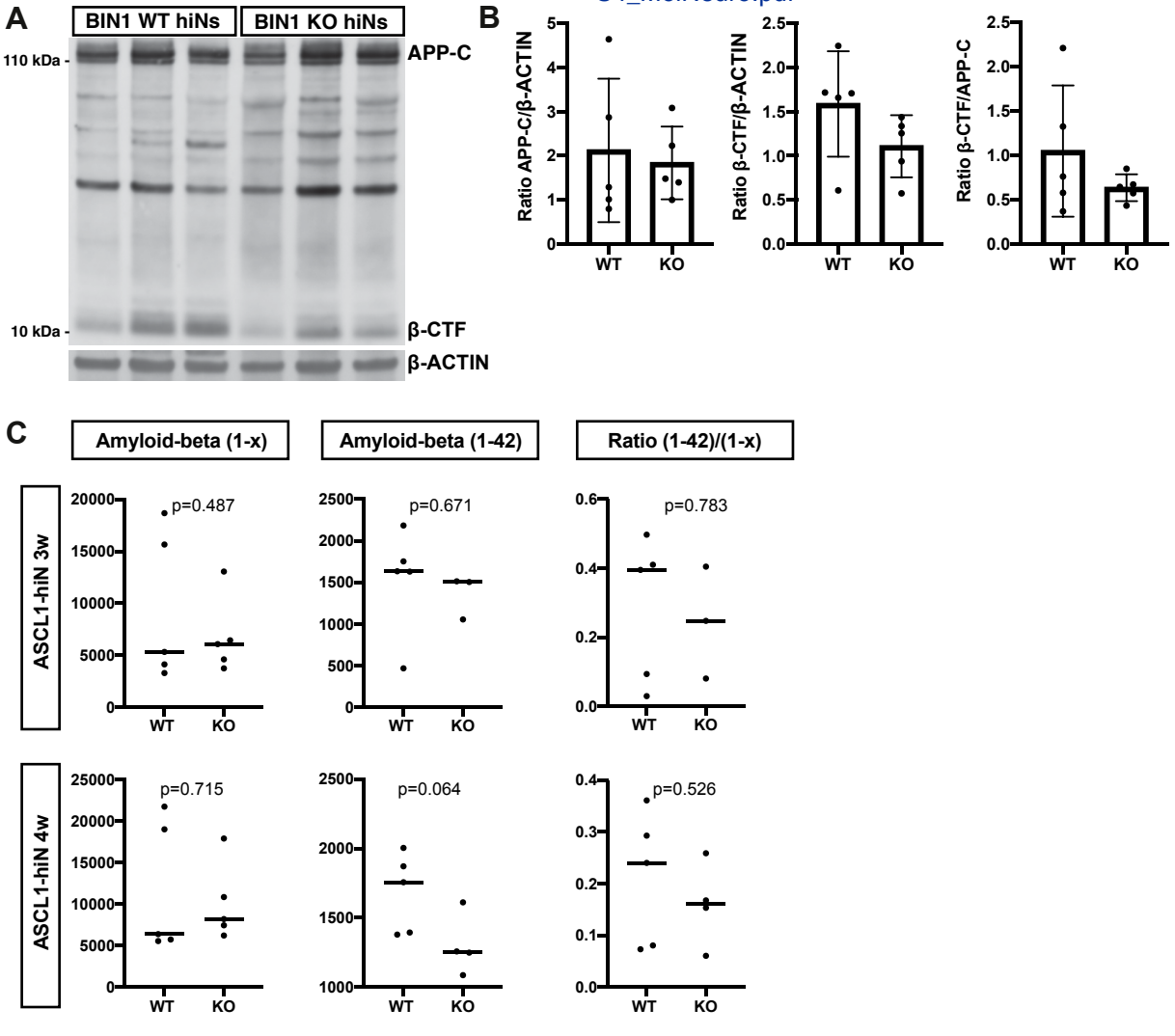

Click here to access/download;Figure;Figure

Figure 5

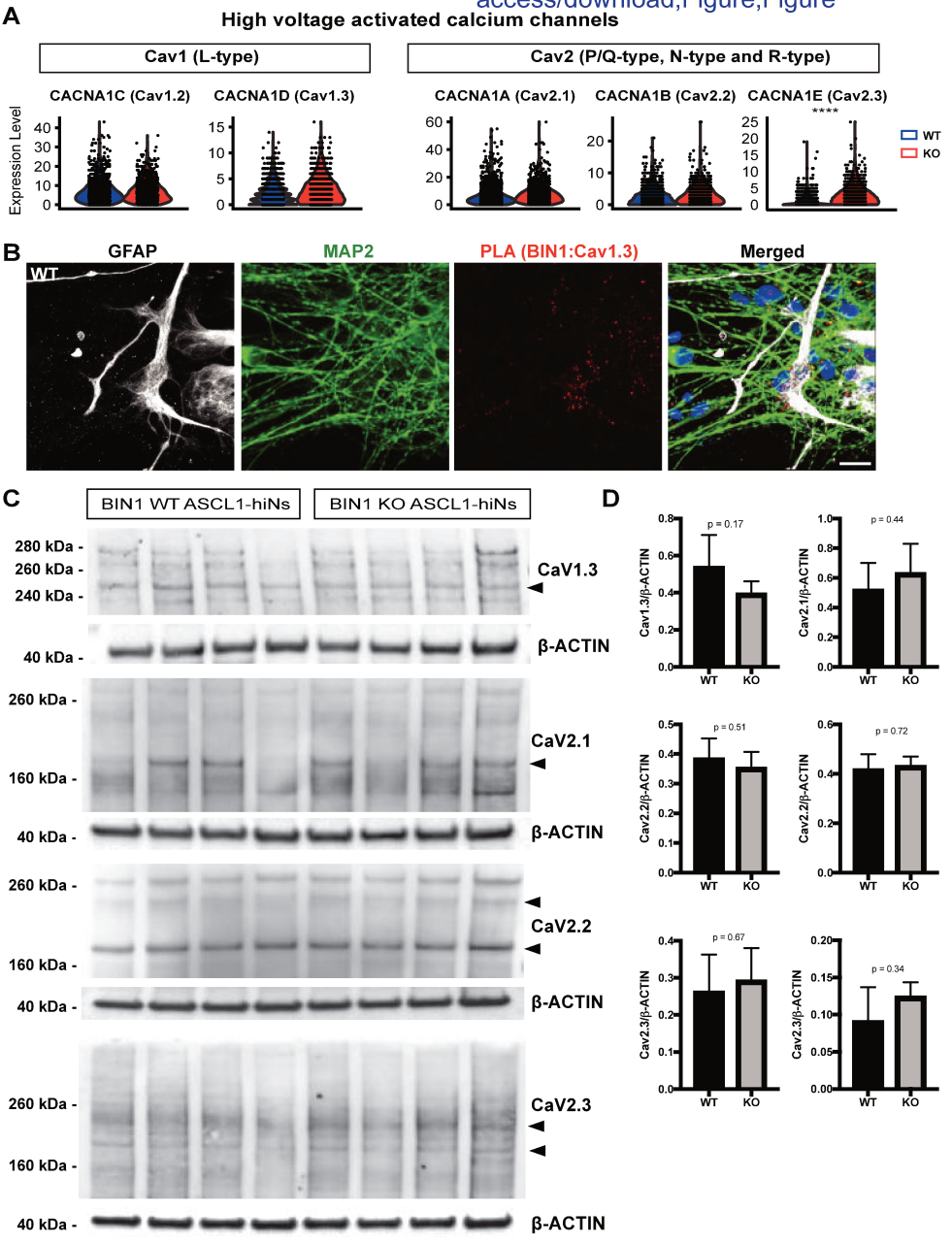

Figure S6

Click here to access/download;Figure;Figure S6_MolNeuro.pdf

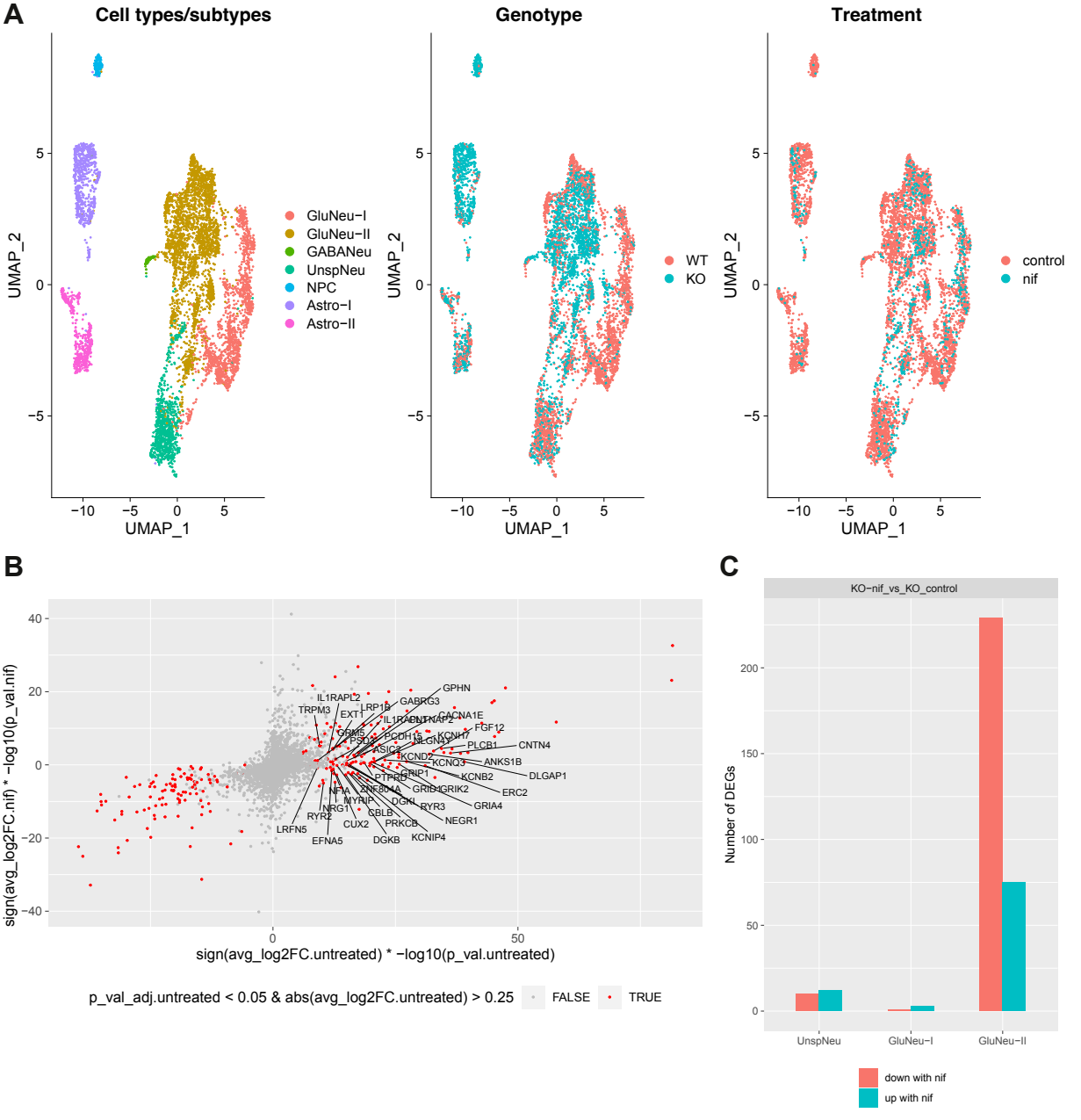

Sup. Table 1

Click here to access/download
Supplementary Material
Sup. Table 1_DEGs in organoids.xlsx

Sup. Table 2

Click here to access/download
Supplementary Material
Sup. Table 2_GOST organoids DEGs.xlsx

Sup. Table 3

Click here to access/download
Supplementary Material
Sup. Table 3_ARGs list.xlsx

Sup. Table 4

Click here to access/download
Supplementary Material
Sup. Table 4_DEGs ASCL1-hiNs.xlsx

Sup. Table 5

Click here to access/download
Supplementary Material
Sup. Table 5_GOST for DEGs in ASCL1-hiNs.xlsx

Click here to access/download
Supplementary Material
Sup. Table 6_DEGs ASCL1-hiNs plus nifedipine.xlsx

Click here to access/download
Supplementary Material
Sup. Table 7_GOST for DEGs in ASCL1-hiNs plus nifedipine.xlsx

Sup. Table 8

Click here to access/download
Supplementary Material
Sup. Table 8_DEGs in AD brains.xlsx

Sup. Table 9

Click here to access/download

Supplementary Material

Sup. Table 9_GO organoids&ADbrain common DEGs.xlsx

Sup. Movie 1

Click here to access/download

Supplementary Material

Movie S1_iGLUSnFr_Bin1WT_Ascl1_4weeks.avi

Sup. Movie 2

Click here to access/download

Supplementary Material

Movie S2_iGLUSnFr_Bin1KO_Ascl1_4weeks.avi

Sup. Movie 3

Click here to access/download

Supplementary Material

Movie S3_OGB_BIN1 WT_Ascl1hiNs.avi

Sup. Movie 4

Click here to access/download

Supplementary Material

Movie S4_OGB_BIN1 KO_Ascl1hiNs.avi

Article IV

4. Amyloid-beta peptides trigger premature functional and gene expression alterations in human-induced neurons

Ana Raquel Melo de Farias1,2,#, Alexandre Pelletier4,#,&, Lukasda Cruz CarvalhoIohan3,#,Orthis Saha1, Amelie Bonnefond4, Philippe Amouyel1,Fabien Delahaye4, Jean-CharlesLambert1and Marcos R. Costa

 # Equal contributions

Biomedicines, 2023 (under review)

4.1 Context and objectives

Alzheimer's disease is characterized by various brain abnormalities, including the accumulation of Aβ plaques, neuroinflammation, and neuronal dysfunction. The prevailing theory, known as the "Amyloid cascade hypothesis", suggests that Aβ deposition is a key trigger for AD pathology. However, the detailed molecular mechanisms connecting Aβ to neuronal dysfunction are not fully understood. The primary objective of this study is to explore how Aβ accumulation affects the functional properties of hiNs. Specifically, to understand the impact of Aβ on neuronal electrical activity by monitoring calcium transients, which are a measure of neuronal excitability. We sought to identify early gene expression alterations triggered by Aβ in hiNs and human-induced astrocytes (hiAs). Using single-nucleus RNA sequencing (snRNA-seq), we aim to uncover how Aβ influences the gene expression profiles of these cells and might affect intercellular communication

By leveraging snRNA-seq data, we intend to identify patterns of communication between different cell types that were influenced by Aβ oligomers. Our results indicate that even slight increases in Aβ concentrations can lead to significant transcriptional changes in human neurons, with potential long-lasting consequences for neural network activity. Additionally, we suggest that Aβ may impact synapses through the activation of specific signaling pathways involving semaphorin, ephrin, and nectin. Overall, this study contributes to our understanding of how Aβ contributes to neuronal dysfunction in Alzheimer's disease by using a human culture model.

4.2 Personal contributions to the work

I contributed to this study in several aspects of the experimental research. In particular, by culturing and differentiating several independent lines of wild-type human iPSCs into neurons/astrocytes using a 2D culture model.

Additionally, I administered treatments with synthetic AB peptides and conducted electrophysiological recordings in calcium imaging, followed by conducting a comprehensive analysis of the results. Moreover, I conducted a part of the single cell RNA-sequencing experiments, including nuclear extraction and library preparation. I also contributed to the writing, reviewing, and editing process.

Amyloid-beta peptides trigger premature functional and gene expression alterations in human-induced neurons

Ana Raquel Melo de Farias[1,2,#], Alexandre Pelletier[4,#,&], Lukas da Cruz Carvalho Iohan[3,#], Orthis Saha[1], Amelie Bonnefond[4], Philippe Amouyel[1], Fabien Delahaye[4], Jean-Charles Lambert[1] and Marcos R. Costa[1,2,*]

1. Univ. Lille, Inserm, CHU Lille, Institut Pasteur de Lille, U1167-RID-AGE facteurs de risque et déterminants moléculaires des maladies liées au vieillissement, DISTALZ, 1 rue du Professeur Calmette 59019 Lille, France
2. Brain Institute, Federal University of Rio Grande do Norte, Av. Senador Salgado Filho, 3000, Campus Universitário, Lagoa Nova, 59078-970 Natal, Brazil
3. Bioinformatics Multidisciplinary Environment, Federal University of Rio Grande do Norte, Natal, Brazil
4. Univ. Lille, Inserm, CNRS, CHU Lille, Institut Pasteur de Lille, U1283-UMR 8199 EGID, Pôle Recherche, 1 Place de Verdun, 59045 Lille Cedex, France

[#]Equal contribution

[&]Current address: The Department of Pharmacology, Physiology & Biophysics. Boston University, Chobanian & Avedisian School of Medicine, MA 02118

* Correspondence should be addressed to:

Marcos Costa, MD, PhD

Inserm U1167

Institut Pasteur de Lille

1 rue du Pr. Calmette

59019 Lille CEDEX, France

Tel: 00 33 (0)3 20 87 77 10

marcos.costa@pasteur-lille.fr

Abstract

Background: Alzheimer's disease (AD) is the most prevalent cause of dementia in the elderly, characterized by the presence of amyloid beta (Aβ) plaques, neurofibrillary tangles, neuroinflammation, synapse loss and neurodegeneration in the brain. The amyloid cascade hypothesis postulates that deposition of Aβ peptides is the causative agent of AD pathology, but we still lack comprehensive understanding about the molecular mechanisms connecting Aβ peptides to neuronal dysfunctions in AD. In this work, we investigated the early effects of Aβ peptides accumulation on the functional properties and gene expression profiles of human-induced neurons (hiNs).

Methods: We exposed 6-weeks-old hiNs to low concentrations of cell-secreted Aβ oligomers or synthetic Aβ and performed time-lapse time microscopy to detect fast calcium transients as an indirect readout of neuronal electrical function. Next, we used single-nucleus RNA sequencing (snRNA-seq) to probe early Aβ-mediated gene expression alterations in hiNs and human-induced astrocytes (hiAs). Lastly, we leveraged snRNA-seq data to identify patterns of intercellular communication modulated by Aβ oligomers.

Results: We show that hiNs acutely exposed to low concentrations of both cell-secreted Aβ peptides or synthetic $A\beta_{1-42}$ exhibit alterations in the frequency of calcium transients suggestive of increased neuronal excitability. We also show that cell-secreted Aβ up-regulates the expression of several synaptic-related genes and down-regulates the expression of genes associated with metabolic stress mainly in glutamatergic neurons and to a lesser degree in GABAergic neurons and astrocytes. These neuronal alterations correlate with activation of SEMA5, EPHA and NECTIN signaling pathways, which are important regulators of synaptic plasticity.

Conclusions: Our findings indicate that slight elevations in Aβ concentrations are sufficient to elicit transcriptional changes in human neurons with long lasting consequences to neural network activity and suggest that at least part of the effects of Aβ on synapses might be mediated by semaphorin, ephrin and nectin signaling pathways.

Keywords:

Amyloid-beta peptides; Human-induced neurons; Single nucleus RNA-sequencing; Calcium imaging; Intercellular communication

Background

Alzheimer's disease (AD) is a neurodegenerative disorder associated with severe cognitive impairment in which memory loss is one of the most predominant features. Worldwide, AD accounts for 60 to 80 percent of dementia cases and represents an increasing burden for ageing populations [1]. Analysis of post-mortem human brains reveal two key features of AD, namely the presence of amyloid plaques - extracellular accumulations of amyloid-β (Aβ) peptides, that are derived from the proteolytic processing of the amyloid precursor protein (APP); and neurofibrillary tangles - intracellular accumulations of the microtubule-associated protein tau. The identification of familial, AD-linked mutations in the genes for amyloid-β precursor protein (APP) and presenilin (PS1 and PS2) associated with deregulation of Aβ peptide production suggests that APP metabolism is at the heart of the disease process through the statement of the amyloid cascade hypothesis [2]. Remarkably, recent treatments developed from this hypothesis and based on immunotherapies against Aβ peptides have shown significant but limited clinical effects in slowing down disease progression [3]. However, even if encouraging, we are still far from benefiting from an effective treatment and we greatly need a better understanding of the pathophysiological processes of AD potentially related to Aβ peptides to develop complementary and original therapeutics approaches.

Alterations in neuronal electrical activity and network oscillations are among the first signals in the brain of AD patients and are intimately associated with Aβ deposits even prior to the onset of clinical symptoms [4–8]. In rodents, treatment with soluble Aβ peptides can lead to neuronal hyperexcitation [9,10] and modulation of excitatory synaptic activity, in turn, regulates the proteolysis of APP and release of Aβ peptides [11,12], creating positive feedback between Aβ accumulation and neuronal electrical activity/synapse dysfunction. Early impairment of neuronal circuits is also observed in the brain of transgenic AD animal models, including the APP23xPS45 double-transgenic mice [13] and the 5XFAD mice that over-expresses human amyloid precursor protein (APP) and presenilin 1 (PS1) harboring five familial AD mutations [14,15]. Moreover, human-induced pluripotent stem cells (hiPSC)-derived neurons carrying mutations in *APP* or *PSEN1* show altered electrical properties [16], suggesting that Aβ peptides modulate the functional properties of human neurons. However, the precise molecular mechanisms associated with Aβ-mediated neuronal hyperexcitability and the exact contribution of $A\beta_{1-42}$ peptides for this process remains elusive.

In this work, we investigated the early functional and gene expression alterations in human-induced neurons (hiNs) and astrocytes (hiAs) exposed to low concentrations of cell-secreted

Aβ peptides. We show that a single exposure to low concentrations Aβ peptides is sufficient to promote an increase in the frequency of calcium transients in hiNs associated with specific synaptic-related gene expression alterations in glutamatergic neurons. These results suggest that slight (and repetitive) changes in Aβ concentrations in the brain may have long lasting consequences for neural networks by impacting gene expression in glutamatergic neurons.

Methods

1. *Maintenance of hiPSCs and neural induction*

For this project, we took advantage of a commercially available hiPSC cell line (ASE-9109, Applied StemCell Inc. CA, USA). The maintenance of the iPSC cultures was done in adherence with manufacturer's protocols which can be found on the webpage of Stemcell Technologies. Briefly, hiPSCs were maintained in mTeSR1+5X supplemented medium in non-treated cell culture dishes/plates pre-coated with 10 ug/ml of vitronectin fresh-diluted in Cell Adhere Dilution Buffer (StemCell Technologies) during 1 h at room temperature. Full medium change was performed daily until the confluence reached about 80%, when the cells were passed. Cell number and viability were recorded using a LUNA™ Automated Cell Counter. To induce a neural lineage from iPSCs, we used either a monolayer or an embryoid body methods. Both consisting of a serum-free system validated by StemCell Technologies and based on the dual SMAD-inhibition (SMADi) method [17]. Briefly, on the monolayer system, hiPSCs are cultured at high density and passaged for 3 times in STEMdiff™ Neural Induction Medium + SMADi (StemCell Technologies) for approximately to 3 weeks. Alternativly, on the embryoid body procedure, the iPSCs are seeded on AggreWell plates (StemCell Technologies) to produce the embryoid bodies. Which are then replated in classic plates followed by a Neural Rosette selection to retain the neural cells. After this period, the hiNPCS generated are maintained for up to 9 passages in treated cell culture dishes pre-coated with poly-L-ornithine (PLO) and laminin (10 µg/mL), using supplemented STEMdiff™ Neural Progenitor Medium (NPM; Stemcell Technologies) fully changed daily. PLO solution was made in water (0.001%) while laminin was diluted in PBS 0.01M with Ca^{2+} and Mg^{2+}.

2. *Differentiation of hiNPCs and mixed cultures of hiNs and hiAs*

To obtain mixed 2D cultures comprising hiNs and hiAs from hiNPCs, we followed the spontaneous differentiation protocol detailed by StemCell Technologies. Following this spontaneous protocol, 100,000 hiNPCs/well were plated in 24-well cell imaging plates from Eppendorf (Cat # 0030741005) pre-coated with PLO (0.001%) and laminin (10µg/mL). Cells were kept in 0.5 mL of NPC medium per well for 24 hours. Following this, equal volume of complete BrainPhys medium (supplemented with BDNF, GDNF, laminin, dibutyryl-cAMP,

ascorbic acid, N2, and SM1) was added to each well to begin the process of differentiation [18]. Subsequently, media was changed in the plates bi-weekly. The media change consisted of removing half of the existing medium in each well and replacing it with an equal volume of fresh complete BrainPhys medium. Mixed cultures of hiNs and hiAs were exposed to cell-secreted or synthetic Aβ peptides (see below) after 5-6 weeks of differentiation and then processed for calcium imaging, western blotting, immunocytochemistry or snRNA-sequencing.

3. Cell-secreted Aβ peptides treatment

Chinese hamster ovary (CHO) cell lines overexpressing the human APP695 (CHO-APP^{WT}) or the London mutated APP695 (CHO-APP^{V717L}) were previously described [19]. CHO cells were grown in DMEM/F-12 1:1 medium, supplemented with 10% heat-inactivated foetal bovine serum, 0.2% Pen/Strep, 2% HT supplement and 300 µM Proline (Sigma). One day before CHO supernatant media collection, a full-medium replacement was performed with Brainphys. CHO cell conditioned Brainphys medium was collected 24h later and Aβ concentrations were measured using Alpha-LISA kits specific for human Aβ1–X (AL288C, PerkinElmer) and Aβ1–42 (AL276C, PerkinElmer). Briefly, the human Aβ analyte standard was diluted in the BrainPhys medium. For the assay, 2 µL of cell culture medium or standard solution was added to an Optiplate-384 microplate (PerkinElmer). 2 µL of 10X mixture including acceptor beads and biotinylated antibody was then added to the wells with culture media or standard solution. Following incubation at room temperature for an hour, 16 µL of 1.25X donor beads was added to respective wells and incubated at room temperature for 1 hour. Luminescence was measured using an EnVision-Alpha Reader (PerkinElmer) at 680 nm excitation and 615 nm emission wavelengths. Control treatment was performed using unconditioned/blank Brainphys medium.

4. Synthetic Aβ$_{1-42}$ treatment

Commercially available lyophilized Aβ$_{1-42}$ (Anaspec) was reconstituted in 1% DMSO as the solvent, followed by PBS 10mM at the concentration of 1 uM and re-diluted in 500 ul/well of supplemented BrainPhys medium to reach a final concentration of 100 pM. The inverted control peptide (Aβ$_{42-1}$, Anaspec) at the same final concentration and vehicle only (1% DMSO in PBS 10 mM) were used as controls. After 5 weeks of spontaneous differentiation, half of the medium was removed from each well and kept aside for later replacement. Then, either the Aβ$_{1-42}$, the inverted peptide or the vehicle were added at proper concentration and the cells

were kept in the incubator for 24 hours. After that period, the medium in each well was replaced followed by the calcium imaging procedures and protein extraction.

5. *Calcium Imaging Experiments*

Spontaneously differentiated 5-6 weeks cultures containing hiNs and hiAs were treated with cell conditioned medium or synthetic $A\beta_{1-42}$ (and respective controls) for 48 hours and 24 hours, respectively, prior to real-time calcium imaging recordings. Cells were incubated with Oregon Green™ 488 BAPTA-1 (OGB-1) acetoxymethyl (AM) (ThermoFisher Scientific) for 1 h immediately before the recordings. A 2.5 mM stock solution of the calcium-indicator dye was prepared in Pluronic™ F-127 (20% solution in DMSO) (ThermoFisher Scientific). 1 µL of the dye solution was added to 500 µL of existing BrainPhys medium in each well of a 24-well cell imaging plate. The other half of existing BrainPhys media from the wells of the plate was removed and kept aside at 37 °C while the calcium-indicator dye was incubated in fresh BrainPhys medium. After 1 h of incubation, the medium which was kept aside was replaced to each well. The 2D cultures were then ready to be imaged using a Spinning Disk Microscope (Nikon) housed at the Institut Pasteur de Lille, Lille, France using the MetaMorph imaging software. We took 1000 images using a 20x (synthetic peptide treatment) or 40x objective (conditioned medium treatment) with 10 ms exposure time and 200 ms intervals, totalizing up to 3 minutes of recording per field. For each well, up to 5 random fields were chosen, and at least two wells from 3 (for cell conditioned medium) or 4 (for synthetic Aβ) independent culture batches were imaged for each condition.

6. *Analyses of Calcium Transients*

Time-series data from calcium imaging recordings were at first converted to .avi format after background subtraction by use of ImageJ software. The videos were subsequently opened on CALciumIMagingAnalyzer (CALIMA) software [20]. Each video recording of a field of cells was first downscaled to 2X in terms of size with a 10X zoom and was checked for the frame average mode. Moreover, in this first detection stage, pre-set filter parameters were adjusted and applied to enable the detection of the maximum number of fluorescent neurons (regions of interest - ROIs) in each field. During this step, the detected cells were checked several times to ensure that only neurons were selected, based both on cell morphologies and the presence of

fast calcium transients. Fluorescence signal noise was filtered using the median of 3 each consecutive images. Fluorescence changes in all detected ROIs was then recorded. Fast (< 400 ms) increases of fluorescence signal above 2 or more standard deviations of the average background was considered a calcium transient (or spike). Detected spikes and cross-correlation matrices of all cells from each field of imaging were extracted and exported as .csv files.

7. Single-nucleus RNA-sequencing

6-week-old mixed cultures of hiNs and hiAs were washed in the 24-well plate wells with 1 mL of Deionized Phosphate Buffer Saline 1X (DPBS, GIBCO™, Fisher Scientific 11590476). Cells were Lysed with wide bore tips in 1 mL Lysis Buffer (Tris-HCL 10mM, NaCl 10mM, MgCl2 3mM, Tween-20 0,1%, Nonidet P40 Substitute 0,1%, Digitonin 0,01%, Invitrogen™ RNAseout™ recombinant ribonuclease inhibitor 0,04 U/µL). Multiple mechanical resuspensions in this buffer were performed for a total lysis time of 15 min. 500 µL of washing buffer was added (Tris-HCL 10mM, NaCl 10 mM, MgCl2 3 mM, Tween-20 0.1%, BSA 1%, Invitrogen™ RNAseout™ recombinant ribonuclease inhibitor 0,04 U/µL) and the lysis suspension was centrifuged 8 mins at 500 g at 4°C (used for all following centrifugation steps) Nuclei pellets were washed 2 times using washing buffer with one filtration step by MACS pre-separation filter 20µm (Miltenyi Biotec). Nuclei pellets were resuspended in 100 µL of staining buffer (DPBS BSA 2%, Tween-20 0.01%, 0,04 U/µl Invitrogen™ RNAseout™ recombinant ribonuclease inhibitor), 10 µL of Fc blocking reagent HumanTruStainFc™ (422302, Biolegend) and incubated 5 min at 4°C. 1µl of anti-Vertebrate Nuclear Hashtag Antibody (Total-Seq™-A, Biolegend) was added and incubated 15 mins at 4°C. Nuclei pellets were washed three times in staining buffer with one filtration step by MACS pre-separation filter 20 µm (Miltenyi Biotec) to a final resuspension in 300 µL of staining buffer for Malassez cell counting with Trypan blue counterstaining (Trypan Blue solution, 11538886, Fisherscientific). Isolated nuclei were loaded on a Chromium 10X genomics controller following the manufacturer protocol using the chromium single-cell v3 chemistry and single indexing and the adapted protocol by Biolegend for the HTO library preparation. The resulting libraries were pooled at equimolar proportions with a 9 for 1 ratio for Gene expression library and HTO library respectively. Finally, the pool was sequenced using 100pb paired-end reads on NOVAseq 6000 system following the manufacturer recommendations (Illumina).

Unique Molecular Index (UMI) Count Matrices for gene expression and for Hash Tag Oligonucleotide (HTO) libraries were generated using the CellRanger count (Feature Barcode)

pipeline. Reads were aligned on the GRCh38-3.0.0 transcriptome reference (10x Genomics). Filtering for low quality cells according to the number of RNA, genes detected, and percentage of mitochondrial RNA was performed. For HTO sample, the HTO matrix was normalized using centered log-ratio (CLR) transformation and cells were assigned back to their sample of origin using HTODemux function of the Seurat R Package. Then, normalizations of the gene expression matrix for cellular sequencing depth, mitochondrial percentage and cell cycle phases using the variance stabilizing transformation (vst) based Seurat::SCTransform function were performed.

To integrate the experimental replicates of the single cell experiments, the harmony R package (https://github.com/immunogenomics/harmony) was used. In order to integrate the datasets, the SCTransform normalized matrices was merged and PCA was performed using Seurat::RunPCA default parameter. The 50 principal components (dimensions) of the PCA were corrected for batch effect using harmony::RunHarmony function. Then, the 30 first batch corrected dimensions were used as input for graph-based cell clustering and visualization tool. Seurat::FindNeighbors using default parameters and Seurat::FindClusters function using the Louvain algorithm were used to cluster cells according to their batch corrected transcriptomes similarities. To visualize the cells similarities in a 2-dimension space, the Seurat::RunUMAP function using default parameter was used. Cell clusters were then annotated based on cell type specific gene expression markers.

To study effect of conditioned media from CHO cells expressing APP WT or APP V717L on hiNPCs-derived cells, cell type specific differential expression analysis was performed on 7578 cells (2570 “APPV717L” cells, 2262 “APPWT” cells and 2746 control cells) using wilcoxon rank-sum test after normalization and regularized variance stabilization of the raw count using SCTransform (Hafemeister and Satija, 2019). We used adjusted p-value<0.05 and |log2FC|>0.25 as cut-offs to define differently expressed genes. Functional enrichment analysis was performed using the R package FGSEA (Fast Pre-ranked Gene Set Enrichment Analysis, version 1.26.0). To perform fgsea, we utilized a gene set list at adjusted p-value<0.05 sorted based on log2FC from three comparisons: APPV717L x Control, APPV717L x APPWT, and APPWT x Control. For the fgseaMultilevel function, the minimum gene set size was set to 15, while the maximum was limited to 400. The significance threshold for p-values was defined as p-value < 0.05. To determine the up- or down-regulated terms within the considered ontologies between conditions, we employed the normalized enrichment score (NES). Terms with NES values greater than 0 were classified as up-regulated, while those with NES values less than 0

were classified as down-regulated. The fgsea Multilevel analysis was performed across all cell types identified within the conditions.

8. Statistical Analysis

All statistical analyses and preparation of graphs were performed using Graph-Pad Prism 8 (San Diego, CA, USA) or RStudio (RStudio Team (2020). RStudio: Integrated Development for R. RStudio, PBC, Boston, MA URL http://www.rstudio.com/). For all statistical comparisons, we first tested for the normality of data distribution using the Kolmogorov-Smirnov test and then compared group variances using the appropriate parametric or non-parametric tests, as indicated in figure legends. Data in plots are represented as mean + standard deviation (SD). An α-error level of $p < 0.05$ was considered significant.

Results

Exposure to low concentrations of Aβ peptides increases electrical activity and reduces synchronicity of hiNs

Increased concentrations of Aβ can lead to neuronal hyperexcitation [9,10,13] and reduced synaptic connectivity in AD animal models. To evaluate whether increased concentrations of Aβ could also affect human neurons, we treated 6-weeks-old mixed hiNs/hiAs cultures with cell secreted Aβ peptides (Figure 1). Firstly, we measured the concentrations of soluble Aβ peptides in the conditioned medium derived from CHO cells expressing the APP^{V717L} (CHO-APP^{V717L}) or APP^{WT} (CHO-APP^{WT}) using alphaLISA and observed averaged concentrations of 700 pM $Aβ_{1-x}$ and and 350pM $Aβ_{1-42}$ in CHO-APP^{WT} conditioned medium (Figure 1B). As previously described [19,21], the concentrations of $Aβ_{1-x}$ was 8-folds higher, whereas that of $Aβ_{1-42}$ was 2.5-folds higher in CHO-APP^{V717L} compared to CHO-APP^{WT} conditioned medium (Figure 1B).

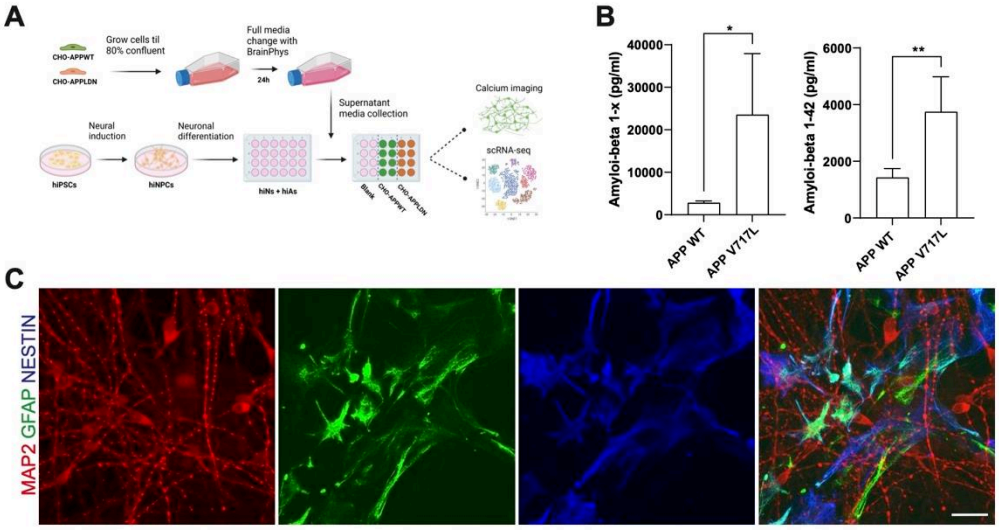

Figure 1: Different concentrations of Aβ peptides in CHO-APP^{WT} and CHO-APP^{V717L} conditioned media. (A) Experimental design showing the generation of hiNs/hiAs cultures, medium conditioning, and treatment. (B) Quantification of $Aβ_{1-x}$ and $Aβ_{1-42}$ peptides in the conditioned medium from CHO-APP^{WT} or CHO-APP^{V717L} (*$p<0.05$; ** $p< 0.01$; Unpaired t-test). (C) Immunocytochemistry in 6-week-old hiNs/hiAs culture using antibodies against MAP2 (red), GFAP (green) and NESTIN (blue). Calibration bar: 20µm.

Forty-eight hours after treatment with conditioned medium, we labeled cells with the calcium sensitive dye Oregon green BAPTA and performed time-lapse video microscopy (Figure 2; Supplementary Movies 1 - 3). Time-series fluorescence images were then analyzed using

CALIMA [20] and calcium spikes were detected when fluorescence change was higher than 2 standard deviations of the average baseline (Methods). We observed a significant higher frequency of calcium spikes in hiNs cultures treated with conditioned medium derived from CHO-APP^{V717L} compared to that from CHO-APP^{WT} (Figure 2C). To evaluate whether this change in the frequency of calcium spikes could be explained in part by a higher concentration of Aβ_{1-42} in the conditioned medium from CHO-APP^{V717L} (Figure 1B), we performed similar calcium imaging experiments in hiNs/HiAs cultures 24 hours after treatment with 100pM of synthetic Aβ_{1-42} or its inverted control peptide (ICP). We observed a significantly higher frequency of calcium spikes in hiNs treated with Aβ_{1-42} compared to both vehicle and ICP (Figure 2D). These observations suggest that the changes in calcium spike frequency observed in hiNs exposed to cell-secreted Aβ peptides are at least partly due to the higher concentrations of Aβ_{1-42} in the CHO-APP^{V717L} conditioned medium.

Next, we measured the synchronicity of calcium transients among hiNs by calculating the eigenvalues of cross-correlation matrices generated by crossing the activity of each individual neuron with all other neurons in the same image field [22]. Despite the increase in the frequency of calcium spikes elicited by Aβ peptides, we observed a lower cross-correlation among inter-neuron calcium spikes in cultures exposed to cell-secreted Aβ or synthetic Aβ_{1-42} (Figure 2F-G), suggesting a reduction in neuronal synchronization. The proportion of active cells (defined as cells showing at least one calcium spike detected during the time of observation) was similar among conditions (Cell-secreted Aβ - Control: 44.36 ± 22.27%; APP WT: 39.68 ± 15.5%; APP V717L: 42.21 ± 20.71%; Synthetic Aβ – Control: 31.31 ± 9.59 %; ICP: 39.61 ± 6.85 %; Aβ_{1-42}: 36.2 ± 11.78 %). Altogether, these observations indicate that exposure to low concentrations of cell-secreted Aβ or synthetic Aβ_{1-42} peptides is sufficient to alter the electrical activity of hiNs circuits.

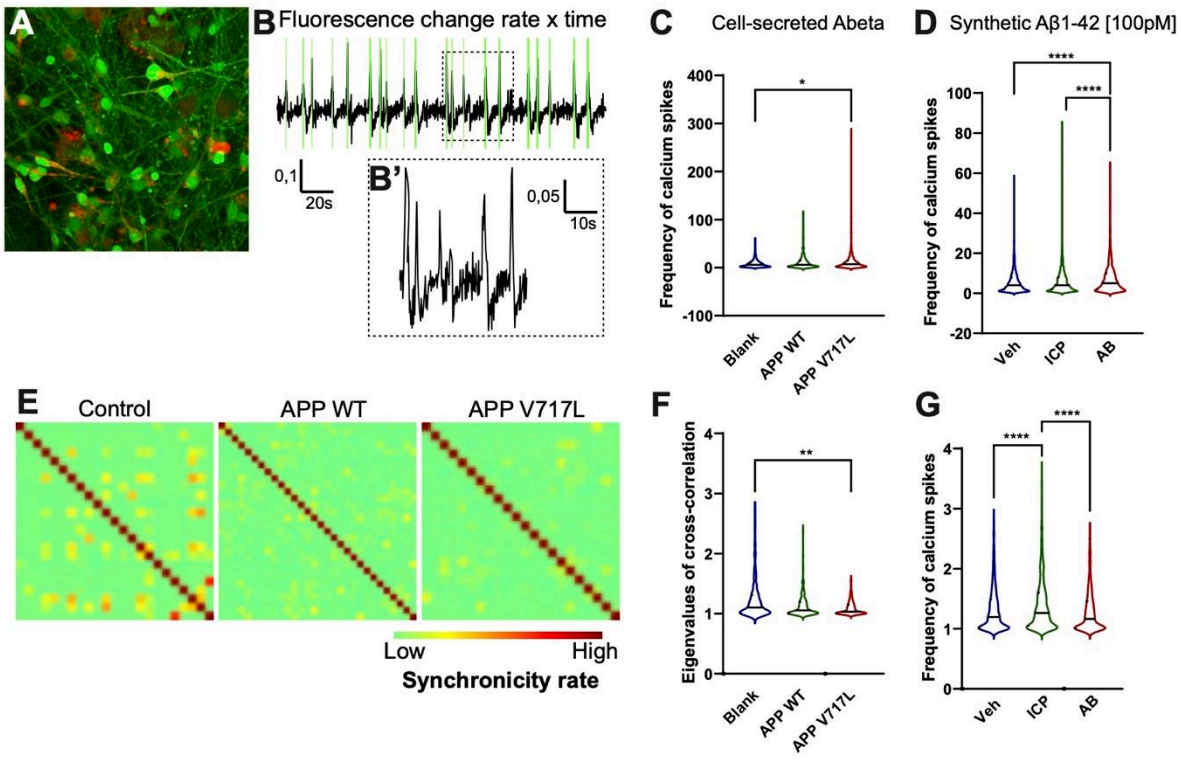

Figure 2: Altered frequency of calcium transients in hiNs exposed to Aβ peptides. (A) Snapshot of 6-week-old hiNs/hiAs culture labeled with Oregon green BAPTA (green) and treated 24h before with 100nM of HiLyte™ Fluor 555-labeled $A\beta_{1-42}$ (red). (B-B') Representative plot of fluorescence change over time in 1000 frames. Green vertical lines indicate detected calcium spikes ($\Delta F > 2$ SDs). Dashed box is magnified in B'. (C) Quantification of calcium spikes in cultures treated with conditioned medium 48h before imaging. (D) Quantification of calcium spikes in cultures treated with 100pM synthetic $A\beta_{1-42}$ 24h before imaging. (E) Representative cross-correlation matrices showing the synchronicity rate of hiNs calcium transients in different conditions. (F) Graphic showing the eigenvalues of cross-correlation matrices in control and cell-secreted treated hiNs/hiAs cultures. (G) Same for cultures treated with synthetic $A\beta_{1-42}$. Statistics in C-D, F-G: *Padj< 0.05; ****Padj<0.0001; Kruskal-Wallis followed by Dunn's multiple comparison test; n= 3 independent cultures for each condition. Number of analyzed cells per condition: Blank Brainphys= 1098; APP^{WT}= 580; APP^{V717L}= 670; Vehicle= 2543; ICP= 3459; $A\beta_{1-42}$= 2472.

Transcriptional changes in hiNs exposed to elevated concentrations of Aβ peptides

We next sought to identify possible changes in gene expression in human-induced astrocytes and neurons elicited by treatment with Aβ. To that, we performed snRNA-seq of mixed hiNs/hiAs cultures treated with conditioned media from CHO-APP^{V717L} or CHO-APP^{WT} and blank Brainphys for 48h (Figure 1). After quality control (Methods), we recovered 7578 nuclei

and identified 17 different cell types/subtypes using unsupervised clustering based on gene expression (Figure 3A). We observed that treatment with conditioned media significantly affected the proportion of cells in clusters 1 and 3, but there was no difference between CHO-APP^{V717L} and CHO-APP^{WT} (Figure 3B). To annotate main cell types in our dataset, we identified the top markers of each cluster (Supplementary Table 1) and evaluated the expression of the astrocyte markers SLC1A3 (GLAST), GFAP and TNC; pan-neuronal markers SNAP25, DCX, MAPT; glutamatergic neurons marker SLC17A6 (VGLUT2); GABAergic neurons marker GAD1 and GAD2; and neural progenitor cells (NPCs) markers HES6, CCND2 and CDK6 in different clusters (Figure 3C). We were able to identify 2 NPCs (14 and 17), 4 astrocytes (2, 3, 4 and 5), 7 glutamatergic neurons (12, 6, 7, 9, 10, 11 and 12) and 3 GABAergic neurons clusters (8, 12 and 15). We were unable to unambiguously assign cluster 16 to any specific cell type based on its gene expression profile and therefore annotated it as "unclassified" (Figure 3D). Although we observed significant statistical differences in the proportions of cell types within a same condition, no differences were observed when we compared the proportion of an individual cell type among conditions (Figure 3E). We also evaluated the expression of putative Aβ ligands [23] in our cultures and found that hiNs mainly expressed acetylcholine receptor subunit alpha-7 (CHRNA7), Glutamate Ionotropic Receptor NMDA Type Subunit 1 (GRIN1), Glutamate Metabotropic Receptor 5 (GRM5) and LDL Receptor Related Protein 1 (LRP1), whereas hiAs mainly expressed LRP1 and Prion Protein (PRNP) (Figure 3F).

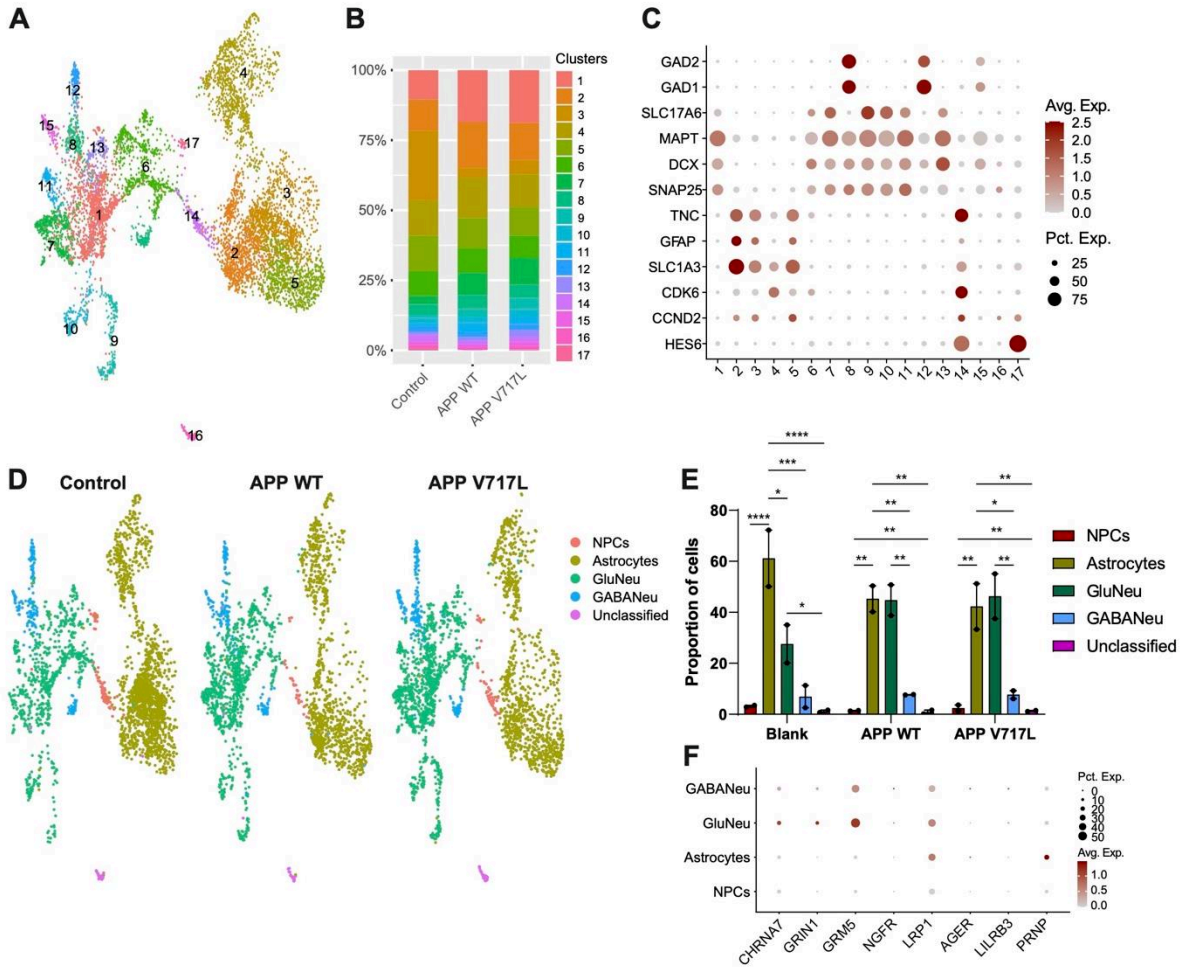

Figure 3: Similar cellular composition of hiNs/hiAs cultures treated with control or CHO-cells conditioned media. (A) UMAP representation of the different cell clusters in hiNs/hiAs cultures. (B) Relative proportion of cell clusters. (C) Dot plot showing the expression of key cell markers used to annotate cell populations. (D) UMAP representation of the annotated cell types/subtypes in hiNs/hiAs cultures in different treatment conditions. (E) Proportion of cell types/subtypes in different conditions (statistics). (F) Dot Plot showing the expression of putative Aβ ligands in different cell types.

To characterize early molecular alterations elicited by conditioned media treatments, we used the Wilcoxon rank-sum test to identify differently expressed genes (DEGs) in NPCs, astrocytes, glutamatergic and GABAergic neurons. We found that treatment with conditioned medium from CHO-APP^{WT} significantly (log2FC>0.25 and FDR<0.05) affected the expression of 252 genes in astrocytes, 32 in GABAergic neurons and 89 in glutamatergic neurons (Figure 4; Supplementary Table 2). Nevertheless, a more significant effect was observed in cultures treated with conditioned medium from CHO-APP^{V717L}, where we identified 235 DEGs in

astrocytes, but 228 in GABAergic neurons and 596 in glutamatergic neurons (Figure 4; Supplementary Table 2). Interestingly, a direct comparison of the transcriptional profile of cultures treated with conditioned medium from CHO-APP^{V717L} or CHO-APP^{WT} revealed a selective alteration in gene expression of glutamatergic neurons (174 DEGs in APP V717L compared to APP WT), but only 2 DEGS in GABAergic neurons and 10 DEGs in astrocytes (Figure 4; Supplementary Table 2). Together, these data indicate that elevated levels of APP and its metabolites modulate gene expression in astrocyte and different neuronal subtypes, and that further increase in Aβ concentrations has a more prominent effect in gene expression of glutamatergic neurons.

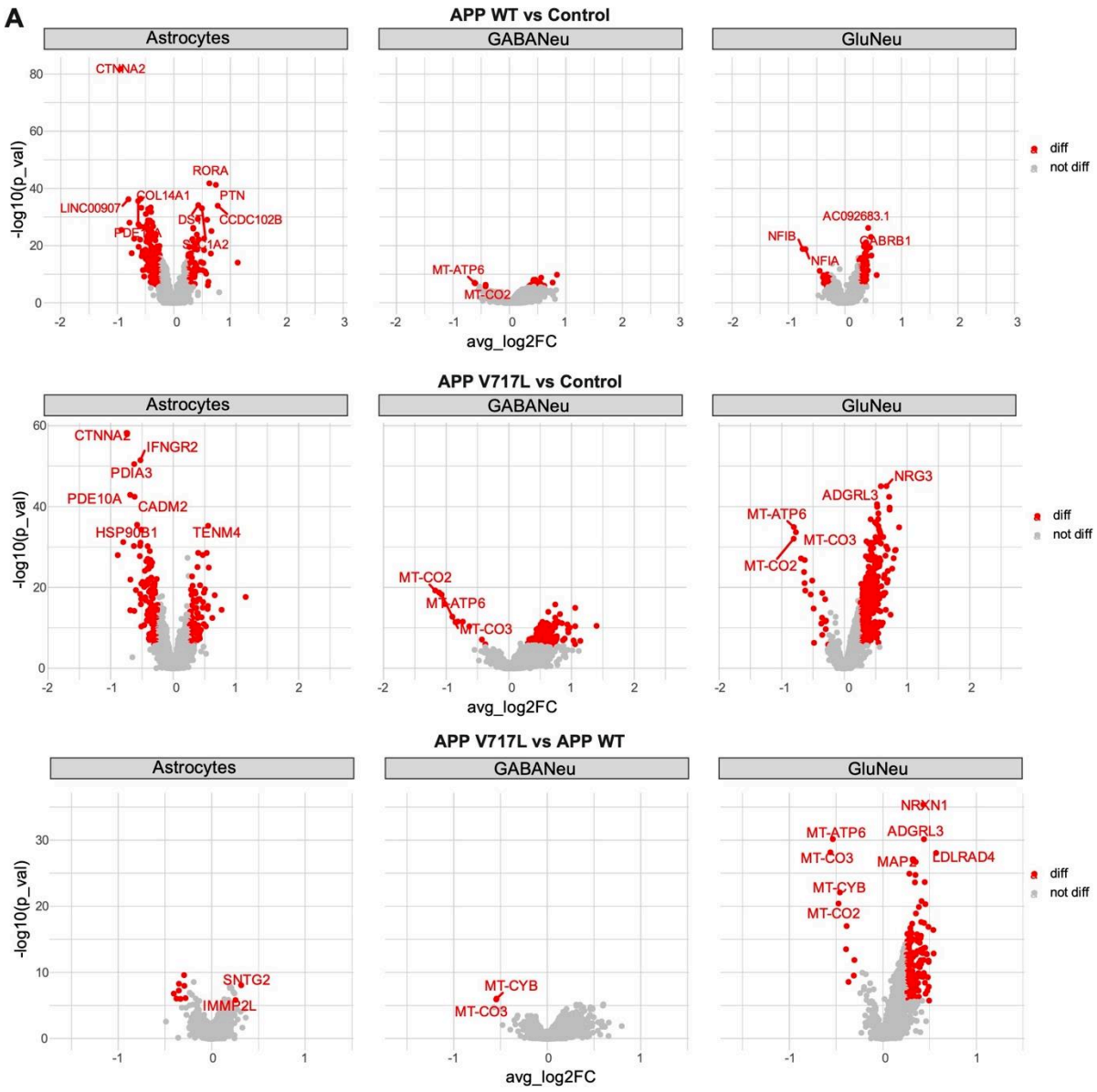

Figure 4: Exposure to Aβ peptides modify gene expression in hiNs and hiAs. (A) Volcano plots representing DEGs (red dots, adjusted p-value <0.05 and |log2FC| >0.25) identified in astrocytes,

glutamatergic and GABAergic neurons when comparing CHO-APP^{WT} vs control, or CHO-APP^{V717L} vs control, and CHO-APP^{V717L} vs CHO-APP^{WT}.

Increased concentrations of Aβ affect pathways associated with oxidative stress and synapse transmission

The above analysis is based on fold-change thresholds and could, therefore, mask small variations in gene expression between CHO-APP^{V717L} and CHO-APP^{WT} treated GABAergic neurons and astrocytes. To overcome this limitation, we performed a gene set enrichment analysis (GSEA), which allowed us to identify functional and pathway enrichments modulated by conditioned media treatments in each cell type based on the ranked gene expression values (Subramanian 2005). We observed significant functional enrichments for the comparisons between CHO-APP^{V717L} vs Control but not CHO-APP^{WT} vs Control conditions (Figure 5). In astrocytes, treatment with conditioned medium from CHO-APP^{V717L} up-regulated genes associated with regulation of cell-differentiation, and down-regulated genes associated with catabolic process and endoplasmic reticulum lumen (Supplementary Table 3). In neurons, up regulated genes were mainly associated with synapse-related terms, whereas down-regulated genes were associated with metabolic processes (Figure A-B; Supplementary Table 3). We also found functional enrichment for gene sets associated with neuronal intrinsic electrical properties, such as ion channels and calcium ion binding, in glutamatergic but not GABAergic neurons treated with CHO-APP^{V717L} conditioned medium compared to controls (Figure 5A; Supplementary Table 3). Furthermore, only glutamatergic neurons displayed functional enrichments for gene sets identified in cultures treated with conditioned medium from CHO-APP^{V717L} compared to CHO-APP^{WT} (Figure 5C; Supplementary Table 3), further suggesting a higher sensibility of this neuronal subtype to Aβ. Up-regulated genes were enriched for cell adhesion, regulation of cellular component biogenesis and post-synapse membrane, whereas down-regulated genes were enriched for transported activity, mitochondrion and catalytic complex (Figure 5C; Supplementary Table 3). Altogether, these findings indicate that at least part of the molecular alterations observed in hiNs are related to the increased Aβ concentration in CHO-APP^{V717L} compared to CHO-APP^{WT} conditioned medium.

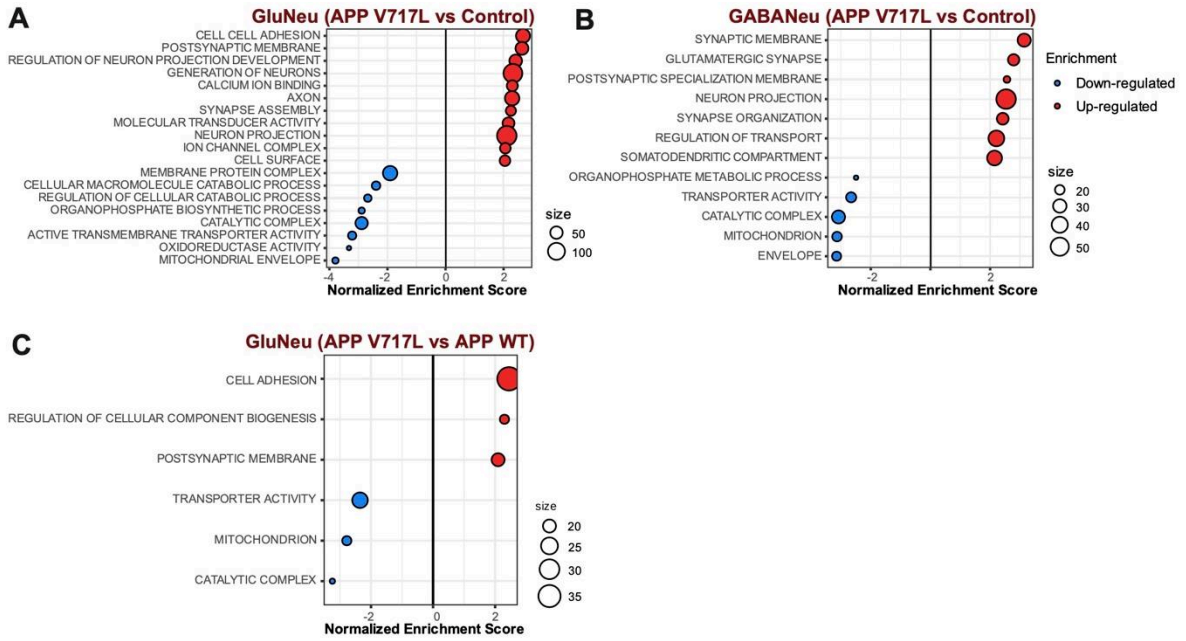

Figure 5: Enrichment for synaptic and metabolic pathways in hiNs treated with Aβ peptides. (A-C) Dot Plots showing the normalized enrichment scores (NES) for pathways enriched for genes differentially expressed in glutamatergic neurons (A, C) and GABAergic neurons (B) when comparing CHO-APP^{V717L} vs control (A-B) or CHO-APP^{V717L} vs CHO-APP^{WT} (C).

Selective effect of Aβ on synaptic processes of glutamatergic neurons

Synapses are fundamental information processing units of the brain and synaptic dysregulation is central to AD pathology. To further characterize our transcriptomic data in a synapse context, we used SynGO, a systematic annotation of synaptic genes and ontology of synaptic processes [24]. Confirming our previous observations using GSEA, we identified the enrichment of several gene ontologies (GOs) related to synaptic biological processes in both glutamatergic and GABAergic neurons (Figure 6; Supplementary Table 4). This enrichment was mainly evident for DEGs identified in neurons exposed to conditioned medium from CHO-APP^{V717L} compared to controls (Figure 6A-B), affecting both the pre- and post-synaptic compartments, and associated with the regulation of presynaptic cytosolic calcium levels, synaptic vesicle cycle, regulation of postsynaptic membrane neurotransmitter receptor levels and synapse assembly, among other synaptic processes (Supplementary Table 4). Also, like our GSEA analysis, we only observed significant enrichments for DEGs identified in glutamatergic neurons when comparing exposed to conditioned medium from CHO-APP^{V717L} compared to CHO-APP^{WT} (Figure 6D; Supplementary Table 4).

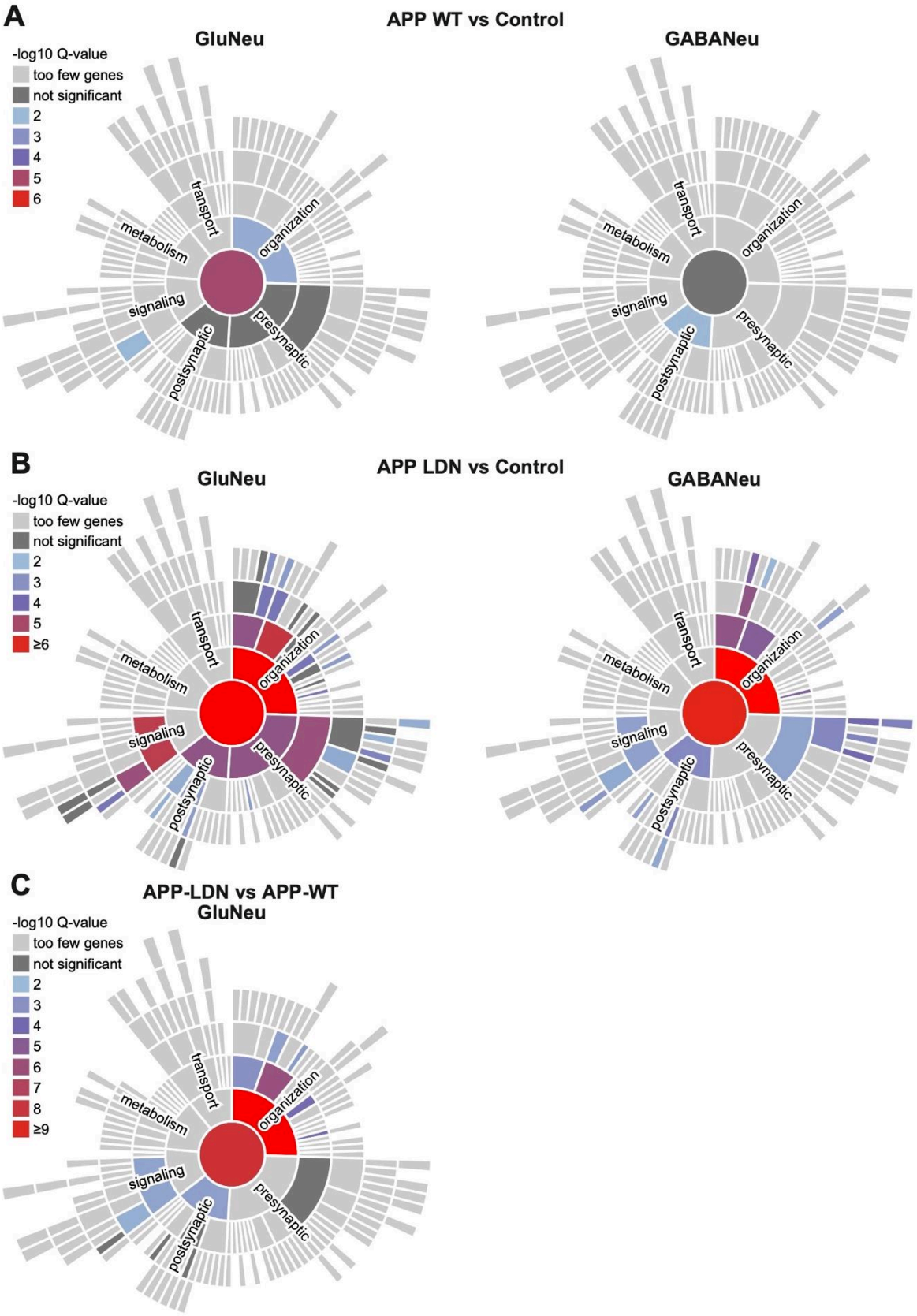

Figure 6: Genes modulated by CHO-APP^{V717L} conditioned medium are involved in synapse organization and signaling. (A-C) Synapse-related gene ontologies for biological processes enriched

for DEGs identified in glutamatergic od GABAergic neurons when comparing CHO-APP^{WT} vs control (A), or CHO-APP^{V717L} vs control (B), and CHO-APP^{V717L} vs CHO-APP^{WT}(C).

Exposure to Aβ peptides alters neuroglial communication

Lastly, we leveraged our snRNAseq data to infer the intercellular communication patterns in our hiNs/hiAs cultures and to evaluate how these patterns could be impacted by the treatment with CHO-APP^{V717L} or CHO-APP^{WT} conditioned medium. To that end, we employed CellChat to predict major signaling inputs and outputs for cells and delineates conserved and context-specific pathways across different conditions [25]. We observed consistent signaling patterns in astrocytes, glutamatergic neurons and GABAergic neurons in all 3 experimental conditions, but some conspicuous differences could also be observed (Figure 7; Supplementary Table 5). Compared to controls, both CHO-APP^{V717L} and CHO-APP^{WT} conditioned media inhibited the neuregulin (NRG), epidermal growth factor (EGF) and myelin protein zero (MPZ) signaling in astrocytes, stimulated cadmium (CADM) signaling in glutamatergic neurons and CD46 signaling in astrocytes, glutamatergic and GABAergic neurons (Figure 7A-B). We also observed specific changes in signaling patterns of cells treated with CHO-APP^{V717L} compared to CHO-APP^{WT} conditioned media, including a higher the relative strength of ephrin-A (EPHA), semaphorin (SEMA5) and NECTIN signaling, and a lower relative strength in midkine (MK; also known as neurite growth-promoting factor 2 - NEGF2) and fibronectin (FN1) signaling (Figure 7C). In accordance with our previous observations in gene expression, we found that treatment with CHO-APP^{V717L} or CHO-APP^{WT} conditioned media increased both the outgoing and incoming interaction strength on the aggregated cell-cell communication network from all signaling pathways in glutamatergic neurons and to a lesser extent in GABAergic neurons (Figure 7D). In contrast, the conditioned media treatment reduced the outgoing and incoming interaction strength in astrocytes (Figure 7D). Collectively, these analyses indicate that small increases in Aβ concentrations may have important consequences for neuroglia communication.

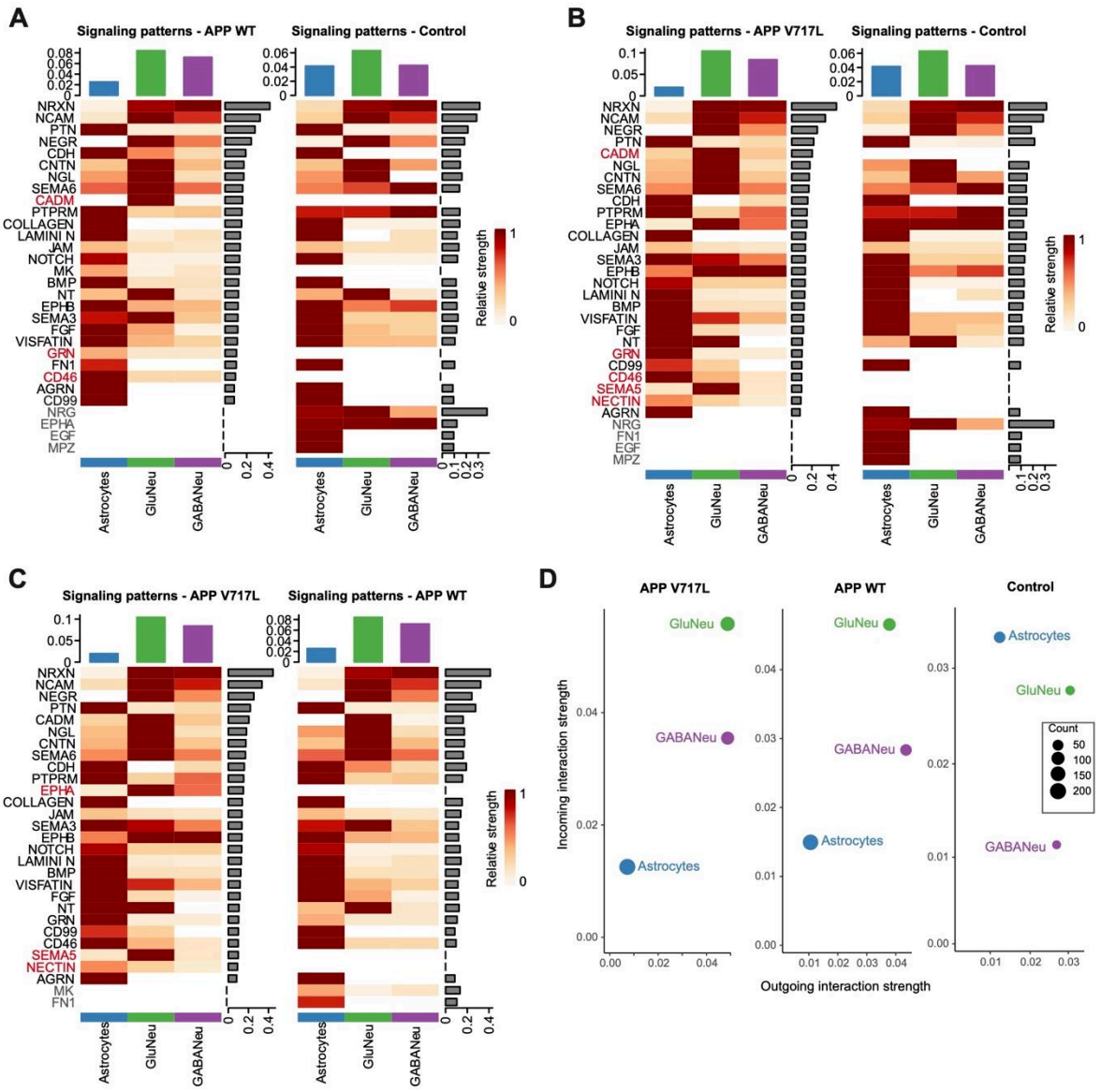

Figure 7: Aβ peptides modulate specific signaling pathways in hiNs/hiAs. (A-C) Heatmaps showing the relative strength of signaling pathways in astrocytes, glutamatergic and GABAergic neurons exposed to conditioned media or control treatments. Signaling pathways specific to one condition are highlighted in gray and red. (D) Dot plots showing the averaged interaction strength for incoming and outgoing signaling in astrocytes, glutamatergic and GABAergic neurons exposed to conditioned media or control treatments. Dot sizes indicate the number of ligand-receptor pairs ("Counts") identified in each cell type.

Discussion

AD patients show aberrant neural network activity in the form of both hyper- and hypo-excitability, and several lines of evidence indicate that these network alterations result from changes in neuronal excitability and synaptic transmission tied to elevated Aβ levels [13,26–28]. Yet, the molecular mechanisms underlying Aβ-induced hyper-excitability remain unclear. In this work, we show that human-induced neurons acutely exposed to low concentrations of both cell-secreted Aβ peptides (including $A\beta_{1-42}$) or synthetic $A\beta_{1-42}$ present alterations in the frequency of calcium transients suggestive of increased neuronal excitability. We also show that cell-secreted Aβ up-regulates the expression of several synaptic-related genes and down-regulates the expression of genes associated with metabolic processes in mitochondria mainly in glutamatergic neurons and to a lesser degree in GABAergic neurons and astrocytes. Collectively, these findings suggest that slight elevations in Aβ concentrations are sufficient to elicit transcriptional changes in human neurons that can contribute to early alterations on neural network activity.

Aβ peptides play a central role in the pathogenesis of AD. When they accumulate abnormally in the brain, they can have detrimental effects on neurons, such as the induction of neuritic plaques, disruption of calcium homeostasis, synaptic loss and oxidative stress [29,30], thus directly contributing to neuronal dysfunction and death. Aβ peptides also affect astrocytes [14,31–33], which can indirectly contribute to neuronal dysfunctions in AD. Moreover, the presence of Aβ in the brain can activate microglia, the immune cells of the central nervous system, leading to neuroinflammation [34,35]. Chronic neuroinflammation can further exacerbate neuronal damage and contribute to the progression of AD. Therefore, Aβ-mediated signaling mediates both cell-autonomous and non-cell-autonomous processes impacting neuronal function and neurodegeneration. In our work, we only model the possible effects of Aβ peptides in neurons and astrocytes. Future work should evaluate the effects of those peptides in more complex hiPSC-derived cellular system harboring neurons, astrocytes, oligodendrocytes, microglia and endothelial cells, thus better representing the complex cellular landscape of the brain.

Despite this limitation, our results reveal some important features of the acute neuronal response to low concentrations of APP and Aβ peptides, which can partly mirror early stages of AD pathology. Here, we show that exposure to CHO-APP^{V717L} conditioned medium, which mainly differ from CHO-APP^{WT} conditioned medium by a higher concentration of Aβ

oligomers enriched for $A\beta_{1-42}$ [19,21], leads to a higher frequency and lower synchronicity of calcium spikes in hiNs. We also describe similar alterations in cultures treated with purified $A\beta_{1-42}$ peptide, suggesting that acute exposition to a low concentration of $A\beta_{1-42}$ is sufficient and necessary to induce human neuron hyperexcitability and reduced coordination of network activity. These finding agree with previous work showing that hiPSC-derived neurons bearing AD-related mutations in presenilin-1 or amyloid precursor protein show a higher frequency of spontaneous action potential compared to isogenic gene corrected controls that is reversed via either γ-Secretase or BACE1 inhibition [16]. It also coincides with work in mice showing that low concentrations (200pM) of $A\beta_{1-42}$ induces an increase of frequency of miniature EPSCs, a decrease of paired pulse facilitation, an increased length of postsynaptic density and an increased expression of plasticity-related proteins [9,26]. These effects were present upon extracellular but not intracellular application of the peptide and involved the activation of α7 nicotinic acetylcholine receptors [26], which are also expressed in a fraction of hiNs (mainly glutamatergic neurons) in our cultures.

The alterations in calcium dynamics together with the gene expression pattern of known $A\beta_{1-42}$ ligands in our cultures may suggest a direct effect of this peptide in the regulation of neuronal functional properties. However, our experimental design does not allow us to unambiguously disentangle the direct effects of Aβ peptides in neurons from potential indirect effects mediated by astrocytes. In fact, inclusions of aggregated Aβ in astrocytes critically affect their ability to support neuronal function [33] and recovery of astrocytic calcium activity normalizes neuronal hyperactivity in a mouse model of amyloidopathy [32], suggesting that at least part of the neuronal alterations observed in response to Aβ peptides are mediated by astrocytes. Yet, our transcriptomic data indicate that exposure to Aβ peptides directly modulate gene expression in glutamatergic neurons, since only this cell type show significant alterations in gene expression when exposed to CHO-APP^{V717L} compared to CHO-APP^{WT} conditioned medium. Moreover, the higher expression of putative Aβ receptors in hiNs compared to hiAs, together with the predominant number of genes differentially expressed in glutamatergic neurons exposed to CHO-APP^{V717L} conditioned medium compared to GABAergic neurons or astrocytes, suggest a primarily cell-autonomous effect of Aβ-mediated signaling in glutamatergic neurons.

Our transcriptional data also reveal critical effects of Aβ-mediated signaling on the regulation of metabolism, electrical activity and synaptic plasticity in hiNs, especially glutamatergic ones. These finding are in accordance with previous studies in AD animal models at early stages of amyloidopathy [36–38] and in the brains of patients with AD at early Braak stages [36,39–42].

Thus, we believe that our results in hiNs may provide insightful information on the molecular mechanisms mediating Aβ-mediated neuronal hyperexcitability in AD. Moreover, our innovative approach to identify intercellular signaling pathways impacted by Aβ peptides via the identification of interactions among ligands, receptors and their cofactors expressed by hiNs and hiAs may contribute to unravel new targetable molecules to prevent Aβ-mediated toxicity.

We show that treatment with CHO-APP^{V717L} conditioned medium activates EPHA, SEMA5 and NECTIN signaling mainly in glutamatergic neurons and, to a lesser extent, in GABAergic neurons and astrocytes. Ephrin ligands and their associated Eph receptors guide axons during neural development and regulate synapse formation and neuronal plasticity in the adult [43]. Similarly, members of the nectin and semaphorin signaling pathways regulate several aspects of synapse formation and maintenance during development and adulthood [44,45]. Among the pathways activated in hiNs treated CHO-APP^{V717L} compared to CHO-APP^{WT} conditioned medium, SEMA5B regulates the elimination of synaptic connections in cultured hippocampal neurons [46], EPHA1 is a risk-modifying locus for AD [47,48]. Therefore, it is plausible to speculate that at least part of the functional and gene expression alterations observed in hiNs exposed to Aβ peptides are mediated by those signaling pathways.

Although we cannot formerly rule out the contribution of soluble APP products rather than Aβ peptides to the alterations observed on the activity and gene expression of hiNs, the fact that they are mainly observed in cells treated with CHO-APP^{V717L} conditioned medium strongly suggest that soluble Aβ peptides are key regulators of neuronal plasticity. On the other hand, the milder alterations observed in the expression of synaptic-related genes of hiNs exposed to the CHO-APP^{WT} conditioned medium could suggest that even lower amounts of Aβ peptides, APP itself or other APP metabolites also affect these cells, as previously suggested in AD mouse models [9,49]. Future studies could employ our system to evaluate the impact of Aβ and other APP metabolites at different concentrations and aggregation states to the regulation of the functional properties and gene expression in human neurons, thus further advancing our understanding about the physiological and pathological roles of theses complex signaling molecules.

Conclusions

Our results indicate that slight elevations in Aβ concentrations are sufficient to elicit transcriptional changes in human neurons, contributing to early alterations on neural network activity, and suggest targetable candidate intercellular signaling pathways mediating Aβ-induced neuronal hyperexcitability.

List of abbreviations

Aβ - amyloid beta

hiNs – human-induced neurons

hiAs - human-induced astrocytes

snRNA-seq – single nucleus RNA-sequencing

APP – amyloid precursor protein

CHO - Chinese hamster ovary

CHO-APP^{WT} – CHO cell line overexpressing the human APP695

CHO-APP^{V717L} - CHO cell line overexpressing the human London mutated APP695

DEG – differentially expressed gene

GSEA – gene-set enrichment analysis

Declarations

Ethics approval and consent to participate

Not applicable

Consent for publication

Not applicable

Availability of data and materials

Count table and metadata from snRNA-seq experiments are available at Mendeley Data, V1, doi: 10.17632/mjcsph7mbs.1

Time-lapse video-microscopy images are available upon reasonable request.

Competing interests

The authors declare no competing interests.

Funding

This work was co-funded by the European Union under the European Regional Development Fund (ERDF) and by the Hauts de France Regional Council (contract no.18006176), the MEL (contract_2016_ESR_05), the French State (contract no. 2018-3-CTRL_IPL_Phase2), and Brazilian National Council for Scientific and Technological Development (CNPq). The UMR 8199 LIGAN-PM Genomics platform (Lille, France) belongs to the 'Federation de Recherche' 3508 Labex EGID (European Genomics Institute for Diabetes; ANR-10-LABX-46) and was supported by the ANR Equipex 2010 session (ANR-10-EQPX-07-01; 'LIGAN-PM'). The LIGAN-PM Genomics platform (Lille, France) is also supported by the FEDER and the Region Nord-Pas-de-Calais-Picardie and is a member of the “France Génomique” consortium (ANR-10-INBS-009). L.C.C.I. was supported by a scholarship from the Coordenação de Aperfeiçoamento de Pessoal de Nível Superior (CAPES), Brazil.

Authors' contributions

Conceptualization, M.R.C.; Methodology, M.R.C., F.D.; Investigation, A.R.M.F., O.S., A.P., M.R.C.; Writing - Original Draft, M.R.C.; Writing - Reviews & Editing, M.R.C., J.C.L., A.P., A.R.M.F., L.C.C.I.; Figures preparation: M.R.C., A.R.M.F., L.C.C.I., A.P. Supervision, M.R.C., F.D., J.C.L.; Funding Acquisition, M.R.C., J.C.L., F.D. All authors have read and approved the manuscript.

Acknowledgements

The authors thank the BioImaging Center Lille (BICeL; US 41 - UMS 2014). The authors also thank Dr. Frédéric Checler (Institut de Pharmacologie Moléculaire et Cellulaire, UMR6097 CNRS/Université de Nice-Sophia-Antipolis, France) for kindly providing CHO-APP^{V717L} and CHO-APP^{WT} cells.

References

1. Prince M, Ali GC, Guerchet M, Prina AM, Albanese E, Wu YT. Recent global trends in the prevalence and incidence of dementia, and survival with dementia. Alzheimer's Res Ther [Internet]. Alzheimer's Research & Therapy; 2016;8. Available from: http://dx.doi.org/10.1186/s13195-016-0188-8

2. Karran E, Mercken M, Strooper B De. The amyloid cascade hypothesis for Alzheimer's disease: an appraisal for the development of therapeutics. Nat Rev Drug Discov [Internet]. 2011;10:698–712. Available from: https://doi.org/10.1038/nrd3505

3. Lacorte E, Ancidoni A, Zaccaria V, Remoli G, Tariciotti L, Bellomo G, et al. Safety and Efficacy of Monoclonal Antibodies for Alzheimer's Disease: A Systematic Review and Meta-Analysis of Published and Unpublished Clinical Trials. J Alzheimer's Dis. 2022;87:101–29.

4. Palop JJ, Mucke L. Network abnormalities and interneuron dysfunction in Alzheimer disease. Nat Rev Neurosci. Nature Publishing Group; 2016;17:777–92.

5. Vossel KA, Tartaglia MC, Nygaard HB, Zeman AZ, Miller BL. Review Epileptic activity in Alzheimer's disease: causes and clinical relevance [Internet]. 2017. Available from: www.thelancet.com/neurology

6. Canter RG, Penney J, Tsai LH. The road to restoring neural circuits for the treatment of Alzheimer's disease. Nature. Nature Publishing Group; 2016. p. 187–96.

7. Styr B, Slutsky I. Imbalance between firing homeostasis and synaptic plasticity drives early-phase Alzheimer's disease. Nat. Neurosci. Nature Publishing Group; 2018. p. 463–73.

8. Harris SS, Wolf F, De Strooper B, Busche MA. Tipping the Scales: Peptide-Dependent Dysregulation of Neural Circuit Dynamics in Alzheimer's Disease. Neuron [Internet]. Elsevier Inc.; 2020;1–19. Available from: https://doi.org/10.1016/j.neuron.2020.06.005

9. Gulisano W, Melone M, Ripoli C, Tropea MR, Li Puma DD, Giunta S, et al. Neuromodulatory action of picomolar extracellular Aβ42 oligomers on presynaptic and postsynaptic mechanisms underlying synaptic function and memory. J Neurosci. Society for Neuroscience; 2019;39:5986–6000.

10. Zott B, Simon MM, Hong W, Unger F, Chen-Engerer HJ, Frosch MP, et al. A vicious cycle of β amyloid−dependent neuronal hyperactivation. Science (80-). American Association for the Advancement of Science; 2019;365:559–65.

11. Cirrito JR, Yamada KA, Finn MB, Sloviter RS, Bales KR, May PC, et al. Synaptic activity regulates interstitial fluid amyloid-β levels in vivo. Neuron. 2005;48:913–22.

12. Bero AW, Yan P, Roh JH, Cirrito JR, Stewart FR, Raichle ME, et al. Neuronal activity regulates the regional vulnerability to amyloid-β 2 deposition. Nat Neurosci. 2011;14:750–6.

13. Busche MA, Chen X, Henning HA, Reichwald J, Staufenbiel M, Sakmann B, et al. Critical role of soluble amyloid-β for early hippocampal hyperactivity in a mouse model of Alzheimer's disease. Proc Natl Acad Sci U S A. 2012;109:8740–5.

14. Andersen J V., Skotte NH, Christensen SK, Polli FS, Shabani M, Markussen KH, et al. Hippocampal disruptions of synaptic and astrocyte metabolism are primary events of early amyloid pathology in the 5xFAD mouse model of Alzheimer's disease. Cell Death Dis. 2021;12.

15. Chen C, Ma X, Wei J, Shakir N, Zhang JK, Zhang L, et al. Early impairment of cortical circuit plasticity and connectivity in the 5XFAD Alzheimer's disease mouse model. Transl Psychiatry. Springer US; 2022;12:1–12.

16. Ghatak S, Dolatabadi N, Trudler D, Zhang X, Wu Y, Mohata M, et al. Mechanisms of hyperexcitability in alzheimer's disease hiPSC-derived neurons and cerebral organoids vs. Isogenic control. Elife. 2019;8:1–22.

17. Chambers SM, Fasano CA, Papapetrou EP, Tomishima M, Sadelain M, Studer L. Highly efficient neural conversion of human ES and iPS cells by dual inhibition of SMAD signaling. Nat Biotechnol [Internet]. 2009;27:275–80. Available from: https://doi.org/10.1038/nbt.1529

18. Bardy C, Van Den Hurk M, Eames T, Marchand C, Hernandez R V., Kellogg M, et al. Neuronal medium that supports basic synaptic functions and activity of human neurons in vitro. Proc Natl Acad Sci U S A. National Academy of Sciences; 2015;112:E2725–34.

19. Guillot-Sestier MV, Sunyach C, Ferreira ST, Marzolo MP, Bauer C, Thevenet A, et al. α-secretase-derived fragment of cellular prion, N1, protects against monomeric and oligomeric amyloid β(Aβ)-associated cell death. J Biol Chem. 2012;287:5021–32.

20. Radstake FDW, Raaijmakers EAL, Luttge R, Zinger S, Frimat JP. CALIMA: The semi-automated open-source calcium imaging analyzer. Comput Methods Programs Biomed. Elsevier B.V.; 2019;179.

21. Kilinc D, Vreulx A-C, Mendes T, Flaig A, Marques-Coelho D, Verschoore M, et al. Pyk2 overexpression in postsynaptic neurons blocks amyloid β1–42-induced synaptotoxicity in microfluidic co-cultures. Brain Commun. 2020;2:1–18.

22. Umakantha A, Morina R, Cowley BR, Snyder AC, Smith MA, Yu BM. Bridging neuronal correlations and dimensionality reduction. Neuron [Internet]. Elsevier Inc.; 2021;109:2740-2754.e12. Available from: https://doi.org/10.1016/j.neuron.2021.06.028

23. Chen GF, Xu TH, Yan Y, Zhou YR, Jiang Y, Melcher K, et al. Amyloid beta: Structure, biology and structure-based therapeutic development. Acta Pharmacol Sin [Internet]. Nature Publishing Group; 2017;38:1205–35. Available from: http://dx.doi.org/10.1038/aps.2017.28

24. Koopmans F, van Nierop P, Andres-Alonso M, Byrnes A, Cijsouw T, Coba MP, et al. SynGO: An Evidence-Based, Expert-Curated Knowledge Base for the Synapse. Neuron. 2019;103:217-234.e4.

25. Jin S, Guerrero-Juarez CF, Zhang L, Chang I, Ramos R, Kuan CH, et al. Inference and analysis of cell-cell communication using CellChat. Nat Commun [Internet]. Springer US; 2021;12:1–20. Available from: http://dx.doi.org/10.1038/s41467-021-21246-9

26. Gulisano W, Melone M, Li Puma DD, Tropea MR, Palmeri A, Arancio O, et al. The effect of amyloid-β peptide on synaptic plasticity and memory is influenced by different isoforms, concentrations, and aggregation status. Neurobiol Aging. Elsevier Inc.; 2018;71:51–60.

27. Kazim SF, Seo JH, Bianchi R, Larson CS, Sharma A, Wong RKS, et al. Neuronal network excitability in alzheimer's disease: The puzzle of similar versus divergent roles of amyloid B and TAU. eNeuro. Society for Neuroscience; 2021.

28. Willem M, Tahirovic S, Busche MA, Ovsepian S V., Chafai M, Kootar S, et al. σ-Secretase processing of APP inhibits neuronal activity in the hippocampus. Nature. Nature Publishing Group; 2015;526:443–7.

29. Spires-Jones TL, Hyman BT. The intersection of amyloid beta and tau at synapses in Alzheimer's disease. Neuron. United States; 2014;82:756–71.

30. Kwart D, Gregg A, Scheckel C, Murphy E, Paquet D, Duffield M, et al. A Large Panel of Isogenic APP and PSEN1 Mutant Human iPSC Neurons Reveals Shared Endosomal Abnormalities Mediated by APP β-CTFs, Not Aβ. Neuron. Cell Press; 2019;104:256-270.e5.

31. Mitew S, Kirkcaldie MTK, Dickson TC, Vickers JC. Altered synapses and gliotransmission in alzheimer's disease and AD model mice. Neurobiol Aging. 2013;34:2341–51.

32. Shah D, Gsell W, Wahis J, Luckett ES, Jamoulle T, Vermaercke B, et al. Astrocyte calcium dysfunction causes early network hyperactivity in Alzheimer's disease. Cell Rep [Internet]. 2022;40:111280. Available from: https://www.sciencedirect.com/science/article/pii/S2211124722011007

33. Konstantinidis E, Portal B, Mothes T, Beretta C, Lindskog M, Erlandsson A. Intracellular deposits of amyloid-beta influence the ability of human iPSC-derived astrocytes to support neuronal function. J Neuroinflammation [Internet]. BioMed Central; 2023;20:1–17. Available from: https://doi.org/10.1186/s12974-022-02687-5

34. d'Errico P, Ziegler-Waldkirch S, Aires V, Hoffmann P, Mezö C, Erny D, et al. Microglia contribute to the propagation of Aβ into unaffected brain tissue. Nat Neurosci. Springer US; 2022;25:20–5.

35. Joshi P, Turola E, Ruiz A, Bergami A, Libera DD, Benussi L, et al. Microglia convert aggregated amyloid-β into neurotoxic forms through the shedding of microvesicles. Cell Death Differ [Internet]. 2014;21:582–93. Available from: https://doi.org/10.1038/cdd.2013.180

36. Iohan L da CC, Lambert J-C, Costa MR. Analysis of modular gene co-expression networks reveals molecular pathways underlying Alzheimer's disease and progressive supranuclear palsy. PLoS One [Internet]. Public Library of Science; 2022;17:e0266405. Available from: https://doi.org/10.1371/journal.pone.0266405

37. Shao F, Wang M, Guo Q, Zhang B, Wang X. Characterization of Alzheimer's Disease-Associated Excitatory Neurons via Single-Cell RNA Sequencing Analysis. Front Aging Neurosci. Switzerland; 2021;13:742176.

38. Wan YW, Al-Ouran R, Mangleburg CG, Perumal TM, Lee T V., Allison K, et al. Meta-Analysis of the Alzheimer's Disease Human Brain Transcriptome and Functional Dissection in Mouse Models. Cell Rep. 2020;32.

39. Mathys H, Davila-Velderrain J, Peng Z, Gao F, Mohammadi S, Young JZ, et al. Single-cell transcriptomic analysis of Alzheimer's disease. Nature. Nature Publishing Group; 2019;570:332–7.

40. Grubman A, Chew G, Ouyang JF, Sun G, Choo XY, McLean C, et al. A single-cell atlas of entorhinal cortex from individuals with Alzheimer's disease reveals cell-type-specific gene expression regulation. Nat Neurosci. Nature Research; 2019;22:2087–97.

41. Leng K, Li E, Eser R, Piergies A, Sit R, Tan M, et al. Molecular characterization of selectively vulnerable neurons in Alzheimer's disease. Nat Neurosci [Internet]. Springer US; 2021;24:276–87. Available from: http://dx.doi.org/10.1038/s41593-020-00764-7

42. Marques-Coelho D, Iohan L da CC, Melo de Farias AR, Flaig A, Letournel F, Martin-Négrier ML, et al. Differential transcript usage unravels gene expression alterations in Alzheimer's disease human brains. npj Aging Mech Dis. Nature Research; 2021;7.

43. Klein R. Bidirectional modulation of synaptic functions by Eph/ephrin signaling. Nat Neurosci [Internet]. 2009;12:15–20. Available from: https://doi.org/10.1038/nn.2231

44. Mizutani K, Miyata M, Shiotani H, Kameyama T, Takai Y. Nectin-2 in general and in the brain. Mol Cell Biochem. Netherlands; 2022;477:167–80.

45. Carulli D, de Winter F, Verhaagen J. Semaphorins in Adult Nervous System Plasticity and Disease. Front Synaptic Neurosci. Switzerland; 2021;13:672891.

46. O'Connor TP, Cockburn K, Wang W, Tapia L, Currie E, Bamji SX. Semaphorin 5B mediates synapse elimination in hippocampal neurons. Neural Dev. 2009;4:1–19.

47. Lambert JC, Ibrahim-Verbaas CA, Harold D, Naj AC, Sims R, Bellenguez C, et al. Meta-analysis of 74,046 individuals identifies 11 new susceptibility loci for Alzheimer's disease. Nat Genet. Nature Publishing Group; 2013;45:1452–8.

48. Bellenguez C, Küçükali F, Jansen IE, Kleineidam L, Moreno-Grau S, Amin N, et al. New insights into the genetic etiology of Alzheimer's disease and related dementias. Nat Genet. 2022;54.

49. Lee SH, Kang J, Ho A, Watanabe H, Bolshakov VY, Shen J. APP Family Regulates Neuronal Excitability and Synaptic Plasticity but Not Neuronal Survival. Neuron [Internet]. Elsevier Inc.; 2020;108:676-690.e8. Available from: https://doi.org/10.1016/j.neuron.2020.08.011

Bibliography

1. Lambert E, Saha O, Soares Landeira B, Melo De Farias AR, Hermant X, Carrier A, et al. The Alzheimer susceptibility gene BIN1 induces isoform-dependent neurotoxicity through early endosome defects. acta neuropathol commun. 2022 Dec;10(1):4.

2. Saha O, Melo De Farias AR, Pelletier A, Siedlecki-Wullich D, Gadaut J, Landeira BS, et al. The Alzheimer's disease risk gene BIN1 modulates neural network activity via the regulation of L-type calcium channel expression in human-induced neurons [Internet]. Neuroscience; 2022 Jan [cited 2023 Aug 20]. Available from: http://biorxiv.org/lookup/doi/10.1101/2022.01.18.476601

3. Stelzmann RA, Norman Schnitzlein H, Reed Murtagh F. An english translation of alzheimer's 1907 paper, ?&#65533;ber eine eigenartige erkankung der hirnrinde? Clin Anat. 1995;8(6):429–31.

4. Hippius H, Neundörfer G. The discovery of Alzheimer's disease. Dialogues in Clinical Neuroscience. 2003 Mar 31;5(1):101–8.

5. Grundke-Iqbal I, Wisniewski HM, BINDERt LI. Abnormal phosphorylation of the microtubule-associated protein X (tau) in Alzheimer cytoskeletal pathology. Medical Sciences.

6. Selkoe DJ, Abraham CR, Podlisny MB, Duffy LK. Isolation of Low-Molecular-Weight Proteins from Amyloid Plaque Fibers in Alzheimer's Disease. 1986; Available from: https://onlinelibrary.wiley.com/doi/abs/10.1111/j.1471-4159.1986.tb08501.x?sid=nlm%3Apubmed

7. Serrano-Pozo A, Frosch MP, Masliah E, Hyman BT. Neuropathological Alterations in Alzheimer Disease. Cold Spring Harbor Perspectives in Medicine. 2011 Sep 1;1(1):a006189–a006189.

8. Bekris LM, Yu CE, Bird TD, Tsuang DW. Review Article: Genetics of Alzheimer Disease. J Geriatr Psychiatry Neurol. 2010 Dec;23(4):213–27.

9. De Strooper. Loss-of-function presenilin mutations in Alzheimer disease. 2007;

10. Lanoiselée HM, Nicolas G, Wallon D, Rovelet-Lecrux A, Lacour M, Rousseau S, et al. APP, PSEN1, and PSEN2 mutations in early-onset Alzheimer disease: A genetic screening study of familial and sporadic cases. Miller BL, editor. PLoS Med. 2017 Mar 28;14(3):e1002270.

11. Gatz M, Reynolds CA, Fratiglioni L, Johansson B, Mortimer JA, Berg S, et al. Role of Genes and Environments for Explaining Alzheimer Disease. Arch Gen Psychiatry. 2006 Feb 1;63(2):168.

12. Gowing E, Roher AE, Woods AS, Cotter RJ, Chaney M, Little SP, et al. Chemical characterization of A beta 17-42 peptide, a component of diffuse amyloid deposits of Alzheimer disease. Journal of Biological Chemistry. 1994 Apr;269(15):10987–90.

13. Bitan G, Kirkitadze MD, Lomakin A, Vollers SS, Benedek GB, Teplow DB. Amyloid &#65533;-protein (A&#65533;) assembly: A&#65533;40 and A&#65533;42 oligomerize through distinct pathways.

14. O'Brien RJ, Wong PC. Amyloid Precursor Protein Processing and Alzheimer's Disease. Annu Rev Neurosci. 2011 Jul 21;34(1):185–204.

15. Zhang Y wu, Thompson R, Zhang H, Xu H. APP processing in Alzheimer's disease. Mol Brain. 2011;4(1):3.

16. Mattson MP, Cheng B, Culwell AR, Esch FS, Lieberburg I. Evidence for excitoprotective and intraneuronal calcium-regulating roles for secreted forms of the β-amyloid precursor protein. 1993; Available from: https://www.sciencedirect.com/science/article/abs/pii/089662739390315I?via%3Dihub

17. Ring S, Weyer SW, Kilian SB, Waldron E, Pietrzik CU, Filippov MA, et al. The Secreted β-Amyloid Precursor Protein Ectodomain APPsα Is Sufficient to Rescue the Anatomical, Behavioral, and Electrophysiological Abnormalities of APP-Deficient Mice. J Neurosci. 2007 Jul 18;27(29):7817–26.

18. Habib A, Sawmiller D, Tan J. Restoring sAPPα functions as a potential treatment for Alzheimer's disease. 2017;

19. Goodman Y, Mattson MP. Secreted Forms of β-Amyloid Precursor Protein Protect Hippocampal Neurons against Amyloid β-Peptide-Induced Oxidative Injury. 1994; Available from: https://www.sciencedirect.com/science/article/abs/pii/S0014488684711071?via%3Dihub

20. Deng J, Ahsan H, Obregon DF, Barger SW, Giunta B. Soluble amyloid precursor protein alpha (sAPPα) inhibits tau phosphorylation through modulation of GSK3β signaling pathway. 2015;

21. Mockett BG, Richter M, Abraham WC, Müller UC. Therapeutic Potential of Secreted Amyloid Precursor Protein APPsα. 2017;

22. Tackenberg, Nitsch. The secreted APP ectodomain sAPPα, but not sAPPβ, protects neurons against Aβ oligomer-induced dendritic spine loss and increased tau phosphorylation. 2019;

23. Moreno L, Rose C, Mohanraj A, Alliquant B, Billard JM. sAβPPα Improves Hippocampal NMDA-Dependent Functional Alterations Linked to Healthy Aging. 2015; Available from: https://pubmed.ncbi.nlm.nih.gov/26402095/

24. Dahlgren KN, Manelli AM, Stine WB, Baker LK, Krafft GA, LaDu MJ. Oligomeric and Fibrillar Species of Amyloid-β Peptides Differentially Affect Neuronal Viability. Journal of Biological Chemistry. 2002 Aug;277(35):32046–53.

25. Deshpande A, Mina E, Glabe C, Busciglio J. Different Conformations of Amyloid β Induce Neurotoxicity by Distinct Mechanisms in Human Cortical Neurons. J Neurosci. 2006 May 31;26(22):6011–8.

26. Selkoe DJ. Amyloid β-Protein and the Genetics of Alzheimer's Disease. Journal of Biological Chemistry. 1996 Aug;271(31):18295–8.

27. Gong. Alzheimer_s disease-affected brain Presence of oligomeric Aβ ligands (ADDLs) suggests a molecular basis for reversible memory loss. 2003;

28. Holtta. Evaluating Amyloid-β Oligomers in Cerebrospinal Fluid as a Biomarker for Alzheimer's Disease. 2013;

29. Murphy MP, LeVine H. Alzheimer's Disease and the β-Amyloid Peptide. 2010;

30. Selkoe DJ, Hardy J. The amyloid hypothesis of Alzheimer's disease at 25 years. EMBO Mol Med. 2016 Jun;8(6):595–608.

31. Lei M, Xu H, Li Z, O'Malley TT, Zhang D. Soluble Aβ Oligomers Impair Hippocampal LTP by Disrupting Glutamatergic/GABAergic Balance. 2016;

32. Zott B, Simon MM, Hong W, Unger F, Chen-Hsing-Jung. A vicious cycle of β amyloid-dependent neuronal hyperactivation. 2019;

33. Ferreira ST, Lourenco MV, Oliveira MM, De Felice FG. Soluble amyloid-β oligomers as synaptotoxins leading to cognitive impairment in Alzheimer's disease. 2015;

34. Hu NW, Klyubin I, Anwyl R, Rowan MJ. GluN2B subunit-containing NMDA receptor antagonists prevent A$^{N}_{L}$-mediated synaptic plasticity disruption in vivo.

35. Ramser. Amyloid-β oligomers induce tau-independent disruption of BDNF axonal transport via calcineurin activation in cultured hippocampal neurons. 2013;

36. Cirrito JR. P-glycoprotein deficiency at the blood-brain barrier increases amyloid-deposition in an Alzheimer disease mouse model. Journal of Clinical Investigation. 2005 Nov 1;115(11):3285–90.

37. Bero. Bidirectional Relationship between Functional Connectivity and Amyloid-β Deposition in Mouse Brain. 2012;

38. Iaccarino HF, Singer AC, Martorell AJ, Rudenko A, Gao F, Gillingham TZ, et al. Gamma frequency entrainment attenuates amyloid load and modifies microglia. Nature. 2016 Dec 8;540(7632):230–5.

39. Busche MA, Eichhoff G, Adelsberger H, Abramowski D, Wielderhold KH. Clusters of hyperactive neurons near amyloid plaques in a mouse model of Alzheimer's disease - PubMed. 2008; Available from: https://pubmed.ncbi.nlm.nih.gov/18802001/

40. Verret L, Mann EO, Hang GB, Barth AMI, Cobos I, Ho K, et al. Inhibitory Interneuron Deficit Links Altered Network Activity and Cognitive Dysfunction in Alzheimer Model. Cell. 2012 Apr;149(3):708–21.

41. Gavello D, Calorio C, Franchino C, Cesano F, Carabelli V. Early Alterations of Hippocampal Neuronal Firing Induced by Abeta42 - PubMed. 2018; Available from: https://pubmed.ncbi.nlm.nih.gov/27999123/

42. Gulisano W, Melone M, Ripoli C, Tropea MR, Li Puma DD, Giunta S, et al. Neuromodulatory Action of Picomolar Extracellular Aβ42 Oligomers on Presynaptic and Postsynaptic Mechanisms Underlying Synaptic Function and Memory. J Neurosci. 2019 Jul 24;39(30):5986–6000.

43. Mitroshina EV, Yarkov RS, Mishchenko TA, Krut' VG, Gavrish MS, Epifanova EA, et al. Brain-Derived Neurotrophic Factor (BDNF) Preserves the Functional Integrity of Neural Networks in the β-Amyloidopathy Model in vitro. Front Cell Dev Biol. 2020 Jul 8;8:582.

44. Teipel S, Grothe MJ, Zhou J, Sepulcre J, Dyrba M, Sorg C, et al. Measuring Cortical Connectivity in Alzheimer's Disease as a Brain Neural Network Pathology: Toward Clinical Applications. J Int Neuropsychol Soc. 2016 Feb;22(2):138–63.

45. Blurton-Jones M, LaFerla FM. Pathways by which Abeta facilitates tau pathology. 2006; Available from: https://pubmed.ncbi.nlm.nih.gov/17168643/

46. Hurtado. Aβ Accelerates the Spatiotemporal Progression of Tau Pathology and Augments Tau Amyloidosis in an Alzheimer Mouse Model. 2010;

47. Stalder M, Phinney A, Probst A, Sommer B, Staufenbiel M, Jucker M. Association of Microglia with Amyloid Plaques in Brains of APP23 Transgenic Mice. The American Journal of Pathology. 1999 Jun;154(6):1673–84.

48. Simard AR, Soulet D, Gowing G, Julien JP, Rivest S. Bone Marrow-Derived Microglia Play a Critical Role in Restricting Senile Plaque Formation in Alzheimer's Disease. Neuron. 2006 Feb;49(4):489–502.

49. Bolmont T, Haiss F, Eicke D, Radde R, Mathis CA, Klunk WE, et al. Dynamics of the Microglial/Amyloid Interaction Indicate a Role in Plaque Maintenance. J Neurosci. 2008 Apr 16;28(16):4283–92.

50. Goedert M, Jakes R. Expression of separate isoforms of human tau protein: correlation with the tau pattern in brain and effects on tubulin polymerization. The EMBO Journal. 1990 Dec;9(13):4225–30.

51. Buée L, Bussière T, Buée-Scherrer V, Delacourte A, Hof PR. Tau protein isoforms, phosphorylation and role in neurodegenerative disorders. 2000; Available from: https://www.sciencedirect.com/science/article/abs/pii/S0165017300000199?via%3Dihub

52. Hefti MM, Farrell K, Kim S, Bowles KR, Fowkes ME, Raj T, et al. High-resolution temporal and regional mapping of MAPT expression and splicing in human brain development. Buratti E, editor. PLoS ONE. 2018 Apr 10;13(4):e0195771.

53. Goedert M, Wischik CM, Crowther RA, Walker JE, Klug A. Cloning and sequencing of the cDNA encoding a core protein of the paired helical filament of Alzheimer disease: identification as the microtubule-associated protein tau. Proc Natl Acad Sci USA. 1988 Jun;85(11):4051–5.

54. Lee VMY, Goedert M, Trojanowski JQ. Neurodegenerative Tauopathies. 2001; Available from: https://www.annualreviews.org/doi/pdf/10.1146/annurev.neuro.24.1.1121#article-denial

55. Pirscoveanu. Tau protein in neurodegenerative diseases – a review.

56. Köpke E, Tung YC, Shaikh S, Alonso AC, Iqbal K, Grundke-Iqbal I. Microtubule-associated protein tau. Abnormal phosphorylation of a non-paired helical filament pool in Alzheimer disease. Journal of Biological Chemistry. 1993 Nov;268(32):24374–84.

57. Yuan A, Kumar A, Peterhoff C, Duff K, Nixon RA. Axonal Transport Rates *In Vivo* Are Unaffected by Tau Deletion or Overexpression in Mice. J Neurosci. 2008 Feb 13;28(7):1682–7.

58. Gotz J, Probst A, Spillantini MG, Schäfer T, Jakes R, Bürki K, et al. Somatodendritic localization and hyperphosphorylation of tau protein in transgenic mice expressing the longest human brain tau isoform. The EMBO Journal. 1995 Apr;14(7):1304–13.

59. Cho jae H, Johnson GVW. Primed phosphorylation of tau at Thr231 by glycogen synthase kinase 3β (GSK3β) plays a critical role in regulating tau's ability to bind and stabilize microtubules. 2004; Available from: https://pubmed.ncbi.nlm.nih.gov/14690523/

60. Braak H, Braak E. Staging of alzheimer's disease-related neurofibrillary changes. 1995; Available from: https://www.sciencedirect.com/science/article/abs/pii/0197458095000216?via%3Dihub

61. Rudrabhatla. Direct evidence of phosphorylated neuronal intermediate filament proteins in neurofibrillary tangles (NFTs) - phosphoproteomics of Alzheimer's NFTs. 2011;

62. Braak H, Braak E. Braak, H., Braak, E., 1991. Neuropathological stageing of Alzheimer-related changes. Acta Neuropathol. (Berl.) 82, 239–259. 1991; Available from: https://doi.org/10.1007/BF00308809

63. DeVos SL, Miller RL, Schoch KM, Holmes BB, Kebodeaux CS, Wegener AJ, et al. Tau reduction prevents neuronal loss and reverses pathological tau deposition and seeding in mice with tauopathy. Sci Transl Med. 2017 Jan 25;9(374):eaag0481.

64. Grabowska-Pyrzewicz W, Want A, Leszek J, Wojda U. Antisense oligonucleotides for Alzheimer's disease therapy: from the mRNA to miRNA paradigm. eBioMedicine. 2021 Dec;74:103691.

65. Dickerson BC, Salat DH, Greve DN, Chua EF, Rand-Giovannetti E, Rentz DM, et al. Increased hippocampal activation in mild cognitive impairment compared to normal aging and AD. Neurology. 2005 Aug 9;65(3):404–11.

66. Busche. Critical role of soluble amyloid-β for early hippocampal hyperactivity in a mouse model of Alzheimer_s disease. 2012;

67. Ghatak S, Dolatabadi N, Trudler D, Zhang X, Wu Y, Mohata M, et al. Mechanisms of hyperexcitability in Alzheimer's disease hiPSC-derived neurons and cerebral organoids vs isogenic controls. eLife. 2019 Nov 29;8:e50333.

68. Palop JJ, Mucke L. Network abnormalities and interneuron dysfunction in Alzheimer disease. Nat Rev Neurosci. 2016 Dec;17(12):777–92.

69. Lam AD, Deck G, Goldman A, Eskandar EN, Noebels J, Cole AJ. Silent hippocampal seizures and spikes identified by foramen ovale electrodes in Alzheimer's disease. Nat Med. 2017 Jun;23(6):678–80.

70. Gotz, Ittner. Amyloid-β and tau — a toxic pas de deux in Alzheimer_s disease. 2011;

71. Busceti CL, Biagioni F, Riozzi B, Battaglia G, Storto M, Cinque C, et al. Enhanced Tau Phosphorylation in the Hippocampus of Mice Treated with 3,4-Methylenedioxymethamphetamine ("Ecstasy"). J Neurosci. 2008 Mar 19;28(12):3234–45.

72. Alves M, Kenny A, De Leo G, Beamer EH, Engel T. Tau Phosphorylation in a Mouse Model of Temporal Lobe Epilepsy. Front Aging Neurosci. 2019 Nov 12;11:308.

73. Angulo E, Noé V, Casado V, Mallol J, Gomez-Isla T. https://onlinelibrary.wiley.com/doi/epdf/10.1111/j.1471-4159.2004.02771.x. 2004; Available from: https://onlinelibrary.wiley.com/doi/epdf/10.1111/j.1471-4159.2004.02771.x

74. Ciccone. Amyloid β-Induced Upregulation of Nav1.6 Underlies Neuronal Hyperactivity in Tg2576 Alzheimer's Disease Mouse Model. 2019;

75. Vitvitsky VM, Garg SK, Keep RF, Albin RL, Banerjee R. Na+ and K+ ion imbalances in Alzheimer's disease. Biochimica et Biophysica Acta (BBA) - Molecular Basis of Disease. 2012 Nov;1822(11):1671–81.

76. Terry RD, Masliah E, Salmon DP, Butters N, DeTeresa R. Physical basis of cognitive alterations in alzheimer's disease: Synapse loss is the major correlate of cognitive impairment. 1991; Available from: https://onlinelibrary.wiley.com/doi/abs/10.1002/ana.410300410

77. Lansbury PT. Evolution of amyloid: What normal protein folding may tell us about fibrillogenesis and disease. Proc Natl Acad Sci USA. 1999 Mar 30;96(7):3342–4.

78. Roberts G, Gentleman S, Lynch A, Graham DI. beta A4 amyloid protein deposition in brain after head trauma. 1991; Available from: https://pubmed.ncbi.nlm.nih.gov/1683421/

79. Scheff S, Price D, Schmitt F, DeKosky ST, Mufson E. Synaptic alterations in CA1 in mild Alzheimer disease and mild cognitive impairment. 2007; Available from: https://pubmed.ncbi.nlm.nih.gov/17470753/

80. the Synaptic Health Endpoints Working Group, Colom-Cadena M, Spires-Jones T, Zetterberg H, Blennow K, Caggiano A, et al. The clinical promise of biomarkers of synapse damage or loss in Alzheimer's disease. Alz Res Therapy. 2020 Dec;12(1):21.

81. Masliah E, Mallory M, Hansen L, Alford M, Albright T. Patterns of aberrant sprouting in alzheimer's disease. 1991; Available from: https://www.sciencedirect.com/science/article/abs/pii/0896627391901705

82. Head E, Corrada MM, Kahle-Wrobleski K, Kim RC, Sarsoza F, Goodus M, et al. Synaptic proteins, neuropathology and cognitive status in the oldest-old. Neurobiology of Aging. 2009 Jul;30(7):1125–34.

83. Dejanovic B, Huntley MA, De Mazière A, Meilandt WJ, Wu T, Srinivasan K, et al. Changes in the Synaptic Proteome in Tauopathy and Rescue of Tau-Induced Synapse Loss by C1q Antibodies. Neuron. 2018 Dec;100(6):1322-1336.e7.

84. Selkoe. Alzheimer's disease is a synaptic failure. 2002; Available from: https://pubmed.ncbi.nlm.nih.gov/12399581/

85. Venkitaramani DV, Chin J, Netzer WJ, Gouras GK, Lesne S, Malinow R, et al. β-Amyloid Modulation of Synaptic Transmission and Plasticity. J Neurosci. 2007 Oct 31;27(44):11832–7.

86. Brody AH, Strittmatter SM. Synaptotoxic Signaling by Amyloid Beta Oligomers in Alzheimer's Disease Through Prion Protein and mGluR5. In: Advances in Pharmacology [Internet]. Elsevier; 2018 [cited 2023 Sep 1]. p. 293–323. Available from: https://linkinghub.elsevier.com/retrieve/pii/S1054358917300856

87. Um JW, Nygaard HB, Heiss JK, Kostylev MA, Stagi M, Vortmeyer A, et al. Alzheimer amyloid-β oligomer bound to postsynaptic prion protein activates Fyn to impair neurons. Nat Neurosci. 2012 Sep;15(9):1227–35.

88. Mroczko B, Groblewska M, Litman-Zawadzka A, Kornhuber J, LewCzuk P. Cellular Receptors of Amyloid β Oligomers (AβOs) in Alzheimer's Disease. 2018;

89. Taniguchi K, Yamamoto F, Amano A, Tamaoka A, Sanjo N. Amyloid-β oligomers interact with NMDA receptors containing GluN2B subunits and metabotropic glutamate receptor 1 in primary cortical neurons: Relevance to the synapse pathology of Alzheimer's disease. 2022; Available from: https://www.sciencedirect.com/science/article/abs/pii/S0168010222000761

90. Tracy TE, Gan L. Tau-mediated synaptic and neuronal dysfunction in neurodegenerative disease. Current Opinion in Neurobiology. 2018 Aug;51:134–8.

91. Coomans EM, Schoonhoven DN, Tuncel H, Verfaillie SCJ, Wolters EE, Boellaard R, et al. In vivo tau pathology is associated with synaptic loss and altered synaptic function. Alz Res Therapy. 2021 Dec;13(1):35.

92. Appelbaum LG, Shenasa MA, Stolz L, Daskalakis Z. Synaptic plasticity and mental health: methods, challenges and opportunities. Neuropsychopharmacol. 2023 Jan;48(1):113–20.

93. Feldman DE. The Spike-Timing Dependence of Plasticity. Neuron. 2012 Aug;75(4):556–71.

94. Andrade-Talavera Y, Rodríguez-Moreno A. Synaptic Plasticity and Oscillations in Alzheimer's Disease: A Complex Picture of a Multifaceted Disease. Front Mol Neurosci. 2021 Jun 17;14:696476.

95. Di Lorenzo F, Ponzo V, Motta C, Bonni S, Picazio S. Impaired Spike Timing Dependent Cortico-Cortical Plasticity in Alzheimer's Disease Patients. 2018; Available from: https://pubmed.ncbi.nlm.nih.gov/30372679/

96. Fauth M, Tetzlaff C. Opposing Effects of Neuronal Activity on Structural Plasticity. Front Neuroanat [Internet]. 2016 Jun 28 [cited 2023 Sep 1];10. Available from: http://journal.frontiersin.org/Article/10.3389/fnana.2016.00075/abstract

97. Badimon A, Strasburger HJ, Ayata P, Chen X, Nair A, Ikegami A, et al. Negative feedback control of neuronal activity by microglia. Nature. 2020 Oct 15;586(7829):417–23.

98. Alzheimer's Disease International Organization. Available from: https://www.alzint.org/

99. Brodaty H, Breteler MM, DeKosky ST, Dorenlot P, Fratiglioni L. The world of dementia beyond 2020. 2011; Available from: https://pubmed.ncbi.nlm.nih.gov/21488846/

100. Harvey RJ, Skelton-Robinson M, Rossor MN. The prevalence and causes of dementia in people under the age of 65 years. Journal of Neurology, Neurosurgery & Psychiatry. 2003 Sep 1;74(9):1206–9.

101. Hall AM, Roberson ED. Mouse models of Alzheimer's disease. Brain Research Bulletin. 2012 May;88(1):3–12.

102. Oakley H, Cole SL, Logan S, Maus E, Shao P, Craft J, et al. Intraneuronal β-Amyloid Aggregates, Neurodegeneration, and Neuron Loss in Transgenic Mice with Five Familial Alzheimer's Disease Mutations: Potential Factors in Amyloid Plaque Formation. J Neurosci. 2006 Oct 4;26(40):10129–40.

103. GERAD consortium, Chapuis J, Hansmannel F, Gistelinck M, Mounier A, Van Cauwenberghe C, et al. Increased expression of BIN1 mediates Alzheimer genetic risk by modulating tau pathology. Mol Psychiatry. 2013 Nov;18(11):1225–34.

104. Alexander AG, Marfil V, Li C. Use of Caenorhabditis elegans as a model to study Alzheimerâ€™s disease and other neurodegenerative diseases. Front Genet [Internet]. 2014 Sep 5 [cited 2023 Aug 20];5. Available from: http://journal.frontiersin.org/article/10.3389/fgene.2014.00279/abstract

105. Dourlen P, Fernandez-Gomez FJ, Dupont C, Grenier-Boley B, Bellenguez C, Obriot H, et al. Functional screening of Alzheimer risk loci identifies PTK2B as an in vivo modulator and early marker of Tau pathology. Mol Psychiatry. 2017 Jun;22(6):874–83.

106. Israel MA, Yuan SH, Bardy C, Reyna SM, Mu Y, Herrera C, et al. Probing sporadic and familial Alzheimer's disease using induced pluripotent stem cells. Nature. 2012 Feb;482(7384):216–20.

107. Hou Y, Dan X, Babbar M, Wei Y, Hasselbalch SG, Croteau DL, et al. Ageing as a risk factor for neurodegenerative disease. Nat Rev Neurol. 2019 Oct;15(10):565–81.

108. Schmidt R, Launer LJ, Nilsson LG, Pajak A, Sans S, Berger K, et al. Magnetic Resonance Imaging of the Brain in Diabetes. Diabetes. 2004 Mar 1;53(3):687–92.

109. De Bruijn RF, Ikram MA. Cardiovascular risk factors and future risk of Alzheimer's disease. BMC Med. 2014 Dec;12(1):130.

110. Hardy JA, Higging GA. Alzheimer's disease: the amyloid cascade hypothesis. 1992; Available from: https://pubmed.ncbi.nlm.nih.gov/1566067/

111. Hardy, Selkoe. The amyloid hypothesis of Alzheimer's disease: progress and problems on the road to therapeutics. 2002; Available from: https://pubmed.ncbi.nlm.nih.gov/12130773/

112. Karran E, Mercken M, De Stooper B. The amyloid cascade hypothesis for Alzheimer's disease: an appraisal for the development of therapeutics. 2011; Available from: https://pubmed.ncbi.nlm.nih.gov/21852788/

113. Price JL, Morris JC. Tangles and plaques in nondemented aging and "preclinical" Alzheimer's disease. 1999; Available from: https://pubmed.ncbi.nlm.nih.gov/10072051/

114. Rodrigue KM, Kennedy KM, Park DC. Beta-Amyloid Deposition and the Aging Brain. Neuropsychol Rev. 2009 Dec;19(4):436–50.

115. Duran-Aniotz C, Morales R, Moreno-Gonzalez I, Hu PP, Soto C. Brains from non-Alzheimer's individuals containing amyloid deposits accelerate Aβ deposition in vivo. acta neuropathol commun. 2013 Dec;1(1):76.

116. Lambert JC, Ramirez A, Grenier-Boley B, Bellenguez C. Step by step: towards a better understanding of the genetic architecture of Alzheimer's disease. Mol Psychiatry [Internet]. 2023 May 2 [cited 2023 Aug 20]; Available from: https://www.nature.com/articles/s41380-023-02076-1

117. De Strooper B, Karran E. The Cellular Phase of Alzheimer's Disease. Cell. 2016 Feb;164(4):603–15.

118. Dourlen P, Kilinc D, Malmanche N, Chapuis J, Lambert JC. The new genetic landscape of Alzheimer's disease: from amyloid cascade to genetically driven synaptic failure hypothesis? Acta Neuropathol. 2019 Aug;138(2):221–36.

119. Celone KA, Calhoun VD, Dickerson BC, Atri A, Chua EF, Miller SL, et al. Alterations in Memory Networks in Mild Cognitive Impairment and Alzheimer's Disease: An Independent Component Analysis. J Neurosci. 2006 Oct 4;26(40):10222–31.

120. Palop JJ, Chin J, Roberson ED, Wang J, Thwin MT, Bien-Ly N, et al. Aberrant Excitatory Neuronal Activity and Compensatory Remodeling of Inhibitory Hippocampal Circuits in Mouse Models of Alzheimer's Disease. Neuron. 2007 Sep;55(5):697–711.

121. Vossel KA, Beagle AJ, Rabinovici GD, Shu H, Lee SE, Naasan G, et al. Seizures and Epileptiform Activity in the Early Stages of Alzheimer Disease. JAMA Neurol. 2013 Sep 1;70(9):1158.

122. Wang R, Reddy PH. Role of Glutamate and NMDA Receptors in Alzheimer's Disease. JAD. 2017 Apr 19;57(4):1041–8.

123. Huang Y ru, Xie X xiu, Yang J, Sun X ying, Niu X yun, Yang C gang, et al. ArhGAP11A mediates amyloid-β generation and neuropathology in an Alzheimer's disease-like mouse model. Cell Reports. 2023 Jun;42(6):112624.

124. Hindorff LA, Sethupathy P, Junkins HA, Ramos EM, Mehta JP, Collins FS, et al. Potential etiologic and functional implications of genome-wide association loci for human diseases and traits. Proc Natl Acad Sci USA. 2009 Jun 9;106(23):9362–7.

125. Yang J, Benyamin B, McEvoy BP, Gordon S, Henders AK, Nyholt DR, et al. Common SNPs explain a large proportion of the heritability for human height. Nat Genet. 2010 Jul;42(7):565–9.

126. European Alzheimer's Disease Initiative (EADI), Genetic and Environmental Risk in Alzheimer's Disease (GERAD), Alzheimer's Disease Genetic Consortium (ADGC), Cohorts for Heart and Aging Research in Genomic Epidemiology (CHARGE), Lambert JC, Ibrahim-Verbaas CA, et al. Meta-analysis of 74,046 individuals identifies 11 new susceptibility loci for Alzheimer's disease. Nat Genet. 2013 Dec;45(12):1452–8.

127. Bellenguez C, Küçükali F, Jansen IE, Kleineidam L, Moreno-Grau S. New insights into the genetic etiology of Alzheimer's disease and related dementias. Nature Genetics. 2022;54.

128. Alzheimer Disease Genetics Consortium (ADGC), The European Alzheimer's Disease Initiative (EADI), Cohorts for Heart and Aging Research in Genomic Epidemiology Consortium (CHARGE), Genetic and Environmental Risk in AD/Defining Genetic, Polygenic and Environmental Risk for Alzheimer's Disease Consortium (GERAD/PERADES), Kunkle BW, Grenier-Boley B, et al. Genetic meta-analysis of diagnosed Alzheimer's disease identifies new risk loci and implicates Aβ, tau, immunity and lipid processing. Nat Genet. 2019 Mar;51(3):414–30.

129. Harold D, Abraham R, Hollingworth P, Sims R, Gerrish A, Hamshere ML, et al. Genome-wide association study identifies variants at CLU and PICALM associated with Alzheimer's disease. Nat Genet. 2009 Oct;41(10):1088–93.

130. Naj AC, Jun G, Beecham GW, Wang LS, Vardarajan BN, Buros J, et al. Common variants at MS4A4/MS4A6E, CD2AP, CD33 and EPHA1 are associated with late-onset Alzheimer's disease. Nat Genet. 2011 May;43(5):436–41.

131. Marques-Coelho D, Iohan LDCC, Melo De Farias AR, Flaig A, The Brainbank Neuro–CEB Neuropathology Network, Letournel F, et al. Differential transcript usage unravels gene expression alterations in Alzheimer's disease human brains. npj Aging Mech Dis. 2021 Jan 4;7(1):2.

132. Butler MH, David C, Ochoa GC, Freyberg Z, Daniell L, Grabs D, et al. Amphiphysin II (SH3P9; BIN1), a Member of the Amphiphysin/Rvs Family, Is Concentrated in the Cortical Cytomatrix of Axon Initial Segments and Nodes of Ranvier in Brain and around T Tubules in Skeletal Muscle. The Journal of Cell Biology. 1997 Jun 16;137(6):1355–67.

133. Taga M, Petyuk VA, White C, Marsh G, Ma Y, Klein HU, et al. BIN1 protein isoforms are differentially expressed in astrocytes, neurons, and microglia: neuronal and astrocyte BIN1 are implicated in tau pathology. Mol Neurodegeneration. 2020 Dec;15(1):44.

134. Zhou Y, Hayashi I, Wong J, Tugusheva K, Renger JJ, Zerbinatti C. Intracellular Clusterin Interacts with Brain Isoforms of the Bridging Integrator 1 and with the Microtubule-Associated Protein Tau in Alzheimer's Disease. Götz J, editor. PLoS ONE. 2014 Jul 22;9(7):e103187.

135. Sudwarts A, Ramesha S, Gao T, Ponnusamy M, Wang S, Hansen M, et al. BIN1 is a key regulator of proinflammatory and neurodegeneration-related activation in microglia. Mol Neurodegeneration. 2022 May 7;17(1):33.

136. Voskobiynyk Y, Roth JR, Cochran JN, Rush T, Carullo NV, Mesina JS, et al. Alzheimer's disease risk gene BIN1 induces Tau-dependent network hyperexcitability. eLife. 2020 Jul 13;9:e57354.

137. Padhy B, Hayat B, Nanda GG, Mohanty PP, Alone DP. Pseudoexfoliation and Alzheimer's associated CLU risk variant, rs2279590, lies within an enhancer element and regulates CLU, EPHX2 and PTK2B gene expression. Human Molecular Genetics. 2017 Nov 15;26(22):4519–29.

138. Li YQ, Tan MS, Wang HF, Tan CC, Zhang W. Common variant in PTK2B is associated with late-onset Alzheimer's disease: A replication study and meta-analyses. 2016; Available from: https://www.sciencedirect.com/science/article/abs/pii/S0304394016302257?via%3Dihub

139. Schwartzentruber J, Cooper S, Liu JZ, Barrio-Hernandez I, Bello E, Kumasaka N, et al. Genome-wide meta-analysis, fine-mapping and integrative prioritization implicate new Alzheimer's disease risk genes. Nat Genet. 2021 Mar;53(3):392–402.

140. Harwood JC, Leonenko G, Sims R, Escott-Price V, Williams J, Holmans P. Defining functional variants associated with Alzheimer's disease in the induced immune response. Brain Communications. 2021 Apr 5;3(2):fcab083.

141. Zhu X, Bao Y, Guo Y, Yang W. Proline-Rich Protein Tyrosine Kinase 2 in Inflammation and Cancer. Cancers. 2018 May 8;10(5):139.

142. Naser R, Aldehaiman A, Díaz-Galicia E, Arold S. Endogenous Control Mechanisms of FAK and PYK2 and Their Relevance to Cancer Development. Cancers. 2018 Jun 11;10(6):196.

143. Momin AA, Mendes T, Barthe P, Faure C, Hong S, Yu P, et al. PYK2 senses calcium through a disordered dimerization and calmodulin-binding element. Commun Biol. 2022 Aug 9;5(1):800.

144. Bennett DA, Schneider JA, Arvanitakis Z, Kelly JF, Aggarwal NT. Neuropathology of older persons without cognitive impairment from two community-based studies. 2006; Available from: https://n.neurology.org/content/66/12/1837

145. Kilinc D, Vreulx AC, Mendes T, Flaig A, Marques-Coelho D, Verschoore M, et al. Pyk2 overexpression in postsynaptic neurons blocks amyloid β1–42-induced synaptotoxicity in microfluidic co-cultures. Brain Communications. 2020 Jul 1;2(2):fcaa139.

146. Dikic I, Dikic I, Schlessinger J. Identification of a New Pyk2 Isoform Implicated in Chemokine and Antigen Receptor Signaling. Journal of Biological Chemistry. 1998 Jun;273(23):14301–8.

147. Xiong WC, Macklem M, Parsons JT. Expression and characterization of splice variants of PYK2, a focal adhesion kinase-related protein. Journal of Cell Science. 1998 Jul 30;111(14):1981–91.

148. Avraham S, London R, Fu Y, Ota S, Hiregowdara D, Li J, et al. Identification and Characterization of a Novel Related Adhesion Focal Tyrosine Kinase (RAFTK) from Megakaryocytes and Brain. Journal of Biological Chemistry. 1995 Nov;270(46):27742–51.

149. Sasaki H, Nagura K, Ishino M, Tobioka H, Kotani K, Sasaki T. Cloning and Characterization of Cell Adhesion Kinase β, a Novel Protein-tyrosine Kinase of the Focal Adhesion Kinase Subfamily. Journal of Biological Chemistry. 1995 Sep;270(36):21206–19.

150. Menegon A, Burgaya F, Baudot P, Dunlap DD, Girault JA. FAK+ and PYK2/CAKβ, two related tyrosine kinases highly expressed in the central nervous system: similarities and differences in the expression pattern. 1999; Available from: https://onlinelibrary.wiley.com/doi/abs/10.1046/j.1460-9568.1999.00798.x

151. Huang YQ, Lu WY, Ali DW, Pelkey KA, Pitcher GM, Lu YM, et al. CAK␤/Pyk2 Kinase Is a Signaling Link for Induction of Long-Term Potentiation in CA1 Hippocampus. 2001;

152. Giralt A, Brito V, Chevy Q, Simonnet C, Otsu Y, Cifuentes-Díaz C, et al. Pyk2 modulates hippocampal excitatory synapses and contributes to cognitive deficits in a Huntington's disease model. Nat Commun. 2017 May 30;8(1):15592.

153. Salazar SV, Cox TO, Lee S, Brody AH, Chyung AS, Haas LT, et al. Alzheimer's Disease Risk Factor Pyk2 Mediates Amyloid-β-Induced Synaptic Dysfunction and Loss. J Neurosci. 2019 Jan 23;39(4):758–72.

154. Sheehan TP, Neve RL, Duman RS, Russell DS. Antidepressant effect of the calcium-activated tyrosine kinase Pyk2 in the lateral septum. 2003; Available from: https://www.biologicalpsychiatryjournal.com/article/S0006-3223(02)01815-2/fulltext

155. Montalban E, Al-Massadi O, Sancho-Balsells A, Brito V, De Pins B, Alberch J, et al. Pyk2 in the amygdala modulates chronic stress sequelae via PSD-95-related micro-structural changes. Transl Psychiatry. 2019 Jan 15;9(1):3.

156. Giralt A, Coura R, Giralut JA. Pyk2 is essential for astrocytes mobility following brain lesion. 2015; Available from: https://pubmed.ncbi.nlm.nih.gov/26663135/

157. Combs CK, Johnson DE, Cannady SB, Lehman TM, Landreth GE. Identification of Microglial Signal Transduction Pathways Mediating a Neurotoxic Response to Amyloidogenic Fragments of ℕ-Amyloid and Prion Proteins. 1999;

158. Tian D, Litvak V, Lev S. Cerebral Ischemia and Seizures Induce Tyrosine Phosphorylation of PYK2 in Neurons and Microglial Cells. J Neurosci. 2000 Sep 1;20(17):6478–87.

159. Lev S, Moreno H, Martinez R, Canoll P, Peles E, Musacchio JM, et al. Protein tyrosine kinase PYK2 involved in Ca2+-induced regulation of ion channel and MAP kinase functions. Nature. 1995 Aug;376(6543):737–45.

160. Hayashi I, Vuori K, Liddington RC. The focal adhesion targeting (FAT) region of focal adhesion kinase is a four-helix bundle that binds paxillin. 2002; Available from: https://pubmed.ncbi.nlm.nih.gov/11799401/

161. Arold ST, Hoellerer MK, Noble MEM. The Structural Basis of Localization and Signaling by the Focal Adhesion Targeting Domain. Structure. 2002 Mar;10(3):319–27.

162. Ceccarelli DFJ, Song HK, Poy F, Schaller MD, Eck MJ. Crystal Structure of the FERM Domain of Focal Adhesion Kinase. Journal of Biological Chemistry. 2006 Jan;281(1):252–9.

163. Lakkakorpi PT, Bett AJ, Lipfert L, Rodan GA, Duong LT. PYK2 Autophosphorylation, but Not Kinase Activity, Is Necessary for Adhesion-induced Association with c-Src, Osteoclast Spreading, and Bone Resorption. Journal of Biological Chemistry. 2003 Mar;278(13):11502–12.

164. Zhao M, Finlay D, Zharkikh I, Vuori K. Novel Role of Src in Priming Pyk2 Phosphorylation. Buday L, editor. PLoS ONE. 2016 Feb 11;11(2):e0149231.

165. Blaukat A, Ivankovic-Dikic I, Grönroos E, Dolfi F, Tokiwa G, Vuori K, et al. Adaptor Proteins Grb2 and Crk Couple Pyk2 with Activation of Specific Mitogen-activated Protein Kinase Cascades. Journal of Biological Chemistry. 1999 May;274(21):14893–901.

166. Li X, Dy RC, Cance WG, Graves LM, Earp HS. Interactions between Two Cytoskeleton-associated Tyrosine Kinases: Calcium-dependent Tyrosine Kinase and Focal Adhesion Tyrosine Kinase. Journal of Biological Chemistry. 1999 Mar;274(13):8917–24.

167. Faure C, Ramos M, Girault JA. Pyk2 cytonuclear localization: mechanisms and regulation by serine dephosphorylation. Cell Mol Life Sci. 2013 Jan;70(1):137–52.

168. Corsi JM, Rouer E, Girault JA, Enslen H. Organization and post-transcriptional processing of focal adhesion kinase gene. BMC Genomics. 2006 Dec;7(1):198.

169. Fan Y, Qu X, Ma Y, Qu J, Liu Y. Cbl-b accelerates trypsin-induced cell detachment through ubiquitination and degradation of proline-rich tyrosine kinase 2. 2014; Available from: https://link.springer.com/article/10.1007/s13277-014-2296-z

170. Verma N, Müller AK, Kothari C, Panayotopoulou E, Kedan A. Targeting of PYK2 Synergizes with EGFR Antagonists in Basal-like TNBC and Circumvents HER3-Associated Resistance via the NEDD4-NDRG1 Axis. 2016; Available from: https://pubmed.ncbi.nlm.nih.gov/27793840/

171. Kadaré G, Toutant M, Formstecher E, Corvol JC, Carnaud M, Boutterin MC, et al. PIAS1-mediated Sumoylation of Focal Adhesion Kinase Activates Its Autophosphorylationn. Journal of Biological Chemistry. 2003 Nov;278(48):47434–40.

172. Faure C, Corvol JC, Toutant M, Valjent E, Hvalby Ø, Jensen V, et al. Calcineurin is essential for depolarization-induced nuclear translocation and tyrosine phosphorylation of PYK2 in neurons. Journal of Cell Science. 2007 Sep 1;120(17):3034–44.

173. De Pins B, Mendes T, Giralt A, Girault JA. The Non-receptor Tyrosine Kinase Pyk2 in Brain Function and Neurological and Psychiatric Diseases. Front Synaptic Neurosci. 2021 Oct 6;13:749001.

174. Meng XQ, Zheng KG, Yang Y, Jiang MX, Zhang YL, Sun QY, et al. Proline-rich tyrosine kinase2 is involved in F-actin organization during in vitro maturation of rat oocyte. Reproduction. 2006 Dec;132(6):859–67.

175. Aoto H, Sasaki H, Ishino M, Sasaki T. Nuclear Translocation of Cell Adhesion Kinase β/Proline-rich Tyrosine Kinase 2.

176. Kohno T, Matsuda E, Sasaki H, Sasaki T. Protein-tyrosine kinase CAKβ/PYK2 is activated by binding Ca2+/calmodulin to FERM F2 α2 helix and thus forming its dimer. 2008; Available from: https://portlandpress.com/biochemj/article-abstract/410/3/513/43534/Protein-tyrosine-kinase-CAK-PYK2-is-activated-by?redirectedFrom=fulltext

177. Schindler EM, Baumgartner M, Gribben EM, Li L, Efimova T. The Role of Proline-Rich Protein Tyrosine Kinase 2 in Differentiation-Dependent Signaling in Human Epidermal Keratinocytes. Journal of Investigative Dermatology. 2007 May;127(5):1094–106.

178. Lim ST, Miller NLG, Nam JO, Chen XL, Lim Y, Schlaepfer DD. Pyk2 Inhibition of p53 as an Adaptive and Intrinsic Mechanism Facilitating Cell Proliferation and Survival. Journal of Biological Chemistry. 2010 Jan;285(3):1743–53.

179. Hum JM, Day RN, Bidwell JP, Wang Y, Pavalko FM. Mechanical Loading in Osteocytes Induces Formation of a Src/Pyk2/MBD2 Complex That Suppresses Anabolic Gene Expression. Leipzig ND, editor. PLoS ONE. 2014 May 19;9(5):e97942.

180. Bartos JA, Ulrich JD, Li H, Beazely MA, Chen Y, MacDonald JF, et al. Postsynaptic Clustering and Activation of Pyk2 by PSD-95. J Neurosci. 2010 Jan 13;30(2):449–63.

181. Rico B, Beggs HE, Schahin-Reed D, Kimes N, Schmidt A, Reichardt LF. Control of axonal branching and synapse formation by focal adhesion kinase. Nat Neurosci. 2004 Oct;7(10):1059–69.

182. Cooper LA, Shen TL, Guan JL. Regulation of Focal Adhesion Kinase by Its Amino-Terminal Domain through an Autoinhibitory Interaction. Molecular and Cellular Biology. 2003 Nov 1;23(22):8030–41.

183. Lietha D, Cai X, Ceccarelli DFJ, Li Y, Schaller MD, Eck MJ. Structural Basis for the Autoinhibition of Focal Adhesion Kinase. Cell. 2007 Jun;129(6):1177–87.

184. Loving HS, Underbakke ES. Conformational Dynamics of FERM-Mediated Autoinhibition in Pyk2 Tyrosine Kinase. 2019; Available from: https://pubmed.ncbi.nlm.nih.gov/31403288/

185. Park SY, Avraham HK, Avraham S. RAFTK/Pyk2 Activation Is Mediated by Trans-acting Autophosphorylation in a Src-independent Manner. Journal of Biological Chemistry. 2004 Aug;279(32):33315–22.

186. Brami-Cherrier K, Gervasi N, Arsenieva D, Walkiewicz K, Boutterin MC, Ortega A, et al. FAK dimerization controls its kinase-dependent functions at focal adhesions. The EMBO Journal. 2014 Feb 18;33(4):356–70.

187. Goñi GM, Epifano C, Boskovic J, Camacho-Artacho M, Zhou J, Bronowska A, et al. Phosphatidylinositol 4,5-bisphosphate triggers activation of focal adhesion kinase by inducing clustering and conformational changes. Proc Natl Acad Sci USA [Internet]. 2014 Aug 5 [cited 2023 Sep 1];111(31). Available from: https://pnas.org/doi/full/10.1073/pnas.1317022111

188. Xie YF, Belrose JC, Lei G, Tymianski M, Mori Y, MacDonald JF, et al. Dependence of NMDA/GSK-3b Mediated Metaplasticity on TRPM2 Channels at Hippocampal CA3-CA1 Synapses. 2011;

189. Seabold GK, Burette A, Lim IA, Weinberg RJ, Hell JW. Interaction of the Tyrosine Kinase Pyk2 with the N-Methyl-d-aspartate Receptor Complex via the Src Homology 3 Domains of PSD-95 and SAP102. Journal of Biological Chemistry. 2003 Apr;278(17):15040–8.

190. Zhang WB, Ross PJ, Tu Y, Wang Y, Beggs S, Sengar AS, et al. Fyn Kinase regulates GluN2B subunit-dominant NMDA receptors in human induced pluripotent stem cell-derived neurons. Sci Rep. 2016 Apr 4;6(1):23837.

191. Siciliano J, Gelman M, Girault JA. Depolarization and neurotransmitters increase neuronal protein tyrosine phosphorylation. 1994; Available from: https://pubmed.ncbi.nlm.nih.gov/7509378/

192. Arold ST, Ulmer TS, Mulhern TD, Werner JM, Ladbury JE, Campbell ID, et al. The Role of the Src Homology 3-Src Homology 2 Interface in the Regulation of Src Kinases. Journal of Biological Chemistry. 2001 May;276(20):17199–205.

193. Xu J, Chatterjee M, Baguley TD, Brouillette J, Kurup P, Ghosh D, et al. Inhibitor of the Tyrosine Phosphatase STEP Reverses Cognitive Deficits in a Mouse Model of Alzheimer's Disease. Khosla C, editor. PLoS Biol. 2014 Aug 5;12(8):e1001923.

194. Chatterjee M, Singh P, Xu J, Lombroso PJ, Kurup PK. Inhibition of striatal-enriched protein tyrosine phosphatase (STEP) activity reverses behavioral deficits in a rodent model of autism. Behavioural Brain Research. 2020 Aug;391:112713.

195. Lee S, Salazar SV, Cox TO, Strittmatter SM. Pyk2 Signaling through Graf1 and RhoA GTPase Is Required for Amyloid-β Oligomer-Triggered Synapse Loss. 2019;

196. Brukman NG, Nunez SY, Puga Molina LDC, Buffone MG, Darszon A. Tyrosine phosphorylation signaling regulates Ca2+ entry by affecting intracellular pH during human sperm capacitation. 2019; Available from: https://pubmed.ncbi.nlm.nih.gov/30203545/

197. Lysechko TL, Cheung SMS, Ostergaard HL. Regulation of the Tyrosine Kinase Pyk2 by Calcium Is through Production of Reactive Oxygen Species in Cytotoxic T Lymphocytes. Journal of Biological Chemistry. 2010 Oct;285(41):31174–84.

198. Li C, Götz J. Pyk2 is a Novel Tau Tyrosine Kinase that is Regulated by the Tyrosine Kinase Fyn. Reddy PH, editor. JAD. 2018 Jun 8;64(1):205–21.

199. Miyamoto T, Stein L, Thomas R, Djukic B, Taneja P, Knox J, et al. Phosphorylation of tau at Y18, but not tau-fyn binding, is required for tau to modulate NMDA receptor-dependent excitotoxicity in primary neuronal culture. Mol Neurodegeneration. 2017 Dec;12(1):41.

200. Brody AH, Nies SH, Guan F, Smith LM, Mukherjee B, Salazar SA, et al. Alzheimer risk gene product Pyk2 suppresses tau phosphorylation and phenotypic effects of tauopathy. Mol Neurodegeneration. 2022 May 3;17(1):32.

201. Hildebrand JD, Schaller MD, Parsons JT. Identification of sequences required for the efficient localization of the focal adhesion kinase, pp125FAK, to cellular focal adhesions. The Journal of cell biology. 1993 Nov 15;123(4):993–1005.

202. Zheng C, Xing Z, Bian ZC, Guo C, Akbay A, Warner L, et al. Differential Regulation of Pyk2 and Focal Adhesion Kinase (FAK). Journal of Biological Chemistry. 1998 Jan;273(4):2384–9.

203. Girault JA, Labesse G, Mornon JP, Callebaut I. Janus Kinases and Focal Adhesion Kinases Play in the 4.1 Band: A Superfamily of Band 4.1 Domains Important for Cell Structure and Signal Transduction. Mol Med. 1998 Dec;4(12):751–69.

204. Lipinski CA, Tran NL, Menashi E, Rohl C, Kloss J, Bay RC, et al. The Tyrosine Kinase Pyk2 Promotes Migration and Invasion of Glioma Cells. Neoplasia. 2005 May;7(5):435–45.

205. Schaller MD. Cellular functions of FAK kinases: insight into molecular mechanisms and novel functions. Journal of Cell Science. 2010 Apr 1;123(7):1007–13.

206. Felsch JS, Cachero TG, Peralta EG. Activation of protein tyrosine kinase PYK2 by the m1 muscarinic acetylcholine receptor. Proc Natl Acad Sci USA. 1998 Apr 28;95(9):5051–6.

207. Xiong Z gang, Pelkey KA, Lu WY, Lu YM, Roder JC, MacDonald JF, et al. Src Potentiation of NMDA Receptors in Hippocampal and Spinal Neurons Is Not Mediated by Reducing Zinc Inhibition. J Neurosci. 1999 Nov 1;19(21):RC37–RC37.

208. Salter MW, Kalia LV. Src kinases: a hub for NMDA receptor regulation. Available from: https://www.nature.com/articles/nrn1368

209. Hou XY, Zhang GY, Wang DG, Guan QH, Yan JZ. Suppression of postsynaptic density protein 95 by antisense oligonucleotides diminishes postischemic pyramidal cell death in rat hippocampal CA1 subfield. 2005; Available from: https://www.sciencedirect.com/science/article/abs/pii/S0304394005005847?via%3Dihub

210. Citri A, Malenka RC. Synaptic Plasticity: Multiple Forms, Functions, and Mechanisms. Neuropsychopharmacol. 2008 Jan;33(1):18–41.

211. Girault JA, Costa A, Derkinderen P, Studler JM, Toutant M. FAK and PYK2/CAKbeta in the nervous system: a link between neuronal activity, plasticity and survival? 1999; Available from: https://pubmed.ncbi.nlm.nih.gov/10354603/

212. Mastrolia V, Al Massadi O, De Pins B, Girault JA. Pyk2 in dorsal hippocampus plays a selective role in spatial memory and synaptic plasticity. Sci Rep. 2021 Aug 11;11(1):16357.

213. Ni B, Farrar JS, Chen S, Lownik JC, Celi FS. A novel role for PTK2B in cultured beige adipocyte differentiation. 2018; Available from: https://www.sciencedirect.com/science/article/abs/pii/S0006291X18310702

214. Li HY, Cui XY, Wu W, Yu FY, Yao HR. Pyk2 and Src mediate signaling to CCL18-induced breast cancer metastasis. 2004; Available from: https://pubmed.ncbi.nlm.nih.gov/24142406/

215. Xu CS, Wang ZF, Huang XD, Dai LM, Cao CJ, Li ZQ. Involvement of ROS-alpha v beta 3 integrin-FAK/Pyk2 in the inhibitory effect of melatonin on U251 glioma cell migration and invasion under hypoxia. J Transl Med. 2015 Dec;13(1):95.

216. Lee D, Hong JH. Activated PyK2 and Its Associated Molecules Transduce Cellular Signaling from the Cancerous Milieu for Cancer Metastasis. IJMS. 2022 Dec 7;23(24):15475.

217. Behmoaram E, Bijian K, Jie S, Xu Y, Darnel A, Bismar TA, et al. Focal Adhesion Kinase-Related Proline-Rich Tyrosine Kinase 2 and Focal Adhesion Kinase Are Co-Overexpressed in Early-Stage and Invasive ErbB-2-Positive Breast Cancer and Cooperate for Breast Cancer Cell Tumorigenesis and Invasiveness. The American Journal of Pathology. 2008 Nov;173(5):1540–50.

218. Giralt A, De Pins B, Cifuentes-Díaz C, López-Molina L, Farah AT, Tible M, et al. PTK2B/Pyk2 overexpression improves a mouse model of Alzheimer's disease. Experimental Neurology. 2018 Sep;307:62–73.

219. Yamamoto S, Shimizu S, Kiyonaka S, Takahashi N, Wajima T. TRPM2-mediated Ca2+ influx induces chemokine production in monocytes that aggravates inflammatory neutrophil infiltration. Available from: https://www.nature.com/articles/nm1758

220. Leissring MA, Murphy MP, Mead TR, Akbari Y, Sugarman MC, Jannatipour M, et al. ⁄-secretase-derived intracellular.

221. De Felice FG, Velasco PT, Lambert MP, Viola K, Fernandez SJ, Ferreira ST, et al. Aβ Oligomers Induce Neuronal Oxidative Stress through an N-Methyl-D-aspartate Receptor-dependent Mechanism That Is Blocked by the Alzheimer Drug Memantine. Journal of Biological Chemistry. 2007 Apr;282(15):11590–601.

222. Beecham GW, Hamilton K, Naj AC, Martin ER, Huentelman M, Myers AJ, et al. Genome-Wide Association Meta-analysis of Neuropathologic Features of Alzheimer's Disease and Related Dementias. Gibson G, editor. PLoS Genet. 2014 Sep 4;10(9):e1004606.

223. Wang X, Lopez OL, Sweet RA, Becker JT, DeKosky ST, Barmada MM, et al. Genetic Determinants of Disease Progression in Alzheimer's Disease. JAD. 2014 Nov 21;43(2):649–55.

224. Nettiksimmons J, Tranah G, Evans DS, Yokoyama JS, Yaffe K. Gene-based aggregate SNP associations between candidate AD genes and cognitive decline. AGE. 2016 Apr;38(2):41.

225. Chambers SM, Fasano CA, Papapetrou EP, Tomishima M, Sadelain M, Studer L. Highly efficient neural conversion of human ES and iPS cells by dual inhibition of SMAD signaling. Nat Biotechnol. 2009 Mar;27(3):275–80.

226. Bardy C, Van Den Hurk M, Eames T, Marchand C, Hernandez RV, Kellogg M, et al. Neuronal medium that supports basic synaptic functions and activity of human neurons in vitro. Proc Natl Acad Sci USA [Internet]. 2015 May 19 [cited 2023 Sep 1];112(20). Available from: https://pnas.org/doi/full/10.1073/pnas.1504393112

227. Lancaster MA, Knoblich JA. Generation of cerebral organoids from human pluripotent stem cells. Nat Protoc. 2014 Oct;9(10):2329–40.

228. Yang J, Zhao H, Ma Y, Shi G, Song J, Tang Y, et al. Early pathogenic event of Alzheimer's disease documented in iPSCs from patients with PSEN1 mutations. Oncotarget. 2017 Jan 31;8(5):7900–13.

229. Hao Y, Hao S, Andersen-Nissen E, Mauck WM, Zheng S, Butler A, et al. Integrated analysis of multimodal single-cell data. Cell. 2021 Jun;184(13):3573-3587.e29.

230. Korotkevich G, Sukhov V, Sergushichev A. Fast gene set enrichment analysis. 2019; Available from: https://www.biorxiv.org/content/10.1101/060012v2

231. Tyssowski KM, DeStefino NR, Cho JH, Dunn CJ, Poston RG, Carty CE, et al. Different Neuronal Activity Patterns Induce Different Gene Expression Programs. Neuron. 2018 May;98(3):530-546.e11.

232. Hrvatin S, Hochbaum DR, Nagy MA, Cicconet M, Robertson K, Cheadle L, et al. Single-cell analysis of experience-dependent transcriptomic states in the mouse visual cortex. Nat Neurosci. 2018 Jan;21(1):120–9.

233. Wagenaar DA, Pine J, Potter SM. An extremely rich repertoire of bursting patterns during the development of cortical cultures. BMC Neurosci. 2006 Dec;7(1):11.

234. Plumbly W, Brandon N, Deeb TZ, Hall J, Harwood AJ. L-type voltage-gated calcium channel regulation of in vitro human cortical neuronal networks. Sci Rep. 2019 Sep 25;9(1):13810.

235. Liang G, Zhang Y. Genetic and Epigenetic Variations in iPSCs: Potential Causes and Implications for Application. Cell Stem Cell. 2013 Aug;13(2):149–59.

236. Trujillo CA, Gao R, Negraes PD, Gu J, Buchanan J, Preissl S, et al. Complex Oscillatory Waves Emerging from Cortical Organoids Model Early Human Brain Network Development. Cell Stem Cell. 2019 Oct;25(4):558-569.e7.

237. Krishnankutty A, Kimura T, Saito T, Aoyagi K, Asada A. In vivo regulation of glycogen synthase kinase 3β activity in neurons and brains. 2017;

238. Irtegun S, Wood RJ, Ormsby AR, Mulhern TD, Hatters DM. Tyrosine 416 Is Phosphorylated in the Closed, Repressed Conformation of c-Src. Lewis P, editor. PLoS ONE. 2013 Jul 26;8(7):e71035.

239. Guise S, Braguer D, Carles G, Delacourte A, Briand C. Hyperphosphorylation of tau is mediated by ERK activation during anticancer drug-induced apoptosis in neuroblastoma cells. Available from: https://pubmed.ncbi.nlm.nih.gov/11170175/

240. Maphis N, Jiang S, Xu G, Kokiko-Cochran ON, Roy SM. Selective suppression of the α isoform of p38 MAPK rescues late-stage tau pathology. 2016;

241. Radstake FDW, Raaijmakers EAL, Luttge R, Zinger S, Frimat JP. CALIMA: The semi-automated open-source calcium imaging analyzer. Available from: https://www.sciencedirect.com/science/article/pii/S0169260718313701?via%3Dihub

242. Leng K, Li E, Eser R, Piergies A, Sit R, Tan M, et al. Molecular characterization of selectively vulnerable neurons in Alzheimer's disease. Nat Neurosci. 2021 Feb;24(2):276–87.

243. Zhang Y, Pak C, Han Y, Ahlenius H, Zhang Z, Chanda S, et al. Rapid Single-Step Induction of Functional Neurons from Human Pluripotent Stem Cells. Neuron. 2013 Jun;78(5):785–98.

244. Neddens J, Temmel M, Flunkert S, Kerschbaumer B, Hoeller C, Loeffler T, et al. Phosphorylation of different tau sites during progression of Alzheimer's disease. acta neuropathol commun. 2018 Dec;6(1):52.

245. Brown J, Camporesi E, Lantero-Rodriguez J, Olsson M, Wang A, Medem B, et al. Tau in cerebrospinal fluid induces neuronal hyperexcitability and alters hippocampal theta oscillations. acta neuropathol commun. 2023 Apr 24;11(1):67.

246. Williamson R, Scales T, Clark BR, Gibb G, Reynolds CH, Kellie S, et al. Rapid Tyrosine Phosphorylation of Neuronal Proteins Including Tau and Focal Adhesion Kinase in Response to Amyloid-β Peptide Exposure: Involvement of Src Family Protein Kinases. J Neurosci. 2002 Jan 1;22(1):10–20.

247. Esposito Z, Belli L, Toniolo S, Sancesario G, Bianconi C, Martorana A. Amyloid β, Glutamate, Excitotoxicity in Alzheimer's Disease: Are We on the Right Track? CNS Neurosci Ther. 2013 Aug;19(8):549–55.

248. Bukke VN, Archana M, Villani R, Romano AD, Wawrzyniak A, Balawender K, et al. The Dual Role of Glutamatergic Neurotransmission in Alzheimer's Disease: From Pathophysiology to Pharmacotherapy. IJMS. 2020 Oct 9;21(20):7452.

249. Gong CX, Liu F, Grundke-Iqbal I, Iqbal K. Post-translational modifications of tau protein in Alzheimer's disease. 2005; Available from: https://pubmed.ncbi.nlm.nih.gov/15517432/

250. Wakahara R, Kunimoto H, Tanino K, Kojima H, Inoue A, Shintaku H, et al. Phospho-Ser727 of STAT3 regulates STAT3 activity by enhancing dephosphorylation of phospho-Tyr705 largely through TC45: Role of phospho-Ser727 of STAT3. Genes to Cells. 2012 Feb;17(2):132–45.